Springer Series in
MATERIALS SCIENCE 55

Springer-Verlag Berlin Heidelberg GmbH

Physics and Astronomy ONLINE LIBRARY
http://www.springer.de/phys/

Springer Series in

MATERIALS SCIENCE

Editors: R. Hull R. M. Osgood, Jr. J. Parisi A. Zunger

The Springer Series in Materials Science covers the complete spectrum of materials physics, including fundamental principles, physical properties, materials theory and design. Recognizing the increasing importance of materials science in future device technologies, the book titles in this series reflect the state-of-the-art in understanding and controlling the structure and properties of all important classes of materials.

51 **Microscopic and Electronic Structure of Point Defects in Semiconductors and Insulators**
Determination and Interpretation of Paramagnetic Hyperfine Interaction
Editors: J. M. Spaeth and H. Overhof

52 **Polymer Films with Embedded Metal Nanoparticles**
By A. Heilmann

53 **Synthesis and Characterization of Nanocrystalline Ceramics**
By M. Winterer

54 **Electronic Structure and Magnetism of Complex Materials**
Editors: D.J. Singh and A. Dimitrios

55 **Quasicrystals**
An Introduction to Structure, Physical Properties and Applications
Editors: J.-B. Suck, M. Schreiber, P. Häussler

56 **SiO_2 in Si Microdevices**
By M. Itsumi

Series homepage – http://www.springer.de/phys/books/ssms/

Volumes 1–50 are listed at the end of the book.

J.-B. Suck M. Schreiber
P. Häussler (Eds.)

Quasicrystals

An Introduction to Structure, Physical Properties and Applications

With 270 Figures

Springer

Professor Jens-Boie Suck
TU Chemnitz, Institut für Physik, 09107 Chemnitz, Germany

Professor Michael Schreiber
International University Bremen, Postfach 75 05 61, 28725 Bremen, Germany

Professor Peter Häussler
TU Chemnitz, Institut für Physik, 09107 Chemnitz, Germany

Series Editors:

Professor Alex Zunger
NREL, National Renewable Energy Laboratory
1617 Cole Boulevard, Golden Colorado 80401-3393, USA

Professor R. M. Osgood, Jr.
Microelectronics Science Laboratory, Department of Electrical Engineering
Columbia University, Seeley W. Mudd Building, New York, NY 10027, USA

Professor Robert Hull
University of Virginia, Dept. of Materials Science and Engineering, Thornton Hall
Charlottesville, VA 22903-2442, USA

Professor Jürgen Parisi
Universität Oldenburg, Fachbereich Physik, Abt. Energie- und Halbleiterforschung
Carl-von-Ossietzky-Strasse 9-11, 26129 Oldenburg, Germany

ISSN 0933-033x

ISBN 978-3-642-08390-7 ISBN 978-3-662-05028-6 (eBook)
DOI 10.1007/978-3-662-05028-6

Library of Congress Cataloging-in-Publication Data.

Quasicrystals: an introduction to structure, physical properties, and applications/ J.-B. Suck, M. Schreiber, P. Häussler (eds.) p. cm. – (Springer series in materials science, ISSN 0933-033X; 55) Includes bibliographical references and index. 1. Quasicrystals. I. Suck, J.B. II. Schreiber, Michael, 1954– . III. Häussler, Peter. IV. Springer series in materials science; v. 55. QC173.4.Q36 Q32 2002 530.4'1–dc21 2002023604

This work is subject to copyright. All rights are reserved, whether the whole or part of the material is concerned, specifically the rights of translation, reprinting, reuse of illustrations, recitation, broadcasting, reproduction on microfilm or in any other way, and storage in data banks. Duplication of this publication or parts thereof is permitted only under the provisions of the German Copyright Law of September 9, 1965, in its current version, and permission for use must always be obtained from Springer-Verlag. Violations are liable for prosecution under the German Copyright Law.

http://www.springer.de

© Springer-Verlag Berlin Heidelberg 2002
Ursprünglich erschienen bei Springer-Verlag Berlin Heidelberg New York 2002.

Softcover reprint of the hardcover 1st edition 2002
The use of general descriptive names, registered names, trademarks, etc. in this publication does not imply, even in the absence of a specific statement, that such names are exempt from the relevant protective laws and regulations and therefore free for general use.

Typesetting: Camera-ready copy produced by the author using a Springer TeX macro package
Cover concept: eStudio Calamar Steinen
Cover production: *design & production* GmbH, Heidelberg

Printed on acid-free paper SPIN: 10980064 57/3111 5 4 3 2 1

Preface

Quasicrystals have been the object of intense research efforts for a good 16 years now. In recent years, this area of solid state physics and crystallography has grown into a mature field in its own right. Hence, several books on quasicrystals have appeared in the interim (see Appendix) and chapters on quasicrystals have been introduced into new books on solid state physics and into new editions of existing monographs. However, most[1] of the former have been written for scientists specialised in this field rather than for students, and the latter additions are often rather brief.

We therefore decided to fill the gap between these two extremes with a book which provides an *introduction to the structure and physical properties of quasicrystals* and covers, in sufficient detail, all important fields in quasicrystal research and even applications. The chapters have been written by specialists and each is based on the author's insight into this field. However, much effort has been put into achieving an introductory character and making the text accessible to newcomers to the field.

In recent years research on quasicrystals has made much progress. Thermodynamically stable quasicrystalline alloys have been discovered and monograins (single crystals) of these quasicrystals are now available. Likewise, computer simulations of quasicrystals – inherently difficult due to the complicated aperiodic atomic structure and the chemical composition, which have to be taken into account in these simulations – have also made much progress, thanks to more efficient computers, which allow us to calculate the physical properties of large and complicated structures, and with the generation of *ab initio* pair potentials, enabling realistic calculations to be performed. Thus, in contrast to most of the earlier books on quasicrystals, where – apart from structure determinations – theoretical approaches have been dominant, there are now so many investigations of the physical properties of quasicrystals and especially of quasicrystalline monograins, that we were able, in most cases, to contrast experimental and theoretical investigations of the same property of the quasicrystalline alloy, thus providing both points of view.

After a brief look at related research prior to the autumn of 1984, when Shechtman, Blech, Gratias and Cahn published their remarkable results, the subject is introduced by two articles on *tilings*. Part II is then devoted to the

[1] An exception here is the monograph of C. Janot cited in the Appendix.

crystallography of quasicrystals and to structural studies using diffraction methods, microscopy, and computer simulations of the atomic structure. This part also emphasizes the importance of clusters for the formation of quasicrystals and presents both models and computer simulations of the growth of aperiodic lattices. From the point of view of an experimentalist, the *production* of quasicrystals is the prerequisite for all research work, and therefore the properties of the undercooled melt of the alloys from which the quasicrystal is drawn, their phase diagrams, and the production of quasicrystals are discussed in Part III. For the investigation of the physical properties of quasicrystals, the perfectness of the aperiodic lattice usually plays an important role and thus the rich variety of possible *defects* and especially of matching rule violations, called 'phasons' in quasicrystals and investigated with diverse methods, are discussed next. Subsequent chapters in Part IV are devoted to the *mechanical* and *electronic* properties and the electrical conduction in quasicrystalline bulk samples and thin films. In Part V *vibrational* and *thermodynamic* properties and, in Part VI, *magnetic* properties are discussed in some detail, always contrasting theoretical and experimental results. The book is then completed with a discussion of the *surface* properties and the technical *applications* of quasicrystals. Finally, the appendix gives a fairly comprehensive compilation of literature on this topic.

The idea for producing this volume was born on the occasion of a 'Heraeus Summer School' held in Chemnitz in autumn 1997. Its aim was and is to inform interested students not yet working on quasicrystals about this exciting topic, and to support young scientists starting their work on quasicrystals, especially within the framework of the 'Schwerpunktprogramm: Quasikristalle', initiated in Germany by the Deutsche Forschungsgemeinschaft. We would like to take this opportunity to express again our gratitude for the support we received from the 'W.-E. Heraeus Stiftung' on the occasion of the summer school. It is a great pleasure to thank Karin Nerger and Ute Vales for their help in the final preparation of the manuscripts.

Chemnitz, May 2002

Jens-Boie Suck
Michael Schreiber
Peter Häussler

Contents

Part I Background

1 Prehistory of Quasicrystals
Jens-Boie Suck 3

1.1 Introduction 3
1.2 Mathematics 4
1.3 Crystallography 6
1.4 Incommensurate Structures 9
1.5 Structure Models of Amorphous Solids 11
1.6 Supercooled Liquids 12
References 14

2 A Guide to Mathematical Quasicrystals
Michael Baake 17

2.1 Introduction 17
2.2 Non-Crystallographic Symmetries 19
2.3 Diffraction 20
2.4 Quasiperiodicity and the Projection Method 24
2.5 Minimal Embedding and Further Examples 27
2.6 LI Classes and Symmetry 31
2.7 Parametrization of LI Classes 32
2.8 Local Derivability and MLD Classes 34
2.9 Local Equivalence and Limit Translation Module 36
2.10 Local Derivability and Symmetry Preservation 37
2.11 Inflation Symmetries and Matching Rules 38
2.12 A Summary of the Perfect World 41
2.13 Alternatives: Disorder and Random Tilings 41
2.14 Concluding Remarks 45
References 46

3 Aperiodic Tilings on the Computer
Uwe Grimm, Michael Schreiber 49

3.1 Introduction 49
3.2 How to Construct Quasiperiodic Tilings 50

3.3 A Small Example Program: Inflating the Chair Tiling 51
3.4 Once Again: The Ubiquitous Fibonacci Chain 55
3.5 The Octagonal Tiling: Projection and Inflation 59
3.6 De Bruijn's Ingenuity: The Dualization Method 61
3.7 Giving It a Trial: A Penrose-Tiling Puzzle 63
3.8 Concluding Remarks 64
References 65

Part II Atomic Structure and Growth

4 Quasicrystallography
Ted Janssen 69

4.1 Introduction 69
4.2 Symmetry 70
4.3 Embedding 71
4.4 Superspace Groups 74
4.5 The Icosahedral Groups 76
4.6 Dihedral Groups 78
4.7 Wyckoff Positions 80
4.8 Diffraction 80
References 81

5 Experimental Determination of the Structure of Quasicrystalline Alloys: Experimental Techniques and Modeling
Michel Boudard 82

5.1 Introduction 82
5.2 X-Ray and Neutron Diffraction 83
5.3 Quasicrystallography or How to Extract Information about the Structure from the Diffraction Data 87
5.4 An Example: The Structure of the i-AlPdMn Icosahedral Phase .. 94
5.5 Further Ideas for Building Models 108
References 113

6 Electron Microscopy and Surface Investigations of Quasicrystals
Hans-Ude Nissen, Conradin Beeli 115

6.1 Introduction 115
6.2 High-Resolution Electron Micrographs and Their Interpretation .. 121
6.3 Decagonal Quasicrystals 126
6.4 Icosahedral Quasicrystal Structures 139
6.5 Dodecagonal, Octagonal, and Cubic Quasicrystals 148
6.6 Special Electron Diffraction Techniques Applied to Quasicrystals . 152

6.7 Surface-Sensitive Techniques Applied to Quasicrystals 155
References 161

7 Structure of Quasicrystals via Pair Potentials
Marek Mihalkovič 167

7.1 Introduction 167
7.2 Pair Potentials 168
7.3 Approaches to Structure Determination from Structural Energies . 169
7.4 Tiling-Decoration Approach 171
7.5 Summary 181
References 181

8 Quasicrystals as Hierarchical Packing of Overlapping Clusters
Christian Janot, Jean-Marie Dubois 183

8.1 Introduction 183
8.2 Penrose Tiling with a Single Prototile 185
8.3 The Jellium Model for Clusters and Quasicrystals 187
8.4 The Cluster Structure of AlPdMn Quasicrystals 191
8.5 Conclusion 196
References 196

9 Modeling Quasicrystal Growth
Uwe Grimm, Dieter Joseph 199

9.1 Introduction 199
9.2 Growing Ideal Penrose Tilings 201
9.3 Growth in the Random Scenario 204
9.4 Atomistic Growth Models 205
9.5 Algorithmically Motivated Cluster Growth Models 208
9.6 Physically Motivated Cluster Growth Models 209
9.7 Random Tiling Growth Models 211
9.8 Concluding Remarks 214
References 216

Part III Production of Quasicrystalline Alloys

10 Production of Quasicrystalline Alloys and Phase Diagrams
Reinhard Lück 221

10.1 Introduction 221
10.2 Establishing and Mapping of High-Order Phase Diagrams 221
10.3 Methods of Investigation 223
10.4 Examples of Ternary Systems 225
10.5 Calculation of Phase Diagrams 228

10.6 Using Phase Diagrams of Quasicrystal-Forming Systems 229
10.7 Conclusion 231
References 231

11 Undercooling of Quasicrystal-Forming Liquid Alloys
Dirk Holland-Moritz 233

11.1 Introduction 233
11.2 Undercooling and Nucleation 234
11.3 Experimental Studies on the Nucleation Behavior of Quasicrystalline and Polytetrahedral Phases 238
11.4 Estimation of the Energy of the Solid–Liquid Interface 244
11.5 Conclusions 246
References 246

Part IV Defects and Mechanical Properties

12 Phasons, Dislocations, and Cracks
Hans-Rainer Trebin 251

12.1 Introduction 251
12.2 Phasons 251
12.3 Plasticity 256
12.4 Cracks 259
12.5 Conclusion 259
References 261

13 Defects
Markus Wollgarten, Volker Franz, Michael Feuerbacher, Knut Urban .. 262

13.1 Introduction 262
13.2 Observation and Characterization of Phason Defects 262
13.3 Observation and Characterization of Dislocations 268
13.4 Dislocation Motion and Dissociation 275
References 277

14 Ion Channeling in Quasicrystals
Dieter Plachke, Heinz Dieter Carstanjen 280

14.1 Introduction 280
14.2 Basics of Channeling 281
14.3 Lindhard's Theory of Channeling 288
14.4 Experimental 291
14.5 Ion Channeling in Quasicrystals 294
References 304

15 Mechanical Properties of Quasicrystals
Knut Urban, Michael Feuerbacher, Markus Wollgarten 305

15.1 Introduction 305
15.2 High-Temperature Plastic Deformation 306
15.3 Discussion 315
References 317

Part V Electronic Properties

16 Electronic Conductivity of Quasicrystals and Approximants
Stephan Roche, Claire Berger, Didier Mayou 321

16.1 Introduction 321
16.2 Electronic Conductivity of Quasicrystals 322
16.3 Localization in Quasiperiodic Systems 325
16.4 Kubo–Greenwood Conductivity 328
16.5 Conclusion 334
References 335

17 Electron Densities of States in Quasicrystals and Approximants
Esther Belin-Ferré 338

17.1 Introduction 338
17.2 Photoemission Spectroscopies 338
17.3 X-Ray Emission and Photoabsorption Spectroscopies 343
17.4 Electron Energy Loss Spectroscopy 354
17.5 Optical Measurements 356
17.6 Conclusion 359
References 360

18 Electronic Transport Properties of Quasicrystalline Thin Films
Roland Haberkern 364

18.1 Introduction 364
18.2 Preparation of Thin Quasicrystalline Films 365
18.3 Amorphous to Quasicrystalline Transition 367
18.4 Comparing the a- with the i-Phase – The Scattering Approach ... 369
18.5 The Al-Pd-Re System 373
18.6 Conclusion 376
References 377

19 Electron Transport in a Magnetic Field: A Landauer-Formula Approach
Gerald Kasner, Holger Wegmann, Harald Böttger 379

19.1 Introduction 379
19.2 The Model 380
19.3 Density of States and Magnetoconductance 382
19.4 Spectra in a Magnetic Field 384
19.5 Conclusions 391
References 392

20 Phonons and Electrons in Quasicrystals
Marián Krajčí, Jürgen Hafner 393

20.1 Introduction 393
20.2 Reciprocal Quasilattice, Quasi-Brillouin Zone 394
20.3 Numerical Techniques for the Calculation of Spectra of Elementary Excitations in Quasicrystals 396
20.4 Phonons in Quasicrystals 402
20.5 Electrons in Quasicrystals 408
20.6 Conclusion 418
References 419

Part VI Atomic Dynamics and Thermodynamics

21 Computer Simulations of Lattice Dynamics in Quasicrystals
Ted Janssen 423

21.1 Introduction 423
21.2 Phonons in IC-Modulated Phases and IC Composites 424
21.3 Models for Phonons in Quasicrystals 427
21.4 Model Calculations 429
21.5 The Character of Spectra and Eigenvectors 432
21.6 Surface Phonons in Quasicrystals 433
References 434

22 Experimental Determination of the Dispersion of Vibrations in Monodomain Quasicrystalline Alloys
Bernard Hennion, Marguerite Quilichini 436

22.1 Introduction 436
22.2 Inelastic Neutron Scattering on Three-Axis Spectrometer 437
22.3 Experimental Results with Ultrasonic and Brillouin Measurements 442
22.4 Neutron Scattering Measurements on Monodomain Quasicrystals . 442
22.5 Conclusion 451
References 452

23 Vibrational Density of States of Stable and Metastable Quasicrystalline Alloys
Jens-Boie Suck 454

23.1 Introduction 454
23.2 Determination of the Generalized Vibrational Density of States by Neutron Inelastic Scattering 456
23.3 Results for Metastable Quasicrystalline Alloys 460
23.4 Stable Quasicrystalline Alloys 462
23.5 Temperature Dependence of the GVDOS 466
References 469

24 Thermodynamics of Quasicrystals
Reinhard Lück 472

24.1 Introduction 472
24.2 Molar Heat 473
24.3 Thermodynamic Functions of Formation 474
24.4 Metastable Quasicrystals and Heat of Transformation 477
24.5 Stability Arguments 478
24.6 Conclusion 482
References 483

Part VII Magnetic Properties

25 Magnetic Properties of Quasicrystals and Approximants
Guy Trambly de Laissardière, Didier Mayou 487

25.1 Introduction 487
25.2 Localized Moments on Transition Metal Impurity 489
25.3 One Transition Atom in a Realistic Effective Metallic Medium ... 494
25.4 Interaction Between Transition Metal Atoms 498
25.5 Conclusion 502
References 503

Part VIII Surfaces and Applications

26 Bulk and Surface Properties of Quasicrystalline Materials and Their Potential Applications
Jean-Marie Dubois 507

26.1 Introduction 507
26.2 Recurrent Localization of Electronic States 508
26.3 Phase Selection and Preparation Conditions 510
26.4 Potential Applications of Transport Properties 514
26.5 Surface Properties 518

26.6 Strengthening of Metallic Matrices 527
26.7 Hydrogen Storage 529
26.8 At the Edge of a New Era in Quasicrystals Science 531
References 532

A Further Reading: Literature on Quasicrystals
Michael Baake, Uwe Grimm 539

Index 545

List of Contributors

Michael Baake
Universität Greifswald
Institut für Mathematik
und Informatik
Jahnstraße 15a
D-17487 Greifswald
Germany
mbaake@uni-greifswald.de

Conradin Beeli
ETH-Zürich
Laboratorium
für Festkörperforschung
ETH-Hönggerberg
CH-8093 Zürich
Switzerland
beeli@solid.phys.ethz.ch

Esther Belin-Ferré
Université Pierre et Marie Curie
Laboratoire de Chimie Physique
F-75231 Paris, Cedex 5
France
belin@moka.ccr.jussieu.fr

Claire Berger
CNRS, LEPES
B.P. 166
F-38042 Grenoble, Cedex 9
France
berger@lepes.polycnrs-gre.fr

Harald Böttger
Universität Magdeburg
Institut für Theoretische Physik
D-39016 Magdeburg
Germany
harald.boettger
@physik.uni-magdeburg.de

Michel Boudard
LTPCM, ENSEEG
BP 75
F-38402 St. Martin d'Heres, Cedex
France
Michel.Boudard@ltpcm.inpg.fr

Heinz Dieter Carstanjen
Max-Planck-Institut
für Metallforschung
Institut für Physik
D-70569 Stuttgart
Germany
carstanjen
@vaxph.mpi-stuttgart.mpg.de

Jean-Marie Dubois
Université de Nancy I
Laboratoire de Science et Génie
des Matériaux Métalliques
Parc de Saurupt
F-54042 Nancy, Cedex
France
Jean-Marie.Dubois
@mines.u-nancy.fr

Michael Feuerbacher
Forschungszentrum Jülich
Institut für Festkörperforschung
D-52425 Jülich
Germany
m.feuerbacher@fz-juelich.de

Volker Franz
Forschungszentrum Jülich
Institut für Festkörperforschung
D-52425 Jülich
Germany
volkerfranz@yahoo.de

Uwe Grimm
Applied Mathematics Department
Faculty of Mathematics
and Computing
The Open University
Walton Hall
Milton Keynes MK7 6AA
United Kingdom
u.h.grimm@open.ac.uk

Roland Haberkern
Technische Universität Chemnitz
Institut für Physik
D-09107 Chemnitz
Germany
Roland.Haberkern@infineon.com

Jürgen Hafner
Technische Universität Wien
Institut für Theoretische Physik
A-1040 Wien
Austria
Juergen.Hafner@univie.ac.at

Bernard Hennion
Laboratoire Léon Brillouin
CEA-CNRS, CEN-Saclay
F-91191 Gif sur Yvette, Cedex
France
lb-sec@llb.saclay.cea.fr

Dirk Holland-Moritz
DLR
Institut für Raumsimulation
D-51140 Köln
Germany
Dirk.Holland-Moritz@dlr.de

Christian Janot
Institut Laue-Langevin
B.P. 156
F-38042 Grenoble, Cedex 9
France
janot@uniroma1.it

Ted Janssen
Katholieke Universiteit
Faculteit der Wiskunde
en Natuurwetenschappen
Instituut voor Theoretische Fysica
NL-6525 ED Nijmegen
The Netherlands
ted@sci.kun.nl

Dieter Joseph
Universität Tübingen
Institut für Theoretische Physik
D-72076 Tübingen
Germany
Dieter.Joseph@Infineon.com

Gerald Kasner
Universität Magdeburg
Institut für Theoretische Physik
D-39016 Magdeburg
Germany
Gerald.Kasner
@physik.uni-magdeburg.de

Marián Krajčí
Technische Universität Wien
Institut für Theoretische Physik
A-1040 Wien
Austria
fyzikraj@savba.sk

Reinhard Lück
Max-Planck-Institut
für Metallforschung
Institut für Werkstoffwissenschaft
D-70174 Stuttgart
Germany
lueck@mf.mpi-stuttgart.mpg.de

Didier Mayou
CNRS, LEPES
B.P. 166
F-38042 Grenoble, Cedex 9
France
mayou@polycnrs-gre.fr

Marek Mihalkovič
Technische Universität Chemnitz
Institut für Physik
D-09107 Chemnitz
Germany
m.mihalkovic
@physik.tu-chemnitz.de
or
Institute of Physics
Slovak Academy of Sciences
84228 Bratislava
Slovakia

Hand-Ude Nissen
ETH-Zürich
Laboratorium
für Festkörperforschung
ETH-Hönggerberg
CH-8093 Zürich
Switzerland
nissen@solid.phys.ethz.ch

Dieter Plachke
Max-Planck-Institut
für Metallforschung
Institut für Physik
D-70569 Stuttgart
Germany
plachke@gmx.de

Marguerite Quilichini
Laboratoire Léon Brillouin
CEA-CNRS, CEN-Saclay
F-91191 Gif sur Yvette, Cedex
France
lb-sec@llb.saclay.cea.fr

Stephan Roche
DRFMC/SPSMS
Commissariat a l'Energie Atomique
7 rue des Martyrs
38054 Grenoble
France
roche@drfmc.ceng.cea.fr

Michael Schreiber
Technische Universität Chemnitz
Institut für Physik
D-09107 Chemnitz
Germany
schreiber@physik.tu-chemnitz.de
or
International University Bremen
School of Engineering and Science
Campus Ring 1
D-28759 Bremen
Germany
m.schreiber@in-bremen.de

Jens-Boie Suck
Technische Universität Chemnitz
Institut für Physik
D-09107 Chemnitz
Germany
suck@physik.tu-chemnitz.de

Guy Trambly de Laissardiére
CNRS, LEPES
B.P. 166
F-38042 Grenoble, Cedex 9
France
guy.trambly@ptm.u-cergy.fr

Hans-Rainer Trebin
Universität Stuttgart
Institut für Theoretische
und Angewandte Physik
D-70550 Stuttgart
Germany
trebin@itap.physik.
uni-stuttgart.de

Knut Urban
Forschungszentrum Jülich
Institut für Festkörperforschung
D-52425 Jülich
Germany
K.Urban@fz-juelich.de

Holger Wegmann, né Schwabe
IFAK
Schleinufer 11
39104 Magdeburg
Germany
hsc@ifak-system.com

Markus Wollgarten
Institute of Applied Physics
ETH-Hönggerberg
CH-8093 Zürich
Switzerland
wollgarten@iap.phys.ethz.ch

Part I

Background

1 Prehistory of Quasicrystals

Jens-Boie Suck

Summary. In this short introductory review on the "prehistory" of quasicrystals, written for the students of the Heraeus Summer School, five different roots are briefly mentioned, from which ideas grew, which helped to understand and accept these alloys, which led to an extension of classical crystallography and of our understanding of solid state physics of non-periodic crystals. Some basic tools are mentioned which are used in relation with quasicrystals and could be helpful in the context of other topics described in the following chapters.

1.1 Introduction

The discovery of quasicrystals was announced on the 5 November 1984 in a Physical Review Letter entitled "Metallic Phase with Long-Range Orientational Order and No Translational Symmetry" by D. Shechtman, I. Blech, D. Gratias, and J.W. Cahn [46]. Three days before, D. Levine and P.J. Steinhardt submitted a paper to the same journal with the title "Quasicrystals: A New Class of Ordered Structures" which offered the structural model of a crystal with quasiperiodic lattice, or "quasicrystal" for short, for the new alloys [31]. This fact clearly demonstrates that even though quasicrystals came as a surprise for most physicists, crystallographers, and material scientists in November 1984, quite a few ideas had been developed earlier, which were related to them after the discovery of quasicrystals. They helped considerably to get acquainted with the new perspectives and theoretical techniques [4] provoked by the discovery of alloys with "non-crystallographic", i.e. icosahedral [46], dodecagonal [22], decagonal [8], and octagonal [55] point symmetry. In what follows, some of these roots of helpful ideas will be briefly mentioned, especially those which will most likely reappear, without going back to their origins, in other contributions in this introduction to quasicrystals, their properties, and applications.

Quasicrystals have most likely been produced occasionally before, even though this cannot be proved subsequently. Hardy and Silkock reported on AlCuLi alloys, one of which they named the (cubic) R-phase, today the rational approximant to the icosahedral alloy in its vicinity in the phase diagram. The alloy next to or at the concentration of the i-phase they named the T2-phase and said: "The pattern appeared fairly simple, although it did not correspond to a cubic structure" [18]. Likewise Padezhnova and collaborators

J.-B. Suck et al. (eds.), *Quasicrystals*
© Springer-Verlag Berlin Heidelberg 2002

report on $Zn_{60}Mg_{30}Y_{10}$ which they called the Z-phase with "unknown structure" [39] – today this alloy is the prototype of the non-Al-based i-phases of Frank–Kasper or Bergman type. With the exception of Ishimasa and collaborators, who found a phase with twelve-fold symmetry in a NiCr alloy with long-range orientational but no translational symmetry, analyzed carefully its tiling by TEM and submitted their paper to *Physical Review Letters* in December 1984 [22] – in contrast to Shechtman and collaborators, the authors mentioned before did not follow up these "unknown structures". If one recalls the partly violent discussions [37], which the announcement of a solid with long-range ordered structure and icosahedral (i-) point symmetry, i.e. with a five-fold rotational axis, provoked in the middle of the 1980s, one may wonder whether such a discovery in the 1950s without all the "preparative" work done in the 1970s would have been accepted at all. This resistance against the acceptance of this new phase with long-range ordered structure was caused by the fact that at that time for nearly all crystallographers, physicists, and material scientists "long range ordered" and "with translational symmetry" were practically synonymous. Therefore no other symmetry axes but 2-, 3-, 4-, and 6-fold were expected in a solid with long-range order in 3D Euclidean space. Time has to be ripe for the acceptance of a discovery. Thus a different way of putting the underlying question of this article could be: "What was done before November 1984 which helped to make this new discovery acceptable?".

In the rest of this chapter, from the possible choices, five different roots will be briefly mentioned from the viewpoint of a material scientist, which have contributed to this preparatory work: mathematics, crystallography, the investigation of incommensurate phases, computer simulations of amorphous metals and finally the important contribution from the computer study of the structure of supercooled liquids.

1.2 Mathematics

Mathematics (and mathematical physics which will not be distinguished in this context) is certainly one of the most important roots of the idea of a quasiperiodic structure. Here many tools had already been completed before quasicrystals were discovered. Two of these will be mentioned briefly. A much more extended discussion is given by M. Baake in this volume [4].

1.2.1 Theory of Functions

Quasiperiodic functions had already been studied within their thesis work by P. Bohl 1893 and by N. Escanglon, who named them "quasiperiodic" in 1919. They were extensively investigated later by Harald Bohr in his work on almost periodic functions [10,25,4]. They are distinguished from non-periodic functions by having a *finite* number of linearly independent basis vectors which

span its Fourier module (the reciprocal lattice in the case of a crystal). The number of independent basis vectors needed defines the rank of the Fourier module. For a periodic function, this rank is equal to the dimension of the lattice; for a quasiperiodic function it is larger and it defines the dimension of the (higher dimensional) space, also often called the superspace, in which the quasiperiodic function can be embedded as a periodic function in each of its coordinates [4]. Restricting the discussion to one-dimensional (1D) functions, the periodic function $f(x) = f(x+1)$ can be expressed by a convergent sum of exponentials $\exp(\mathrm{i}2\pi nx)$ (plane waves) with n an integer. A 1D quasiperiodic function can also be expressed by a convergent sum of exponentials, which however are of the type $\exp(\mathrm{i}2\pi(n_1 \times 1 + n_2 \times 2 + ... + n_N \times N))$ where N is a *finite* number. In the case $N = \infty$ one deals with non-periodic functions.

1.2.2 Tilings

The second, perhaps even more important chapter, is that of tilings, which in a probably more curious and playful way goes at least back to A. Dürer and especially J. Kepler and which was more firmly installed as a mathematical discipline by the end of the 19th century. Here mainly one question of this discipline is of importance for the prehistory of quasicrystals: "How many tiles are needed at least to tile the Euclidean space (primarily 2D) in a purely aperiodic manner without overlapping tiles or empty spaces between them?". Here "non-periodic" and "Euclidean" are of importance because for periodic lattices one unit cell is sufficient [3] and in curved space the answer to this question is completely different [27]. This question has interested quite a few mathematicians and theoretical physicists and in the answers given to this question the number of tiles reduced with time, arriving in 1974 at "2 tiles" in Roger Penrose's aperiodic tiling of the plane [41].[1] As shown in Fig. 3.1 in [4] he used two rhombi with equal side length but different opening angles of 36 ("skinny" rhombus) and 72 degrees ("fat" rhombus) respectively, implying five-fold symmetry and hence non-periodic tiling, and he imposed matching rules for the addition of tiles to an existing tiling. The resulting tiling is non-periodic, it has long-range bond orientational order (BOO) with five-fold symmetry (due to the chosen angles 360/10 and 360/5) and it is self-similar, i.e. one can produce new tilings by inflation or deflation of the existing tiling. It consists of an infinite repetition of the same local structure in an always slightly different surrounding and it is much more difficult to build up [42] than one would expect from looking at Fig. 3.1 in [4] (see also the article on growth models of Grimm and Joseph in this volume). While Penrose claimed in his very charmingly written article on "The rôle of Aesthetics in

[1] Admitting overlapping tiles with overlapping rules one will succeed (at least in 2D) with 1 decagonal tile only (see P. Gummelt, Geometriae Dedicata **62** (1996) 1, P.J. Steinhardt, H.-C. Jeong, K. Saitoh, M. Tanaka, E. Abe, A.P. Tsai, Nature **396** (1998) 55).

Pure and Applied Mathematical Research" to have invented his tiling as a game [41,43], N.G. de Bruijn displayed the mathematical potential of the method in two articles called "Algebraic theory of Penrose's non-periodic tiling of the plane" [12], in which he already discussed the basis of many of the methods like the grid method, projection from higher-dimensional space (hdsp), inflation, and deflation, etc., which were used later in connection with models of quasicrystals. Similarly the aperiodic tiling of the plane with eight-fold point symmetry by R. Ammann [2] was analyzed mathematically by Beenker [7]. Most of them will be discussed in subsequent articles of this volume.

The potential of Penrose break through was immediately recognized and its first generalization to 3D (end of the 1970s, beginning of the 1980s) using the corresponding two rhombohedra instead of the rhombi discussed above is said to be due to R. Ammann [2]. In 1981 A.L. Mackay published his 3D tiling using the same two rhombohedra (see below) and parallel to this P. Kramer produced a centrosymmetric 3D tiling with full icosahedral symmetry using seven different tiles with four different shapes while three were copies scaled by the irrational number $\tau = 0.5(1 + \sqrt{5})$ (the golden mean which is related to the tile angles of 360/5 and 360/10) [29]. This tiling was afterwards generalized to n dimensions using the projection from hdsp [30].

1.3 Crystallography

If a new atomic structure is detected, crystallography is concerned, perhaps challenged in the first place. And here in fact very important insights and ideas have been accumulated which helped to understand the atomic structure as far as we do now.

If metals are concerned, and in fact all quasicrystals known so far are alloys, dense packing of hard or soft spheres, tetrahedral geometry, etc., will most likely come into play. From this point of view the work on "Complex Structures of Alloys as Packing of Spheres" of F.C. Frank and J.S. Kasper is of great importance [15]. Working with spheres of equal size, at most 12 such spheres can be in contact with a 13th in the middle. If the spheres of equal diameter are hard, fcc, hcp, and icosahedral clusters are energetically equivalent. This is not the case if one is working with spheres which can relax. In this case the icosahedral configuration can gain binding energy from inward relaxation, because in this geometry the hard spheres do not touch each other, while in the fcc and hcp configuration the atoms already touch each other before relaxation and therefore cannot relax further [14]. The relaxation of the icosahedral configuration only happens if the atom in the middle leaves enough space, e.g. by having a 5% smaller radius than the outer atoms or a soft potential which allows inward relaxation [14]. (Therefore many arguments have been based on the fact that Al just has an atomic radius 5% larger than Mn when the first icosahedral alloy AlMn was found.) This is

the onset of the work of Frank and Kasper which then proceeded to describe complex alloy structures, nowadays called Frank–Kasper phases, on the basis of large building units, clusters of icosahedral shape or with parts of icosahedra, which are assembled to form a *periodic* lattice. $Mg_{32}(AlZn)_{49}$ with its 162 atoms per unit cell also belongs to these structures. The "cracking" of this structure, one of the most complicated structures solved in the 1950s [9], not only led to a lively discussion on the structure of the quasicrystals right after their discovery – because Linus Pauling suspected a similar complicated periodic structure at their basis as in the case of Mg(AlZn) [40] – but also to one of the two basic building units which are discussed nowadays in connection with the structure of icosahedral alloys: the Bergman cluster (BC). This is a cluster of several shells around an inner atom, the first shell of 12 atoms being an icosahedron (see the right-hand side of Fig. 1.1). The building of the next shells normally follows the scheme: put atoms in the middle of the surfaces of the polyhedron defined by the atomic positions in the previous shell, here 20 atoms above the 20 equilateral triangles of the inner iscosahedron, which puts them in the nearest position to the center of the cluster forming a pentagonal dodecahedron. Then cut the edges of the polyhedron defined by these atomic positions which will make it more sphere-like, and then occupy the newly won space, here by 12 further atoms in the pentagonal places of the dodecahedron (above the corners of the (first shell) icosahedron). Thus the atoms in this second shell are at the corners of a rhombic triacontrahedron. This again has 60 triangles (half-rhombs) on its surface above which now 60 new atoms can be put, forming the third shell with 60 atoms at the 60 corners of a truncated icosahedron (the 12 corners cut off giving five new corners each time). Adding 12 further atoms as before one arrives at 72 atoms lying on the faces of an cuboctahedron. Cuboctahedra can be packed in a periodic lattice in 3D Euclidean space and a bcc lattice can therefore be formed by these clusters resulting in a structure with 162 atoms per unit cell.

The second of the building units just mentioned is the Mackay icosahedron (MI). A.L. Mackay was motivated for this investigation by a very similar sphere packing described by J.D. Bernal and considerations of the architect Buckminster Fuller.[2] Mackay investigated the packing of an assembly of spheres (several atomic shells) with icosahedral point group symmetry. Compared to the cuboctahedra, which usually represent the first coordination shell in close packed cubic structures, one would gain a 5% shorter binding length towards the center of the cluster if this center is occupied by an atom with smaller diameter or soft potentials would allow relaxation towards the center. The MI consists of a first shell of 12 atoms, surrounding a thirteenth in the center, at the corners of an icosahedron (see the left-hand side of Fig. 1.1). The second icosahedral shell of exactly twice the size of the first contains 42 atoms, of which the 12 atoms along the five-fold axes, which are defined by

[2] His ideas influenced crystallography a second time in connection with the discovery of the Fullerenes one year after the discovery of the quasicrystalline alloys.

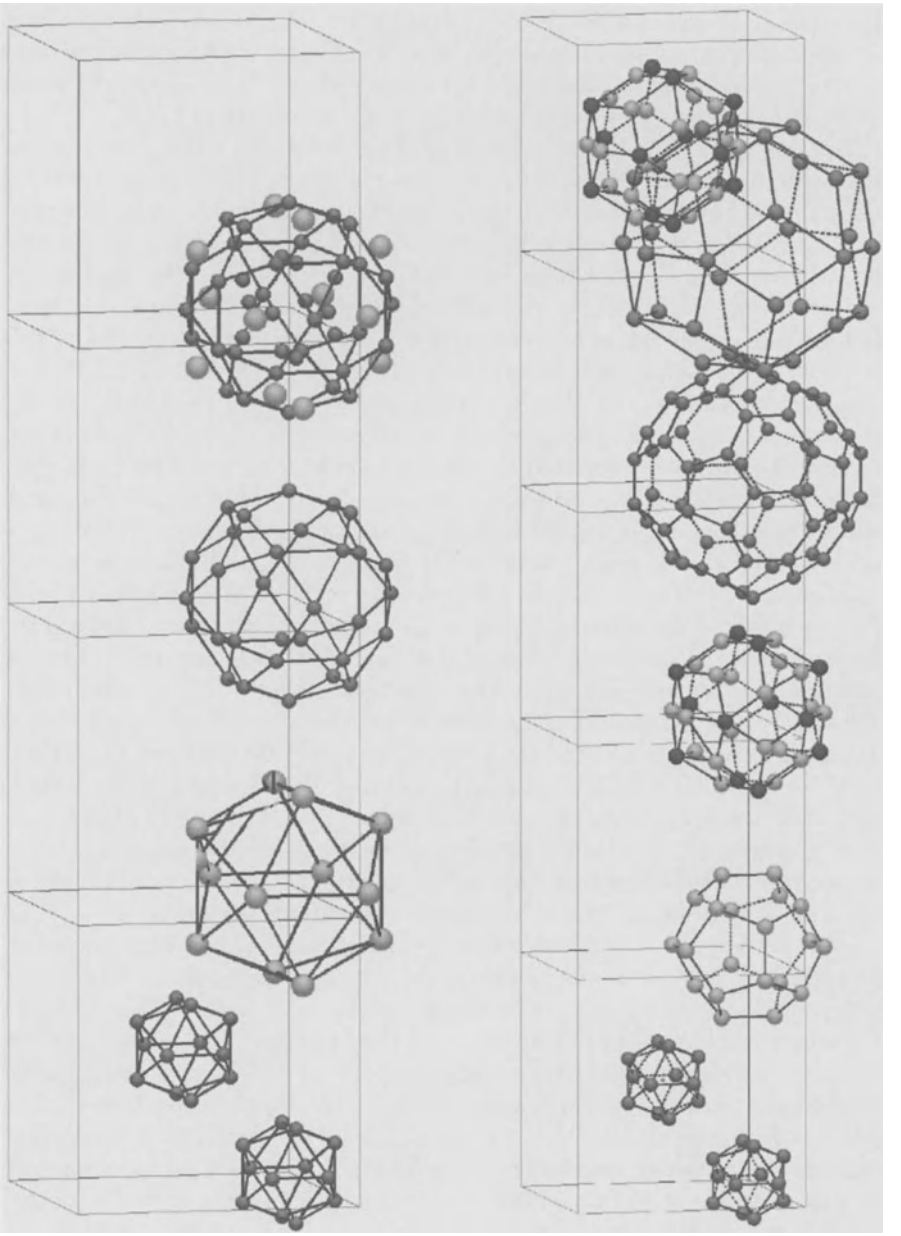

Fig. 1.1. Left: Mackay cluster, right Bergman cluster

the atom at the center and the 12 corners of the icosahedron of the first shell, are in contact with each other. The spheres of equal size are not close packed in the faces of the second shell icosahedron but have about 5% space between them ($d = 1.05146$ times their diameter). This unit, including a central atom, has 55 atoms and further layers could be added, the next one containing 92 further atoms.

Each icosahedron, by a small deformation, can be transformed into a cuboctahedron which could then be arranged in a close packed cubic structure. Each icosahedron can be easily divided into 20 slightly deformed tetrahedra, the underlying building unit of most densely packed structures of atoms with spherical symmetric potentials (like Coulomb potentials). It is therefore not too surprising that the MI has a packing density (0.698 with central atom, 0.724 without, due to inward relaxation) not too far from that of a close packed cubic structure (0.74) and that continuing with further shells one arrives at a packing density of 0.688 which is slightly larger than that of bcc phases (0.680). As bcc is often the high-temperature structure of metals and alloys [1] the packing described by Mackay also offers an atomic structure with just slightly larger packing density for a high-temperature phase. As the MI (without deformation) cannot be used as a building unit in periodic crystals, Mackay published his multishell icosahedron under the heading "A dense non-crystallographic packing of equal spheres" [33].

A further contribution from crystallography to the understanding of the structure of QC likewise came from A.L. Mackay. It concerned the crystallographic investigation of the extension of the Penrose tiling from 2D to 3D, as done before by Ammann, using two rhombohedra instead of two rhombs and corresponding matching rules, and appeared under the title of "Crystallography and the Penrose tiling" [34]. To my knowledge he was the first to coin the term "quasilattice", he showed how to obtain the 3D quasilattice using an acute and an obtuse rhombohedron via recursive subdivision and quotes the inflation rules which led to the limit τ of the ratio of occurrence frequency of the two types of rhombohedra as for the rhombi in the Penrose pattern. He demonstrated the formation of rhombic triacontahedra in this 3D tiling by 10 acute and 10 obtuse rhombohedra corresponding to the decagons found in the 2D Penrose tiling and he explained the use of 6 Miller indices to address the points in reciprocal space of the 3D quasiperiodic tiling. He also showed how to obtain this Penrose tiling by a cut from the 3D structure and he obtained the first diffraction pattern from the Penrose tiling with "atoms" on its vertices.

1.4 Incommensurate Structures

A third discipline which contributed considerably to the understanding of the QC structure was the investigation of incommensurate phases. As a consequence of the variation of external parameters, e.g. lowering of the tempera-

ture or application of pressure, a structural phase transition can be triggered, which normally takes the system to another periodic structure. In some cases however, if competing interactions exists, a new structure may be formed which is incommensurable with the remaining basic structure. This formation of an incommensurable modulation of the structure literally leads to an aperiodic structure. However the Bragg peaks of the original lattice still persist and the incommensurable modulation shows up as satellites (or streaks) aside of these Bragg peaks only [24]. Obviously it was the existence of this "parent" crystal on which the incommensurable modulation appeared as a "disturbance" which made it easier for crystallographers to swallow this kind of aperiodic lattice than the QC model and treat them within traditional crystallography.[3] A vivid example of a compositional incommensurate modulation – in contrast to a displacive incommensurate modulation which can, e.g., be caused by a competition of conduction electrons (charge density waves) and the atomic lattice (especially also at surfaces) [44] – of a 2D system is a gas condensed on a surface built by atoms of a different diameter than that of the gas atoms (e.g. Kr on graphite). As long as the density and the temperature of the first layer of gas atoms on the surface is low, the atoms will arrange in phase with the surface structure of the substrate for energetic reasons. When the layer gets denser, geometrical constraints will become dominant and the atoms are forced to arrange themselves out of phase with the supporting surface structure, or form a domain structure with soliton-like domain walls at the domain border which are out of phase with the periodicity of the substrate. In 3D, graphite layers intercalated with metal atoms are a good example for a system with a tendency to form compositional incommensurate phases [5].

These structures and their properties had been investigated intensively especially in the 1970s [24,5], and it was therefore not surprising that specialists in this field immediately imagined quasicrystals as "ultimate incommensurate" structures [6]. More surprising was the initial resistance of other scientists against non-periodic lattices and against the interpretation of QC structures in higher dimensions, as both had been extensively used for some time already in connection with incommensurate structures [23]. These phases in some sense can therefore be regarded as having paved the way for the acceptance of QC models. Different from QC, incommensurate structures essentially retain a basic periodic structure and the modulation is also periodic but incommensurate with the original periodicity of the lattice.

The 3D structure and its modulation can be presented in 4d space ("superspace") in which the fourth dimension "stores" the phase information as a new coordinate and degree of freedom. It is interesting to note that this new degree of freedom can be excited – due to the restoring forces which want to keep the incommensurable modulation – and can lead to new collective exci-

[3] See for comparison the concept of a "periodic average structure of particular quasicrystals" by W. Steurer and T. Haibach, Acta Cryst. **A 55** (1999) 48-57.

tations which are called phasons in analogy to phonons. The dispersion of the phasons, which has its origin ($\omega = 0$) at a wave vector incommensurable with those of the phonons of the same crystal, has in fact been observed in neutron inelastic scattering experiments [13]. In the context of QC one uses the same word "phasons" but with a *different* meaning. Here one normally does not mean collective excitations in the phase system (internal or perpendicular space) but matching rule violations. For QC one adapts essentially the same description in higher-dimensional space, dividing this into a parallel space where the translational information is stored as in the case of incommensurate phases and a perpendicular space where the phase information, now no longer one-dimensional, is stored. However there are at least two differences between incommensurate phases and QC: QC have no related periodic crystal which dominates their Fourier module (though QC may have "relatives" in the form of rational approximants [4,54]); and QC have one basic length scale (plus related distances scaled by some multiple of the point symmetry characteristic irrational number (e.g. τ in the case of ten-fold or five-fold, $(1+\sqrt{2})$ in the case of eight-fold point symmetry which is related to the tile angles of $360/8$), while incommensurate phases are determined by two length scales, the lattice constant of the periodic crystal and the wavelength of its incommensurable modulation.

1.5 Structure Models of Amorphous Solids

The static structure factor determined in diffraction experiments done on disordered condensed matter reduces the 3D structure to 1D information, the radial distribution function $g(r)$, which contains information only on distances and the number of atoms in the nearer neighbor shells. In order to get some insight into the 3D structure, one therefore has to perform computer simulations of the structure, of which a large number have been done and which have to agree with the experimentally determined $g(r)$. Here only very few are mentioned which concern metallic amorphous systems. A simulation of metal cluster formation based on rather simple approximations already showed that clusters of 13 atoms have a strong tendency to form icosahedra even if in the growth process, where one atom was added after the other, they had passed through an fcc cluster before [11]. The authors concluded from this that icosahedral clusters should be frequent building blocks of amorphous metals, a hypothesis which was later supported by experimental results [52,53]. Based on *ab initio* pseudopotentials for binary amorphous alloys of simple metals J. Hafner showed that the structure which forms depends on the choice of the ratio of the radii of the majority component in the alloy: if the smaller atoms are the majority, Frank–Kasper phases form; if the number of larger atoms dominates an amorphous structure, icosahedral subunits are formed [16]. On the basis of more elaborate computer simulations on large systems, it was shown later by D.R. Nelson [38] that a model for the structure

of metallic amorphous solids can be based on defect lines in a system with icosahedral bond orientational order (BOO) in 3D Euclidean space, where the Frank–Kasper phases, which contain icosahedral building units, would be ordered networks of these lines. That QC and amorphous alloys can both be related to Frank–Kasper phases is not that surprising, as both structures are built from atoms with largely centrosymmetric bonding potential. This leads to a dense packing of spheres, the starting idea of Frank and Kasper. One then easily realizes that the dense packing of four spheres leads to a tetragonal structure and that 20 slightly deformed tetragons can be joined to form an icosahedron. More surprising is perhaps that such icosahedral and rhombicosidodecahedral building blocks are also formed in computer simulations when a liquid is quenched below the glass transition temperature T_g [26], very similar to the structures obtained by an atom by atom systematic construction of an amorphous cluster [20]. Thus from the modeling of amorphous alloys the conviction was transferred to QC that icosahedral building units could be abundant in a system without translational symmetry and which can be approximated by the dense packing of spheres. This computer experiment on quenching leads to the last root in the prehistory of QC which will be mentioned in this chapter.

1.6 Supercooled Liquids

If icosahedral building units are observed in an amorphous solid after the very fast quench in a computer simulation one has to suspect that they had existed already – at least to a certain approximation – in the undercooled liquid before the quench, as there will most likely not be enough time to form them in the quenching process itself. The question "do icosahedral clusters exist in supercooled liquid metals and are they the reason for the observed supercoolability?" had already been discussed by Frank in 1952 [14] and it has regained much interest nowadays [21,47]. From a somewhat different point of view, namely "does a phase with bond directions, characteristic of an icosahedral geometry, form in supercooled liquids?", this question was investigated in a thorough computer simulation of a Lennard–Jones liquid by Steinhardt, Nelson, and Ronchetti 30 years later [49].

This investigation was a consequent step to a 3D liquid from a very successful study of a 2D liquid during and just after melting by Halperin and Nelson [17], which again went back to a new kind of phase transition discussed by Kosterlitz and Thouless [28]. This latter work is based on the idea that dislocations should preferably form in pairs with opposite Burgers vectors, as the formation of this lattice defect will cost less energy if the same dislocation is created near the first one which compensates the effect of the first – a cheap way of regaining an unperturbed lattice at some distance from the dislocation pair. Kosterlitz and Thouless investigated the unbinding of these dislocation pairs as a phase transition following an energy increase. Starting from these

ideas, Nelson and Halperin found in their investigation of melting of a triangular lattice on a smooth surface a new phase between the 2D crystal and the completely disordered liquid, the hexatic phase, which is characterized by a hexagonal long-range order in the bond orientations (BOO) (with algebraic decay) after unbinding of the dislocation pairs has taken place and the long-range order in the atomic positions (LRO) has already been lost (exponential decay). Bond directions are here defined by the shortest connection between neighboring atoms. The defects in this hexatic phase with BOO are disclinations ("dislocations" in the bond direction) which, like the dislocations in the phase with LRO and for the same reason, again form preferably in self-compensating pairs. It is finally the unbinding of these disclination pairs on further energy increase which leads to the completely disordered phase. Experimentally many efforts have been made to prove the existence of the hexatic phase [51,36]. The discovery of the hexatic phase is of great importance for our understanding of long-range order because it showed the (nearly independent) existence of two kinds of long-range order: in the atomic positions – the usual meaning of LRO – and the BOO which is necessarily linked to the LRO in a crystal but can survive the loss of the LRO under certain conditions. Intellectually, this discovery was very helpful for the acceptance of the models for quasicrystals some years later, where the BOO plays such an important role in decorated tilings [35], and even in the understanding of competing models like the icosahedral glass, in which BOO alone can lead to the appearance of peaks with finite width in the diffraction patterns [50].

The investigation of a supercooled liquid in order to look for traces of a corresponding phase with icosahedral BOO in 3D [49], an icosahedratic phase, was encouraged also by Frank's argument on the existence of clusters with icosahedral point symmetry in supercooled liquid metals [14]. Following his arguments these are energetically favored (after inward relaxation under a soft potential) and could form there without being constrained by translational symmetry conditions and could therefore prevent the transition of the liquid into a periodic crystal and thus support supercooling. Steinhardt and collaborators investigated (rotational invariant) mean values of the bond orientation in their liquid and found no significant correlations at $T > T_{\mathrm{m}}$, the melting temperature. However at about 10% careful supercooling, the bond orientation correlation function increased considerably and the icosahedral one ($\mathrm{l} = 6$) had a preferred extension compared with that of cubic symmetry ($\mathrm{l} = 4$). In all cases the BOO was longer ranged than the LRO, like in 2D, i.e. the BOO is more stable and has a locally dominant icosahedral component. A true phase with long-range icosahederal BOO was not reached; the maximum achieved was 35% of a long-range icosahedral phase. In addition, the range of the icosahedral BOO depends critically on the quenching rate, the slower the quench the farther extended the icosahedral BOO.

A study similar to this one on the question: "Do pre-existing clusters with either icosahedral or cuboctahedral (local fcc) geometry in a dense 3D liquid

align via orientation-sensitive interaction leading to a long-range bond oriented phase without long-range positional order?" was investigated by A.D.J. Haymet within a mean field approximation [19]. The predictions, based on the same rotational invariant order parameters and criteria as were used by P.J. Steinhard and collaborators, of his study are: on lowering the temperature from $T > T_m$ there is a transition out of the isotropic liquid to a phase with cuboctahedral BOO, which was assigned to ordinary freezing. In the supercooled liquid, however, below this freezing temperature, the system undergoes a transition to a phase with long-range icosahedral BOO. On further supercooling this state should get trapped due to the strong decrease of the viscosity and finally lead to a glass with long-range icosahedral BOO.

These very important investigations, which were the first systematic searches for an icosahedral phase in condensed matter and therefore helped to pave the way for the acceptance of the QC model, were at the origin of two different developments. D.R. Nelson and collaborators used these results for modeling the structure of amorphous metals via a defective icosahedral phase [38,45], while P.J. Steinhardt and collaborators looked for a perfect icosahedral phase in a solid, which was still excluded by the authors with regret from the discussion of possible crystalline phases a few years before [1], but which lead them directly to the model mentioned at the beginning of this chapter [31,32,48].

This promenade through some of the works which helped to prepare our understanding and acceptance of QC turned out to be a closed tour - with five-fold symmetry, of course. I am aware that the selection of topics is incomplete and a personal choice from the point of view of a material scientist. Still I believe that some of the topics touched on here will come back in the following chapters, and back-reference may therefore be helpful.

Acknowledgment

It is a pleasure to acknowledge helpful discussions with Michael Baake, Ted Jannsen and Christian Janot. I am grateful to Marc Audier for providing me with Fig. 1.1.

References

1. Alexander S., McTague J., Phys. Rev. Lett. 41 (1978) 702
2. Ammann (1977) cited in "Tilings and Patterns", ed. B. Grünbaum, G.C. Shephard (Freeman & Co. New York 1985), and by D. Levine, P.J. Steinhardt, J. Non-Cryst. Sol. 75 (1985) 85
3. Ashcroft N.W., Mermin N.D. "Solid State Physics" (Saunders Coll. Publ. 1976)
4. See e.g. Baake M. (2002): Chapter 2 of this book. See also: Grimm U., Schreiber M. (2002): Chapter 3 of this book
5. Bak P., Rep. Prog. Phys. 45 (1982) 587

6. Bak P., Phy. Rev. Lett. 54 (1985) 1517
7. Beenker F.P.M., Techn. Hogeschool Eindhoven Rep. No. 82-WSK-04 (1982)
8. Bendersky L., Phys. Rev. Lett. 55 (1985) 1461
9. Bergman G., Wangle J.T.C., Pauling L., Acta Cryst. 10 (1957) 254
10. Bohr H., Acta Math. 45 (1924) 29; 46 (1925) 101; 52 (1928) 127
11. Briant C.L., Burton J.J., Phys. Stat. Solidi (b) 85 (1978) 393
12. de Bruijn N.G., Ned. Akadem. Wetensch. Proc. Ser. A 84 (1981) 39 and 53
13. Currat R., Janssen T., Solid State Phys. 41, ed. H. Ehrenreich, D. Turnbull (Academic Press 1988) p. 202
14. Frank F.C., Proc. Roy. Phys. Soc. London A215 (1952) 43
15. Frank F.C., Kasper J.S., Acta Cryst. 11 (1958) 184; 12 (1959) 483
16. Hafner J., Phys. Rev. B 21 (1980) 406
17. Halperin B.I., Nelson D.R., Phys. Rev. Lett. 41 (1978) 121; Phys. Rev. B 19 (1979) 2457
18. Hardy H.K., Silcock J.M., J. Inst. Metals 84 (1955) 423
19. Haymet A.D.J., Phys. Rev. B27 (1983) 1725
20. Hoare M.R., J. Non-Cryst. Solids 31 (1978) 157
21. Holland-Moritz D. (2002): See Chapter 11 of this book
22. Ishimasa T., Nissen H.-U., Fukano, Y., Phys. Rev. Lett. 55 (1985) 511
23. Janner A., Physica 114A (1982) 614
24. Janssen T., Janner, A., Adv. in Phys. 36 (1987) 519 and ref. therein
25. Janssen T., Phys. Rep. 168 (1988) 55
26. Jonsson H., Andersen H.C., Phys. Rev. Lett. 60 (1988) 2295
27. Kleman M., Sadoc J.-F., J. Phys. (France) Lett. 40 (1979) L 569
28. Kosterlitz J.M., Thouless D.J., J. Phys. C 6 (1973) 1181
29. Kramer P., Acta Cryst. A38 (1982) 257
30. Kramer P., Neri R., Acta Cryst. A40 (1984) 580
31. Levine D., Steinhardt J.P., Phys. Rev. Lett. 53 (1984) 2477
32. Levine D., Steinhardt P.J., Phys. Rev. B 34 (1986) 596
33. Mackay A.L., Acta Cryst. 15 (1962) 916
34. Mackay A.L., Kristallografiya 26 (1981), 909, Physica 114A (1982) 609
35. Mihalkovič M. (2002): See Chapter 7 of this book
36. Murray C.A., Gammel P.L., Bishop D.J., Mitzi D.B., Kapitulnik A., Phys. Rev. Lett. 64 (1990) 2312
37. Nature 319 (1986) 102 (several letters)
38. Nelson D.R., Phys. Rev. Lett. 50 (1983) 982
39. Padezhnova E.M., Mel'nik E.V., Miliyevskiy R.A., Dobatkina T.V., Kinzhibalo V.V., Russ. Metall 3 (1982) 185
40. Pauling L., Nature 317 (1985) 512
41. Penrose R., J. Inst. Math. Appl. 10 (1974) 266
42. Penrose R. in "Aperiodicity and Order", ed. M.V. Jaric (Academic Press, Boston 1988)
43. In 1977 these and other important result together with graphics from Escher appeared under the title "Mathematical Games" in Scientific American 236 (1977) 110
44. Pynn R., Nature 281 (1979) 433
45. Sachdev S., Nelson D.R., Phys. Rev. Lett. 53 (1984) 1947, Phys. Rev. B 32 (1985) 4592
46. Shechtman D., Blech I.A., Gratias D., Cahn J.W., Phys. Rev. Lett. 53 (1984) 1951

47. Simonet V., Hippert F., Klein H., Audier M., Bellissent R., Fischer H., Murani A.P., Boursier D., Phys. Rev. B 58 (1998) 6273
48. Socolar J.E.S., Steinhardt P.J., Phys. Rev. B 34 (1986) 617
49. Steinhardt P.J., Nelson D.R., Ronchetti M., Phys. Rev. Lett. 47 (1981), Phys. Rev. B28 (1983) 784
50. Stephens P.W., Goldman A.I., Phys. Rev. Lett. 56 (1986) 1168; 57 (1986) 2331
51. Strandburg K.J., Rev. Mod. Phys. 60 (1988) 161
52. Suck J.-B., Bretscher H., Rudin H., Grütter P., Güntherodt H.-J., Phys. Rev. Letters 59 (1987) 102
53. Suck J.-B., Güntherodt H.-J., in "Phonons 89", ed. by Hunklinger, S., Ludwig, W., Weiss, G. (World Scientific, Singapore, 1990) p. 573
54. Tamura N., Phil. Mag. A 76 (1997) 337
55. Wang N., Chen H., Kuo K.H., Phys. Rev. Lett. 59 (1987) 1010

2 A Guide to Mathematical Quasicrystals

Michael Baake

Summary. This contribution deals with mathematical and physical properties of discrete structures such as point sets and tilings. The emphasis is on proper generalizations of concepts and ideas from classical crystallography. In particular, we focus on their interplay with various physically motivated equivalence concepts such as local indistinguishability and local equivalence. Various discrete patterns with non-crystallographic symmetries are described in detail, and some of their magic properties are introduced. This perfectly ordered world is augmented by a brief introduction to the stochastic world of random tilings.

2.1 Introduction

The discovery of alloys with long-range orientational order and sharp diffraction images of non-crystallographic symmetry [37,69] has initiated an intensive investigation of the possible structures and physical properties of such systems. Although there were various precursors, both theoretically and experimentally [73], it was this renewed and amplified interest that established a new branch of solid-state physics, and also of discrete geometry. It is usually called the theory of quasicrystals, even though it also covers ordered structures that are more general than those with a pure Bragg diffraction spectrum.

It is now rather common to think of the regime between crystallographic and amorphous systems as an interesting area with a hierarchy of ordered states. This was not so some 15 years ago, and it is the purpose of this contribution, and of the book as a whole, to introduce some of the ideas and methods that are needed to handle this new zoo. In particular, I will summarize some mathematical and conceptual issues connected with it, with special emphasis on proper equivalence concepts. This is more important than it might appear at first sight, because non-periodic order shows both new features and new hazards – and it is worthless to talk about a property of one specific structure if it is lost for others that are locally indistinguishable.

To develop some of these ideas, one has to start with a valid idealization of the physical structures that one has in mind. Since we are interested in solids of some relevant size here, it is reasonable to replace their atomic arrangements by suitable infinite point sets. These should be uniformly discrete (i.e. there should be a uniform minimal distance between the points)

J.-B. Suck et al. (eds.), *Quasicrystals*
© Springer-Verlag Berlin Heidelberg 2002

and, usually, they should be relatively dense (i.e. there should be a maximal hole). Sets with this property are called Delone sets and are widely used for this purpose.

By analogy with ordinary crystallography, many people prefer to think in terms of cells or tiles [57]. Here, one may start from a (usually finite) number of proto-tiles that fit together to tile space without gaps or overlaps. If we now decorate the tiles by finitely many points (giving the atomic positions, say), we return to a Delone set. Vice versa, given a Delone set $\varLambda$, we can perform the Voronoi construction that attaches to each point $x \in \varLambda$ the region of all points of ambient space that are closer to x than to any other point of $\varLambda$. In this way, we come back to a tiling (whose dual, the so-called Delone tiling [66], is an even better candidate). Under an additional, but rather mild, condition, namely that $\overline{\varLambda - \varLambda}$ is discrete,[1] it will actually show only finitely many different tiles, and in this sense the two concepts are equivalent [48].

In what follows, in line with other expositions [23,42,47], we shall usually illustrate the concepts with examples from the class of tilings made from finitely many proto-tiles, but all concepts will be formulated in a way that allows us to switch between such tilings and Delone sets. In particular, the central equivalence concepts will be described in that way, and this will actually make this very connection between tilings and point sets more precise.

As mentioned before, it is the aim of this contribution to summarize several rather central concepts that are needed for the description of quasicrystals. Since it is impossible to give a self-contained exposition of the present body of knowledge in this survey, the following text is often a pointer in nature, and further details have to be taken from the references given. Also, even though some definitions and results are highlighted, the exposition is rather informal and contains no proofs, although we will try to sketch the ideas behind them, whenever that is possible in fairly non-technical terms. For more details, in particular on more mathematical issues, we refer to [10] and [55].

The chapter is organized as follows. After an introduction to non-crystallographic symmetries, we will recall some concepts from diffraction theory, followed by Sect. 2.4 on quasiperiodicity and the projection method, which is vital for the description of perfect quasicrystals. We then explain the issue of minimal embedding, illustrated with the most important examples. Then, as a first equivalence concept, local indistinguishability (also called local isomorphism) is introduced. This allows for the proper definition of (generalized) symmetry, but also calls for an effective control of the corresponding equivalence classes, which is then provided by the torus parametrization.

This is followed by the introduction of the important equivalence concept of mutual local derivability, or local equivalence. This paves the way for a

[1] A point set S is discrete if each point $x \in S$ can be surrounded by a non-empty open ball that does not contain any point from S except x. Note that uniform discreteness is a lot stronger than mere discreteness!

generalization of translation and space group concepts from "ordinary" crystallography, without using Fourier transforms. Also, this setting enables a simple and unified setting for inflation/deflation symmetries and perfect matching rules as invariants of local equivalence classes. After some speculations on a possible classification scheme (which is presently still pretty incomplete), a brief introduction to the alternative approach via so-called "random tilings" is given, which is, in a way, the stochastic counterpart of the theory of perfect quasiperiodic tilings.

2.2 Non-Crystallographic Symmetries

To understand the impact of the discovery of quasicrystals, we first have to know what non-crystallographic symmetries are (to be described in this section) and then why their appearance in the diffraction images of solids is, at least at first sight, astonishing (to be addressed in Sect. 2.3).

To begin with, we need some crystallographic concepts, in particular that of a lattice in n-dimensional (nD) Euclidean space. A set $\varGamma \subset \mathbb{R}^n$ is called a *lattice* if it is a discrete subgroup of $\mathbb{R}^n$ such that the factor group $\mathbb{R}^n/\varGamma$ is compact. This is equivalent to saying that there is a set of linearly independent vectors, basis of the lattice, such that

$$\varGamma = \mathbb{Z}\boldsymbol{b}_1 \oplus \cdots \oplus \mathbb{Z}\boldsymbol{b}_n, \tag{2.1}$$

i.e. $\varGamma$ consists of all integer linear combinations of the basis vectors. So, $\mathbb{Z}$ is a lattice in one dimension, and $\mathbb{Z}^2$ is one in the plane, but $\mathbb{Z}$ is not a lattice in two or more dimensions because its basis only spans a 1D ambient space.

Next, we call a set S periodic if $S + \boldsymbol{t} = S$ for some $\boldsymbol{t} \neq 0$. Such a $\boldsymbol{t}$ is a period of S. S is called *crystallographic* if its periods form a lattice, i.e. if its periods span ambient space [53]. If we now ask for the possible rotation symmetries of a crystallographic point set, we hit an obstruction, usually called the crystallographic restriction [68].

Theorem 1 *Let S be a crystallographic point set in $\mathbb{R}^n$, and R an orthogonal transformation that maps S onto itself. Then, R is of finite order, i.e. $R^k = \mathbb{1}$ for some k. In particular, we have $k \in \{1, 2\}$ for $n = 1$, and $k \in \{1, 2, 3, 4, 6\}$ both for $n = 2$ and $n = 3$. In general, the characteristic polynomial of R has integer coefficients only.*

The reason for this is that the invariance of S implies the invariance of its lattice of periods. The discreteness of the lattice forbids R from being of infinite order. Next, R must map the basis vectors onto integer linear combinations of them, so it must be similar to an integer matrix, from which the last statement follows. The case $n = 1$ is trivial, while $n = 2$ and $n = 3$ result from considering the traces of orthogonal matrices in their standard form: if φ is the rotation angle (around an axis in three dimensions), then $2\cos(\varphi)$ must be an integer.

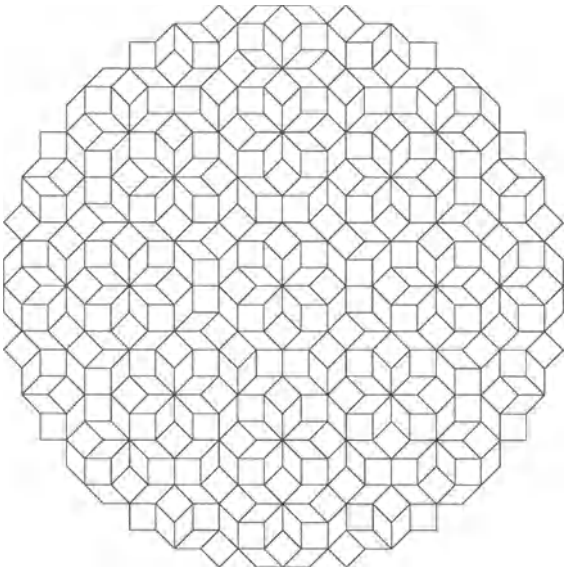

Fig. 2.1. The central patch of an exactly eight-fold symmetric ABT

As a consequence, the so-called Ammann–Beenker tiling (ABT) of Fig. 2.1, showing exact eight-fold symmetry even in the infinite area limit where it covers the plane, cannot be crystallographic [1,4,30]. What is more, it cannot possess any period, because the symmetry would immediately complete any single period to a basis of a lattice. Therefore, this is not a model of a 2D crystal, nor is any atomic decoration of its two cells, a square and a rhomb. The simplest such decoration, which is typical and exhaustive in a sense that we will understand shortly, consists of points on all vertices of the entire tiling. If we take the diffraction image of this, with scatterers of equal strength on all points, we nevertheless obtain an image that resembles that of crystals pretty closely; see Fig. 2.2. Let us thus turn our attention to diffraction for a while.

2.3 Diffraction

To simplify things, we will only talk about kinematic diffraction, i.e. diffraction that can be understood in terms of single scattering in the Fraunhofer picture. This is quite appropriate for X-ray and neutron diffraction, but not for electron diffraction where multiple scattering is essential [19]. Kinematic diffraction from a structure, in turn, is closely related to the Fourier transform of the corresponding potential in the sense that the observed intensities of sharp spots (Bragg peaks) are proportional to the absolute squares of the Fourier amplitudes [19].

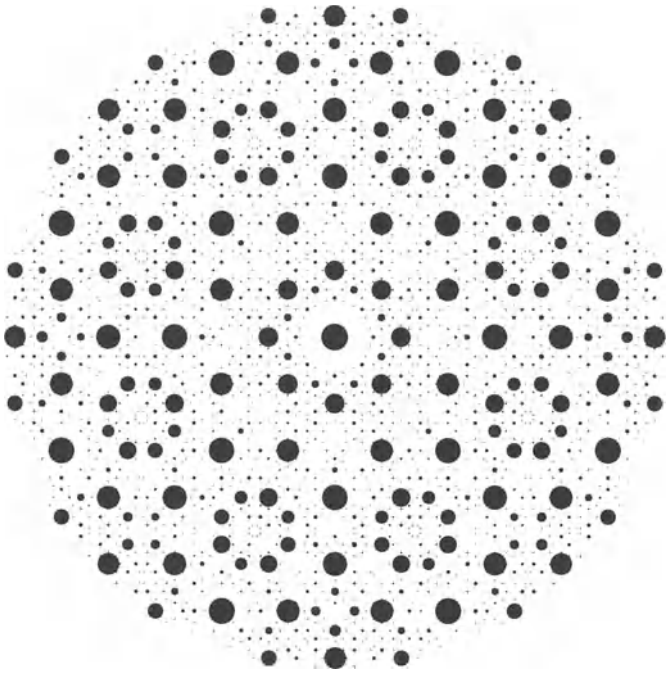

Fig. 2.2. A diffraction image of the ABT of Fig. 2.1. The area of each disc is proportional to the intensity of the corresponding peak, and the cut-off is at 0.1 % of the central intensity

In our idealized world, with atoms etc. replaced by point scatterers (Dirac distributions) on a set $\varLambda$, we thus consider the so-called Dirac comb of $\varLambda$,

$$\omega \;=\; \omega_{\varLambda} \;:=\; \sum_{\boldsymbol{x}\in\varLambda} \delta_{\boldsymbol{x}}\,, \tag{2.2}$$

where $\delta_{\boldsymbol{x}}$ is Dirac's distribution (or measure) at point $\boldsymbol{x}$, i.e. $(\delta_{\boldsymbol{x}}, \psi) = \psi(\boldsymbol{x})$ for all test functions ψ. Here, (T, ϕ) denotes the linear form defined by a distribution T acting on a test function ϕ [65]. In a second step, one defines a so-called *autocorrelation* or Patterson function [19]

$$\gamma_{\omega} \;:=\; \lim_{r\to\infty} \frac{1}{\mathrm{vol}(B_r(\mathbf{0}))} \sum_{\boldsymbol{x},\boldsymbol{y}\in\varLambda\cap B_r(\mathbf{0})} \delta_{\boldsymbol{x}-\boldsymbol{y}}\,, \tag{2.3}$$

where $B_r(\mathbf{0})$ is the (solid) ball of radius r around $\mathbf{0}$, $\mathrm{vol}(B)$ denotes the volume of B, and the limit is assumed to exist. Furthermore, we will tacitly assume that this limit stays the same if we replace the ball by any other convex region centered around the origin (with r interpreted as its inradius)

– actually a rather non-trivial feature to establish. The autocorrelation is a distribution of the form

$$\gamma_\omega \;=\; \sum_{\boldsymbol{z}\in\Delta} \nu(\boldsymbol{z})\delta_{\boldsymbol{z}}, \tag{2.4}$$

where $\Delta = \Lambda - \Lambda$ and the coefficient $\nu(\boldsymbol{z})$ equals the density of points $\boldsymbol{x} \in \Lambda$ such that, also, $\boldsymbol{x} + \boldsymbol{z} \in \Lambda$. In particular, the coefficient of $\delta_{\mathbf{0}}$ is $\nu(\mathbf{0}) = d = \mathrm{dens}(\Lambda)$.

The observed intensity pattern is now given by the Fourier transform of this autocorrelation, denoted by $\hat{\gamma}_\omega$. Here, the following convention for the Fourier transforms of functions is used:

$$\hat{f}(\boldsymbol{k}) \;=\; \int_{\mathbb{R}^n} \mathrm{e}^{-2\pi \mathrm{i}\boldsymbol{k}\boldsymbol{x}} f(\boldsymbol{x})\mathrm{d}\boldsymbol{x}, \quad \check{g}(\boldsymbol{x}) \;=\; \int_{\mathbb{R}^n} \mathrm{e}^{2\pi \mathrm{i}\boldsymbol{k}\boldsymbol{x}} g(\boldsymbol{k})\mathrm{d}\boldsymbol{k}\,. \tag{2.5}$$

With this convention, one has $\hat{\check{g}} = g$ and $\check{\hat{f}} = f$. Also, there is no need to distinguish between dual and reciprocal lattices (the factor 2π is absorbed into the argument of the exponential function) and the convolution theorem takes the nice form $\widehat{f * g} = \hat{f} \cdot \hat{g}$, where

$$(f * g)(\boldsymbol{x}) \;=\; \int_{\mathbb{R}^n} f(\boldsymbol{x}-\boldsymbol{y})g(\boldsymbol{y})\mathrm{d}\boldsymbol{y}\,. \tag{2.6}$$

Finally, the Fourier transform of a tempered distribution [65] T is defined by $(\hat{T}, \psi) := (T, \hat{\psi})$, as usual. In this way, the coefficient of $\delta_{\mathbf{0}}$ in $\hat{\gamma}_\omega$ is d^2.

Let us take a closer look at the diffraction from a lattice Γ. Here, $\Delta = \Gamma$ and, obviously, the autocorrelation coefficients are $\nu(\boldsymbol{z}) \equiv d = \mathrm{dens}(\Gamma)$. So

$$\gamma_\omega \;=\; d \sum_{\boldsymbol{x}\in\Gamma} \delta_{\boldsymbol{x}}\,. \tag{2.7}$$

It is now a direct consequence of the so-called Poisson summation formula that the diffraction image consists of Bragg peaks (or Dirac peaks) only. They are supported by the dual (or reciprocal) of the lattice of periods, and are hence distributed in a discrete fashion. The Poisson summation formula reads

$$\widehat{\sum_{\boldsymbol{x}\in\Gamma} \delta_{\boldsymbol{x}}} \;=\; d \cdot \sum_{\boldsymbol{y}\in\Gamma^*} \delta_{\boldsymbol{y}}, \tag{2.8}$$

with the dual lattice $\Gamma^* = \{\boldsymbol{y} \mid \boldsymbol{x}\cdot\boldsymbol{y} \in \mathbb{Z} \text{ for all } \boldsymbol{x} \in \Gamma\}$. Therefore, we obtain

$$\hat{\gamma}_\omega \;=\; d^2 \sum_{\boldsymbol{y}\in\Gamma^*} \delta_{\boldsymbol{y}}\,. \tag{2.9}$$

It is worthwhile to note that the Poisson summation formula (2.8) also provides an explicit form of the Fourier transform of ω itself, which is well-defined in this case. Since the autocorrelation is essentially a volume-weighted convolution $(*)$ of ω with itself, the convolution theorem explains why the

coefficients of $\hat{\gamma}_\omega$ are the absolute squares of those of $\hat{\omega}$. This is usually summarized in a so-called Wiener diagram:

$$\begin{array}{ccc} \omega & \xrightarrow{\ *\ } & \gamma_\omega \\ {\scriptstyle \mathrm{FT}}\downarrow & & \downarrow{\scriptstyle \mathrm{FT}} \\ \hat{\omega} & \xrightarrow{\ |.|^2\ } & \hat{\gamma}_\omega \end{array} \tag{2.10}$$

Whenever this situation applies, in the sense that all quantities exist and the diagram is commutative, things are rather simple. In particular, given the situation of a lattice, atomic profiles (extended scatterers) or more complicated decorations of a fundamental domain (multiple atoms per unit cell) can be incorporated by means of convolutions with ω and can then be processed through the Wiener diagram. Formally, the same process is then always used (at least for the Bragg part), but this needs extra justification, and often difficult analysis [34,71]. We will come back to this around (2.15).

This procedure seems perfectly well-defined and robust if applied to the diffraction from finite patches or samples, but the problems mentioned are then only shifted to the question of the sense in which larger and larger samples show diffraction images that converge – again, not at all an easy one.

What other situations give rise to well-defined diffraction? In other words, which distribution of matter diffracts? The answer to this question is far from clear. Therefore, we shall only sketch some aspects that are relevant to the understanding of the diffraction of quasicrystals and related structures. There is not much freedom to obtain sharp diffraction spots that are arranged in a discrete fashion, and this is indeed essentially restricted to diffraction from crystallographic arrangements (up to deviations of density zero, because the autocorrelation of a set of positive density is not changed by adding or removing points of density zero). Therefore, if one restricts one's attention to such sets, it is obvious that non-crystallographic symmetries cannot show up. This was the point of view of "classical" crystallography – and this was challenged by the discovery of quasicrystals.

Beyond any doubt, the observed diffraction spots of quasicrystals are sharp and show non-crystallographic symmetries, such as a five-fold axis or the full icosahedral group. The solution to the emerging puzzle lies in the answer to the question as to whether the distribution of spots is really discrete,[2] i.e. whether the spots are clearly separated from one another. For a given resolution, this seems to be the case – and this is certainly the reason why quasicrystals were discovered (for a given resolution, they show up through a

[2] We only talk about diffraction from "single crystals" here or its analog for quasicrystals. A somewhat similar discussion appears for diffraction from powders, but should be distinguished clearly, because this case has a rather different explanation; see Chap. 16 of [19].

discrete diffraction pattern). However, if one increases the sensitivity (e.g. by doubling the exposure time of the photographic plate), more peaks become visible, and this process does not come to an end: the set of all peaks would lie dense, and only those of an intensity beyond a given threshold result in a discrete pattern, similar to the diffraction of a crystal, but with non-crystallographic symmetry. One example has been shown in Fig. 2.1; another important example is the rhombic Penrose tiling (PT) [9,22,60] of Fig. 2.3.

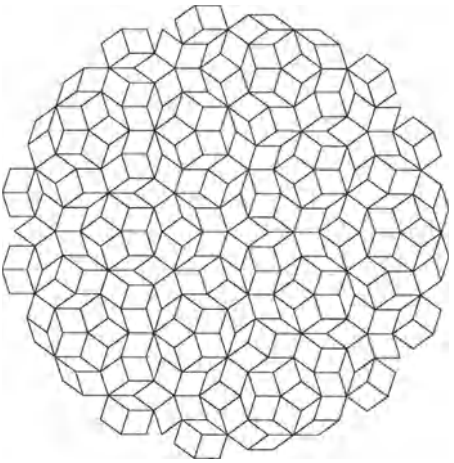

Fig. 2.3. An example of a rhombic PT

2.4 Quasiperiodicity and the Projection Method

It is now time to explain how such a strange diffraction behavior can come about. Its foundation goes back to the beginning of the 20th century, when Harald Bohr, the younger brother of Niels, developed what is now called the theory of almost periodic functions. Let us consider the example

$$f(x) \;=\; \sin(x) + \sin(\tau x), \tag{2.11}$$

where $\tau = (1+\sqrt{5})/2$ is the golden ratio. This is the most irrational number, as can be seen from its continued fraction expansion, whence $f(x)$ is certainly not periodic. Nevertheless, for any given $\varepsilon > 0$, there are "almost-translations" t such that $|f(x) - f(x+t)| < \varepsilon$, for all $x \in \mathbb{R}$. Furthermore, such translations are not rare, but lie relatively dense in $\mathbb{R}$, i.e. there is a maximal distance between any two consecutive ones. The set of continuous functions with this property is closed under uniform convergence, and can be uniformly approximated by trigonometric polynomials. This results in a generalization of a Fourier series, and this is essentially the core of Bohr's work [16]. For a more recent introduction, with additional material, see [18].

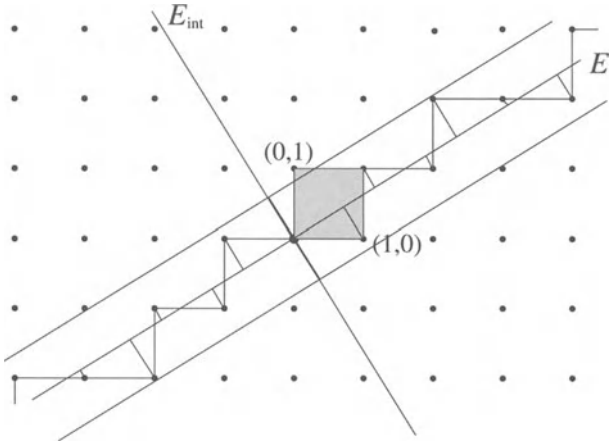

Fig. 2.4. The projection method for the Fibonacci chain and the torus parametrization of its LI class (cf. Sect. 2.7)

In these generalized Fourier series, pairwise incommensurate base frequencies occur (such as 1 and τ in the above example). If their number is finite, the corresponding function is called quasiperiodic. This subclass of functions has the property that it can be obtained as a section through a periodic function of more variables; e.g., in our example,

$$f(x) \;=\; \sin(x) + \sin(y)|_{y=\tau x}. \tag{2.12}$$

This is also the essential idea for understanding the diffractivity of quasicrystals; see [24,41,45] and various articles in [72].

Let us therefore construct non-periodic point sets by suitable sections through a crystallographic structure in higher dimension. As a first step, let us take a look at the so-called cut-and-project method, an example of which is shown in Fig. 2.4. Starting with the square lattice in the plane, $\mathbb{Z}^2$, a line E with an irrational slope is drawn, surrounded by a parallel strip of finite width. All lattice points inside the strip are then projected to E. The result is a sequence of points that forms a non-periodic Delone set (due to the irrationality of the slope – otherwise it would be periodic). If the slope (as in Fig. 2.4) is $1/\tau$, and if the width of the strip coincides with the projection of a fundamental square to the internal (in this case perpendicular) direction E_{int}, we obtain what is called the Fibonacci chain, the most common and best studied non-periodic 1D point set; see [29] for a tutorial introduction into the different possibilities for looking at this structure.

This projection scheme, which has an obvious generalization in higher dimensions, does not seem to be an exact analog of the section idea mentioned before, but it is equivalent to it. To see this, take the intersection of the strip with E_{int}, which is an interval here. This set, W, is called the window or acceptance domain, and our Fibonacci chain F is then given by

$$F \;=\; \{P(\boldsymbol{x}) \mid \boldsymbol{x} \in \mathbb{Z}^2 \;\text{ and }\; P_{\text{int}}(\boldsymbol{x}) \in W\}\,, \tag{2.13}$$

where P and P_{int} denote the canonical projections to E and E_{int}, respectively (for a more general and systematic formulation, we refer to [55,66,67]). The same set is obtained if, instead of using the strip method, we take an inverted copy of the window, $-W$, stitch it to each lattice point of $\mathbb{Z}^2$, and modify the rule by saying that we obtain a point of F whenever E cuts one of the copies. It can be considered as a target or a kind of atomic hypersurface, which is point-like in the direction of the "physical" space, E, and is extended only in "internal" space, E_{int}. A third method to describe the same object goes under the name of the "dualization scheme" and has the advantage of directly giving cells rather than point sets [9,47,58,66]. Note that we have not given a formal definition of a quasicrystal, and we will not do so because the present use of the word is far from being context-free, a really natural approach not yet being in sight. A reasonable working definition of a quasicrystal would include all discrete patterns that possess an autocorrelation whose Fourier transform (i.e. the diffraction) is either purely discrete or has at least a non-trivial discrete part.

In view of the Fourier transform, the construction method with the atomic hypersurfaces seems most attractive, because it is closest to the idea of describing a quasiperiodic arrangement of scatterers as a section through a crystallographic arrangement in higher dimensions. Now consider a Fibonacci chain, F, with point scatterers of equal strength on all its points, i.e. consider the Dirac comb

$$\omega_F \;=\; \sum_{x\in F} \delta_x \,. \tag{2.14}$$

By a simple (formal) calculation, one finds that the Fourier transform consists of Dirac peaks on all points $P(\boldsymbol{k})$, where $\boldsymbol{k}$ is a point of the dual of the embedding lattice. Its amplitude, $a(P(\boldsymbol{k}))$, is formally given by

$$a(P(\boldsymbol{k})) \;=\; \frac{d}{\mathrm{vol}(W)} \int_{-W} \mathrm{e}^{-2\pi \mathrm{i}\, k_{\mathrm{int}} x_{\mathrm{int}}}\, \mathrm{d}x_{\mathrm{int}}, \tag{2.15}$$

where $x_{\mathrm{int}} = P_{\mathrm{int}}(\boldsymbol{x})$ etc. and $d = \mathrm{dens}(F)$. The diffraction image is composed of Bragg peaks at the points $P(\boldsymbol{k})$ of intensity $|a(P(\boldsymbol{k}))|^2$. The derivation of this can be found in many articles, but has to be taken with a pinch of salt: it is purely formal, because the resulting expression for $\hat{\omega}_F$ is not a locally summable distribution and hence not a valid representation of a tempered distribution. That this formal way of calculating the intensities is nevertheless correct was proved only much later [34].

In what sense does all of this resolve the puzzle that we started from? If we take a closer look at (2.15), we realize that, if W is an interval, the absolute squares of the amplitudes are of the form $\sin(2\pi k_{\mathrm{int}})^2/(2\pi k_{\mathrm{int}})^2$, and hence are bounded by $c/|k_{\mathrm{int}}|^2$ with some constant c – and this means that only finitely many peaks per unit volume have an intensity beyond a given threshold, because $|k_{\mathrm{int}}|$ is the distance of the (dual) lattice point $\boldsymbol{k}$ from the cut space. A cut-off for the intensities thus has an effect that is similar to that

of the projection method itself! This is perhaps one of the most important observations in this context: a point set can be diffractive, and show a clear signature of this, without being crystallographic. If this is the case, then there is no longer any reason why non-crystallographic symmetries should not show up. If they do, however, we know immediately that the system cannot be crystallographic, and we would try to use the idea of a section through a lattice in higher dimensions to describe the structure.

Let me add another warning. The success of the projection method does not indicate that there is any need for higher-dimensional physics. It is only a convenient description of a certain class of ordered structures. Clearly, it is tempting to derive all sorts of generalizations of common properties and theorems (e.g. Bloch's theorem) by employing the embedding scheme and a chain of formal calculations. Quite frequently, this leads to wrong conclusions, and extreme care is required. For example, there is no easy analog of Bloch's theorem. In fact, its naive generalization fails just about as badly as is possible: In the infinite size limit, the standard tight-binding model on the Fibonacci chain has no bands at all, and the spectrum is neither absolutely continuous nor pure point, but purely singular continuous! In other words, it is precisely of the form that was argued to be impossible for physical structures not too long ago. For more on this, and on the existence of a Cantor-type gap structure with topological quantum numbers, see [2,13,74].

2.5 Minimal Embedding and Further Examples

In spite of the warnings given above, the projection method, if used properly, is an extremely powerful tool, e.g. for practically indexing a diffraction pattern. However, given a diffractive system with non-crystallographic point symmetry, what is the right embedding dimension (which equals the indexing dimension) to start from? Fortunately, the answer is known:

Theorem 2 *The description of a planar quasiperiodic point set with n-fold symmetry by means of the projection method requires a lattice of dimension at least $\phi(n)$. A 3D quasiperiodic point set with icosahedral symmetry requires an embedding lattice of dimension at least 6.*

Here, $\phi(n)$ is Euler's totient function, i.e. the number of positive integers less than n which are coprime to n. The proof of the icosahedral case is based on the representation theory of the icosahedral group [23]. The statement about the planar symmetries is a direct and rather simple consequence of the structure of the so-called cyclotomic polynomials; see Appendix A of [5] for an explicit proof.

Let us note that the minimal dimension is usually sufficient (unless one wants to describe "modulated" quasicrystals, where it doubles), and using more than the minimal number only results in ambiguities of the indexing scheme – an altogether undesirable feature.

Having settled the question for the correct dimension, we need to know what the "right" lattice is. It turns out that the higher-dimensional analogies of the square and cubic lattices, the hypercubic lattices, are not sufficient. The most common example where this becomes apparent is the PT of Fig. 2.3. It has five-fold (actually ten-fold) symmetry (cf. Sect. 2.6), and the above theorem then tells us that a 4D lattice is the right choice, because $\phi(5) = \phi(10) = 4$. However, it is not possible to use the lattice $\mathbb{Z}^4$ in this case. Very often, one finds a description of the PT based upon $\mathbb{Z}^5$ in which one extra dimension has been introduced. This has the disadvantage mentioned above. A simpler choice is the so-called root lattice A_4, which can be seen as the 4D lattice that is obtained by intersecting $\mathbb{Z}^5$ with the 4D hyperplane through the origin, and orthogonal to the space diagonal $(1,1,1,1,1)$. In general, root lattices provide a very nice class of simple lattices that is general enough to cover the observed cases [7] in a maximally symmetric way. For background material on root lattices, and all sorts of interesting connections to other branches of mathematics, we refer to the bible [17].

Let us briefly mention some other planar examples [29]. The ABT of Fig. 2.1 shows eight-fold symmetry, and requires a 4D lattice ($\phi(8) = 4$). The standard choice [4] is $\mathbb{Z}^4$, but the face-centered lattice in 4D is also possible, i.e. the root lattice D_4. The latter has the advantage that, with a different choice of the cut space, patterns with 12-fold symmetry ($\phi(12) = 4$, once more) can also be obtained [5]. Sometimes, 12-fold symmetry is easier to describe with another root lattice, namely $A_2 \times A_2$.

Most prominent, in this context, are tilings made from squares and equilateral triangles, such as that shown in Fig. 2.5. It is compatible with 12-fold symmetry (the triangles cover half the area), and was obtained by the projection method. Its window, however, shows a more complicated structure: it is a 12-fold symmetric region, is compact, is the closure of its interior, but has a fractal boundary; see Fig. 2.6. It is a well-accepted conjecture that all square–triangle tilings with 12-fold symmetry, obtained by projection, require a fractally shaped window, and, in a certain sense, the one of Fig. 2.5 is an example with a "maximally smooth" window boundary [6]: almost everywhere, the boundary is locally smooth (a line segment, in fact), but at an uncountable set of boundary points (of vanishing Lebesgue measure) the fractal dimension is non-integral, and rather close to 2.

After these planar examples, let us briefly sketch the situation in three dimensions. Clearly, there are the so-called T-phases (where T stands for "thumbtack", to mimic their geometric structure) which are quasiperiodic in a plane and periodic along the perpendicular line. They can be modeled by 3D tilings that are stacked layers, each single layer being made from prisms (as tiles) whose base pattern forms one of the classic planar tilings. Clearly, their Fourier image needs one extra Miller index, i.e. the Bragg peaks of standard decagonal T-phases are indexed by five integers, four being needed

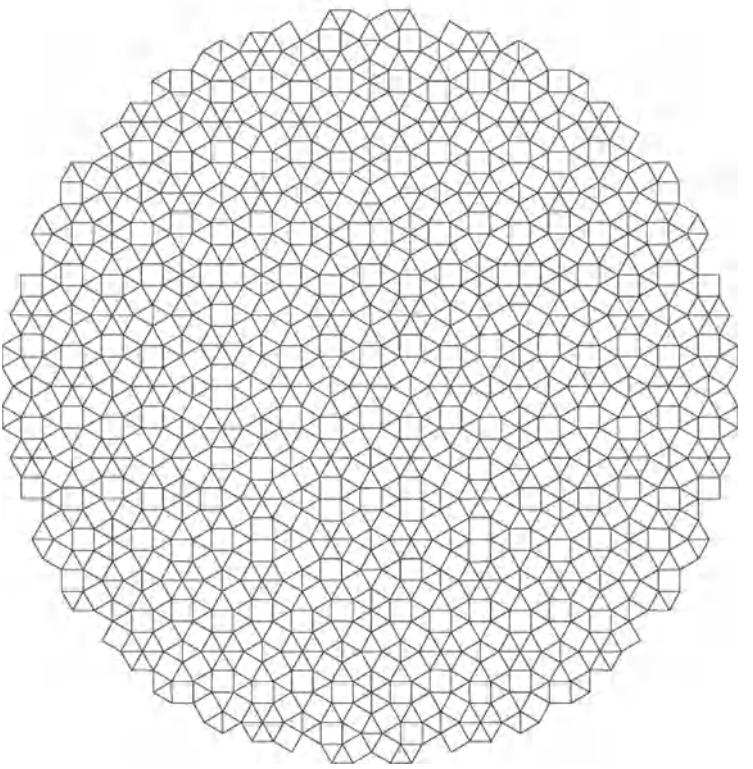

Fig. 2.5. A finite patch of a quasiperiodic square–triangle tiling

for the non-periodic planar degrees of freedom and one extra index for the periodic direction.

Of greatest importance, probably, are the tilings with icosahedral symmetry. Here, one has to distinguish three different types. All can be obtained by the projection method from hypercubic lattices in 6D space. There are three different Bravais types, primitive ($\mathbb{Z}^6$), face-centered (D_6) and body-centered (D_6^*) [68]. The three different icosahedral classes [23] are then also called primitive (or P-type), face-centered (F-type) and body-centered (B-type), respectively. Since no application of the B-type models is presently known, we will skip details of them.

The standard P-type tiling is made from two rhombohedra, an acute and an obtuse one. It has, in various degrees of completeness, a long history [73] and was first described by means of the projection technique by Kramer and Neri (KN) [45]. The diffraction shows icosahedral symmetry and a clear scaling with inflation multiplier τ^3. (The meaning of this will become clear in Sect. 2.11.) This is characteristic of P-type structures, and makes the distinction from F-type rather simple, as the latter displays scaling with an inflation multiplier τ (the same would be true of the B-type).

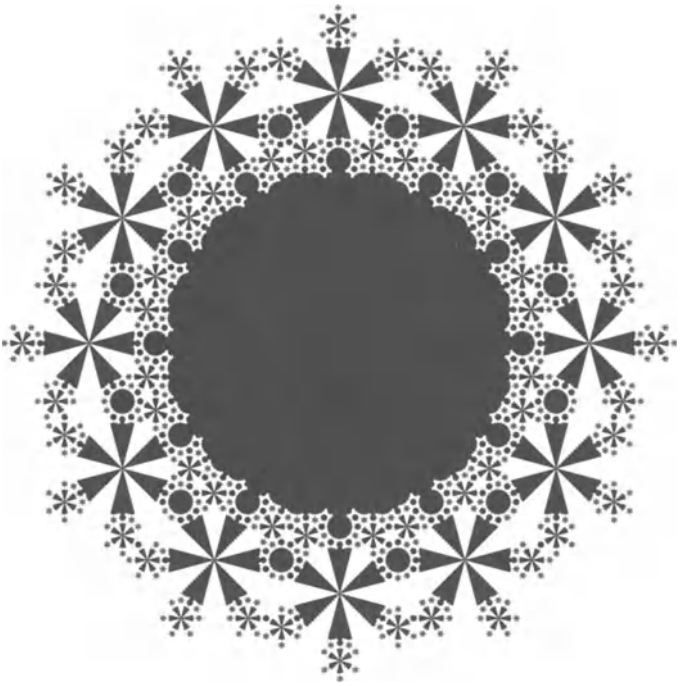

Fig. 2.6. The window for the square–triangle tiling of Fig. 2.5

The more important class (in terms of applications) is that of F-type tilings. One of the earliest examples is the zonohedral tiling [70] by Socolar and Steinhardt (SS). It is built from four proto-tiles, namely the acute rhombohedron met above, the rhombic dodecahedron, the rhombic icosahedron and the famous triacontahedron, also known as Kepler's body [30]. Another example [20], Danzer's tiling (DT), is very closely related (i.e. locally equivalent), as we shall see later. It is built from four tetrahedra. Finally, on the basis of the projection technique, several other F-type tilings have been investigated [8,46]. The most important, $\mathcal{T}^{*(2F)}$, is built from six tetrahedra and is again very closely related to SS and DT, although it contains more local information – a concept to be made more precise shortly.

Up to this point, no further mathematical details or concepts have been needed to gain a first impression (see [61] for a general construction scheme). However, for a better understanding of the structures, their symmetries and some of the new features, we now have to dive a little deeper into the world of discrete geometry. In particular, we definitely need some good tools with which to handle the zoo of possibilities. Later, we shall see that the number of "known" examples, at least those with "nice" properties, is actually rather small, and can be handled with little more difficulty than is needed for the crystallographic patterns.

2.6 LI Classes and Symmetry

One basic concept for the general analysis of global order properties of discrete structures is the equivalence concept of *local indistinguishability* (LI), also known as local isomorphism [50]. Since the latter term is used with a different meaning in other (connected) areas, we suggest replacing the word "isomorphism" by "indistinguishability" here. Since the infinite (mathematical) structure is considered as an approximation to large but finite physical objects, it is natural to identify those structures that are locally indistinguishable on arbitrarily large but finite scales.

We will use this term frequently in what follows, so for a precise definition we introduce some notation. The mathematical objects that we deal with are, most generally, discrete structures in Euclidean space, i.e. sets of (possibly decorated) bounded subsets of space which are locally finite in the sense that each ball of finite radius meets only finitely many structure elements. If A is such a discrete structure, then we call each subset of A that is completely contained in a ball of radius r an r-patch of A. Now, two structures A and B are locally indistinguishable if each r-patch of A is, up to a translation, also an r-patch of B and vice versa (a moment's reflection reveals that, in the general case, this "vice versa" is necessary to obtain a proper equivalence relation). The corresponding equivalence class of a structure is called its LI class.

It should be emphasized that this formal definition does not quite reflect the intuitive description of the first paragraph, because we have insisted on identity of r-patches up to translations only, rather than up to more general Euclidean motions. This more restrictive relation will prove useful for other concepts to be introduced in Sect. 2.7, and especially for the definition of generalized point symmetries.

One of the most outstanding properties of experimentally observed aperiodically ordered structures such as quasicrystals is the occurrence of crystallographically forbidden symmetries in their diffraction spectra, e.g. five-fold axes. On the other hand, it is clear that, for example, a 3D discrete structure can possess at most one axis of exact five-fold point symmetry in a given direction, because otherwise there would be a dense set of such axes, which is impossible for a locally finite structure. Therefore, to also take into consideration spatially homogeneous structures with non-crystallographic symmetry properties, one has to enlarge the symmetry concept slightly. This is easily done with the help of LI as defined above: we say that the isometric linear transformation T is a generalized point symmetry element of the structure A if, and only if, A and $T(A)$ belong to the same LI class.

What do these concepts mean in the crystallographic case? First, one sees at once that a structure A is locally indistinguishable from a crystallographic structure B if and only if there is a translation vector $\boldsymbol{t}$ which translates A to B: $B = \boldsymbol{t} + A$. As a consequence, in the crystallographic case, the

generalized point symmetry of a structure coincides with the conventional point symmetry, as it should do.

For aperiodic patterns, the generalized symmetry is a proper extension of exact symmetry. For example, the PT may have exact five-fold symmetry, i.e. there are precisely four representatives (up to translations) in its LI class LI(PT) which have one point of exact (global) five-fold symmetry each; most of the members of LI(PT) have no exact symmetry at all. The generalized point symmetry group of each element of LI(PT) coincides, however, with the symmetry group of the regular decagon, i.e. it is the dihedral group D_{10}. (The symbol D_n appears in two different meanings, once for the corresponding root lattice and once for the dihedral group of order $2n$. Since both are standard in the literature, and misunderstandings are unlikely, we will stick to this convention.)

2.7 Parametrization of LI Classes

Having given the definition of an LI class is not quite the same as understanding its structure. The latter is, in fact, more complicated than one might expect. To see this, let us first consider the case of a crystallographic pattern $\mathcal{P}$: its LI class $\mathrm{LI}(\mathcal{P})$ consists of all its translates, and can thus be parametrized by the points of a fundamental domain of the corresponding lattice, Γ, of translations (e.g. its Voronoi or Wigner–Seitz cell, to be specific) because $\mathcal{P} = \mathcal{P}+\boldsymbol{t}$ for all $\boldsymbol{t} \in \Gamma$. In particular, $\mathrm{LI}(\mathcal{P})$ simply consists of one translation class of patterns.

The correspondence between patterns in $\mathrm{LI}(\mathcal{P})$ and points of a fundamental domain is called the *torus parametrization* of $\mathrm{LI}(\mathcal{P})$ because such a domain, upon identifying Γ-equivalent boundary points, becomes a torus of the dimension of the lattice. Clearly, the answer cannot be this simple for non-crystallographic patterns. Here, $\mathrm{LI}(\mathcal{P})$ does not only contain all translates of $\mathcal{P}$, but also all other patterns that can be obtained as limits of these (w.r.t. the obvious topology of patch-wise comparison) – and "most" members are of the latter type. In fact, for repetitive[3] patterns, the LI class contains uncountably many ($2^{\aleph_0}$) translation (even congruence) classes [66] – so, things are a lot more complicated, and a parametrization would be handy.

It is not known how to achieve this in general, but, for certain patterns, it is indeed possible. Among these are those point sets and tilings that can be constructed by the projection method introduced in Sect. 2.3. Let us take another look at Fig. 2.4. This shows, in addition to the ingredients needed to visualize the projection mechanism, a shaded square that represents a fundamental domain of the lattice $\mathbb{Z}^2$. It becomes a 2D torus on identifying opposite faces in the usual way. Now, let us mark a special point of the line E by a handle (this can be thought of as a reference point for the pattern). If

[3] "Repetitive" means that for each radius r there is another radius $R = R(r)$, such that each $\mathcal{P}$-patch of radius r can be found in every $\mathcal{P}$-patch of radius R.

we move E around, and with it the strip, we obtain different cut-and-project sets for each position of the handle in the fundamental domain, but we do not get anything new beyond it, due to the periodicity of the embedding lattice. Therefore, the points on the torus parametrize different Fibonacci chains, and it is well known that one actually exhausts the entire LI class in this way [66]. This is the torus parametrization of quasiperiodic LI classes [3].

There is one subtlety that we have suppressed so far. The projection method is unique as long as no lattice point lies on the boundary of the strip – in which case the corresponding projected object is called regular. Such regular members form the majority of the LI class. In turn, situations in which lattice points fall on the boundary of the strip correspond to the union of several singular patterns, each of which can be seen as a limit of regular patterns. The singular patterns also belong to the LI class. In this new light, the torus parametrization is one-to-one for regular members of the LI class, but multiple-to-one for singular members. This point will become important in any potential classification of LI classes beyond the torus parametrization. We will briefly come back to this in Sect. 2.8.

In our Fibonacci example, the parametrization of singular members is two-to-one. An interesting question is how different from one another two such singular chains are. The answer relies on the structure of the window. As long as its boundary (the intersection of the strip with E_{int}) is of vanishing Lebesgue measure, the different singular members attached to the same torus parameter differ from one another only at places of zero density – hence, their identification is physically reasonable.[4] In turn, a vanishing Lebesgue measure of the boundary of the window does not seem to be too restrictive. In particular, the example of Fig. 2.6 is still included, as are all other compact sets in $\mathbb{R}^n$ with a boundary of Hausdorff (or fractal) dimension $< n$.

The great advantage of the torus parametrization is its universality, in the sense that we can use the same torus for all projection structures attached to the same embedding lattice and for the same choice of the cut space E. Some individual properties of the LI classes are then encoded in the precise way in which the singular members behave, but they are usually less important or even irrelevant for considerations such as symmetry, inflation invariance, etc. In particular, the torus parametrization allows us to find all members of an LI class that show exact invariance under a given symmetry operation, including new types of symmetry, such as inflation/deflation symmetry, to be discussed later. This is based on lifting the symmetry operation under consideration to a mapping on the torus. Then, the number of fixed points can be determined by calculating certain determinants. For details, together with explicit examples and a full treatment of the physically relevant symmetries, see [3,33].

[4] For certain applications, it is advantageous to distinguish regular and singular patterns and to adopt a topological point of view, e.g. for questions such as the spectra of Schrödinger operators [13].

Table 2.1. Point symmetries of the 64 inversion-symmetric tilings for the three different types of icosahedral LI classes

Group	B-type	P-type	F-type
Y_h	1	2	4
D_{5d}	18	12	0
D_{3d}	30	20	0
D_{2h}	15	30	60

An extension of this analysis to groups of transformations (rather than single operations) is possible, and it is instructive to look at subgroups of the icosahedral group and their actions on the three possible types of LI classes, see Table 2.1. In each case, there are precisely 64 inversion-symmetric members of the LI class, and they are distributed in a very peculiar way on the subgroups of Y_h, the full icosahedral group. To be more specific, there are two rhombohedral tilings in LI(KN) with full Y_h symmetry, one being regular and the other singular, while there are four such members in LI(DT), say, three regular and one singular. As a consequence of this analysis, and using the implications of LI, it must be concluded that F-type tilings or Delone sets have a denser distribution of clusters with exact (or almost exact) icosahedral symmetry – an idea pretty close to the concept of a Frank–Kasper phase. This would suggest that F-type icosahedral quasicrystals should be more frequent than P-type ones, as is indeed the case.

2.8 Local Derivability and MLD Classes

LI as defined above is certainly a useful tool for the study of various properties of individual tilings. However, for the description of more general aspects of their order (regardless of local details that might be more accidental), one has to extend the equivalence concept under consideration [11]. Let us make this vague statement a bit more concrete by considering a crystallographic structure. Its order is, up to a scaling factor, fully described by its space group, without caring about how the fundamental domain is actually decorated. Also, it does not matter which representative of the fundamental domain we actually choose – we can certainly transfer the detailed description from one choice to another in a strictly local way. Now, in the aperiodic case, the (naively defined) space group is almost always trivial and therefore cannot serve as a classification tool. One way out is to consider the diffraction intensities of the structure [54,63]. Although this (non-rigorous!) approach works for a large class of structure types, it has a number of shortcomings. First, it is confined to the case of structures which show Bragg diffraction, i.e. are essentially almost periodic. Next, the method is indirect – namely, working in $\boldsymbol{k}$-space – and therefore offers no good intuition for the things going on in real

space. Finally, such an approach might lead to a rather coarse picture, not distinguishing between locally inequivalent structures. This does not happen in the crystallographic case, but it does so in the extension of this approach to quasicrystals.

To describe an appropriate alternative, let us consider, as an example, two tilings which certainly are to be considered equivalent: the PT and its Robinson decomposition (RD) into isosceles golden triangles [9]. By definition, there is a clear-cut rule for transforming a PT into its corresponding RD, and it is not hard to see that, for a given RD, the underlying PT can be reconstructed at each location by observing just a few triangles in the vicinity; see Figs. 2.3, 2.7 and 2.8. In particular, this means that we can transfer any decoration of RD into one of PT, and vice versa – eventually for the price that we have to distinguish several congruent copies of the proto-tiles from one another, depending on their (uniformly!) local neighborhood in the tiling.

Let us put this type of equivalence into more formal terms. It is clear that the details of the transformation process described above are not important, e.g. we will certainly not care about tiles being properly dissected or composed, or in fact about tiles at all: quite frequently a representative discrete point set [43] is what one really needs or wants! The essential feature that allows the abstraction from local details while keeping track of the global order is the uniform locality of the transformation rule. It is easy to see that such a uniformly local rule for the transformation of some structure A into a structure B exists precisely under the following condition: there is a fixed finite radius r such that if the r-patches of A around two points, $\boldsymbol{p}$ and $\boldsymbol{q}$, are equal up to the translation $\boldsymbol{t} = \boldsymbol{p} - \boldsymbol{q}$, then the structure B at the points $\boldsymbol{p}$ and $\boldsymbol{q}$ is the same, again up to the translation $\boldsymbol{t}$.

If this condition is fulfilled, then we call B locally derivable [12] from A. If it is also fulfilled with the roles of A and B interchanged (with a possibly different radius r'), then we call A and B *mutually locally derivable* (MLD) from one another, or locally equivalent.

It is clear that this equivalence relation can be extended to entire LI classes. That is, if A and B are locally equivalent, then, for any A' in the LI class of A, some B' can be found in a canonical fashion (just using "the same rule") such that A' and B' are locally equivalent, thereby defining a one-to-one correspondence between the two LI classes. Therefore, we can combine these equivalences defining the MLD class of a structure A to be the set of all structures that are locally indistinguishable from some structure that is

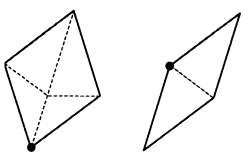

Fig. 2.7. Robinson's decomposition of the PT

locally equivalent to A. Needless to say that PT and RD in the above example belong to the same MLD class in this sense.

Let A and B be locally equivalent structures. Obviously, if A is invariant under a certain translation $\boldsymbol{t}$, then B must be invariant under $\boldsymbol{t}$ as well, by the very definition of local equivalence. A little further reflection shows that, on the other hand, if A and B are crystallographic with the same translation lattice, $\varGamma$, then they are locally equivalent, by "transformation rules" involving only a couple of fundamental domains. Therefore, local equivalence is a generalization of "having the same translation lattice" in the periodic case:

Theorem 3 *Two crystallographic patterns, A and B, are locally equivalent if and only if they share the same translation lattice $\varGamma$.*

This result also explains why we restricted our definition of LI (or patch-equivalence) to translations only, rather than using a version involving congruence. Below, we will refine the MLD concept in order to achieve a generalization of the space group classification.

2.9 Local Equivalence and Limit Translation Module

In general, it may be a difficult problem to decide whether or not two given structures are locally equivalent. As one tool for this task, we introduce an object associated to each discrete structure. It also generalizes the translation lattice of a periodic structure in a certain sense, but contains less information.[5]

Let A be a discrete structure. For each radius r, one can collect all translation vectors $\boldsymbol{t}$ which "move patches inside A", that is, for which an r-patch P exists in A such that the translate $\boldsymbol{t} + P$ is also an r-patch of A. These translation vectors for fixed r generate a $\mathbb{Z}$-module, $\varLambda_r$, which simply consists of all integer linear combinations of the translations found. This module gets smaller if r becomes larger: $r \leq r'$ implies $\varLambda_r \supseteq \varLambda_{r'}$. This property allows us to define a limit,

$$\varLambda := \bigcap_{r>0} \varLambda_r, \tag{2.16}$$

which is again a $\mathbb{Z}$-module. We call $\varLambda$ the *limit translation module* (LTM) of the structure A. It is obviously an invariant of LI classes.

In the crystallographic case, the LTM is just the translation lattice itself. On the other hand, in the general case, $\varLambda$ may turn out to be trivial, and this might even be the "typical" situation. However, there is a large class of structures where this LTM is non-trivial and provides important information on the order of the structure, among them being point sets or tilings obtained by the projection method. In any case, the LTM is an invariant of MLD

[5] This slightly more difficult section may be skipped on first reading.

classes: if A and B are locally equivalent, then their LTMs must coincide; furthermore, if B' is locally indistinguishable from B, then its LTM is the same as well. On the other hand, if B is derivable from A, one can only conclude that $\mathrm{LTM}(A) \subseteq \mathrm{LTM}(B)$. Therefore, the determination of the LTM is a natural first step for proving or disproving the local equivalence of two given structures.

That the LTM does not specify the MLD class completely, even if it is non-degenerate, can also be studied in the special case of cut-and-project patterns as introduced above. If A is such a quasiperiodic structure, minimally embedded [66] into the periodic structure S (this is important!), then $\mathrm{LTM}(A)$ turns out to be just the projection image of $\mathrm{LTM}(S)$ (i.e. its lattice of translations, which then serves as the embedding lattice) into the subspace containing A, i.e. into E. This also explains the connection of $\mathrm{LTM}(A)$ to the Fourier module of A in such a situation: the latter is the (generally dense) set of points in $\boldsymbol{k}$-space where we have to expect Bragg peaks. It is obtained by projecting the dual of the embedding lattice into E, as explained earlier. However, given the higher-dimensional lattice and the cut space, the quasiperiodic structures obtained by cut-and-project are by no means all in the same MLD class.

In fact, one has the following simple necessary and sufficient criterion for two cut-and-project structures to share the same MLD class: it must be possible to reconstruct the acceptance domains of A from those of A' by finitely many union, intersection and set complement operations, and vice versa (for a more detailed account of the relationship between the projection formalism and local derivability, see [12]). In this way, one can actually prove that PT and the so-called Tübingen triangle tiling (TTT), another decagonal tiling built from the golden triangles (see Fig. 2.8 and [9]), are not in the same MLD class (although it is possible to rescale PT such that it becomes locally derivable from TTT). These two LI classes actually differ in the distribution of singular tilings, and the transformation rule from TTT to PT maps certain sets of singular tilings of LI(TTT) onto single, but regular, members of LI(PT) – something that clearly cannot be inverted. This is remarkable, as TTT and PT certainly have the same space group according to [63], i.e. they cannot be distinguished on the basis of the symmetry properties of their Fourier transforms.

2.10 Local Derivability and Symmetry Preservation

The careful reader will have noticed that we did not include rotations etc. in the definition of local derivability – for very good reasons. Nevertheless, symmetry is important, in particular for many physical applications, and it is obvious how to include it by one further step of refinement [11]. Let us say that a certain local derivation rule preserves the symmetry of a structure if the derivation rule and the symmetry operation commute. This then de-

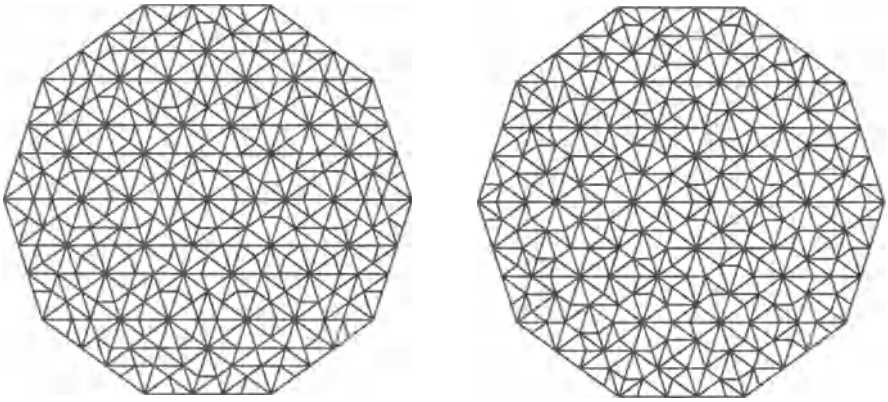

Fig. 2.8. Decagonal patch of the TTT (left) versus RD of the rhombic PT (right)

fines symmetry-preserving (S-)MLD classes which obviously form (pairwise disjoint) subclasses of MLD classes.

As in the case of MLD classes, the specialization of the S-MLD concept to the periodic case fits well into classical crystallography: two crystallographic structures belong to the same S-MLD class if and only if their space groups are identical (for a true generalization of the crystallographic classification scheme of periodic structures, one has to broaden the S-MLD classes by allowing for global similarity transformations). Simultaneously, this fact shows that S-MLD is a proper refinement of MLD, i.e. there are MLD classes that contain several S-MLD classes. An aperiodic planar example of such a form of behavior will be given at the end of Sect. 2.11.

In 3D space, SS and DT are in the same S-MLD class [21,64]. Therefore, in this sense, they really describe the same class of structures. One of the D_6-based tilings allows the local derivation of DT from it, but there is no local rule to go back to the D_6-based tiling – a 3D analog of the situation previously met with TTT versus PT.

2.11 Inflation Symmetries and Matching Rules

Let us now investigate how the MLD concept works in the context of two outstanding properties which important aperiodic structures exhibit: inflation/deflation (I/D) symmetry and perfect matching rules (MRs) (cf. [40,42, 49,51,53] for commonly used definitions).

As there are various I/D concepts in the literature, we have to be precise about what we mean, thereby taking the opportunity to put the MLD concept into operation. Usually, a deflation of a structure consists of a certain rule for a local transformation of structure elements into patches of a new structure which turns out to be of the same type as the original one, but on a smaller scale. For example, the dissection of the golden triangles depicted in Fig. 2.9

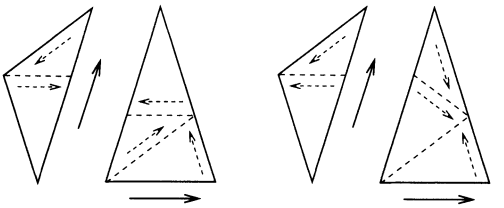

Fig. 2.9. The inflation rule for TTT (left) and RD (right)

gives the inflation rules both for the triangles of TTT and of RD. So far, this does not seem to be too interesting, as one can carry out this sort of procedure with the periodic tiling of the plane by squares. However, in certain cases, such an operation does not result in any loss of information on the original structure, i.e. it is possible to recover it by an inverse transformation, also in a local fashion.

Re-reading the definitions in recent sections, one sees that the above description is precisely what is meant by the following formal definition: a structure A has an I/D symmetry related to a similarity transformation T if $T(A)$ is in the same MLD class as A (i.e. if $T(A)$ is locally indistinguishable from a structure which, in turn, is locally equivalent to A – it is necessary to phrase it in this way because the situation in which $T(A)$ is already locally equivalent to A is too special).

From Sect. 2.10, we may conclude that no periodic structure can have any I/D symmetry related to a non-trivial T, i.e. where T is not just a rigid motion. The reason can be glimpsed from the following example: subdividing the square cells of the lattice $\mathbb{Z}^2$ into smaller squares of half the edge length, say, is obviously a local rule. But the converse, re-grouping four adjacent squares into a larger square, is not – it requires knowledge of where the process was started to guarantee fault-free operation, and this means that it is not possible by a local rule. On the other hand, the existence of non-trivial I/D seems to be a very common feature among the interesting aperiodic structures [53]. In many cases, T is just a rescaling, but there are important examples where rotation–dilations are needed, as in certain 2D tilings with 12-fold symmetry [5,56]. We have the following:

Theorem 4 *The existence of an I/D symmetry is a property of an entire MLD class: either all members share it, or none has it.*

This fact may be exploited into two directions. First, having established the existence of I/D for a single structure, one already has I/D for its entire MLD class. Second, simultaneous (non-)existence of I/D provides a necessary criterion for two structures to be locally equivalent.

The study of perfect MRs is another subject where the concept of local equivalence proves fruitful. We say that a structure A possesses perfect MRs (essentially in the sense of [51]) if its LI class is determined by the set of its r-patches for some finite radius r (which we call, if chosen minimally, the MR radius of A), i.e. if every other structure which contains, up to translations,

only r-patches which also occur in A necessarily belongs to the LI class of A. In the case of LI(PT), a very simple version in terms of tiles with oriented edges can be given [28]. For obvious reasons, this property of a structure is particularly interesting in the case in which this structure is supposed to describe the global order of physically realized structures such as quasicrystals [40,42]. One may think of a Hamiltonian that favors the patches of the atlas, in this way restricting the ground state to a member of the LI class.

It is almost immediate that every structure that is locally equivalent to one with perfect MRs must itself possess perfect MRs:

Theorem 5 *The existence of perfect MRs is a property of an entire MLD class: either all LI classes contained in this MLD class possess perfect MRs, or none of the LI classes can have them.*

Note, however, that the MR radius is not an invariant of MLD classes. This is of some relevance in the physical context, if one tries to relate the MRs to the local interaction of some suitable Hamiltonian, i.e. if one searches for a Hamiltonian whose ground states form a specific LI class with perfect MRs. This is due to the fact that the information contained in a structure may be delocalized (gradually) by the local derivation of another structure. An estimate for the MR radius of a structure A which is locally equivalent to a structure B with perfect MRs [27] involves the MR radius of B and the relevant radii for the transition from B to A, and vice versa. It is an interesting question to ask what the infimum of all MR radii of the LI classes inside one MLD class is. It has been conjectured that it might actually be zero under some mild extra condition. This is rather plausible for systems with I/D symmetry, as shrunk-down representatives exist on arbitrarily small scales.

It should be noted that there are certain tilings, such as the Ammann–Beenker octagonal tiling [1] or Gähler's dodecagonal "shield" tiling [26], which do not possess perfect MRs if one considers only undecorated tiles, but can be transformed into structures with MRs by convenient decorations. In these cases, the introduction of the decoration cannot be achieved in a local fashion [26]: the naked and decorated tilings form different MLD classes and should therefore be distinguished clearly [44].

One might ask about the number of different possibilities of constructing tilings of a given symmetry with perfect MRs (e.g. for the 8-, 10- and 12-fold symmetric cases [52]). Here, one is not interested in the (infinite) variety of representatives of one and the same MLD class, but in different MLD classes with perfect MRs, such as those defined by LI(PT) and LI(TTT). At the moment, the only candidate for an infinite family of different tilings with perfect MRs is provided by the generalized Penrose patterns [49] with parameter $\gamma = m + n\tau$. A closer inspection [36,49] shows that these tilings belong to only one MLD class, or to two S-MLD classes – one with fivefold and one with tenfold symmetry (which contains LI(PT)). This analysis has been extended [49] to rational values of γ, which results in an entire tower of LI classes that allow a local derivation down the tower, but not upwards.

On the bottom of this tower, we find a well-known friend: the rhombic PT. Similar towers certainly exist for other examples, e.g. in 3D space, but, to our knowledge, they have not yet been analyzed in detail.

2.12 A Summary of the Perfect World

So far, it has been outlined, in rather elementary terms, how equivalence concepts such as LI and MLD are helpful in sorting out local properties of locally finite tilings or other discrete patterns. Furthermore, we believe that concepts along the lines presented above are needed to continue a sound classification program of aperiodically ordered structures, and for various aspects it is advantageous not to depend on Fourier transforms.

Let us continue with a speculation. We have seen that there were serious connections between different examples of patterns with perfect MRs. An interesting question is how serious these connections are. From the past 15 years of research on quasicrystals and aperiodic order, we have the feeling that the variety of S-MLD classes with all magic properties is limited, if organized properly. To this end, one has to form towers of them, in which two consecutive members allow a local derivation down the tower, but not up – as in the case of MLD(TTT) being on top of MLD(PT). With this, we tend to the following conjecture: the number of towers of quasiperiodic S-MLD classes with fixed symmetry, LTM of minimal rank,[6] local I/D symmetry (with fixed inflation multiplier) and local perfect MRs is finite.

This statement is rather fragile: essentially, removing any of its conditions makes it invalid. Therefore, a further exploration of this question (and a proof or disproof) would be a logical next step in the classification of aperiodic structures – complementing and perhaps even completing the existing classification of Fourier modules [38,54] (mainly based on symmetry alone).

Although a good classification of order, even along these lines, is not in sight (and it might actually be very far away), one should not shut one's eyes to other possibilities. In fact, even if we had the answer to the above question, it would not be sufficient physically: so far, we have totally, and deliberately, ignored any stochastic aspect of point sets or tilings. This is not really tolerable, and Sect. 2.13 is devoted to a very brief and sketchy introduction to a totally different (but, fortunately, not totally disconnected) universe.

2.13 Alternatives: Disorder and Random Tilings

The first indication on incompleteness of the above approach comes from the observation that quasicrystals will also show defects (in fact, probably more

[6] Minimal w.r.t. the symmetry, e.g. rank 4 for ten-fold symmetry in the plane or rank 6 for icosahedral symmetry in 3D space.

than ordinary crystals), and one would like to know the possible scenarios. As a first step, one can investigate so-called defective vertex configurations within the geometric setting of a tiling; cf. [14] for a survey. Although this provides rather interesting insights, and even allows for some simplistic, but not too unrealistic, models, we shall focus here on an alternative to perfect tilings or Delone sets that starts from a rather different, if not opposing, point of view.

The above discussion has implicitly concentrated on discrete structures that could be seen as idealizations of energetically stabilized structures, and LI classes with perfect MRs may be interpreted in this way: in principle, there exists a Hamiltonian whose ground state is necessarily an element of the LI class defined by the perfect MRs. Although this idea seems attractive, it has a number of pitfalls. On the one hand, such a Hamiltonian will be rather artificial and unrealistic, and on the other hand, such MRs do not lead to local growth rules [28,59] unless the structure is crystallographic. Therefore, even if MRs can provide a toy model for energetic stabilization, they cannot explain why quasicrystals form and how they grow. A similar problem is also present in a slightly relaxed scenario, known as "maxing rules" [31,39].

An alternative or complementary idea is provided by statistical physics. Recall that stability is related to minimizing the free energy, which is given as $F = U - TS$, where U is the internal energy, S is the entropy and T is the temperature. Therefore, stabilization can also have a significant entropic contribution, and we will now briefly sketch some ideas that have been developed along that route. To this end, we assume that U is essentially degenerate, and thus that minimizing F means maximizing S. Therefore, we are talking about an idealization (first pointed out by Elser [25]) which corresponds to a high-temperature phase – a picture that is not at all absurd in view of the experimental observations!

Let us go back to the Fibonacci chain for a moment. It showed two different atomic distances a and b, say, between neighboring points. Their arrangement is entirely deterministic, with frequencies $1/\tau$ and $1/\tau^2$, respectively. Furthermore, one can show that precisely $n+1$ different words (in a and b) of length n occur in an infinite Fibonacci chain – no matter which representative of its LI class we take. Therefore, its (combinatorial) entropy density per letter vanishes, as can easily be calculated:

$$s = \lim_{n\to\infty} \frac{\log(n+1)}{n} = 0. \tag{2.17}$$

The same phenomenon happens for the entropy density of all other deterministically ordered structures obtained by the projection method or by an inflation rule [15]. This is caused by the inherent long-range repetitive order of those structures, which is also the reason for a well-defined diffraction spectrum.[7] Therefore, if we want to introduce some entropy, we have to go

[7] Inflation-generated tilings need not have a pure point diffraction spectrum. This depends on the nature of the inflation multiplier [71].

beyond such structures, but we certainly want a scheme that does not totally destroy the long-range (orientational) order.

The simplest idea is to relax the possible configurations of letters. If we allow any sequence of a's and b's subject to the sole restriction that their frequencies ν_a and ν_b match those of the Fibonacci chain, we obtain a Bernoulli-type ensemble of infinite chains, this time with a positive entropy density:

$$s = -\nu_a \log(\nu_a) - \nu_b \log(\nu_b) = \frac{\tau+2}{\tau+1} \log(\tau) \simeq 0.665\,. \tag{2.18}$$

This (essentially unrestricted) ensemble has two disadvantages: first, the maximal entropy would occur for $\nu_a = \nu_b = 1/2$ as $\log(2) \simeq 0.693$, and not for the Fibonacci frequencies. Second, the new ensemble is so random that the typical ensemble member no longer shows sharp diffraction peaks. Consequently, this model is not suitable for an explanation of Fibonacci-type structures.

To overcome these difficulties, at least in dimensions two and higher, the idea of a *random tiling* was put forward by the Cornell group [32]. Starting from the same proto-tiles as in a perfect quasiperiodic tiling, one allows all gap-less space-fillings that are face-to-face and overlap-free, and eventually subject to further restrictions. It is this set of local, geometric constraints that transforms the unrestricted Bernoulli-type ensemble into a more interesting and realistic Markov-type ensemble. For example, one could start from the two rhombs of the PT of the plane but relax the MRs. In this way, one obtains a random tiling ensemble with a unique entropy maximum at the tile frequencies of the perfect tiling, and this maximum also corresponds to the unique point (in parameter space) of maximum symmetry, D_{10}. So far, the situation seems to be considerably improved. However, the diffraction side is not yet fully satisfactory: such planar tiling ensembles display sharp peaks, but there are, in general, no Bragg peaks.

Since we live in three dimensions, we should ultimately be concerned only with that situation. But then, carrying out the analogous exercise with the tilings of 3D space by the two rhombohedra mentioned earlier, we again find the entropy maximum at the point in parameter space that shows icosahedral symmetry. This time, because statistical fluctuations of a 3D ensemble are bounded, the diffraction would still show Bragg reflexes, plus a structured diffuse background. Furthermore, the entropy around the maximum, as a function of the parameters (e.g. the densities of different proto-tiles), is a strictly concave function, with the maximum being locally quadratic. This allows us to develop a kind of entropic elasticity theory around the maximum, and the corresponding symmetry-adapted invariant forms are characterized by what are called the elastic constants [32].

We have now met the basic ingredients. The collection of all tilings of nD space from a given set of proto-tiles (face-to-face, gap-less and overlap-free, as usual, plus, eventually, some extra constraints) is called a random tiling ensemble if it has a positive entropy density in the sense that the number

of possibilities of covering a ball of radius r grows exponentially in r^n. Such ensembles, if well-defined statistically, have some rather general features, two of which are often stated as kinds of axioms. They are the so-called random tiling hypotheses (RTHs) [32] which, in our language, read as follows:

RTH1. The point of maximum entropy is automatically a point of maximum symmetry.

RTH2. The entropy, around the maximum, is a locally quadratic function of the parameters.

It might be interesting to note that RTH1 is actually a theorem and follows by some group-theoretic arguments from considerably simpler assumptions. The status of RTH2, however, is more difficult: this really is an assumption that has to be verified, as explicit counterexamples are known [62].

To give an impression, let us, at this point, present one example of a planar random tiling, made from two proto-tiles, a rhombus and a dart – see Fig. 2.10. Both proto-tiles are built from two copies of an isosceles triangle, and thus they share the same area. Rhombs occur in three orientations, and darts in six. In addition to the usual rules about putting them together, we also demand that the rhombs observe an alternation rule, i.e. no two rhombs that are mere translates of one another are allowed to share an edge. This is one of the very few non-trivial examples that can be solved completely, in an exact and even rigorous way, by methods from statistical mechanics. Although it is only compatible with six-fold symmetry (and could thus be called a crystallographic random tiling ensemble), it shows many features that are also typical of "quasicrystalline" random tilings (although the diffraction is different). In particular, it displays a unique entropy maximum of quadratic nature [RTH2] at the point of maximal symmetry [RTH1]. Furthermore, somewhere else in the phase diagram, it shows an order–disorder phase transition (of Onsager type) which can alternatively be interpreted as a percolation phase transition [35,62]. In Fig. 2.11 we show a typical snapshot from the ensemble at its entropy maximum, which turns out to be

$$s \;=\; \tfrac{1}{3}\log(2) \;\simeq\; 0.231\,. \tag{2.19}$$

This result is so simple that it must be, and is indeed [35,62], possible to give a direct derivation of it, without referring to the somewhat elaborate exact solution of the underlying dimer model.

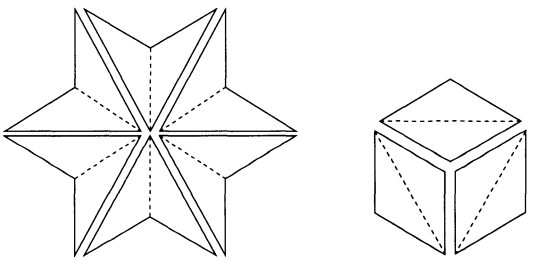

Fig. 2.10. Proto-tiles of the dart–rhombus random tiling

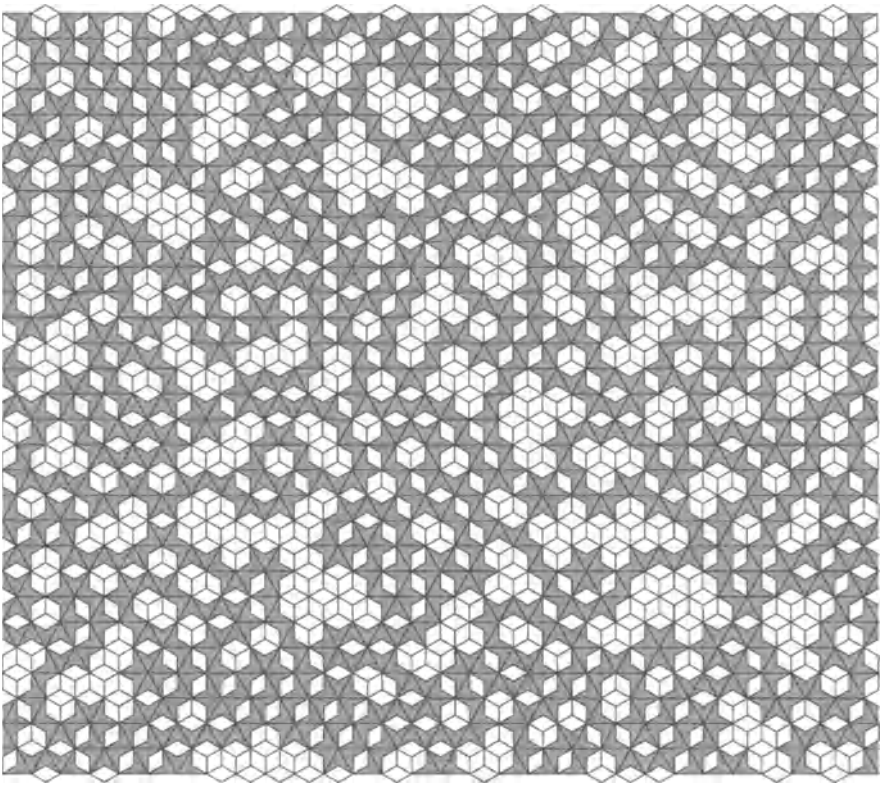

Fig. 2.11. A snapshot of a dart–rhombus random tiling at maximum entropy

2.14 Concluding Remarks

After this little excursion into the world of aperiodic order, one should realize that the displayed material was not only a short (and possibly insufficient) glimpse – it was also highly biased. This resulted not so much in a strange view at the things discussed, I hope, but in the omission of many other aspects – often fascinating, sometimes frustratingly complicated, occasionally in the t2c2e-category[8] or just unnoticed by the ignorant author. But, even 20 years after the field took off, it is still in its infancy, and any other statement runs the risk of delusive security. It is amazing how many things seem to be known, or almost known, and how few of them are really established, or fully known. And, for many aspects, we have just scratched the surface.

In view of this, I should try to mention some of the points not discussed above. However, even that would be biased again, and it is probably better to give the advice to read on in this volume, and to consult the introductory

[8] Things too complicated to explain, at least on a few pages.

articles from other summer or winter schools, some of which are given in the references below. Anyway, one "take-home" message should be to remain open-minded to new aspects, to challenge "common knowledge", to follow interesting paths and – last but not least – to have fun!

Acknowledgments

This survey is partially based upon results obtained in collaboration with a number of colleagues, in particular with Uwe Grimm, Dieter Joseph, Peter Kramer, Robert V. Moody, Peter A. B. Pleasants and Martin Schlottmann. Many results would not be in their present form without this cooperation. Also, I am grateful to my students Moritz Höffe, Joachim Hermisson and Christoph Richard for their help and supply of material. Finally, I would like to thank Shelomo I. Ben-Abraham, Veit Elser, Franz Gähler, Albertus Hof, Jeffrey C. Lagarias and Hans-Ude Nissen for valuable discussions. Many other names should be mentioned here, but I apologize for not doing so and hope that the selection of references is a valid substitute.

References

1. Ammann R., Grünbaum B., Shephard G.C. (1992): Discr. Comput. Geom. **8**, 1
2. Baake M., Grimm U., Joseph D. (1993): Int. J. Mod. Phys. **B7**, 1527
3. Baake M., Hermisson J., Pleasants P.A.B. (1997): J. Phys. A **30**, 3029
4. Baake M., Joseph D. (1990): Phys. Rev. B **42**, 8091
5. Baake M., Joseph D., Schlottmann M. (1991): Int. J. Mod. Phys. B **5**, 1927
6. Baake M., Klitzing R., Schlottmann M. (1992): Physica A **191**, 554
7. Baake M., Kramer P., Joseph D., Schlottmann M. (1990): J. Phys. A **23**, L1037
8. Baake M., Kramer P., Papadopolos Z., Zeidler D. (1991): in *Group Theoretical Methods in Physics*, ed. V.V. Dodonov, V.I. Man'ko, Springer, Berlin, p. 543
9. Baake M., Kramer P., Schlottmann M., Zeidler D. (1990): Int. J. Mod. Phys. B **4**, 2217
10. Baake M., Moody R.V. (eds.) (2000): *Directions in Mathematical Quasicrystals*, CRM Monograph Series, vol. 13, AMS, Providence, RI
11. Baake M., Schlottmann M. (1995): in *Quasicrystals*, ed. C. Janot, R. Mosseri, World Scientific, Singapore, p. 15
12. Baake M., Schlottmann M., Jarvis P.D. (1991): J. Phys. A **24**, 4637
13. Bellissard J., Bovier A., Ghez J.M. (1992): Rev. Math. Phys. **4**, 1
14. Ben-Abraham S.I. (1993): Int. J. Mod. Phys. B **7**, 1415
15. Berthé V. (1995): in *Beyond Quasicrystals*, ed. F. Axel, D. Gratias, Springer, Berlin, p. 441
16. Bohr H. (1932): *Fastperiodische Funktionen*, Springer, Berlin, reprinted 1974
17. Conway J.H., Sloane N.J.A. (1993): *Sphere Packings, Lattices and Groups* (2nd ed.), Springer, New York
18. Corduneanu C. (1989): *Almost Periodic Functions* (2nd ed.), Chelsea, New York
19. Cowley J.M. (1995): *Diffraction Physics* (3rd ed.), North Holland, Amsterdam
20. Danzer L. (1989): Discr. Math. **76**, 1

21. Danzer L., Papadopolos Z., Talis A. (1993): Int. J. Mod. Phys. **7**, 1379
22. de Bruijn N.G. (1981): Math. Proc. A **84**, 39 and 53
23. Duneau M. (1994): in *Lectures on Quasicrystals*, ed. F. Hippert, D. Gratias, Les Editions de Physique, Les Ulis, p. 153
24. Duneau M., Katz A. (1985): Phys. Rev. Lett. **54**, 2688
25. Elser V. (1985): Phys. Rev. Lett. **54**, 1730
26. Gähler F. (1993): J. Non-Cryst. Solids **153 & 154**, 160
27. Gähler F., Baake M., Schlottmann M. (1994): Phys. Rev. B **50**, 12458
28. Grimm U., Joseph D. (2002): See Chapter 9 of this book.
29. Grimm U., Schreiber M. (2002): See Chapter 3 of this book.
30. Grünbaum B., Shephard G.C. (1987): *Tilings and Patterns*, W.H. Freeman, New York
31. Gummelt P. (1996): Geom. Ded. **62**, 1
32. Henley C.L. (1991): In *Quasicrystals: The State of the Art*, ed. D.P. DiVincenzo, P.J. Steinhardt, World Scientific, Singapore, p. 429
33. Hermisson J., Richard C., Baake M. (1997): J. Phys. I (France) **7**, 1003
34. Hof A. (1997): In [55], p. 239
35. Höffe M. (1997): *Zufallsparkettierungen und Dimermodelle*, Diplomarbeit, Universität Tübingen
36. Ingersent K. (1991): In *Quasicrystals: The State of the Art*, ed. D.P. DiVincenzo, P.J. Steinhardt, World Scientific, Singapore, p. 185
37. Ishimasa T., Nissen H.-U., Fukano Y. (1985): Phys. Rev. Lett. **55**, 511
38. Janssen T. (1988): Phys. Rep. **168**, 55
39. Jeong H.-C., Steinhardt P.J. (1997): Phys. Rev. B **55**, 3520
40. Katz A. (1995): In *Beyond Quasicrystals*, ed. F. Axel, D. Gratias, Springer, Berlin, p. 141
41. Katz A., Duneau M. (1986): J. Phys. **47**, 181
42. Katz A., Gratias D. (1994): In *Lectures on Quasicrystals*, ed. F. Hippert, D. Gratias, Les Editions de Physique, Les Ulis, p. 187
43. Klitzing R., Baake M. (1994): J. Phys. I (France) **4**, 893
44. Klitzing R., Schlottmann M., Baake M. (1993): Int. J. Mod. Phys. **B7**, 1455
45. Kramer P., Neri R. (1984): Acta Crystallogr. **A40**, 580; and **A41**, 619 (1985) [Erratum]
46. Kramer P., Papadopolos Z. (1997): In [55], p. 307
47. Kramer P., Schlottmann M. (1989): J. Phys. A **22**, L1097
48. Lagarias J.C. (1999):
Discr. Comput. Geom. **21**, 161; and **21**, 345
49. Le T.Q.T. (1997): In [55], p. 331
50. Levine D., Steinhardt P.J. (1986): Phys. Rev. B **34**, 596
51. Levitov L.S. (1988): Commun. Math. Phys. **119**, 627
52. Lück R. (1993): Int. J. Mod. Phys. B **7**, 1437
53. Lunnon W.F., Pleasants P.A.B. (1987): J. Math. Pures Appl. **66**, 217
54. Mermin N.D. (1991): In *Quasicrystals: The State of the Art*, ed. D.P. DiVincenzo, P.J. Steinhardt, World Scientific, Singapore, p. 133
55. Moody R.V. (ed.) (1997): *The Mathematics of Long-Range Aperiodic Order*, NATO ASI C 489, Kluwer, Dordrecht
56. Niizeki K. (1989): J. Phys. A **22**, 205
57. Nissen H.-U., Beeli C. (1993): Int. J. Mod. Phys. **B7**, 1387
58. Oguey C., Duneau M., Katz A. (1988): Commun. Math. Phys. **118**, 99

59. Ophuysen G. van, Weber M., Danzer L. (1995): J. Phys. A **28**, 281
60. Penrose R. (1974): Bull. Inst. Math. Appl. **10**, 266
61. Pleasants P.A.B. (1995): In *Quasicrystals*, ed. C. Janot, R. Mosseri, World Scientific, Singapore, p. 22
62. Richard C., Höffe M., Hermisson J., Baake M. (1998): J. Phys. A **31**, 6385
63. Rokhsar D.S., Mermin N.D., Wright D.C. (1988): Acta Crystallogr. A **44**, 197
64. Roth J. (1993): J. Phys. A **26**, 1455
65. Rudin W. (1991): *Functional Analysis* (2nd ed.), McGraw Hill, New York
66. Schlottmann M. (1993): *Geometrische Eigenschaften quasiperiodischer Strukturen*, Dissertation, Univ. Tübingen; and Int. J. Mod. Phys. B **7**, 1351
67. Schlottmann M. (1998): "Projection formalism for locally compact Abelian groups", in *Quasicrystals and Discrete Geometry*, ed. J. Patera, Fields Institute Monographs, vol. 10, AMS, Rhode Island, p. 247
68. Schwarzenberger R.L.E. (1980): *N-dimensional Crystallography*, Pitman, San Francisco
69. Shechtman D., Blech I., Gratias D., Cahn J. (1984): Phys. Rev. Lett. **53**, 1951
70. Socolar J.E.S., Steinhardt P.J. (1986): Phys. Rev. B **34**, 617
71. Solomyak B. (1997): Ergod. Theory Dynam. Syst. **17**, 695
72. Steinhardt P.J., Ostlund S. (eds.) (1987): *The Physics of Quasicrystals*, World Scientific, Singapore
73. Suck J.B. (2001): See Chapter 1 of this book.
74. Sütö A. (1995): In *Beyond Quasicrystals*, ed. F. Axel, D. Gratias, Springer, Berlin, p. 481

3 Aperiodic Tilings on the Computer

Uwe Grimm and Michael Schreiber

Summary. We briefly review the standard methods used to construct quasiperiodic tilings, such as the projection, the inflation and the grid method. A number of sample *Mathematica* programs, implementing the different approaches for one- and two-dimensional examples, are discussed. Apart from small examples, the corresponding programs are not contained in the text, but are archived on the WWW.

3.1 Introduction

Structure models of quasicrystals are based on tilings of space, either on perfect quasiperiodic patterns or on random tilings. However, besides their physical applications, many of these tilings are also esthetically appealing – not by chance is Penrose's original article [29] entitled "The rôle of esthetics in pure and applied mathematical research"! Thus, even a reader who does not plan to enter the subject of quasicrystals on a deeper level might be interested to know how such tilings can be produced on the computer.

The computer programs discussed here were provided for two afternoon sessions of the summer school. Because no knowledge of particular programming languages could be assumed, and since good graphic tools were essential for this purpose, we decided to use an algebraic computer package that provides all that one needs. Which of the commercially available packages one chooses is mainly a matter of taste, and we decided in favor of *Mathematica*[1] [36]. Note that the actual *Mathematica* programs, apart from a small example, are not reproduced in this text – instead, the routines are archived on the WWW [16] and can be downloaded free of charge. At present, this directory contains a total of six files:

- `Read.Me`
- `ChairTiling.m`
- `FibonacciChain.m`
- `OctagonalTiling.m`
- `GridMethod.m`
- `PenrosePuzzle.m`

[1] *Mathematica*® is a registered trademark of Wolfram Research.

J.-B. Suck et al. (eds.), *Quasicrystals*
© Springer-Verlag Berlin Heidelberg 2002

including some documentation, but we may choose to update or supplement the content in the future.

During the summer school, the participants worked with *Mathematica* "notebooks". The corresponding front end of *Mathematica* provides a rather nice programming environment. Nevertheless, there are several reasons why we prefer to use a standard package format [27] for the archived programs: first of all, these are much smaller in size; secondly, they are less version-dependent (the notebook format in *Mathematica* has changed recently, and notebooks prepared with version 3.0 of *Mathematica* cannot be used with earlier versions); and finally, as these are simple ASCII files, file transfer should pose no problems. Furthermore, if desired, our programs can of course easily be included in the notebook environment by the user himself.

After a short survey on the different approaches employed to construct quasiperiodic tilings, we first present a simple example – a *Mathematica* program for the inflation of the so-called chair tiling [17]. This is followed by concise descriptions of our *Mathematica* programs. We also briefly sketch the theory behind the constructions, for a more detailed account we refer the reader to the literature compiled in [14], and to the other chapters of this volume.

3.2 How to Construct Quasiperiodic Tilings

Whether one wants to describe the structure of real (albeit idealized) quasicrystals, or whether one is just after a more elaborate way to tile the bathroom floor, one faces the problem of constructing quasiperiodic tilings. There exists a variety of mathematical procedures [2,18,33], the most popular being the projection (or cut-and-projection) method [7,10,20,23,25]. Here, one starts from a higher-dimensional *periodic* lattice, cuts a certain slice out of it and projects this slice onto a lower-dimensional (the "physical" or "parallel") space (the remaining directions are usually referred to as "orthogonal", "perpendicular" or "internal" coordinates). In fact, there are several slightly different, albeit equivalent, formulations of this method; for details, see [2].

The simplest example – and in fact the only one that can easily be visualized on the computer – is given by a projection from a periodic two-dimensional (2D) lattice to a 1D quasiperiodic structure, the usual toy model being the Fibonacci chain, which is related to the golden mean $\tau = (1+\sqrt{5})/2$. This is part of one of the programs that is described in detail in Sect. 3.4. It also contains the description of the Fibonacci chain as a substitution sequence, which is a common method for constructing aperiodic (in general not quasiperiodic) self-similar sequences. These serve as toy models of 1D aperiodic order in many areas of physics [3].

Inflation rules [17] provide a concept for the construction of self-similar, and in particular quasiperiodic, tilings in the same spirit. The rules describe in which way each tile of a given set is decomposed into scaled copies of the

tiles, such that, after applying the rules to a patch of a tiling, one obtains a patch consisting of the same tiles, but with all lengths scaled by a common factor. Iterating this procedure on some initial patch and rescaling after each step such that the tiles stay the same, one generates larger and larger patches that approach an infinite self-similar tiling. In Sect. 3.5, an example for both the projection and the inflation approach is given for the 2D octagonal (Ammann–Beenker) tiling [1,4,8,21].

Another approach, the dualization or grid method, is due to de Bruijn [6] (see also [22]): Rotating equidistant parallel lines by angles $2\pi k/n$, $k = 0, 1, \ldots, n-1$, yields an n-fold grid. Its dualization gives an n-fold tiling in which each p-gon of the grid corresponds to a vertex with p neighbors in the tiling. This method can very easily be translated into a computer program, see Sect. 3.6, and it is also straightforward to generalize it to higher dimensions.

Finally, quasiperiodic tilings may also be constructed via so-called matching rules [17,29,30]. Starting with a fixed set of proto-tiles, these give an atlas of the allowed local configurations. If these are *perfect* matching rules, the quasiperiodic tiling is essentially determined; more precisely, it is the corresponding "local indistinguishability" or "local isomorphism" (LI) class that is fixed [2]. At a first view, this looks like a constructive prescription that should allow us to model the growth of such structures, but this turns out to be a fallacy, because it contains an inherent non-locality (cf. [15]). In practice, this means that an erroneous tile addition during construction may only show up much later and at a completely different place; see, e.g., [31] for a nice example. In Sect. 3.7, we present a program that allows the reader to try this for the rhombic Penrose tiling.

3.3 A Small Example Program: Inflating the Chair Tiling

Before we address our main subject, the generation of quasiperiodic tilings, we first present a small program to give the reader a taste of the syntax and the structure of the programs. Clearly, we cannot give an extensive introduction to the *Mathematica* language; for this, the reader is referred to [27,34,36] and to the vast literature on *Mathematica* (including a regularly published journal with electronic supplements) and its applications in science, particularly in mathematics and theoretical physics – it is beyond the scope of this article to list all of these. Let us only mention a few features that we use frequently, so that even the non-committed reader gets some feeling of how to change the provided *Mathematica* programs if he wants to intervene and produce his own tilings according to his own esthetic preferences.

The main ingredient in our programs is the manipulation of lists of objects, as we represent a tiling in a natural way as a list of its tiles (and the tiles, occasionally, as a list of its vertices, which in turn are lists of their coordinates). For this, functions are used, which are either explicitly defined

Fig. 3.1. The inflation rule of the chair tiling

(such as, for instance, `f[x_]:=x^2`, which defines the function $f(x) = x^2$) or are used as so-called "pure functions". The latter are expressions delimited by an ampersand (`&`) involving arguments `#1` (or just `#`), `#2`, `#3` and so on (for instance, to compute $x^2 + y^2$ one may use `(#1^2+#2^2)&[x,y]` or, synonymously, `Function[#1^2+#2^2][x,y]`). Such functions can easily be applied to the elements of a list by using the command `Map`. For example, `Map[#^3&,{1,2,3,4,5}]` or, in a shorter form, `#^3&/@{1,2,3,4,5}` results in the output `{1,8,27,64,125}`. There is also a functional operation `Nest` that allows us to apply a function iteratively, as we are going to do with the inflation rule. For instance, `Nest[f,x,3]` is equivalent to `f[f[f[x]]]`.

For simplicity, we consider a tiling that consists of a single tile only. We choose the so-called chair tiling, and generate it by iterated application of the inflation rule given in Fig. 3.1. Note that the chair tiling, though aperiodic, is not quasiperiodic – it is an example of a limit-periodic tiling, which means that its Fourier module, though discrete, is not finitely generated [12]. The "chair-formed" tile, which occurs in four different orientations, can be thought of as a combination of three congruent squares; hence the tiling belongs to the class of so-called "triomino" (a term that is deduced from the word "domino"; the general case is referred to as "polyomino") tilings [13].

An implementation of the inflation rule of Fig. 3.1 is shown in Fig. 3.2. `ScaleFactor` gives the linear scaling factor of the inflation rule, which is 2 in this case. In an inflation step, we rescale all lengths by this factor such that, provided that one starts with a patch with integer coordinates of the vertices, the coordinates of the inflated patch are integers. A single tile is represented in the form `{or,{x0,y0}}`, where `or` denotes the angular orientation of the tile, with values 0, 1, 2 and 3 (mod 4), and `{x0,y0}` denote the coordinates of the reference point. The function `TileCoordinates` computes the actual coordinates of the six vertices of a tile, which is used in the graphics function `PlotTiling`. All displacements are expressed in terms of four 2D vectors, namely `TwoVector[0]={1,1}` and its m-times 90°-rotated copies `TwoVector[m]`. The inflation rule is encoded in the function `TileInflation`, which produces a list of the four tiles into which a single tile is dissected. Since tiles in all orientations are dissected in the same way, it is sufficient to use a single definition by employing the rotated vectors `TwoVector[m]`. To perform an n-fold inflation of a patch, consisting of a list of one or more tiles, the function `Inflation` is used, with n as its second argument. Finally, `PlotTiling` enables one to plot the tiling, with optional arguments that allow us to give different colors to the four orientations of the tile and to change the color and width of the lines that outline the tiles.

```
Clear[ScaleFactor,TwoVector,TileCoordinates,TileInflation,
      Inflation,PlotTiling];

ScaleFactor = 2;

TwoVector[num_Integer] :=
  TwoVector[num] =
  Dot[MatrixPower[{{0,-1},
                   {1, 0}},num],{1,1}];

TileCoordinates[{tile_Integer,refpoint_List}] :=
  Map[(refpoint+#)&,
      {0,(#3+#4)/2,#4,#1,#2,(#2+#3)/2}]&[TwoVector[tile],
                                         TwoVector[tile+1],
                                         TwoVector[tile+2],
                                         TwoVector[tile+3]];

TileInflation[{tile_Integer,refpoint_List}] :=
  {{#1,#4},
   {#2,#4+TwoVector[#2]},
   {#1,#4+TwoVector[#1]},
   {#3,#4+TwoVector[#3]}}&[Mod[tile,4],
                           Mod[tile-1,4],
                           Mod[tile+1,4],
                           ScaleFactor*refpoint];

Inflation[tiling_List,
          num_Integer:1] /; num>=0 :=
  Nest[Flatten[Map[TileInflation,#],1]&,tiling,num];

PlotTiling[tiling_List,
           tilecol_List:Table[GrayLevel[1],{4}],
           linecol_:GrayLevel[0],
           linewidth_:1/200] :=
  Graphics[Table[{tilecol[[i+1]],
                  Map[Polygon,#],
                  linecol,Thickness[linewidth],
                  Map[Line[Join[#,Take[#,2]]]&,#]}&[
                    Map[TileCoordinates,
                        Select[tiling,Mod[First[#],4]==i&]]],
                 {i,0,3}],
           AspectRatio->1];
```

Fig. 3.2. The *Mathematica* program `ChairTiling.m` [16] for the inflation of the chair tiling. It is also available in electronic form [16]

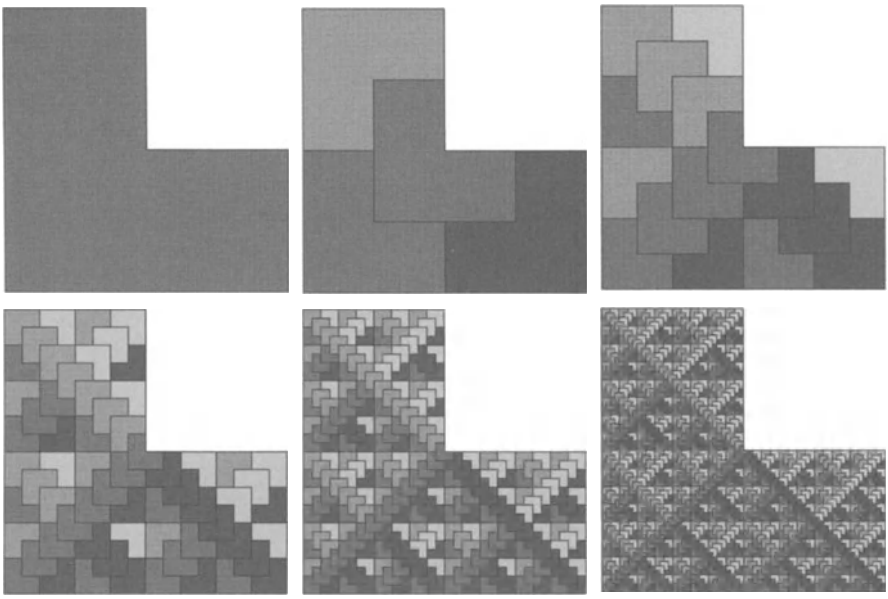

Fig. 3.3. Inflation of the chair tiling. The four orientations of the tile are distinguished by different shadings

The result can be seen in Fig. 3.3, where the first five inflation steps of a single tile are shown, giving different shadings to the four orientations of the tile. This figure has been produced by the following input

```
GraphicsArray[Partition[
  Table[PlotTiling[Inflation[{{2,{0,0}}},n],
                   Map[GrayLevel,{0.8,0.6,0.4,0.2}],
                   GrayLevel[0],
                   1/500],
        {n,0,5}],3],GraphicsSpacing->0];
```

within a `Show` or `Display` command to display the result on the screen or write it to a PostScript file, respectively. Note that our rescaling by `ScaleFactor` has effectively been reversed by *Mathematica*, since the different subgraphs in a `GraphicsArray` arrangement are scaled to the same total size. For completeness, we mention that Fig. 3.1 was produced by

```
GraphicsArray[
  {PlotTiling[{{2,{0,0}}},Map[GrayLevel,{1,1,1,1}],
              GrayLevel[0],1/100],
   Graphics[{GrayLevel[0],Polygon[{{1/4,-1/3},{1,0},{1/4,1/3}}],
             GrayLevel[1],Disk[{1/8,0},{1/4,7/20}],
             GrayLevel[0],Thickness[1/50],Line[{{-1,0},{4/5,0}}]},
             AspectRatio->1,PlotRange->{{-2,2},{-2,2}}],
```

```
PlotTiling[Inflation[{{2,{0,0}}}],Map[GrayLevel,{1,1,1,1}],
        GrayLevel[0],1/100]};
```

where the second part of the argument of `GraphicsArray` produces the arrow.

This completes our little excursion into the mysteries of *Mathematica*. Of course, the preceding remarks can only offer a glimpse of the possibilities of this algebraic computer package; although – on purpose – our example program of Fig. 3.2 is not written in the simplest possible way, but already contains some little tricks to show at least some of the ingredients of the programs discussed below.

3.4 Once Again: The Ubiquitous Fibonacci Chain

The toy model of a 1D quasicrystal is the Fibonacci chain – one is unlikely to find any introductory text on quasicrystals where this example is not discussed. The usual way to introduce the Fibonacci sequence employs an inflation-like procedure, a so-called substitution rule,

$$\varrho: \begin{cases} S \to L \\ L \to LS, \end{cases} \tag{3.1}$$

on two letters S and L, generating a semi-infinite word w_∞ by iterated application $w_{n+1} = \varrho(w_n)$ on some initial word, say $w_0 = S$,

$$\begin{aligned} w_0 &= S, & w_4 &= LSLLS, \\ w_1 &= L, & w_5 &= LSLLSLSL, \\ w_2 &= LS, & w_6 &= LSLLSLSLLSLLS, \\ w_3 &= LSL, & w_7 &= LSLLSLSLLSLLSLSLLSLS, \end{aligned} \tag{3.2}$$

and so forth. Obviously, in place of the substitution rule (3.1), one can use concatenation of subsequent words to generate the same sequence

$$w_0 = S, \qquad w_1 = L, \qquad w_{n+1} = w_n w_{n-1}\,, \tag{3.3}$$

where $w_n w_{n-1}$ denotes the word obtained by appending w_{n-1} to w_n. From this, it is easy to see that the length of the word w_n (i.e. the number of its letters) is given by the Fibonacci number $|w_n| = f_{n+1}$, defined by the recursion

$$f_0 = 0, \qquad f_1 = 1, \qquad f_{n+1} = f_n + f_{n-1}\,, \tag{3.4}$$

and that w_n contains precisely f_n letters L and f_{n-1} letters S [for $n > 0$; otherwise, one has to extend the definition (3.4) to negative values of n, which amounts to setting $f_{-n} = (-1)^{n+1} f_n$ for $n > 0$]. Thus, the frequency of the predominant letter L in the limit word w_∞ is given by

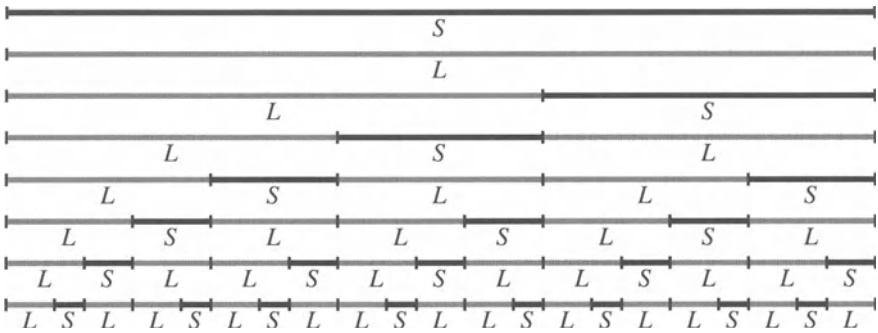

Fig. 3.4. Inflation of the Fibonacci chain

$$\begin{aligned} \nu_L &= \lim_{n\to\infty} \frac{f_n}{f_{n+1}} = \lim_{n\to\infty} \frac{f_n}{f_n + f_{n-1}} \\ &= 1 + \left(\lim_{n\to\infty} \frac{f_{n-1}}{f_n} \right)^{-1} = 1 + \nu_L^{-1} \\ \Longrightarrow \quad \nu_L &= \frac{\sqrt{5}-1}{2} = \tau - 1 = \tau^{-1}, \end{aligned} \tag{3.5}$$

where $\tau = (1+\sqrt{5})/2 = \lim_{n\to\infty}(f_{n+1}/f_n)$ is the golden ratio. As this is an irrational number, we have thus proved that the Fibonacci sequence is aperiodic. Such statistical properties of the sequence can also be derived from the associated substitution matrix

$$M_\varrho = \begin{pmatrix} 0 & 1 \\ 1 & 1 \end{pmatrix}, \qquad \lambda^\pm = \pm\tau^{\pm 1}, \qquad v^+ = \begin{pmatrix} \tau^{-2} \\ \tau^{-1} \end{pmatrix}, \tag{3.6}$$

whose elements just count the number of letters S and L appearing in $\varrho(S)$ and $\varrho(L)$, respectively. Its largest eigenvalue λ^+, related to the exponential growth of the word length in a substitution step, is just τ; and the elements of the corresponding eigenvector v^+, when properly normalized, encode the frequencies of the two letters; cf. (3.6). Obviously, substitution rules with an irrational maximum eigenvalue of the corresponding substitution matrix generically give aperiodic (but, in general, not quasiperiodic) chains. However, a rational or integer maximum eigenvalue does not imply that the sequence that one obtains is periodic; the Thue–Morse sequence with substitution $a \to ab$, $b \to ba$, is a prominent example: it is aperiodic although the two eigenvalues of the substitution matrix (whose elements are all equal to 1) are 2 and 0.

In the file `FibonacciChain.m` [16], a program `SubstitutionSystem` is contained that defines several functions (`SubstitutionRule`, `Substitution`, `SubstitutionMatrix`, `SubstitutionSequence` and `SubstitutionWord`) to generate arbitrary substitution sequences. The substitution rule and an initial word have to be given as parameters, and the defaults (which are `{"S"->{"L"}, "L"->{"L","S"}}` for the rule and `{"S"}` as initial word) yield the

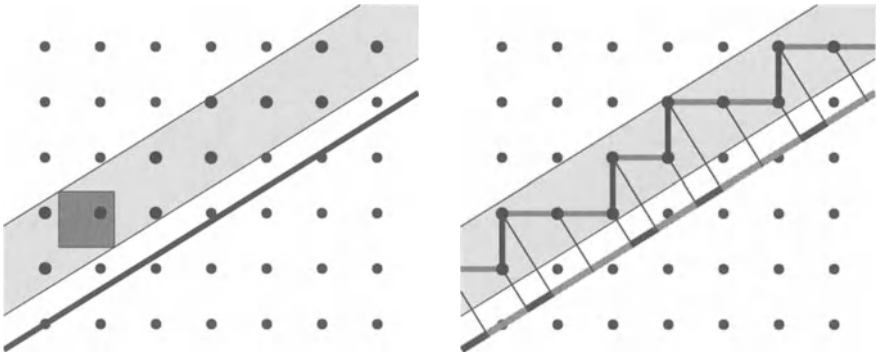

Fig. 3.5. A projection of the Fibonacci chain from the square lattice in the "strip projection" scheme. The slope of the "physical space" is τ^{-1}. For details, see the text

Fibonacci sequence as in (3.1) and (3.2). The recursive definition (3.3) is also implemented (`FibonacciRecursionSequence`, `FibonacciRecursionWord`). Here, the Fibonacci (or other substitution) words may be represented in two ways; for instance, $w_4 = LSLLS$ may either be represented as a list of single letters `{"L","S","L","L","S"}` (e.g. `FibonacciRecursionSequence[4]`) or as a string `{"LSLLS"}` (e.g. `FibonacciRecursionWord[4]`). There are a number of functions to analyze the statistical properties of the sequence, which are written such that they can simultaneously deal with both representations of the words. For example, `SubWordCount[w1,w2]` counts the number of occurrences of the word `w2` in the word `w1`. Furthermore, the Fibonacci numbers are defined (`FibonacciNumber[n]` gives f_n), and a small program `PlotLinearChain` for a geometric representation of n-letter sequences as linear arrangements of n intervals is included. We used this to prepare Fig. 3.4 with

```
PlotLinearChain[Table[SubstitutionSequence[i],{i,0,7}],
                True,
                {N[GoldenRatio],1},
                {GrayLevel[0.45],GrayLevel[0]},
                {GrayLevel[0],GrayLevel[0]}]
```

where the length ratio of the two intervals is the golden mean τ, with L corresponding to the "long" and S to the "short" interval, respectively. In this way, the substitution rule may be interpreted as an inflation procedure for the geometric object; and, upon suitable rescaling of lengths (i.e. by a factor of τ), the semi-infinite line representing the limit word w_∞ is a fixed point under this procedure.

This "geometric Fibonacci chain", however, can also be obtained by a suitable projection from the 2D square lattice. As mentioned previously, there are several variants of projection schemes, which are essentially equivalent,

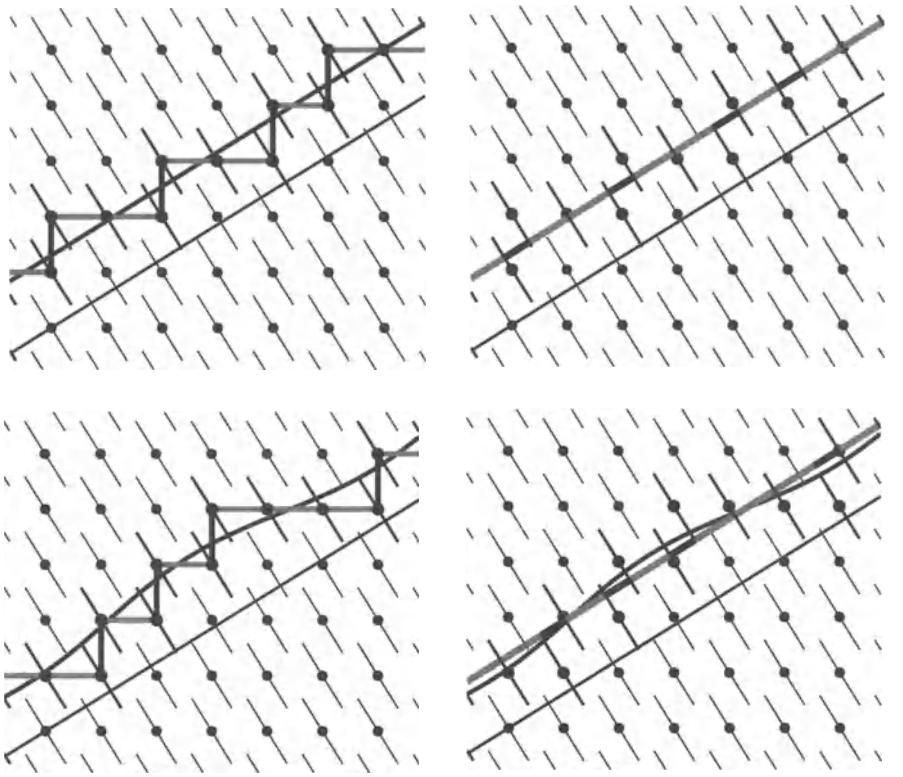

Fig. 3.6. A projection of the Fibonacci chain from the square lattice in the "atomic hypersurface" scheme. Below, small "phasonic" fluctuations in the cut space lead to "phason jumps", creating subwords ($LSLSLS$ and LLL) that are not present in a perfect Fibonacci sequence

see Figs. 3.5–3.7. The file `FibonacciChain.m` [16] contains the three functions `StripProjection`, `AtomicSurfaceProjection` and `KlotzConstruction`, which show, in a sequence of pictures, three variations of the projection to a line. Among others, the slope can be given as a parameter, the default value $1/\tau$ again yielding the Fibonacci chain. As is common, the "window" or "acceptance domain", which determines which part of the square lattice is projected, is chosen as the projection of a unit cell (e.g. the dark grey square in the left-hand part of Fig. 3.5) of the square lattice onto "perpendicular space", i.e. in the direction orthogonal to the cut line which corresponds to the "physical space" and is indicated by the thick line in the left-hand part of Fig. 3.5. In the "strip projection" shown in Fig. 3.5, this determines the width of the strip, and its vertical position can be chosen as a parameter. The actual sequence obtained by projection depends on this parameter, but one always stays within the same LI class [2], except for some "singular" cases that are obtained if one lattice point falls precisely on the boundary

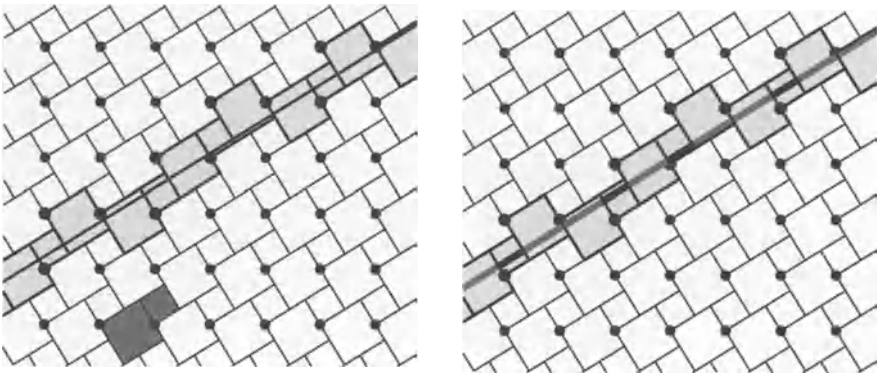

Fig. 3.7. A projection of the Fibonacci chain from the square lattice in the "Klotz construction" or "dualization" scheme

of the strip. In the method of the "atomic (hyper)surfaces" [5,19] shown in Fig. 3.6, the cut line is dissected by "atomic surfaces" attached to the vertices of the square lattice. The function `AtomicSurfaceProjection` also allows us to introduce fluctuations of the cut space (mimicking "phason" degrees of freedom; see [35]), an example is shown in the lower part of Fig. 3.6. Finally, the "Klotz construction" or "dualization" scheme [24,26,28,32] shown in Fig. 3.7 employs a different unit cell of the square lattice (e.g. consisting of the two dark grey squares in the left-hand part of Fig. 3.7), chosen such that all of its boundaries are parallel or perpendicular to the "physical space". In addition to the pictures shown in Fig. 3.7, the function `KlotzConstruction` also gives a detailed description of the construction of this unit cell.

We now turn our attention to arguably more interesting examples of 2D quasiperiodic tilings, both from an esthetic and a physical point of view. Nevertheless, the methods that we are going to use are very similar to the 1D case considered above: in particular, the projection scheme is a straightforward generalization of the method shown in Figs. 3.5–3.7.

3.5 The Octagonal Tiling: Projection and Inflation

We now consider the canonical octagonal (also known as Ammann–Beenker) tiling [1,4,8,21]. The corresponding programs are contained in the file `OctagonalTiling.m` [16]. The tiling can be obtained by projection from the 4D hypercubic lattice, choosing the orientation of the "physical space" as one of the two unique invariant subspaces with respect to the action of the dihedral group D_8 (the symmetry group of the regular octagon), which is a subgroup of the point group of the 4D hypercubic lattice. The acceptance domain is the orthogonal projection of the hypercube: it is a regular octagon, as shown in Fig. 3.8, which was produced with the function `PlotCubeOrthogonalProjection`.

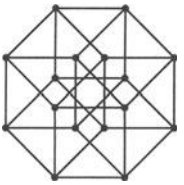

Fig. 3.8. A projection of the 4D hypercube

The projection of a small portion of the hypercubic lattice, together with the orthogonal projection of the vertices, is shown in Fig. 3.9. The patch comprises 177 vertices and 536 edges; it was obtained by considering all points that can be reached by at most eight steps along the hypercubic edges from the origin, which corresponds to the center of this eight-fold symmetric patch. Here, we used the commands `PlotParallelProjection` and `PlotOrthogonalProjection` defined in `OctagonalTiling.m` [16].

The octagonal tiling can also be obtained by inflation. The inflation rule, i.e. the description of how to cut tiles into smaller pieces, can be read off from Fig. 3.10, which shows three subsequent inflation steps. Apparently, the inflation rule is rather complicated: first, the parts obtained by inflating a tile sometimes cover only half a tile at the smaller scale, and secondly, the square tile is dissected in an asymmetric way. The best way to represent the inflation rule is therefore in terms of two triangular tiles obtained by cutting the rhomb along the short diagonal, and cutting the square such that the two halves, when oriented properly, are dissected in the same way. This inflation procedure has been implemented in `OctagonalInflation`, and only at the end, when using `PlotOctagonalTiling` to display the tiling, may one choose to recombine the triangles into squares and rhombs, as has been done in Fig. 3.10.

In the programs, the tilings are always treated in terms of integer coordinates – only for the purpose of the graphical presentation is it necessary to translate these into real 2D coordinates. In the projection approach, it is

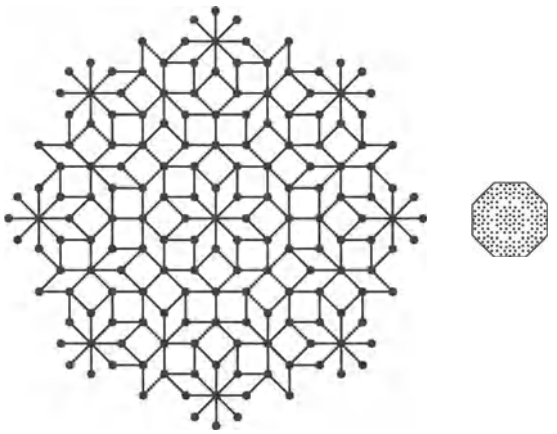

Fig. 3.9. A parallel (vertices and edges, left side) and perpendicular (vertices only, right side) projection of part of the hypercubic lattice, drawn at the same scale. The octagon is the projection of the 4D hypercube; cf. Fig. 3.8

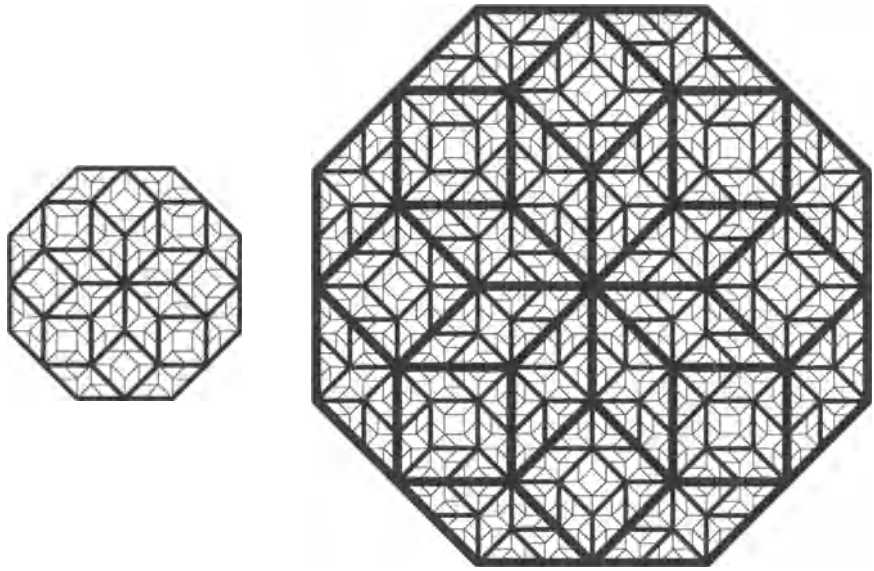

Fig. 3.10. Two (left) and three (right) inflation steps of the octagonal tiling

natural to use the coordinates of the 4D hypercubic lattice point, whereas in the inflation approach we, instead, performed all calculations in the module $\mathbb{Z} + \sqrt{2}\mathbb{Z}$.

3.6 De Bruijn's Ingenuity: The Dualization Method

Another method that is particularly easy to program is de Bruijn's famous grid (or dualization) method [6,22]. Here, one starts from an n-fold grid that is created rotating a set of equidistant parallel lines by angles $2\pi k/n$, $k = 0, 1, \ldots, n-1$, and shifting them by certain amounts. The sum of these shifts, Γ, plays an important role – in general, the tilings constructed with different values of Γ (modulo 1) belong to different LI classes. A grid is called "regular" if there are no intersection points where more than two lines meet. From this, an n-fold tiling is obtained by dualization, so that each p-gon of the grid yields a vertex with p neighbors in the tiling. Its coordinates can be calculated easily. For a regular grid, each intersection point of the grid thus corresponds to a rhombic tile. Note that for odd values of n one could equally well have considered the case $2n$, since a rotation by an angle of π is irrelevant.

In Fig. 3.11, we present a grid and the corresponding rhombic tiling for the Penrose case, i.e. for $n = 5$ where the shifts (grid parameters) satisfy the condition $\Gamma = 0$. The portion of a regular lattice on the boundary of the patch is due to the finiteness of the grid (because we used only seven grid

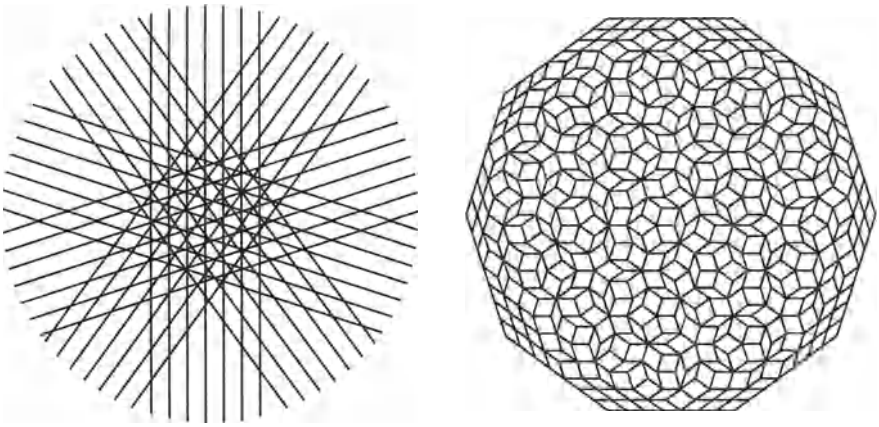

Fig. 3.11. A pentagrid (left) and the corresponding part of a ten-fold tiling (right, disregarding the boundary region), which belongs to the LI class of the Penrose tiling ($\Gamma = 0$)

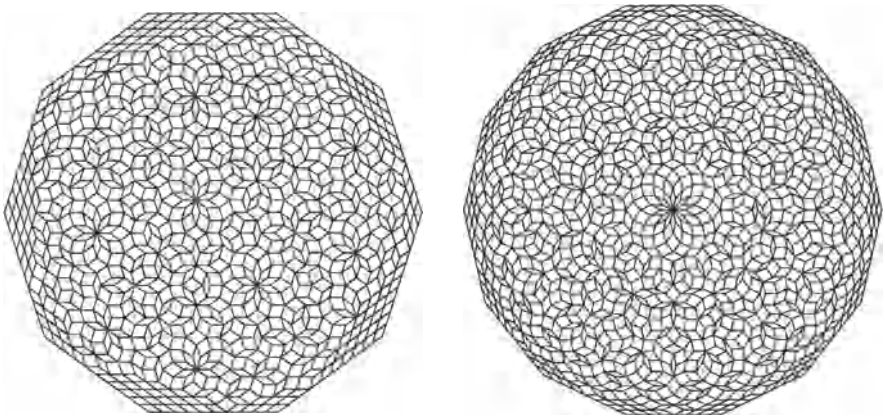

Fig. 3.12. Two tilings obtained by the grid method: a ten-fold tiling (left) in the LI class of the "anti-Penrose" tiling ($\Gamma = 1/2$) and an example for $n = 7$ (right), again disregarding the boundary region which is due to the finite grid

lines for each direction). The picture has been produced with the commands `PlotGrid` and `PlotDualTiling` defined in `GridMethod.m` [16]. Note that in the dualization, performed in `DualizeGrid`, the regularity of the grid is not verified, although it is assumed in the construction; hence the results are unpredictable in the case in which the grid is not regular. Figure 3.12 shows, on the left, another example for $n = 5$, but now with $\Gamma = 1/2$ which is "maximally remote" from the Penrose case $\Gamma = 0$, for which reason it is occasionally referred to as an "anti-Penrose tiling". Although it is built from the same two rhombic tiles as the Penrose tiling, it obviously belongs to a

different LI class, because it contains vertex configurations that are forbidden in a perfect Penrose tiling such as, for instance, the star of ten "thin" rhombs. On the right-hand side of Fig. 3.12, an example for $n = 7$ is shown. We note that the grid method is equivalent to the projection scheme; see, e.g., [32] for details.

3.7 Giving It a Trial: A Penrose-Tiling Puzzle

Finally, we would like to invite the reader to take the part of the pitiable craftsman who, unsuspectingly, accepted the honorable commission to tile a hypocrite quasicrystallographer's bathroom floor with a portion of a rhombic Penrose tiling. Prudently, the quasicrystallographer provided two sets of rhombic tiles with edges that only fit in certain ways, thus encoding the matching rules of the Penrose tiling as in Fig. 3.13.

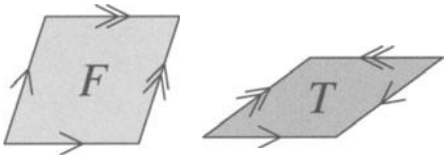

Fig. 3.13. The two Penrose rhombs ("fat" and "thin") with arrow decorations encoding the matching rules

To understand the desperate situation of the tiler, the reader should use the program `PenrosePuzzle` contained in the file `PenrosePuzzle.m` [16]. One may give an arbitrary initial patch as input: the default is a single "fat" rhomb. Once started, the program asks whether to add or to remove tiles. An addition is specified by the letter `A` followed by the type of the new tile (`F` for the "fat" and `T` for the "thin" rhomb, respectively) and by the number of the surface edge at which the new tile should be attached. This leaves only one possible way to attach the tile without creating an overlap with the tile that it is attached to; and for each addition the program checks whether it leads to an arrow mismatch in the resulting tiling, or whether an overlap occurs between the new tile and a tile of the previous patch. If that happens, an error message is produced and one may choose whether to continue with the addition. A tile removal is simply specified by the letter `R` together with the number of one of the surface edges of the tile to be removed (thus only tiles that are on the surface of the patch can be removed). The edges are numbered consecutively; the patch with the edge labels is shown after each successful addition or removal of a tile – see Fig. 3.14.

Of course, matching rules just state that one has constructed a perfect Penrose tiling when one has succeeded in tiling the entire plane without violating the rules. However, since both tiles and bathrooms are usually of finite size, the tiler might in the end turn up with a finite "legal" patch (i.e. the matching rules are not violated) that nevertheless is not "correct", i.e.

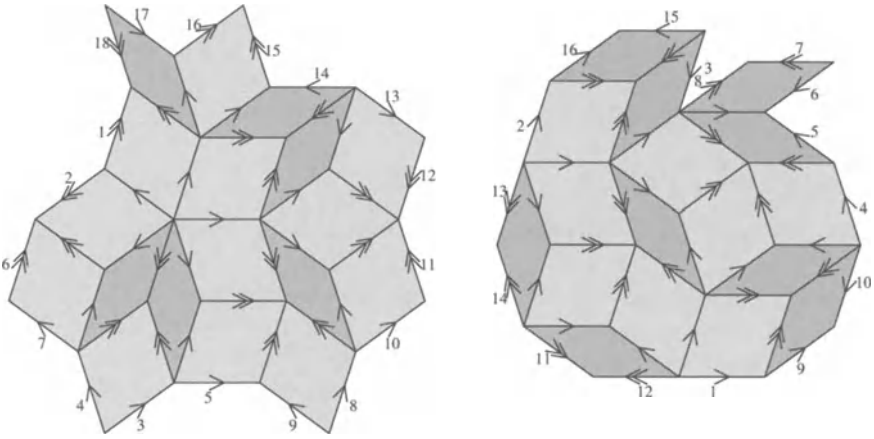

Fig. 3.14. Two patches consisting of Penrose rhombs, grown with `PenrosePuzzle`. In the right-hand example, the two crevices with surfaces edges $(5, 6)$ and and $(3, 8)$ cannot be filled with the tiles of Fig. 3.13 – any attempted addition of a tile will produce an error due to a mismatch of the arrows or an overlap of two tiles. Note that it does not suffice to remove the tile with surface edges 6, 7 and 8 – one also has to remove the thin rhomb with surface edge 5 in order to obtain a patch that occurs in a perfect Penrose tiling

it does not occur in a perfect Penrose tiling. In other words, it is impossible to continue the addition of further tiles without violating the matching rules at some point; see the right-hand part of Fig. 3.14 for a simple example and [15,31] for more details.

3.8 Concluding Remarks

Clearly, the programs introduced here form a by no means complete package that allows one to create all of those tilings that quasicrystallographers play around with – but this was not what we had intended. Instead, it was our purpose to show, with a few comparatively simple examples, how quasiperiodic tilings can be produced, and thereby give an insight into the different approaches that one may choose. In particular, we have restricted ourselves to 1D and 2D examples, not because it would be substantially more difficult to generate higher-dimensional tilings, but mainly because it requires much more effort to visualize the result on a 2D screen. For the 3D case, commercially available balls-and-sticks kits, e.g. [37], which allow us to build icosahedral structures, may still prove more useful than computer-generated pictures – however, there is also a *Mathematica* implementation of the balls-and-sticks tools [11].

Nevertheless, our sample programs [16] may serve as a starting point for the layman who aims to generate some beautiful pictures of tilings, whether

his or her interest is of a mathematical, physical or purely esthetical nature. Whether or not experts may still profit from our small example programs, they will have to judge for themselves – we did not expend too much effort in finding the most elegant or most concise (but probably also quite unreadable) form of the program code, nor did we try to optimize our programs with respect to CPU time or memory consumption (which sooner or later – more likely sooner – becomes the limiting factor in using *Mathematica*). Still, it should be rather easy to modify our programs in order to treat most of the quasiperiodic tilings that one may encounter in the literature.

Finally, we would like to note that computer programs generating quasiperiodic tilings can also be found in other places. For example, some *Mathematica* programs are contained in the book [33], and there even exists an interactive WWW site [9] devoted to quasiperiodic tilings.

References

1. Ammann, R., Grünbaum, B., Shephard, G.C. (1992): Discr. Comput. Geom. **8**, 1
2. Baake, M. (2002): See Chapter 2 of this book
3. Baake, M., Grimm, U., Joseph, D. (1993): Int. J. Mod. Phys. B **7**, 1527
4. Baake, M., Joseph, D. (1990): Phys. Rev. B **42**, 8091
5. Bak, P. (1986): Scr. Metall. **20**, 1199
6. de Bruijn, N.G. (1981): Proc. Kon. Ned. Akad. Wet. A (Indagationes Mathematicae) **84**, 39 and 53
7. Duneau, M., Katz, A. (1985): Phys. Rev. Lett. **54**, 2688
8. Duneau, M., Mosseri, R., Oguey, C. (1989): J. Phys. A **22**, 4549
9. Durand, E. (1994): *QuasiTiler 3.0* (WWW front end by P. Burchard, D. Meyer and E. Durand, Geometry Center, University of Minnesota) `http://www.geom.umn.edu/apps/quasitiler`
10. Elser, V. (1986): Acta Crystallogr. A **42**, 36
11. Elser, V. (1998): *IQtools* (for detailed information, please contact the author by email: `ve10@cornell.edu`)
12. Gähler, F., Klitzing, R. (1997): In *The Mathematics of Long-Range Aperiodic Order* (NATO ASI C 489), ed. R.V. Moody, Kluwer, Dordrecht, p. 141
13. Golomb, S. (1994): *Polyominoes: Puzzles, Patterns, Problems and Packings* (2nd ed.), Princeton University Press, Princeton
14. Grimm, U., Baake, M. (2002): See the Appendix of this book
15. Grimm, U., Joseph, D. (2002): See Chapter 9 of this book
16. Grimm, U., Schreiber, M. (1998): *Constructing Aperiodic Tilings with Mathematica: Some Example Programs*, `http://www.tu-chemnitz.de/physik/HERAEUS/2000/springer.html`
17. Grünbaum, B., Shephard, G.C. (1987): *Tilings and Patterns*, W.H. Freeman, New York
18. Janot, C. (1994): *Quasicrystals: A Primer* (2nd ed.), Clarendon Press, Oxford
19. Janner, A., Janssen, T. (1986): Phys. Rev. B **15**, 643
20. Kalugin, P.A., Kitayev, A.Y., Levitov, L.S. (1985): JETP Lett. **41**, 145; J. Phys. Lett. (France) **46**, L601

21. Katz, A., Gratias, D. (1994): In *Lectures on Quasicrystals*, ed. F. Hippert, D. Gratias, Les Editions de Physique, Les Ulis, p. 187
22. Korepin, V.E., Gähler, F., Rhyner, J. (1988): Acta Crystallogr. A **44**, 667
23. Kramer, P. (1982): Acta Crystallogr. A **38**, 257
24. Kramer, P. (1987): Mod. Phys. Lett. B **1**, 7
25. Kramer, P., Neri, R. (1984): Acta Crystallogr. A **40**, 580; **41**, 691 (1985) [Erratum]
26. Kramer, P., Schlottmann, M. (1989): J. Phys. A **22**, L1097
27. Maeder, R. (1990): *Programming in Mathematica*, Addison–Wesley, Redwood City (California)
28. Oguey, C., Duneau, M, Katz, A. (1988): Commun. Math. Phys. **118**, 99
29. Penrose, R. (1974): Bull. Inst. Math. Applics. **10**, 266
30. Penrose, R. (1978): Eureka **39**, 16; reprinted in Math. Intell. **2**, 32 (1979)
31. Penrose R. (1989): In *Introduction to the Mathematics of Quasicrystals* (Aperiodicity and Order, vol. 2), ed. M.V. Jarić, Academic Press, San Diego, p. 53
32. Schlottmann, M. (1993): Int. J. Mod. Phys. B **7**, 1351; and *Geometrische Eigenschaften quasiperiodischer Strukturen*, PhD Thesis, Universität Tübingen
33. Senechal, M. (1995): *Quasicrystals and Geometry*, Cambridge University Press, Cambridge
34. Skiena, S. (1990): *Implementing Discrete Mathematics: Combinatorics and Graph Theory with Mathematica*, Addison–Wesley, Redwood City (California)
35. Trebin H.-R. (2002): See Chapter 12 of this book
36. Wolfram, S. (1991): *Mathematica: A System for Doing Mathematics by Computer* (2nd ed.), Addison–Wesley, Reading (Massachusetts)
37. Zometool Marketing, 1526 South Pearl Street, Denver, CO 80210, USA; `http://www.zometool.com`

Part II

Atomic Structure and Growth

4 Quasicrystallography

Ted Janssen

Summary. Quasicrystals and other aperiodic, but quasiperiodic, structures lack lattice periodicity. Nevertheless, they have the same degree of order as lattice-periodic crystals. The crystallographic notion of symmetry can be generalized. One way to do this is to introduce a higher-dimensional space, but such an approach is equivalent to a three-dimensional formulation. Superspace groups are discussed, and applied to the symmetry of icosahedral and dihedral quasicrystals.

4.1 Introduction

A solid is usually considered to be an ordinary crystal if it is lattice-periodic. That means that there are three independent translation vectors that leave the crystal structure invariant. This is reflected in the diffraction pattern, which consists of sharp Bragg peaks on the positions of a lattice, called the reciprocal lattice. For a couple of decades, other materials have been found that show a diffraction pattern with sharp spots as well, but these spots, instead of belonging to a reciprocal lattice, have positions

$$\boldsymbol{k} = \sum_{i=1}^{n} h_i \boldsymbol{a}_i^* \qquad (\text{integer } h_i) \tag{4.1}$$

that are linear integral combinations of a finite number ($n > 3$) of basis vectors. We call the vectors $\boldsymbol{a}_i^*$ a basis only if they are not rationally dependent. If the number n is larger than the dimension of the space, the structure is not lattice-periodic, but is called quasiperiodic. The set $\{\sum_i h_i \boldsymbol{a}_i^*\}$ forms a $\mathbb{Z}$-module, with the property that each sum of two elements belongs to the module, and that an integer multiple of an element belongs to the module. In this case, the module is called the Fourier module. The number of basis vectors is the rank of the module. If the rank is larger than the dimension, there is a dense set of vectors and this is not considered as a lattice in crystallography.

Of course, experimentally it can be hard to determine the rank, because every irrational number can arbitrarily well be approximated by a rational number. But, actually, this is no different from the problem of saying whether a lattice is orthorhombic or monoclinic with an angle of almost 90°.

J.-B. Suck et al. (eds.), *Quasicrystals*
© Springer-Verlag Berlin Heidelberg 2002

Although initially considered as an oddity, quasiperiodicity occurs very frequently. A substantial part of the Earth's crust has minerals with this property. The consequences of the absence of lattice periodicity are important, because many treatments of solid-state systems are based on concepts such as lattice periodicity and Brillouin zone.

One can distinguish three major classes of materials with a quasiperiodic structure. These occur in addition to other types of quasiperiodicity, such as that found in magnetic systems. The first class is that of incommensurate (IC) modulated crystals. These can be described as starting from a normal lattice-periodic structure, where one has a periodic change, with a period that is not compatible with that of the basic structure. For example, this can be a spatially periodic displacement. Another possibility is that certain sites in the lattice-periodic structure are occupied with a probability that depends periodically in space on the position. If the periodicity is IC with the lattice of the starting structure, the modulated structure is quasiperiodic. A simple example is a crystal with lattice positions $\boldsymbol{n}$ and average positions $\boldsymbol{r}_j$ in the unit cell. If the positions of the modulated structure are $\boldsymbol{n} + \boldsymbol{r}_j + \boldsymbol{a}_j \cos(\boldsymbol{Q} \cdot \boldsymbol{n} + \phi_j)$, with a wave vector $\boldsymbol{Q}$ that does not belong to the reciprocal lattice of the basic structure, the modulation will be reflected in the appearance of satellites in the diffraction pattern. In this case, the positions of the diffraction spots are

$$h_1 \boldsymbol{a}_1^* + h_2 \boldsymbol{a}^* + h_3 \boldsymbol{a}_3^* + m\boldsymbol{Q}.$$

The spots with $m \neq 0$ are called satellites. The rank of the Fourier module here is four.

Another class is formed by the IC composites. These consist of two or more subsystems which are themselves (possibly modulated) crystal structures. If the lattices of the basic structures are mutually IC, the structure is quasiperiodic. A simple example is a host lattice of urea molecules that has channels in which alcane molecules are situated. If the alcane molecules order lattice-periodically, but such that the lattice constant is IC with that of the urea lattice, the composite structure is quasiperiodic.

The third class is that of quasicrystals. In these materials one cannot distinguish a basic structure. However, often these show sharp diffraction spots and a rotation symmetry of the diffraction pattern that is not crystallographic. For example, in AlMnPd the diffraction patterns shows five-fold symmetry along certain axes. The sharp spots indicate a high degree of ordering, the non-crystallographic symmetry indicates that there is no lattice periodicity. The spots can be labeled by six indices h_i in this case, and therefore this quasicrystal is quasiperiodic of rank six [1].

4.2 Symmetry

Consider a function that describes a crystal property, for example, the electron density $\rho(\boldsymbol{r})$. This function is lattice-periodic if there is a three-dimen-

sional (3D) lattice (a module of rank three with linearly independent basis) with elements $\boldsymbol{a}$ such that $\rho(\boldsymbol{r}) = \rho(\boldsymbol{r} - \boldsymbol{a})$. Then the Fourier transform consists of delta functions on the reciprocal lattice of the lattice that leaves $\rho(\boldsymbol{r})$ invariant. This implies that the function has space group symmetry: there are Euclidean transformations $\{R|\boldsymbol{t}\}$ such that

$$\rho(\boldsymbol{r}) = \rho(\{R|\boldsymbol{t}\}^{-1}\boldsymbol{r}) = \rho(R^{-1}(\boldsymbol{r} - \boldsymbol{t})), \tag{4.2}$$

and these transformations form the space group of the system. For the Fourier transform, this equality implies

$$\hat{\rho}(\boldsymbol{k}) = \exp(-\mathrm{i}\boldsymbol{k} \cdot \boldsymbol{t})\hat{\rho}(R\boldsymbol{k}). \tag{4.3}$$

Every motion for which this equality holds belongs to the space group. In particular, for the modulus of $\hat{\rho}(\boldsymbol{k})$ one has

$$|\hat{\rho}(\boldsymbol{k})| = |\hat{\rho}(R\boldsymbol{k})| \tag{4.4}$$

for every element R of the point group.

For a quasiperiodic system, the space-group symmetry can be very low, although the diffraction pattern may look very symmetric. Actually there is, generally, much hidden symmetry, which can be made explicit by generalizing the concept of symmetry [3,8,9].

If R belongs to the point group of the diffraction pattern, it maps the position of a spot on to another element of the Fourier module. Therefore, one has, in particular,

$$R\boldsymbol{a}_i^* = \sum_{j=1}^{n} \Gamma^*(R)_{ji}\boldsymbol{a}_j^*. \tag{4.5}$$

Here $\Gamma(R)$ is an integer $n \times n$ matrix. These matrices form an nD representation of the point group of the diffraction pattern. Because the intensities of two spots connected by R are the same, and the pattern of spots above a certain threshold is discrete, the point group is finite. Then it follows that the representation Γ is equivalent to an nD orthogonal representation. This implies that there is an nD crystallographic point group associated with the 3D symmetry point group of the diffraction pattern. In the next section, we shall give an interpretation of this relation.

For modulated crystals, there is another approach to the symmetry problem. The periodic modulation transforms with a representation of the space group of the basic structure. We shall not enter into the fine detail of this approach.

4.3 Embedding

It is simple to construct an example of a quasiperiodic function of rank n. Consider a function in R^n that is periodic with period 1 in each of its arguments:

$$f(x_1, x_2, \ldots, x_n) = f(x_1 + 1, x_2, \ldots, x_n) = \ldots$$

Then consider n real numbers α_i that are mutually IC (α_i/α_j is irrational), and define the function of one variable:

$$g(x) = f(\alpha_1 x, \alpha_2 x, \ldots, \alpha_n x).$$

The Fourier transforms of the functions f and g are

$$f(x_1, \ldots) = \sum_{\mathbf{m}} \hat{f}(m_1, \ldots, m_n) \exp(2\pi \mathrm{i} \sum_i m_i x_i)$$

$$\rightarrow g(x) = \sum_{k \in L} \hat{g}(k) \exp(\mathrm{i}kx),$$

with $L \doteq \{k = \sum_i 2\pi m_i \alpha_i\}$ and $\hat{g}(k) \doteq \hat{f}(m_1, \ldots)$. This means that L is the Fourier module of rank n, and that $g(x)$ is quasiperiodic.

On the other hand, each quasiperiodic function can be obtained by restricting a periodic function in n dimensions to a subspace. To that end, consider the basis vectors of the Fourier module as the projection of n linearly independent vectors of an nD reciprocal lattice. In this way, each vector of the Fourier module corresponds in a unique way to a reciprocal lattice vector in n dimensions. If the projection of the nD reciprocal lattice vector $\boldsymbol{k}_s$ is $\hat{\pi}\boldsymbol{k}_s = \boldsymbol{k}$, and $\hat{f}(\boldsymbol{k})$ is the Fourier transform of the quasiperiodic function $f(\boldsymbol{r})$, there is a lattice-periodic function

$$f_s(\boldsymbol{r}_s) = \sum_{\boldsymbol{k}_s} \hat{f}(\hat{\pi}\boldsymbol{k}_s) \exp(\mathrm{i}\boldsymbol{k}_s \cdot \boldsymbol{r}_s), \tag{4.6}$$

for which the restriction to the physical space is $f(\boldsymbol{r})$. This may look like a mathematical property without any physical meaning. However, the Fourier components of the nD periodic structure are exactly the same as those of the 3D quasiperiodic structure. The information in both approaches is then also the same. Working with a lattice-periodic function allows us to use the terminology and the techniques of normal crystallography. In addition, several features of quasiperiodic systems have a simple interpretation when considered in higher-dimensional space. But, after all, this is only a matter of convenience.

To the nD reciprocal lattice Σ^* there corresponds a direct lattice Σ. Each point in physical space corresponds via lattice translations from Σ to a point in the unit cell of Σ. By definition, the value of the function f_s at this point of the unit cell is the value of f in the corresponding point in physical space. In this way, the information given by the function f is simply folded into the unit cell of Σ.

In particular, if the density is given by delta peaks at the atomic positions, the density in n dimensions is concentrated on $(n-3)$-dimensional hypersurfaces in nD space, called atomic surfaces. A very simple example is that of an IC modulated crystal, as considered in Sect. 4.1. In that case the rank of the

Fourier module is four, and the quasiperiodic structure stems from a lattice periodic structure in four dimensions. Embedding gives lines in 4D space:

$$[\boldsymbol{n} + \boldsymbol{r}_j + \boldsymbol{a}_j \cos(\boldsymbol{Q} \cdot \boldsymbol{n} + \phi_j + t), \quad t],$$

where t is the internal coordinate running from minus infinity to plus infinity. Each atom corresponds to a line in 4D space, and the intersection with physical space ($t = 0$) gives the physical IC structure. The lines here are the atomic surfaces. If one does the same for a 3D tiling with icosahedral symmetry, the atomic surfaces are copies of the projection of the 6D unit cell on the 3D internal space. These are finite objects. An atomic surface gives an atomic position when it intersects physical space.

The symmetry of the lattice-periodic function f_s is an nD space group [6,10,11]. Because the function f_s is obtained via the lifting of a projection, the length scale in the internal space is not fixed. This means that point group transformations cannot mix physical and internal space and, therefore, the point group of the nD space group must leave the physical space invariant. It is $(3 + d)$-reducible.

Now we can come back to the question of symmetry. If $\{R_s|\boldsymbol{t}_s\}$ is an element of the nD space group, it leaves the embedded function invariant. Analogously to Sect. 4.1, the implied consequence for the Fourier transform is

$$\hat{f}(\boldsymbol{k}) \;=\; \exp(\mathrm{i}\boldsymbol{k}_s \cdot \boldsymbol{t}_s)\hat{f}(R\boldsymbol{k}). \tag{4.7}$$

Because of the construction, the argument of $\hat{f}$ is the 3D vector $\boldsymbol{k}$, and not the nD vector $\boldsymbol{k}_s$. Also, the action of the nD point group element on $\boldsymbol{k}$ is given by its physical component R. Writing the physical and internal components of the non-primitive translation $\boldsymbol{k}_s$, one obtains the relation

$$\hat{f}(\boldsymbol{k}) \;=\; \exp(\mathrm{i}\boldsymbol{k}_I \cdot \boldsymbol{t}_I)\exp(\mathrm{i}\boldsymbol{k}_E \cdot \boldsymbol{t}_E)\hat{f}(R\boldsymbol{k}). \tag{4.8}$$

If $\boldsymbol{t}_I$ vanishes this is just the condition for having the motion $\{R|\boldsymbol{t}_E\}$ as a symmetry element of $f(\boldsymbol{r})$. Therefore, the above condition is a generalization of the condition for space-group symmetry for a lattice-periodic function to that for a quasiperiodic function. The additional term is a shift in internal space, and corresponds to a shift in the phase of the structure, in particular for a modulated structure. The term can be considered as a hidden or internal symmetry, which is the reason for its name. In the theory of particles interacting with electromagnetic fields, this phase shift is in fact a gauge transformation. In that context, the shift in internal space can be considered as a compensating gauge transformation [2] – compensating, because without this term the element $\{R|\boldsymbol{t}_E\}$ would not be a symmetry operation.

Equation (4.7) is an expression in 3D reciprocal space. This is a kind of dual description to that using nD space groups. Being each other's Fourier transform, they are equivalent. However, use of both approaches has advantages [7,8]. For example, to describe the atomic structure it often gives more insight if one uses the direct space.

4.4 Superspace Groups

A superspace group is an nD space group with a point group K that leaves invariant a subspace with the dimension of the physical space (usually 3D). Such a superspace group can be the symmetry group of an aperiodic crystal if this invariant space is in an IC direction, i.e. if at most one lattice point belongs to it. The superspace group G has an invariant subgroup A of nD lattice translations and the quotient G/A is isomorphic to the point group K. The elements of K can be written as direct sum of an orthogonal transformation R_E in physical space and an orthogonal transformation R_I in internal or perpendicular space. In the same way, each translation, be it a lattice translation, or a non-primitive translation, can be written as $\boldsymbol{a} = (\boldsymbol{a}_E, \boldsymbol{a}_I)$.

The elements of an nD space group consist of pairs of an orthogonal transformation R_s and a translation $\boldsymbol{t}_s$. The elements R_s form the point group of the space group.

Orthogonal transformations in nD can, by a real transformation, be transformed into the direct sum of 1D and 2D components. The 1D components are ± 1, and the 2D components are rotations

$$\begin{pmatrix} \cos(2\pi ip/q) & -\sin(2\pi ip/q) \\ \sin(2\pi ip/q) & \cos(2\pi ip/q) \end{pmatrix} \tag{4.9}$$

of finite order. A crystallographic transformation leaves an nD lattice invariant. Therefore, the transformation is conjugated to an integer matrix. This puts restrictions on the possible values of q if n is given. A necessary condition for having a crystallographic transformation is that the invariants, in particular the trace, are integers, because such a transformation is equivalent to an integer matrix. If $\exp(2\pi ip/q)$ is an eigenvalue, the trace can only be integer if all conjugates, i.e. all complex numbers $\exp(2\pi ir/q)$ with r and q mutually prime, are eigenvalues. The number of these is the Euler function $\Phi(q)$, i.e. the number of integers smaller than, and mutually prime with, q. For q equal to 3, 4 or 6, this is two, but for 5, 8, 10 or 12 it is four. Therefore, a crystallographic transformation of order five is necessarily of dimension equal to, or larger than, four.

The point groups of a superspace group are reducible into a dD (d is the dimension of physical space) and an $(n-d)$-dimensional component. If the elements R_E generate a point group K_E and the elements R_I a point group K_I, the point group is a subgroup of $K_E \times K_I$. It is a so-called subdirect product of K_E and K_I. This suggests the following notation: the point group K_E is a finite, not necessarily crystallographic, point group in physical space. It has, therefore, a standard crystallographic symbol, introduced by Mauguin and Hermann. In this symbol, generators of K_E are indicated. Each such generator is associated with a transformation R_I. Therefore, one can denote the point group by the symbol of the 3D point group with, in parentheses, the corresponding elements R_I. For example, the basic structure of the IC phase of K_2SeO_4 is Pcmn. The basic structure is orthorhombic, and the modulation

wave vector $\boldsymbol{Q}$ is along the c-axis. The point group of the diffraction pattern then is mmm. The corresponding matrices Γ for the generators are then

$$\begin{pmatrix} -1 & 0 & 0 & 0 \\ 0 & 1 & 0 & 0 \\ 0 & 0 & 1 & 0 \\ 0 & 0 & 0 & 1 \end{pmatrix}, \quad \begin{pmatrix} 1 & 0 & 0 & 0 \\ 0 & -1 & 0 & 0 \\ 0 & 0 & 1 & 0 \\ 0 & 0 & 0 & 1 \end{pmatrix}, \quad \begin{pmatrix} 1 & 0 & 0 & 0 \\ 0 & 1 & 0 & 0 \\ 0 & 0 & -1 & 0 \\ 0 & 0 & 0 & -1 \end{pmatrix},$$

and the symbol for this group is mmm($11\bar{1}$).

For the quasicrystal AlMnPd, the point group of the diffraction pattern is the symmetry point group of the icosahedron ($5\bar{3}$m). One of the five-fold rotations is given by the matrix Γ:

$$\begin{pmatrix} 1 & 0 & 0 & 0 & 0 & 0 \\ 0 & 0 & 1 & 0 & 0 & 0 \\ 0 & 0 & 0 & 1 & 0 & 0 \\ 0 & 0 & 0 & 0 & 1 & 0 \\ 0 & 0 & 0 & 0 & 0 & 1 \\ 0 & 1 & 0 & 0 & 0 & 0 \end{pmatrix}.$$

This matrix is equivalent to the direct sum of a 2D rotation over $2\pi/5$ and a 2D rotation over $4\pi/5$. Therefore, it is equivalent to the pair $(5,5^2)$, the rotations over $2\pi/5$ and over $4\pi/5$, respectively. The Euler function $\Phi(5) = 4$. Therefore, the crystallographic five-fold rotation is minimally of four dimensions.

The elements of an nD space group are of the form

$$\{R_s|\boldsymbol{t}_s\} = \{(R, R_I)|(\boldsymbol{t}_E, \boldsymbol{t}_I)\}.$$

The translational parts $\boldsymbol{t}_s$ can be expressed in lattice coordinates x_i. For example, the superspace group of K_2SeO_4 in the IC phase has generators

$$\left(\begin{array}{cccc|c} -1 & 0 & 0 & 0 & \frac{1}{2} \\ 0 & 1 & 0 & 0 & 0 \\ 0 & 0 & 1 & 0 & \frac{1}{2} \\ 0 & 0 & 0 & 1 & 0 \end{array}\right), \quad \left(\begin{array}{cccc|c} 1 & 0 & 0 & 0 & 0 \\ 0 & -1 & 0 & 0 & \frac{1}{2} \\ 0 & 0 & 1 & 0 & 0 \\ 0 & 0 & 0 & 1 & \frac{1}{2} \end{array}\right),$$

$$\left(\begin{array}{cccc|c} 1 & 0 & 0 & 0 & \frac{1}{2} \\ 0 & 1 & 0 & 0 & \frac{1}{2} \\ 0 & 0 & -1 & 0 & \frac{1}{2} \\ 0 & 0 & 0 & -1 & 0 \end{array}\right).$$

The symbol for this group is Pcmn($1s\bar{1}$). The space groups for 3D crystals of rank 4 have been tabulated [6].

4.5 The Icosahedral Groups

An important class of quasicrystals are those showing a diffraction pattern with the symmetry of an icosahedron. Actually, the first quasicrystal discovered, AlMn, had this property, and this fact in particular raised a lot of interest. The point group of an icosahedron, which is also the point group of a dodecahedron, is of order 120. Its subgroup of rotations of order 60 has five conjugacy classes. The group is generated by a five-fold and a three-fold rotation (A and B, respectively). The group of order 120 ($5\bar{3}$m) is the direct product of the group 532 and the group of order two generated by the total inversion $\bar{1}$. The character table of the rotation group is given in Table 4.1.

Table 4.1. Character table of the group 532. The ordinals in the first column number the irreducible representation, $\tau = (\sqrt{5}-1)/2$

Representative	E	A	A^2	B	AB
Order of elements	1	5	5	3	2
Order of class	1	12	12	20	15
1.	1	1	1	1	1
2.	3	$1+\tau$	$-\tau$	0	-1
3.	3	$-\tau$	$1+\tau$	0	-1
4.	4	-1	-1	1	0
5.	5	0	0	-1	1

It is immediately clear that there is no invariant lattice in three dimensions, because there is no faithful representation with integer character. There are 4D and 5D faithful representations, but these cannot occur as point groups of a quasiperiodic structure, because they do not have an invariant 3D subspace. The lowest dimension then is six: the sum of the second and third irreducible representations has integer character, and has an invariant 3D subspace. This is indeed the possibility that is realized in quasicrystals.

The Fourier module of an icosahedral quasicrystal consists of vectors with Cartesian coordinates $m + n\tau$ with m and n integers [4]. As basis for the module, the following can be chosen:

$$\begin{aligned} &\boldsymbol{a}_1^* = (1,\Phi,0), \quad \boldsymbol{a}_2^* = (-1,\Phi,0), \quad \boldsymbol{a}_3^* = (0,1,\Phi), \\ &\boldsymbol{a}_4^* = (\Phi,0,1), \quad \boldsymbol{a}_5^* = (\Phi,0,-1), \quad \boldsymbol{a}_6^* = (0,1,-\Phi), \\ &\Phi = 1/\tau = (\sqrt{5}+1)/2. \end{aligned}$$

On this basis, the two generators of the rotation subgroup are given by the matrices

$$\Gamma(A) = \begin{pmatrix} 1 & 0 & 0 & 0 & 0 & 0 \\ 0 & 0 & 1 & 0 & 0 & 0 \\ 0 & 0 & 0 & 1 & 0 & 0 \\ 0 & 0 & 0 & 0 & 1 & 0 \\ 0 & 0 & 0 & 0 & 0 & 1 \\ 0 & 1 & 0 & 0 & 0 & 0 \end{pmatrix}, \quad \Gamma(B) = \begin{pmatrix} 0 & 0 & 0 & 0 & 0 & 1 \\ 1 & 0 & 0 & 0 & 0 & 0 \\ 0 & 0 & 0 & 0 & 1 & 0 \\ 0 & 0 & -1 & 0 & 0 & 0 \\ 0 & 0 & 0 & -1 & 0 & 0 \\ 0 & 1 & 0 & 0 & 0 & 0 \end{pmatrix}.$$

The representation of 532 generated by these two matrices has character (6,1,1,0,−2), which shows that it is equivalent to the sum of the two 3D irreducible representations. It is a 6D crystallographic point group, which is generated by the elements $5(5^2)$ and $3(3)$. Therefore, it can be denoted by $532(5^232)$. The group of order 120 then has symbol $\bar{5}\bar{3}\mathrm{m}(\bar{5}^2\bar{3}\mathrm{m})$.

In six dimensions, a lattice left invariant by the 6D point group has a metric tensor $g_{ij} = \boldsymbol{a}_i \cdot \boldsymbol{a}_j$ that is determined by the condition

$$\Gamma^{\mathrm{T}}(A) g \Gamma(A) = \Gamma^{\mathrm{T}}(B) g \Gamma(B) = g.$$

The general solution is the metric tensor with two free parameters:

$$g = \begin{pmatrix} a & b & b & b & b & b \\ b & a & b & -b & -b & b \\ b & b & a & b & -b & -b \\ b & -b & b & a & b & -b \\ b & -b & -b & b & a & b \\ b & b & -b & -b & b & a \end{pmatrix}.$$

A realization of a basis with such a metric tensor is

$$\begin{aligned} \boldsymbol{a}_1 &= (1, \Phi, 0, f, f\Phi, 0), & \boldsymbol{a}_2 &= (-1, \Phi, 0, f, -f\Phi, 0), \\ \boldsymbol{a}_3 &= (0, 1, \Phi, -f\Phi, 0, -f), & \boldsymbol{a}_4 &= (\Phi, 0, 1, 0, -f, f\Phi), \\ \boldsymbol{a}_5 &= (\Phi, 0, -1, 0, -f, -f\Phi), & \boldsymbol{a}_6 &= (0, 1, -\Phi, -f\Phi, 0, f). \end{aligned}$$

Here f is an arbitrary scale factor. When put equal to unity, the lattice becomes hypercubic. The full holohedral point group of such a lattice has order 46 080 and is irreducible. Therefore, there is no invariant subspace, and consequently the corresponding space groups cannot be used for quasiperiodic structures. Nevertheless, the parameter f is arbitrary. The solution of this problem is that, although the lattice of the embedded structure can be chosen to be hypercubic, the filling of the unit cell breaks this symmetry to an icosahedral subgroup.

There are three different Bravais classes within this lattice system: the primitive (s.i. = simple icosahedral), a body-centered (b.c.i.), and an all-face-centered (f.c.i.) lattice. There are only two point groups that lead to the same metric tensor: 532 and $\bar{5}\bar{3}\mathrm{m}$. Other subgroups leave more general metric tensors invariant, with more free parameters. An important example is the subgroup $\mathrm{m}\bar{3}$. This is a 3D crystallographic group that occurs as point group

of a commensurate approximant. It has three free parameters in the invariant metric tensor. It is generated by the matrices

$$\Gamma(C) = \begin{pmatrix} 0 & 0 & 0 & 0 & 0 & 1 \\ 0 & 0 & -1 & 0 & 0 & 0 \\ 0 & 0 & 0 & -1 & 0 & 0 \\ 0 & 1 & 0 & 0 & 0 & 0 \\ 1 & 0 & 0 & 0 & 0 & 0 \\ 0 & 0 & 0 & 0 & 1 & 0 \end{pmatrix}, \quad \Gamma(D) = \begin{pmatrix} 1 & 0 & 0 & 0 & 0 & 0 \\ 0 & 1 & 0 & 0 & 0 & 0 \\ 0 & 0 & 0 & 0 & 0 & 1 \\ 0 & 0 & 0 & 0 & 1 & 0 \\ 0 & 0 & 0 & 1 & 0 & 0 \\ 0 & 0 & 1 & 0 & 0 & 0 \end{pmatrix}$$

of order 3 and 2, respectively. The 6D point group is a reducible representation of the tetrahedral group of order 24: it is twice the ungerade irreducible representation of dimension 3. Thus the group is $m\bar{3}(m\bar{3})$. The fact that the group has two equivalent irreducible components implies that there are three free parameters for the metric tensor. The commensurate approximant of an icosahedral structure can be obtained by replacing the numbers Φ in the internal coordinates by a rational number p/q. The metric tensor then becomes

$$g = \begin{pmatrix} a & b & c & c & c & c \\ b & a & c & -c & -c & c \\ c & c & a & c & -c & -b \\ c & -c & c & a & b & -c \\ c & -c & -c & b & a & c \\ c & c & -b & -c & c & a \end{pmatrix}, \quad \begin{cases} a = 2 + \Phi + f^2(1 + (p/q)^2) \\ b = \Phi + f^2(1 - (p/q)^2) \\ c = \Phi - f^2 p/q \end{cases}.$$

Here f is again an arbitrary scale factor. The change from the IC value Φ, which gives a quasiperiodic structure, to the commensurate value p/q, corresponding to a 3D lattice-periodic structure, breaks the point group symmetry. However, between the two values the point group symmetry is $m\bar{3}(m\bar{3})$, but the structure is still quasiperiodic. This is an example of a symmetry-breaking phase transition inside the quasicrystalline phase.

In the s.i. Bravais class there are four space groups, in the b.c.i. class three and in the f.c.i. class four. They can be specified by the generators of the point groups and the associated translation components. For example, in the s.i. class there are the two symmorphic groups with zero translation components for the generators of the point groups (532, and $\bar{5}\bar{3}$m, respectively), and two non-symmorphic groups. One has point group $532(5^232)$ and a translation $(1/5,0,0,0,0,0)$ associated with the generator A, the other point group $\bar{5}\bar{3}m(\bar{5}^23m)$ and a translation $(0,2/5,2/5,2/5,2/5,2/5)$ being associated with the rotation A.

4.6 Dihedral Groups

Besides the icosahedral quasicrystals, there are also layered crystals with 8-, 10- or 12-fold symmetry in the planes. These correspond to the finite point

groups in three dimensions that do not have a faithful integer representation in three, but do have one in four dimensions. These groups are the dihedral groups, with one axis around which there is a p-fold rotation. These groups have irreducible representations of dimensions one and two. Because there is, for these layered structures, a translation symmetry perpendicular to the layers, the rank of the Fourier module is five.

If one takes a vector in 2D reciprocal space, a 5-, 8-, 10- or 12-fold rotation creates a star of vectors that generate a module of rank four. The star and the module generated by it are by construction invariant under the rotation, and in addition also under mirror operations perpendicular to or through the basis vectors. These orthogonal transformations generate a dihedral group. Because the module is invariant under the total inversion, which, here, is a two-fold rotation, a module invariant under five is also invariant under ten. Therefore, the symmetry groups of the modules are the groups 8mm, 10mm and 12mm. If one adds a perpendicular 1D space with a basis lattice vector, the modules are invariant under 8/mmm, 10/mmm and 12/mmm of order 32, 40 and 48, respectively. The modules can be lifted to 5D reciprocal lattices, and the corresponding 5D holohedral point groups are $8\mathrm{mm}(8^3\mathrm{mm})\perp\mathrm{m}$, $10\mathrm{mm}(10^3\mathrm{mm})\perp\mathrm{m}$ and $12\mathrm{mm}(12^5\mathrm{mm})\perp\mathrm{m}$. These symbols mean that the point groups are direct products of a 4D point group of order 16, 20 or 24, respectively, and a 1D group m, whereas the two subgroups act on mutually perpendicular spaces. As an example, the group $8\mathrm{mm}(8^3\mathrm{mm})\perp\mathrm{m}$ has the following generators:

$$8(8^3) = \begin{pmatrix} 0 & 0 & 0 & -1 & 0 \\ 1 & 0 & 0 & 0 & 0 \\ 0 & 1 & 0 & 0 & 0 \\ 0 & 0 & 1 & 0 & 0 \\ 0 & 0 & 0 & 0 & 1 \end{pmatrix}, \quad m(m) = \begin{pmatrix} 0 & 0 & 0 & 1 & 0 \\ 0 & 0 & 1 & 0 & 0 \\ 0 & 1 & 0 & 0 & 0 \\ 1 & 0 & 0 & 0 & 0 \\ 0 & 0 & 0 & 0 & 1 \end{pmatrix},$$

$$m = \begin{pmatrix} 1 & 0 & 0 & 0 & 0 \\ 0 & 1 & 0 & 0 & 0 \\ 0 & 0 & 1 & 0 & 0 \\ 0 & 0 & 0 & 1 & 0 \\ 0 & 0 & 0 & 0 & -1 \end{pmatrix}.$$

The element $8(8^3)$ is equivalent to the direct sum of a rotation through an angle $\pi/4$ and a rotation through $3\pi/4$. The element m(m) has two eigenvalues -1 and three eigenvalues $+1$.

There are five Bravais classes in 5D in these three families: two in the octagonal case, two in the decagonal case, and one in the dodecagonal case. The number of space groups is much larger than in the icosahedral case: 73 in the octagonal family, 52 in the decagonal family, and 25 in the dodecagonal family. Up to now, only a small proportion of these have been found to be the symmetry group of a quasicrystal.

4.7 Wyckoff Positions

A point in a unit cell has a site symmetry that is defined as the point group of the subgroup of the space group that leaves the point invariant to within lattice translations. The points are put into equivalence classes, called Wyckoff positions. Two points belong to the same Wyckoff position if the subgroups of the space group that leave them invariant up to lattice vectors are conjugated. In particular, the orbit of a point under the space group belongs to one Wyckoff position. Site symmetry and the number of points in the orbit are important for characterization of structures, and for the study of local properties. If one knows the number of atoms of a certain species in the unit cell, there are restrictions on the possible occupied Wyckoff positions. For a general point in the unit cell, the site symmetry is the identity and the length of the orbit is equal to the order of the point group. In the case of centering, invariance is considered up to the vectors of the conventional lattice, and the length of the orbit is the length in the primitive unit cell times the index of the centering.

If an atom A belongs to a Wyckoff position w, every two points in the orbit should remain separated by a minimal distance. This also applies to the atomic surfaces in a quasiperiodic structure. Moreover, if an atomic surface is located in a Wyckoff position w, the site symmetry must leave the atomic surface invariant. In other words, the site symmetry should be compatible with the shape of the atomic surface in a quasicrystal.

Consider as an example the symmorphic space group in the s.i. family with point group $532(5^232)$. According to the generating matrices $\Gamma(A)$ and $\Gamma(B)$ given in Sect. 4.5, the point (x, y, y, y, y, y) has site symmetry $5(5^2)$: it is left invariant by $\Gamma(A)$. This means that there are ten points in the orbit. The mutual distances in physical space of atoms in the orbit depend on the values x and y, and on the lattice constant. An atomic surface for such a quasicrystal is parallel to the internal space. The additional condition is that the internal point group $K_I = 5^2$ acting in V_I leaves the atomic surface invariant: it has five-fold symmetry.

4.8 Diffraction

Diffraction measures, in principle, the modulus of the structure factor

$$S(\boldsymbol{k}) = \sum_j f_j \exp(\mathrm{i}\boldsymbol{k} \cdot \boldsymbol{r}_j). \tag{4.10}$$

Here f_j is the atomic scattering factor, and the sum runs over all atoms of the system. There is scattering only for the vectors belonging to the Fourier module. There is a one-to-one correspondence between the vectors $\boldsymbol{k}$ of the Fourier module and the reciprocal lattice vectors in nD space. Therefore, the

structure factor is the same as that for a periodic nD system with atomic surfaces in the unit cell. This can be formulated as follows:

$$S(\boldsymbol{k} = \hat{\pi}\boldsymbol{k}_s) = \sum_j \int_{\Omega_j} f_j(\boldsymbol{t}) \exp(\mathrm{i}\boldsymbol{k} \cdot \boldsymbol{r}_E(j, \boldsymbol{t})) \exp(\mathrm{i}\boldsymbol{k}_I \cdot \boldsymbol{t}) \mathrm{d}\boldsymbol{t}. \tag{4.11}$$

The integration is over all atomic surfaces in the unit cell. This structure factor has the usual behavior under a symmetry operation $\{(R, R_I)|\,(\boldsymbol{t}_E, \boldsymbol{t}_I)\}$:

$$S(\boldsymbol{k}) = \exp(\mathrm{i}\boldsymbol{k}_I \cdot \boldsymbol{t}_I) S(R\boldsymbol{k}) \exp(\mathrm{i}\boldsymbol{k} \cdot \boldsymbol{t}_E). \tag{4.12}$$

Without internal shift $\boldsymbol{t}_I$ this is just the condition for a 3D Euclidean transformation $\{R|\boldsymbol{t}_E\}$ to be a symmetry operator. In this sense, it is a generalization of the usual procedure. From this follow extinction rules. If $\boldsymbol{k}$ is invariant under R, the structure factor is zero if $\boldsymbol{k} \cdot \boldsymbol{t}_E + \boldsymbol{k}_I \cdot \boldsymbol{t}_I \neq 0 \pmod{2\pi}$.

As an example, take the non-symmorphic s.i. space group with point group $532(5^2 32)$ mentioned in Sect. 4.5. The five-fold rotation has as translation $\boldsymbol{a}_1/5$. It leaves the module vector $\boldsymbol{k} = [h_1 h_2 h_2 h_2 h_2 h_2]$ invariant. The condition for the structure factor to vanish at this position is that $\boldsymbol{k}_s \cdot \boldsymbol{t}_s = \sum_i h_i x_i = h_1/5$ is equal to zero modulo integers, in order to have a non-vanishing $S(\boldsymbol{k})$. Therefore, one has the condition that h_1 is a multiple of five. These general extinction rules can be tabulated for all 11 icosahedral space groups. They have been given for all 5D and 6D quasicrystals [5,11].

References

1. Cahn J.W., Shechtman D., Gratias D. (1986): J. Mat. Res. **1**, 13
2. Janner A., Janssen T. (1971): Physica **53**, 1
3. Janner A., Janssen T. (1977): Phys. Rev. **B15**, 643
4. Janssen T. (1986): Acta Crystallogr. **A42**, 261
5. Janssen T. (1988): Phys. Rep. **168**, 57
6. Janssen T., Janner A., de Wolff P.M., Looijenga-Vos A. (1992): In *Internal Tables for Crystallography*, Vol. C, ed. A.J.C. Wilson, Kluwer, Dordrecht, p. 797
7. Lifshitz R. (1996): Physica **A232**, 633
8. Mermin N.D., Rokhsar D.S., Wright D.C. (1987): Phys. Rev. Lett. **58**, 2099
9. Opechowski W. (1986): *Crystallographic and Metacrystallographic Groups*, North-Holland, Amsterdam
10. van Smaalen S. (1995): Cryst. Rev. **4**, 79
11. Yamamoto A. (1996): Acta Crystallogr. **A52**, 509

5 Experimental Determination of the Structure of Quasicrystalline Alloys: Experimental Techniques and Modeling

Michel Boudard

Summary. The diffraction and analysis techniques for the structure determination of quasicrystals are reviewed with examples of 1D and 3D quasicrystals. The various strategies for modeling are then presented.

5.1 Introduction

The atomic structure of matter can be studied by means of diffraction techniques, such as electron, X-ray and neutron diffraction [13,18]. Indeed the diffraction pattern of a given system depends directly on its structure. In a very schematic way Fig. 5.1 shows general results expected for gases, liquids, amorphous solids and crystals. Each pattern of the distribution of intensities is characteristic of the different systems, and thus information on the structure can be obtained from the analysis of these diffraction spectra. Quasicrystals (QCs) present diffraction patterns very similar to those of crystals

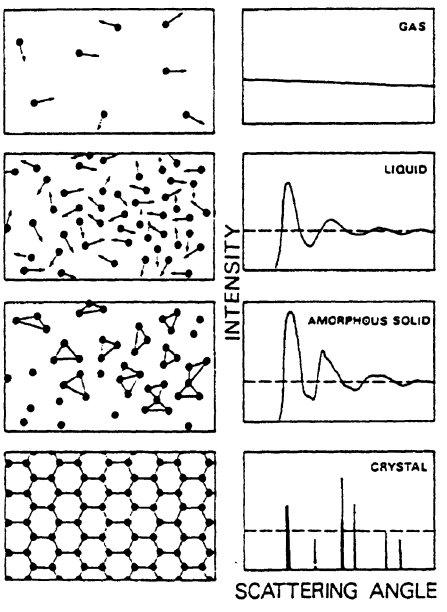

Fig. 5.1. Pictorial representation of atom distribution in matter and expected typical diffraction patterns [13]

J.-B. Suck et al. (eds.), *Quasicrystals*
© Springer-Verlag Berlin Heidelberg 2002

in that they consist of sharp diffraction peaks (Bragg reflections) which are characteristic of a long-range order present in these materials. It is possible to get all the information necessary to describe the structure from a limited set of such Bragg peaks. This problem is solved for crystals by crystallography (which groups different techniques and concepts such as Patterson analysis, contrast variation, direct methods, point group and space group determination, and symmetry analysis). As we will see throughout this chapter, for QCs it is solved in a very similar way.

5.2 X-Ray and Neutron Diffraction

First of all we will recall some basic features necessary to understand a diffraction experiment. Diffraction arises from collective scattering. In a very schematic way Fig. 5.2 represents the scattering of a monochromatic beam by one particle. We will consider either the scattering of an X-ray or a thermal neutron beam (the associated wavelength is of the order of 1Å). In the

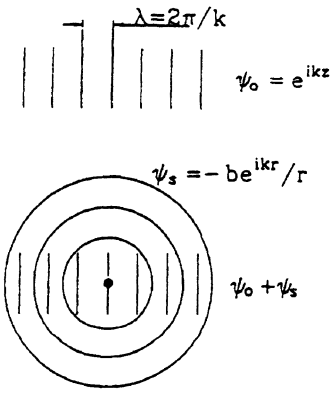

Fig. 5.2. Scattering of a monochromatic beam by one particle [18]

case of neutron scattering, the scattered wave by one particle takes, under certain approximations the form [18]

$$\psi_{1,\mathrm{scatt}}(\boldsymbol{r}) = -\frac{2\pi m}{h^2}\frac{\mathrm{e}^{\mathrm{i}2\pi kr}}{r}\widetilde{V}_1(\boldsymbol{k})\,. \tag{5.1}$$

This equation represents a spherical wave with amplitude proportional to $\widetilde{V}_1(\boldsymbol{k})$: the Fourier transform (FT) of the interaction potential over the region of interest. The scattering process arises from the interaction of neutrons with the nucleus. The interaction range of the strong force between the nucleus and neutron is of the order of a fm (10^{-15}m) i.e. is point-like scattering and the interaction potential can be approximate by a delta function. This approximation leads to the Fermi pseudo-potential $V_1(\boldsymbol{r}) = \alpha_1\delta(\boldsymbol{r} - \boldsymbol{r}_j)$ and

so it turns out that $\frac{2\pi m}{h^2}\widetilde{V}(\boldsymbol{k}) = b$, where b is a constant which is called the neutron scattering length.

Let us take a second scattering center located at $\boldsymbol{r_2}$ from the origin. Then

$$\psi_{2,\mathrm{scatt}}(\boldsymbol{r}) = -\frac{2\pi m}{h^2}\frac{\mathrm{e}^{\mathrm{i}2\pi kr}}{r}\widetilde{V}_2(\boldsymbol{k})\,\mathrm{e}^{\mathrm{i}\boldsymbol{k}\cdot r_2}\,. \tag{5.2}$$

The total amplitude can be written for N atoms

$$\psi_{\mathrm{scatt}}(\boldsymbol{r}) = -\frac{2\pi m}{h^2}\frac{\mathrm{e}^{\mathrm{i}2\pi kr}}{r}\widetilde{V}(\boldsymbol{k}) \tag{5.3}$$

where the term $\widetilde{V}(\boldsymbol{k})$ is the FT of the interaction potential due to the N particles, $V(\boldsymbol{r})$, and both terms are written in the general form

$$V(\boldsymbol{r}) = \sum_j \alpha_j \delta(\boldsymbol{r} - \boldsymbol{r}_j) \tag{5.4}$$

$$\widetilde{V}(\boldsymbol{k}) = \sum_j \widetilde{V}_j(\boldsymbol{k})\,\mathrm{e}^{\mathrm{i}\boldsymbol{k}\cdot\boldsymbol{r}}\,. \tag{5.5}$$

We can now introduce in (5.3) the scattering length of the different scattering Centrex

$$\psi_{\mathrm{scatt}}(\boldsymbol{r}) = -\frac{\mathrm{e}^{\mathrm{i}2\pi kr}}{r}\sum_j b_j\,\mathrm{e}^{\mathrm{i}\boldsymbol{k}\cdot\boldsymbol{r}}\,. \tag{5.6}$$

The sum in (5.6) is known as the structure factor and we will generally write it as

$$F(\boldsymbol{k}) = \sum_j b_j\,\mathrm{e}^{\mathrm{i}\boldsymbol{k}\cdot\boldsymbol{r}}\,. \tag{5.7}$$

For X-rays, the elementary scattering is due to Thomson scattering from a single electron. The incident X-ray photon has an electric field that exerts a force on the electron and gives an instantaneous acceleration. The accelerated electron then radiates like a dipole antenna. When considering an atom one has to take into account all electrons present in the atom. The situation is similar to that described above for the neutron: each electron has a phase term and finally one arrives at an expression of the form

$$\psi_{1,\mathrm{scatt}}(\boldsymbol{r}) = \text{constant}\,\widetilde{f}_1(\boldsymbol{k}) \tag{5.8}$$

where $\widetilde{f}_1(\boldsymbol{k})$ is the FT of the electron density of each individual atom (numbered 1 for (5.8)) and is known as the form factor of the atom. When considering several atoms one gets an expression similar to (5.3) where the diffracted amplitude is proportional to the FT $\widetilde{\rho}(\boldsymbol{k})$ of the electron density $\rho(\boldsymbol{r})$.

Thus the amplitude of the scattered wave is proportional to the FT either of the potential (neutron) or to the electron density (X-ray). The characteristic features of diffraction from crystals (and QCs) follows from the special distribution of the atoms in a periodic (respectively quasiperiodic) way.

Let us consider for example a 3D periodic distribution of atoms. The structure is completely specified if ones knows the unit cell (generally defined by three vector $\boldsymbol{a}, \boldsymbol{b}, \boldsymbol{c}$) and the distribution of atoms inside the unit cell. The crystal is then built by a periodic distribution of the unit cell along the three direction defined by the vectors $\boldsymbol{a}, \boldsymbol{b}, \boldsymbol{c}$ and thus the resulting periodic (Fermi pseudo-) potential (neutron case) can be expanded in a Fourier series (plane waves)

$$V(\boldsymbol{r}) = \sum_{\boldsymbol{k}} V_{\boldsymbol{k}} \mathrm{e}^{\mathrm{i}\boldsymbol{k}\cdot\boldsymbol{r}} \,. \tag{5.9}$$

The different values of $\boldsymbol{k}$ belong to the reciprocal lattice of the lattice just defined in real space and is defined as:

$$\boldsymbol{k} = n\boldsymbol{a}^* + m\boldsymbol{b}^* + l\boldsymbol{c}^* \tag{5.10}$$

with $\boldsymbol{a}\cdot\boldsymbol{a}^* = \boldsymbol{b}\cdot\boldsymbol{b}^* = \boldsymbol{c}\cdot\boldsymbol{c}^* = 1$ and $\boldsymbol{a}^*\cdot\boldsymbol{b} = \boldsymbol{a}^*\cdot\boldsymbol{c} = \cdots = \cdots = 0$. The coefficients $V_{\boldsymbol{k}}$ are then

$$V_{\boldsymbol{k}} = \frac{1}{\mathrm{Vol}_c} \int_{\text{unit cell}} V(\boldsymbol{r}) \mathrm{e}^{-\mathrm{i}2\pi\boldsymbol{k}\cdot\boldsymbol{r}} \mathrm{d}^3\boldsymbol{r} \tag{5.11}$$

where Vol_c corresponds to the unit cell volume. These coefficients $V_{\boldsymbol{k}}$ are directly related to the FT of the potential $\widetilde{V}(\boldsymbol{k})$ used in (5.3) and we have

$$\widetilde{V}(\boldsymbol{k}) = \text{constant.} \sum_{\boldsymbol{k}'} V_{\boldsymbol{k}'} \delta(\boldsymbol{k} - \boldsymbol{k}') \tag{5.12}$$

where the sum is over the vectors defined by (5.10). Thus the periodicity of the potential $V(\boldsymbol{r})$ is responsible of the geometry of the reciprocal space: the scattered amplitude is directly related to $\widetilde{V}(\boldsymbol{k})$ (see (5.3)) and is according to (5.12) non-zero only for $\boldsymbol{k}$ vectors belonging to the reciprocal lattice defined by (5.10).

It is thus possible from the diffraction experiments to get information about the distribution of atoms: in particular indexing a diffraction pattern gives the three vectors a, b, c defining the unit cell. To go further, i.e. to know what is inside the unit cell one has to know all the coefficients $V_{\boldsymbol{k}}$ in (5.9). This idea is summarized in Fig. 5.3. The 1D crystal is obtained as a convolution of a Poisson distribution by a function over one period. The coefficients $V_{\boldsymbol{k}}$ depend only on the content of the unit cell (see (5.11)) and conversely the $V_{\boldsymbol{k}}$ give information about the content of the unit cell (see (5.9)).

Some of these ideas can be generalized for QCs, i.e quasiperiodic structures, by introducing a periodic image in a higher-dimensional space [1,2,14].

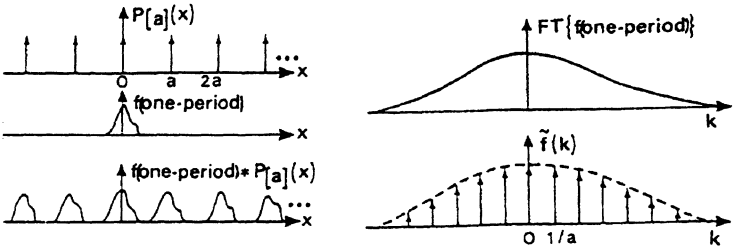

Fig. 5.3. A 1D crystal obtained as the convolution of a Poisson distribution by a function over one period [18]

This concept will be developed in the next section but we will first briefly consider in the next two subsections two difficulties that appear in the determination of structures via diffraction experiments and how they can be overcome.

5.2.1 Patterson Analysis

In a diffraction experiment we do not measure the complex amplitude (for example $V_{\boldsymbol{k}}$) but the intensity ($V_{\boldsymbol{k}}V_{\boldsymbol{k}}^*$). Thus if we want to find the distribution of either the electronic density or the distribution of potentials in the unit cell from a simple FT of $\widetilde{V}(\boldsymbol{k})$ we need to find the phase of the coefficients $V_{\boldsymbol{k}}$ as the intensity will only provide the square of the modulus of $V_{\boldsymbol{k}}$. The direct methods developed for crystals allow us to find relations between the phases of different coefficients and to propose a starting set of phases for solving the structure. These methods have not been developed for QCs. However, some information about the structure can be obtained by performing the FT of the intensity, called the Patterson function (PF), which is defined as

$$P(\boldsymbol{r}) = \sum_{\boldsymbol{k}} (V_{\boldsymbol{k}}V_{\boldsymbol{k}}^*)\mathrm{e}^{\mathrm{i}\boldsymbol{k}\cdot\boldsymbol{r}}\,. \tag{5.13}$$

The FT of a product of functions is given by a convolution product

$$P(\boldsymbol{r}) = \rho(\boldsymbol{r}) * \rho(-\boldsymbol{r}) = \int_{all\ space} \rho(\boldsymbol{u})\rho(\boldsymbol{u}+\boldsymbol{r})\mathrm{d}^3\boldsymbol{u}\,. \tag{5.14}$$

This function is the density correlation function, or pair correlation function: it takes non-zero values only if there is density both at $\boldsymbol{u}$ and $\boldsymbol{u}+\boldsymbol{r}$ (see (5.14)), i.e., at points separated by $\boldsymbol{r}$. Thus this function gives a distribution of all interatomic distances. In the case of periodic structures the PF has the same periodicity as the structure and is always centrosymmetrical due to the fact that $V_{\boldsymbol{k}}V_{\boldsymbol{k}}^* = V_{-\boldsymbol{k}}V_{-\boldsymbol{k}}^*$. These features of the PF are represented for a 1D periodic example in Fig. 5.4. For very simple structures it is possible to get from the PF all the information about $V(\boldsymbol{r})$ or $\rho(\boldsymbol{r})$ in the unit cell. However when one deals with several atoms per unit cell and with different chemical

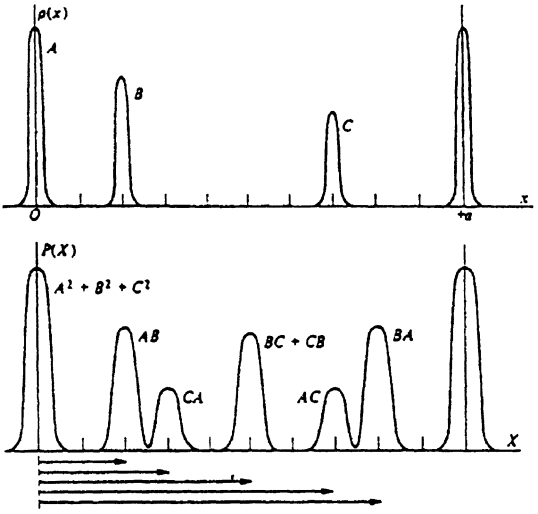

Fig. 5.4. Construction of the PF from a 1D periodic structure having three atoms A, B and C. Top panel: the corresponding electron density function. Lower panel: the corresponding PF [16]

species the problem can be difficult to solve from a Patterson analysis alone. Figure 5.4 indicates the complexity which can arise in such a case.

5.2.2 Contrast Variation

A very powerful method to overcome the problem of the presence of different chemical species (see the difference of height of $\rho(\boldsymbol{r})$ in Fig. 5.4) is contrast variation. The idea of this method is to vary either the scattering length or the form factor (see (5.7)) for a given element and thus perform the corresponding diffraction experiments for each scattering length (or form factor). Figure 5.5 shows the results for a pseudo-binary alloy A-T in which the scattering length of the element T has been varied by isomorphic substitution, i.e. one substitutes one element by another with a different scattering length. The information contained in these different diffraction patterns (note the different distribution of relative intensities) allows us to separate the contribution of atoms A and T. One ended in particular with $|\widetilde{V_A}(\boldsymbol{k})|$, $|\widetilde{V_T}(\boldsymbol{k})|$ and can thus perform a simplified Patterson analysis for the elements A and T separately.

5.3 Quasicrystallography or How to Extract Information About the Structure from the Diffraction Data

It is possible to introduce a periodic image in a higher-dimensional space to describe the quasiperiodic structure by the so-called cut method [1,2,14]. We will now see how one can use this method to extract information on

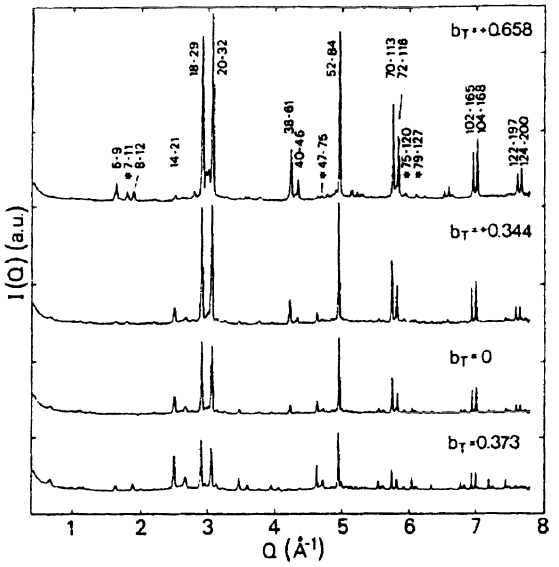

Fig. 5.5. Neutron diffraction patterns corresponding to a contrast variation experiment [3]. The different scattering lengths corresponding to T are indicated. The principal peaks are indexed with the N, M indices following [5]

a quasiperiodic structure from diffraction data. We will start with several simple 1D models in order to explain how one solves a quasiperiodic structure keeping in mind that in the case of a periodic structure one has to determine:

(a) the unit cell;
(b) the distribution of atoms in the unit cell.

5.3.1 The Cut Method. A 1D Example

The cut method allows the construction of a quasiperiodic model using a periodic image in a higher-dimensional space. The 2D periodic image represented in Fig. 5.6 gives rise to the 1D quasiperiodic model of the Fibonacci chain. This 2D image is obtained by decorating a square lattice with segments. A point is then generated along the 1D line perpendicular to the segments (dashed line in Fig. 5.6 corresponding to physical space) whenever a segment intersects the line. The quasiperiodic structure is thus obtained by cut of the 2D periodic image. The 2D space can be obtained as the direct sum

$E = E_{\text{par}} \oplus E_{\text{per}}$ of two orthogonal subspaces each of dimension 1:

E_{par} the physical space or parallel space (dashed line orthogonal to the segments decorating the square lattice in Fig. 5.6);

E_{per} the perpendicular (or orthogonal) space.

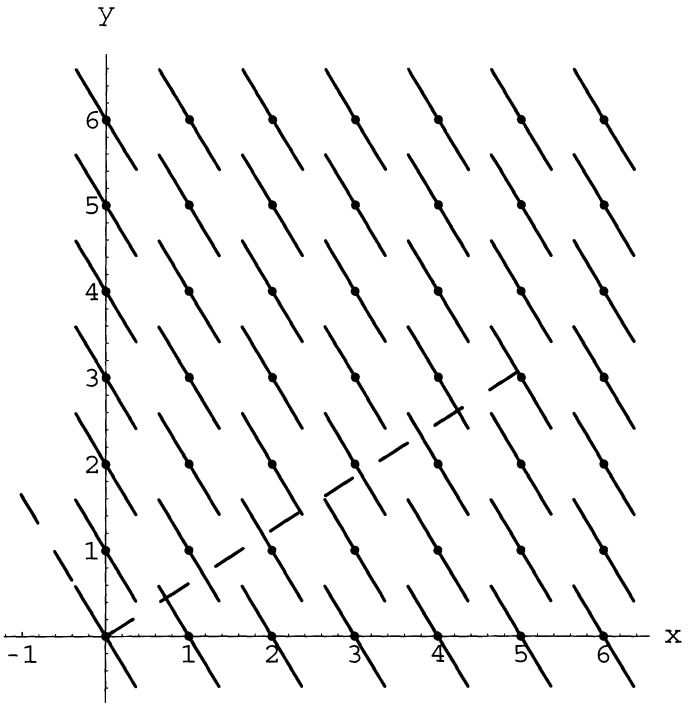

Fig. 5.6. A 2D periodic image generating the 1D Fibonacci chain

We can associate a different set of segment to the square unit cell. Figure 5.7 represents another example built of two segments in each unit cell:

(1) a segment S_{perp} (A) decorating the point of the square lattice generating atoms of chemical species A;
(2) a segment S_{perp} (B) decorating the middle point of each square cell generating atoms of chemical species B.

The periodic image is then determined by:

(1) the periodic lattice (i.e. the unit cell);
(2) the sites occupied in the unit cell (e.g. origin and center in Fig. 5.7);
(3) the shape, dimension and chemical species of the different segments (segments S_{perp} (A) and S_{perp} (B) in Fig. 5.7).

Solving a quasiperiodic structure means the determination of these three elements associated with the periodic image. In the more general case (e.g. for 6D periodic images) we will refer to the objects that are decorating the lattice (the segments for previous 2D examples) as atomic objects (AOs) (also called "atomic surfaces").

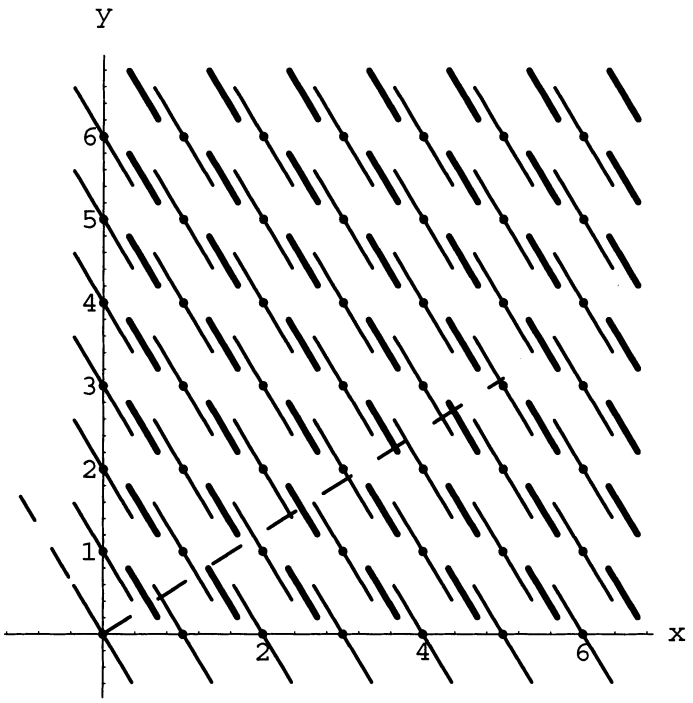

Fig. 5.7. 2D periodic image built with two segments

5.3.2 Crystallography of QCs

It is possible to generalize the basic concepts of crystallography for the periodic image involving the AOs. The formalism is completely equivalent to the case of periodic crystals and allows a direct use of the experimental data obtained from diffraction experiments for solving the quasiperiodic structure.

Usually the density of a (periodic) crystal, with a unit cell defined by the vectors $\boldsymbol{a}$, $\boldsymbol{b}$ and $\boldsymbol{c}$, can be written as a 3D Fourier series:

$$\rho(\boldsymbol{r}) = \sum_{k} \widetilde{\rho}(\boldsymbol{k}) \exp(\mathrm{i}\boldsymbol{k}\cdot\boldsymbol{r}) \tag{5.15}$$

where $\boldsymbol{r}$ represents a position vector in the direct space (physical space) and the sum extends over the set of points of reciprocal space (see (5.9) and (5.10)). The position vector can be expressed as

$$\boldsymbol{r} = x\boldsymbol{a_1} + y\boldsymbol{a_2} + z\boldsymbol{a_3} \tag{5.16}$$

and thus (5.15) can be written

$$\rho(x,y,z) = \sum_{n,l,m} F_{n,l,m} \exp(\mathrm{i}2\pi(nx + ly + mz)) \tag{5.17}$$

where $F_{n,l,m}$ are the Fourier coefficients (FCs) (or structure factors of the crystal).

These concepts can be generalized to the periodic image associated to the QC. The density of the 2D periodic image described in Fig. 5.6 is periodic and can be written as

$$\rho(x,y) = \sum_{n,l} F_{n,l} \exp(\mathrm{i}2\pi(nx + ly)) \,. \tag{5.18}$$

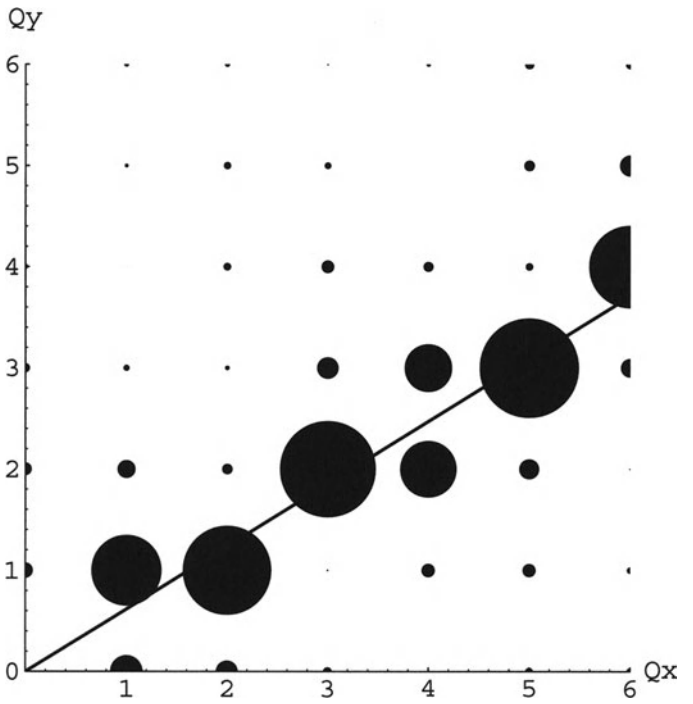

Fig. 5.8. Intensities corresponding to the model of Fig. 5.6

The difference with respect to a crystal is the introduction of AOs (segments in Figs. 5.6 and 5.7) instead of atoms. We will see how this point affects the FCs $F_{n,l}$. These coefficients (or structure factors $F_{n,l}$) can be calculated by Fourier transforming the density $\rho(x,y)$ corresponding to the square lattice decorated by a segment $S_{\mathrm{perp}}(\boldsymbol{r})$. This density can be written as a convolution product:

$$\rho(\boldsymbol{r}) = \sum_{j} \delta(\boldsymbol{r} - \boldsymbol{r}_j) * S_{\mathrm{perp}}(\boldsymbol{r}) \tag{5.19}$$

where $S_{\text{perp}}(\boldsymbol{r})$ is a window function depending only on $\boldsymbol{r}_{\text{perp}}$ defined as:

$$S_{\text{perp}}(\boldsymbol{r}) = 1 \text{ if } \boldsymbol{r}_{\text{perp}} \in \left[\frac{-S_{\text{perp}}}{2}, \frac{S_{\text{perp}}}{2}\right] \tag{5.20}$$

$$0 \text{ if } \boldsymbol{r}_{\text{perp}} \notin \left[\frac{-S_{\text{perp}}}{2}, \frac{S_{\text{perp}}}{2}\right] . \tag{5.21}$$

One obtains the reciprocal space by the FT of the density in the direct space. It is built of a discrete set of delta functions defining the square reciprocal lattice multiplied by the FT of the AO (segment in Figs. 5.6 and 5.7). This will be denoted $G_{S_{\text{perp}}}(\boldsymbol{Q})$ (a vector of the reciprocal space $\boldsymbol{k}$ will be denoted hereafter as $\boldsymbol{Q}$). The FT of the density is

$$\widetilde{\rho}(\boldsymbol{Q}) = \frac{1}{a^2}\left[\sum_j \delta(\boldsymbol{Q} - \boldsymbol{Q_j}) G_{S_{\text{perp}}}(\boldsymbol{Q})\right] \tag{5.22}$$

with

$$G_{S_{\text{perp}}}(\boldsymbol{Q}) = \frac{\sin(X)}{X} \tag{5.23}$$

and

$$X = \frac{Q_{\text{perp}} S_{\text{perp}}}{2} \tag{5.24}$$

Thus each Bragg peak is the result of a delta peak multiplied by the function $G_{S_{\text{perp}}}$ evaluated at $Q_{j\text{perp}}$. These results are represented in Fig. 5.8. The square of the modulus of the structure factor corresponding to each Bragg peak is represented by the area of the circles. The points j which have a small component $Q_{j\text{perp}}$ have larger areas due to the behavior of the function describe by (5.23) (this function has its maximum at 0 and decays rapidly when considering increasing X values).

The 1D quasiperiodic structure in physical space was obtained by a cut. The corresponding operation in reciprocal space is a projection, i.e. the reciprocal space of the 1D quasiperiodic structure in Fig. 5.8 is obtained by projecting along the perpendicular direction of the Bragg peaks lying in the square lattice. This construction leads to a dense set of Bragg peaks distributed quasiperiodically in the 1D reciprocal space.

This method can easily be extended to the structure represented in Fig. 5.7. The density can be written as

$$\rho(\boldsymbol{r}) = \sum_j \delta(\boldsymbol{r} - \boldsymbol{r_j}) * S^{\text{A}}_{\text{perp}}(\boldsymbol{r}) + \sum_j \delta(\boldsymbol{r} - \boldsymbol{r_j} - \boldsymbol{r_{BC}}) * S^{\text{B}}_{\text{perp}}(\boldsymbol{r}) . \tag{5.25}$$

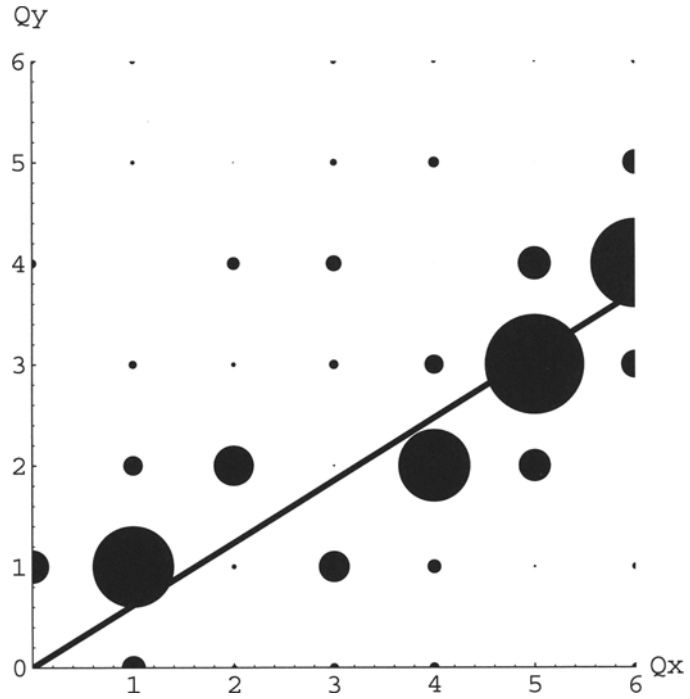

Fig. 5.9. Intensities corresponding to the model of Fig. 5.7

This expression is the extension of (5.19) for the case of two segments. The additional segment is centered on the body center position (BC) of the square lattice identified by the vector $\boldsymbol{r}_{\mathbf{BC}}$. The FT of the density is

$$\widetilde{\rho}(\boldsymbol{Q}) = \frac{1}{a^2}\left[\sum_j \delta(\boldsymbol{Q}-\boldsymbol{Q}_j)\right]\left[G^{\mathrm{A}}_{S_{\mathrm{per}}}(\boldsymbol{Q}) + \exp(\mathrm{i}\boldsymbol{Q}\cdot\boldsymbol{r}_{\mathbf{BC}})G^{\mathrm{B}}_{S_{\mathrm{per}}}(\boldsymbol{Q})\right] \quad (5.26)$$

The FCs (5.18) are

$$F_{n,m} = \frac{1}{a^2}\left[G^{\mathrm{A}}_{S_{\mathrm{perp}}}(\boldsymbol{Q}_{j,perp}) + \exp(\mathrm{i}\boldsymbol{Q}_j\cdot\boldsymbol{r}_{\mathbf{BC}})G^{\mathrm{B}}_{S_{\mathrm{perp}}}(\boldsymbol{Q}_{j,\mathrm{perp}})\right] \quad (5.27)$$

These results are represented in Fig. 5.9. The square of the modulus of the structure factor corresponding to each Bragg peak is represented by the area of the circles. The points j which have a small component $Q_{j,\mathrm{perp}}$ have larger areas.

5.4 An Example: The Structure of the i-AlPdMn Icosahedral Phase

We will now see how the basic tools of quasicrystallography described in the previous section apply when solving the structure of the i-AlPdMn QC [3,4].

5.4.1 Neutron Contrast Variation on Powder Samples

We have already shown in Fig. 5.5 the four different neutron diffraction patterns obtained by varying the scattering length of the Mn [3]. This is done by replacing a certain amount of the Mn atoms (with a neutron scattering length $b = -3.73$ fm) by a mixture of Fe and Cr whose scattering length is $b = 6.58$ fm (the Mn-(Fe,Cr) mixture will be called T hereafter). The (Fe,Cr) atoms substitute the Mn atoms randomly and this kind of substitution is called isomorphic. By varying the amount of (Fe,Cr) in T one varies its corresponding scattering length and it is possible to extract the modulus of the partial structure factors $|F_{\mathrm{Al,Pd}}|$, $|F_{\mathrm{Mn}}|$ and also their phase difference $\delta\phi$ [3]. $|F_{\mathrm{Al,Pd}}|$ and $|F_{\mathrm{Mn}}|$ correspond respectively to the contribution of the Al and Pd atoms grouped together and to the Mn atoms. The regrouping of the Al and Pd atoms is due to the fact that we are performing the substitution on Mn atoms only, which allows us to separate the contribution of this element from the rest. Thus the ternary alloy AlPdMn is treated as a binary alloy AMn (Al and Pd have very close scattering lengths, $b_{\mathrm{Al}} = 3.4$ fm and $b_{\mathrm{Pd}} = 5.9$ fm, though it is difficult to separate the individual contributions).

5.4.1.1 Indexing of the Diffraction Pattern. The first step in the determination of the structure is the indexing of the diffraction pattern [5,10]. The point group symmetry (equivalent to the Laue class for crystals) of the diffraction pattern is usually determined by a TEM experiment. For the alloy studied here it is the one corresponding to an icosahedron. In 6D this symmetry corresponds to a hypercubic reciprocal lattices and a hypercubic Bravais lattice in the direct space and there are three possibilities to be considered for the Bravais lattices: primitive (P), face centered (F) and body centered (I) (see Duneau in [16]). Each of these 6D periodic Bravais lattices corresponds to a unique distribution of the position of diffraction peaks in the 3D reciprocal physical space. This is shown in Fig. 5.10 (from Duneau in [16]) for a 2-fold scattering plane for the P and F Bravais lattices (in this figure additional symbols represent the extinction rules which allow the determination of the possible space group). The i-AlPdMn phase corresponds to a I hypercubic reciprocal lattice as the one represented in Fig. 5.10b and its diffraction pattern presents no systematic extinction. Thus the Bravais hypercubic lattice in the direct space is F type and there are only two possible space groups: $Fm\bar{3}\bar{5}$ (centrosymmetric) or Fm35 (non centrosymmetric). The lattice constant of the F hypercubic cell is a_{F}=12.9 Å.

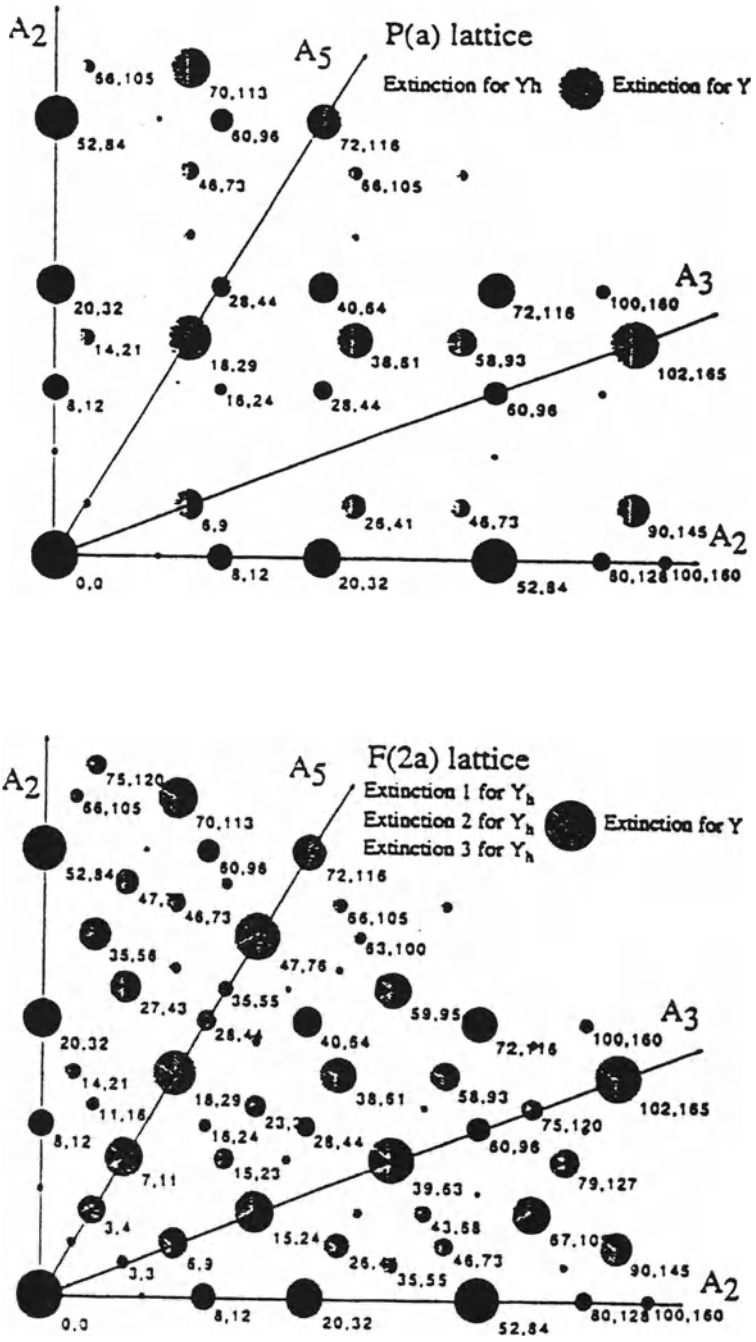

Fig. 5.10. Simulated extinction rules for two different Bravais lattices. Top panel: P direct lattice; lower panel: F direct lattice

It is interesting to compare the i-AlPdMn diffraction pattern with that corresponding to the i-AlMn phase (as in Fig. 5.10a) which has a primitive hypercubic lattice. The reciprocal lattice of the i-AlPdMn phase presents additional peaks with respect to the reciprocal lattice of the i-AlMn phase. These peaks can be related to a superstructure.

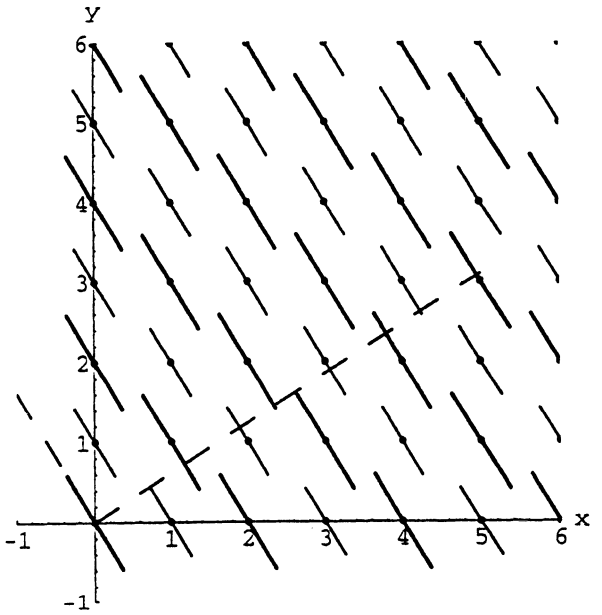

Fig. 5.11. 2D example showing a superstructure with respect to the model of Fig. 5.6

Figures 5.11 and 5.12 show a 2D example in order to clarify the idea of the structural modifications leading to a superstructure. The structure of Fig. 5.11 and its diffraction pattern (Fig. 5.12) are very similar to the one presented in Fig. 5.6 and Fig. 5.8. However a slight difference has been introduced for the size of the segment at the origin between two adjacent cells. The resulting structure presents a doubling of the cell parameter (usually known as a superstructure) and leads to a new diffraction pattern which contains additional peaks (see Fig. 5.12). As the difference between both structures is not very important these additional peaks are weak. This is the case for i-AlPdMn as can be seen in Fig. 5.5. (The additional peaks with respect to i-AlMn which are characteristic for the F bravais lattice of the i-AlPdMn are weak and correspond to those peaks marked with an asterix in Fig. 5.5. These peaks will be referred to as superstructure reflections.) Thus it is more convenient to consider the F direct lattice as resulting from an ordering on the P lattice with the 6D lattice constant $a_P = a_F/2 = 6.45$ Å.

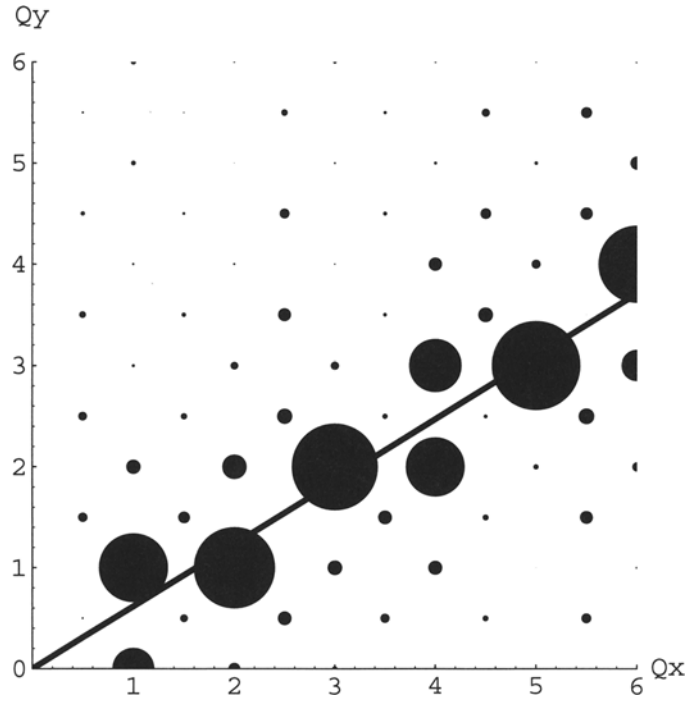

Fig. 5.12. Intensities corresponding to the model of Fig. 5.11

5.4.1.2 Patterson Analysis. Once the four diffraction patterns have been indexed and the integrated intensity has been calculated, it is possible to get the partial structure factor $|F_{\mathrm{AlPd}}|$ and $|F_{\mathrm{Mn}}|$ as described before [3] and thus we can perform a Patterson analysis by FT of the intensities, $|F_{\mathrm{Mn}}|^2$ and $|F_{\mathrm{Al,Pd}}|^2$. The PF of the Mn sublattice is very simple: there is only a contribution at the nodes corresponding to the primitive hypercubic lattice as shown in Fig. 5.13. The description of the atomic structure will be done in the primitive unit cell (a_{P}), considering two classes of atomic coordinates: their sum is either even (as [0,0,0,0,0,0] or [2,0,0,0,0,0]) or odd (as [1,0,0,0,0,0]). Figure 5.13 is very similar to those present for the 1D example (e.g. Fig. 5.6). Actually it is a section of the 6D PF in a plane containing two 5-fold directions: one in the physical space $[1, \tau, 0]_{\mathrm{par}}$ and one in the perpendicular space $[-\tau, 1, 0]_{\mathrm{perp}}$. The PF extends mainly along the perpendicular direction. This implies that, to a first approximation, the AOs describing the Mn quasiperiodic structure are confined in the perpendicular space.

Figure 5.14 shows the profile of the PF scanned along the perpendicular direction. It also shows that the contribution from the even nodes sites, N_0,(e.g. [0,0,0,0,0,0]) is slightly larger than that from the odd nodes sites, N_1, (e.g. [1,0,0,0,0,0]). For such a simple example the link with the density

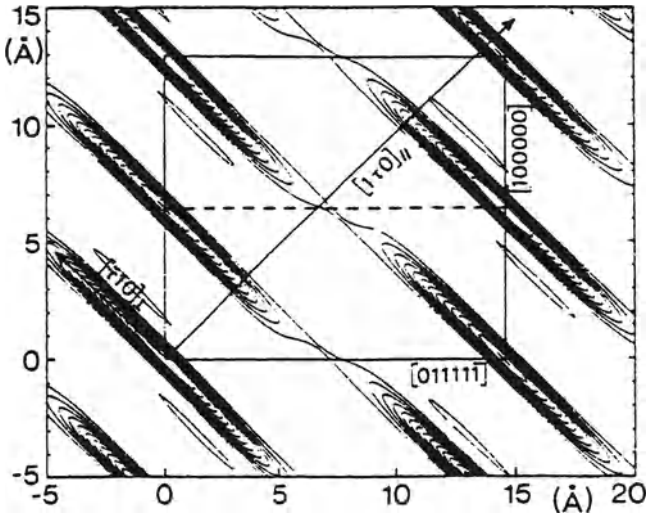

Fig. 5.13. Rational 2D cut, containing a 5-fold direction in both the physical and the perpendicular spaces, of the 6D PF corresponding to the Mn sublattice

function can easily be found: there are two different Mn AOs with slightly different sizes on N_0 and N_1.

Thus we have information on:

(a) which sites are occupied by Mn on the hyperlattice (primitive);
(b) the size and geometry of the AOs on each site.

In particular the different occupation on the odd and on the even nodes leads to an F-type sublattice for Mn atoms (see the 1D example in Fig. 5.11).

A more precise evaluation of the volume of the AOs and also a phase reconstruction can be realized by looking at the behavior of the structure factor along the perpendicular direction of reciprocal space (Fig. 5.15). Similarly to what happens in 1D the structure factor is modulated by the FT of the AOs and thus there is a very special dependence in perpendicular space. The equivalent of (5.27) is:

$$F(Q) = \frac{1}{2a^6}[G_{N_0}(Q_{\text{perp}}) \pm G_{N_1}(Q_{\text{perp}})] \tag{5.28}$$

where $G_{N_0}(Q_{\text{perp}})$ and $G_{N_1}(Q_{\text{perp}})$ are the FTs of the two AOs attached to, respectively, even and odd nodes. The sign ($\pm$) is positive for fundamental reflections and negative for superstructure reflections. As a direct consequence of this relation, superstructure reflections are sensitive to the difference between even and odd sites.

As for the 1D case corresponding to the square window function (Fig. 5.6) generally the FT of the AO presents a maximum value at $\boldsymbol{Q}_{\text{perp}} = \mathbf{0}$ and

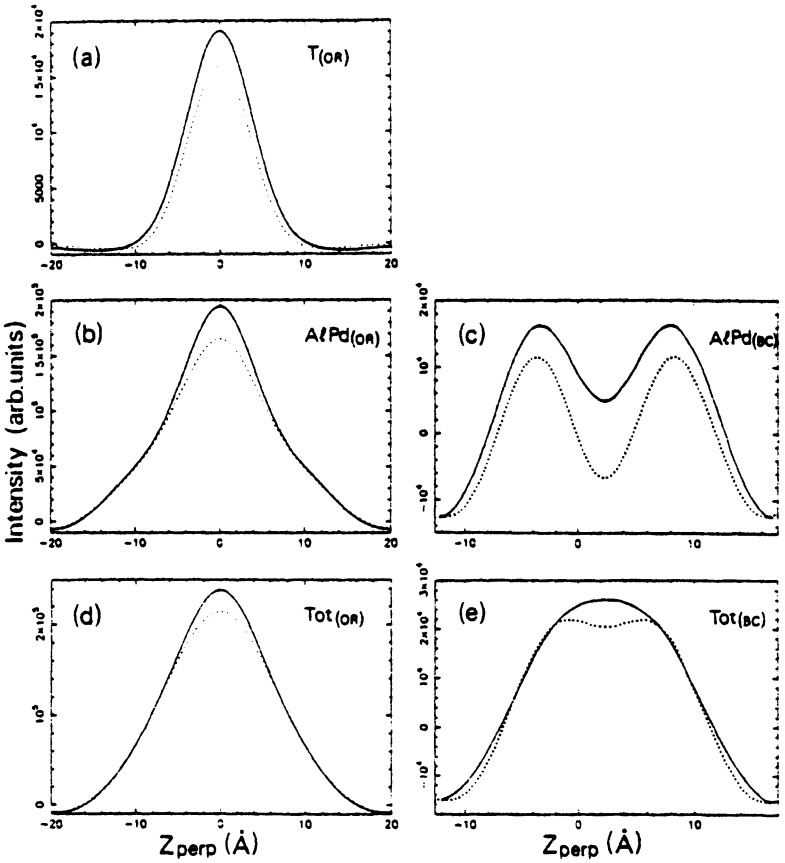

Fig. 5.14. Profile of the PFs. Full (dashed) lines corresponds to even (odd) sites. (**a**) T origin node, (**b**) A origin node, (**c**) A body center node, (**d**) total PF (T+A) at origin node, (**e**) as (**d**) for body center node

then decays slowly as Q_{perp} increases. The value at $\boldsymbol{Q}_{\text{perp}} = \mathbf{0}$ is proportional to the volume of the AO and the decay is due to the destructive interference taking place between different parts of the AO when Q_{perp} increases and it depends directly on the shape of the AO. Thus from Fig. 5.15 it is possible to get information on the volumes V_0 and V_1 and the shapes of the AOs attached to N_0 and N_1.

In particular from (5.28) it appears that for $\boldsymbol{Q}_{\text{perp}} = \mathbf{0}$ we have $F(0)$ proportional to $V_0 + V_1$ and $V_0 - V_1$. In order to extrapolate the value of the structure factor to $\boldsymbol{Q}_{\text{perp}} = \mathbf{0}$ we model the AOs by spheres and the corresponding structure factor is shown in Fig. 5.16. The smooth decay follows the general trend of the structure factor represented in Fig. 5.15. The density (0.066 at/Å^3) and the atomic composition of the sample $Al_{70}Pd_{20}Mn_{10}$ fixed the total volume:

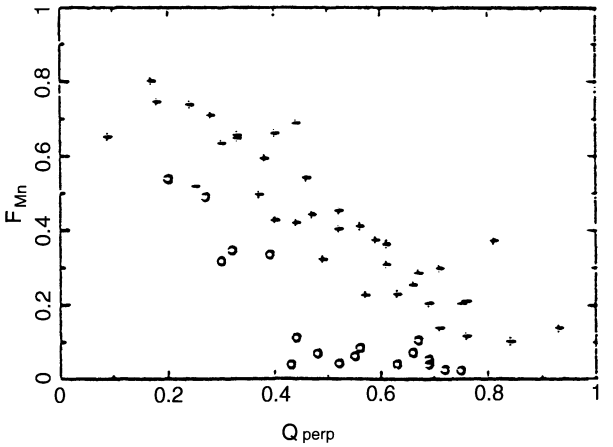

Fig. 5.15. Q_{perp} dependence of the structure factor

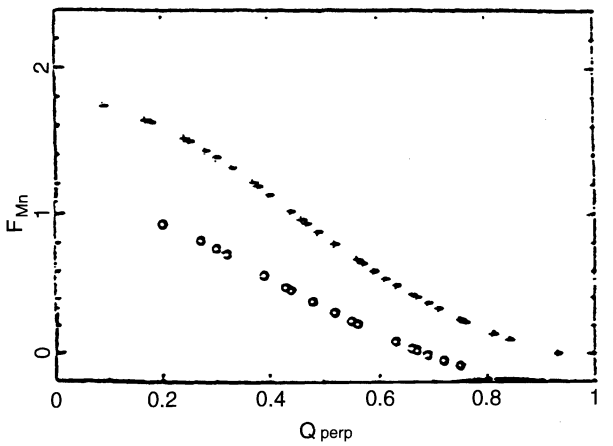

Fig. 5.16. Structure factor corresponding to a model built with spheres

$$0.0066\left[\frac{\text{at}}{\text{Å}^3}\right] = \frac{1}{2a^6}(V_0 + V_1)\,. \tag{5.29}$$

The final volumes retained correspond to two spheres with radius $R_0 = 5.68$ Å and $R_1 = 3.55$ Å($R_0/R_1 = 1.6$). Even though the AOs are certainly not spheres, they are well approximated by spheres and in particular they have a very similar decay with Q_{perp} (compare Fig. 5.15 and Fig. 5.16). This comparison allows us to reconstruct the phase, i.e. to give the sign of the spherical model to F_{Mn} (where all signs are positive in the present case). As explained in [3] it is now possible from the sign of F_{Mn} to assign the sign of the partial structure factor $F_{\text{Al,Pd}}$ by their phase difference $\delta\phi$. Indeed the results of the contrast variation experiment shows that $\delta\phi$ is either 0 or π, i.e. F_{Mn} and $F_{\text{Al,Pd}}$ have either the same sign ($\delta\phi = 0$) or the opposite

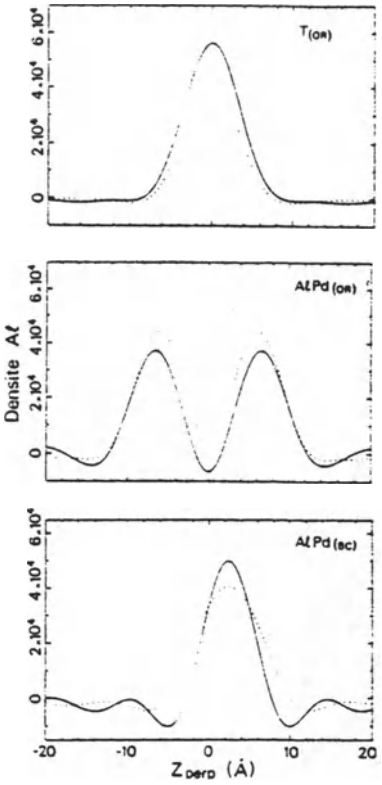

Fig. 5.17. Density profiles

sign ($\delta\phi = \pi$). Figure 5.17 shows the results of the density profiles along one direction of the perpendicular space and Fig. 5.18 shows a 2D cut of the 6D density function. These results were obtained by FT of F_{Mn} and $F_{\mathrm{Al,Pd}}$. For Mn we find results consistent with the Patterson analysis, that is the N_0 and N_1 sites are occupied with two AO which are slightly different. For the Al, Pd atoms we find that there is a contribution at BC_0 (corresponding for example to coordinates $1/2[3,1,1,1,1,-1]$) and at BC_1(corresponding for example to coordinates $1/2[1,1,1,1,1,-1]$) and also a contribution at N_0 and N_1. Contributions at BC are very similar to those of Mn at origin nodes, i.e. there are nearly spherical AOs with a radius of the order of 4 Å (the AO at BC_1 being the largest of the two AOs at the BC sites). The AOs of AlPd attached to N_0 and N_1 are much larger and correspond to nearly spherical shells around the Mn AO and their external radius is of the order of 10 Å, as can be seen in Fig. 5.17. These results are consistent with the Patterson profiles show in Fig. 5.14. Indeed considering that the AO at the BC is much smaller than the one at the N, the BC Patterson profiles give direct information on the AO at N (the AOs at the BC act as a delta function in the convolution product, see (5.14)). The AlPd contribution to the PF at the BC present similar profiles as that corresponding to the density (i.e. an

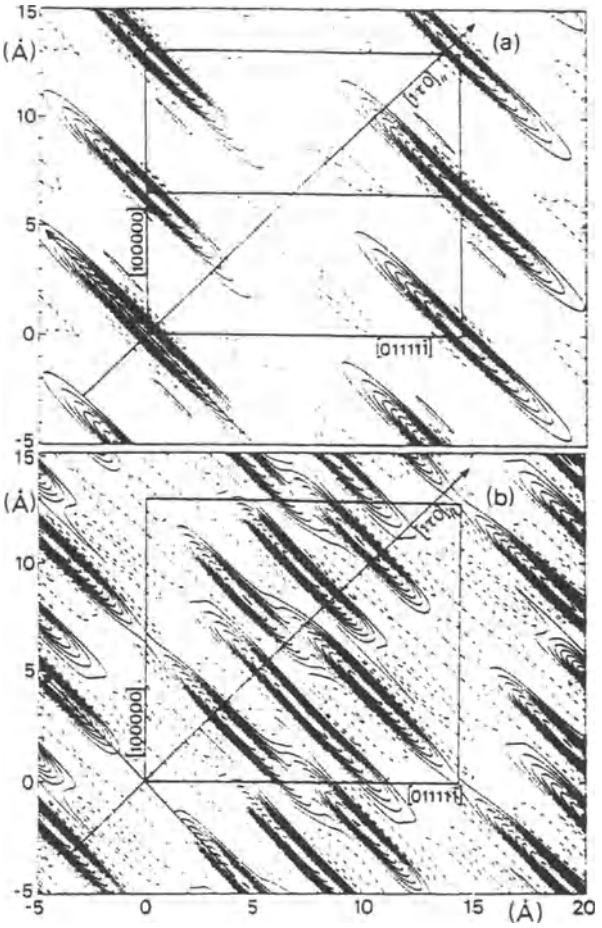

Fig. 5.18. 2D cut of the 6D density function containing a 5-fold direction in both the physical and the perpendicular spaces. (**a**) Mn; (**b**) Al+Pd

almost spherical shell with an empty core) whereas the total contribution (Mn+AlPd) no longer shows the presence of the empty core because it is now filled by Mn.

5.4.1.3 Resume and Limitation. We have presented the application of the contrast variation method, of Patterson analysis and also the method of reconstructing the phase looking at the Q_{perp} dependence of the structure factor. The distribution of AOs for the Mn and A atoms is as follows: a core of Mn is surrounded by an A AO for N_0 and N_1, and the BC are occupied by small AOs of A. The equivalent site N_0 and N_1 (respectively BC_0 and BC_1) of the primitive hypercubic lattice are occupied in a different way leading to an F- type hypercubic lattice. However there are still several limitations to this approach:

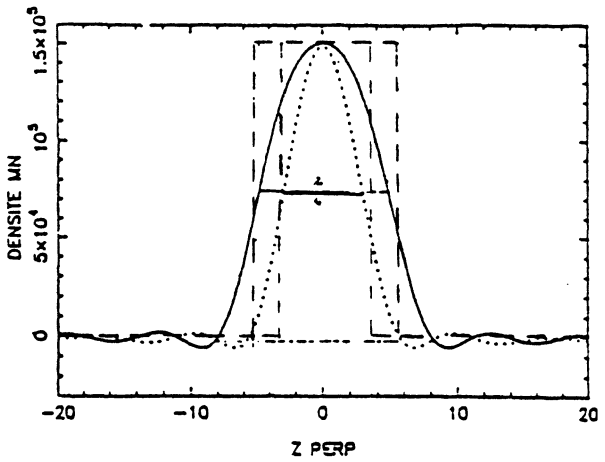

Fig. 5.19. Truncation effects

- The method allows the separation of only the contribution of the Mn from the rest which is treated as a single chemical species A. It is not possible to separate the Al from the Pd contribution (no contrast variation is possible and both elements have a similar scattering length).
- Cut effects and limited data sets: this limitation arises from cut effects i.e. only a limited data set is accessible from diffraction experiments. These truncation effects concern both variables Q_{par} (because of the limited range accessible in Q_{par} due to the experimental set up) and Q_{perp} (as for Q_{par} and with the additional difficulty that the intensity of the reflections is correlated with Q_{perp}, i.e. reflections with large Q_{perp} are very weak). These limitations are shown in Fig. 5.19 where the profile of the density corresponding to two spherical AOs with different radii (dashed lines) are compared with the profiles obtained by FT using a limited set of FC of the density. The set used here is quite large but the truncation effects are already important. When using the set limited to the FC corresponding to the measured reflections one obtains profiles very similar to those shown in Fig. 5.17a.

5.4.2 Neutron and X-ray Diffraction Experiments on Single QCs

In this section we will discuss neutron diffraction experiments on single QCs (monograin sample) [4] which represent a more complete data set than the one obtained with powder samples and allows in principle a more precise determination of the structure although essential features that can be obtained by a first-order solution (as the spherical model that will be presented) are the same as those obtained in previous sections. We will also see how we can proceed in our structural determination using X-ray diffraction experiments on single quasicrystals. This is due to the fact that in X-rays experiments the PF is directly related to the electron density (see Sect. 5.2). The in-

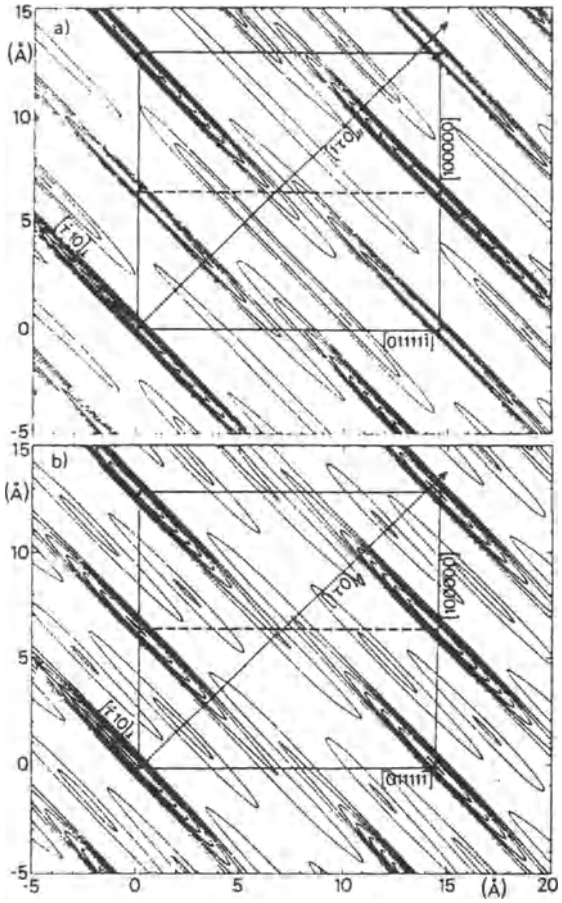

Fig. 5.20. 2D cut of the 6D PF containing a 5-fold direction in both physical and perpendicular spaces: (**a**) X-ray; (**b**) Neutron

teraction between X-ray and matter depends on the number of electron of each element. Thus for the i-AlPdMn alloy the X-rays will be very sensitive to the Pd and will be much less scattered by Al (Z(Pd)=46, Z(Mn)=25, Z(Al)=13). Thus X-rays provide an additional contrast that is very sensitive to Pd with respect to the previous neutron experiment. This will allow us to disentangle the Al and the Pd contribution in the Patterson analysis. Figures 5.20 and 5.21 show sections and profiles of the 6D PF (similar to those presented in previous sections) corresponding to the four-circle data obtained with neutron and X-rays diffraction. For the neutron data we obtained the same results as before and the differences in comparison with Figs. 5.14d and 5.14e are due to the fact that in the present case we have introduced the scattering length (in particular note that the minus sign of the Mn scattering length, b(Mn), leads to a negative contribution to the PF at BC sites). The

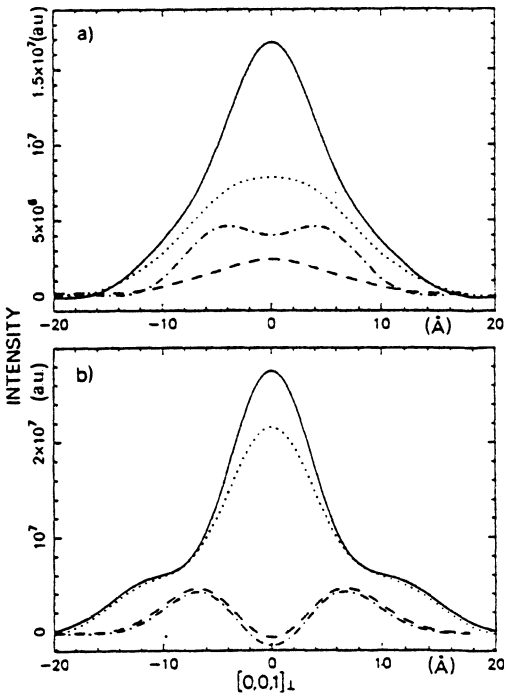

Fig. 5.21. Patterson profiles corresponding to the experiment: (**a**) X-ray; (**b**) Neutron

PF obtained with X-ray data are very different (see Fig. 5.21a). First of all the N_0 and N_1 (resp. BC_0 and BC_1) contributions are very different. This fact indicates that there is a very important superstructural ordering due to Pd, that is Pd is likely to be unevenly distributed according to the parity of the site: for example all in N_0 and in BC_0. The profile of the PF at BC_0 is qualitatively similar to that at BC_0 and BC_1 for the neutron data (Fig. 5.21b). This suggests that for one of the two sites N_0 or N_1, the main features correspond to a central core of Mn surrounded by Pd while for the other the central core of Mn is surrounded by Al. However a quantitative analyzes (a precise determination of the volume and distribution of the different AOs directly from the PF) remains difficult due to the fact that we have no access to the atomic density but rather to the electronic density (or distribution of potential for the neutron data) and also due to the truncation effect explained in previous sections. At this point it is necessary to construct a model in order to get more structural information. In a first approach the model can be constructed by considering AOs with spherical symmetry. The choice of these volumes is based on the qualitative information obtained up to now. An initial spherical model is then constructed with:

- two spherical cores of Mn at the origin sites N_0 and $N_1$with different sizes;

- these two cores are surrounded by a spherical shell of Al and Pd and the Pd is probably only distributed in one of the two sites N_0 or N_1 (this distribution and also the order for the Pd and Al shells are the important points to be solved);
- the BC sites are occupied by small spheres of either Al or Pd (this point has to be solved).

The precise distribution of the AOs and the evaluation of their sizes has been carried out by comparison of the predictions of the model with the experimental results, either in real space (PF) or in reciprocal space (intensities). Although these methods are equivalent, as they are related by an FT, some features are more easily seen in real space while others are better seen in reciprocal space. In direct space we can compare the shape of the profile of the PFs as those presented in Fig. 5.21 with those corresponding to a spherical model (see Fig. 5.22). This allows us to verify the different hypotheses concerning the distribution of the AOs. Once the order of the AOs has been determined, their respective volumes can be reliably evaluated in reciprocal space by comparing the calculated structure factor with the experimental one. This method is similar to that presented in Sect. 5.4.1 for the evaluation of the sizes of the AOs of Mn at the N_0 and N_1 nodes. In this case we

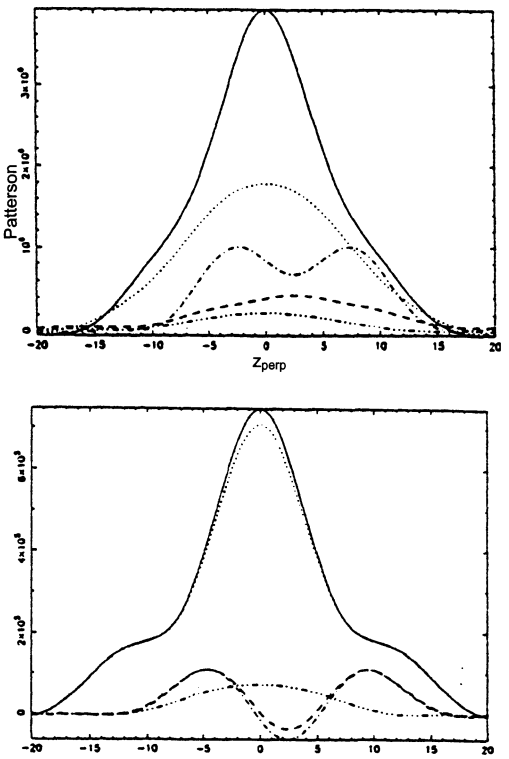

Fig. 5.22. Patterson profiles corresponding to the model: (**a**) X-ray; (**b**) Neutron

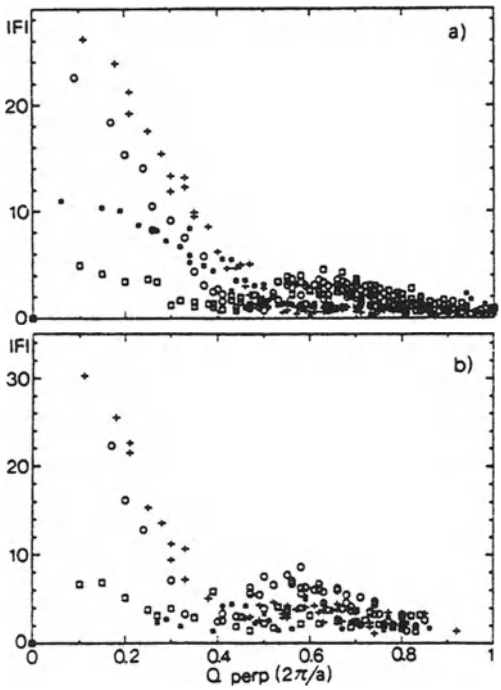

Fig. 5.23. Dependence of the modulus of the structure factors with Q_{perp}; four branches are visible: (**a**) X-ray; (**b**) Neutron

consider different AOs placed on N_0, N_1 , BC_0 and BC_1 which leads to four different branches at low Q_{perp} values according to the parity of N and M, rather than two as for the Mn partial structure factor [4]. These four branches can be clearly seen in the experimental data as shown in Fig. 5.23. Taking into account only the atomic density as an additional physical constraint (i.e. density and chemical composition of the sample) the following 10 volumes of the spherical AOs were determined by adjusting both the PF profiles and the low Q_{perp} dependence of the structure factors:

- centered at N_0 a core of Mn with radius $0.8a_{\mathrm{P}}$ (a_{P}=$a_F/2 = 6.45$ Å is the parameter of the 6D primitive hypercubic lattice) surrounded successively by a shell of Pd with an external radius of $1.26a_{\mathrm{P}}$ and a shell of Al with an external radius of $1.55a_{\mathrm{P}}$;
- centered at N_1 a core of Mn with radius $0.52a_{\mathrm{P}}$ surrounded by a shell of Al with an external radius of $1.64a_{\mathrm{P}}$;
- centered at BC_0 a small ball of Al ($0.3a_{\mathrm{P}}$) or nothing;
- centered at BC_1 a small ball of Pd ($0.71a_{\mathrm{P}}$).

The resulting model is represented in Fig. 5.24. This spherical model fits the data relatively well and, as expected from a spherical model, is better at low Q_{perp} value. The residual factor, R, defined as:

$$R = \sum \frac{|I_{\mathrm{obs}} - I_{\mathrm{calc}}|}{\sum I_{\mathrm{obs}}} \tag{5.30}$$

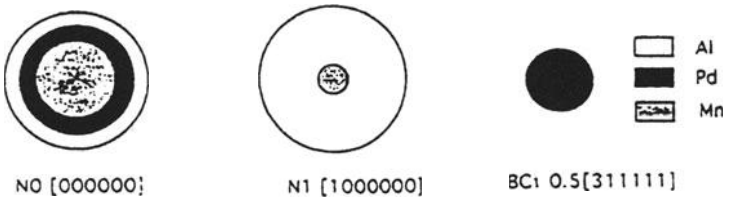

Fig. 5.24. The model built with spherical AOs

is 9% for X-rays and 16% for neutrons when considering values of Q_{perp} lower than 0.5 (in $\frac{2\pi}{a_{\text{P}}}$units) and 14% (X-ray) and 24% (neutrons) if all data are included.

Although we have learned a lot about the structure, we are still far away from what is usually achieved for (periodic) crystals (the R factor is of the order of 5% for all the data). This is due to the fact that we have very few constraints and free parameters in our model and the final details are not accessible. We will briefly see in the next section what ideas are presently being developed to improve the models.

5.5 Further Ideas for Building Models

Modeling with spheres offers an easy analytical calculation of the structure factors and gives good agreement for low Q_{perp} values. It gives a good estimate of the occupied sites in the 6D unit cell and can evaluate the size of the corresponding AOs for the different chemical species. This model is only a first approach to a realistic model and it will be compared to two other 6D models based on more complicated AOs. We will illustrate how additional constraints arising from density, chemical composition and minimum distances between atoms in physical space can be introduced in the models.

Figure 5.25 compares the AOs at N_0 and N_1 for the spherical model with that proposed by Duneau and Oguey [9] for the AlMnSi icosahedral phase (hereafter the DO model). In the DO model, the AOs were constructed in order to generate a lot of Mackay icosahedra (MI) [17,6]. This cluster (see Fig. 5.26) is built up of a small Al icosahedron surrounded by a Mn icosahedron and an Al icosidodecahedron. It is present in the α-AlMnSi crystalline phase which is a rational approximant of the icosahedral phase. Besides the condition of generating a lot of MIs the DO model does not create interatomic short distances. This model can be built starting from a unique AO located at the nodes of the 6D unit cell. This AO is a triacontahedron (TR) which is the AO corresponding to the standard Penrose tiling (see Fig. 5.27). It is possible to increase the density of the Penrose tiling by taking a TR τ times larger than the canonical one (LTR). In particular, a new distance is generated along the 2-fold axis (see Fig. 5.28). There is no short distance along this direction and also along the 3-fold direction (see Fig. 5.29). However there

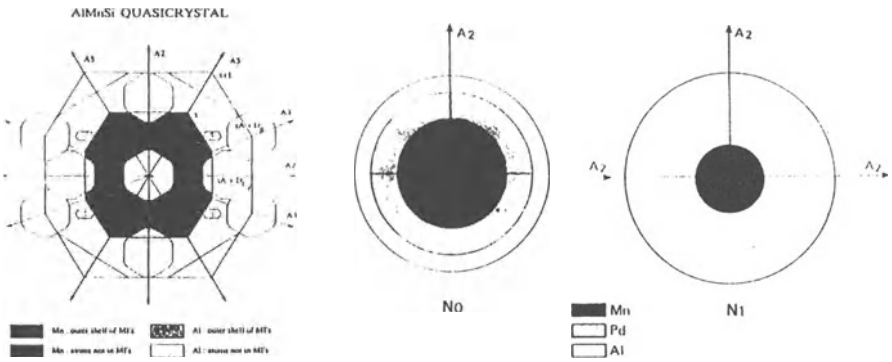

Fig. 5.25. Comparison between the DO model and the spherical model

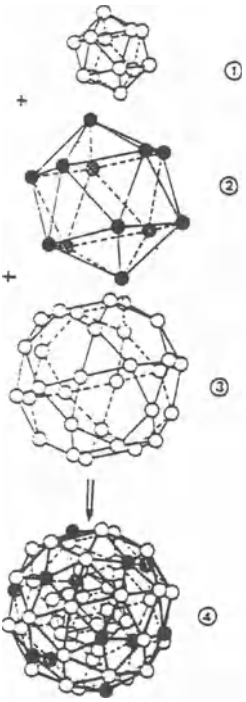

Fig. 5.26. Mackay icosahedron

is a problem of short distances along the 5-fold direction as can be seen in Fig. 5.30: the two AOs centered at [2,0,0,0,0,0] and [0,1,1,1,1,−1] define, in the parallel space, a short distance.

In order to avoid this problem the two polyhedra (LTR) considered must have different coordinates in perpendicular space, i.e. the projection in perpendicular space of these polyhedra along the parallel space must have no intersection. This problem is shown for the LTR in Fig. 5.31. This condition

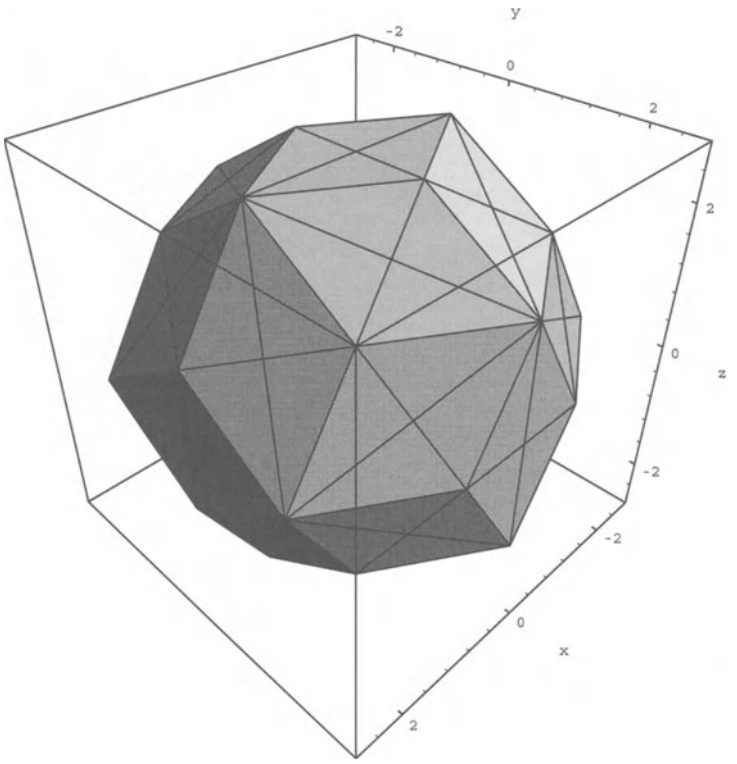

Fig. 5.27. TR generating the standard 3D Penrose tiling

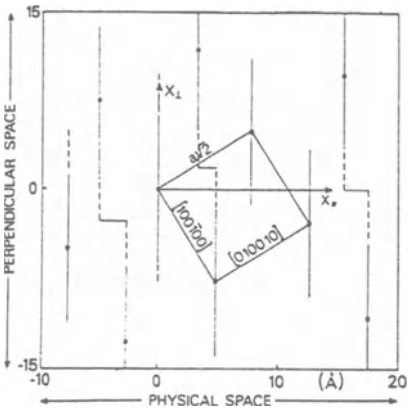

Fig. 5.28. 2D cut containing a 2-fold direction in both physical and perpendicular spaces. The AO corresponding to the canonical TR is the full line and the inflation by τ is drawn with the dashed lines

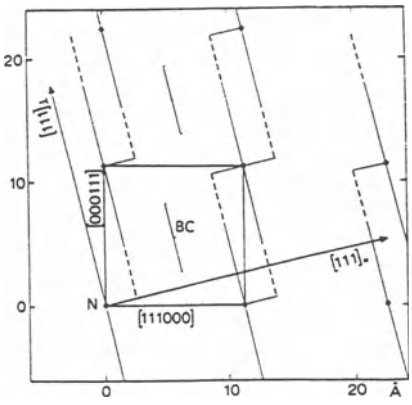

Fig. 5.29. 2D cut containing a 3-fold direction in both physical and perpendicular spaces. The AOs corresponding to the canonical TR are the plain line and the inflation by τ is drawn with the dashed lines

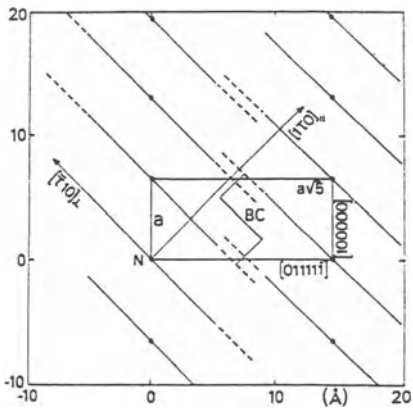

Fig. 5.30. 2D cut containing a 5-fold direction in both physical and perpendicular spaces. The AOs corresponding to the canonical TR are the plain line and the inflation by τ is drawn with the dashed lines

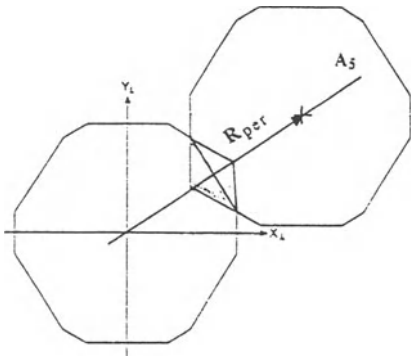

Fig. 5.31. Projection of the AOs corresponding to the LTR

can be fulfilled by cutting both AOs by planes perpendicular to the 5-fold axes (only one is represented in Fig. 5.31). These planes define a dodecahedron. The AO of the origin is thus a LTR truncated by a dodecahedron. It is possible to added a small polyhedron at the BC site whose maximum diameter along the 5-fold direction is represented in Fig. 5.30. In the DO model the polyhedron retained is a small dodecahedron. This model presents no superstructure, i.e. no difference is considered for the origin sites N_0 and N_1 (resp. BC_0 and BC_1) but it can be generalized to the i-AlPdMn phase just by considering different chemical occupation of the sites according to the parity. Without additional modifications the LTR AO truncated by a dodecahedron will generate a pseudo-Mackay cluster which has, instead of the inner Al icosahedron, a central Mn atom (not present in the cluster generated by the DO model) surrounded by an incomplete dodecahedron (with 6 or 7 atoms). In the DO model the central part of the AO at the origin is removed in order to avoid the generation of an atom at the center of the MI. In the same way the external part of this AO is removed along the 3-fold axes in order to avoid short distances due to additional small AOs which are added in order to generate the inner Al icosahedron of the MI (this modification allows an increase in the density by 5%). Another solution which avoids short distances along 5-fold axes has been proposed by Katz and Gratias and will be called the K model hereafter [15,16]. The AO centered at nodes equivalent to [2,0,0,0,0,0] is the LTR, while the AO retained at nodes equivalent to [0,1,1,1,1,−1] is now a similar LTR but with holes corresponding to the intersection with the LTR at [2,0,0,0,0,0] (see Figs. 5.30, 5.31, and 5.32). As shown in Fig. 5.33 with these two AOs at the nodes it is possible to have a supplementary AO only at one of the two BC positions but with a diameter along the 5-fold axis two times larger than in the previous DO model. This AO is taken as a small TR (see Fig. 5.32). This model is in qualitative agreement with the spherical model. The DO and K models fit the measured density well ($0.064 < \rho < 0.07$ at/Å^3). Similarly to the DO model, it is possible to increase the density of the K model up to 0.067 at/Å^3 by adding AOs for generating the small icosahedron in the MI. The K model is built in order to connect the different AOs. This fact allows a translation of the cut space along the perpendicular direction preserving the number of atoms in the structure (closeness condi-

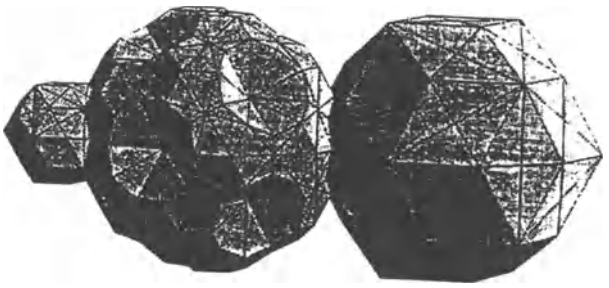

Fig. 5.32. The AOs corresponding to the K model [16]

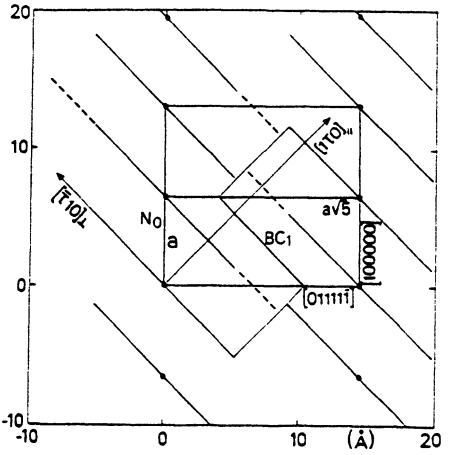

Fig. 5.33. 2D cut containing a 5-fold direction in both physical and perpendicular space. The AOs correspond to the K model

tions). If one takes into account this additional hypothesis and continuous volumes limited by sharp planes (as in the LTR) there is only a limited set of solutions with a realistic density. However there is no experimental evidence for these hypotheses and in particular other models can be described by fractal AOs. Although the K model represents an improvement by taking into account the physical constraint (no short distances and closeness condition), the agreement of this model with the diffraction data (measured by the R factor) is of the same order of magnitude as for the spherical model.

References

1. Bak, P. (1986), Phys. Rev. Lett., **56**, 861.
2. Bak, P. (1986), Scripta Met., **20**, 1199.
3. Boudard, M., de Boissieu, M., Janot, C., Dubois, J. M. and Dong, C. (1991), Phil. Mag. Lett., **64 (4)**, 197.
4. Boudard, M., Deboissieu, M., Janot, C., Heger, G., Beeli, C., Nissen, H. U., Vincent, H., Ibberson, R., Audier, M. and Dubois, J. M. (1992), J Phys-Condens Matter, **4**, 10149.
5. Cahn, J. W., Shechtman, D. and Gratias, D. (1986), J. Mat. Res., **1**, 13.
6. Cooper, M. and Robinson, K. (1966), Acta Cryst., **20**, 614.
7. Cornier-Quiquandon, M., Quivy, M., Lefebvre, S., Elkaim, E. and Heger, G. (1991), Phys. Rev. B, **44**, 2071.
8. Cornier-Quiquandon, M., Bellissent, R., Calvayrac, Y., Cahn, J. W., Gratias, D. and Mozer, B. (1993), J Non-Cryst Solids, **153**, 10.
9. Duneau, M. and Oguey, C. (1989), J. Phys. (France), **50**, 135.
10. Elser0 Elser, V. (1985), Phys. Rev. B, **32**, 4892.
11. Elser V. and Henley C. L. (1985), Phys. Rev. Lett. **55**, 2883.
12. Guyot P. and Audier M. (1985), Phil. Mag. B, **52**, L15.
13. Janot, C., Ed. (1992). Quasicrystals: A primer. Oxford, Oxford Science Publications.

14. Janssen, T. (1986), Acta Cryst., **A42**, 261.
15. Katz, A.,(1989), Proceedings of the Workshops "Number Theory and Physics", Les Houches Luck, J. M., Moussa, P., Waldschmidt, M. Eds Springer Proceedings in Physics **47**, Springer-Verlag.
16. Hippert, F. and Gratias, D. (1994), Lectures on Quasicrystals , Les Editions de Physique.
17. Mackay, A. L. (1962), Acta Crystallogr., **15**, 916.
18. Baruchel, J., Hechon, J. L., Lehnar, M. S., Regrard, J. R., Schlenker, C. (1993), Neutron and Synchrotron Radiation for Condensed Matter Studies Les Editions de Physique.

6 Electron Microscopy and Surface Investigations of Quasicrystals

Hans-Ude Nissen and Conradin Beeli

Summary. A review of recent results on electron-microscopy investigations of quasicrystalline materials is presented with special emphasis on thermodynamically stable quasicrystals. Also, an introduction into the technique of high-resolution transmission electron microscopy (HRTEM) as well as into convergent beam electron diffraction and Kikuchi line pattern techniques is given. Additionally, techniques sensitive to thin surface layers and especially their application to quasicrystals are discussed: secondary electron imaging, X-ray photoelectron scattering, electron backscattering diffraction and scanning tunneling microscopy.

The HRTEM technique is illustrated with examples of the structural investigation of decagonal d-Al–Mn–Pd and d-Al–Co–Ni quasicrystals as well as the icosahedral (i-) phases in the systems Al–Cu–Li, Al–Mn–Pd and Al–Cu–Fe. The role of atom clusters in the structural analysis of quasicrystals is emphasized and reviewed. It is shown that a statistical analysis of the long-range translational order in stable decagonal quasicrystals can be made using HRTEM images. Investigations of the structure of dodecagonal, octagonal and cubic quasicrystals by HRTEM imaging in combination with electron-diffraction techniques are discussed, and the application of aperiodic twelve-fold symmetric tilings is treated.

6.1 Introduction

6.1.1 Early Work on Electron Microscopy of Quasicrystals

It is a remarkable fact that, more than any other major novelty in materials science in this century, the discovery as well as the early development of research on quasicrystalline metals is almost exclusively due to the use of transmission electron microscopy (TEM) as a method of investigation. A material with icosahedral point symmetry in its selected area electron diffraction (SAED) patterns and long-range orientational order but no translational symmetry in real space was first found by Shechtman et al. [124]. By the end of 1984, SAED patterns taken from extremely fine-grained, but structurally homogeneous, alloys had been observed which contained sharp Bragg reflections but exhibited symmetry elements characteristic of point-group symmetries which, for geometric reasons, crystalline materials could not possess. These symmetry elements were a five-fold symmetry axis of Al_6Mn with a $(\overline{5}3m)$ icosahedral point-group symmetry, first observed by Shechtman et al. [124], and a twelve-fold symmetry axis found in certain regions of Cr–Ni

J.-B. Suck et al. (eds.), *Quasicrystals*
© Springer-Verlag Berlin Heidelberg 2002

fine particles which had a 1D periodic structure with point-group symmetry 12/mmm and were first observed by Gähler [47,48] and Ishimasa et al. [71]. Then a few months later, in 1985, Bendersky [12] also described a 1D periodic Al–Mn alloy (called T-phase) with a ten-fold axial symmetry element. By a first application of the convergent beam electron diffraction (CBED) technique to quasicrystals he subsequently showed that this decagonal quasicrystal had the point-group symmetry 10/mmm [13].

Evidently, all these materials had aperiodic structures, i.e. they were lacking periodic translation symmetry, since all the point-group symmetries found were incompatible with any crystalline structure and its Bravais lattice. Yet the sharp diffraction spots (Bragg peaks) pointed to the presence of a long-range ordered structure contrasting the amorphous structures and establishing a general class of ordered solids positioned between the crystalline and the amorphous structures. The term quasicrystals for this class of materials was first used by Levine and Steinhardt in 1984 [92].

Subsequently, in further TEM studies, the following new aperiodic structures were discovered: A 1-dimensional periodic structure with an eight-fold symmetry axis was found in extremely fast-cooled Cr–Ni–Si alloys [141], and, more recently, two different cubic 3D aperiodic structures were discovered, respectively, in rapidly cooled V–Ni–Si alloys [46] and $Mg_{61}Al_{39}$ [34].

In the twelve years following the initial discoveries, a large amount of new quasicrystals were found, mostly in alloys containing Al. The metallurgical investigations indicated that a number of them were stable phases, while the majority were metastable. New quasicrystal phases have been discovered each year since then. A survey of the presently known systems containing stable quasicrystals is given in Table 6.1. Note that the existence of stable decagonal quasicrystals in the systems Ga–Co–Cu, Ga–Cu–Fe–Si and Ga–Ni–Si–V has also recently been reported [50]. However, these phases have not been included in Table 6.1, since only preliminary results have been published so far. In contrast, all the quasicrystals listed in Table 6.1 have been documented at least twice in the literature, in most cases in studies including at least certain crystallographic data.

The continuation of this work lead to a close collaboration between groups of scientists whose aim was to determine the equilibrium phase diagrams of ternary alloys containing the quasicrystal phases and other groups who were able to separate and identify the phases contained in the different synthesized ingots, mainly by using transmission electron microscopy or X-ray powder diffraction techniques [45,49,51,53,147].

6.1.2 Penrose Tilings and Related Quasiperiodic Tilings as an Aid in the Interpretation of Electron Micrographs

Shortly after the appearance of the first electron microscopy description of an icosahedral quasicrystal [124], Levine and Steinhardt [92] introduced

Table 6.1. Stable quasicrystal phases

Typical composition	Icosahedral quasilattice respectively approximate c-axis parameters [nm]	References
Icosahedral quasicrystals		
$Al_{57}Cu_{10.8}Li_{32.2}$	0.504	[119]
$Al_{43}Mg_{43}Pd_{14}$	0.513	[87]
$Ga_{20}Mg_{43}Zn_{37}$	0.509	[102]
$Ni_{17}Ti_{41.5}Zr_{41.5}$	0.516	[84]
$Mg_{42}RE_8Zn_{50}$ [1])	0.104	[93,99]
$Al_{62}Cu_{25}TM_{13}$ [2])	0.89 to 0.905	[137]
$Al_{70}Mn_9Pd_{21}$	0.912	[138]
$Al_{70}Pd_{21}Re_9$	0.920	[138]
Decagonal quasicrystals		
$Al_{64}Co_{16}Cu_{20}$ [3])	0.8 (also 0.4)	[56,60,136]
$Al_{71.5}Co_{14}Ni_{14.5}$ [3])	0.8 (also 0.4)	[53,136]
$Al_{71}Fe_5Ni_{24}$	0.4	[57]
$Mg_{20}SE_{10}Zn_{70}$ [4])	0.51	[118,126]
$Al_{69.8}Mn_{12.1}Pd_{18.1}$	1.2	[9,51]
$Al_{40}Fe_{15}Ge_{20}Mn_{25}$	1.2	[148]
$Al_{70}Pd_{17}TM_{13}$ [2])	1.6	[139]
$Al_{74}Ni_{15}Ru_{11}$ [2])	1.6 (also 0.4)	[134]
$Al_{72}Cr_{16}Cu_{12}$	3.6	[103]
Dodecagonal quasicrystals		
$Ta_{1.6}Te$	2.0	[29]

[1]) RE = Y, Gd, Tb, Dy, Ho, Er
[2]) TM = Fe, Ru, Os
[3]) rather wide range of existence
[4]) SE = Dy, Ho

3D tilings by two rhombohedra, the previously known so-called Ammann–Kowalevski–Kramer (AKK) rhombohedra [91], as the building blocks of a basic quasiperiodic tiling model for any icosahedral quasicrystal. In the "perfect quasiperiodic structure model" of Levine and Steinhardt, the concept of an ideal quasicrystal is defined and described (for a more complete description of these 3D quasiperiodic tilings, see the contribution by Baake in this volume). 3D tilings like those by AKK-rhombohedra are a 3D analog of quasiperiodic Penrose tilings found earlier by Penrose [106], long before quasicrystals were known. These were later applied very successfully to model decagonal quasicrystals.

Several models for aperiodic structures as well as for the growth of these materials were proposed immediately after the discovery by Shechtman et al. and now form the theoretical basis for structural interpretations. For the case

of an ideal quasicrystal, the terms used to describe the complete symmetries of a crystal were complemented by additional terms: The term periodicity is replaced by quasiperiodicity, the term Bravais lattice by the aperiodic (but deterministic) quasilattice (or tiling) and, generally, 3D crystallography is replaced by higher-dimensional crystallography (i.e. crystallography using $(3+n)$D geometric space as an embedding space for quasicrystal structures). For example, icosahedral quasicrystals are described using the so-called cut-and-projection methods and the concept of embedding of the 3D icosahedral structure into a 6D cubic periodic structure [35,40,76].

It was initially impossible to directly interpret high-resolution transmission electron micrographs of quasicrystals in terms of the atomic structure. This was mainly due to insufficient point-to-point resolution as well as to the strong influence of dynamical electron scattering. However, the projection of the quasilattice along the direction of the electron beam could be observed in the high-resolution electron micrographs and then be interpreted as a 2D tiling. The most significant progress in finding the atom positions in quasicrystals therefore was the application of the above-mentioned embedding methods. In the most significant examples of icosahedral and decagonal structures, the application of these methods resulted in the so-called average atom structure (as opposed to the actual real-quasicrystal structures with their specific defects) [15,20,23,30,131,132,145].

Accordingly, tilings are useful to find the structure of quasicrystals in two different contexts: First, in the applications made in connection with the higher-dimensional space embedding techniques. An example of this first context is the case of the icosahedral 3D tilings consisting of the AKK-rhombohedra mentioned above [92]. Most of these tilings are strictly quasiperiodic, although the methods for their generation can be modified in such a way that so-called random tilings are obtained [61]. Random tilings have quasiperiodicity only on the average, but possess long-range positional order. By contrast, "polyhedral glass models" (e.g. the icosahedral glass model) have bond-orientational order only and very short-ranging positional order [130]. (Note that quasiperiodic structures have infinite-range positional order.)

A second, principally different, way of construction and use of a tiling has also been very successful (see, for example, [63,81,100]). Here a tiling is constructed directly as an overlay of a HRTEM micrograph in such a way that all small regions having the same shape and the same contrast configurations in that micrograph are bounded by edges of one copy of the same type of tile, i.e. a polygon with a given constant shape. The resulting tiling usually has a small number of tiles (2 to 6), and the tiles have a single, constant edge length. However, the tiling may occasionally also contain small regions, the outlines of which do not correspond to one of the types of tiles. These regions usually indicate the positions of a locally disordered domain in the specimen.

The interpretation of tilings constructed in this way cannot only aid in the determination of the structure, once the atom decoration of each type of

tiles is assumed or found experimentally, it is also helpful in localizing defects (e.g. phason defects) and, especially, in determining the degree to which a quasicrystal approaches the (ideal) quasiperiodic state or else a random tiling state.

6.1.3 Synthesis of Quasicrystals as Related to Phase Diagrams

The objective of this chapter is to present and underline the fundamental importance of metallurgy for the production of high-quality metal alloys and thus of quasicrystals. Because of the complexity of this subject, only a brief introduction will be given here. For details we refer to the chapters by Lück in this volume. The first quasicrystalline materials in the Al–TM systems (TM = V, Cr, Mn, Fe, Co, Ni, Mo, etc.) are unstable compounds and were invariably produced by melt spinning [125]. With the addition of Si it finally became possible to produce single-phase materials with the composition $Al_{74}Mn_{22}Si_4$ [14]. However, the structural quality could not be further improved by long-time annealing, since these compounds were metastable. Accordingly, the discovery of stable quasicrystals in the Al–Cu–Li system [119] led to hopes that high quality could be reached by annealing. A pseudobinary section of the Al–Cu–Li phase diagram was determined in 1986 [119], but the subsequent X-ray investigations invariably showed an intrinsic disorder indicating a correlation length of only 30 nm [54]. This last study [54] revealed that the icosahedral glass model can be used to explain certain diffuse scattering effects in the Al–Cu–Li quasicrystal [130]. However, these authors emphasized that, by contrast, the structure of the stable i-Al–Cu–Fe quasicrystal cannot be explained by such a model containing intrinsic disorder. In fact, the best i-Al–Cu–Fe as well as Al–Mn–Pd quasicrystals show X-ray peak widths which are only limited by the instrumental resolution [20,30]. Therefore, these quasicrystals are frequently termed "perfect" quasicrystals.

The preceding overview has shown that the growth of "perfect" quasicrystals has led to such an exceptional improvement in the quality of quasicrystal structures, that these now approach an ordered structure which can be modeled by an ideal, quasiperiodic structure model.

The systematic growth of high-quality samples, however, requires the precise knowledge of the equilibrium phase diagrams for the ternary systems. This has recently been strongly emphasized by Calvayrac [24], but it is also evident from the work by Kortan et al. [86] on Al–Cu–Li, by Grushko [56] on Al–Cu–Co as well as by Gödecke and Lück [51] on Al–Mn–Pd.

As examples, we discuss here two temperature versus concentration diagrams: A section through the decagonal phase region as well as the icosahedral phase region in the Al–Mn–Pd system [51,52] (Fig. 6.1) and the Al-70 at.% section of the Al–Co–Ni system containing stable decagonal quasicrystals [53] (presented by Lück in this volume). As is evident from Fig. 6.1, in Al–Mn–Pd the decagonal phase, D, exists (within experimental limits) for a singular composition only, i.e. $Al_{69.8}Mn_{18.1}Pd_{12.1}$. Therefore, it is represented in

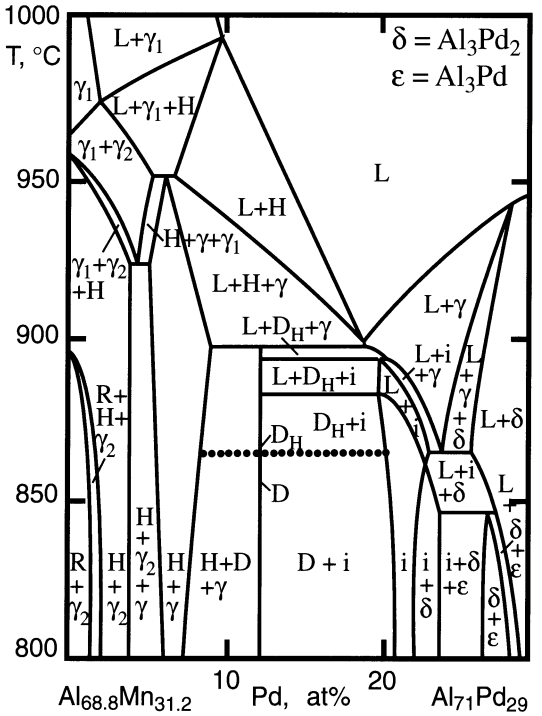

Fig. 6.1. Temperature versus concentration section of the Al–Mn–Pd system which contains both the decagonal (D) and the icosahedral phase (i). Note the high-temperature modification D_H of the D-phase. The letters denote the following phases: L liquid, H orthorhombic $Al_{11}Mn_4$, R monoclinic $Al_{11}Mn_4$, γ and γ_1 high-temperature AlMnPd phases related to the W-type structure, γ_2-Al_8Cr_5-type phase ("distorted" γ-brass), δ-Al_3Ni_2-type phase, ϵ-Al_3Pd orthorhombic phase

the diagram by a vertical line only. Notice also that, at temperatures above 860°C, the decagonal phase was found to be replaced by a pseudodecagonal approximant, D_H [10]. By contrast, the icosahedral phase, i, at a temperature around 860°C has an existence region with a width of up to 2 at.%. However, at a temperature of 800°C the width is only 1 at.% and reduces even further at lower temperatures. In order to produce i-phase single-crystals stable at low temperatures, it is very important to know this behavior. The necessary data for the growth of the stable Al–Mn–Pd i-phase have been obtained by Gödecke et al. [51,52]. They are in good agreement with the results by different groups growing single-quasicrystals using the Czochralski method [26]. The Al-70 at.% section of the Al–Co–Ni phase diagram (given by Lück in this volume) has been selected for discussion, since most of the publications on stable d-Al–Co–Ni report $Al_{70}Co_{15}Ni_{15}$ as the sample composition; but, as can be seen in that diagram, a quasicrystal of this composition is not stable below 800°C. However, at a composition with slightly higher Al-content,

e.g. 71 at.%, the quasicrystal is in fact stable to low temperatures [122]. This observation leads to the conclusion that probably most publications have actually reported a nominal bulk composition and not the composition of their sample, or, even worse, that some of the samples contained precipitates of a few per cent of crystalline phases (X- and/or Al_3Ni_2 phases). In summary, we conclude that in experimental studies it is of the utmost importance to report the precise procedures used for the production of the alloys as well as their exact composition. Without this information it will be impossible, or meaningless, to compare the results of different studies.

6.2 High-Resolution Electron Micrographs and Their Interpretation

For an introduction, a very comprehensive and up-to-date treatment of high-resolution transmission electron microscopy (HRTEM) can be found in Williams and Carter [144]. More theoretical treatments are given in the textbooks by Cowley [31] and by Horiuchi [67]; the latter includes many examples of applications. A text concentrating on high-resolution imaging is the book by Spence [127], while a short, but useful general introduction is "Electron Microscopy and Analysis" by Goodhew and Humphreys [55]. The textbooks by Hirsch et al. [66] and Reimer [107] are both still very useful, even though they are early publications in this field. In these textbooks useful details on the transmission electron microscope and on image interpretation can be found.

The description of the image formation and the diffraction process is possible by using one of three different physical concepts, i.e. the geometrical optics approach, the kinematical theory (wave optics) and the dynamical theory of electron-matter interaction, which is based on quantum theory.

6.2.1 The Abbé Principle

Incident radiation passing through an object produces an amplitude distribution $q(x, y)$ (the object transmission function) in the object plane, which is the exit plane of the object for the passing radiation. This distribution function is transferred by a lens with a focal length f onto the image plane, yielding the object function $\Psi(x, y)$. The image is a recreation of $q(x, y)$, inverted and magnified by a factor $M = R'/R$, see Fig. 6.2: $\Psi(x, y) = q(-Rx/R', -Ry/R')$, where R is the object-to-lens distance and R' the lens-to-image distance. All electrons (or light) scattered by an angle φ are brought to a focus at one point in the back-focal plane. This is equivalent to the statement that the distribution function on the back-focal plane is given by the Fourier transform of $q(x, y)$, $Q(x/\lambda f, y/\lambda f)$, called the Fraunhofer diffraction function. Further, the amplitude distribution (x, y) in the image plane is similarly related by a Fourier transform to the Fraunhofer diffraction function $Q(k_x, k_y)$.

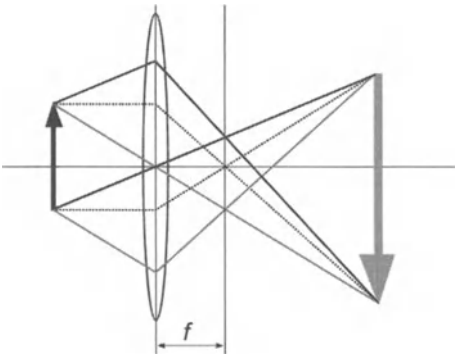

Fig. 6.2. Electron-ray diagram used in the wave-optics description of the image formation process according to the Abbé principle

The intensity distribution in the back-focal plane can be observed as the diffraction pattern. Thus the imaging process may be described in terms of two Fourier transforms: The scattered radiation from the object interferes at the back-focal plane to produce the Fraunhofer diffraction function, and then the radiation from the back-focal plane again forms an interference pattern on the image plane. Thus the image is given by the Fourier transform of the interference pattern in the back-focal plane. As a consequence, every point in the back-focal plane receives a contribution from all points in the object plane and contributes to all points in the image plane. This statement is the Abbé principle, first introduced by Abbé. Note that up to now we have neglected all lens aberrations. The theory including aberrations will be presented in Sect. 6.2.3.

6.2.2 Selected Area Electron Diffraction

As discussed, the diffraction pattern contains information from the whole area of the illuminated specimen. Such a pattern is generally not very useful, since the specimen may contain different phases and/or crystal orientations. A specific region of the specimen may be selected by converging the electron beam, using the condensor lens system. However, because of the convergent illumination, this results in a so-called convergent beam electron diffraction (CBED) pattern, consisting of disks instead of diffraction spots. Furthermore, the coherence of the illumination is lost as a result of the strong convergence of the beam. A mode very specific to transmission electron microscopy (TEM) is the so-called selected area electron diffraction (SAED) technique, which allows us to select a specific area from which we want to obtain a diffraction pattern. In order to select this specific region, a selecting aperture is inserted in the image plane, after the objective lens. This has two major advantages: First, the image is typically magnified 30 times as compared to the specimen, and therefore this technique allows the use of an aperture, 15 μm in diameter, to select a region having a diameter of only 0.5 μm. While it is technically

almost impossible to produce a circular aperture of 0.5 μm diameter, it is rather easy to make one of 15 μm. Secondly, a parallel, non-convergent (and thus highly coherent) illumination can be used, which results in sharply defined diffraction spots.

In an obvious way, in the SAED technique use is made of the Abbé principle mentioned above. In the SAED mode, the diffraction pattern, appearing on the final viewing screen, is formed with only those electrons which pass through the SAED aperture in the image plane. According to the Abbé principle, this corresponds exactly, in the object plane, to a specimen region defined by the virtual image of the selected area aperture. In practice, however, there is a lower limit to the size of the SAED aperture, since the substantial spherical aberration of the objective lens leads to contributions of higher-order Bragg reflections from regions adjacent to the selected one [144]. Practically, for a modern 300-kV transmission electron microscope, this limits the smallest diameter of a selected area in the object plane to approximately 0.5 μm. Nevertheless, the SAED technique is still one of the most important methods to investigate the fine structure of a material, since only in such patterns can weak and/or diffuse intensity maxima or satellite reflections be observed. Additionally, for dark field and bright field imaging, it is necessary to first form a SAED pattern and then select the particular Bragg reflection or satellite reflection by using an aperture (the so-called objective aperture).

6.2.3 Interpretation by the Dynamical Theory

HRTEM imaging of specimens involves two main physical processes: the scattering of the electron wave within the object and the transfer of information on the wave function at the exit plane of the object by the optical system of the microscope to the final image.

The first process is a quantum-mechanical process and involves, in principle, multiple scattering processes for any 3D object. This results from the fact that any Bragg-diffracted electron beam has the proper orientation for being re-diffracted by the same set of atom planes. Two different theoretical approaches have been used for the formulation of the so-called dynamical theory of diffraction: The first is based on the formulation of quantum mechanics as differential equations, i.e. the Schrödinger equation in a crystal lattice, while the second one is based on the integral formulation. The integral formulation is also called the physical optics approach and represents the object as a set of thin layers, and the propagation of radiation through the object as an initial plane wave scattered successively, layer by layer, within the object. The scattered wave components are added according to the principles of Huygens and Fresnel. This formulation has been used by Cowley [31] to suggest the so-called multi-slice technique for image simulations of high-resolution images. By contrast, the formulation based on differential equations results in the so-called Bloch-wave method. It has been shown that the two methods are identical in the limiting case of infinitely thin slices.

The second physical process which is important in HRTEM imaging is the transfer of information by the transmission electron microscope from the exit plane of the specimen to the image. This process is decisive in the determination of the point-to-point resolution of an HRTEM image. The transfer of information (or contrast) is described mathematically by the so-called contrast transfer function (CTF). In a real-space description, the wave function at the exit plane of the object is convoluted by the contrast transfer function, which results in the observed image contrast. The higher the resolution, the greater the amount of high spatial frequencies which have to be included in the imaging process. This is equivalent to the inclusion, by a large objective aperture, of high-order Bragg reflections, far apart from the optical axis. Therefore, the spherical aberration and the defocus of the objective lens significantly influence any HRTEM image. The CTF is usually described in reciprocal space, since in that treatment the (object) wave function and the image contrast are related by a simple multiplication instead of a convolution in real space. The following three main contributions to the CTF have to be considered: The aperture function, $A(k)$, the attenuation of the wave due to chromatic aberrations, together with the detector influence (film or CCD camera), $E(k)$, and the aberration of the lenses, $B(k)$. If we write $H(k)$ for the CTF we obtain:

$$H(k) = A(k) \cdot E(k) \cdot B(k)\,, \tag{6.1}$$

where $B(k) = \exp[\mathrm{i}\chi(k)]$, with $\chi(k) = \pi\Delta f k^2 + \pi C_\mathrm{s}\lambda^3 k^4/2$. Here, C_s is the spherical aberration constant (typically of the order of 1 mm), λ the electron wavelength and Δf the defocus value. $B(k)$ of the CTF is mainly determined by the objective lens. This is evident from the consideration that the objective lens magnifies the image by a factor of 30 and therefore demagnifies in reciprocal space by the same factor. Therefore, all diffracted beams are approximately parallel to the optical axis for all the following lenses. Accordingly, the spherical aberration of all these lenses becomes negligible. However, the spherical aberration of the objective lens of a transmission electron microscope cannot be neglected!

We now discuss the influence of the CTF on the wave function at the exit plane of the object. In many cases the so-called weak phase object approximation (WPOA) can be adopted as a first approximation which allows us to describe, in a simple way, the effect of a very thin specimen. Actually, a metallic specimen can only be referred to as very thin if its thickness is below 1 nm [31,144]. In the WPOA the wave function is represented as $q(x,y) = 1 - \mathrm{i}\sigma V_\mathrm{t}(x,y)$, where higher order terms in σV_t are neglected. $V_\mathrm{t}(x,y)$ represents the projected potential of the thin specimen, and σ is a constant depending on the wavelength of the electrons. Since here the main interest is on the influence of the spherical aberration on the image contrast, *coherent* illumination is assumed, which implies, to a first approximation, $E(k) = 1$ (no damping of high spatial frequencies). The more general case of a strongly scattering object and partially coherent illumination has been developed

by Ishizuka [74]. In this general case the transfer of information is described by transmission cross-coefficients, and it is this more detailed theory which is used for HRTEM image simulations [128]. The aperture function, $A(k)$, is 1 inside a disk of radius k_0 and zero outside. Thus the amplitude of the image contrast $\Psi(x, y)$ is the convolution of $q(x, y)$ with the CTF. In order to calculate this, it is convenient to Fourier transform $q(x, y)$, which gives $Q(k) = \delta(k) - \mathrm{i}\sigma\Phi_\mathrm{t}(k)$, and to separate $H(k)$ into real and imaginary parts $H(k) = \cos(\chi(k)) + \mathrm{i}\sin(\chi(k))$. The intensity of the Fourier transform of the image contrast can therefore be calculated as follows:

$$\begin{aligned} I(k) &= |\Psi(k)|^2 = |Q(k)[\cos(\chi(k)) + \mathrm{i}\sin(\chi(k))]|^2 \\ &= |1 + \sigma\Phi_\mathrm{t}(k)\sin(\chi(k)) - \mathrm{i}\sigma\Phi_\mathrm{t}(k)\cos(\chi(k))|^2 . \end{aligned} \tag{6.2}$$

We will again neglect higher powers of $\sigma\Phi_\mathrm{t}$, which results in:

$$I(k) = 1 + 2\sigma\Phi_\mathrm{t}(k)\sin\chi(k) . \tag{6.3}$$

This equation implies that in this approximation (WPOA with coherent illumination conditions) we have to consider only the imaginary part of the CTF, i.e. $B(k) = \sin\chi(k)$. It is obvious from (6.3) that the image contrast is linearly proportional to the projected potential $V_\mathrm{t}(x, y)$ of the specimen. However, the influence of the convolution with the Fourier transform of $\sin\chi(k)$ has to be considered. The optimum setting of the electron microscope for HRTEM imaging is now given for a defocus value Δf, which compensates, as much as possible, the influence of the spherical aberration. This defocus value is obtained if $\sin\chi(k)$ is close to 1 (i.e. substantially different from 0) and does not change sign from $k = 0$ up to a spatial frequency k_res, which limits the point-to-point resolution of the microscope. The objective aperture diameter should be selected in such a way that, in reciprocal space, it approximately corresponds to a radius $k_0 = k_\mathrm{res}$. It has been shown by Scherzer that the best compromise is obtained near $\Delta f = -1.15 C_\mathrm{s}^{1/2}\lambda^{1/2}$; this defocus condition is now known as the Scherzer defocus value. The function $\sin\chi(k)$ for this defocus value is represented in Fig. 6.3. In this case, the first zero of the function $\sin\chi(k)$ occurs at $k_\mathrm{res} = k_\mathrm{Sch} = 1.51\ C_\mathrm{s}^{-1/4}\lambda^{-3/4}$, which has been accepted as that reciprocal distance which defines the point-to-point resolution of a TEM instrument. Therefore, the corresponding point-to-point resolution is $r_\mathrm{Sch} = 0.66\ C_\mathrm{s}^{1/4}\lambda^{3/4}$. If $\sin\chi(k)$ is (nearly) equal to 1 for all important space frequencies contributing to the HRTEM image, the observed image intensity $I(x, y)$ varies proportional to the projected potential $I(x, y) = 1 + 2\sigma V_t(x, y)$; i.e. for a very thin specimen and for the Scherzer defocus condition the image contrast can then be interpreted as the projected potential of the specimen. For a modern 300-kV TEM with a spherical aberration constant $C_\mathrm{s} = 0.6\,\mathrm{mm}$ the point-to-point resolution corresponds to $r_\mathrm{Sch} = 0.17\,\mathrm{nm}$.

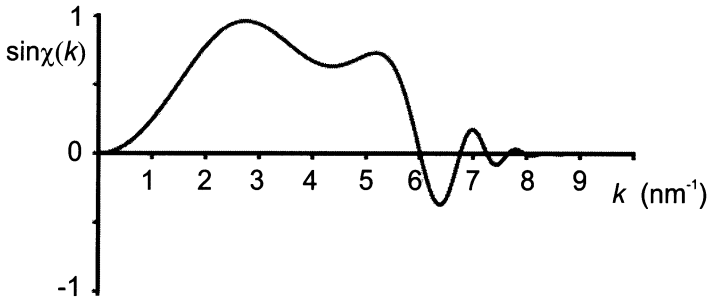

Fig. 6.3. Plot of $\sin\chi(k)$ against reciprocal distance in [nm^{-1}], used to define the point-to-point resolution of an electron microscope

6.3 Decagonal Quasicrystals

After the discovery of decagonal quasicrystals [12], electron microscopy investigations have mainly been made in three systems, i.e. Al–Mn–Pd [9], Al–Co–Cu [60] and Al–Co–Ni [136]. A special investigation on phase transformations from the crystalline to the quasicrystalline state has been made in the systems Al–Co–Cu–Si and Al–Mn–Pd [2]. Here we present results on d-Al–Mn–Pd and d-Al–Co–Ni alloys.

6.3.1 Description of the Decagonal Al–Mn–Pd Quasicrystal

The ternary phase diagram of Al–Mn–Pd in the region of the two stable quasicrystals has been determined with unprecedented precision by Gödecke and Lück [51]. Figure 6.4 shows part of an SAED pattern of the stable decagonal quasicrystal taken along the 10-fold axis. This is an example of a relatively well-ordered specimen of this phase. Nevertheless, small shifts, especially of some weaker diffraction spots, away from their ideal position, can be recognized. As reported by Beeli et al. [11], decagonal material with a high degree of order can best be obtained by first producing a rapidly quenched (melt-spun) specimen, which consists of a polycrystalline texture of icosahedral, supersaturated quasicrystals. Subsequently, this material is annealed at 830°C for several days and thereby converts, without any long-range diffusion process, into a decagonal quasicrystal having only a small amount of linear phason strain.

A HRTEM image (corresponding to the SAED pattern, Fig. 6.4) is presented in Fig. 6.5. This micrograph was obtained with a high voltage (800 kV), HRTEM instrument at NIRIM, Tsukuba, Japan. This instrument has, at this voltage, a point-to-point resolution of 0.14 nm. The micrograph shows part of a thin edge with increasing thickness from approximately 4 nm (top of Fig. 6.5) to 8 nm at the bottom. The main contrast feature of this micrograph is an aperiodic arrangement of disks having the shape of regular decagons containing white, nearly triangular spots at their centers.

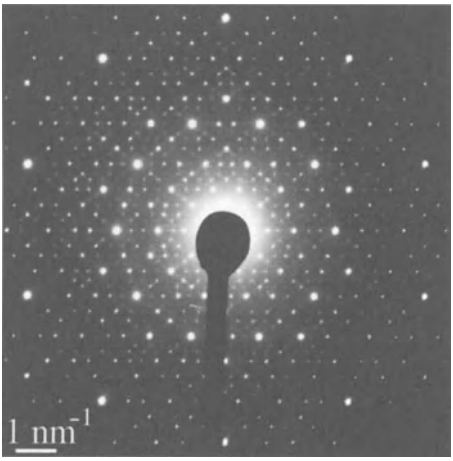

Fig. 6.4. SAED pattern of d-Al–Mn–Pd, taken along the 10-fold axis

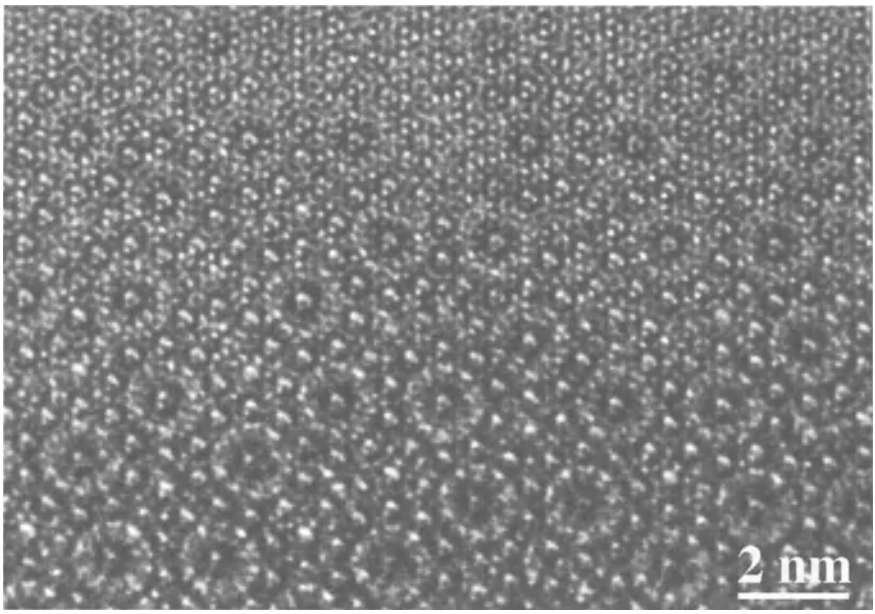

Fig. 6.5. HRTEM image of d-Al–Mn–Pd quasicrystal, taken along the 10-fold axis, observed in a rapidly quenched tape of composition $Al_{70}Mn_{15}Pd_{15}$, annealed at 820°C for 6.5 h

The centers of these discs are frequently arranged as regular pentagons of 2 nm edge length, and their interior has the shape of a pentagonal star. Such decagons are marked by white lines in Fig. 6.6; this micrograph was taken from a specimen region adjacent to that shown in Fig. 6.5. The outlines of two banana-shaped larger tiles are also marked in Fig. 6.6, and it can be

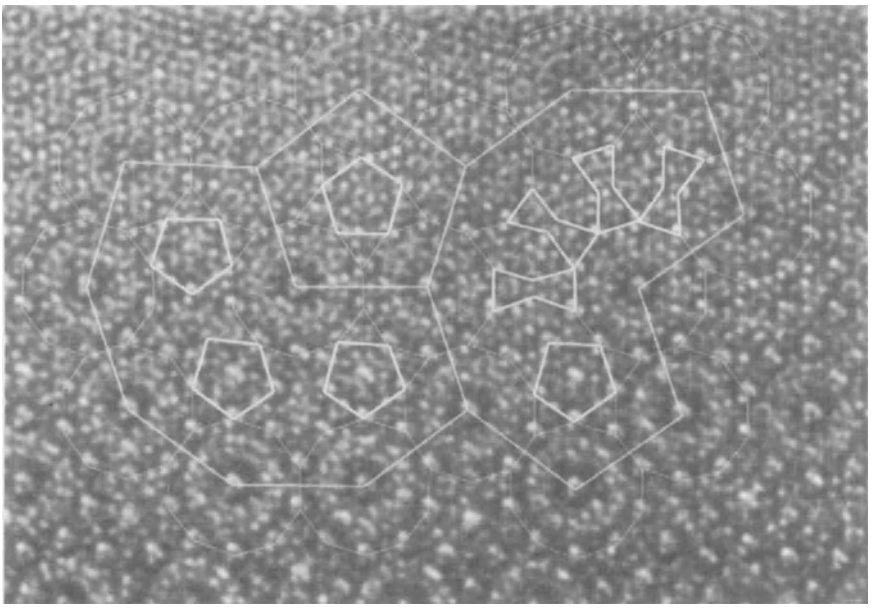

Fig. 6.6. HRTEM image similar to Fig. 6.5. The outlines of two banana-shaped tiles and a pentagon (edge length 2 nm) are marked by *white lines*. Note the different contrast in the interior of the banana-shaped tiles

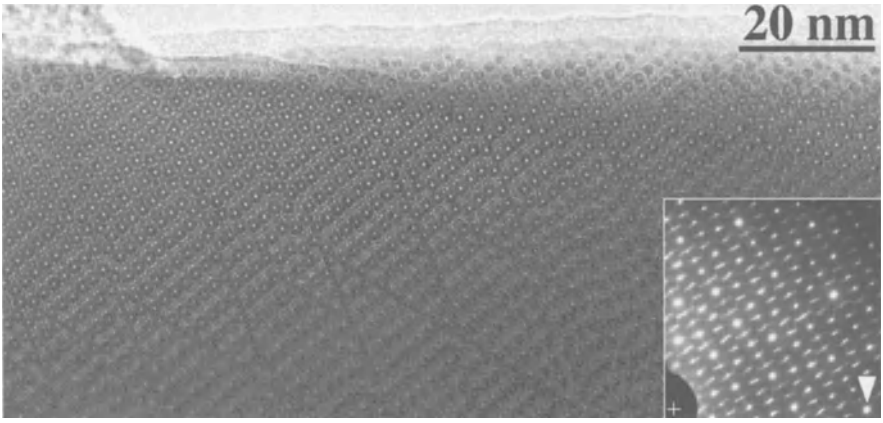

Fig. 6.7. Electron micrograph of a quenched $Al_{69.8}Mn_{18.1}Pd_{12.1}$ alloy, annealed at 892°C for 1 day, showing rhomb-shaped crystalline domains. A quarter of the corresponding SAED pattern is inserted; the *arrow head* marks a reflection corresponding to a d-value of 0.235 nm

recognized that the contrast details and outlines of the smaller tiles are very different inside the two larger tiles. This can be interpreted by assuming that

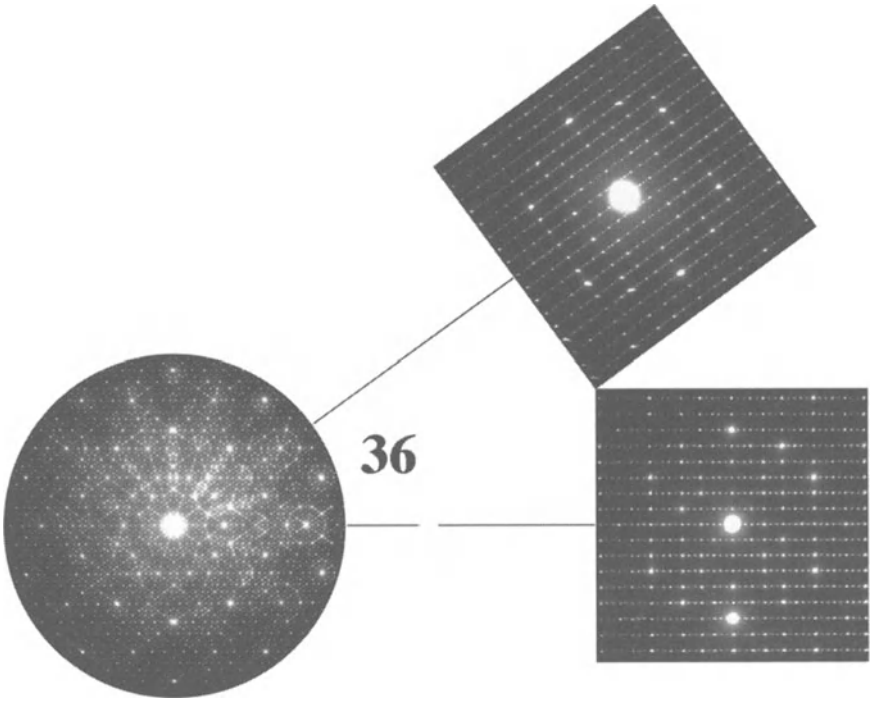

Fig. 6.8. SAED patterns taken along the three main projection directions of an orthorhombic approximant structure in Al–Mn–Pd. All patterns are to the same scale. The period along the pseudo-10-fold axis, visible in the two 2-fold SAED patterns, corresponds to 1.25 nm

the same tile of the structure may, at different places, be composed of two different spatial arrangements of subunits [8]. This interpretation has been corroborated by dynamical-contrast simulations [128] based on two models for the interior structure of the banana-shaped tile: One of these models, which is consistent with an arrangement shown on the left side of Fig. 6.6, was proposed on the basis of HRTEM images of Hiraga and Sun [65], while the arrangement shown (in the upper part of the banana tile) on the right-hand side corresponds to models introduced by Steurer et al. [132] and by Yamamoto [145] which have been obtained on the basis of two rather different X-ray structure refinement methods. Note that the arrangement in the banana on the left side is much more frequently observed in HRTEM images. In a recent refinement of d-Al–Mn–Pd by Weber and Yamamoto [143] the arrangement of atoms inside the banana-shaped tile is similar to the model of Hiraga and Sun and thus in better agreement with HRTEM images [8]. As mentioned before, at temperatures above approximately 860°C, d-Al–Mn–Pd undergoes an unusual transformation into an approximant phase, called the D_H-phase [10,52]. This phase can be described by an orthorhombic B-centered

unit cell (a=2.03 nm, b=1.25 nm, c=6.25 nm). In the projection along the b-axis, which is the pseudodecagonal direction, HRTEM images, such as the micrograph shown in Fig. 6.7, exhibit a very regular domain structure consisting of rhomb-shaped domains with 36° smaller angle, bounded by dark contrast. These domains can be interpreted as antiphase domains. Besides the D_H-approximant, an orthorhombic approximant with an even larger unit cell (a=6.25 nm, b=1.25 nm and c=8.65 nm) has been observed in this system. It is not yet known whether this approximant phase is a stable or rather a metastable phase. Figure 6.8 gives high-voltage SAED patterns along three major projection directions arranged on the corners of a 36-degree sector in the reciprocal space. Notice (in the round subfigure) that, as a result of the large unit cell, not only the stronger reflections approach decagonal symmetry, that the minor diffraction spots, clustering around strong reflections, are also approximately arranged as the vertices of small regular decagons.

6.3.2 The Al–Co–Ni Decagonal Quasicrystal, a System with Eight Structural Modifications

An unusual multitude of quasicrystalline states has been described from the Al–Co–Ni alloy system [108,115]. Figures 6.9 present a survey of the presently known structural modifications of decagonal, respectively, pentagonal and 1D quasicrystals in the Al–Co–Ni system, each represented by an SAED pattern projected along the unique periodic 10-fold axis of symmetry. These patterns have all been obtained at room temperature from ingots quenched in water from the selected annealing temperature. Figure 6.9a corresponds to the structural state referred to as the basic Ni-rich state. It is characterized by an exceptional degree of approximation to a truly quasiperiodic atom structure [108,113,115]. The very large number of reflections can all be indexed by referring to a basic decagonal structure.

The HRTEM images of the basic Ni-rich structure in the projection direction parallel to the periodic 10-fold axis can be described by a tiling approaching a quasiperiodic Penrose pentagon tiling (see Sect. 6.3.3). Figures 6.9b-d and 6.9e-h comprise the patterns made from structural modifications which all contain one type of basic pentagonally symmetric atom cluster [110] arranged and oriented in different ways. It is at present not clear which of these modifications can be called phases in the thermodynamic sense. In our opinion, this problem requires further discussion [94]. Figure 6.9b represents one of the states with a decagonal superstructure called the S1-state [39,109]. This state is closely related to the type I superstructure, of which a pattern is shown in Fig. 6.9c [39,109]. The type I superstructure was discovered by Edagawa et al. [39], and an indexing scheme was introduced by these authors, whereby the superstructure reflections of this state can be differentiated into two classes, S1 and S2. The type I state is a low-temperature state which transforms into the S1-state at a temperature between 750°C and 850°C, depending on composition. During this transformation the S2-intensities disap-

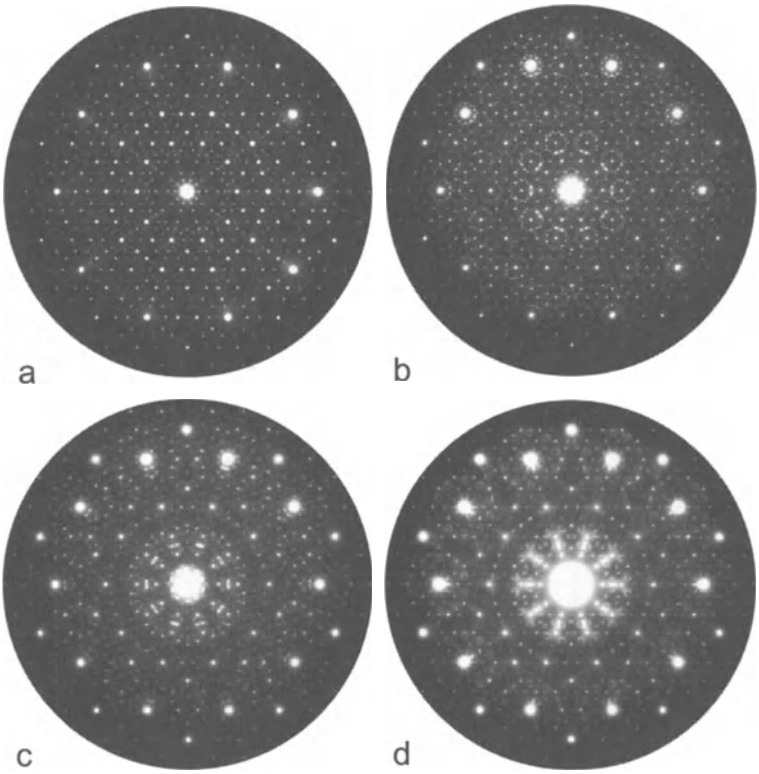

Fig. 6.9. SAED patterns taken along the 10-fold axis of Al–Co–Ni quasicrystals (courtesy S. Ritsch). (**a**): basic Ni-rich phase, $Al_{70}Co_{11}Ni_{19}$, 1050°C for 12 h. (**b**): S1 state, $Al_{72.5}Co_{13.5}Ni_{14}$, 900°C for 2 d. (**c**): Type I, $Al_{71.5}Co_{13}Ni_{15.5}$, 400°C for 90 d. (**d**): Type II, $Al_{71.5}Co_{15.5}Ni_{13}$, 850°C for 3 d

pear, whereas the S1-reflections remain. Figure 6.10 shows a HRTEM image of an Al–Co–Ni quasicrystal in the S1-state, which renders an SAED pattern similar to that of Fig. 6.9b. The contrast details in the thin part of the region shown in this micrograph clearly contain a dark pentagon-shaped contrast feature in which a bright spot in the center is surrounded by a disk-shaped region of intermediate contrast. This pentagonal contrast has successfully been interpreted as evidence for a pentagonal symmetry of the atom cluster in the projection along the 10-fold axis [110]. It can be recognized in Fig. 6.10 that most of these disks have their pentagon-shaped center in an *antiparallel* orientation with respect to their next-neighbors. This feature is typical for both, the S1-state and for the type I superstructure. In quasicrystalline material with a slightly lower Ni-content, Ritsch [109] observed a second decagonal superstructure, the type II modification (Fig. 6.9d). This superstructure is characterized by additional reflections located on small pentagons, arranged with their centers on regular decagons around the strongest basic reflections.

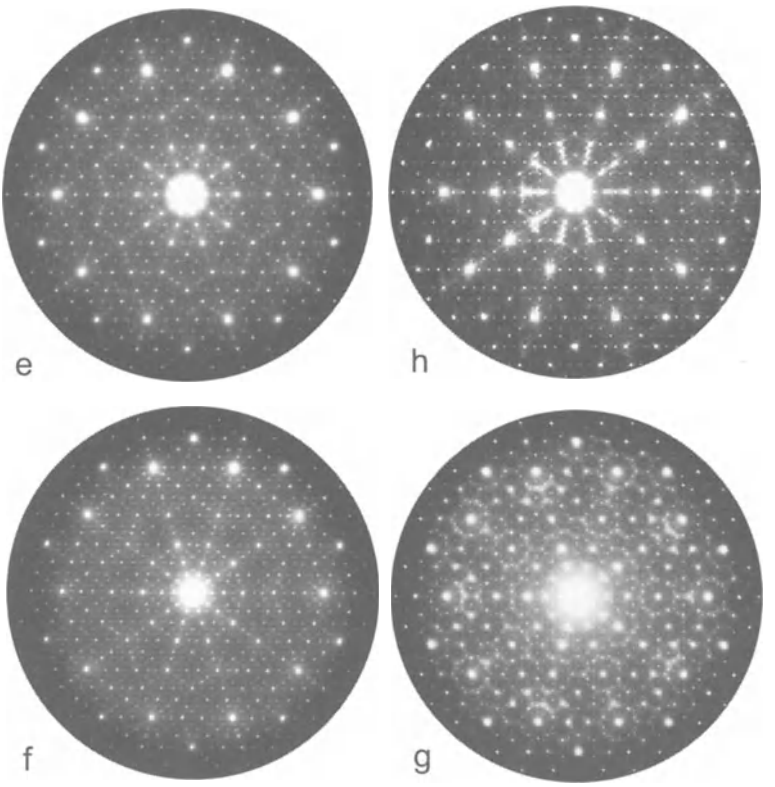

Fig. 6.9. (**e**): basic Co-rich state, $Al_{72.5}Co_{16.5}Ni_{11}$, 850°C for 3 d. (**f**): 5-fold state, $Al_{72.5}Co_{20}Ni_{7.5}$, 1050°C for 10 h. (**g**): 5-fold with type I state, $Al_{71.5}Co_{25.5}Ni_3$, 1160°C for 2 h. (**h**): 1D quasicrystal, $Al_{71}Co_{19}Ni_{10}$, 1080°C for 17 h. For all figures: Along the horizontal axis the two strongest reflections correspond to a *d*-value of 0.236 nm

The indexing of this superstructure has been shown by Ritsch et al. to be possible by the introduction of half-integer indices. The origin of these superstructure reflections is still not well understood. The 1D periodic 5-fold modification (Fig. 6.9e) occurs in the most Co-rich region of the stability field of the decagonal phase [112,114]. This structure is characterized by a *parallel* orientation over extended distances of most of the pentagonal atom clusters mentioned above. This SAED pattern definitely has 5-fold rather than 10-fold symmetry. This break of the 10-fold symmetry, which would principally be expected according to the inherent inversion symmetry of a diffraction experiment (Friedel's law), is caused by dynamical scattering effects due to the mainly parallel orientation of the pentagonally symmetric atom clusters.

This can be concluded from a simulated SAED pattern (Fig. 6.11) which has been calculated with the multi-slice method on the basis of a large supercell containing pentagonally symmetric clusters in parallel orientation only.

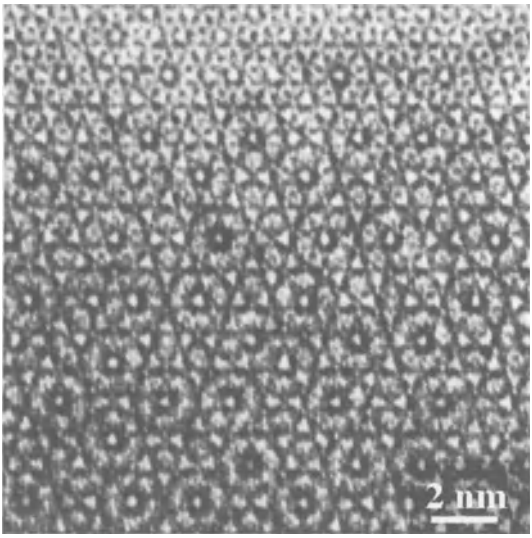

Fig. 6.10. HRTEM image taken along the 10-fold axis of quenched $Al_{72.5}Co_{13.5}Ni_{14}$ annealed at 900°C for 2 d. The image has been taken with a 300-kV electron microscope (C_s=1.1 mm) at a defocus of 30 nm in order to enhance the contrast of the pentagonal cluster centers. The thickness increases from the top to the bottom

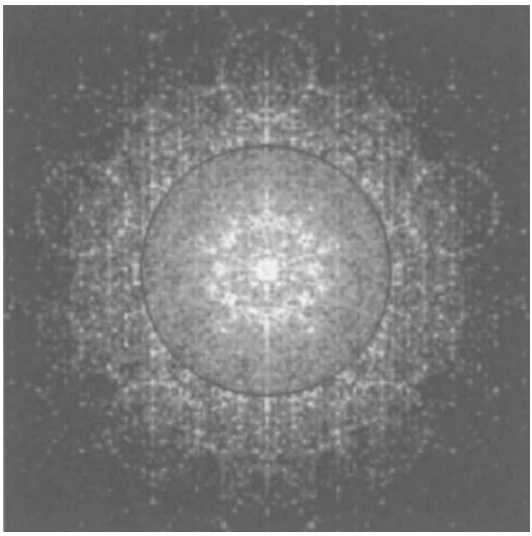

Fig. 6.11. Simulated SAED pattern of a 5-fold quasicrystal (periodic along the third dimension). The simulation takes account of the dynamical scattering effects. The center of the pattern (marked by a *black circle*) is shown with a different cut-off value in order to also present the weaker reflections with high space frequencies

The details for this simulation have been presented in [112]. The intensity of the power spectrum of the calculated wave function is represented in Fig. 6.11. The data here are plotted with two different logarithmic scales for the central part and the part with high space frequencies, respectively, since in the raw data the primary beam intensity was too high to allow a representation of the weaker reflections and thus a comparison with the experimental pattern. The simulation results in a satisfactory correspondence with Fig. 6.9e.

While in the 5-fold symmetric modification the domains of pentagonal clusters in parallel orientation extend over at least several micrometers, the basic Co-rich modification is characterized by only nanometer-sized domains in which the orientation of the pentagonal clusters is parallel [108,115]. However, both states, i.e. the decagonal basic Co-rich and the 5-fold state, contain only basic reflections in their SAED patterns. In samples quenched from a temperature around 1160°C and for a composition $Al_{71.5}Co_{25.5}Ni_3$ a variant of the type I superstructure modification occurs in the 1D periodic 5-fold modification; this variant, shown in Fig. 6.9g, is characterized by the presence of both, the S1-type and the S2-type superstructure reflections. Additionally, strong diffuse intensity around the superstructure reflections is present [116]. Ritsch et al. [117] have obtained SAED patterns (Fig. 6.9h) in the projection direction along the pseudodecagonal axis, which can best be interpreted as a 1D quasicrystal: Along the periodic axis in this pattern (which is shown oriented horizontally in Fig. 6.9h) a period of 6.15 nm can be inferred. In the direction perpendicular to this periodic axis an aperiodic sequence (which is part of the Fibonnacci sequence) of two distances approximately related by the golden mean, $\tau = 1.618...$, can be recognized in Figs. 6.9. Additionally, along the c-axis (pseudodecagonal axis) a period of approximately 0.8 nm has been observed. So far, we have in most cases observed the 1D Al–Co–Ni quasicrystal modification as fine-grained, twined material. A similar interpretation of a high-resolution synchrotron radiation diffraction experiment of a multiply twined sample has recently been presented [82].

6.3.3 A Quasiperiodic Decagonal Al–Co–Ni Quasicrystal?

As presented in Sect. 6.3.2, the basic Ni-rich phase of Al–Co–Ni quasicrystals reveals a very high degree of perfection in its SAED patterns. A magnified detail of a SAED pattern in the projection along the 10-fold axis is presented in Fig. 6.12. This pattern shows many sharp reflections and only weak diffuse background intensity (which in Fig. 6.12 is in part due to an incipient S1-type superstructure order).

The basic Ni-rich structure has been analyzed in detail on the basis of a set of electron micrographs by Ritsch et al. [108,113]. Image simulations were performed on the basis of a structure proposed by Steurer et al. [131] and resulted in a close agreement with the observed image contrast. This comparison also revealed that the individual clusters in this structure have basically decagonal (and not pentagonal) symmetry in the projection along

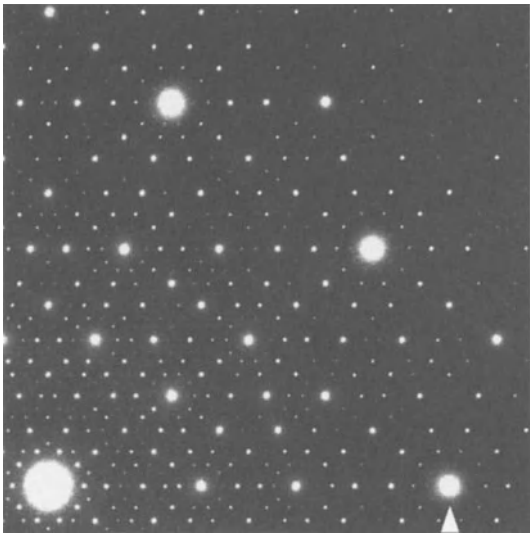

Fig. 6.12. Highly magnified SAED pattern (one quadrant) of a basic Ni-rich quasicrystal ($Al_{70}Co_{11}Ni_{19}$, 1050°C for 12 h). The *arrow head* indicates a reflection with a *d*-value of 0.236 nm

the 10-fold axis. This indicates that there must be considerable chemical disorder in the atomic arrangement of the clusters in the basic Ni-rich state. The centers of these clusters form the vertices of a tiling with a unique edge length of 2.0 nm, which almost precisely corresponds to a portion of a strictly quasiperiodic Penrose pentagon tiling. This tiling is shown in the central drawing of Fig. 6.13. Additionally, the details of the local image contrast configurations allows us to superimpose another tiling (related by a deflation with the factor τ) with an edge length of 3.24 nm, shown at the bottom of Fig. 6.13. Similarly, by composition, a tiling inflated by a factor $1/\tau$ can be constructed and superimposed onto the original electron micrograph (top of Fig. 6.13). In this tiling a certain number of the vertices are not recognized in the contrast of the micrograph; these have therefore been omitted in the drawing of the corresponding tiling with the smallest edge length of 1.24 nm.

The coordinates of all vertices in a 10-fold random tiling can be expressed as integer linear combinations of the five edge vectors of a regular pentagon. A 5-dimensional coordinate is obtained in this way for each vertex after arbitrarily selecting an origin. Coordinates which differ by an integral multiple of (11111) represent the same point in 5D space. As a result, the structure can be discussed in terms of a 4D space. By lifting the tiling in this way to 4D space, coordinates of vertices near a 2D hyperplane, the so-called parallel space, are obtained. The other two dimensions of the 4D space are then referred to as perpendicular space. The lines connecting these coordinates in 4D space result in a fluctuating hypersurface without tears. The projection of the coordinates on this hypersurface onto perpendicular space defines a region which, for a quasiperiodic tiling corresponds to the acceptance region associated with the vertices of the hypercubic lattice. The broadness of the

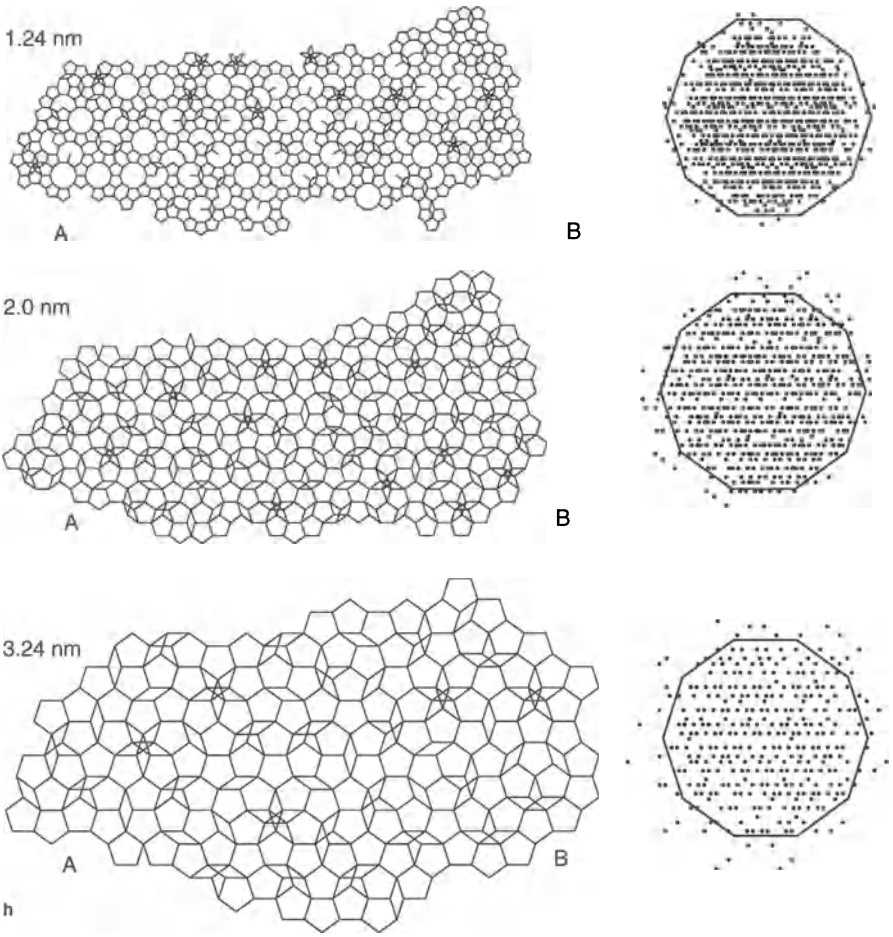

Fig. 6.13. Tilings with three different edge lengths, constructed as overlays onto an electron micrograph of a highly ordered Ni-rich decagonal state. The diagrams on the right give the perpendicular space plot corresponding to each of these tilings, superimposed with the decagon-shaped perpendicular space window for a Penrose pentagon tiling

distribution of the projected vertices in perpendicular space gives a measure of the degree of randomness of the tiling. If the distribution is anisotropic, this is evidence for a (uniform or linear) phason strain, which is due to an inclination of the lifted hypersurface with respect to the hyperplane of an ideal 10-fold symmetric tiling.

For the three tilings shown on the left side of Fig. 6.13, these perpendicular space (or internal space) vertex distributions have been constructed for the corresponding tilings with three different tile sizes (shown on the right-hand side of Fig. 6.13). In these plots the decagon corresponds to the outline of the

perpendicular space window of a (strictly quasiperiodic) Penrose pentagon tiling. An analogous analysis using a perpendicular space plot was made for micrographs of the S1-superstructure modification.

An example for $Al_{72.5}Co_{13.5}Ni_{14}$, annealed at 900°C for two days, is presented in Fig. 6.14, together with the corresponding tiling. This tiling consists of large tiles which are characteristic for the S1-type modification of the Al–Co–Ni quasicrystal. These large tiles can be decomposed into either the tiles of a Penrose rhombus tiling or into those of a Penrose pentagon tiling. These "interior" vertices inside the large tiles could not be recognized in the micrographs and have therefore been omitted from the tiling in Fig. 6.14. This absence is not related to a lower quality of the HRTEM images, but characteristic for the S1-state. In contrast, in the type I state most of these "interior" vertices can be recognized [108,109]. Their absence in the S1-state has been interpreted on the basis of HRTEM image simulations as due to phason-related stacking disorder in the direction parallel to the 10-fold axis [111]. This effect is caused by the superposition, parallel to the 10-fold axis, of different local tiling configurations from different levels within the specimen (also called "stacking randomness"). In HRTEM only those centers of decagonal atom clusters can be recognized which are positioned along the same projected vertex position throughout most of the specimen thickness (typically, for 75%, or more, of the thickness). The corresponding plot of the distribution of the perpendicular space on the right-hand side of Fig. 6.14 shows a remarkable clustering of these points around the center of the plot within the perpendicular space window of an ideal Penrose pentagon tiling. The perpendicular space plots considered separately are no safe indication of the presence of either an almost quasiperiodic tiling (e.g. Fig. 6.13) or a random

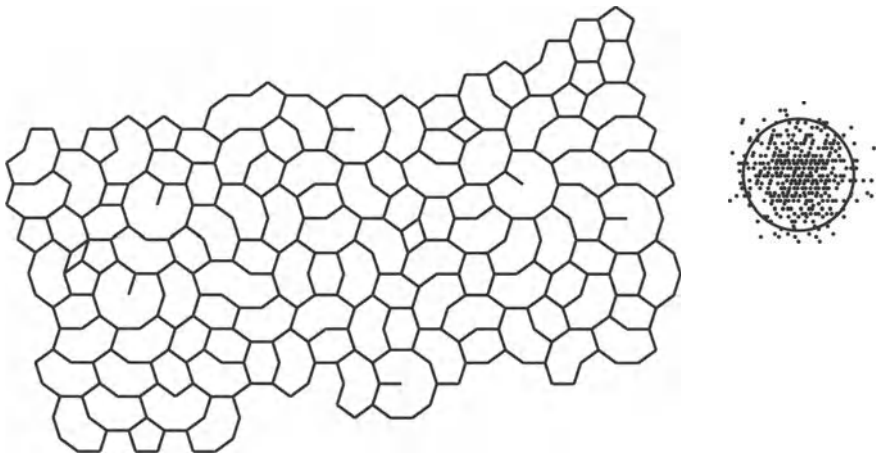

Fig. 6.14. Tiling and perpendicular space plot of the S1-superstructure observed in an $Al_{72.5}Co_{13.5}Ni_{14}$ alloy, 900°C for 2 d (courtesy S. Ritsch)

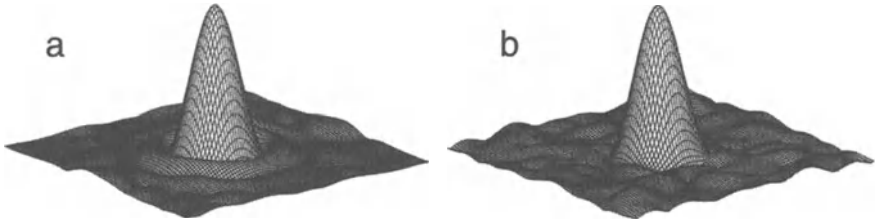

Fig. 6.15. Absolute value of the Fourier transform of the perpendicular space distributions for (**a**) the basic Ni-rich state and (**b**) the S1-superstructure (courtesy D. Joseph)

tiling (e.g. Fig. 6.14). Therefore an alternative method, based on a statistical analysis of the perpendicular space distribution, has been developed [81] in order to provide a measure of the degree to which an experimental tiling approaches a quasiperiodic one. The absolute value of the Fourier transformation of the perpendicular space point distributions from Figs. 6.13 (center) and 6.14 are presented in Fig. 6.15. The Fourier transform of a Gaussian distribution is again a Gaussian distribution, while the Fourier transform of a cylindrical box function is an oscillating rotation-symmetric function. The perpendicular space distribution of a random tiling is a Gaussian distribution, whereas for a quasiperiodic tiling it is a prismatic box function [79]. Accordingly, the oscillating function recognized in Fig. 6.15a indicates that the tiling constructed as an overlay onto the micrograph of the basic Ni-rich phase is exceptionally close to a quasiperiodic tiling. By contrast, the tiling of the S1-state is obviously a random tiling, since the distribution function in Fig. 6.15b is a Gaussian distribution.

It has been argued by Henley [62] that the basic Ni-rich phase could nevertheless be interpreted as a structural state with a long-range order corresponding to that of a random tiling. This argument is based on the result by Shaw et al. [123], that for a sufficiently thick specimen (typically more than 10 nm) the HRTEM images cannot reveal the presence of phason disorder. Even though this argument has only been formulated for an icosahedral tiling, similar considerations might apply for the stacking of different decagonal random tilings in which one layer is related to the next one by a certain amount of reshuffling of tiles due to phason flips. This argument is not compatible with the following experimental observations:

1. The 2-fold SAED patterns of the S1-state show strong diffuse scattering in the layers perpendicular to the 10-fold axis, while diffuse intensity is nearly absent in the case of the Ni-rich perfect decagonal state [113]. This has also been observed in X-ray diffraction patterns of d-Al–Co–Ni [4]. This diffuse scattering is mostly due to the phason disorder present in the S1-state, which is clearly a state corresponding to a random tiling.

2. The tilings of the S1-state quasicrystals do not show the appearance of a perfect decagonal tiling, even for very large specimen thicknesses. By contrast, in HRTEM images of the basic Ni-rich state there is almost no extinction of vertices as would be expected for a stacking of many different random pentagon tilings (related layer-by-layer with a varying amount of phason flips) [111]. Instead, a tiling similar to that presented in Fig. 6.14 is invariably observed. In the case of quasicrystals periodic in 1D, such as the decagonal phases, this observation can be taken as evidence against the argument by Shaw et al. [123].
3. The 10-fold SAED patterns of the basic Ni-rich state contain an exceptionally large number of weak diffraction spots. No measurable displacement from the ideal decagonal symmetric positions can be recognized. (Compare, for example, the SAED pattern Fig. 6.4 of d-Al–Mn–Pd with that of the basic Ni-rich phase in Fig. 6.12. Note that the diffuse intensity in the diffraction patterns of d-Al–Mn–Pd has recently been successfully explained [95].) Also the presence of weak reflections in Fig. 6.12 indicates a small amount of overall phason disorder [40]. Since the weak reflections are not shifted from their ideal positions, this is further evidence for a very low density of phason defects.

In summary, the basic Ni-rich state is assumed to possess a long-range order close to truly quasiperiodic. However, the observation that the basic Ni-rich phase is only stable at temperatures above approximately 800°C indicates that it is probably a phase *additionally* stabilized by an entropy contribution. This entropy contribution originates from the chemical disorder present in this phase and *not* from the configurational entropy of a random tiling. This argument has been discussed in more details in [81]. In a recent contribution [129] a rather small region, approximately 11 nm in diameter, of basic d-Al–Co–Ni has been analyzed by a HRTEM image. These authors concluded that the quasicrystal was ordered according to a perfect Penrose tiling. It is evident from the present discussion that further HRTEM investigations of the basic Ni-rich phase should be made.

6.4 Icosahedral Quasicrystal Structures

6.4.1 Icosahedral Al–Cu–Li Quasicrystals

The investigation of icosahedral quasicrystals poses special problems caused by the aperiodic atom arrangement along any projection direction of the structure in contrast to quasicrystals periodic in 1D. The first stable icosahedral phase was found in the Al–Cu–Li system [119]. While X-ray and neutron diffraction studies invariably indicated a structure with icosahedral symmetry [16,33,42], transmission electron microscopy revealed considerable deviations from icosahedral symmetry in SAED patterns taken from sub-micrometer size regions [5,25,101,150]. However, these TEM results are consistent with

the observation of strong diffuse scattering and short correlation lengths measured by X-ray diffraction [54,86].

The attempts to solve the structure of i-Al–Cu–Li were greatly facilitated by the X-ray structure refinement of the cubic R-phase, which has a composition very close to that of the icosahedral phase [1]. On this basis full structure determinations were finally made by Yamamoto [145] and Jaric and Qui [77]. Elswijk et al. [42] proposed a first simplified structure model based on a decoration of a quasiperiodic AKK-rhombohedra tiling. Later, de Boissieu et al. [16], using a 6D embedding approach, made a more refined structure determination in which a combination of X-ray and neutron data was used. Jaric and Qui [77] developed a novel crystallographic refinement method, whereby a rational approximant (the cubic R-phase) was used to obtain the unknown phases of the measured quasicrystal reflections. The structure model by Yamamoto [145] was based on the set of experimental data by de Boissieu et al. [16]. This structure determination used perpendicular space acceptance domains in the form of complicated polyhedra for each of the different sites in a 3D quasiperiodic AKK-tiling. This was done in such a way that the icosahedral cluster of the cubic R-phase was present on all the so-called 12-fold sites of the icosahedral tiling. A similar idea has also been proposed by Hiraga [63].

Figure 6.16a presents a HRTEM image in the 2-fold projection direction. In this micrograph one of the 2-fold axes is parallel to the vertical direction and another one parallel to the horizontal direction (the directions of 3- and 5-fold axes are indicated by arrows). (The 2-fold projection direction gives

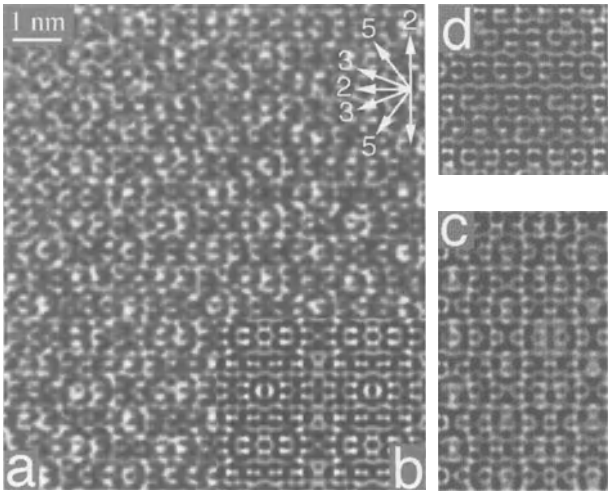

Fig. 6.16. HRTEM image of i-Al–Cu–Li in the 2-fold projection (**a**) and corresponding contrast simulations by Yamamoto (**b**), de Boissieu et al. (**c**) and Elswijk et al. (**d**), respectively. All images are in the same scale

the most important structural information, since all important symmetry axes are present within this image plane.) The imaging conditions of this micrograph are as follows: 300-kV, point-to-point resolution 0.20 nm, specimen thickness less than 10 nm, and the Scherzer defocus condition. The micrograph Fig. 6.16a should be compared with three different dynamical image contrast simulations [5,7] shown in the same scale in Figs. 6.16b–d: Fig. 6.16b is based on the model of Yamamoto, Fig. 6.16c was made using the model of de Boissieu et al., and Fig. 6.16d is based on the model of Elswijk et al. Evidently, the best fit between observed and calculated image contrast is obtained for Fig. 6.16b. The two main contributions of HRTEM investigations of Al–Cu–Li for finding the average structure of this quasicrystal are the corroboration of the basic structural features of the X-ray structure determinations (especially those by Yamamoto and by Jaric and Qui), and the unequivocal evidence for the overall presence of regions with strong deviations from icosahedral symmetry [5].

6.4.2 Icosahedral Al–Mn–Pd and Al–Cu–Fe Quasicrystals

A typical set of SAED patterns along four major symmetry directions of an $Al_{70}Mn_9Pd_{21}$ quasicrystal is presented in Fig. 6.17. This specimen has been annealed at 800°C for two days. Three diffraction patterns (Figs. 6.17a–c) reveal a τ-scaling in the arrangement of the reflections, characteristic for the face-centered icosahedral (F-type) quasilattice [37,73]. The usual F-type Al–Mn–Pd quasicrystal, shown in Fig. 6.17, is for certain compositions also stable at low temperatures, e.g. 600°C, see Fig. 6.18a.

The SAED patterns of two further variants of this quasicrystal (observed at temperatures between 500 to 700°C) are described in Figs. 6.18b–d. These figures present magnified details taken from corresponding regions of SAED patterns taken with the electron beam oriented along a 2-fold axis. The first of these, called F2-phase [70] is shown in Fig. 6.18b. It has a P-type quasilattice and a quasilattice parameter which is τ-times larger than that of the F-type quasicrystal [69]. In Fig. 6.18c narrow-spaced superstructure reflections (average modulation period 15.7 nm) are recognized, corresponding to a modulation in the direction of a 3-fold axis. The superstructure was first observed by Ishimasa and Mori [70] in a specimen of bulk composition $Al_{69}Mn_9Pd_{22}$. This SAED pattern was taken from a specimen with composition $Al_{70}Mn_8Pd_{22}$ [59].

In another region (Fig. 6.18d) of the same specimen SAED patterns could be obtained which had two sets of superstructure reflections parallel to both 3-fold axes in SAED pattern taken in the [1/1 1/1 0/0] projection direction (indexing system by Cahn et al. [22]; this type of zone axis contains in the diffraction pattern two 3-fold axes and one 2-fold axis).

Our recent HRTEM investigations indicate that a new interpretation of these superstructure reflections is possible by a modulated quasicrystal phase with modulations along the four 3-fold axes of a cube. A similar complicated

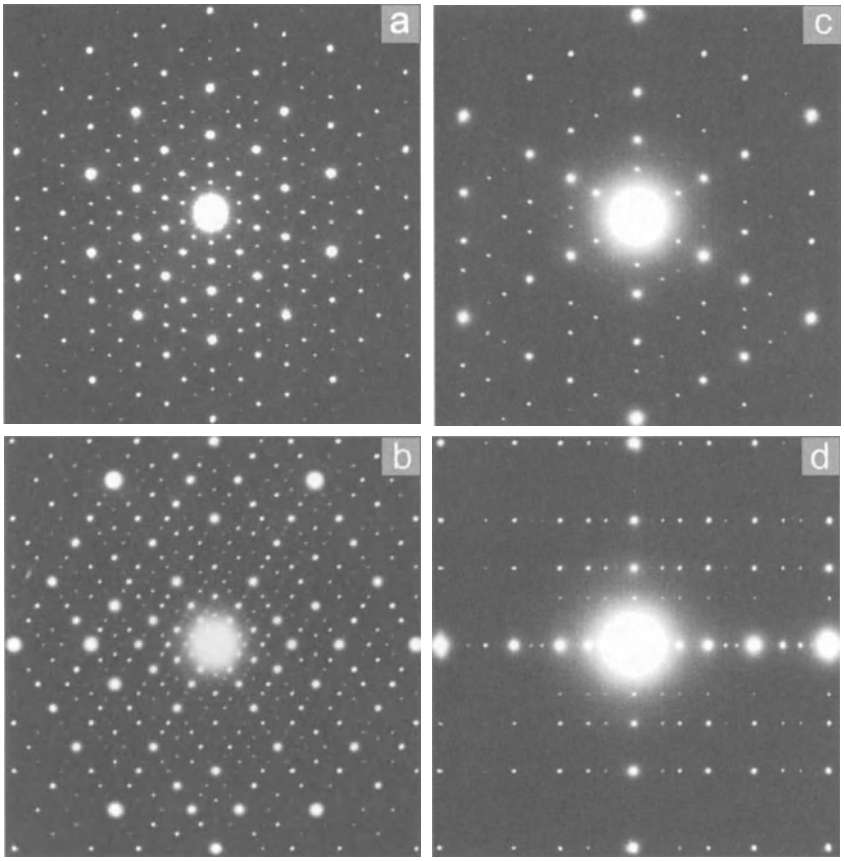

Fig. 6.17. SAED patterns of i-$Al_{70}Mn_9Pd_{21}$ in the 5-fold (**a**), 2-fold (**b**), and 3-fold projection direction (**c**), and a direction normal to a mirror plane (**d**)

superstructure has also been studied by de Boissieu et al. [17]. An additional corroboration of the assumption that the modulation has (approximate) cubic symmetry (m3) can be obtained from the SAED pattern Fig. 6.18d. In this pattern the modulated structure is observed along the projection direction parallel to one edge of the cube, the space diagonals of which are parallel to the four modulated 3-fold axes.

HRTEM images obtained from i-Al–Mn–Pd quasicrystals indicate a highly ordered structure, i.e. an average quasiperiodic structure with long-range order. An example of such a highly ordered material is presented for a 2-fold projection direction in Fig. 6.19. When observed at a grazing angle along different symmetry directions, no evidence of phason defects can be found, i.e. the lattice lines are continuous in the entire region of the micrograph. (Notice that the image Fig. 6.19 has not been taken in the Scherzer defocus

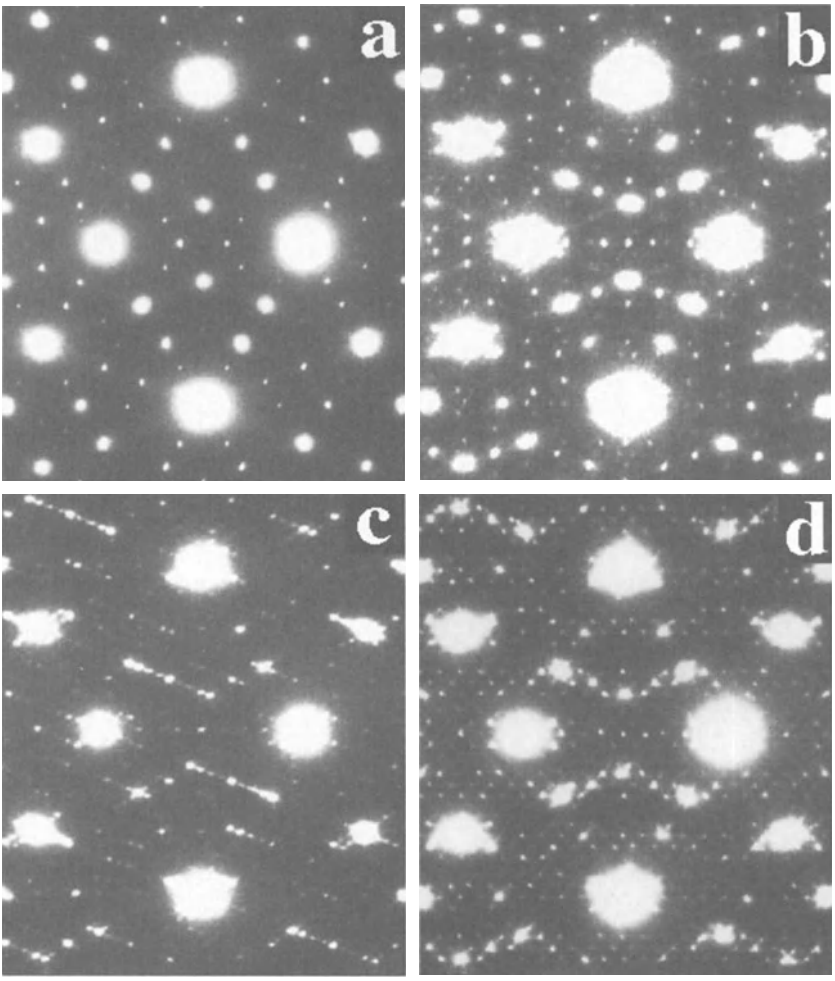

Fig. 6.18. Portions of SAED patterns of i-Al–Mn–Pd in the 2-fold projection, obtained from different samples quenched from 600°C. (**a**) F-type, (**b**) P-type (F2-phase) and the modulated F_{2M}-phase (also called F*-phase) (**c, d**)

condition, but at a higher defocus in order to enhance certain aperiodically repeated contrast features.)

Besides the stable Al–Mn–Pd quasicrystal, the i-Al–Cu–Fe phase, typically with a composition close to $Al_{63}Cu_{25}Fe_{12}$, has been the most frequently used material for electron microscopy investigations of icosahedral phases [64,70,73,89]. Figure 6.20 shows a HRTEM image of i-Al–Cu–Fe projected along the 5-fold axis. The thickness of the specimen increases from the right-hand margin to the left. Again the continuity of all lattice planes indicates

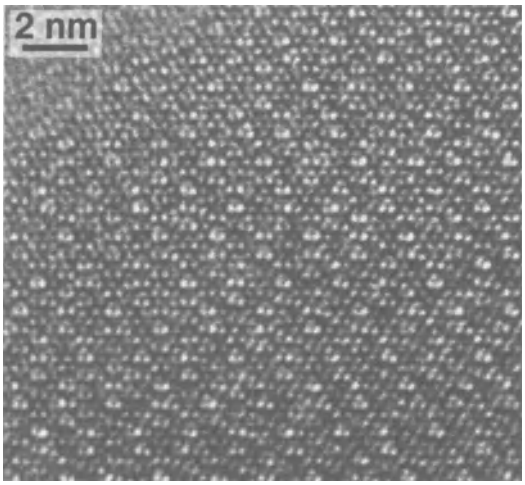

Fig. 6.19. High-voltage (800 kV) HRTEM image of F-type i-Al–Mn–Pd in 2-fold projection, obtained in a sample quenched from 800°C

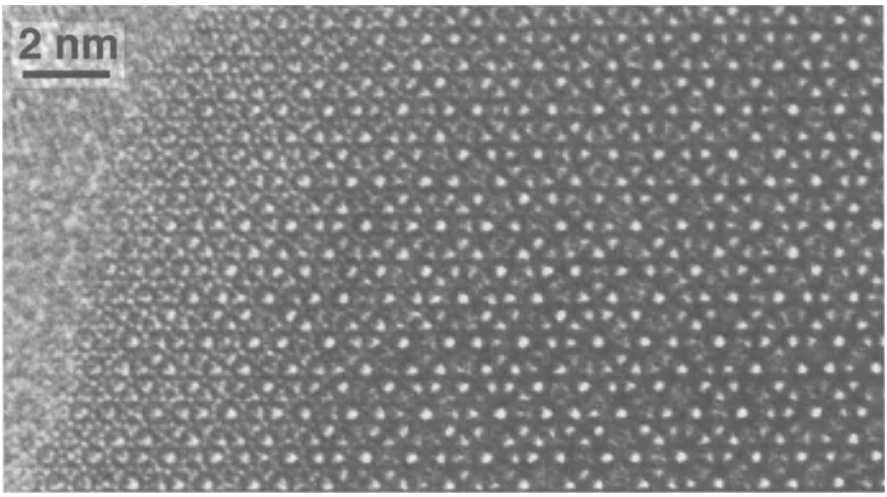

Fig. 6.20. HRTEM image of F-type i-Al–Cu–Fe in 5-fold projection, obtained in a sample quenched from 800°C (courtesy K. Kifune)

a very high degree of order. As often, the thin margin of the wedge-shaped specimen allows us to recognize finer structural details.

In order to visualize individual phason defects in an icosahedral quasicrystal of high structural quality, a dynamical contrast calculation would be necessary, in which both thickness and defocus (of the objective lens) are varied. For thick specimens the argument put forward by Shaw et al. [123], may still be valid, i.e. that phason defects cannot be recognized in HRTEM images of relatively thick specimens because of the projection effects.

6.4.3 Icosahedral Clusters and Cluster Models of Icosahedral Phases

As discussed in Sect. 6.4.1, the identification of large icosahedral clusters in crystalline phases of similar composition to that of the icosahedral quasicrystal has been one of the most successful ideas which allowed a realistic average structure model for i-Al–Cu–Li to be found [145]. In i-Al–Mn–Si, the so-called Mackay cluster (Fig. 6.21) has been used with similar success to model the average structure [36]. Accordingly, it seems natural to propose related cluster models for other icosahedral quasicrystals. The first structure determinations by X-ray and neutron diffraction techniques for i-Al–Cu–Fe [30] and i-Al–Mn–Pd [20] were published in 1991 and 1992, respectively. Nevertheless, up to now there is no generally accepted structure model for these two structures. In order to make progress in the future, it is therefore necessary to know which icosahedral clusters exist and then to select those clusters as basic building blocks that are in accordance with the experimental 6D Patterson maps of the two icosahedral phases. In addition, it will be helpful to ascertain the existence of the corresponding cluster in one or several approximant crystal structures.

In the structure determination of the i-Al–Mn–Pd, Boudard et al. [20] have found evidence for the presence of the so-called pseudo-Mackay cluster (Fig. 6.22), in which the inner icosahedron of a regular Mackay cluster is replaced by a dodecahedron. However, since this would correspond to 20 instead of 12 atoms inside the same outer shell, not all of these positions can

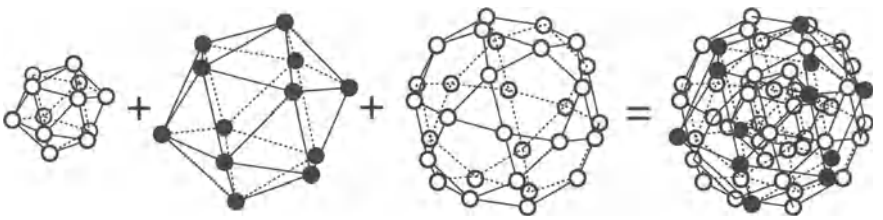

Fig. 6.21. The Mackay cluster, as observed in α-Al–Mn–Si

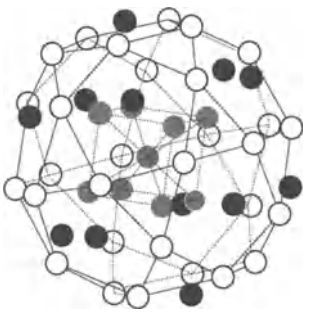

Fig. 6.22. The pseudo-Mackay cluster, as observed in i-Al–Mn–Pd. The innermost icosahedron of the Mackay cluster is replaced by a central atom which is surrounded by 7 or 8 atoms, arranged on the 20 vertices of a dodecahedron

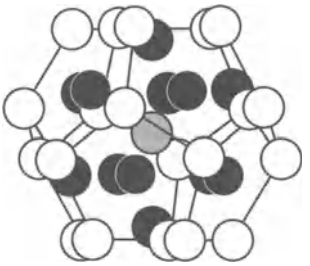

Fig. 6.23. The Bergmann cluster, as observed in i-Al–Mn–Pd and i-Al–Cu–Fe

be occupied. On the basis of their data, Boudard et al. [20] assumed only eight or nine atoms to be situated on this inner shell. The connection between adjacent pseudo-Mackay clusters influences the occupancy on this inner shell. In a report on a Pd-rich approximant phase in the Al–Mn–Pd system [21], Boudard et al. have confirmed the presence of the Bergmann cluster (Fig. 6.23). The Bergmann cluster in the approximant phase has, however, a different chemical decoration from that of the icosahedral phase. Presently, it is generally agreed that both, the Bergmann cluster and the pseudo-Mackay cluster are present in both these icosahedral structures, i.e. i-Al–Cu–Fe and i-Al–Mn–Pd.

If Si is added to the Al–Mn–Pd system, the icosahedral phase is only formed up to a Si-content of approximately 2 at.% and is subsequently replaced by two different cubic approximant phases with large unit cells [70]. It would appear that this approximant is a good candidate for finding an icosahedral atom cluster for i-Al–Mn–Pd. A recent structure determination [133] has established a new icosahedral cluster in the Al–Mn–Pd–Si [2/1,2/1,2/1]-approximant phase. The twelve (!) successive icosahedral shells found in this X-ray investigation are presented in Fig. 6.24.
This cluster can be viewed as an extension of the Bergmann cluster. In this situation the question arises as to whether this approach of transferring the clusters found in approximants to the corresponding quasicrystal, which was very successful for the Al–Cu–Li quasicrystal, can be applied analogously to i-Al–Mn–Pd or i-Al–Cu–Fe. Recently, this has been attempted by Yamamoto and Hiraga [146]. It should be kept in mind that further new clusters may be found with continued investigation of chemically different approximant crystals and new stable icosahedral quasicrystals.

Katz and Gratias [83] have presented a part of their final results (i.e. a 5-fold and a 2-fold projection of a slice of the structure) on the 3D structure of i-Al–Cu–Fe. Clearly, this structure proposal allows an interpretation in terms of two different clusters arranged quasiperiodically on the vertices of a binary tiling when projected, for example, along a 5-fold axis. Elser [41] has also proposed a model of the structure of i-Al–Mn–Pd and i-Al–Cu–Fe quasicrystals in terms of two clusters: the Bergmann cluster and the pseudo-Mackay cluster. This model is a random tiling model formulated in 3D space

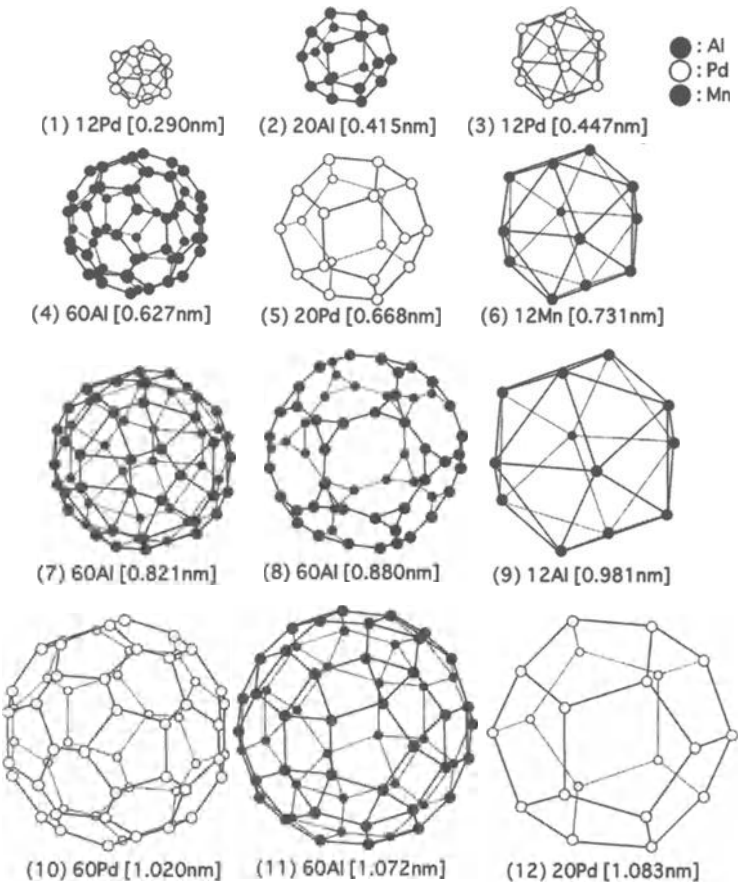

Fig. 6.24. The complex icosahedral cluster, as observed in the [2/1,2/1,2/1]-approximant phase of Al–Mn–Pd–Si. After Sugiyama et al. [133]

based on the data from Katz and co-workers [30,83] for Al–Cu–Fe and for Al–Mn–Pd on data from Boudard et al. [20]. A Bergmann cluster is positioned on all even sites of a AKK-rhombohedra tiling (with τ-times a basic edge length, which is 0.4465 nm for Al–Cu–Fe and 0.4561 nm for Al–Mn–Pd) and a pseudo-Mackay cluster on the odd sites of the same tiling; the two clusters share six atoms along the 5-fold axis. This decoration of the AKK-tiling results in an F-type lattice. The details of the structure as well as a probable mechanism for the phason movements are described in detail in [41]. A similar model has been applied to interpret the surface structure of i-Al–Mn–Pd by Papadopolos et al. [105].

In summary, the cluster description of icosahedral phases appears, at present, to be a natural way to propose a structure model for i-Al–Mn–Pd and the i-Al–Cu–Fe. There is even a theoretical argument as to why clusters could

be a key for the understanding of the formation of quasicrystal structures: For decagonal tilings, Gummelt [58] has proved that a single decagonal cluster can cover the plane in a strictly quasiperiodic way if certain overlaps are allowed. Subsequently, Steinhardt and Jeong [78] have shown that this is equivalent to maximizing the density of this overlapping decagonal cluster in the tiling. Accordingly, it could be conjectured for icosahedral quasicrystals, that similarly the maximized density of overlapping an analogous 3D polyhedral cluster leads to a strictly quasiperiodic structure. However, Kramer [90] has proved for an icosahedral tiling that a single covering cluster is not sufficient to cover the entire volume without voids.

6.5 Dodecagonal, Octagonal, and Cubic Quasicrystals

Dodecagonal quasicrystals have been produced in four different systems: the Cr–Ni system [71,72] and the related Ni–V and Ni–V–Si systems [27], the Bi–Mn system [149] and the Ta–Te system [29]. A short review on the most relevant structural aspects of the Cr–Ni and Ni–V–(Si) dodecagonal quasicrystals has recently been published by Beeli [6]. Figure 6.25 shows the upper half of an SAED pattern made from a small area of a Cr–Ni small particle. This pattern is characteristic for the dodecagonal quasicrystal structure found in these particles. As a result of a slight off-axis tilt a larger number of diffraction spots with high indices appear [72]. As is obvious from the SAED pattern, these spots can be connected to form a ring of overlapping regular dodecagons (around (2400)-type reflections) and a ring of edge-sharing dodecagons (around (5353)-type reflections). The most probable stable dodecagonal

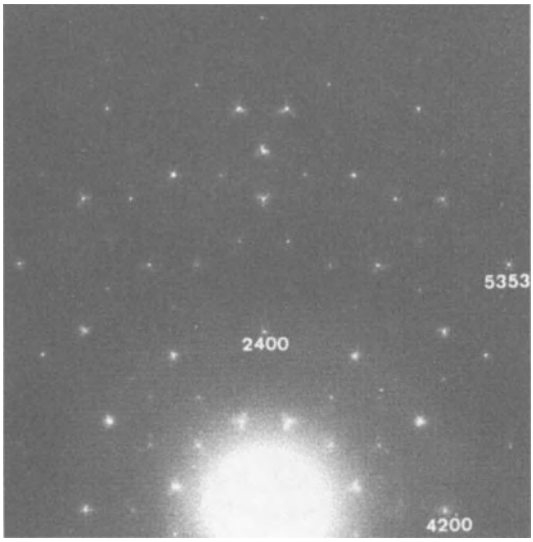

Fig. 6.25. SAED pattern of a Cr–Ni dodecagonal quasicrystal small particle with indices. The electron beam was slightly tilted against the c-axis of the quasicrystal (courtesy T. Ishimasa)

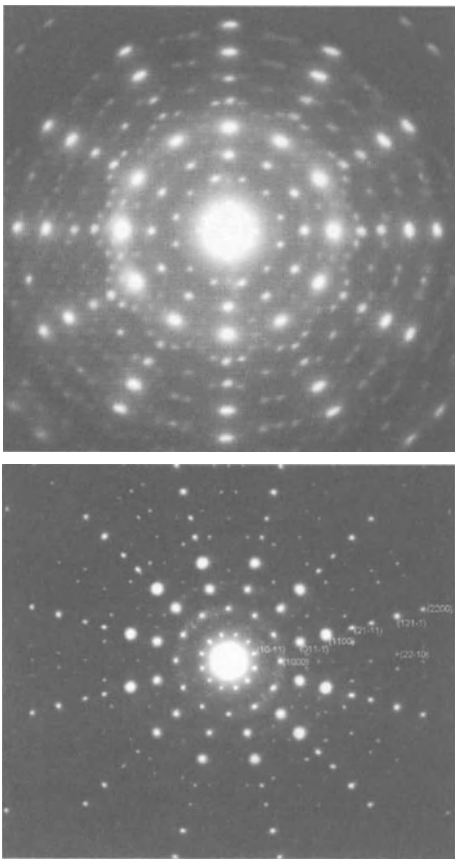

Fig. 6.26. Comparison of two SAED patterns from differently produced Ta–Te dodecagonal quasicrystals. (**a**) Ta–Te quasicrystal obtained by a solid-state diffusion reaction at 1300 K (courtesy M. Uchida and Horiuchi). (**b**) Thin region of a $Ta_{1.61}Te$ single-quasicrystal unit (courtesy M. Conrad, B. Harbrecht and F. Krumeich)

Ta–Te quasicrystal shows a different and denser arrangement of diffraction spots. This can be recognized, for example, in the SAED pattern (Fig. 6.26a) taken from a Ta–Te quasicrystal obtained by a diffusion reaction around 1300 K in the interdiffusion layer of $TaTe_2$ and pure Ta [140]. This pattern has approximately 12-fold symmetry and the somewhat diffuse spots can be connected (in several ways) to form a network of squares and equilateral triangles. This SAED pattern has been obtained from one grain of a polycrystalline material with sub-micrometer grain size, whereas in Fig. 6.26b, a SAED pattern is shown for comparison which has been obtained from a thin region of morphological units of $Ta_{1.61}Te$ described by Conrad et al. [29], which reach sizes up to several 100 µm. Figure 6.27 presents a HRTEM image from such a quasicrystal; it shows an aperiodic distribution of dodecagonal rings consisting of 12 bright spots. The centers of these dodecagons can be used to construct a tiling of squares and regular triangles (with 2 nm edge length) which can be superimposed onto the image contrast. In the upper part of this micrograph several different periodic arrangements of these

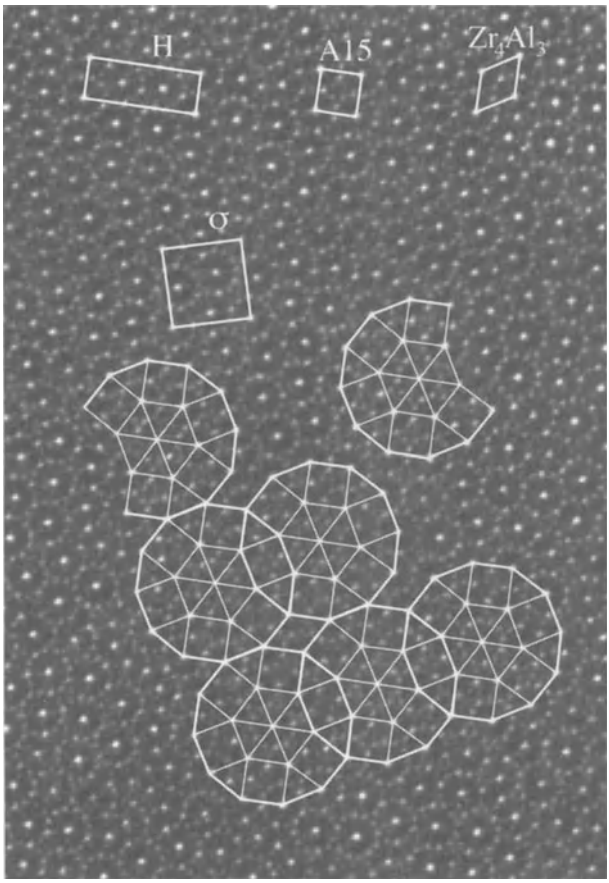

Fig. 6.27. HRTEM micrograph of a dodecagonal Ta–Te quasicrystal. A few unit cells of the phases σ, H, A15 and Zr_4Al_3 as well as dodecagon-shaped regions are marked by white lines (courtesy F. Krumeich)

squares and regular triangles can be recognized. The four unit cells of the basic crystalline structures formed by squares and regular triangles have been outlined: the σ-phase, the A15 structure, the Zr_4Al_3-type structure and the H-phase. In the lower part of the HRTEM image of this 1D periodic structure, an arrangement in the form of several regular dodecagons is indicated by white lines. These dodecagons are partly overlapping or arranged edge-to-edge. Clearly, the tiling which can be superimposed onto this micrograph is a random tiling, with an edge length of the tiles of approximately 2 nm. A portion of such a random tiling is shown in Fig. 6.28. The close correspondence to the observed tiling in the HRTEM image is evident. The random tiling in Fig. 6.28 has been obtained using the growth model for a square-triangle tiling as described by Joseph and Elser [80]. Both tilings contain a

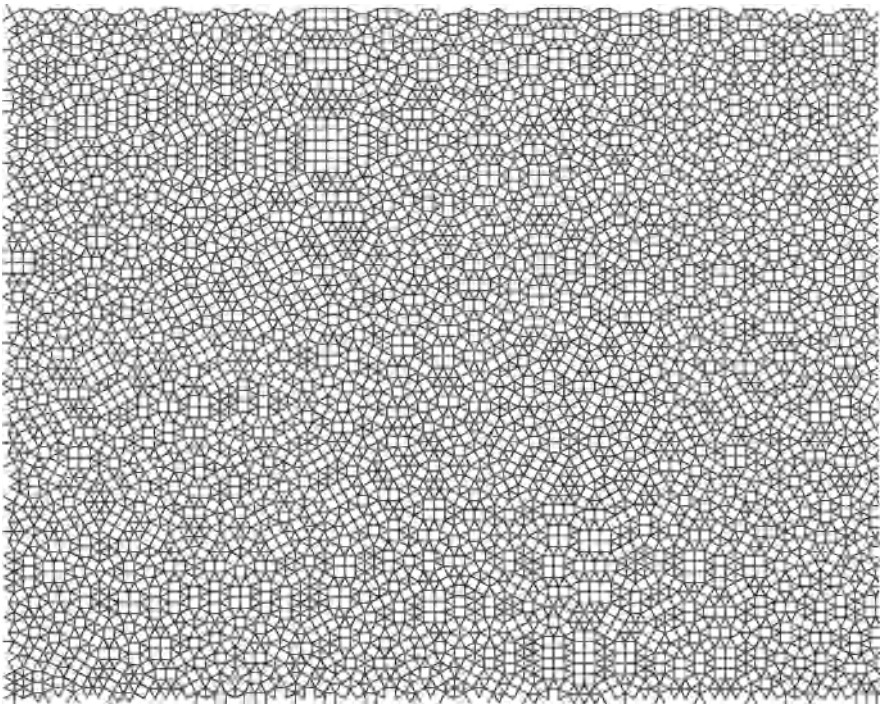

Fig. 6.28. Square-triangle tiling produced by growth algorithm according to Joseph and Elser (courtesy D. Joseph)

few short periodic repetitions of one of the four basic periodic structures described above. This good correspondence may be explained by the fact that the $Ta_{1.6}Te$ phase has been obtained by a reaction from the gas phase, i.e. a gas-solid reaction. Similarly, the growth algorithm by Joseph and Elser for the square-triangle tilings permits diffusion of "atoms" (vertices of the tiling) only at the surface.

The octagonal quasicrystalline alloys are in many ways analogous in their properties to the metastable dodecagonal quasicrystals, e.g. in the Cr–Ni or the Ni–V system. They are all metastable and are produced by very rapid quenching techniques such as the hammer-and-anvil technique [142]. The two octagonal quasicrystal systems reported so far are $Cr_5Ni_3Si_2$ [141] and $Al_3Mn_{82}Si_{15}$ [142]. Similar to Cr–Ni quasicrystals, the structure, judged on the basis of HRTEM images and SAED results, is essentially a 1D periodic quasicrystal composed of two prismatic building blocks, a cube and a 45° rhombic prism, in a random tiling type aperiodic arrangement. Along the periodic axis four layers, ABAB', have been observed, whereby the B'-layers are rotated 45° around the z-axis against the B-layers, so that an 8_4 screw-axis symmetry results [68]. Interestingly, small regions of both an octagonal and a dodecagonal quasicrystal structure have been described from the

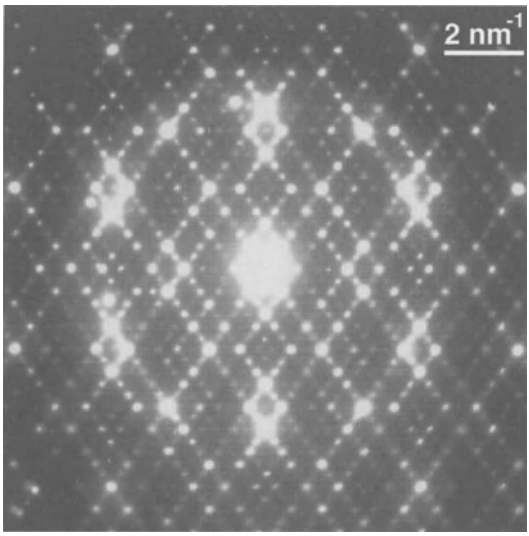

Fig. 6.29. SAED pattern of rapidly quenched $Al_{61}Mg_{39}$ alloy in 2-fold projection (courtesy P. Donnadieu)

same specimen, and a possible transformation between these two structures has been suggested and modeled as a transformation involving a so-called Schur-rotation [3]. In two chemically different systems metastable aperiodic structures with the symmetry elements of a cubic space group, except for a lack of translational symmetry, have been reported [34,46]. Feng et al. [46] found such an aperiodic phase in rapidly solidified $Ni_{16}V_6Si_7$. An interpretation of the possible quasilattice of this structure was given on the basis of the $(3+n)$D crystallography formulation by Janner and Janssen [75]. Donnadieu et al. [34] have investigated a series of Al–Mg structures related to the stable crystal structure β-Al_3Mg_2 (a=2.85 nm, space group Fd3m). In this series, at a certain composition ($Al_{61}Mg_{39}$), a structure interpreted as a cubic quasicrystal was found, while for other compositions various modulated structures occurred. A SAED pattern of this cubic quasicrystal, taken along a 2-fold axis, is shown in Fig. 6.29. The Bragg spots which can be recognized are positioned on the vertices of a lattice defined by two orthogonal sets of parallel lines, each of which forms an aperiodic sequence with two distances related to the factor $(1+\sqrt{3})/2$, which is also the factor determining the geometry of dodecagonal quasicrystals.

6.6 Special Electron Diffraction Techniques Applied to Quasicrystals

6.6.1 Kikuchi Pattern Technique

The technique of Kikuchi line pattern analysis can be applied to any structure which has a discrete diffraction spectrum, i.e. it is also applicable to quasicrystals and can give valuable information on the structure or on the

orientation of a thin quasicrystal specimen in the TEM instrument. In relatively thick regions of such a specimen foil the electron beam generates a large proportion of electrons incoherently scattered in all directions. These electrons can be Bragg-diffracted on any lattice (or quasilattice) planes, and the diffracted beam will lie on one of two cones originating from the incidence point of the beam. For each diffraction vector g these two so-called Kossel cones exist, each pair of cones having a different angle θ to the corresponding (hkl)-plane. The intersection between this set of intercalated cones of diffraction intensity with the Ewald sphere produces a Kikuchi line pattern on the screen of the electron microscope. The line oriented parallel half-way between both Kikuchi lines forming a parallel pair (a Kikuchi band), is the intersection of the (hkl)-plane with the Ewald sphere and can thus be indexed like any SAED pattern [144]. Figure 6.30 shows a Kikuchi pattern of d-Al–Co–Ni oriented parallel to the 10-fold axis. The symmetry can be recognized with high precision, and even very small deviations from a specific symmetry can be measured in such a pattern. Even though the Kikuchi bands indicate 10-fold symmetry, the spots visible in the higher-order Laue zones reveal a clear difference between two adjacent bands (cf. detail images in Fig. 6.30), indicating the presence of 5-fold symmetry only. The Kikuchi pattern tech-

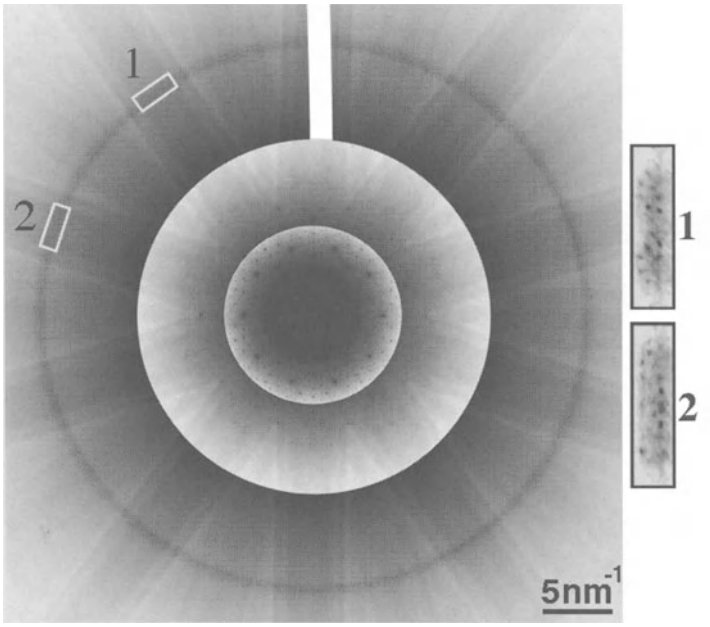

Fig. 6.30. Kikuchi line pattern of a pentagonal quasicrystal oriented parallel to the 5-fold axis ($Al_{71.5}Co_{25.5}Ni_3$). Two detail images show the regions marked in higher magnification. The inner ring-shaped and the circular regions are superimposed details from different patterns which were obtained with shorter exposure times

nique is therefore a valuable tool to identify approximant crystal structures as different from quasicrystals.

6.6.2 Convergent Beam Electron Diffraction Technique

A second special electron diffraction technique used on a TEM instrument is the convergent beam electron diffraction (CBED) technique [144]. This technique was developed in 1938 by Kossel and Möllenstedt [88]. It provides not only diffraction information from an extremely small specimen region but also gives information on certain symmetry elements, for instance in a quasicrystal structure, which cannot be obtained from a single SAED pattern or the usual X-ray techniques. This additional information includes the full space group symmetry of crystals, the presence of enantiomorphism in a crystal, or the point-group symmetry of quasicrystals. The CBED pattern has been used to overcome the limitation in spatial resolution of the SAED technique (cf. Sect. 6.2.2), however, it is now also employed as a very versatile quantitative technique. In an electron microscope the convergence angle of the electron beam can be increased by changing the excitation of the second condensor lens of the instrument. The diffraction pattern thereby can gradually be changed from a SAED pattern with fine sharp spots to a CBED pattern. In the latter all spots are visible in isolated form as small disks, showing contrast details inside the disk which are not available in SAED patterns. The larger the convergence angle, the more information is available from higher-order Laue zones. Finally the disks are strongly overlapping, forming a single pattern.

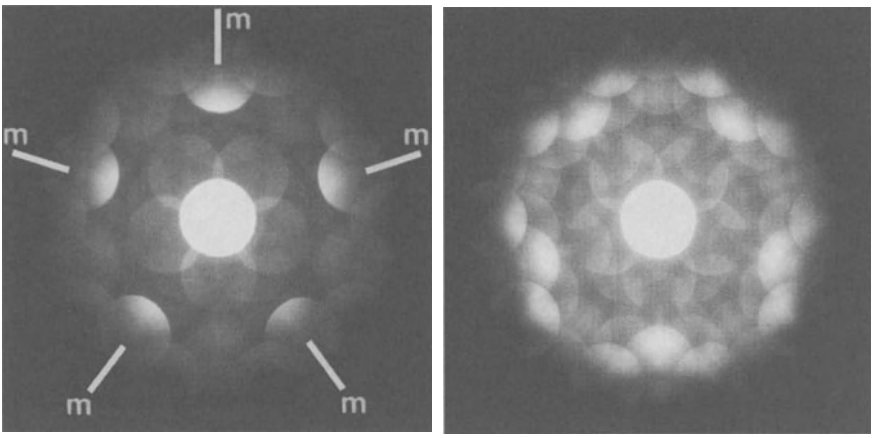

Fig. 6.31. CBED patterns of a pentagonal quasicrystal oriented parallel to the 5-fold axis ($Al_{70}Co_{26}Cu_4$). The *left* pattern is from a thin region, the *right* from an intermediate thick region (courtesy K. Tsuda)

The fine details in the interior of the disks in a CBED pattern can best be recognized and analyzed if the pattern is obtained from a region of the specimen which is carefully aligned parallel to one of the main symmetry directions of the structure. Figure 6.31 presents a CBED pattern of a pentagonal $Al_{70}Co_{26}Cu_4$ quasicrystal in which the 5-fold symmetry corresponding to the space group $P\overline{1}0m2$ can clearly be recognized; for details, see Tanaka et al. [135]. Similar to the 5-fold symmetry in the Al–Co–Ni quasicrystals, the 5-fold symmetric structural state of this quasicrystal can be attributed to a parallel orientation of the pentagonally symmetric clusters which are the main structural units of this quasicrystal.

6.7 Surface-Sensitive Techniques Applied to Quasicrystals

6.7.1 Secondary Electron Imaging

In the secondary electron imaging (SEI) technique [43] the physical process is basically the excitation of the surface layer by an electron beam with an energy around 2-4 keV. The primary electrons which enter the specimen are scattered elastically as well as inelastically at the atoms of the first few layers of 3 to 5 nm, which then act as emitters of secondary electrons. At this energy of the electrons, elastic forward scattering at the neighbor atoms is the main scattering process, and this so-called forward-focusing effect causes the electrons leaving the specimen to be oriented preferentially along the columns of the (quasi-)crystal structure. The inelastically scattered electrons dominate the spectrum of the back scattered intensity. Above a certain critical energy the elastic scattering is weakly energy dependent. Thus the incoherent addition of electrons having different energies only cause an enhancement of the total image contrast. The pattern is observed on a hemispherical screen underlaid by two grids, whereby the outer grid serves to retard the slower electrons emitted from the surface layer, thus acting as a high-pass energy filter. The observed SEI images mark the channeling directions around an average atom in the structure of the surface layer. These directions appear as broad bright spots on the image. The broadness is due to a minor contribution of electron interference effects; by contrast, electron diffraction effects are dominant in the image contrast for low primary electron energies. At an energy of typically 2000 eV the image contrast can therefore be directly interpreted as a real-space (hemispherical) representation of the channeling directions in the structure of the surface layer. The minimum specimen surface required for this technique must presently have a diameter of approximatively 0.3 mm.

Erbudak et al. [44] have successfully applied this technique to i-Al–Mn–Pd quasicrystals, and similar experiments were made by this group on d-Al–Co–Ni quasicrystals [18]. Figure 6.32a shows an SEI pattern (made after heating in vacuum) of i-Al–Mn–Pd oriented parallel to a 5-fold axis. In this pattern

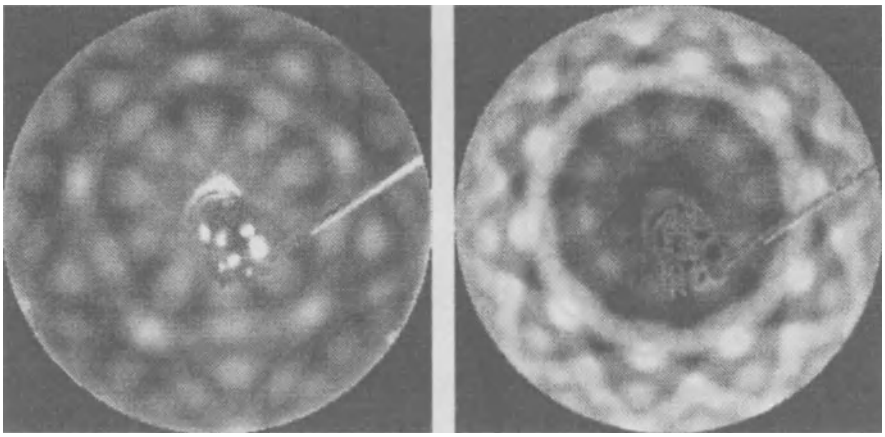

Fig. 6.32. SEI patterns of an i-Al–Mn–Pd quasicrystal oriented parallel to the 5-fold axis (**a**) and of an Al–Co–Ni quasicrystal parallel to the 10-fold axis (**b**) (courtesy M. Erbudak and M. Zurkirch)

the positions of the 5-fold, 3-fold and 2-fold symmetry directions appear as bright spots. In addition, there are somewhat weaker spots, such as the ten spots surrounding the position of a 5-fold axis. For the interpretation of these diagrams the model concept can be used where the centers of the bright spots represent the directions in which the next-neighbor atoms are lying (around an average atom in the structure taken as the origin). Thus the physical interpretation of these SEI images strongly suggest the frequent existence of cluster-shaped arrangements around a central atom, whereby the cluster has icosahedral point symmetry. In fact these images are compatible with the existence of a pseudo-Mackay cluster in i-Al–Mn–Pd.

The recent application of the SEI technique to d-Al–Co–Ni quasicrystals [18] must still be regarded as preliminary, since improvements in both the size and the ordering of the surface layer can be expected. Figure 6.32b presents a new SEI pattern, which is characterized, besides bright spots, by pronounced straight, bright bands connecting these spots. These bands resemble the bright diffuse bands of electron channeling patterns (cf. Sect. 6.7.3). The Al–Co–Ni single quasicrystal used for this SEI study as well as the Al–Co–Cu quasicrystal for the STM image presented below (Fig. 6.35), have been obtained in a multi-zone furnace by passing a temperature gradient of 1000°C to 750°C through the whole sample over a period of 2 to 3 weeks. Subsequently, large single-quasicrystal grains were selected from the resulting ingot and analyzed by single-crystal X-ray diffraction methods.

At present, the configuration of the bright spots in the SEI patterns of d-Al–Co–Ni taken parallel to the 10-fold axis (Fig. 6.32b) as well as normal to that axis, are basically consistent with the two-layer model (periodic axis of 0.41 nm) by Steurer et al. [131].

6.7.2 X-Ray Photoelectron Scattering

X-ray photoelectron spectroscopy has recently been applied to quasicrystals in a form which allows us to obtain real-space information in a very similar way as by the SEI technique. X-ray photoelectron spectroscopy is traditionally used for element analysis of surface layers. However, the photoelectron intensity changes not only due the chemical concentration, but also because of the pronounced forward scattering in the energy range of typically 1000 eV. In the X-ray photoelectron scattering technique, the photoelectron intensity is monitored for a particular core-level over the hemisphere above the sample surface and this results in the projection of the next-neighbor directions starting from the site of the (average) emitter atom [104]. This chemically sensitive surface technique has been termed full-hemispherical X-ray photoelectron diffraction (XPD). It is a surface-sensitive technique, since the photoelectrons have a relatively short mean free path of 1 to 5 nm only. While in

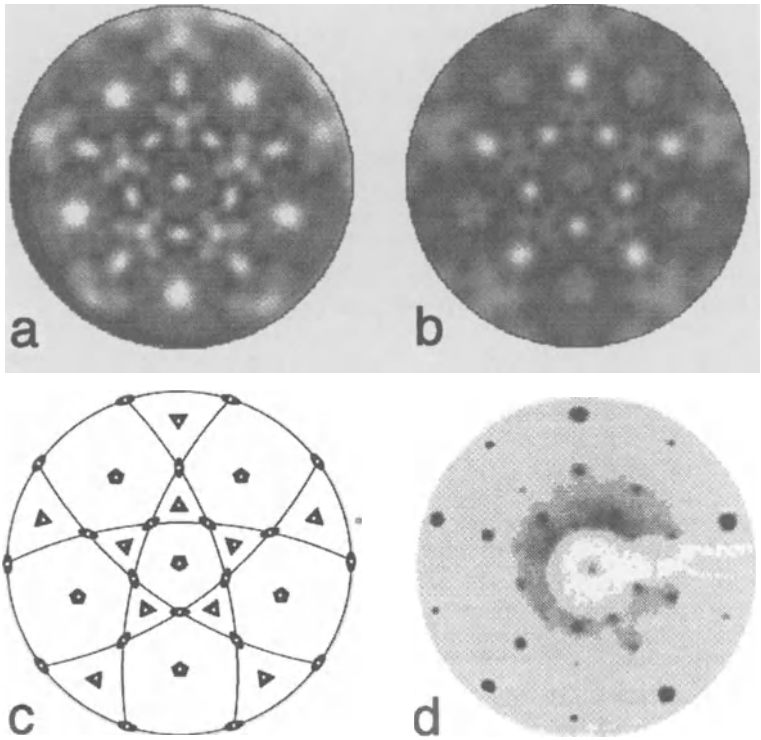

Fig. 6.33. (**a**) XPD pattern of an i-Al–Mn–Pd quasicrystal oriented parallel to the 5-fold axis, (**b**) SSC calculation of based on a pseudo-Mackay cluster, (**c**) stereographic projection indicating the icosahedral symmetry elements (*lines* correspond to 5-fold planes), (**d**) LEED pattern of the 5-fold surface taken at 23.5 eV (courtesy D. Naumovic)

this procedure only one chemical species is selected as emitters of the photoelectrons, the scattering process itself mainly depends on the local crystallographic environment of the emitter atoms and only weakly on the chemical species. In Fig. 6.33a the XPD pattern of a surface cut normal to a 5-fold axis of i-$Al_{70.3}Mn_{21.4}Pd_{8.3}$ is presented [96–98]. It has been obtained from the Pd $3d_{5/2}$ photoelectrons at an energy of 917 eV. Additionally, a single-scattering cluster (SSC) calculation based on a pseudo-Mackay cluster (Fig. 6.33b) as well as the stereographic projection of an icosahedron (Fig. 6.33c) are shown for comparison. The XPD pattern contains high-intensity features at the positions of the main symmetry axes. Note that the 5-fold planes indicated in the stereographic projection can also be recognized in the experimental XPD pattern as weak bands of intensity connecting the 2-fold axes positions. Additionally, finer features can be observed, such as a triplet of spots around each 3-fold axis and ten weak spots around each 5-fold axis. These features are not clearly reproduced in the SSC calculation, while the main features are well reproduced. This indicates that the finer details must originate from atom arrangements of additional clusters adjacent to the pseudo-Mackay clusters used in this calculation, e.g. the Bergmann cluster, as assumed in the model by Elser [41]. The low energy electron diffraction (LEED) pattern (Fig. 6.33d) of this 5-fold surface has been obtained at 23.5 eV. The 5-fold symmetry recognized in this diffraction pattern is due to dynamical scattering effects, as shown by Schaub et al. [121] (compare this result to the SAED patterns of 1D periodic 5-fold Al–Co–Ni quasicrystals).

6.7.3 Electron Channeling Pattern Technique Using a Scanning Electron Microscope

The electron channeling pattern (ECP) technique, also called electron backscattering pattern (EBSP) technique, provides highly useful information on the crystal structure and the perfection of the surface. These orientation-dependent line patterns, discovered by Coates in 1967 [28] and explained by Booker et al. [19] (for a modern explanation we refer to [32]), can easily and in a very short time be produced by the back scattered electrons in a conventional scanning electron microscope (SEM). For this, the electron beam (typically of 15-25 kV) is focused by the objective lens of the SEM onto a specific position of the surface and then continuously changed in its orientation, so that it undergoes a rocking movement within a full cone, leaving the point on the surface constant. In connection with a modern SEM, the ECP technique is frequently used to study textures by measuring quantitatively the orientation differences for all grains in a specimen, with a spatial resolution of typically 0.2 to 1 μm. Even though the geometry of the ECP is similar to the Kikuchi line patterns obtained in a transmission electron microscope, the physical process is different, i.e. the pattern is due to the channeling phenomenon caused by a beam of (partially) coherent electrons with an angle of convergence smaller than 1 mrad. (Regarding the similar

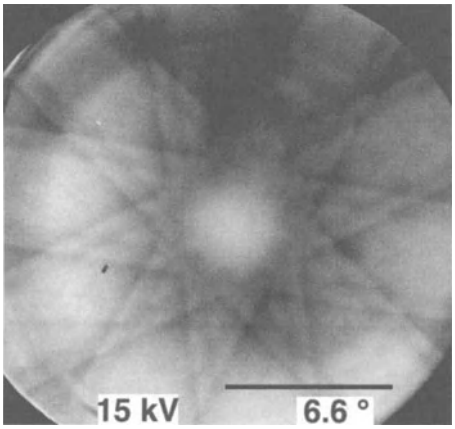

Fig. 6.34. Electron channeling pattern of the 10-fold cleavage plane of a d-Al–Mn–Pd single-quasicrystal

ion-channeling technique and its application to quasicrystals, see the chapter by Carstanjen in this volume.) Further applications of automated versions of the ECP technique to a statistically meaningful analysis of quasicrystal textures may be expected in the near future.

Figure 6.34 is a typical ECP taken along the 10-fold axis of a d-Al–Mn–Pd single-quasicrystal obtained on a freshly cleaved surface. Similar ECPs of an i-Al–Mn–Pd single quasicrystal have been presented in [20]. Similar to Kikuchi line patterns, these patterns allow the recognition of grain boundaries as well as the specific symmetry around the axis parallel to the electron beam.

6.7.4 Scanning Tunneling Microscopy

For a long time, in spite of many attempts, it was not possible to obtain scanning tunneling microscopy (STM) images of the surfaces of quasicrystals which would resolve the atomic structure similar to that deduced from HR-TEM micrographs. Kortan et al. [85] were able to improve the perfection of the surface, and thus became the first group to obtain (nearly) atomic resolution on the surface of a mm-sized $Al_{65}Co_{20}Cu_{15}$ decagonal quasicrystal. Figure 6.35a shows an example of the STM image contrast of d-Al–Co–Cu quasicrystal before further enhancement by Fourier filtering methods [85]. This image shows very flat terraces normal to the unique periodic 10-fold axis. The measured step height of 0.41 nm corresponds to the period of this decagonal phase. Inside each terrace the STM image contrast reveals basic decagonal clusters, similar to the results obtained from HRTEM images discussed above.

Schaub et al. [120] first observed nearly atomically resolved contrast details in STM images taken of a 5-fold surface of an i-$Al_{68}Mn_9Pd_{23}$ quasicrystal. In this case the specimen was prepared by a repeated sequence of ion-sputtering and subsequent annealing. In the STM image (Fig. 6.35b) se-

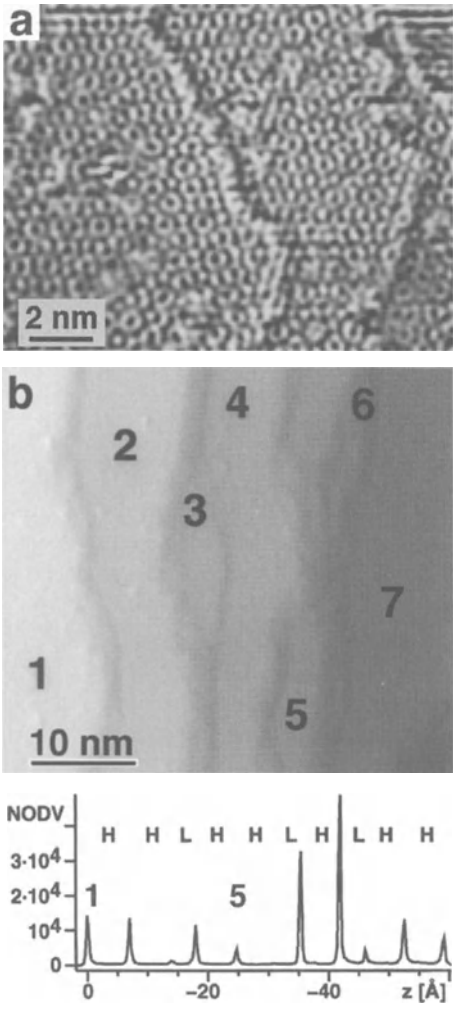

Fig. 6.35. (**a**) STM image of the 10-fold surface of a d-Al–Co–Cu single-quasicrystal (courtesy A.R. Kortan). (**b**) STM image of a stepped 5-fold surface of an i-Al–Mn–Pd single-quasicrystal. A histogram of the absolute frequency of different heights (z-axis) is shown below the image. NODV: number of data values (courtesy T.M. Schaub)

veral terraces normal to the 5-fold axis can be recognized. The diagram below the STM image shows the histogram of the measured sequence of step heights. It reveals two different heights, H=0.422 nm and L=0.678 nm (with an error of $\pm$0.025 nm), alternating in an aperiodic sequence, which is part of a Fibonnacci sequence. These two step heights can be compared to the values 0.408 nm and 0.660 nm taken from the data in [20,105], indicating that the surface step structure corresponds to heights of the slabs in the bulk structure.

Recently, a new STM investigation of in-situ cleaved i-Al–Mn–Pd quasicrystals has been presented [38]. Details of this challenging study can be found in the contribution by Feuerbacher in this volume.

Acknowledgment

We are very grateful to the editors of this book to have invited one of us (H.-U. N.) to lecture at the Heraeus Summer School on Quasicrystals at the Technical University Chemnitz, with its very stimulating atmosphere. We are also especially thankful for the efficient help provided by U. Grimm (Technical University Chemnitz) in the finalization of this manuscript. Our sincere thanks go to many colleagues who very kindly provided us with data and, especially, with high quality images documenting their work. Among these are M. Baake (University of Tübingen), E. Cockayne (Yale University, USA), M. Conrad and B. Harbrecht (University of Marburg), P. Donnadieu (Laboratoire d'Etude des Microstructures, Chatillon, France), S. Ritsch, M. Erbudak, M. Zurkirch, F. Krumeich, R. Wessicken and P. Wägli (ETH Zürich), F. Gähler (University of Stuttgart), T. Gödecke, R. Lück and M. Scheffer (MPI for Metal Research, Stuttgart), D. Häussler (MPI for Microstructure Physics, Halle), K. Hiraga, K. Tsuda and M. Tanaka (Tohoku University, Sendai), S. Horiuchi, M. Uchida, S. Weber and A. Yamamoto (NIRIM, Tsukuba), T. Ishimasa (Hokkaido University, Sapporo), D. Joseph, V. Elser and C.L. Henley (Cornell University, USA), K. Kifune (Osaka Women's University), A.R. Kortan (Lucent Technologies, Bell Labs Innovations, Murray Hill), as well as D. Naumovic and P. Aebi (University of Fribourg).

References

1. Audier M., Pannetier J., Leblanc M., Janot C., Lang J.-M., Dubost B. (1988): Physica **B 153**, 136
2. Audier M., Guyot P., de Boissieu M., Menguy N. (1993): J. Non-Cryst. Solids **153&154**, 591
3. Baake M., Joseph D., Kramer P. (1993): *Crystal-Quasicrystal Transitions*, eds. M.J. Yacaman and M. Torres, Elsevier, Amsterdam, pp. 173–191
4. Baumgarte A., Schreuer J., Estermann M.A., Steurer W. (1997): Philos. Mag. **A 75**, 1665
5. Beeli C. (1992): Ph.D. thesis, ETH Zurich, No. 9801
6. Beeli C. (1994): Phys. Rev. **B 49**, 6398
7. Beeli C. (1997): Proc. Group 21, *Physical Appl. and Math. Aspects of Geometry, Groups and Algebras*, eds. H.-D. Doebner, W. Scherer and C. Schulte, World Scientific, Singapore, Vol. II, pp. 939–946
8. Beeli C., Horiuchi S. (1997): Proc. 6th Int. Conf. on Quasicrystals, eds. S. Takeuchi and T. Fujiwara, World Scientific, Singapore, p. 31–34
9. Beeli C., Nissen H.-U., Robadey J. (1991): Philos. Mag. Lett. **63**, 87
10. Beeli C., Stadelmann P., Gödecke T., Lück R. (1995): Proc. Aperiodic '94, World Scientific, Singapore, p. 362
11. Beeli C., Stadelmann P., Gödecke T., Lück R. (1995): *Quasicrystals*, eds. C. Janot and R. Mosseri, World Scientific, Singapore, pp. 664–667
12. Bendersky L. (1985): Phys. Rev. Lett. **55**, 1461
13. Bendersky L.(1986): J. Phys. France, **47**, C3, 457

14. Biggs B.D., Pierce F.S., Poon S.J. (1992): Europhys. Lett. **19**, 415
15. de Boissieu M., Janot C., Dubois J.-M. (1988): Europhys. Lett. **7**, 593
16. de Boissieu M., Janot C., Dubois J.-M., Audier M., Dubost B. (1988): J. Phys.: Condens. Matter **3**, 1
17. de Boissieu M., Boudard M., Ishimasa T., Elkaim E., Lauriat J.P., Letoublon A., Audier M., Duneau M., Davroski A. (1998): Philos. Mag. **A 78**, 305
18. Bolliger B., Erbudak M., Hochstrasser M., Kortan A.R., Zurkirch M. (1996): Phys. Rev. **B 54**, R15598 ; and Zurkirch M. (1997): Ph.D. thesis, ETH Zurich, No. 12444
19. Booker G.R., Shaw A.M.B., Whelan M.J., Hirsch P.B. (1967): Philos. Mag. **16**, 1185
20. Boudard M., de Boissieu M., Vincent H., Heger G., Beeli C., Nissen H.-U., Ibberson R., Audier M., Dubois J.-M., Janot C. (1992): J. Phys.: Condens. Matter **4**, 10149
21. Boudard M., Klein H., de Boissieu M., Audier M., Vincent H. (1996): Philos. Mag. **A 74**, 939
22. Cahn J.W., Shechtman D., Gratias D. (1986): J. Mater. Res. **1**, 13
23. Cahn J.W., Gratias D., Mozer B. (1988): J. Phys. France **49**, 1225
24. Calvayrac Y. (1996): J. Phys. IV France **6**, C2, 21
25. Cantoni M., Nissen H.-U., Beeli C. (1989): Proc. 3eme Colloque sur les Quasicristaux, Nancy, p. C1
26. Capitan M.J., Bessiere M., Lefebvre S., Calvayrac Y., Quivy A., Gratias D. (1995): *Quasicrystals*, eds. C. Janot and R. Mosseri, World Scientific, Singapore, pp. 652–655
27. Chen H., Li D.X., Kuo K.H. (1988): Phys. Rev. Lett. **60**, 1645
28. Coates D.G. (1967): Philos. Mag. **16**, 1179
29. Conrad M., Harbrecht B., Krumeich F. (1998): Proc. Aperiodic '97, World Scientific, Singapore, 199; see also Krumeich F., Conrad M., Nissen H.-U., Harbrecht B. (1998): Philos. Mag. Lett. **78**, 357
30. Cornier-Quiquandon M., Quivy A., Lefebvre S., Elkaim E., Heger G., Katz A., Gratias D. (1991): Phys. Rev. **B 44**, 2071
31. Cowley J.M.(1990): *Diffraction Physics*, North Holland, Amsterdam, 2nd edn.
32. Dingley D.J. (1981): Scanning Electron Microscopy **4**, 273
33. Dénoyer F., Heger G., Lambert M., Lang J.-M., Sainfort P. (1987): J. Phys. France **48**, 1357
34. Donnadieu P., Su H.L., Harmelin M., Effenberg G., Aldinger F. (1996): J. Phys. I France **6**, 1153
35. Duneau M., Katz A. (1985): Phys. Rev. Lett. **54**, 2688
36. Duneau M., Oguey C. (1989): J. Phys. France **50**, 135
37. Ebalard S., Spaepen F. (1989): J. Mater. Res. **4**, 39
38. Ebert Ph., Feuerbacher M., Tamura N., Wollgarten M., Urban K. (1996): Phys. Rev. Lett. **77**, 3827
39. Edagawa K., Ichihara M., Suzuki K., Takeuchi S. (1992): Philos. Mag. Lett. **61**, 15
40. Elser V. (1986): Acta Crystallogr. **A42**, 36
41. Elser V. (1996): Philos. Mag. **B 73**, 641
42. Elswijk H.B., de Hosson J.T.M., van Smaalen S., de Boer J.L. (1988): Phys. Rev. **B38**, 1681
43. Erbudak M., Hochstrasser M., Schulthess T., Wetli E. (1993): Philos. Mag. Lett. **68**, 179

44. Erbudak M., Nissen H.-U., Wetli E., Hochstrasser M., Ritsch S. (1994): Phys. Rev. Lett. **72**, 3037; and Bolliger B., Erbudak M., Vvedensky D.D., Zurkirch M., Kortan A.R. (1998): Phys. Rev. Lett. **80**, 5369
45. Fadot F. (1993): Ann. Chim. France **18**, 445–456
46. Feng Y.C., Lu G., Ye H.Q., Kuo K.H., Withers L.R., van Tendeloo G. (1990): J. Phys. Condens. Matter **2**, 9749
47. Gähler F. (1988): In *Quasicrystalline Materials*, eds. C. Janot and J.-M. Dubois, World Scientific, Singapore, pp. 272–284
48. Gähler F. (1988): Ph.D. thesis ETH Zurich, Switzerland, No. 8414
49. Gayle F.W., Shapiro A., Biancaniello F.S., Boettinger W.J. (1992): Metal. Trans. **A 23**, 2409
50. Ge S.P., Kuo K.H. (1997): Philos. Mag. Lett. **75**, 245
51. Gödecke T., Lück R. (1995): Z. Metallkd. **85**, 695
52. Gödecke T., Lück R., Beeli C. (1995): *Quasicrystals*, eds. C. Janot and R. Mosseri, World Scientific, Singapore, pp. 644–47
53. Gödecke T., Scheffer M., Lück R., Ritsch S., Beeli C. (1997): Z. Metallkd. **88**, 687
54. Goldman A.I., Guryan C.A., Stephens P.W., Parsey Jr. J.M., Chen H.S., Aeppli G., Gayle F.W. (1988): Phys. Rev. Lett. **61**, 1962
55. Goodhew P.J., Humphreys F.J. (1988): *Electron Microcopy and Analysis*, 2nd edn. Talor & Francis, London
56. Grushko B. (1993): Mater. Trans. JIM **34**, 116
57. Grushko B., Wittmann R., Urban K. (1994): Philos. Mag. Lett. **67**, 25
58. Gummelt P. (1996): Geometriae Dedicata **62**, 1 and (1995): *Quasicrystals*, eds. C. Janot and R. Mosseri, World Scientific, Singapore, pp. 84–87
59. Häussler D., Beeli C., Nissen H.-U. (1997): Philos. Mag. Lett. **75**, 117
60. He L.X., Zhang Z., Wu Z.K., Kuo K.H. (1988): Proc. EUREM 88, Inst. Phys. Conf. Ser. **93**, 501 and (1990): Philos. Mag. Lett. **61**, 15
61. Henley C.L. (1991) in: *Quasicrystals: The State of the Art*, eds. C.P. DiVincenzo and P.J. Steinhardt, World Scientific, Singapore, pp. 429–524; and (1987): Comments Condens Matter Phys. **13**, 59
62. Henley C.L. (1997): private communication, ICQ6 Tokyo
63. Hiraga K. (1990): Springer Series in Solid State Physics Vol. 93, *Quasicrystals*, eds. T. Fujiwara amd T. Ogawa, Springer, Berlin, pp. 68–77
64. Hiraga K., Shindo D. (1989): Jpn. J. Appl. Phys. **28**, 2556
65. Hiraga K., Sun W. (1993): Philos. Mag. Lett. **67**, 117
66. Hirsch P.B., Howie A., Nicholson R.B., Pashley D.W., Whelan M.J (1977): *Electron microscopy of thin crystals*, 2nd rev. edition, Malabar, Florida Krieger (ISBN 0-88275-376-2)
67. Horiuchi S. (1994): *Fundamentals of high-resolution transmission electron microscopy*, North Holland, Amsterdam
68. Hovmöller S., Liang J.C. (1995): Phil. Mag. Lett. **71**, 123
69. Ishimasa T. (1995): Philos. Mag. Lett. **71**, 65
70. Ishimasa T., Mori M. (1992): Philos. Mag. **B66**, 513
71. Ishimasa T., Nissen H.-U., Fukano Y. (1985): Phys. Rev. Lett. **55**, 511
72. Ishimasa T., Nissen H.-U., Fukano Y. (1988): Philos. Mag. **A 58**, 835
73. Ishimasa T., Fukano Y., Tsuchimori M. (1988): Philos. Mag. Lett. **58**, 157
74. Ishizuka K. (1980): Ultramicroscopy **5**, 55
75. Janner A., Janssen T. (1977): Phys. Rev. **B 15**, 643

76. Janssen T. (1986): Acta Crystallogr. **A 42**, 261
77. Jaric M.V., Qiu S.Y. (1990): In *Quasicrystals*, Springer Series in Solid State Sciences Vol. 93, eds. T. Fujiwara and T. Ogawa, Springer, Berlin, p. 48; as well as in (1993): Acta Crystallogr. **A 49**, 576; and in (1994): Phys. Rev. **B 49**, 6614
78. Jeong H.C., Steinhardt P.J. (1996):Nature **382**, 433 and (1997): Phys. Rev. **B 55**, 3520
79. Joseph D., Baake M. (1996): J. Math. Gen. **A 29**, 6709
80. Joseph D., Elser V. (1997): Phys. Rev. Lett. **79**, 1066
81. Joseph D., Ritsch S., Beeli C. (1997): Phys. Rev. **B 55**, 8175
82. Kalning M., Kek S., Krane H.G., Dorna V., Press W., Steurer W. (1997): Phys. Rev. **B 55**, 187
83. Katz A., Gratias D. (1995): *Quasicrystals*, eds. C. Janot and R. Mosseri, World Scientific, Singapore, pp. 164–167
84. Kelton F., Kim W.J., Stroud R.M. (1997): Appl. Phys. Lett. **70**, 3230
85. Kortan A.R., Becker R.S., Thiel F.A., Chen K.S. (1990): Phys. Rev. Lett. **64**, 200
86. Kortan A.R., Thiel F.A., Kopylov N., Chen H.S. (1993): J. Cryst. Growth **128**, 1086
87. Koshikawa N., Edagawa K., Honda Y., Takeuchi S. (1993): Mater. Trans. JIM **34**, 188
88. Kossel W., Möllenstedt G. (1938): Naturwissenschaften **26**, 660
89. Krakow W., diVincenzo S.P., Bancel P.A., Cockayne E., Elser V. (1993): J. Mater. Res. **8**, 24
90. Kramer P. (1999): J. Phys. A: Math. Gen. **32**, 5781
91. Kramer P., Neri R. (1984): Acta Crystallogr. **A 40**, 580
92. Levine D., Steinhardt P.J. (1984): Phys. Rev. Lett. **53**, 2477
93. Luo Z. , Zhang S., Tang Y., Zhao D. (1993): Scr. Met. Mater. **28**, 1513
94. Lück R., Scheffer M., Gödecke T., Ritsch S., Beeli C. (1998): *Quasicrystals*, MRS Symposium Proceedings Vol. **553**, 25
95. Mihalkovic M. (1997): Mater. Sci. Eng. **A 226–228**, 961
96. Naumovic D., Aebi P., Schlapbach L., Beeli C. (1997): *New Horizons in Quasicrystals, Research and Applications*, eds. A.I. Goldmann, D.J. Sordelet, P.A. Thiel, J.M. Dubois, World Scientific, Singapore, p. 86
97. Naumovic D., Aebi P., Beeli C., Schlapbach L. (1999): Surface Sci. **435**, 302
98. Naumovic D., Aebi P., Schlapbach L., Beeli C., Lograsso T.A., Delaney D.W. (1999): Phys. Rev. **B 60**, R16330
99. Niikura A., Tsai A.P., Inoue A., Masumoto T. (1994): Philos. Mag. Lett. **66**, 259
100. Nissen H.-U., Beeli C. (1993): J. Mod. Phys. **B 7**, 1387
101. Nissen H.-U., Beeli C. (1993): J. Non-Cryst. Solids **153&154**, 68
102. Ohashi W., Spaepen F. (1987): Nature **320**, 555
103. Okabe T., Furihata J.I., Morishita K., Fujimori H. (1993): Philos. Mag. Lett. **66**, 259
104. Osterwalder J., Greber T., Stuck A., Schlapbach L. (1991): Phys. Rev. **B 44**, 13764 and (1993): Naumovic D., Stuck A., Greber T. , Osterwalder J., Schlapbach L., Phys. Rev. **B 47**, 7462
105. Papadopolos Z., Kramer P., Kasner G., Bürgler D.E. (1998): *Quasicrystals*, Symposium Proceedings Vol. 553, p.231, Materials Research Society (MRS), Warrendale, Pensylvania, USA

106. Penrose R. (1974): J. Inst. Math. Appl. **10**, 266
107. Reimer L. (1993): *Transmission Electron Microscopy*, 3rd edn. Springer, Berlin
108. Ritsch S. (1996): Ph.D. thesis, ETH Zurich, No. 11730
109. Ritsch S., Beeli C., Nissen H.-U., Lück R. (1995): Philos. Mag. **A 71**, 671
110. Ritsch S., Nissen H.-U., Beeli C. (1995): *Quasicrystals*, eds. C. Janot and R. Mosseri, World Scientific, Singapore, pp. 216–219
111. Ritsch S., Nissen H.-U., Beeli C. (1996): Phys. Rev. Lett. **76**, 2507
112. Ritsch S., Beeli C., Nissen H.-U. (1996): Philos. Mag. Lett. **74**, 203
113. Ritsch S., Beeli C., Nissen H.-U., Gödecke T., Scheffer M., Lück R. (1996): Philos. Mag. Lett. **74**, 99
114. Ritsch S., Beeli C., Nissen H.-U. (1997): Phil. Mag. Lett. **75**, 49, addendum to Ref. [112]
115. Ritsch S., Nissen H.-U., Beeli C. (1997): Proc. 6th Int. Conf. on Quasicrystals, eds. S. Takeuchi and T. Fujiwara, World Scientific, Singapore, pp. 367–370
116. Ritsch S., Beeli C., Lück R., Hiraga K. (1999): Philos. Mag. Lett. **79**, 225
117. Ritsch S., Radulescu O., Beeli C., Warrington D.H., Lück R., Hiraga K. (2000): Philos. Mag. Lett. **80**, 107
118. Sato T.J., Abe E., Tsai A.P. (1997): Jpn. J. Appl. Phys. **36**, L1038
119. Sainfort P., Dubost B., Dubus A. (1985): Comptes Rendues Acad. Sc. Paris, **301**, serie II, 689 and (1986): J. Phys. France **47**, C3, 321
120. Schaub T.M., Bürgler D.E., Güntherodt H.-G., Suck J.-B. (1994): Phys. Rev. Lett. **73**, 1255
121. Schaub T.M., Bürgler D.E., Güntherodt H.-G., Suck J.-B., Audier M. (1995): *Quasicrystals*, eds. C. Janot and R. Mosseri, World Scientific, Singapore, pp. 132–138
122. Scheffer M., Gödecke T., Lück R. (1997): Proc. 6th Int. Conf. on Quasicrystals, eds. S. Takeuchi and T. Fujiwara, World Scientific, Singapore, pp. 269–272
123. Shaw L.J., Elser V., Henley C.L. (1991): Phys. Rev. **B 43**, 3423
124. Shechtman D., Blech I., Gratias D., Cahn J.W. (1984): Phys. Rev. Lett. **53**, 1951
125. Shechtman D. (1988): In: *Quasicrystalline Materials*, eds. C. Janot and J.-M. Dubois, World Scientific, Singapore, p. 3
126. Shimizu T., Ishimasa T. (1998): Jpn. J. Appl. Phys. **37**, 5691
127. Spence J.C.H. (1980): *Experimental high resolution electron microscopy*, Oxford University Press
128. Stadelmann P. (1987): Ultramicroscopy **21**, 131
129. Steinhardt P.J., Jeong H.-C., Saitoh K., Tanaka M., Abe E., Tsai A.P. (1998): Nature **396**, 55
130. Stephens P.W., Goldman A.I. (1986): Phys. Rev. Lett. **56**, 1168; see also: Stephens P.W. (1989): in *Aperiodicity and Order 3, Extended Icosahedral Structures*, ed. M.V. Jaric Academic Press, Boston, pp. 37–104
131. Steurer W., Haibach T., Zhang B., Kek S., Lück R. (1993): Acta Crystallogr. **B 49**, 661
132. Steurer W., Haibach T., Zhang B., Beeli C., Nissen H.-U. (1994): J. Phys.: Condens. Matter **6**, 613
133. Sugiyama K., Kaji N., Hiraga K., Ishimasa T. (1998): Z. Kristallogr. **213**, 90
134. Sun W., Hiraga K. (2000): Philos. Mag. Lett. **80**, 157
135. Tanaka M., Terauchi M., Tsuda K. (1994): *Convergent-Beam Electron Diffraction III*, JEOL Ltd. Tokyo, pp. 89–115; see also Vol. I of this series.

136. Tsai A.P., Inoue A., Masumoto T. (1989): Mater. Trans. JIM **30**, 463
137. Tsai A.P., Inoue A., Masumoto T. (1987): Jpn. J. Appl. Phys. **26**, L1505 and (1989): Mater. Trans. JIM **30**, 666
138. Tsai A.P., Inoue A., Yokoyama Y., Masumoto T. (1990): Philos. Mag. Lett. **61**, 9
139. Tsai A.P., Inoue A., Masumoto T. (1991): Philos. Mag. Lett. **61**, 163
140. Uchida M., Horiuchi S. (1997): Jpn. J. Appl. Phys. Part 2, **36**, L1523
141. Wang N., Chen H., Kuo K.H. (1987): Phys. Rev. Lett. **59**, 1010
142. Wang N., Feng K:K:, Kuo K.H. (1988): Appl. Phys. Lett. **52**, 2120
143. Weber S., Yamamoto A. (1997): Philos. Mag. **A 76**, 85
144. Williams D.B., Carter C.B. (1996): *Transmission electron microscopy* Plenum Press, New York
145. Yamamoto A. (1992): Phys. Rev. **B 45**, 5217, see also (1996): Acta Crystallogr. **A 52**, 509
146. Yamamoto A., Hiraga K. (1999): Abstract OB4 at the 7th Int. Conf. Quasicrystals (ICQ7) (http://icq6.uni-stuttgart.de), Stuttgart, Germany
147. Yokoyama Y., Tsai A.P., Inoue A., Masumoto T. (1991): Mater. Trans. JIM **32**, 1089
148. Yokoyama Y., Yamada Y., Fukaura K., Sunada H., Inoue A., Note R. (1997): Jpn. J. Appl. Phys. **36**, 6470
149. Yoshida K., Yamada T., Taniguchi Y. (1989): Acta Crystallogr. **B 45**, 40 and (1991): Philos. Mag. Lett. **63**, 127
150. Yu K., Portier R., Yu-Zhang K., Bigot J. (1988): Philos. Mag. Lett. **57**, 35

7 Structure of Quasicrystals via Pair Potentials

Marek Mihalkovič

Summary. Quasicrystal structures are commonly described as a cut through a density distribution in higher-dimensional space. When adopted in a diffraction approach to the structure solution, such a scheme in general only provides information about an *averaged* density distribution in real space, and fails to account for correlations in the occupancy of some partially occupied sites. An alternative and complementary approach described here combines a tiling-decoration description of the structure, and cohesive energies calculated using realistic pair potentials, in order to propose plausible atomic configurations, compatible with the diffraction data. The approach is illustrated on the example of a large cubic approximant to the icosahedral AlZnMg quasicrystal.

7.1 Introduction

Despite the remarkable progress in production of high-quality thermodynamically stable quasicrystals (icosahedral i-AlCuFe, i-AlPdMn, i-YZnMg, decagonal d-AlNiCo, d-AlCoCu and others), the task of solving the quasicrystal structures turned out to be an extremely difficult one. The intrinsic difficulty is the lack of translational order: the diffraction pattern consists of a set of delta functions covering densely reciprocal space [6] and in principle there is no upper bound limiting the number of parameters necessary to solve the structure. This fact itself does not imply the quasicrystal structure *must* be complicated: some quasicrystal models are crystallographically simple when viewed as an irrationally oriented cut through a convenient hypercrystal [1], or a *decoration rule* of a tiling-decoration model can be simple, even when the corresponding hyperspace description is not. This is in general (to a different extent when considering particular phases case by case) the experience emerging from the diffraction-data structure refinements, suggesting that the additional complexity, related to disorder phenomena specific to quasicrystals, is the rule rather than the exception, and that the diffraction data themselves are not sufficient to fix the structure completely.

This chapter discusses a systematic approach to the optimization and comparison of quasicrystal models on the basis of structural energies, calculated from realistic pair potentials. In this approximation, the energies can be evaluated rapidly enough even for large systems of translationally independent atoms, which is necessary to explore the parameter space of quasicrystal models, and eliminate the uncertainties that are difficult to resolve

J.-B. Suck et al. (eds.), *Quasicrystals*
© Springer-Verlag Berlin Heidelberg 2002

by diffraction refinement. Comparison of the optimized structural energies of quasicrystal or related crystalline structures provides hints about the origins of quasicrystal stability, and the optimized models can be used as a starting point for more accurate energetic considerations. Additional benefits are applications to atomic dynamics, phason dynamics, phonon–phason coupling, diffusion processes, dislocations, etc.

After briefly reviewing a few approaches to the problem of discovering low-energy quasicrystal structures, given the atomic pair interactions, we focus on the tiling-decoration approach to quasicrystal structure refinement. Within this framework, we illustrate with the example of Frank–Kasper AlZnMg approximant structures, how the structural energies may be used to complement the diffraction data refinements.

7.2 Pair Potentials

As noted in the introduction, the specific appeal to calculate cohesive energies of quasicrystal models via pair potentials lies in the fact that their structure is not known in sufficient detail, while the lack of translational periodicity requires that the models are represented by large number of independent atoms, which limits the applicability of the *ab initio* methods. *Ab initio* calculations of the quasicrystal electronic structure are typically performed using idealized models, in which atomic positions are rigidly dictated by an abstract geometry of the tiling, or by cut and projection from the hyperspace; very likely, this may distort calculated energies. On the other hand, sensitivity of the pair potentials to the atomic positions and chemical ordering suggests their use in conjunction with diffraction refinements.

For simple-metal systems like i-AlZnMg, the conduction electrons can be regarded as nearly free; replacing the electron–ion interaction by an effective (empty-core) pseudopotential results in pair potentials that are dependent on the atomic volume Ω, valence Z and empty-core radius r_c. The main features of these potentials are the steep repulsive part at short range distances, and the tail oscillating with the periodicity of π/k_F, k_F being the Fermi wave vector.

Systematic exploration of the parameter space of these pair potentials has been performed at both zero [22], and finite temperature [3] with the main result that the quasicrystal structures are *stable* with respect to a collection of competing crystalline phases in a narrow range of the parameter space, between the closely packed and open structures [9]. In a rather crude virtual crystal approximation, neglecting the chemical ordering, these results may be extrapolated to existing ternary quasicrystals.

Pseudobinary simple-metal pair potentials were used to test the mechanical stability and atomic dynamics of the quasicrystal models in AlZnMg [8,12] and AlCuLi [28] systems. It has been pointed out [12,22] that the oscillating tails of the potentials may be important for stability, when the

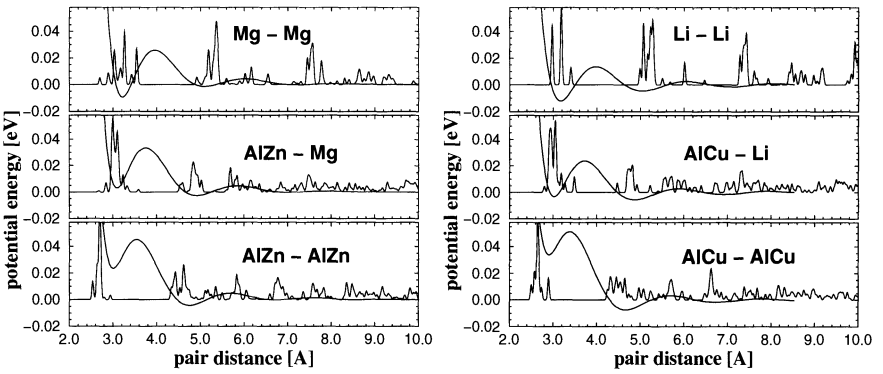

Fig. 7.1. Pair potentials for pseudobinary $(AlZn)_{49}Mg_{32}$ and $(AlCu)_{80}Li_{20}$ alloys, together with the partial pair distribution functions for the 160-atom 1/1 approximant cubic α phase

respective minima of the pair potential match the maxima in the pair distribution functions, in accordance with the Hume–Rothery scenario [7]. Figure 7.1 shows such pair potentials for pseudobinary i-(AlZn)Mg [12] and pseudobinary i-(AlCu)Li [28], together with the corresponding partial pair distribution functions (PPDF) for the 1/1 approximant cubic α phase with 160 atoms in the unit cell (space group $Im\bar{3}$). The matching of the PPDF with the oscillations of the potentials is pronounced for AB and BB pairs, where A denotes the "smaller" atom (AlZn) or (AlCu) and B the "bigger" (Mg, Li).

Recently the generalized pseudopotential theory has been successfully used to derive *ab initio* potentials for Al–TM (transition metal) [18] systems, explicitly including d–d interactions, with full treatment of sp–d hybridization and the volume and concentration dependence of the total energy. As the majority of the known icosahedral and decagonal phases form in Al-rich aluminides containing TM, one may hope to obtain new insights into the structure and energetics of these systems.

7.3 Approaches to Structure Determination from Structural Energies

The method unbiased by any prejudice about the optimal structure is simulation of the *solidification process*, by means of molecular dynamics. In practice, such simulations can be performed for systems of a few hundred atoms, achieving cooling rates that are roughly two orders of magnitude faster than the "fast-cooling" experimental condition: apparently, such a method would not seem appropriate for studying the details of the equilibrium quasicrystal structures, but it turned out to be of considerable inspirative value even for this purpose. First of all, it provides testing grounds for the propensity of cer-

tain atomic interactions to form quasicrystal structures: special monoatomic interaction disfavoring formation of simple crystalline structures, and tailored actually to produce an amorphous phase, formed a *dodecagonal* quasicrystal [5] with Frank–Kasper like local order. On the other hand, Lennard–Jones type pair interaction optimized to support formation of the Frank–Kasper like *icosahedral* quasicrystal [20] eventually led to formation of a novel *decagonal* quasicrystal with the Frank–Kasper local order [21]. Detailed analysis of the frozen samples enabled an idealized description of the structure as a decoration of rectangle–triangle or two-level decagonal tilings, and clarified relationships between icosahedral and decagonal Frank–Kasper phases.

Alternatively, in order to achieve a laboratory time scale for the cooling/equilibration cycles, one can judiciously discretize the positional degrees of freedom of the atoms, so as to freeze out the phonon degrees of freedom, and focus on the "phasons" that are specific to quasicrystals. The discretization can be achieved by extending "standard" atomic surfaces (that impose a certain hard-core condition in the real space) along the perpendicular space, so as to create a lattice of "candidate" sites. These are subsequently populated by atoms in a Monte Carlo simulation. This method has been earlier used to construct optimal quasicrystal sphere packings [13] or optimize the i-AlMn structural model [14]. More recently, it has been employed in conjunction with realistic AlCo pair potentials to resolve the detailed structure, and analyze the finite-temperature phason disorder under equilibrium condition in orthorhombic $Al_{13}Co_4$ [26], and approximants to the d-AlCo system [27]. In the latter case, the simulation carried out at $T = 1000$ K resulted in an identification of the tiling geometry describing the equilibrium state of the system, in which the vertices of the 2D decagonal hexagon–boat–star (HBS) tiling are occupied by pentagonal bipyramid clusters. The tiling-decoration model inferred from the simulation comprises a fixed skeleton of stable Al and Co atomic positions that could be assigned to the tiling patterns, and other partially occupied Al sites, with an important consequence that the "internal" entropy associated with Al disorder within a fixed tiling pattern was estimated to be larger than the configurational entropy arising from the tile reshufflings. As a byproduct of the simulation, the phasonic motions of individual atoms were associated with the reshufflings and puckerings of the tiling patterns.

The ambition common to all of the approaches to the energetic structure refinement is to establish the often assumed, but not sufficiently understood link between the abstract tilings, and detailed atomic structure, subject to realistic atomic interactions. A corollary of a successful "energetic" structure determination should be formulation of the *tiling Hamiltonian*, creating a one-to-one correspondence between an ensemble of tilings, and the atomic structure, via the structural energies. In the following section, we describe in detail the direct tiling-decoration approach, in which the optimal tiling

geometry is taken as an assumption, thus enabling resolution of fine details of the structure by systematic variation of plausible atomic motifs.

7.4 Tiling-Decoration Approach

In this section we focus on the direct tiling-decoration approach to structure determination, as has been developed and applied to the structural modeling of the i-AlMn system [15,16,19]. In order to emphasize the link between "energetic" and diffraction-data structure refinements, we apply the tiling-decoration machinery to the example of the Frank–Kasper i-AlZnMg approximants, taking advantage of recent progress on the experimental side.

In a quasiperiodic structure, no two atoms have a strictly equivalent environment, if we compare shells around them within the cutoff radius R_{cut}, and $R_{\mathrm{cut}} \to \infty$. In practice, however, atomic interactions are of finite range, and a choice of a finite R_{cut} will produce an R_{cut} atlas of topologically (nearly) equivalent site classes. Any attempt to determine the structure of a quasicrystal involves an interplay between the required resolution of the model, and the actual effective interaction cutoff R_{cut}, via a *parametrization*.

There are two possible approaches: hyperspace, as corroborated by Yamamoto [29] and used for diffraction refinement, or real space, via tiling and decoration, as has been applied to the pair-potential structural analysis in the AlMn system [16]. Although the two approaches are parallel in principle, there is one substantial difference: the hyperspace approach derives the constraints on the degrees of freedom of the topologically equivalent sites from the assumption of *global* quasiperiodic ordering, while in the tiling-decoration picture these constraints are derived *locally* from the point symmetries of tiling objects, and the global quasiperiodic ordering may or may not occur.

7.4.1 Definitions

The tiling-decoration model associates appropriate atomic motifs with the chosen set of tiling objects (nodes, linkages, faces, bonds): we call this association *binding*. We naturally demand that the point group of an atomic motif bound to a certain object is a subgroup of the object's point group. Consequently, the atoms are grouped into *canonical orbits*, characterized by positional and other (occupation factor, energy, DW factor, ...) parameters, that are identical (up to the object's point-group symmetry relations) for all atoms in the group. The positional parameters assigned to the canonical orbit are defined with respect to a conveniently chosen origin of the tiling object, most conveniently to its symmetry center.

In the context of structure refinement via pair potentials, we will make use of the following quantities:

– "raw" cohesive energies E_{raw}, calculated from atomic positions (given by diffraction-data refinement or by relaxation of atomic positions with respect to the pair potentials);

– symmetrized energies $E_{\rm can}$, obtained from atomic positions after they were symmetrized to satisfy decoration-model local symmetry constraints;
– root mean square displacements of the "raw" atomic positions from the symmetrized positions, $d_{\rm can}^{\rm RMS}$, measuring symmetry breaking of the decoration rule.

Cohesive energies $E_{\rm can}$ and displacements $d_{\rm can}^{\rm RMS}$ are an important measure of goodness of the decoration model: $E_{\rm can} \gg E_{\rm raw}$ and/or big $d_{\rm can}^{\rm RMS}$ means the tiling-decoration model is not sensible. All of the above quantities can be averaged either over all atoms to give a simple characterization of the model, or over each canonical orbit separately, to reveal which particular site(s) is responsible for the spuriously high energy, or large $d_{\rm can}^{\rm RMS}$.

For a given structure the binding of tiling and decoration is *not* necessarily unique. A convenient refinement procedure is to start with the simplest, "minimal" binding, yielding the smallest number of parameters. Roughly speaking, this corresponds to the effective interaction cutoff – as discussed above – of the order of the tiling bond length. A failure of a particular binding indicated by the above diagnostics may just mean a necessity to formulate a higher-resolution binding using more complex binding with larger effective interaction cutoff.

The corollary of this approach is that the model becomes independent of the particular arrangement of tiles, in the sense that all the parameters (and the quantities that are a function of these parameters – e.g. energy as a function of atomic coordinates) refined using a certain tiling can be straightforwardly transferred to another tiling.

In the following, we analyze in detail the structure of the AlZnMg quasicrystal, using pair potentials taken from [12], the canonical-cell tiling (CCT) decoration machinery and the structural data from two cubic phases in this system – the familiar 1/1 α phase [2] (Im$\bar{3}$ space group) and 2/1 approximant (Pa$\bar{3}$), whose structure has been solved recently [23].

7.4.2 Structure and Cohesive Energies of i-AlZnMg Approximants

Historically, the first stable quasicrystals were the Frank–Kasper icosahedral phases i-AlCuLi and i-GaZnMg. As these suffered from certain intrinsic disorder manifested by finite correlation length, the relatively small diffraction-data sets did not allow refinement of the details of the structure.

Nevertheless, it is the Frank–Kasper type quasicrystal, that promises a feasible diffraction-data vs energy refinement: first of all, for the simple-metal systems like e.g. AlZnMg the realistic pair potentials can be rather easily calculated (see Sect. 7.2), and while the diffraction data provide sufficient contrast to resolve (AlMg) vs Zn chemical ordering, the cohesive energies are sensitive to the (AlZn)–Mg chemical ordering. Recently, it has been clarified that there exists a stable i-AlZnMg phase (at 44 % Mg content), and stable 2/1 cubic approximant at 43 % Mg [24], while replacement of the Al by

Al_xGa_{1-x} at ≈ 39 % Mg content leads to an intriguing sequence of stabilities ranging from 1/1 through 2/1 and orthorhombic 3/2-2/1-2/1 approximants to the icosahedral phase as x goes from 0 to 1 [17].

7.4.2.1 Tiling of Canonical Cells. The two prominent families of icosahedral quasicrystals – the Frank–Kasper class represented by AlZnMg and the Al–TM class by AlMnSi – have 1/1 approximant phases, in which large icosahedral clusters (the Bergman cluster in the case of AlZnMg, and the Mackay icosahedron in the case of AlMnSi) are centered at the nodes of a bcc lattice. Henley [10] suggested that the most natural tiling description of quasicrystals should be accordingly based on cluster-to-cluster linkages, with maximal density of nodes, decorated by the clusters.

An optimal icosahedral geometry based on the bcc nearest-neighbor linkages is the CCT [10]. The four canonical cells A, B, C and D are constituted by the two kinds of bcc nearest–neighbor bonds called here b (2-fold) and c (3-fold), $b = 2c/\sqrt{3}$, and three kinds of faces X (bcc tetrahedron facet), Y (equilateral triangle of b bonds) and Z (rectangle made up of a pair of c and a pair of b bonds), see Fig. 7.2.

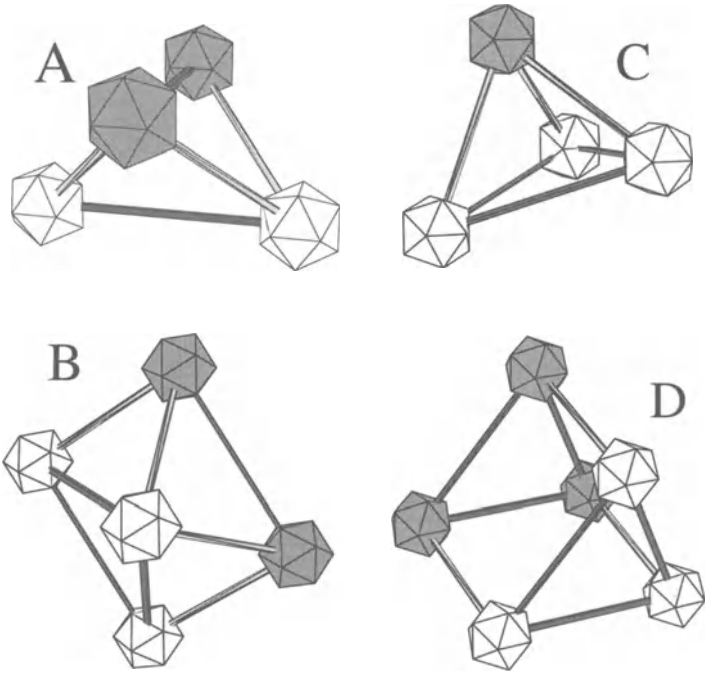

Fig. 7.2. Four cells in the icosahedral canonical-cell tiling

CCT is *bipartite*: nodes can be uniquely partitioned into two flavors (even and odd) such that the b bonds always link the nodes with the same flavor, while the 3-fold c bonds link even nodes with odd nodes. In Fig. 7.2, the nodes of the CCT are represented by small icosahedra, whose gray level corresponds to their flavor.

7.4.2.2 Decoration. We start from the models of the cubic 1/1 [2] and 2/1 [23] Frank–Kasper phases, derived from the single-crystal diffraction data. The most economic description of their structure is in terms of Bergman clusters decorating nodes of the canonical tiling, as illustrated in Fig. 7.3. The succession of shells around the canonical nodes is: small icosahedron (SMI), unit triacontahedron (UT), soccer ball (SB), and the large triacontahedron (LT) (not shown). The link between the cluster description and the CCT model can be established by inspecting Fig. 7.3 and the third column of Table 7.1. The corresponding CCT frameworks are pure A tiling for the 1/1

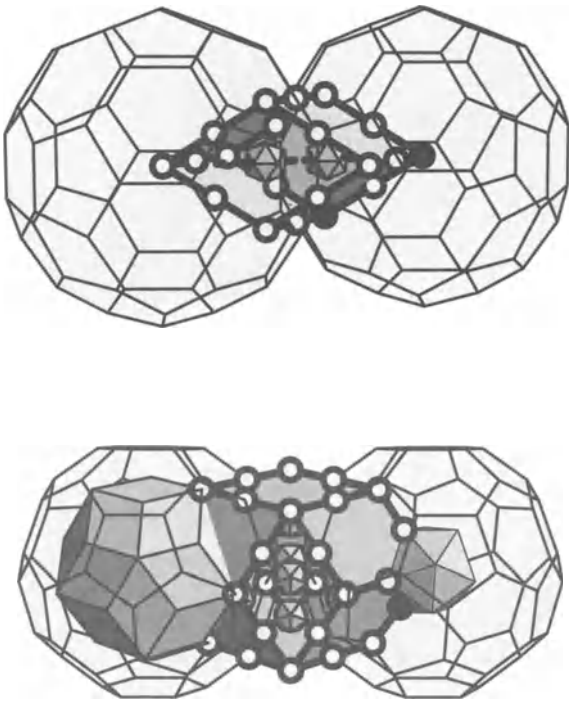

Fig. 7.3. Decoration of the canonical c bond by a prolate rhombohedron (PR), and SB shell of the Bergman cluster (top); the same for the 2-fold b bond and rhombic dodecahedron (RD) (bottom), plus the UT shell (left sharp RD tip) and the SMI. One front facet of each polyhedron is omitted to show the Mg atoms in the interior, represented by icosahedral balls. Empty circles represent (AlZn) atoms

Table 7.1. List of canonical orbits, objects they were bound to, the corresponding shell in the cluster description, total number of atoms N_{at} in the orbit (and for a single object), displacements d_{HE}^{RMS} (d_{can}^{RMS}) from Henley–Elser idealized positions (or symmetrically averaged positions, respectively), and cohesive energy per atom E_{coh} for different 1/1 and 2/1 AlZnMg models (subscript notation explained in Sect. 7.4.2.2). E_{coh} is given relative to the $2/1_{r1}$ model (last column, bold)

orbit	object	shell	$N_{at}(\mu)$	model	d_{HE}^{RMS} Å$\times 10^{-3}$	d_{can}^{RMS} Å$\times 10^{-3}$	ΔE_{coh} meV
Al(α,N)	node	SMI	24(12)	$1/1_d$	91	21	+247.4
			96(12)	$2/1_d$	80	65	+65.9
				$1/1_r$	9	8	−12.1
				$2/1_{r1}$	62	72	**405.2**
				$2/1_{r2}$	162	166	−38.2
Al(β,N)	node	UT	24(12)	$1/1_d$	254	133	+17.3
			96(12)	$2/1_d$	185	151	+2.2
				$1/1_r$	269	262	−7.7
				$2/1_{r1}$	233	221	**410.9**
				$2/1_{r2}$	380	366	−49.6
Mg(δ,N)	node	UT	40(20)	$1/1_d$	194	70	+9.0
			160(20)	$2/1_d$	122	76	−7.2
				$1/1_r$	87	41	+2.4
				$2/1_{r1}$	98	58	**49.8**
				$2/1_{r2}$	122	106	+13.1
Al(α,c)	c bond	SB	48(6)	$1/1_d$	206	184	+11.3
			168(6)	$2/1_d$	86	70	+31.2
				$1/1_r$	129	124	−9.7
				$2/1_{r1}$	119	113	**311.1**
				$2/1_{r2}$	108	87	+13.2
Mg(δ_z,b)	b bond	LT	12(2)	$1/1_d$	156	–	+80.0
			48(2)	$2/1_d$	424	333	+144.9
				$1/1_r$	143	–	+6.4
				$2/1_{r1}$	148	62	**82.7**
				$2/1_{r2}$	438	288	+50.9
Mg(δ_y,b)	b bond	SB	12(2)	$1/1_d$	64	–	−7.9
			48(2)	$2/1_d$	343	343	+75.2
				$1/1_r$	3	–	+54.2
				$2/1_{r1}$	120	116	**171.3**
				$2/1_{r2}$	358	353	+330.3
Al(β,Y)	Y face	glue	8(1)	$2/1_d$	306	–	+290.3
				$2/1_{r1}$	160	–	**615.3**
				$2/1_{r2}$	212	–	+4.7
Mg(δ,Y)	Y face	LT	8(1)	$2/1_d$	36	–	−9.1
				$2/1_{r1}$	41	–	**109.8**
				$2/1_{r2}$	35	–	−42.7
Al(α_1,Y)	Y face	SB	24(3)	$2/1_d$	63	18	+101.5
				$2/1_{r1}$	122	19	**371.9**
				$2/1_{r2}$	535	5	−46.0
Al(α_2,Y)	Y face	SB	24(3)	$2/1_{d1}$	49	15	+103.7
				$2/1_{d2}$	1597	9	+264.0
				$2/1_{r1}$	105	2	**279.7**
				$2/1_{r2}$	1510	15	+221.9

approximant and ABC tiling for the 2/1 approximant. A list of the tiling objects used in our "minimal"-binding decoration rule, their point symmetries, number of atoms in the unit cell, Mg fractional content x and lattice parameters, are summarized in Table 7.2. Each canonical orbit merges together a few Wyckoff orbits, that are topologically nearly equivalent.

Table 7.2. Frequencies of tiling objects in the cubic 1/1 and 2/1 canonical tilings, per unit cell

object crystal (symm.)	node $5\bar{3}2/m$	b bond 2/mmm	c bond $\bar{3}m$	Y face 3m	atoms	x(Mg)	a [Å]
1/1 ($Im\bar{3}$)	2	6	8	–	160	0.400	14.2
2/1 ($Pa\bar{3}$)	8	24	28	8	680	0.388	23.0

The diffraction-data model of the 2/1 approximant has a pair of partially occupied Wyckoff orbits displaced by ≈ 1.5 Å. For the purpose of analyzing energetics of the system, we split this model into two variants, denoted $2/1_1$ and $2/1_2$, each with one of the two conflicting sites left vacant. In the following, we label models with atomic coordinates derived from the diffraction data by a subscript "d", those with atomic coordinates obtained after relaxation under the pair potentials by a subscript "r" and the two 2/1 variant models are further subscripted by "1" or "2" (note that $2/1_{d1}$ and $2/1_{d2}$ would have all atomic positions identical up to the single Wyckoff site).

Performing standard decomposition of the CCT into Penrose rhombohedra [10], in which every b linkage is decorated by the rhombic dodecahedron (RD), and every c linkage by a prolate rhombohedron (PR), we recover the one-to-one correspondence with the familiar Henley–Elser (HE) decoration [11], with the exception of the $2/1_2$ model, in which one Wyckoff site has no counterpart in the decoration model. Labels of orbits in Table 7.1 follow the notation introduced by Henley and Elser: α (rhombohedron mid-edge positions), β (vertices) and δ (PR body diagonal positions). The column denoted $d_{\mathrm{HE}}^{\mathrm{RMS}}$ gives diffraction-data (or relaxed) model displacements from the ideal HE model positions. The Wyckoff position obtained from the diffraction data, but missing in the HE model is denoted $\mathrm{Al}(\alpha_2, Y)$; note the extremely large $d_{\mathrm{HE}}^{\mathrm{RMS}}$ for this site in the row of the diffraction data $2/1_{d2}$ and relaxed $2/1_{r2}$ models.

7.4.2.3 Chemistry. A simple geometrical interpretation of the chemical ordering in Frank–Kasper quasicrystals has been suggested in [11] employing a close-packing argument: large Mg atoms naturally fit on the body diagonals of the PR and related sites inside the RD, always below and above the center of the rhombohedron face (in Fig. 7.3 they are represented by small icosahedral balls). On the other hand, smaller (AlZn) atoms occupy vertices and mid-edge points of the rhombohedra.

Table 7.3. Rebinding. Orbits with extremely large canonical symmetry breaking were "rebound" from the b bond (2/mmm point symmetry) to the b_{31} bond with lower symmetry (m)

orbit	object	shell	$N_{at}(\mu)$	model	d_{can}^{RMS} Å$\times 10^{-3}$	ΔE_{coh} meV
Mg(δ_{z+},b_{31})	b_{31} bond	LT	24(1)	d	10	+40.4
				r_1	24	**77.5**
				r_2	15	+83.1
Mg(δ_{z-},b_{31})	b_{31} bond	LT	24(1)	d	14	+249.6
				r_1	20	**87.8**
				r_2	17	+209.2
Mg(δ_{y+},b_{31})	b_{31} bond	SB	24(1)	d	21	+201.3
				r_1	28	**170.4**
				r_2	17	+323.6
Mg(δ_{y-},b_{31})	b_{31} bond	SB	24(1)	d	14	−50.9
				r_1	51	**172.2**
				r_2	64	+59.9

In the 1/1 approximant, the only "intermediate" position is Mg(δ_y,b), sitting just below the RD face that was left transparent in Fig. 7.3. This site is occupied by a large atom (Mg) in 1/1 AlZnMg, and by a small atom (AlCu) in isostructural 1/1 AlCuLi, called the R phase. In the 2/1 structure, there are more such intermediate sites, and the picture is further complicated by the presence of the partially occupied sites that are located nearby. Since the diffraction data cannot distinguish reliably between Al and Mg, we first assigned chemical occupations according to the above simple rule, and subsequently refined the chemical occupation as described in Sect. 7.4.2.5.

7.4.2.4 Cohesive Energies. Both the cohesive energies and displacements gathered in Table 7.1 reflect the fact that the $2/1_d$ model *averages* displacive modulation, resulting from the partially occupied Al(α_2,Y) site. In order to account for the displacive modulation, we have constructed a "context-sensitive" binding, in which the atoms formerly assigned to b bonds (2/mmm point symmetry) were "rebound" to "b_{31}" bonds. (The latter object can be defined after inspecting cells around the b bond.) Consequently, each of the Mg(δ_z,b) and Mg(δ_y,b) were split into two orbits (see Table 7.3).

Table 7.4 summarizes total cohesive energies, and d_{can}^{RMS} displacements for the three models we compare here (1/1, $2/1_1$ and $2/1_2$). Model variant $2/1_{r2}$ has $\approx$ 24 meV higher energy than the "standard" $2/1_{r1}$ model, but remains mechanically stable upon relaxation. The $2/1_d$ model gives peculiarly the symmetrized E_{can} lower than E_{raw} for the "minimal" binding, and $E_{can} > E_{raw}$ for the context-sensitive binding; the opposite is true for the $2/1_{r2}$ model. This is because the canonical symmetrization tends to average away the displacive modulation arising from the intervening Al(α_2,Y) atom.

Table 7.4. Cohesive energies E (in meV) of the 1/1 and two 2/1 models (relative to $2/1_{\mathrm{r1}}$ model, bold). E_{raw} gives "raw" energies of relaxed (diffraction-data) models, E_{can} are energies of the canonically symmetrized models, characterized by displacement $d_{\mathrm{can}}^{\mathrm{RMS}}$ (Å). The last two columns show how the canonically symmetrized quantities reflect the binding

binding	minimal	minimal	minimal	b sensitive	b sensitive
model	1/1	$2/1_1$	$2/1_2$	$2/1_1$	$2/1_2$
E_{raw}	−7(+39)	**253**(+42)	+24(+55)	0(+42)	+24(+55)
E_{can}	+10(+45)	+11(+20)	+136(+157)	+12(+54)	+63(+72)
$d_{\mathrm{can}}^{\mathrm{RMS}}$	0.12(0.12)	0.11(0.15)	0.20(0.15)	0.11(0.08)	0.17(0.08)

On the other hand, the fact that E_{raw} of both $2/1_{\mathrm{d}}$ models, differing only by Al(α_2,Y) position, have nearly equal energies only ≈ 50 meV higher than the relaxed $2/1_{\mathrm{r1}}$ model indicates that the displacive modulation is accommodated *locally* – there is no evidence of global symmetry breaking, as is observed in the 1/1 AlMnSi phase.

Ignoring the x(Mg) dependence of E_{coh} (we will address this point later), the best model is 1/1, with E_{raw} lower by 7 meV than the $2/1_{\mathrm{r1}}$ model. The two canonically symmetrized (relaxed) models have nearly the same energy, but the total $d_{\mathrm{can}}^{\mathrm{RMS}}$ is slightly bigger in the 1/1 case; hence one of the sources of relative stability of the 1/1 model should be a more favorable relaxation distortion (breaking the local point-group symmetry) of some of the cluster shells. Cross-checking with Table 7.1, it appears the shell responsible for this effect is the unit icosahedron, Al(β).

Checking the site energies, we can identify other "problem places" in the 2/1 model: the energy of the Al(β,Y) site near the center of the Y face of the 2/1 tiling (white disk in Fig. 7.4) is 0.2 eV higher than the energy of the topologically similar Al(β, N) site, and by far highest in the model, indicating the vacancy could be energetically more favorable. This site does not occur in the 1/1 model (in the HE model, such sites are vertices of the "isolated" oblate rhombohedra, OR), and in the next section we discuss competition of the 2/1 and 1/1 phases focusing on this structural variation.

7.4.2.5 Relative Stability of the 2/1 and 1/1 Phases. As mentioned in the beginning of this section, the 2/1 Frank–Kasper phase is stable in the AlZnMg system when the Mg content is increased from $x \approx 39$ % to 43 %. On the other hand, the models of the 1/1 or 2/1 phases contain about 32 % of the sites clearly appropriate for "big" atoms (Mg(δ,N) and Mg(δ_z,b), dodecahedron and LT shells), another 6−7% are "intermediate" (Mg(δ_y,b), SB shell). Due to the higher cluster packing fraction in the 1/1 phase, occupying the three sites by Mg leads to higher Mg content in the 1/1 phase (see Table 7.2). On the other hand, the more complex 2/1 phase, due to its lower cluster packing fraction, has more other "intermediate" sites that could be more

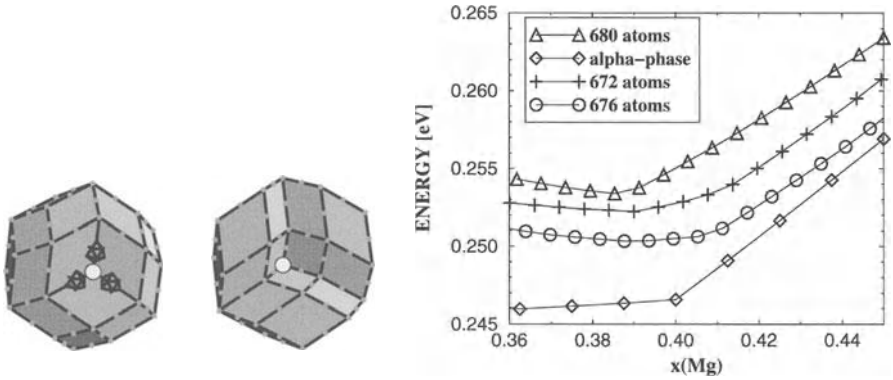

Fig. 7.4. Y face of the CCT decorated by RD, shown from two viewpoints close to its 3-fold axis (left, middle parts of the figure). The white disk near the center of the Y face indicates a Al(β,Y) site with highest energy. The pair potentials favor the modification indicated in the middle figure: the Al(β,Y) site is left vacant, and the three nearby "mid-edge" or SB sites Al(α_1,Y) are preferentially occupied by Mg (icosahedral balls). On the right, plot of the cohesive energy $E_{\rm coh}$ vs Mg content x, for the 1/1 α phase, and the $2/1_1$ model with 0, 4 and 8 vacancies introduced on 680 atomic sites

appropriate for Mg than the next available site in the 1/1 phase. An optimal tool to address the competition in the phase diagram of the Frank–Kasper phases as a function of the Mg content is the pair potentials.

We employ the following procedure: using 680 atomic sites in the $2/1_1$ model, Mg and Al atoms occupy them randomly; then at given x, chemical ordering is optimized with respect to the pair potentials by simulated Metropolis Monte Carlo annealing in a cooling run with temperature $T = 800$ K $\rightarrow$ 100 K. Subsequently, the optimal structure is relaxed by the conjugate gradient method until $\Delta E < 10^{-4}$ eV, and the chemical order is again randomized, but at slightly altered x. The procedure is repeated for $x = 0.35 \rightarrow 0.45$, and for three different atomic densities of 680, 676 and 672 atoms per 2/1 unit cell.

Since we used the pair potentials calculated at a certain atomic volume and Mg content and neglect the leading structure-independent volume term, we rescale the lattice parameters systematically such that the point density is fixed over the whole range of x and for all models. Thus the systematic deviation in $E_{\rm coh}$ is the same for all models; we believe this does not impact significantly on the energy differences between the 1/1 and 2/1 phases at the x of interest.

The plot of $E_{\rm coh}$ vs x in Fig. 7.4 suggests that the optimal atomic density for the 2/1 approximant is 676 atoms, as opposed to the 680 atoms found experimentally. In agreement with the site-energy diagnostics, the vacancies are always at the Al(β,Y) site, but optimally only at half of them. Starting

with Mg at the three best Mg sites Mg(δ,N), Mg(δ_z,b), Mg(δ,Y), the next orbits gradually filled by Mg with increasing Mg content are Mg(δ_y,b) up to $x = 0.39$, Al(α_1,Y) up to $x = 0.41$, and Al(α,c). For the best 2/1 model with 676 atoms and 50 % occupation of the Al(β,Y) site, the energetic balance between the 1/1 and 2/1 phases with increasing Mg content becomes very subtle: the 1/1 phase is more stable by $\approx$4 meV per atom at x(Mg) = 0.4, and by only 1 meV at $x = 0.44$.

7.4.2.6 Electronic Stabilization. It is well known that the ternary Frank-Kasper phases occur typically at the valence-electron per atom ratio at which the Fermi level coincides with a strongly scattering reciprocal lattice vector with high multiplicity [25], invoking the Hume–Rothery stabilization mechanism. *Ab initio* electronic structure calculations (for a review, see the contribution of M. Krajčí in this book) in fact prove the existence of a pseudogap near the Fermi level. It was speculated [4] that in the AlZnMg system phases with higher Mg content are stabilized by appropriately shifting the Fermi level towards the minimum of the pseudogap; at the same time, the close-packing energetic advantage achieved in the 1/1 phase structure is weakened by non-optimal "big" atom (Mg) content. The diagram in Fig. 7.4 appears to support this conjecture, because the relative stability of the 1/1 model with respect to the 2/1 model weakens as the Mg content increases above 40 %.

7.4.3 Conclusion

Using tiling-decoration machinery in conjuction with cohesive energies calculated from pair potentials we have characterized the unusual structural variation, observed in the 2/1 AlZnMg model derived from the diffraction data: occurrence of a partially occupied Wyckoff site, that does not have any counterpart in the familiar HE model, as well as other 6D models proposed previously. Furthermore, a Monte Carlo calculation combined with relaxation under pair potentials predicts that the optimal 2/1 AlZnMg structure has additional partially occupied sites, located at the vertices of the "isolated" OR (HE model), near the center of the Y faces within the CCT geometry. Thus it appears that the close-packing argument clearly applies when the ratio of big to small atoms is optimal ($\approx$ 38 % of big atoms), favoring 1/1 phase formation. At higher big-atom content, there is a subtle energetic competition between vacancies preferentially forming on certain sites (vertices of Penrose rhombohedra in the HE model), and chemical ordering on further "intermediate" sites (accommodating rather easily either a big or a small atom), that exist in the 2/1 structure but are not available in the 1/1 structure. Consequently, with increased Mg content the 2/1 structure becomes more favorable.

Although the 2/1 approximant is still too small to draw conclusions about the i-AlZnMg quasicrystal, the structure of the latter is definitely more complex than previously expected.

7.5 Summary

Calculating cohesive energies of quasicrystalline structures and their approximants is suitable and desired for two mutually entangled purposes: (i) just like in diffraction refinement, to identify the most favorable atomic structure and chemical ordering; (ii) at the same time, cohesive energies provide clues to the understanding of how a particular local ordering, enforced by finite-range atomic interaction, induces peculiar long–range ordering observed in quasicrystalline structures. The methods appropriate for the "energetic" structure refinement range from molecular-dynamics studies, or simulated lattice-gas annealing, in which a tiling-decoration picture is eventually enforced directly by the pair interactions, to the trial tiling-decoration approach, that starts from an *a priori* knowledge of the tiling and systematically varies atomic motifs in order to discover lowest-energy structures. Cohesive energies serve as valuable diagnostics of the validity of a trial parametrization of the structural models.

In general, the pair potential studies of the atomic structure are ideally suited to disentangle and relate two different types of phasonic disorder, arising either from the different *tile* arrangements (with possibly *rigid* atomic motifs bound to the tiles), or from characteristic Al-vacancy disorder. They reveal that the solution of quasicrystal structures is a task of considerably greater complexity than is often assumed.

References

1. Bak P. (1985): Phys. Rev. Lett. **54**, 1517, Bak P. (1986): Phys. Rev. B **32**, 5764
2. Bergman G., Waugh J. L. T., Pauling L. (1957): Acta Cryst. **10**, 254
3. Denton A., Hafner J. (1997): Phys. Rev. B **56**, 2469
4. Dell'Acqua G., Krajčí M., Hafner J. (1997): J. Phys. Cond. Matt. **9**, 10 725
5. Dzugutov M. (1993): Phys. Rev. Lett. **70**, 2924
6. Elser V. (1985): Phys. Rev. B **32**, 4892
7. Friedel J. (1988): Helv. Phys. Acta **61**, 538
8. Hafner J., Krajčí M. (1993): J. Phys. Cond. Matt. **5**, 2489
9. Hafner J., Heine V. (1983, 1986): J. Phys. F **13**, 2479; **16**, 1429
10. Henley C. L. (1991): Phys. Rev. B **43**, 993
11. Henley C. L., Elser V. (1986): Phil. Mag. B **53**, L59
12. Krajčí M., Hafner J. (1992): Phys. Rev. B **46**, 10 669
13. Mihalkovič M., Mrafko P. (1993): Europhys. Lett. **21**, 463
14. Mihalkovič M., Mrafko P. (1994): Phys. Rev. B **49**, 100; Mihalkovič M., Mrafko P. (1992): J. Non-Cryst. Sol. **143**, 225
15. Mihalkovič M., Zhu W.-J., Henley C.L., Oxborrow M. (1996): Phys. Rev. B **53**, 9002
16. Mihalkovič M., Zhu W.-J., Henley C.L., Phillips R. (1996): Phys. Rev. B **53**, 9021
17. Mizutani U., Matsuda T., Itoh Y., Tanaka K., Domae H., Mizuno T., Murasaki S., Miyoshi Y., Hashimoto K., Yamada Y. (1993): J. Non-Cryst. Sol. **156–158**, 882

18. Moriarty J.A., Widom M. (1997): Phys. Rev. B **56**, 7905
19. Oxborrow M. (1993): Ph. D. Thesis, Cornell University, Ithaca
20. Roth J., Trebin H.-R., Schilling R. (1995): Phys. Rev. B **51**, 15 833
21. Roth J., Henley C. L. (1997): Phil. Mag. A **75**, 861
22. Smith A. P. (1991): Phys. Rev. B **43**, 11 635
23. Spiekerman S., PhD Thesis, Fachbereich Chemie, Universität Dortmund (1998)
24. Takeuchi T., Mizutani U. (1995): Phys. Rev. B **52**, 9300
25. Vaks V.G., Kamyshenko V.V., Samolyuk G.D. (1988): Phys. Lett. **132 A**, 131
26. Widom M., Phillips R., Zou J., Carlsson A.E. (1995): Phil. Mag. B **71**, 397
27. Widom M., Cockayne E.: *Proc. Fifth Int. Conf. Quasicrystals*, ed. C. Janot, R. Mosseri (Singapore, World Scientific 1994), p. 343
28. Windisch M., Hafner J., Krajčí M., Mihalkovič M. (1994): Phys. Rev. B **49**, 8701
29. Yamamoto A. (1993): Acta Cryst. A **49**, 337

8 Quasicrystals as Hierarchical Packing of Overlapping Clusters

Christian Janot* and Jean-Marie Dubois

Summary. It is possible to describe quasiperiodic structures in terms of a skeleton of a hierarchical self-similar packing of overlapping atomic clusters. The related inflation rules constrain both composition and atomic valences to have strictly defined values. Stability of the skeleton requires that bonding electrons are recurrently localized at site-forming self-similar isomorphic subsets of the structure and are distributed into "magic cluster" states. Properties can be understood in the framework of such a cluster description of quasicrystals.

8.1 Introduction

Quasicrystals are a form of the solid state which differs from the other two known forms, crystalline and amorphous, by possessing a new type of long-range translational order, quasiperiodicity, and a non-crystallographic orientational order [9,14,23,26,31,33,60]. A central problem in condensed matter physics is to determine whether quasiperiodicity leads to physical properties which are significantly different from those of crystalline and amorphous materials. Such unusual properties have indeed been found in icosahedral alloys of high structural quality [13,15,16,50]. Some of their most striking features, which are not expected for alloys consisting of normal metallic elements, are the very high value of the electrical resistivity (up to $\sim 10\ \Omega$cm at low temperatures in the Al-Pd-Re system [1,6,30,51,52]), a strong negative temperature coefficient of resistivity, an increase of resistivity with increased structural perfection of the samples along with an extreme sensitivity to sample composition, and a low, if any, electronic contribution to the specific heat and thus a vanishing density of states (DOS) at the Fermi level. Other peculiar properties of quasicrystals include thermal insulator behavior, difficult wetting of the surface, low friction coefficient, high hardness, elevated corrosion resistance and a brittle–ductile transition with a very soft plasticity above about 970 K [16,22,49]. Most of these properties combine effectively to give technologically interesting applications [17,34]. The debate concerning structure and stability of quasicrystals revolve about the relative roles of energy and entropy [3,24,29]. But in both cases the description

* Present address: Dipartimento di Scienze della Terra, Universitá di Roma "La Sapienza", Piazzale Aldo Moro, 5 - 00185 Roma, Italy.

J.-B. Suck et al. (eds.), *Quasicrystals*
© Springer-Verlag Berlin Heidelberg 2002

of the structure is based on tiles representing the short-range structure in the material. For an energetically stabilized tiling, growth gets in the way of perfection. Perfect quasiperiodic structures can be obtained via several geometrical methods including inflation-deflation of prototiles, tiling with at least two prototiles and matching rules or physical cut of a higher-dimensional periodic structure [9,14,23,26,31,33,60]. As for perfect crystals described by classical crystallography, the above perfect quasiperiodic structures are irreplaceable when one needs to experimentally approach the structures of real quasicrystals for which they give a very useful average description [9,14]. But these geometrical models suffer several physical drawbacks which have led to some concerns about their suitability to explain what quasicrystals are. For instance, space tiling requires a choice of a small number of prototiles along with the definition of rules to fill space using these tiles, without overlap or holes. Physically, the prototiles must correspond to clusters of atoms which are compatible with the chemistry of the system. The conditions for crystals seem intuitively simple: it is easy to imagine a single building block arising as a low-energy atomic cluster of the given elements. Then, periodicity is also easily obtained by adding again and again clusters identical to this building block prototype. Crystallography teaches us that the procedure works quite well provided the basic building block has no symmetry elements of order five or larger than six. Ordered space tiling without periodicity is far less easy. A leading model for describing quasiperiodic structure has been the Penrose tiling picture [23,26,31,33,60], based on the two-dimensional aperiodic pattern invented by Roger Penrose in 1974 [48]. The Penrose pattern is composed of fat and thin rhombi with matching rules which constrain the way neighboring tiles can join edge-to-edge. The generalization to three-dimensional structures with icosahedral symmetry composed of rhombohedral bricks with matching rules has also been found. In the Penrose tiling pictures, one can imagine that the tiles represent two distinct clusters of atoms and the matching rules represent atomic interactions. But the physical conditions required to emulate a Penrose tiling appear to be much more complex than that needed for periodic crystals. The energetics must be delicately balanced to allow two distinct clusters to be almost equally stable so as to intermix with a specific ratio of densities. Furthermore, the atomic interactions must restrict clusters so that they join only according to the matching rules. This implies arbitrary long-range interaction and precludes growth of structures because a large number of tiles must be rearranged at each step through the whole ensemble. The entropic viewpoint [29,38] allows phason defects to stabilize the structure, relax the matching rules and results in structures that are easier to grow. But beyond basic imperfection of the entropically stabilized structures, this alternative also predicts that quasicrystals are metastable. Yet, some quasicrystals appear to be thermodynamically stable and random tiling does not solve either the delicate energetic problem of having two almost equally stable tiles. The most promising alternative for filling space

with "non-crystallographic clusters" is probably to use a single type of tile combined with overlapping rules. The result is of course an unconventional tiling, because of allowed overlaps, and it is perhaps better to term it as a "covering" of space. The construction implies a closer tie with crystals. Indeed, such coverings can be described in terms of the packing of a single type of cluster and correspond to a generalization in which the "unit cells" overlap for bonding. Furthermore, the formation of the structure may be described also in terms of a low-energy atomic cluster, making it plausible that quasiperiodic systems can be understood by considering the energetics of microscopic clusters. Such concepts have recently been developed in accurate detail [18,27,32,35,37,53] and structures of that sort have experimentally been observed in real quasicrystals [9,20,46,56,62]. Proof of the possibility to cover Penrose and octagonal tilings with a single overlapping cluster was first given by Duneau [18]. Copies of a symmetrical cluster are placed on a quasiperiodic skeleton as on a quasi-Bravais lattice. Gummelt showed subsequently [27] that the size of the clusters can be reduced if symmetry conditions are relaxed and if several "covering matching rules" are used. From Gummelt's results, it was then shown by Jeong and Steinhardt [37] that even the covering matching rules can be somewhat discarded and replaced by a variational principle which leads to maximizing the density of a chosen cluster of tiles. Finally, suggestions on why some clusters should be stable in quasicrystals have been proposed [32,35,36]. The cluster description of quasicrystals is what we are going to discuss in this chapter.

8.2 Penrose Tiling with a Single Prototile

As introduced above, it has been shown that a quasiperiodic covering can be forced using a single type of tile combined with overlapping rules [18,27,37]. An elaborated proof can be found in the original papers. The main results are summarized in Figs. 8.1 and 8.2, which apply to the case of a two-dimensional Penrose tiling. The single tile is chosen to be the decagon shown in Fig. 8.1a, appropriately decorated with shaded regions. The decagons are then permitted to overlap in certain discrete ways as shown in Fig. 8.1b, which allow five types of nearest-neighbor configurations (families A and B in the figure) and two different separations between the centers of neighboring decagons. These two distances, which are in an irrational ratio, replace the two tile types of the usual Penrose tiling. Parts (c) and (d) of Fig. 8.1 illustrate the analogy to a Penrose tiling by inscribing each decagon with a fat rhombus tile marked with the usual single and double arrows (matching rules). Where the rhombi join at a vertex only, there is an open angle where fat or thin rhombi can fit according to the Penrose matching rules. Analyzing in detail all possible configurations of decagons [37], it is possible to demonstrate that the overlap rules force precisely the same nearest-neighbor configurations of rhombi as do the Penrose edge-matching rules. This is illustrated in Fig. 8.2

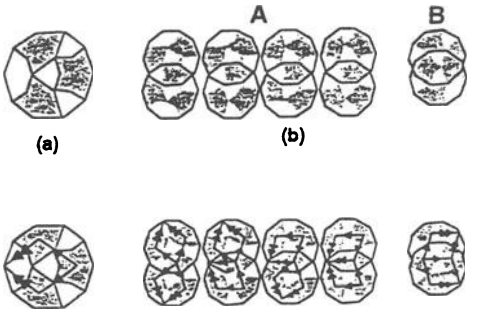

Fig. 8.1. Decagonal cluster used to cover a Penrose tiling (**a**) with possible overlapping situations; (**b**) illustration of the equivalence of the covering scheme in terms of Penrose rhombi (redrawn from [37])

which shows that the nine necessary decagon configurations are in one-to-one correspondence with the nine ways of surrounding a fat rhombus by neighboring fat and thin rhombi in a perfect Penrose tiling. Thus, the two-tile Penrose tiling can be reinterpreted in terms of a single, repeating motif. This reinterpretation of the structure of quasicrystals is a simplification which is valid independently of whether overlap energetics are an important factor in the formation of quasicrystals or not. But this is not the end of it. The same authors [37] have also demonstrated that if one allows any possible configuration of fat and thin rhombi, a perfect Penrose can be picked out by maximizing the density of a particular tile cluster. As a model for quasicrystals the notion is that the chosen cluster represents some low–energy microscopic cluster of atoms. Minimizing the energy naturally maximizes the cluster density and forces quasiperiodicity. This strongly suggests that the energetic conditions required for quasicrystal formation are only that a single chosen cluster has low energy, which is similar to the conditions needed to form periodic crystals, and simpler to envisage than the conditions needed to form two different tiles plus matching rules. This seems to formalize the long–standing consensus that quasiperiodic long–range order should result from a trend of atoms to gather into stable clusters having non–crystallographic symmetries [32,35,36]. Along the way, molecular dynamic calculations by Dzugutov [19] had previously demonstrated that an atomic assembly, when allowed to relax into a locally strong icosahedral potential, reaches long–distance quasiperiodic order.

On the other hand, atomic clusters have been experimentally observed in the structure of real quasicrystals. Indeed, building units of about 50 atoms with geometry close to that of a Mackay icosahedron have been identified in AlPdMn or AlFeCu quasicrystals either in their structures as deduced from diffraction data [9,14,35] or directly with imaging techniques such as secondary electron imaging [62], X-ray photoelectron diffraction [46] or scanning tunneling microscopy [20]. The question now to be addressed is obviously: why should some atomic clusters be more stable than others? This is the purpose of the next section of this chapter.

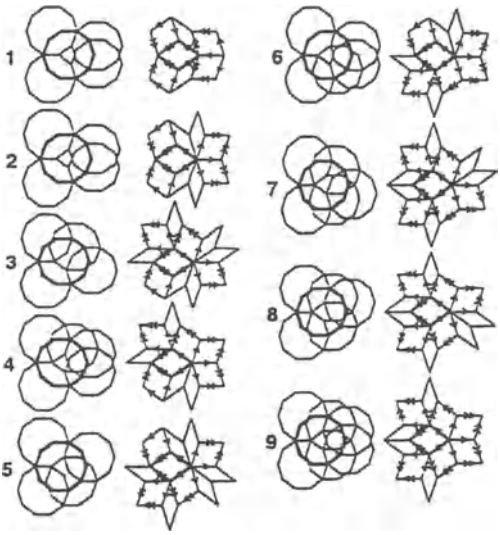

Fig. 8.2. Nine ways of surrounding a decagon corresponding to the nine ways of surrounding a fat rhombus by thin and fat rhombi according to the Penrose matching rules (redrawn from [37])

8.3 The Jellium Model for Clusters and Quasicrystals

Conditions for stability of atomic clusters can be understood from the developing subject of the physics of free atomic clusters. Free clusters are almost always generated and studied in molecular beams. When assembled, most clusters coalesce to form bigger units and the properties evolve to the bulk. This confirms that if the clusters are to serve as building blocks, they have to be such that they will not lose their identity when assembled. This can be accomplished if the clusters are very stable and resist deformation. That this is possible is already evident from the discovery of Fullerides which are crystals of C_{60} clusters. Another cluster with the potential of forming cluster assemblies was discovered by Guo, Kern and Castleman [28]. It is made up of eight transitions metal and 12 carbon atoms and is referred to as a metallo-carbohedrene. Both these are experimental discoveries. Is it possible to develop some fundamental principles which could guide us to identify clusters with the potential for forming cluster materials? To gain an insight into the above question, it is helpful to look at the factors controlling the stability and reactivity of clusters. Let us start with the abundance spectra of Na_n clusters generated in beams [42]. They show that the clusters containing 2, 8, 18, 20, 40, 58, 92, ... Na atoms are far more dominant than other sizes. These special clusters are said to contain "magic numbers" of atoms. Theoretical work shows that this can be understood on the basis of a simple jellium model where one imagines that the positive charges of the ions are distributed over the size of the cluster and the electrons move in this effective potential. This is similar to the case of atoms except that in an atom the positive charge is localized at the nucleus. The one-electron levels in the jellium picture can be

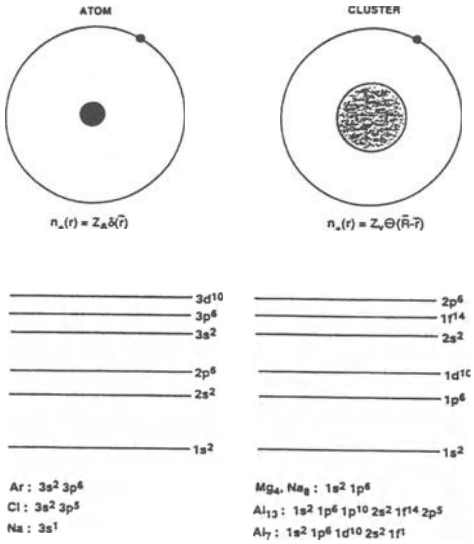

Fig. 8.3. Comparison of the one-electron energy levels in an atom and a cluster (superatom). Examples of clusters simulating different atoms are also given

labeled using the same quantum numbers as in atoms because of the spherical symmetry of the potential. This is shown in Fig. 8.3. In a cluster, the level order is $1s^21p^61d^{10}2s^21f^{14}2p^61g^{18}$... It is easy to see that the magic clusters 2, 8, 20, 34, 40, 58, 92, ... correspond to clusters with filled shells, i.e. $1s^2, 1s^21p^6, 1s^21p^61d^{10}2s^2$, etc. The filled electronic shells should also make these clusters behave like inert gas atoms. In fact they do. For example, the ionization potential on Na_n clusters shows peaks at clusters containing two and eight electrons (atoms) as in the case of atoms where the maxima occur at inert gases with two or eight electrons. The magic clusters are also chemically less reactive. For example, experimental studies of the reactivity of Al_n [44] with oxygen show that whereas Al_{13} reacts strongly, Al_{13}^- with 40 electrons and a filled electronic shell is relatively inert. These results show that the electronic structure of clusters resembles those of atoms and the most stable clusters correspond to filled electronic shells which also render them less reactive. It was Khanna and Jena [39–41] who first argued that it should be possible to design very stable clusters mimicking different elements in the periodic table. They considered an Al_{13} cluster. The ground state is an icosahedron having a central atom surrounded by a first shell of 12 atoms. The cluster is geometrically close packed. Al is trivalent, so that the cluster has 39 bonding electrons, one shy of the magic number 40. The cluster could therefore be made more stable by doping with a tetravalent impurity such as C. Using *ab initio* calculations, they showed that an $Al_{12}C$ cluster is indeed more stable than Al_{13} by 4.4 eV. The electronic shell filling also makes the cluster less reactive. A calculation of the binding energy of a H atom brought towards Al_{13} and $Al_{12}C$ showed that the binding energy is significantly reduced in the case of $Al_{12}C$. The final test of stability and inertia has come from

the recent computer simulations of a molecule composed of two $Al_{12}C$ units. The studies based on Car-Parrinello quantum molecular dynamics show that the structure of the individual $Al_{12}C$ clusters remains intact. We would like to add that a similar study on $Al_{12}Si$ which also has 40 electrons showed that the energy gain is smaller. The energy gain in $Al_{12}C$ is both due to the electronic shell fillings as well as to the fact that C is smaller than Al and therefore allows the surface Al–Al bonds, which are 5% longer than radial bonds in an ideal icosahedron, to relax. In the above, we have discussed relatively inert clusters. One can also form assemblies using molecular units composed of clusters interacting via ionic or covalent bonds. Consider the Al_{13} cluster. In a jellium model, its electronic state corresponds to $1s^2 1p^6 1d^{10} 2s^2 1f^{14} 2p^5$. It therefore requires one more electron to fill the p-shell just as in a halogen atom. A theoretical calculation shows that it does indeed have an electron affinity of 3.7 eV compared to 3.6 eV for the Cl atom. Note that an Al atom has an electron affinity of only 0.6 eV. Similarly, in a KAl_{13} cluster, K loses its electron to Al_{13} and the molecule has a binding energy of 3.04 eV due to the formation of an ionic bond. The above discussion shows that, by controlling the number of atoms and the chemical composition, it is possible to have clusters which can mimic different atoms in the periodic arrangement. These clusters can serve as building blocks much in the same way as atoms. Figure 8.4 shows the one-electron levels (only the valence portion) of an Al atom and an Al_{13} cluster. In an atom, the degeneracy of the one-electron levels is governed by the angular momentum quantum number. In a cluster on the other hand, the degeneracy is governed by the arrangements of atoms. Whereas an atom only undergoes a change in electronic orbital upon chemical bonding, a cluster is a soft superatom where the atomic structure can also change. The resistance to such a change depends on the binding energy of the cluster, the energy cost for deformation and the binding energy between clusters. In this context, growth of icosahedral quasicrystals may result from a special situation regarding the number of valence electrons available in the

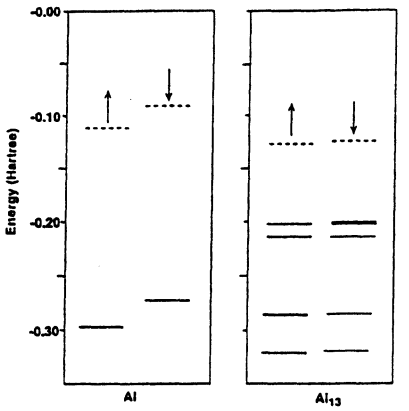

Fig. 8.4. (**a**) Energy levels in an Al atom. (**b**) Energy levels of electrons in an Al_{13} cluster

basic clusters compared to a close magic number [32,35,36]. Consider a cluster made of N atoms, taken as all identical for simplicity, with n valence (or bonding) electrons per atom such that the total number of bonding electrons in the cluster Nn differs from a magic number M by n:

$$\begin{aligned} Nn &= M + n \\ n &= M/(N-1)\,. \end{aligned} \tag{8.1}$$

This means that the cluster has the same "valence" as its constituent atoms. Since it misses the magic number M, the cluster would be slightly reactive and it will have a tendency to assemble with $N-1$ other identical clusters to grow into a supercluster (of N clusters) again containing $Nn = M + n$ bonding electrons, missing again the "magic stability" to allow further growth into inflated self-similar supersuperclusters and so on. At each stage the cluster of clusters keeps the same number of bonding electrons, has the same "valence" and is, so to speak, geometrically and chemically self-similar to the constituent atoms of the system. Alternatively, the clusters may be magic with $Nn = M$, bonding being obtained via overlaps and sharing atoms so that an average of n electrons per cluster is transferred to the next generation of clusters for extending the stability of the structure. From a physical point of view, the picture in both cases assumes the cluster behaves as a square well confining most of the electrons. Only electrons close to the Fermi energy tunnel through the barrier but most of the new states are confined by the well created by the succeeding supercluster and so on. The electron density of states $n\ (E)$ is thus composed of the unlocalized states of one generation falling on to the localized states of the next generation. This is schematically shown in Fig. 8.5. The width of the successive subbands decreases rapidly, following the squared sizes of the successively inflated domains. The density of states at low energy is mastered by the basic "small" cluster and is terminated toward the Fermi level by a succession of self-similar, more and more spiky features. The overall envelope of the spikes follows a power law of the energy $\mathrm{E}^{1/2}$ in good agreement with experimental results [61]. Such a model has observable implications including poor conductivity (increasing with

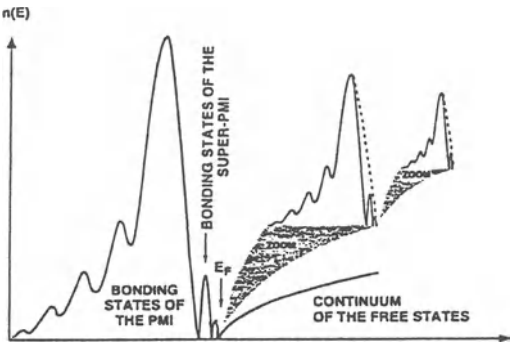

Fig. 8.5. Schematic density of electronic states for AlPdMn quasicrystals. The large feature on the left-hand side is the contribution of the elementary PMI. The successive features come from the inflated PMIs

temperature), low chemical reactivity, diamagnetism or mechanical brittleness [32,35,36]. To go beyond the model toward real quasicrystals, there are difficulties which are not easily overcome: real quasicrystals are never monatomic systems (they belong mostly to ternary systems), it seems that their structures cannot be covered with a single type of cluster and self-similar packing does not necessarily have the expected density. These possible drawbacks of the model are going to be illustrated and partially overcome in the next section with the example of the AlPdMn quasicrystal. Obviously, saying that the structure of quasicrystals can be described by self-similar packing of building blocks is not a discovery: everybody has realized it for a very long time. What is somewhat new and may be useful in the above derivation includes:

- the idea that the structure is solidly quasiperiodic if the building blocks are "magic" or "almost magic" clusters with non–crystallographic symmetries;
- the consequence that most of the valence electrons of the atoms are "virtually" trapped in cluster-like levels within a self-similar Jellium following the constraints of the structure. The result is a sort of multiple site self-similar localization. This has not to be taken too strictly: the atomic clusters are not isolated from each other; electrons may continuously jump from site to site provided that the number of electrons in clusters of any scale remain magic when averaged in time;
- the possibility for building blocks to overlap.

8.4 The Cluster Structure of AlPdMn Quasicrystals

The AlPdMn system is the only one so far which has allowed the formation of icosahedral quasicrystals as perfect big centimeter-size single grains [58,43,7,10]. Despite such a very favorable circumstance, the actual structure has been obtained at a rather low level resolution only. But this appears sufficiently clear to reveal several building rules which are astonishingly simple, with both chemical and geometrical order (Fig. 8.6). First of all, the observed structure is essentially based on atomic units containing 51 atoms in total, named Pseudo-Mackay Icosahedra (PMI) hereafter, and made of three centrosymmetrical shells: an inner small centered core of nine atoms, an intermediate icosahedron of 12 atoms and an external icosadodecahedron of 30 atoms. The last two shells have practically equal radii and constitute altogether the "surface" of the PMI whose diameter is very close to 0.96 nm. The small inner core is a piece of a pentagonal dodecahedron whose 20 atomic sites are only partially occupied in a way which probably fluctuates from PMI to PMI within the structure. Two families of chemically differing PMIs have been identified so far in the structure: one family (PMI-A) has something close to six manganese and six palladium atoms on the icosahedron sites of the external shell, the 39 remaining sites being occupied by

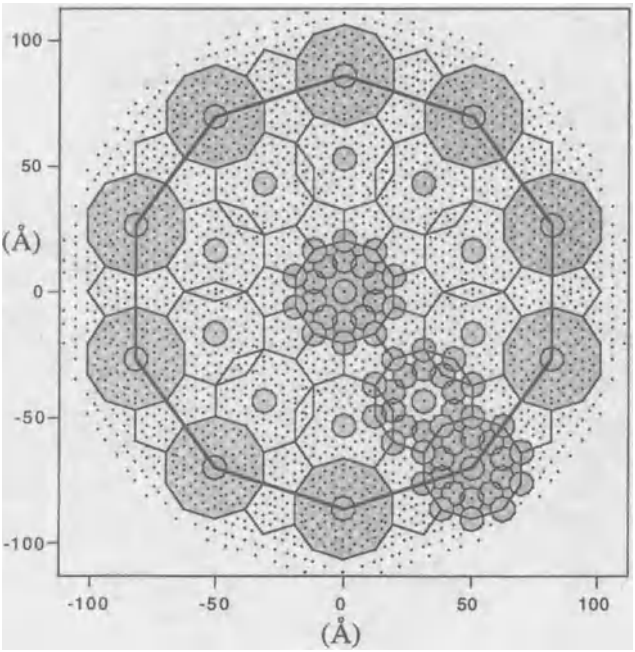

Fig. 8.6. Planar section of the AlPdMn quasicrystal structure. Small rings of 10 atoms are equatorial sections of a basic PMI. Two steps of inflated rings are represented. Overlapping clusters are also visible

aluminium atoms; the second family (PMI-T) has about 20 palladium atoms among the 42 of the external shell, the 31 or so remaining sites being occupied by aluminium atoms. The calculated atomic density of an individual PMI is 64 at/nm^3, which is close to the measured density of the bulk material, within experimental accuracy. Chemical compositions of the PMI-A and PMI-T as reported above cannot be strictly ascertained from diffraction data. But they are self-consistently in agreement with a magic cluster description provided M is taken equal to 92 and valences of the chemical species are $V_{Al} = +3$ for aluminium atoms, V_{Mn} close to -3 for manganese atoms and V_{Pd} slightly negative for palladium atoms [32,36]. Such negative valences for transition metal atoms have been currently suggested in intermetallic compounds; they are consistent with the analysis of Mayou et al. [54,57] in terms of cluster virtual bound states and they suggest the trend of the d-elements in these alloys to saturate their electron d-levels by attracting electrons from Al atoms; the point has indeed received experimental support [4,5]. Even the values $V_{Pd} \sim -0$ and $V_{Mn} \sim -3$ can be qualitatively understood. The electronic structures of Pd and Mn free atoms are $4d^85s^2$ and $3d^54s^2$, respectively; nearest neighbor distances in quasicrystals have been found to be up to more than 5% shorter than in the corresponding metals

which generate large local pressure on electronic states; this has been experimentally shown to force transfer of electrons from s to d states [47] with the consequence that electride-like materials can be obtained where atoms become ions with "interstitial" electrons only. Then the electronic structure of Pd and Mn in quasicrystals should approach $4d^{10}$ and $3d^7$ respectively, with a trend for Mn atoms to attract three more electrons so as to reach the $3d^{10}$ configuration, from a time averaging point of view. Finally, we have also previously explained that the self-similar growth of the structure, or at least its skeleton, can proceed via successive substitutions of atoms by PMI with proper rescaling [32,35,36]. However, it would be dangerous to think that reality is that simple. A minor remark regards the density which must be kept constant at any inflation stage; as substituting atoms by PMI increases the number of atoms by a factor 51, the inflated volume must also be multiplied by 51 to avoid density losses; the scale factor (defining length expansion) must then be $3.7081... = (1.5478...)^3$, involving the number $n = 1.548$ which is very close to the observed value and falls only 4% off the golden mean τ used previously for simplicity [32,35]. The detailed examination of the growth scheme reveals that some clusters overlap at any inflation stage (Fig. 8.6). These overlapping clusters are just the ones deduced by inflation from the atomic sites of the partially occupied dodecahedron of the basic PMI. Atoms cannot overlap; this is why the dodecahedron sites are not all occupied in the basic PMI. But these dodecahedron sites of the inflated PMI can all be occupied by 20 overlapping basic PMI so that they bring altogether 8×51 atoms to the structure (equivalent to eight whole PMI); and this is pursued the same way through the successive inflation steps. In conclusion, in the particular structure of the icosahedral AlPdMn quasicrystals, space covering is obtained using clusters whose geometry is that of a single prototype but with several chemical decorations. On the other hand, some of these clusters overlap, others do not. An interesting consequence of overlapping is that density is preserved even though inflation is used to grow the structure. Short distance atomic jumps (see Fig. 8.6) allow the exchange of overlapping with non-overlapping clusters and vice versa. Another remark concerns what we can call a requirement for intrinsic disorder even if the expression is not fully appropriate. The point is that the three-dimensional real structure of quasicrystals is not unequivocally defined from diffraction data. The best to be expected is the 6-dim periodic image of the 3-dim quasiperiodic system which then results from slicing by physical space. Many configurations, equally probable, are obtained when translating continuously this physical space in hyperspace. The real structure may be a patchwork of domains each taken in one of the possible configurations, with interfaces or connecting regions in between implying phason defects. These defects are frozen in at low temperature but may generate atomic jumps when the thermal energy is high enough, with softening of the material [59] and cleaning of weak diffuse scattering contributions from diffraction patterns [8,11]. Even so,

self-similarity remains the most robust ingredient of the overall structure and this must be considered in its manifold aspect, i.e. not only via the already mentioned geometrical implications. For instance, valences must be extended from atoms to clusters at any stage, with a one-to-one correspondence scheme. This means that, starting with three atomic species, i.e. Al, Pd and Mn, we must continue with three building units, i.e. PMI-Al, PMI-Pd and PMI-Mn. Two types of PMI only being deduced from diffraction data must then be accepted as an experiment-limited result with the PMI-T being the best observable compromise between PMI-Pd and PMI-Mn. Constraints from self-similarity requirements may allow discrimination of the two. Let us first consider that some of the PMI-T are the inflated partners of the Pd atoms. The magic number invariance with inflation ($M = 92$ in the present case) imposes the condition that the number of valence electrons in a PMI-Pd is $92+\mathrm{V_{Pd}}$ ($\mathrm{V_{Pd}}$ valences of the Pd atoms); if x_{Al} is the number of Al atoms over the 51 atoms in the PMI, we have the trivial equation:

$$3x_{\mathrm{Al}} + (51 - x_{\mathrm{Al}})V_{\mathrm{Pd}} = 92 + V_{\mathrm{Pd}} \tag{8.2}$$

in which V_{Pd} must be slightly negative, very close to zero indeed and x_{Al} is an integer; V_{Pd} fixed to zero gives $x_{\mathrm{Al}} = 30,66$ whose closest integers are 30 and 31. Using now $x_{\mathrm{Al}} = 31$ (and $x_{\mathrm{Pd}} = 20$ since PMI-T contains only Al and Pd atoms), one finds $V_{\mathrm{Pd}} = -1/19 = -0.0526...$. With the other possible value $x_{\mathrm{Al}} = 30$ ($x_{\mathrm{Pd}} = 21$) and keeping $V_{\mathrm{Pd}} = -1/19$, we have the second type of PMI-T which happens to contain 88.8947... valence electrons, i.e. 92−3.1053, whose "cluster valence" is then −3.1053 (3 + 2/19 actually). This nicely sounds like a PMI-Mn, the inflated partner of Mn atoms, with common valences equal to −3.1053.... Both PMI-Pd (31 Al + 20 Pd) and PMI-Mn (30 Al + 21 Pd) are fascinatingly close to the experimentally built PMI-T, well within practical resolution. The other experimental family, the PMI-A, can then be confidently assigned to Al atoms, with a +3 valence value (92 + 3 = 95 electrons in the PMI). Again the solution is very close to the experimental insight; with 38 Al atoms, six Mn atoms (half of the large icosahedron) and seven Pd atoms (the other half of the large icosahedron plus probably atoms at centers of the PMIs) we get exactly the expected +3 valency. Thus, refining the experimental results in self-consistency with inflation invariance of the structure and the magic cluster model allows us to approach more closely real atomic clusters. A very pleasant by-product conclusion is that the three ingredients of the overall description (magic clusters, PMI units and global inflation) can be considered very robust. To be completely conclusive on that point, we must also check self-consistency of the model with the alloy composition which may be written as $\mathrm{Al}_x\mathrm{Pd}_y\mathrm{Mn}_z$. After the first inflation stage we must have the following situation:

$$\begin{aligned} &x_{\mathrm{PMI}} - Al \text{ which contains } 38\mathrm{Al} + 7\mathrm{Pd} + 6\mathrm{Mn} \\ &y_{\mathrm{PMI}} - Pd \text{ which contains } 31\mathrm{Al} + 20\mathrm{Pd} \\ &z_{\mathrm{PMI}} - Mn \text{ which contains } 30\mathrm{Al} + 21\mathrm{Pd} \end{aligned} \tag{8.3}$$

with the resulting equations:

$$\begin{aligned} 51x &= 38x + 31y + 30z \\ 51y &= 7x + 20y + 21z \\ 51z &= 6x \end{aligned} \tag{8.4}$$

and the closing condition $x + y + z = 1$. This overdetermined system of equation has actually one and only one solution:

$$\begin{aligned} x &= 0.702666... \\ y &= 0.214666... \\ z &= 0.082666... \end{aligned} \tag{8.5}$$

which is impressively close to the composition of the AlPdMn icosahedral phase as shown in the experimentally built phase diagram [2]. It is noteworthy that the partial volume occupied by all Al atoms in the structure is close to τ^2 as large as the cumulated partial volumes of all Pd and all Mn atoms. We may consider the demonstration as convincing enough to conclude that the distribution of the valence electrons in quasicrystals is based on a hierarchy of recurrently localized states. Each state is defined by the size of a given atomic domain (basic PMI or inflated PMI at any inflation stage) and extends to all identical domains of the structure. In each of these domains M/Nn^{3n} electrons/atoms are confined (timely averaged confinement) over distances scaling as $\Lambda\nu^n$ in which M is still the relevant magic number, N the number of atoms in the basic units (PMI here) of diameter Λ, ν^3 is the inflation scale factor and n, any integer, is the inflation order. Thus, the number of confined electrons decreases as $1/\nu^{3n}$ when the confinement distance increases as ν^n , and most of the bonding electrons are essentially trapped into cluster levels, with exchanges, if any, limited to hopping-like mechanisms [36]. This also suggests that quasicrystals must be poorly reactive to any external action. They actually have a very low mechanical response, they resist corrosion, their surface energy is low and they exhibit small friction coefficients [25]. The effectiveness and impact of the rigid clusters on mechanical properties is especially spectacular, with extremely brittle behavior up to about 100 K prior to melting. The rigid clusters prevent easy simple gliding and these clusters cannot be cut nor deformed without destabilization of the structure. In computer simulations, cracks have been observed to propagate in between the rigid clusters [45]. Surface morphology upon fracture tests shows the features typical of solids with strong anisotropic atomic bonds and in which atomic transport, if any, is only very slow. Finally the magic cluster scheme also raises some questions about the nature of quasicrystal surfaces. These surfaces when in their natural state should be very rough due to emerging rigid clusters. This has actually been observed on cleaved samples [20]. On the other hand, surface reconstruction, when allowed, can occur only if at least a "layer" of cluster is destroyed and rearranged; the corresponding abrupt

cut of the structure by a surface must also account for relaxation of the self-similarity rules mastering the bulk. Chemical compositions as measured on reconstructed quasicrystals surfaces [12,55] of single grains of AlPdMn show a net depletion in Mn which suggests that a layer of the ξ-approximant [2] may form at surfaces, with perhaps some sort of structural gradient profile to reach the icosahedral geometry down in the bulk. Very few other structures of quasicrystals have been analyzed so far within the scheme of atomic overlapping clusters. Decagonal phases of the AlNiCo system [56] also contain columns of two-dimensional clusters whose copies are stacked along a five-fold axis with successive rotations by $2\pi/5$ about this axis. Recent models try to account for the cluster ingredient in the structure of quasicrystals [21].

8.5 Conclusion

Higher-dimensional crystallography and a Penrose-like description of quasicrystals have been, and still are, very useful tools to understand the geometry of these unconventional structures. But the energetics of the problem completely escapes these approaches. Constructions implying overlapping stable clusters of atoms restore a closer tie between quasicrystals and crystals and greatly simplify the problem of searching for structural models for quasicrystals. Extending geometrical self-similarity to chemistry allows us to find stability conditions and explains most of the peculiar physical properties observed with quasicrystals. New quasicrystals may form by bonding any kind of stable atomic clusters having non-crystallographic symmetries.

References

1. Akiyama H., Honda Y., Hashimoto T., Edagawa K., and Takeuchi A. (1993): Jpn. J. Appl. Phys. B 7, L1003
2. Audier M., Durand-Charre M., and de Boissieu M. (1993): Phil. Mag. B 68, 607
3. Baake M. and Joseph D. (1990): Phys. Rev. B 42, 8091
4. Basov D.N., Timusk T., Barakat F., Greedan J., and Grushkjo B. (1994): Phys. Rev. Lett. 72, 1937
5. E. Belin, Z. Dankhazi, A. Sadoc, and J.M. Dubois (1994): J. Phys.: Condens. Matter 6, 8771; (1994): Eur. Phys. Lett. 26, 677
6. Berger C., Grenet T., Lindqvist P., Lanco P., Grieco J.C., Fourcaudot G. and Cyrot-Lackmann F. (1993): Solid State Commun. 87, 977
7. de Boissieu M., Durand-Charre M., Bastie P., Carabelli A., Boudard M., Bessiere M., Lefebvre S., Janot C., and Audier M. (1992): Phil. Mag. Lett. 65, 147
8. de Boissieu M., Boudard M., Hennion B., Bellissent R., Kycia S., Goldman A.I., Janot C., and Audier M. (1995): Phys. Rev. Lett. 75, 89;
9. Boudard M., de Boissieu M., Janot C., Heger G., Beeli C., Nissen H.U., Vincent H., Ibberson R., Audier M., and Dubois J.M. (1992): J. Phys: Condens Matter 4, 10149

10. Boudard M., Bourgeat-Lami E., de Boissieu M., Janot C., Durand-Charre M., H. Klein, M. Audier, and B. Hennion (1995): Phil. Mag. Lett. 71(1) 11
11. Boudard M., de Boissieu M., Letoublon A., Hennion B., Bellissent R., and Janot C. (1996): Europhys. Lett. 33, 199
12. Chang S.L., Anderegg J.W., and Thiel P.A. (1996): J. Non-Cryst. Sol. 195, 95; Chang S.L., Chin W.B., Zhang C.M., Jenks C.J., and Thiel P.A. (1995): Surf. Science 337, 135
13. Chernikov M.A., Bianchi A., and Ott H.R. (1995): Phys. Rev. B 51, 153
14. Cornier-Quiquandon M., Quivy M., Lefebvre S., Elkaim E., Heger G., Katz A., and Gratias D. (1991): Phys. Rev. B 44, 2071
15. Degiorgi L., Chernikov M.A., Beeli C., and Ott H.R. (1993): Solid State Comm. 87, 721
16. Dubois J.M., Kang S.S., and Perrot A. (1994): Mater. Sc. Eng. A179-A180, 122
17. Dubois J.M. (2002): See Chapter 26 of this book; Dubois J.M. (1997) in: New Horizons in Quasicrystals, Goldman A.I., Sordelet D.J., Thiel P.A., and Dubois J.M. (Eds). World Scientific, Singapore
18. Duneau M. (1995) in: Quasicrystals, 5th International Conference on Quasicrystals, Janot C. and Mosseri R. (Eds.). World Scientific, Singapore, 116
19. Dzugutov M. (1992): Phys. Rev. A 46, R2984; (1993): Phys. Rev. Lett. 70, 2924
20. Ebert P., Feuerbacher M., Tamura N., Wollgarten M., and Urban K. (1996): Phys. Rev. Lett. 77, 3827
21. Elser V. (1996): Phil Mag. B 73, 641
22. Feuerbacher M., Baufeld B., Rosenfeld R., Bartsch M., Hanke G., Beyss M., Wollgarten M., Messerschmitt U., and Urban K. (1995): Phil. Mag. Lett. 71, 91
23. Fujivara T. and Ogawa T. (Eds.) (1990): Quasicrystals, Springer-Verlag Berlin
24. Gähler F. and Jeong H.C. (1995): J. Phys. A 28, 1807
25. Gödecke and Lück R. (1995): Z. Metallkd. 86, 2
26. Goldman A.I., Sordelet D.J., Thiel P.A., and Dubois J.M. (Eds.) (1997): New Horizons in Quasicrystals, World Scientific, Singapore
27. Gummelt P. (1996): Geometriae Dedicata 62, 1
28. Guo B.C., Kerns K.P., and Castleman Jr. A.W. (1992): Science 255, 1411
29. Henley C.L. (1991) in: Quasicrystals: The State of the Art, DiVincenzo D.P. and Steindhardt P.J. (Eds.). World Scientific, Singapore, 111
30. Honda Y., Edagawa K., Yoshika A., Hashimoto T., and Takeuchi S. (1994): Jpn. J. Appl. Phys. A 9, 4929
31. Janot, C. (1994): Quasicrystals: A primer, 2nd edition, Oxford University Press, Cambridge
32. Janot C. and de Boissieu M. (1994): Phys. Rev. Lett. 72, 1674.
33. Janot C. and Mosseri R. (Eds.) (1995): Quasicrystals, 5th International Conference on Quasicrystals, World Scientific, Singapore
34. Janot C. (1996): Europhysics News 27, 60;
35. Janot C. (1996): Phys. Rev. B 53, 181
36. Janot C. (1997): J. Phys.: Condens. Matter 9, 1493
37. Jeong H.C. and Steinhardt P.J. (1997): Phys. Rev. B 553, 520
38. Joseph D. and Elser V. (1997): Phys. Rev. Lett. 79, 1066
39. Khanna S.N. and Jena P. (1992): Phys. Rev. Lett. 69, 1664; (1993): ibid. 71, 208
40. Khanna S.N. and Jena P. (1994): Chem. Phys. Lett. 218, 383; Chem. Phys. Lett. 219, 479

41. Khanna S.N. and Jena P. (1995): Phys. Rev. B 51, 13705
42. Knight W.D., Clemenger K., de Heer W.A., Saunders W.A., Chou M.Y., and Cohen M.L. (1984): Phys. Rev. Lett. 52, 2141
43. Kycia S.W., Goldman A.I., Lograsso T.A., Delancy D.W., Sutton M., Dufresne E., Brüning R., and Rodricks B. (1993): Phys. Rev. B 48, 3544
44. Leuchtner R.E., Harms A.C., and Castleman Jr. A.W. (1989): J. Chem. Phys. 91, 2753
45. Mikulla R., Krul F., Gumbsch P., and Trebin H.R. (1997) in: New Horizons in Quasicrystals, Goldman A.I., Sordelet D.J., Thiel P.A., and Dubois J.M. (Eds.). World Scientific, Singapore, 200
46. Naumovic D., Aebi P., Schlapbach L., and Beeli C. (1997) in: New Horizons in Quasicrystals, Goldman A.I., Sordelet D.J., Thiel P.A. and Dubois J.M. (Eds.). World Scientific, Singapore, 86
47. Parker L.J., Atou T., and Badding J. (1996): Science 273, 95
48. Penrose R. (1974): Bull. Inst. Math. Appl. 10, 266
49. Perrot A. and Dubois J.M. (1995) in: Janot C. and Mosseri R. (Eds.) Quasicrystals, 5th International Conference on Quasicrystals. World Scientific, Singapore, 586
50. Pierce F.S., Poon S.J., and Guo Q. (1993): Science 261, 737
51. Pierce F.S., Guo Q., and Poon S.J. (1994): Phys. Rev. Lett. 73, 2220
52. Poon S. J. (1992): Adv. Phys. 41, 303
53. Quemerais P. (1994): J. Phys. (Paris) 4, 1669
54. Roche S., Trambly de Laissardire G., and Mayou D. (1997): J. Math. Phys. 38, 4
55. Schaub T.M., Bürgler D.E., Güntherodt H.J., Suck J.B. and Audier M. (1995): Appl. Phys. A 61, 491
56. Steurer W., Haibach T., and Zhang B. (1993): Acta Cryst. B 49, 661.
57. Trambly de Laissardiere G. and Mayou D. (1997): Phys. Rev. B 55, 2890
58. Tsai A.P., Inoue A., and Masumoto T. (1990): Phil. Mag. Lett. 62 (2), 95
59. Urban K., Wollgarten M., and Wittmann R. (1993): Physica Scripta T 49, 360
60. Di Vincenzo D.P. and Steinhardt P.J. (Eds.)(1991): Quasicrystals: The State of the Art, World Scientific, Singapore
61. Wu X., Kycia S.W., Olson C.G., Benning P.J., Goldman A.I., and Lynch D.W. (1995): Phys. Rev. Lett. 75, 4540
62. Zurkirsh M., Atrei A., Erbudak M., and Hochtstrasser M. (1996): Phil. Mag. Lett. 73, 107

Part III

Production of Quasicrystalline Alloys

9 Modeling Quasicrystal Growth

Uwe Grimm and Dieter Joseph

Dedicated to the memory of Marko V. Jarić

Summary. Understanding the growth of quasicrystals poses a challenging problem, not the least because the quasiperiodic order present in idealized mathematical models of quasicrystals prohibits simple local growth algorithms. This can only be circumvented by allowing for some degree of disorder, which of course is always present in real quasicrystalline samples. In this review, we give an overview of the present state of theoretical research, addressing the problems, the different approaches and the results obtained so far.

9.1 Introduction

How do quasicrystals grow? This has been (and still is) one of the fundamental puzzles in the theory of quasicrystals, and despite the effort employed to provide an answer to this fascinating question, there is still much to be understood. In this review, we want to show the problems that one has to face, and present an overview on the ideas, the models, the methods and the results that have been discussed in the literature to date.

After all, one may ask, what is so different about growing quasicrystals in comparison to the growth of (ordinary) crystals? Certainly, taking a thermodynamic point of view, one would expect that the basic theory of nucleation and crystal growth should be the same as for ordinary crystals; see, e.g., [42] for an introductory textbook on this subject, and [27] for experimental results on undercooled melts of quasicrystalline alloys. In fact, the answer to this question lies in the structure of quasicrystals, and their relationship to ordered crystals on the one hand, and to disordered amorphous materials on the other. An ideal crystal is constructed as a periodic arrangement of a single building block, the unit cell, forming a regular lattice. Thus, in order to understand why the atoms arrange in a crystalline fashion, it is sufficient to consider a small portion of the crystal that contains a few of these unit cells. In amorphous systems, on the other hand, one only finds short-ranged local order, and one can quite easily imagine how such a structure can emerge in a process of aggregation.

For *ideal* quasicrystals (where "ideal" means perfect in the mathematical sense), however, the situation is completely different. Being aperiodic, they possess a long-ranged quasiperiodic order of the atomic positions. This quasi-

J.-B. Suck et al. (eds.), *Quasicrystals*
© Springer-Verlag Berlin Heidelberg 2002

periodic order, if it is perfect, is very restrictive, and one should not think of the quasiperiodic structure as being less ordered than the periodic structure that underlies crystals. In fact, structure models of quasicrystals are typically built on quasiperiodic tilings of space, where the tiles are decorated by the atomic positions. Such tilings can be obtained as sections through higher-dimensional periodic lattices; hence the degree of order in these periodic and quasiperiodic structures is comparable. However, the lack of periodicity makes it much more difficult to build such a structure from its constituents (for example, to construct a quasiperiodic tiling by arranging the tiles like a puzzle) without violating quasiperiodicity [54]. We cordially invite the reader to give it a trial [18].

At first, the tile-by-tile growth of a quasicrystal may even seem to be an impossible task. However, for certain tilings, there exist collections of *local* conditions, so-called matching rules, that enforce quasiperiodicity. Nevertheless, these matching rules do not really solve the problem: they only state that if you managed to tile the space without violating the matching rules, you will indeed have constructed a quasiperiodic tiling. But they do not guarantee that a given finite "legal" patch (i.e. one that does not violate the rules) *can* in fact be extended to an infinite tiling of space. So, in this sense, matching rules are not sufficient to provide a simple algorithm for the construction of ideal quasiperiodic tilings.

With this in mind, one inevitably arrives at the question of how Nature solves this puzzle to grow real quasicrystals. Apparently, this seems to require non-local interaction among the constituents, which we want to exclude on physical grounds. Of course, there is a rather easy way out of this dilemma – namely that in physical reality one *never* encounters real quasicrystals that are absolutely perfect in the mathematical sense. However, the same is true for ideal crystals, and one can nowadays grow real quasicrystals that show at least comparable degrees of perfection to those of real ordinary crystals – judged, for instance, by the sharpness of their experimentally observed diffraction patterns. These high-quality quasicrystals are commonly called "perfect quasicrystals" regardless of whether they resemble an ideal quasiperiodic tiling or a random tiling (see below).

Nevertheless, it turns out that the idea of building defects into the ideal quasiperiodic tilings is rather fruitful, being closely linked to the question of thermodynamic stability of quasicrystals. In principle, there are two possible scenarios: quasicrystals may either be true ground states of the many-particle Hamiltonian, and hence *energetically* stabilized (which means that they are thermodynamically stable at arbitrarily low temperatures), or they are high-temperature phases that are stabilized by *entropic* contributions to the free energy. In the latter case, which is tentatively favored by experimental results [3,4,36], the question of disorder in quasicrystals is crucial, since disorder provides entropy. Examples are, for instance, defects and vacancies (as also frequently observed in crystals), configurational disorder (which can be de-

scribed by randomizing the ideal quasiperiodic tiling, resulting in random tiling models) or chemical disorder (which emerges by interchanging atomic positions between different atomic species). Arguably, all of these sources of entropy appear in quasicrystals, and there is experimental evidence that the description of quasicrystals as random tilings may be more appropriate than those based on ideal quasiperiodic tilings [46]. Most of the models in the literature therefore do not describe the growth of ideal structures, but rather try to grow tilings incorporating defects, or structures resembling random tilings.

This review is organized as follows. First, we concentrate on ideal quasiperiodic tilings, discussing the possibility of growing ideal Penrose tilings as an example. This will also clarify the question of non-locality in ideal quasiperiodic growth. After that, we will briefly address the basic problem of random growth models. Subsequently, a number of semi-realistic growth models are discussed that try to mimic the growth of defective quasiperiodic structures in different ways. We distinguish four different classes of growth models altogether, but we would like to stress that our somewhat arbitrary distribution of models into these groups serves mainly presentational purposes and is not meant as a real classification.

The first group consists of what we refer to as "atomistic" growth models, where single "atoms" are added to the growing cluster according to certain conditions. The second class contains (algorithmically motivated) "cluster-based" models, where the aggregation is driven by the requirement that certain preferred cluster configurations have to be completed. After this, we address more physically motivated cluster-based models, so-called "orientational glasses", which are random packings of (symmetric) building blocks preserving relative orientations, and hence show orientational order. The last group of growth models in our list is based on the random tiling idea, starting from a fixed set of tiles. Finally, we conclude and give an outlook on future developments.

9.2 Growing Ideal Penrose Tilings

There has been a lively debate on the possibility of purely local growth algorithms for ideal quasiperiodic tilings (their inherent non-locality was first pointed out by Elser [11]), particularly after Onoda et al. [49] found an algorithm for the Penrose tiling and claimed that it was local [30,50,106]. In what follows, we shall discuss this algorithm, occasionally referred to as the "OSDS rules", in some detail; cf. also [6,61,62].

As one may have guessed from our introductory comments, the algorithm is based on the matching rules for the Penrose tiling. These *perfect* matching rules [2] are most easily described in terms of two different types of arrows ("single" and "double" arrows) assigned to the edges of the two rhombs ("fat" and "thin" rhombs) as shown in Fig. 9.1. Starting with some initial patch, one

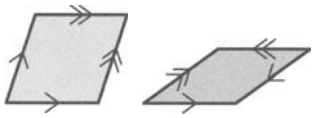

Fig. 9.1. The Penrose rhombs with arrow decorations

successively adds single tiles to the surface, obeying the matching rules. But, as mentioned above, this is not sufficient – in general, sooner or later, one arrives at a situation in which a certain surface vertex cannot be completed without violating the matching rules.

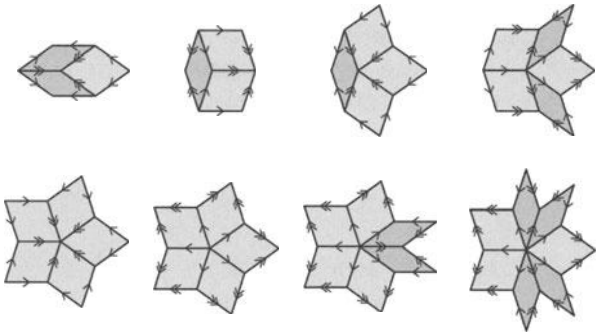

Fig. 9.2. The eight vertex configurations of the Penrose tiling

Thus, one has to be more careful about adding tiles, and in the OSDS rules, going back to a suggestion of Gardner [16], this is achieved by distinguishing two kinds of tile additions: so-called "forced" and "unforced" tiles. As the name suggests, the first kind of addition is one where there is only a *single* possibility of adding a tile (in general, there will be two) at this location without creating a vertex configuration that is not allowed in an ideal Penrose tiling (there are only eight such configurations; see Fig. 9.2).

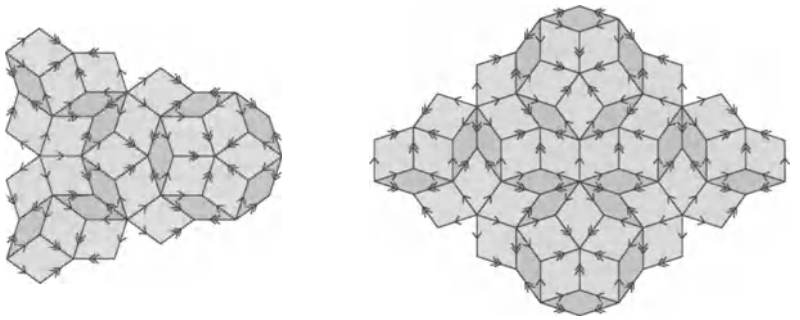

Fig. 9.3. Two examples of a dead surface

Growth according to the OSDS rules now proceeds in two sequential steps. In the first step, one only adds forced tiles at randomly chosen positions, until the entire surface consists of unforced vertices, i.e. incomplete vertices at which no additions are forced. Such surfaces are termed "dead surfaces": two small examples are shown in Fig. 9.3. There exist dead surfaces of arbitrary size that can be cataloged exhaustively [61].

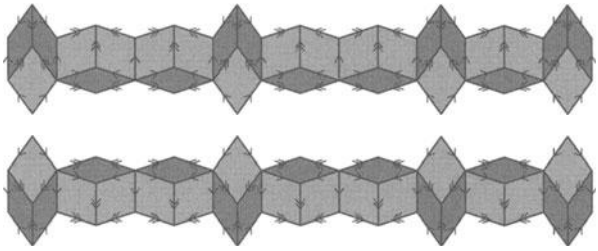

Fig. 9.4. Two worm segments related by a flip

Along the flat parts of a dead surface, one may add segments of so-called "worms" which consist of a linear chain of the two hexagons that contain three rhombs (Fig. 9.4), arranged in a Fibonacci sequence [54]. The complete worm can be "flipped" without affecting the form or arrow decoration of its surface; hence it fits on the dead surface in both orientations (see Fig. 9.5 for an example).

While this shows the freedom that one has to continue the growth process, simply adding worm segments of arbitrary orientations to a dead surface can lead to inconsistencies (there are "dangerous faces" of the dead surface), which may only show up after the addition of many more tiles [54]. Thus, in order to avoid this, one has to formulate a more restrictive rule for adding

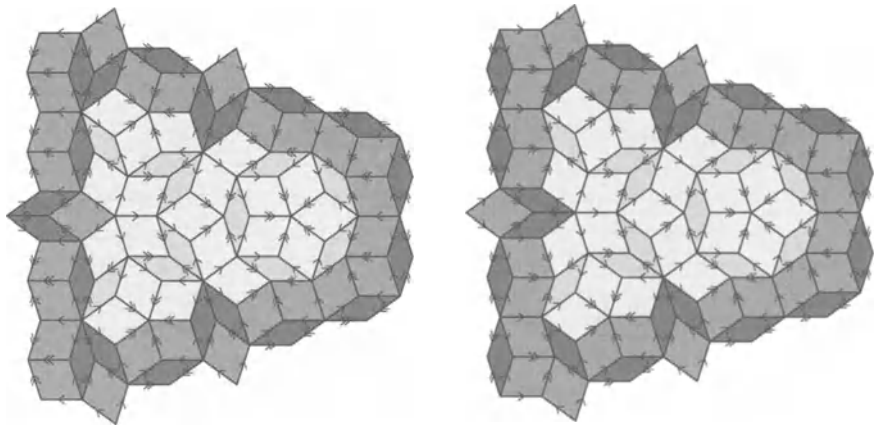

Fig. 9.5. Two possible extensions of a dead surface by worm segments

the next tile, and the second OSDS rule states that one should add a "fat" rhomb at either side of an 108° corner of the dead surface, consistent with the vertex set of Fig. 9.2. This gives one possible rule that ensures that one never encounters inconsistencies [61]. Note that any dead surface has at least two 108° corners, except for certain degenerate cases in which two such corners merge to form a 36° corner.

How does non-locality in growth manifest itself? The crux is hidden in the two-step process: in order to avoid mistakes, one first has to complete a dead surface before making an unforced choice. However, this implies that one has to inspect the *entire* surface of the patch. In other words, vertices at arbitrarily large distance have to be visited as the patch grows. In this sense, the OSDS growth algorithm is clearly non-local [30,48,106]. Beyond this, it is generally not possible to judge locally whether or not an unforced choice will yield inconsistencies [54].

However, it is indeed possible to derive a fully local algorithm if one is willing to pay the price of defects, for instance, by allowing unforced choices with a very small probability. In this way, tilings with an arbitrarily low defect rate (depending on the chosen probability) can be grown. However, the growth of the tiling shows a rather strange time-dependence [58]: while forced tiles are added very quickly, growth becomes completely stalled when a dead surface is approached. Only after an unforced tile is chosen does rapid growth commence again. A number of more general growth rules, allowing defects of various types, were investigated in [51].

Let us close the discussion of ideal tiling growth with two remarks. The first is a warning concerning dead surfaces. It is by no means the case that nothing outside a dead surface is determined by the ideal structure – in general, large parts of the tiling beyond the worm segment are already fixed. The second remark concerns special kinds of defects, so-called "decapods", which are decagons that cannot be filled without violating the matching rules. Starting from such a defect as an initial patch for the growth, one never encounters a dead surface, and forced growth of an (otherwise) ideal structure continues indefinitely [61].

9.3 Growth in the Random Scenario

Beyond the essentially deterministic growth of ideal tilings, non-locality usually poses no problem (for exceptions, refer to Sect. 9.7). Instead of restrictive matching rules, one has to fulfill simple geometric constraints that guarantee symmetry, face-to-face conditions, etc. New atoms, clusters or tiles can be attached to the growing surface using purely local information depending only on a limited number of neighboring objects. The choices in the growth process correspond to the configurational entropy of the system.

Nevertheless, this scenario also has its drawbacks [37,59]. The surface aggregation suffers from a memory effect that generates a considerable rise

in the background strain of the "internal" (also referred to as "orthogonal", "perpendicular" or "phason") coordinates, a so-called phason strain. This terminology refers to the embedding into higher-dimensional space [2,21,67]. In fact, the corresponding phason fluctuations become size-dependent for three-dimensional (3D) quasicrystals. In practice, this means that a grown system shows strong *systematic* deviations from both ideal structure types (ideal quasiperiodic tilings and equilibrium random tilings) rather than the desired random fluctuations in the phason field alone. The behavior can be modeled by a classical Ginzburg–Landau–Langevin equation for the coarse-grained phason field $\Phi(r, z)$,

$$\frac{\partial \Phi(r,z)}{\partial z} = \mathcal{D}\frac{\partial^2 \Phi(r,z)}{\partial r^2} + \rho(r,z)\,, \tag{9.1}$$

where z is the growth direction, r are the surface coordinates, $\rho(r, z)$ represents a δ-correlated noise term and $\mathcal{D}$ is the phason-diffusion constant. This diffusion equation leads to an asymmetry in the fluctuations of the phason coordinates and hence in the spectral density. The intensities of the Fourier spectrum of a grown 3D quasicrystal thus show a power-law decay; the fluctuations of the internal coordinates diverge logarithmically. Altogether, one ends up with an effective "$D - 1$ model", i.e. the system grown in D physical dimensions behaves like a $(D - 1)$-dimensional equilibrium system. For details, we refer to [59] and the overview [21].

Most of the growth models discussed below belong to this class. Although divergent phason fluctuations have been reported for relatively-poor-quality quasicrystals, this is clearly not the case for very-high-quality quasicrystals. On the other hand, the quality of even the best samples benefits from annealing procedures, which means that internal rearrangements over time, after the quasicrystal is first grown, tend to increase the structural order. A possible scenario for avoiding diverging phason strains is discussed in Sect. 9.7.

9.4 Atomistic Growth Models

Envisaging physical growth, the simplest model description grows a cluster atom by atom, for instance, by a diffusion-limited aggregation process. In view of the peculiar properties of quasiperiodic structures, this approach appears to be problematic, because it is difficult to find simple assumptions (for example, on interaction potentials) that will result in the growth of a quasicrystal rather than a periodic or a disordered structure. Monte Carlo investigations hint at the possibility of stable quasicrystalline order; see, e.g., [68] for a two-component system with Lennard–Jones pair potentials. In fact, the models discussed below solve the problem by restricting the possible positions where new atoms may be added to the growing cluster, in this way trying to enforce non-crystallographic symmetries or, at least, preventing simple periodic arrangements. In some cases, these assumptions may appear

rather artificial and hence unphysical. Clearly, as for all models based on random aggregation processes, one cannot expect to grow ideal quasiperiodic systems, but rather more or less disordered structures; and the degree of disorder present in the grown samples gives a first test of the relevance of the model.

The earliest model of this kind was inspired by the binary decoration of Penrose rhombs with two sizes of atoms. Equilibrium states of this system had been studied [40,68]. In a very simple growth model [43,66], atoms may stick to certain positions determined by the tile decoration [40]. After being added to the growing cluster, atoms remain frozen in their positions. The growth is forced to proceed "layer by layer", new positions being taken into consideration only after a full surface layer has been completed. The possible sticking places for atoms are ordered according to an energy that is a sum of pairwise contributions from neighboring atoms ("growth-priority parameters"), the available sites being filled successively according to this ordering. In this way, the only freedom occurs when several such places are degenerate in energy, in which case a random choice is made. As one might expect from such a simplistic model, the outcome is not very close to a realistic quasicrystalline structure. In most cases, the growing cluster generates "tears". However, for certain ranges of the energy parameters, the layer-by-layer growth results in dense structures without holes or tears [66] (we want to avoid the term "perfect structures" [66], since it is prone to misinterpretation). However, these grown samples resemble multiply twined crystalline structures much more than quasicrystals, showing huge local anisotropies.

Olami's growth model [48] follows a somewhat different strategy. It starts from a small cluster of points from an ideal quasiperiodic set, which in this case is not the Penrose tiling, but a simpler pentagonal tiling obtained by projection. In such a finite patch, there will be straight lines in the pentagonal directions ("pentagonal lines") that pass through a number of points in the set. As possible positions of new points, only intersections of such pentagonal lines are considered; and a point is added on a randomly chosen intersection of pentagonal lines if, in fact, it falls on at least four lines. In addition, there is a rule that avoids short distances, discarding the point with the smaller "line number" if a new point comes too close to an existing point in the set (in the case in which the maximum number, i.e. five, pentagonal lines pass through both points, both are kept). These growth rules are fully local, depending only on the environment of a chosen point up to a distance that is at most τ^3 times the minimum distance between two points along a pentagonal line in the ideal structure (τ is the golden mean). Provided that one starts with a sufficiently large initial cluster (of about 30–100 points), one can grow large patches with rather small fluctuations in the phason coordinates, resulting in very narrow diffraction peaks in the Fourier transform. Furthermore, the phason fluctuations grow extremely slowly with increasing system size, and the numerical data from five grown patches with up to 2×10^4 points suggest

that they may stay bounded. In principle [48], a similar growth procedure could also be applied to the Penrose tiling. Due to the more complex shape of the acceptance domain, one expects that grown patches will have larger disorder than in the simpler pentagonal case.

As the last example in this category, we discuss the dodecahedral local ordering (DLO) model [7] for the growth of icosahedral quasicrystals. Here, DLO means that all closest neighbors of an atom are positioned at a subset of the vertices of a regular dodecahedron. Such a local ordering may result from a close packing of two kinds of atoms with different sizes. Again, once stuck to the cluster, atoms are frozen and cannot move or be removed from the growing cluster. Starting from a seed of about 3–50 atoms, trial positions at all vertices of regular dodecahedra around all atoms are taken into account. The position for a new atom is then selected by an energy that is a sum of contributions for each atomic bond, depending only on atomic distances. The energy parameters are chosen [7] such that frustration between short- and medium-range interatomic forces results, mimicking oscillating interatomic potentials. In this way, the growth of crystalline structures is suppressed. Although the energy of a position can be obtained locally, the whole surface must be inspected to find the position of minimal energy. Figure 9.6 shows an

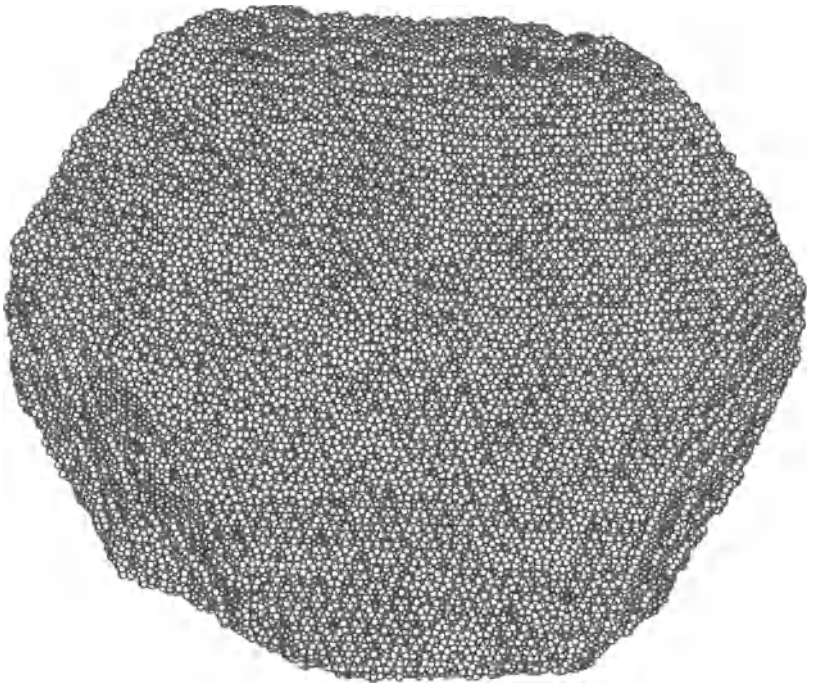

Fig. 9.6. View along a threefold axis of a DLO grown cluster of about one million atoms (courtesy of V. Dmitrienko)

example of a large cluster grown with these rules. The obtained samples are faceted, they have a face-centered icosahedral structure and their phasonic disorder depends on the particular interatomic potentials.

9.5 Algorithmically Motivated Cluster Growth Models

The importance of clusters for the understanding of the structure and the physical properties of quasicrystals was recognized immediately after their discovery; but particularly over the past few years there has been increasing research activity on a cluster-based description of quasicrystals [9,28,31]. While, at first, this may seem to be in conflict with the tiling picture, this is clearly not the case. On the one hand, one may decorate tilings such that certain atomic clusters are predominant in the local arrangements of atoms. On the other hand, at least some quasiperiodic tilings – such as, for instance, the Penrose tiling – can alternatively be described in terms of a covering of space by a *single* cluster [10,19,20]. That is, in contrast to the tiling picture, only a single tile is used, but different kinds of overlaps may occur. For the example of the Penrose tiling, it has been shown that a suitable restriction on the possible overlaps of regular decagons is in fact equivalent to the perfect matching rules. The corresponding picture of a quasicrystal is physically very attractive, as one may imagine the quasicrystal as sort of a densely packed conglomerate of very stable clusters. Recently, it was argued that a quasicrystalline structure may even result from a *maximization* of certain cluster configurations [15,23,32,63], which may also give some new insight into quasicrystal formation. The growth models considered here are of a different nature – they are based on the addition of single "atoms" guided by conditions that certain cluster configurations have to be completed. In this sense, they are in fact "atomistic" models. However, the role of clusters as the fundamental entities of the structure is strongly pronounced, which is the reason why we want to consider them separately.

The first model that we want to mention here, the so-called decahedral-recursive (DR) model [1,56,57] bears, in a sense, some similarity to the DLO model [7], but it is more closely tied to the cluster idea. According to the DR model, the growth proceeds in two steps. First, there is a "decahedral stage", in which atoms are added to an initial seed (which the authors chose to be magic number clusters of atoms, known to be particularly stable) such that they complete irregular decahedra (pentagonal bipyramids). This process is carried out with atoms of one size until, due to geometric frustration, it becomes necessary to use a second type of somewhat (about 5 %) smaller atoms; hence at least two atomic species are required. Note that frustrations necessarily appear due to the different lengths of the edges and the outer radius of an icosahedron (dodecahedron). During this growth, certain atomic positions ("O points") on the surface occur that may act as new nucleation centers. These are located at the centers of (distorted) icosahedra. These O points

have the property that, shifting the whole cluster into them, a large number of coincidences are created. This is exploited to enlarge the cluster further (discarding overlapping atoms), until one arrives at particular O points ("nodes") which give rise to a larger percentage of coincidences than others. The cluster obtained in this way is considered to be the "basic cluster" of the structure, and further growth proceeds by shifting this basic cluster into its nodes, which maximize the fraction of coinciding atomic positions. Thus, the grown structure may be thought of as a packing by overlapping copies of the basic cluster. The DR model can, in principle, lead to quasicrystalline (in particular, decagonal and icosahedral) and to crystalline approximant structures, depending heavily on the initially chosen seed. The DR growth process can be interpreted in terms of a cut-and-projection scheme with a peculiar window function, and the diffraction pattern of DR structures consists, in general, of Bragg peaks together with a diffuse background.

The second model in this category, proposed recently [29], is much simpler than the DR model. Here, growth commences from a given seed that determines a "star" of atomic bondings, for instance, a decagonal star if the initial cluster is a decagon with one atom in its center. This vector star then defines the only possible translations, relative to the surface atoms, for adding new atoms to the cluster. Growth through the star short-distance scheme (SSDS) then proceeds as follows. Choosing an arbitrary surface atom, atoms forming a shifted copy of the basic initial cluster are added around it. Those of the new atoms that are too close to already existing sites (the allowed minimum distance is a parameter of the model) are rejected. Due to the randomness in the choice of the surface atom, this leads to a family of slightly different structures. Details of the possible structures, and their dependence on the choice of the star and the short-distance threshold, are still to be investigated; but it has already been shown that also twined crystals may result.

9.6 Physically Motivated Cluster Growth Models

While the previously presented models use structureless "atoms" to build up the growing cluster, we now turn to models whose building blocks already contain information about the symmetry. More specifically, the orientational models discussed below are random arrangements of symmetric building blocks (regular decagons or icosahedra) subject to certain constraints on relative orientations and distances.

The idea of such a model goes back to Shechtman and Blech [60]. They tried to explain the observed diffraction patterns of icosahedral quasicrystals by describing their structure as random packings of icosahedra, joined along their edges or at their vertices while preserving orientational symmetry. Even though their clusters were rather small (containing about 1000 icosahedra), the computed diffraction pattern of the vertex-connected random packing gave reasonable qualitative agreement with experimental results.

This idea was followed up by Stephens and Goldman [65] (see also the review [64]). Besides vertex- and edge-connected "icosahedral glasses", they also considered face-connected packings. In particular, they investigated the size-dependence of the peak widths, performing simulations of up to 109 454 sites in a sample of cubic shape. The intrinsic peak widths that they obtained turned out to be very small and comparable to those observed experimentally for icosahedral AlMn. For the majority of peaks, the cluster size was still insufficient to resolve the internal width.

Although these results look quite encouraging, the simple models based on non-interpenetrating random packings of clusters are unrealistic in several aspects [55]. First, their density is far too low – only about 60 % of the bcc packing density. Another, unrelated problem is the low, filamentary connectivity of the cluster network. Even reasonably connected networks were found to be broken up into domains by "tears". Accordingly, the phason components behave rather irregularly, and there is a large increase in the phason fluctuations with growing patch size. Finally, the peak positions and the peak shapes calculated from the grown samples do not agree with experimental powder diffraction patterns of higher-quality quasicrystals.

Clearly, to improve the situation, one wants to increase connectivity and suppress the generation of tears. Prior to [55], Elser [12–14] and Nori et al. [47] had already discussed a scenario that strongly improves the quality of the grown clusters. The main idea, first introduced [12] for a 2D random packing model of regular decagons, consists of introducing a finite temperature into the growth process, thus allowing rearrangements close to the surface of the growing sample. More precisely, Elser distinguishes a "growth region" with a non-uniform temperature field, and a "frozen" region in which no further rearrangements are allowed. A lattice gas Hamiltonian with pairwise interactions, including a next-nearest-neighbor term, was chosen to facilitate the formation of nicely connected networks. In particular, the allowed cluster–neighbor relationships were taken from observed approximant phases. The quasicrystal was grown, starting from a single seed, by moving the growth region with its linear temperature profile with constant velocity, and applying a Monte Carlo procedure to the lattice gas Hamiltonian. The whole procedure easily translates to the icosahedral case, and simulations [13,14] show that this growth mechanism, with suitable choices of the parameters, produces well-packed, icosahedrally ordered structures, with intrinsic phason fluctuations that are in good agreement with the behavior of peak widths observed in diffraction experiments. However, due to the anisotropy of the growth conditions, a small but finite phason strain cannot be avoided.

A somewhat different route was followed by Robertson and Moss [55], imposing additional local constraints on the neighborhood of an icosahedron, in this way trying to suppress the formation of tears and to increase the connectivity. The main idea consists of allowing a cluster to have only a discrete set of neighbor distances within its local environment of a certain

size. By suitably tuning their parameters, Robertson and Moss reach packing fractions and connectivities that are comparable to Elser's, but they also find a remaining phason strain that does not seem to vanish with increasing system size.

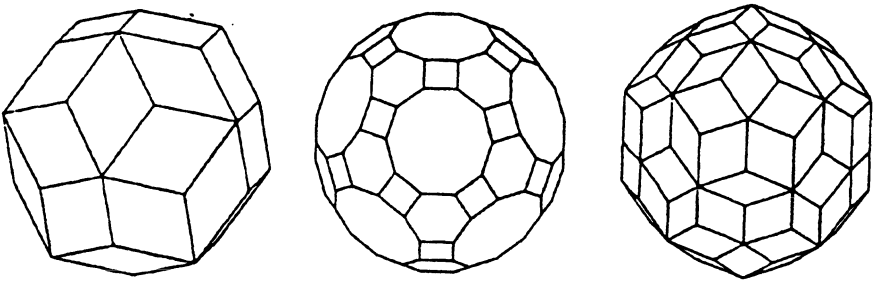

Fig. 9.7. Simple equilibrium shapes of icosahedral bond-oriented glasses (reproduced from [25] with permission, copyright: the American Physical Society 1987)

Finally, we would like to point out that facet formation is not just a characteristic of crystals or ideal quasiperiodic tilings, but may also occur in random tilings and certain classes of bond-oriented glasses (see [24–26,41] for discussions of the possible $T = 0$ equilibrium shapes of systems with icosahedral symmetry). Some simple examples are shown in Fig. 9.7.

9.7 Random Tiling Growth Models

Soon after ideal quasiperiodic tilings came into fashion as geometric models of quasicrystals, Elser [11] pointed out that one may relax the mathematical constraints of these tilings without losing their most important features, such as, for instance, their sharp diffraction peaks. This remark led the way to the so-called random tiling theory [21], where tiles are packed randomly without gaps or overlaps. In a hydrodynamic description, elastic constants and configurational entropy were introduced. The new degrees of freedom were (by analogy with modulated crystals) called phasons, which are long-wavelength modes of the orthogonal coordinates of the quasicrystal. The differences between the physical properties of these random tilings compared to those of the ideal quasiperiodic ones – although mathematically essentially different – are so small that even today it is hard to distinguish between them experimentally [3,4,34,36]. The local character of the random tiling scenario made it attractive for growth modeling, having in mind a cluster decoration of the tiles or the vertices.

Inspired by the structural similarity between the dodecagonal and the σ phases of VNi and VNiSi alloys (which can be described as a periodic net of

squares and equilateral triangles), Kuo et al. [39] considered a growth model of dodecagonal quasicrystals based on the same building blocks, i.e. a square–triangle random tiling. The ensemble consists of squares and equilateral triangles only [52]. The growth process proceeds by attaching complete tiles to a seed following three rules: (1) only the two tiles considered above are used, (2) squares prefer triangles on all sides and (3) when two triangles face each other they are surrounded by four squares. Whereas rules (1) and (2) – according to the authors – yield a modified random tiling with motifs very similar to those found in high-resolution transmission electron microscopy (HRTEM) images of dodecagonal phases, the addition of rule (3) results in a periodic σ phase.

In order to obtain a 3D icosahedral random tiling with two linkages and a high packing density, Henley [22] developed the so-called canonical cell tiling (CCT). Its tiles are two irregular tetrahedra, one irregular square–pyramid and one equilateral prism. Unfortunately, the CCT is much harder to treat than the primitive icosahedral tiling [38]. Motivated by transfer matrix techniques, a method to produce towers of CCTs with periodic boundary conditions in two dimensions was introduced [45], which resembles a growth model. Starting on a layer of canonical cells which span the entire cross-section, new vertices of the canonical cells are constructed, without gaps or overlaps, respecting the boundary conditions. In order to avoid wrong moves and to save computer time, preference is given to the deepest lying vertex (w.r.t. the surface). For the majority of such growing surfaces, there is at least one move that is forced by the surrounding geometry. Following the forced moves, one ends at *locally* dead surfaces where every crevice can be filled at least in two different ways. Here, one has to make a choice to proceed. The surface is only locally dead, i.e. in some cases one ends up with a defective vertex later on. The catalog of these dead surfaces is the key feature in the derivation of estimates of the elastic and entropic properties of the CCT [44]. The appearance of forced moves and dead surfaces reminds one of the growth algorithm for the ideal Penrose tiling described in Sect. 9.2. However, the canonical cells do not have matching rules, and their possible arrangements contain a finite entropy density.

Motivated by the question of how close one can approach an *equilibrium* random tiling via a growth process, Joseph and Elser [35] took a different approach to the square–triangle random tiling. To every vertex i of a tiling, two variables are associated: a uniform chemical potential μ and an angle variable Ω_i. The chemical potential describes the energy difference of a bulk vertex relative to the liquid/vapor phase. The angle Ω_i mimics the influence of the surface: it is simply the portion of the full angle around a vertex that is covered by already completed tiles. Both enter a simple Hamiltonian

$$H = \sum_i (\mu - \Omega_i)\,, \tag{9.2}$$

where the sum extends over all vertices of the tiling. In this way, each bulk vertex has an energy of $\mu - 2\pi$, whereas surface vertices have energies of $\mu - 2\pi n/12$ with $n = 0, 2, 3, 4, \ldots, 9$ (the case $n = 10$ does not occur because the "missing" triangle is always complete, and hence the corresponding vertex belongs to the bulk). Attaching or removing vertices gives rise to a change in bulk and surface energies. The system will try to minimize its surface with respect to the bulk. Using (9.2) as a penalty function in a Monte Carlo simulation, the authors proposed the first *reversible* growth model with a fluctuating surface, i.e. vertices may be attached or removed, and detailed balance is always fulfilled. In the case of the square–triangle tiling, the geometric constraints were minimal: the minimal distance between vertices is given by the bond length, and completed tiles may only be squares or equilateral triangles, while their relative frequency may vary freely.

Starting from a seed, on the plane or a cylinder, Joseph and Elser [35] derived a growth/melting boundary of the form $\mu = 2\pi + TS_0$, where S_0 is the entropy of the equilibrium system. The temperature T enters the simulation through the Boltzmann factor of the Monte Carlo simulation. In this way, it is possible to measure equilibrium properties of a system via a non-equilibrium process such as growth. For a given temperature $T < 2\pi/3$, the system develops tears for all $\mu < 2\pi + TS_0$; and their separation λ_{tear} follows a scaling law

$$\lambda_{\text{tear}} \sim (2\pi + TS_0 - \mu)^{-1} \tag{9.3}$$

that is predicted by a phason instability at the surface. Furthermore, the model shows that the asymmetry in the phason fluctuations (see Sect. 9.3) vanishes when approaching the growth limit. Therefore, in the limit of vanishing growth velocities (i.e. $\mu \to 2\pi + TS_0$), it is possible to produce a grown random tiling that is, on a given length scale, indistinguishable from a member of the equilibrium ensemble. When approaching the growth limit, the system must exploit all of its entropy to grow at all. Thus, it must align its phason strain closer and closer to zero. In practice, the system is growing and retreating repeatedly until large, accidental phason fluctuations are erased. Using this property, even the modeling of surface annealing is possible [33].

The extension to other tilings is straightforward. In Figs. 9.8 and 9.9, we show two cylindrical patches of the unrestricted ten-fold rectangle–triangle random tiling [5], grown at different growth velocities. Although this tiling ensemble can be treated by Bethe-ansatz methods [17], it has not yet been understood in terms of the conventional random-tiling description [53]. On the other hand, a restricted (binary) version of this tiling, which is used to model the decagonal phase of AlPdMn [53], can be treated with random tiling theory without problems. However, it shows a growth instability due to its binary restriction, which acts as a non-local constraint on the tiling ensemble [33]. Hence growth without leaving the ensemble appears impossible.

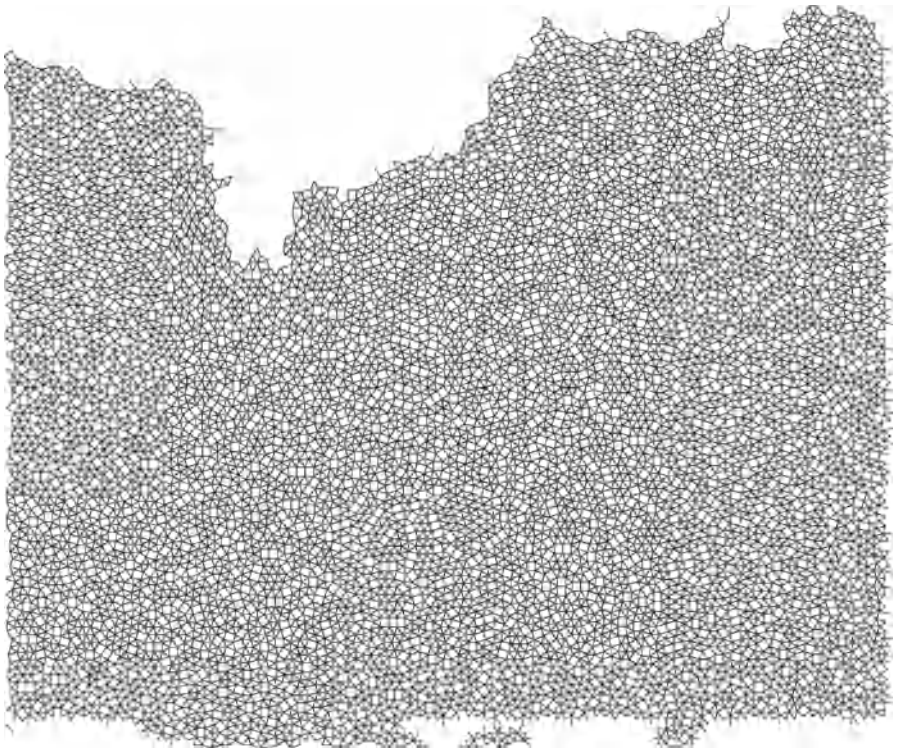

Fig. 9.8. The unrestricted ten-fold rectangle–triangle tiling grown according to the model of Joseph and Elser [35] at temperature $T = \pi/2$ with chemical potential $\mu = 2\pi + 0.160\pi/2$ (rapid growth). For this case, the growth/melting boundary is $\mu \approx 2\pi + 0.175\pi/2$ [17]

The model [35] shows that, in principle, there is no need for collective bulk rearrangements after growth, and that uniform phason strains can be made arbitrarily small on macroscopic length scales. Usually, bulk rearrangements (in the form of flips, zippers, etc.) are needed to approach equilibrium, but they can be kinetically very slow.

9.8 Concluding Remarks

To date, it is fair to state that the growth of quasicrystals has not been understood, and there is still a lot of work to be done in order to arrive at a physical picture of the growth process that can account for the experimental observations. It appears impossible to grow ideal quasiperiodic structures by purely local algorithms without incorporating a certain amount of defects. The structure of quasicrystals may be better described in terms of random

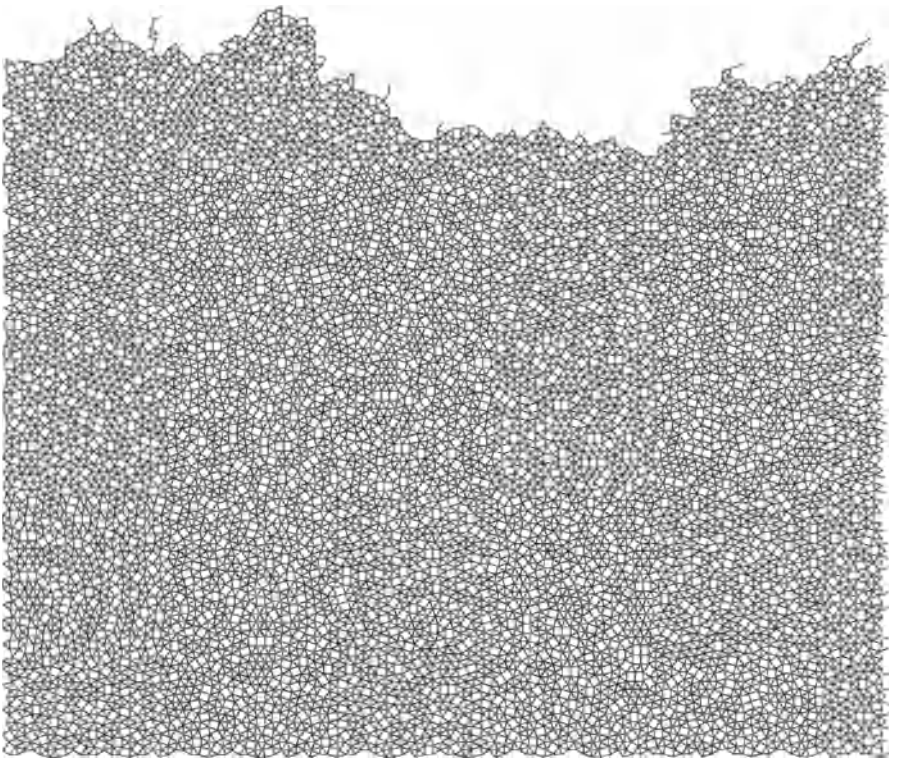

Fig. 9.9. Same as Fig. 9.8, but for $\mu = 2\pi + 0.174\pi/2$ (slow growth)

tilings (or other models including a stochastic component), which points at the importance of entropic contributions in the formation of quasicrystals.

As we have demonstrated, there are a number of different approaches towards an understanding of quasicrystal growth. Most models concentrate on the question of how quasiperiodic order is established, using a greatly simplified set of degrees of freedom. Clearly, some remnants of the orientational symmetry are already implicit in all these models, for instance, by allowing only certain atomic positions or directions of atomic bonding. In this sense, the long-ranged orientational order in the grown samples is not surprising. What one really would like to see is a more pronounced order of atomic positions that can account for the sharp diffraction peaks observed in experiments. The question of whether quasicrystals can be grown by local deposition of atoms of different species or by attachment of pre-formed clusters alone remains to be attacked.

Almost all of the models discussed above employ non-reversible dynamics in their growth algorithms. Usually, this is said to be motivated by the rapid quenching processes used to produce quasicrystals, particularly in the early

days (many quasicrystals are still produced by melt-spinning, with quenching rates of about 10^5 K/s, but these samples contain many defects; and only after annealing at about 20–50 K below their melting point do they become "good" quasicrystals). However, the current picture of growth for crystals suggests diffusion and fluctuation processes on the surface during growth. There is no reason to believe that quasicrystals are different in this respect. In our view, this is probably the reason why most of these models suffer from large anisotropies or phason fluctuations, creating structures that are far from ideal quasicrystals or equilibrium random tilings. Introducing temperature, and allowing reorganization to occur at least at the surface, the growing bulk is given the possibility to reconnoiter the configurational phase space, making full use of its entropy. In this way, structures that resemble equilibrium random tilings may be realized by a physical growth process.

Finally, we emphasize that the inflation properties of quasiperiodic structures allow, in principle, for several physical interpretations of these models (e.g. "atoms" in what we call atomistic models may be thought of as real atoms, but equally well may be considered as clusters containing groups of atoms, or even clusters of such clusters). Thus, rather simplistic models might also well capture the important ingredients that render possible the formation of quasicrystals.

Note Added in Proof

After completion of this review, Dmitrienko et al. [8] published a modified version of the growth model discussed in Sect. 9.4 [7]. They replaced the non-local energy minimization by a local Monte Carlo step.

Acknowledgments

We would like to thank M. Baake, V. Elser, P. Gummelt, C.L. Henley, R. Lück and J.-B. Suck for valuable comments. Furthermore, we are obliged to V.E. Dmitrienko and T.L. Ho for allowing us to include their figures in this review. Financial support from DFG and NSF (Grant No. DMR-9412561) is gratefully acknowledged.

References

1. Aragón J.L., Romeu D., Gómez A. (1991): Phys. Rev. B **44**, 584
2. Baake M. (2002): See Chapter 2 of this book
3. de Boissieu M., Boudard M., Hennion B., Bellissent R., Kycia S., Goldman A., Janot C., Audier M. (1995): Phys. Rev. Lett. **75**, 89
4. Boudard M., de Boissieu M., Letoublon A., Hennion B., Bellissent R., Janot C. (1996): Europhys. Lett. **33**, 199

5. Cockayne E. (1995): Phys. Rev. B **51**, 14958
6. DiVincenzo D.P. (1997): In *The Mathematics of Long-Range Aperiodic Order* (NATO ASI C 489), ed. R.V. Moody, Kluwer, Dordrecht, p. 127
7. Dmitrienko V.E., Astaf'ev S.B. (1995): Phys. Rev. Lett. **75**, 1538
8. Dmitrienko V.E., Astaf'ev S.B., Kléman M. (1999): Phys. Rev. B **59**, 286
9. Dubois J.-M., Janot C. (2002): See Chapter 8 of this book
10. Duneau M. (1995): In *Quasicrystals*, ed. C. Janot, R. Mosseri, World Scientific, Singapore, p. 116
11. Elser V. (1985): Phys. Rev. Lett. **54**, 1730
12. Elser V. (1987): In *Proc. XVth Int. Coll. on Group Theoretical Methods in Physics* (Vol. 1), ed. R. Gilmore, D.H. Feng, World Scientific, Singapore, p. 162.
13. Elser V. (1988): In *Fractals, Quasicrystals, Chaos, Knots and Algebraic Quantum Mechanics*, ed. A. Amman, L. Cederbaum, W. Gans, Kluwer, Dordrecht, p. 121
14. Elser V. (1989): In *Extended Icosahedral Structures* (Aperiodicity and Order, vol. 3), ed. M.V. Jarić, D. Gratias, Academic Press, San Diego, p. 105
15. Gähler F., Jeong H.-C. (1995): J. Phys. A **28**, 1807
16. Gardner M. (1977): Sci. Am. **236**, 110
17. de Gier J., Nienhuis B. (1998): J. Phys. A **31**, 2141
18. Grimm U., Schreiber M. (2002): See Chapter 3 of this book
19. Gummelt P. (1995): In *Quasicrystals*, ed. C. Janot, R. Mosseri, World Scientific, Singapore, p. 84
20. Gummelt P. (1996): Geom. Ded. **62**, 1
21. Henley C.L. (1991): In *Quasicrystals: The State of the Art*, ed. D.P. DiVincenzo, P.J. Steinhardt, World Scientific, Singapore, p. 429
22. Henley C.L. (1991): Phys. Rev. B **43**, 993
23. Henley C.L. (1998): In *Proc. 6th Int. Conf. Quasicrystals*, ed. S. Takeuchi, T. Fujiwara, World Scientific, Singapore, p. 27
24. Ho T.L. (1991): In *Quasicrystals: The State of the Art*, ed. D.P. DiVincenzo, P.J. Steinhardt, World Scientific, Singapore, p. 401
25. Ho T.L., Jaszczak J.A., Li Y.H., Saam W.F. (1987): Phys. Rev. Lett. **59**, 1116
26. Ho T.L., Li Y.H., Saam W.F., Jaszczak J.A. (1989): Phys. Rev. B **39**, 10614
27. Holland-Moritz D. (2002): See Chapter 11 of this book
28. Janot C., de Boissieu M. (1994): Phys. Rev. Lett. **72**, 1674
29. Janot C., Patera J. (1997): Phys. Lett. A **233**, 110
30. Jarić M.V., Ronchetti M. (1989): Phys. Rev. Lett. **62**, 1209
31. Jeong H.-C., Steinhardt P.J. (1994): Phys. Rev. Lett. **73**, 1943
32. Jeong H.-C., Steinhardt P.J. (1997): Phys. Rev. B **55**, 3520
33. Joseph D. (1998): Phys. Rev. B **58**, 8347
34. Joseph D., Baake M. (1996): J. Phys. A **29**, 6709
35. Joseph D., Elser V. (1997): Phys. Rev. Lett. **79**, 1066
36. Joseph D., Ritsch S., Beeli C. (1997): Phys. Rev. B **55**, 8175
37. Kalugin P. (1998): Private communication
38. Kramer P., Neri R. (1984): Acta Crystallogr. A **40**, 580
39. Kuo K.H., Feng Y.C., Chen H. (1988): Phys. Rev. Lett. **61**, 1740
40. Lançon F., Billard L., Chaudhari P. (1986): Europhys. Lett. **2**, 625
41. Lei T., Henley C.L. (1991): Phil. Mag. B **63**, 677
42. Markov I.V. (1995): *Crystal Growth for Beginners: Fundamentals of Nucleation, Crystal Growth and Epitaxy*, World Scientific, Singapore

43. Minchau B., Szeto K.Y., Villain J. (1987): Phys. Rev. Lett. **58**, 1960
44. Newman M.E.J., Henley C.L. (1995): Phys. Rev. B **52**, 6386
45. Newman M.E.J., Henley C.L., Oxborrow M. (1995): Phil. Mag. B **71**, 991
46. Nissen H.-U., Beeli C. (2002): See Chapter 6 of this book
47. Nori F., Ronchetti M., Elser V. (1988): Phys. Rev. Lett. **61**, 2774
48. Olami Z. (1991): Europhys. Lett. **16**, 361 and J. Phys. (France) I **1**, 42
49. Onoda G.Y., Steinhardt P.J., DiVincenzo D.P., Socolar J.E.S. (1988): Phys. Rev. Lett. **60**, 2653
50. Onoda G.Y., Steinhardt P.J., DiVincenzo D.P., Socolar J.E.S. (1989): Phys. Rev. Lett. **62**, 1210
51. Ophuysen G. van, Weber M., Danzer L. (1995): J. Phys. A **28**, 281
52. Oxborrow M., Henley C.L. (1993): Phys. Rev. B **48**, 6966
53. Oxborrow M., Mihalkovic, M. (in press): To appear in *Aperiodic'97* (Proc. Int. Conf. Aperiodic Crystals), ed. M. de Boissieu, R. Currat, J.-L. Verger-Gaugry, World Scientific, Singapore
54. Penrose R. (1989): In *Introduction to the Mathematics of Quasicrystals* (Aperiodicity and Order, vol. 2), ed. M.V. Jarić, Academic Press, San Diego, p. 53
55. Robertson J.L., Moss S.C. (1991): Z. Phys. B **83**, 391
56. Romeu D. (1988): Int. J. Mod. Phys. B **2**, 77; 265
57. Romeu D., Aragón J.L. (1993): In *Crystal–Quasicrystal Transitions*, ed. M.J. Yacamán, M. Torres, North-Holland (Elsevier), Amsterdam, p. 193
58. Ronchetti M., Jarić M.V. (1990): In *Quasicrystals*, ed. M.V. Jarić, S. Lundqvist, World Scientific, Singapore, p. 227
59. Sekimoto K. (1990): Physica A **170**, 150 and in *Quasicrystals* (Springer Solid-State Sciences 93), ed. T. Fujiwara, T. Ogawa, Springer, Berlin, p. 120
60. Shechtman D., Blech I.A. (1985): Metall. Trans. A **16A**, 1005
61. Socolar J.E.S. (1991): In *Quasicrystals: The State of the Art*, ed. D.P. DiVincenzo, P.J. Steinhardt, World Scientific, Singapore, p. 213
62. Steinhardt P.J. (1990): In *Quasicrystals* (Springer Solid-State Sciences 93), ed. T. Fujiwara, T. Ogawa, Springer, Berlin, p. 91
63. Steinhardt P.J., Jeong H.-C. (1996): Nature **382**, 431
64. Stephens P.W. (1989): In *Extended Icosahedral Structures* (Aperiodicity and Order, vol. 3), ed. M.V. Jarić, D. Gratias, Academic Press, San Diego, p. 37
65. Stephens P.W., Goldman A.I. (1986): Phys. Rev. Lett. **56**, 1168; **57**, 2331 (Erratum)
66. Szeto K.Y., Wang Z.M. (1990): Phys. Rev. B **41**, 1347
67. Trebin H.-R. (2002): See Chapter 12 of this book
68. Widom M., Strandburg K.J., Swendsen R.H. (1987): Phys. Rev. Lett. **58**, 706

10 Production of Quasicrystalline Alloys and Phase Diagrams

Reinhard Lück

Summary. Tools for the description and investigation of ternary alloy systems are summarized. The quasicrystal-forming systems Al-Mn-Pd and Al-Co-Ni are described; liquidus projection, isothermal and pseudobinary intersections are represented. The significance of phase equilibria for the production of quasicrystals is outlined, where stable and metastable equilibria are considered.

10.1 Introduction

In the first stage of quasicrystal research metastable quasicrystalline alloys were produced. For instance, these materials were formed from the liquid state by rapid quenching. Later alloys were detected which crystallize with quasiperiodic lattices by slow cooling. Therefore it can be assumed that quasicrystals exist also as stable phases. Formation of metastable phases does not follow the stable phase diagram, but with the knowledge of the stable phase diagram the formation of metastable phases can better be understood. Stable quasicrystals are formed in ternary and higher component systems. In binaries only metastable quasicrystals have been observed, although a few exceptions are discussed. Metastable extensions to the binaries from regions of stable ternary quasicrystal may give further information. Therefore, quasicrystals may be formed in binaries by rapid quenching, provided the formation of competing phases is suppressed by undercooling. The knowledge of the phase diagrams is necessary for further procedures, such as the growing of single crystals and the development of applications. Some ternary phase diagrams are investigated in detail. A compilation of phase diagrams especially for Al-based alloys has been published [24]; however, very few data can be found in such compilations since research on quasicrystal-forming ternaries is quite new and the reader has to use original publications. Some progress has been achieved during the last few years, however, there are some features that are different from other systems.

10.2 Establishing and Mapping of High-Order Phase Diagrams

The investigation of high-order phase diagrams needs some special tools, which will now be summarized. Several methods of data storing of phase dia-

J.-B. Suck et al. (eds.), *Quasicrystals*
© Springer-Verlag Berlin Heidelberg 2002

grams are known. Whereas in the beginning graphical representations were used, the use of computer data is now increasing. The representation of systems with four and more components requires four and more dimensions, numerical documentations therefore have their advantages.

Binary Boundary Systems
Binary systems are represented with temperature and concentration (or mole fraction) as axes. Two- and one-phase fields are separated by lines, three-phase regions are, according to the Gibbs phase rule, horizontal lines with constant temperature. Horizontal lines in the two-phase regions ending at the phase boundaries are the 'tie lines', which describe the two-phase equilibria.

The Gibbs Triangle
Most of the stable quasicrystals are ternary alloys. Ternaries are mapped in equilateral triangles; any point within the triangle represents a particular composition. The corners represent the pure components, the edges represent the binaries. The fourth axis in three dimensions represents the temperature. A quaternary system can be mapped in a similar manner in a tetrahedron. The temperature axis cannot be mapped in three-dimensional space.

Temperature-Concentration Intersections
Temperature versus concentration plots as intersections of the ternary system are often used to represent phase regions and temperatures of transformation. These vertical intersections are sometimes termed pseudobinary intersections (not to be confused with quasibinary intersections) or isopleth; the term isopleth is preferred if a quantity such as the concentration of a component or the ratio of the concentrations of two components is kept constant. There are important differences between pseudobinaries and binaries, so three-phase regions are not necessarily horizontal lines in pseudobinaries. The term 'quasibinary intersection' is used if the intersection follows, in all cases, the tie lines. Consequently, a quasibinary intersection has all the properties of a binary system.

Isothermal Intersections
In order to plot existence regions at a fixed temperature isothermal intersections are used. Lines on the intersection separate one- and two-phase regions and two- and three-phase regions as well. Three-phase regions are represented by three straight lines forming a triangle, i.e. a tie-line triangle. Two-phase regions are separated from the three-phase regions by straight lines; however, they are separated from the one-phase regions by smoothly curved lines. Single-phase regions are separated from the two-phase regions by several pieces of smoothly curved lines. Contact of one-phase regions with the three-phase regions can, in isothermal intersections only, be observed at points.

Surface Projection
Projections along the temperature axis are very important; however, they can be complicated. The most important projection is that of the liquidus surface. The liquidus surface gives information of the primarily crystallizing species during solidification. The separating lines are lines of coexisting three phases and they separate four different regions. Concerning the shape of the whole liquidus surface these lines are termed liquidus grooves. Points of contacting lines (contacting liquidus grooves) are significant for phase transformation.

Some Transformation Types
Whereas in the binary two basic reaction types – i.e. the eutectic/eutectoid (labeled e) and the peritectic/peritectoid reactions (labeled p) – are important, in the ternary an additional basic type – the 'transition type' – is introduced (L = liquid):

$L = \alpha + \beta + \gamma$	ternary eutectic reaction (labeled E)
$L + \alpha = \beta + \gamma$	transition type reaction, formerly named 'ternary quasi-peritectic' (labeled U)
$L + \alpha + \beta = \gamma$	ternary peritectic reaction (labeled P)

Binary reactions are written with lower case letters whereas ternary reactions are written with capitals, more details of labeling ternary reactions have been published recently [20]. These reactions E, U, and P are represented in the three-dimensional diagram by the so-called 'four-phase planes'. The four-phase planes of E and P are triangularly shaped, whereas the four-phase plane of U has the form of a quadrangle.

Reaction Scheme
In a flow chart all reactions of the ternary and the binary boundary systems can be listed to understand the phase diagram; this flow chart is called the Scheil reaction scheme [16,24]. In this reaction scheme each reaction is characterized by its reaction formula, its symbol and its temperature; lines connecting the reactions symbolize three-phase areas.

10.3 Methods of Investigation

Several experimental methods are used to investigate phase diagrams. In addition, calculations of phase diagrams using thermodynamic data are possible. The important methods will be summarized. In-situ methods are used to register phase transitions immediately during heating or cooling procedures. If the reactions are sluggish the methods may not be appropriate. Sometimes, as-cast samples are investigated. Generally, as-cast samples give only a rough impression of phase transformations; a careful heat treatment to equilibrate the samples is necessary. In-situ methods support vertical intersections. Analyzes of heat-treated and subsequently quenched samples support the establishment of isothermal intersections provided all investigated samples are

heat treated at the same temperature and have been in an equilibrium state at this temperature; this state should be quenched in.

Differential Thermal Analysis (DTA)
Thermal analyzes record temperature versus time or register a difference between sample temperature and reference temperature versus time or sample temperature (DTA). An improvement of DTA is differential scanning calorimetry (DSC), where the temperature difference is replaced with a quantitative measurement of difference in heat transfer between sample and reference. Endothermic and exothermic effects can be detected and their temperatures can be determined. The sensitivity of these methods depends in any case on the heating rate.

Thermal Analyzes Using Physical Properties
Physical properties can be measured as they depend on temperature, examples are electrical resistivity, magnetic susceptibility, thermal expansion, etc.. Discontinuous features of recorded curves – such as the changes of slope – can be used to determine phase transitions. Low heating rates can be applied for slow reactions. This is an advantage compared to DTA and DSC.

Phase Identification by Light Microscopy
The metallographic investigation of samples by grinding, polishing and etching in combination with light microscopy has a long tradition. The number of phases as well as their solidification processes or processes of formation during heat treatment can be derived. The use of polarized light is particularly useful to separate icosahedral and cubic crystals from crystals with lower symmetry, since the tensor of electrical conductivity is related to optical properties and this property is isotropic for icosahedral and cubic crystals.

Phase Identification by Electron Microscopy
The application of scanning electron microscopy (SEM) has some advantages similar to light microscopy. Magnification can be performed at a slightly higher scale; and with special equipment, the chemical composition of small areas can be determined.

Transmission electron microscopy (TEM) for phase identification by diffraction – especially when selected area electron diffraction (SAED) is applied – is very important for identification of quasicrystals, of their different variants and of their approximants. High resolution transmission electron microscopy (HRTEM) has its own advantages for phase identification of non-periodic tilings [23].

Phase Identification by X-Ray Diffraction
The identification of phases by X-ray diffraction is well known and has most advantage if a single-phase sample can be used. It has some disadvantages in phase diagram determination: small amounts are not detectable, three and more phases are difficult to be detected simultaneously.

10.4 Examples of Ternary Systems

The first published ternary diagram of a quasicrystal-forming system was the Al-Li-Cu system [5]. Data on isothermal sections and isopleths of quasicrystal-forming systems are widespread in the literature and will not be summarized as often they are incomplete or disputed. I will restrict myself to two examples which are well established.

The Al-Pd-Mn System

Rather complete information is given for the Al-Pd-Mn system [11,12]. This was the first system where stable icosahedral as well as decagonal quasicrystals have been detected [2]. Formation of the icosahedral phase from the

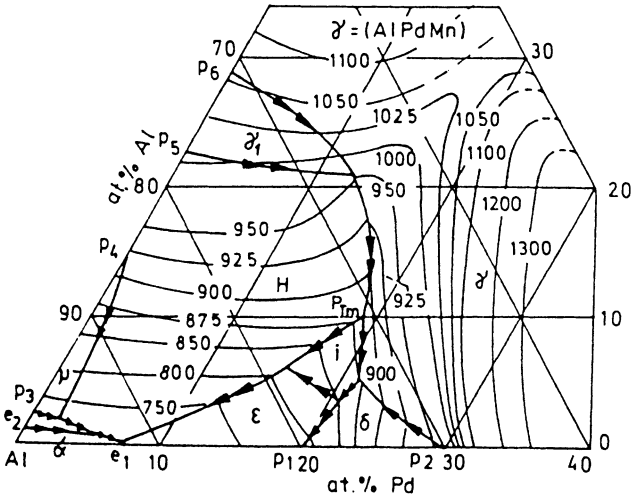

Fig. 10.1. Primary crystallization areas and contour lines of the liquidus of the Al-Pd-Mn system [11]. Formation of the decagonal phase is suppressed due to sluggish reaction. Temperatures are given in °C

liquid state is found in a ternary peritectic reaction, the presentation of the liquidus projection surface (Fig. 10.1) is taken from [11]. The formation of the decagonal phase is sluggish, so the determination of the phase diagram in the region of the decagonal phase is difficult.

An isothermal section at 840°C of the Al-Pd-Mn system is presented in Fig. 10.2. Nine one-phase regions, γ, γ_2, H=$Al_{11}Mn_4$(h), R=$Al_{11}Mn_4$(r), D=decagonal, i=icosahedral, ϵ, δ and L=liquid, are intersected. Several two-phase and three-phase regions are formed by these phases. As the quasicrystalline phases exhibit different modifications further investigations by TEM and HRTEM are necessary [3,4,17].

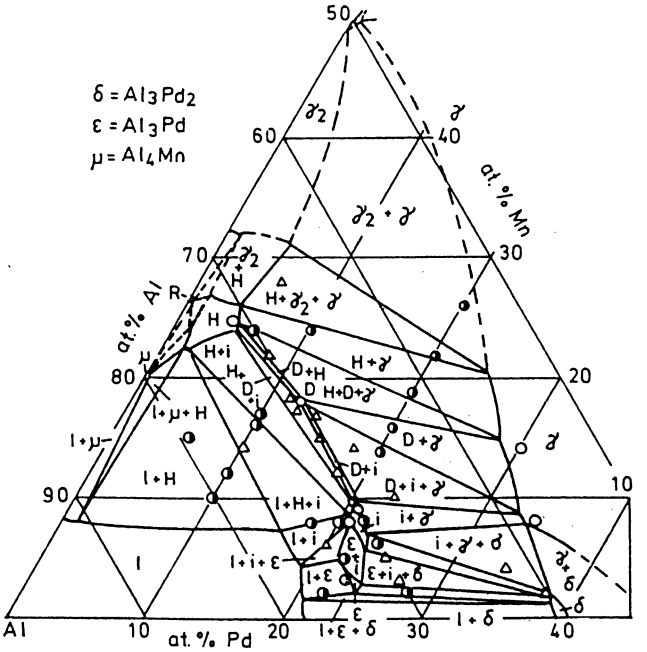

Fig. 10.2. Isothermal section of the Al-Pd-Mn system at 840°C [11]

The Al-Co-Ni System

The ternary systems Al-CoAl-NiAl and Al-CoAl-CuAl are characterized by the formation of decagonal phases; no icosahedral phases have been observed. The investigation of the Al-Co-Ni system is still under progress since Kek [19] presented the first isothermal sections. Meanwhile several papers about the phase equilibria of this system have been published [8–10,13,14,22,28], [30,31,33,34]. The liquidus projection surface (Fig 10.3) is presented according to [8,13]. It is based on data of several investigations. Ten different regions of primary crystallization can be seen in the presented part. The label D designates the primary crystallization of the decagonal phase. This phase dominates the figure. The decagonal phase D is the only ternary phase crystallizing from the liquid state. It is formed at 1175°C in a peritectic reaction where the liquidus groove between liquidus of D and the liquidus of β has a maximum. There are nine four-phase reactions with the melt; eight four-phase reactions are of the transition type and one is a ternary peritectic reaction.

In Fig. 10.4 an isopleth with 70 at.% Al is reproduced [13,34]. Experimental data of differential thermal analyzes and magnetothermal analyzes have been included. Only two single-phase regions, liquid and D, are intersected. Five four-phase planes are intersected. Several phases are involved at the four-phase reactions. The maximum extension of the decagonal phase is found

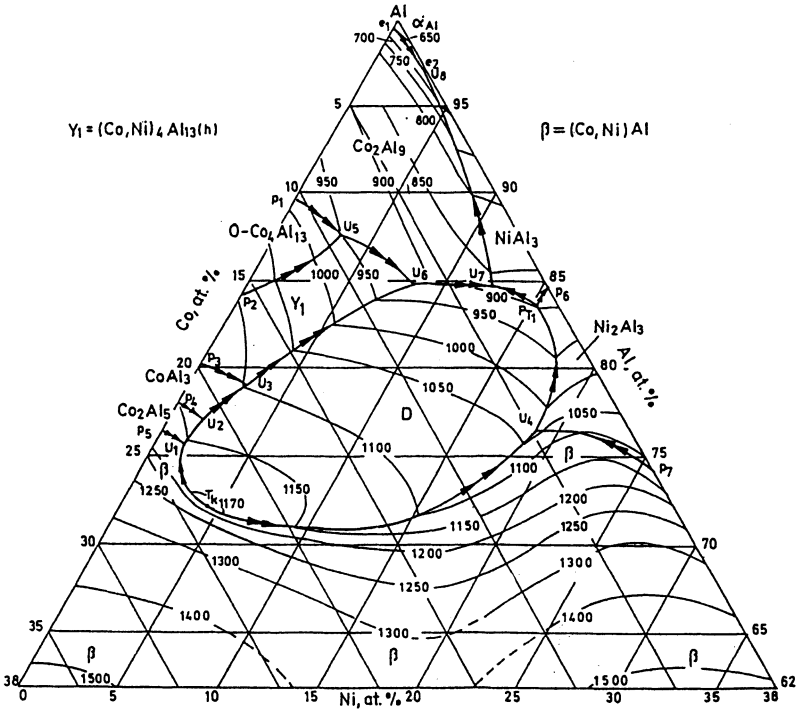

Fig. 10.3. Primary crystallization areas and contour lines of the liquidus of the Al-Co-Ni system [8,13]

along the vertical section $Al_{74}Co_{26}$ – $Al_{69}Ni_{31}$ [33]. The isopleth shows that the shape of the liquidus surface and the magnetic properties of the melt [11] imply that there is an appreciable chemical short-range order in the melt. One can assume that icosahedral clusters are preformed in the melt. The chemical short-range order stabilizes the liquid state. This stabilization has to be taken into account in computer modeling, if the phase diagram is to be computed. It is worthwhile mentioning that in the partial system Al–CoNi–NiAl there are 45 three-phase regions found. This number is determined without taking into account that several variants of the D phase exist [6,7,25–30,57]; modifications with five-fold symmetry, one-dimensional quasicrystals and superstructures were found, most of them could be related to regions in the phase diagram [31]. A summary of the eight variants of D can be found in this volume [23]. An in-situ study by dilatometric measurements could verify transformation of some of these variants and improve the determination of their existence regions [22].

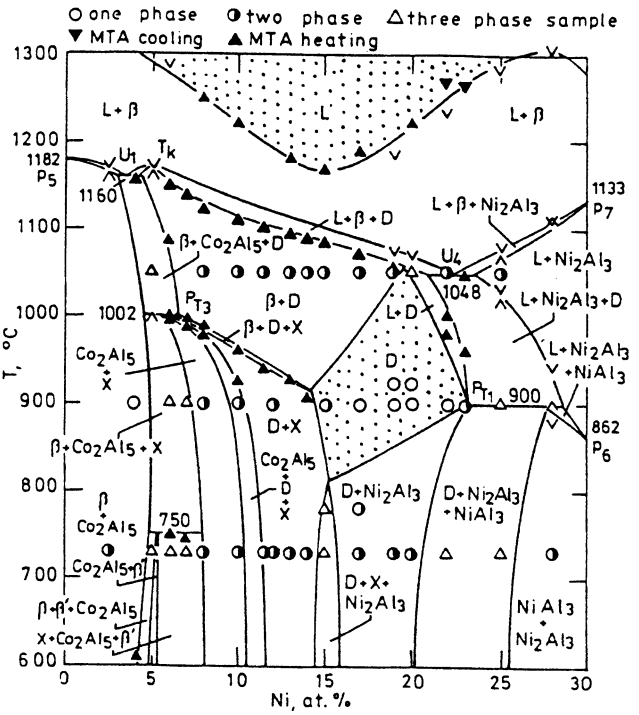

Fig. 10.4. Isopleth at 70 at.% Al in the Al-Co-Ni system [8,34]

10.5 Calculation of Phase Diagrams

The calculation of quasicrystal-forming systems needs thermodynamic data [16] (i.e. application of the CALPHAD method; CALPHAD is the abbreviation of CALculation of PHAse Diagrams; a conference series and a Journal are termed CALPHAD). If such data are not available, they must be modeled by fitting the experimentally determined phase diagram. The calculation is difficult for several reasons:

(i) Very few thermodynamic data of quasicrystals are available; this may change in the future.

(ii) Quasicrystalline phases and related crystalline phases (e.g. 'approximants') generally compete in their formation and will have very similar heats of formation [32].

(iii) The significance of entropy is not clear; an entropic stabilization by particular defects, the so-called phasons, has been proposed; details of entropic stabilization are discussed in [18]. Thermodynamics of quasicrystals are discussed in a separate contribution to this volume [21].

10.6 Using Phase Diagrams of Quasicrystal-Forming Systems

Preparation of Stable Quasicrystals
If a ternary phase diagram of a quasicrystal-forming system is well known, the procedure of preparation can be deduced from the diagram. A section along the quasicrystal–liquid tie-lines yields the composition of the initial composition of the melt during the Czochralski technique. The composition of the melt should be within the liquidus area, e.g. within region i in the liquidus projection, whereas the solidified single crystal should have the composition of the solidus area. The whole system should be kept in the two-phase regime of i + L.

The phase diagrams favor the primary formation of other alloys rather than quasicrystals especially due to peritectic reaction if the composition of the alloy is that of the quasicrystal in the solid state. During solidification, other phases are formed due to segregation. Accordingly, heat treatment after solidification is necessary for equilibration and homogenization. This heat treatment has to be performed carefully beginning with a temperature below the solidus temperature of the phase with the lowest solidus area; this is to avoid remelting. After that, the temperature for the heat treatment can be increased. Naturally, large samples need long times for equilibration due to the slow diffusion rates. If quasicrystalline alloys are formed in the solid state, the tie-lines play the same role as in liquid-state reactions.

Preparation of Metastable Quasicrystals
Supercooling from the liquidus can favor the formation of quasicrystalline phases. One reason is the degree of supercooling of competing phases. To have a first impression of the formation of metastable phases the liquidus of the quasicrystal might be extended into regions where quasicrystals are thermodynamically unstable. This gives an idea where quasicrystals can be formed in binaries as metastable alloys. If the supercoolings of all competing phases are considered, a liquidus surface for supercooling can be designed. Gödecke [8] did it for the Al-CoAl-NiAl system. The results are reproduced in Fig. 10.5. Such supercooling diagrams refer to special cooling rates. The diagram shows that the formation of the decagonal phase is extended. In the binaries of Al–Co and Al–Ni decagonal alloys can be formed as metastable alloys. The isopleth with 10 at.% Ni (Fig. 10.6) shows the range of supercooling (hatched area); supercooling of the β phase is stronger than that of D.

Metastable quasicrystals are prepared by those methods that were initially developed for the production of amorphous and other metastable alloys (see, for example, [1,35]). A very common method is melt quenching. There are several different methods, the most known method is melt spinning where a thin ribbon is produced with a single or a double roller. Other methods have

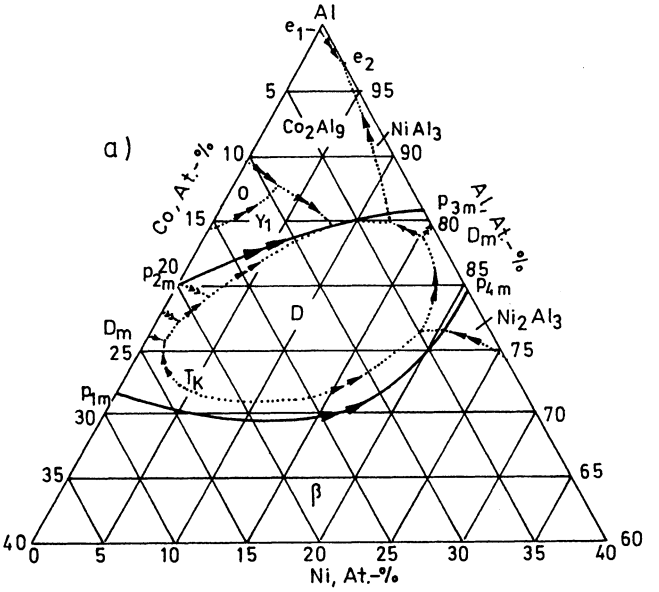

Fig. 10.5. Metastable (*solid lines*) and stable (*dotted lines*) liquidus surface of the decagonal phase of the Al-CoAl-NiAl system [8], the metastable data are taken from cooling experiments and from literature data cited in [8]

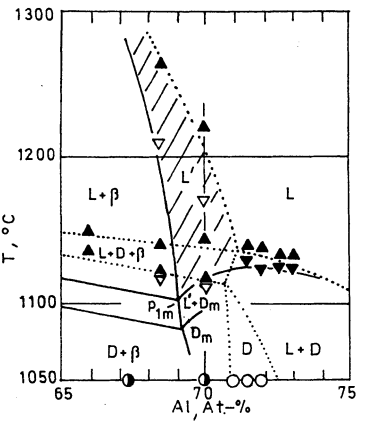

Fig. 10.6. Isopleth with 10 at.% Ni of the Al-CoAl-NiAl system from 65 to 75 at.% Al. Metastable (*solid lines*) and stable (*dotted lines*) solidification of β and D [8]. Cooling rates for supercooling are chosen from 10 to 20 $Kmin^{-1}$

been applied: crystallization from the metastable amorphous state, mechanical alloying, i.e. ball milling, interdiffusion of thin layers.

Metastable variants of the quasicrystals may also be formed during annealing processes. Periodic approximants of the decagonal phase in Al-Co-Ni were observed after some heat treatment of the as-cast state [15,32].

10.7 Conclusion

Methods to investigate quasicrystal-forming alloy systems are well established. The investigations require extensive data, since quasicrystals are beset with competing crystalline phases in the alloy systems. For quasicrystals that are formed from the melt, ternary peritectic reactions have been found. Sluggish reactions can make the phase-diagram determination difficult, so metastable phase diagrams may be determined and regarded for practical purposes as stable diagrams. A combination of different methods enhances the chance to determine phase transformations exactly. Variants of quasicrystals, as periodic approximants, 1D quasicrystals, modulated quasicrystals, quasicrystalline superstructures – in the stable as well as in a metastable state – make the phase diagrams more complex. Sophisticated methods are necessary to understand the equilibria of quasicrystals in detail.

Acknowledgment

This chapter is based on extensive collaboration with T. Gödecke and M. Scheffer, to whom I am grateful. Special thanks are due to S. Ritsch (Sendai), H.-U. Nissen (Zurich) and C. Beeli (Lausanne/Zurich) for cooperation in TEM and HRTEM research and for fruitful discussions. D. Lang gave important technical advice. Financial support from the Deutsche Forschungsgemeinschaft is gratefully acknowledged.

References

1. Anatharaman T.R., Suryanarayana C. (1987): *Rapidly Solidified Metals*, Trans Tech Publications, Aedermannsdorf.
2. Beeli C., Nissen H.-U., Robadey J. (1991): Philos. Mag. Lett. **63**, 87.
3. Beeli C., Stadelmann P., Gödecke T., Lück R. (1995): Proc. Int. Conf. Aperiodic '94, Les Diablerets, Switzerland, 18–22 September 1994, eds. G. Chapuis, W. Paciorek, World Scientific, Singapore, p. 361.
4. Beeli C., Stadelmann P., Lück R., Gödecke T. (1995): Proc. 5th Int. Conf. Quasicrystals, Avignon, 22–26 May 1995, eds. Ch. Janot, R. Mosseri, World Scientific, Singapore, p. 680.
5. Dubost B., Colinet C., Ansara I. (1988): Proc. ILL/CODEST Workshop Quasicrystalline Materials, Grenoble, 21–25 March 1988, eds. Ch. Janot, J.M. Dubois, World Scientific, Singapore, p. 39.
6. Edagawa K. (1995): Proc. 5th Int. Conf. Quasicrystals, Avignon, 22-26 May 1995, Eds. Ch. Janot., R. Mosseri, World Scientific, Singapore, p. 322.
7. Edagawa K., Sawa H., Takeuchi S. (1994): Philos. Mag. Lett. **69**, 227.
8. Gödecke T. (1997): Z. Metallkd. **88**, 557.
9. Gödecke T., Ellner M. (1996): Z. Metallkd. **87**, 854.
10. Gödecke T., Ellner M. (1997): Z. Metallkd. **88**, 382.
11. Gödecke T., Lück R. (1995): Z. Metallkd. **86**, 109.

12. Gödecke T., Lück R., Beeli C. (1995): Proc. 5th Int. Conf. Quasicrystals, Avignon, 22–26 May 1995, eds. Ch. Janot., R. Mosseri, World Scientific, Singapore, p. 644.
13. Gödecke T., Scheffer M., Lück R., Ritsch S., Beeli C. (1997): Z. Metallkd. **88**, 687.
14. Gödecke T., Scheffer M., Lück R., Ritsch S., Beeli C. (1998): Z. Metallkd. **89**, 687.
15. Grushko B., Holland-Moritz D., Wittmann R., Wilde G. (1998): J. Alloys Comp. **280**, 215.
16. Hillert M. (1998): *Phase equilibria, phase diagrams and phase transformations*, Cambridge University Press, Cambridge, UK.
17. Ishimasa T. (1995): Proc. 5th Int. Conf. Quasicrystals, Avignon, 22–26 May 1995, eds. Ch. Janot, R. Mosseri, World Scientific, Singapore, p. 648.
18. Joseph D., Ritsch S., Beeli C. (1997): Phys. Rev. **B 55**, 8175.
19. Kek S.(1991): Ph.D. thesis, Stuttgart University, Stuttgart.
20. Lück R., Gödecke T. (2000): Z. Metallkd. **91**, 692.
21. Lück R. (2002): See Chapter 24 of this book.
22. Lück R., Scheffer M., Gödecke T., Ritsch S., Beeli C. (1999): Proc. MRS Fall Meeting, Nov. 30–Dec. 2, 1998, Symp. on Quasicrystals, Boston, Mass., eds. J.-M. Dubois, P.A. Thiel, A.-P. Tsai, K. Urban, MRS, Warrendale, Pennsylvania, 25.
23. Nissen H.-U., Beeli, C. (2002): See Chapter 6 of this book.
24. Petzow G., Effenberg G. (1988): *Ternary Alloys*, VHC Verlagsgesellschaft, Weinheim.
25. Ritsch S. (1996): Ph.D. thesis, ETH Zürich, Zurich.
26. Ritsch S., Nissen H.-U., Beeli C. (1998): Proc. 6th Int. Conf. Quasicrystals, Tokyo, 1997, eds. S. Takeuchi, T. Fujiwara, World Scientific, Singapore, 367.
27. Ritsch S., Beeli C., Nissen H.-U., Lück R. (1995): Philos. Mag. **A 71**, 671.
28. Ritsch S., Beeli C., Nissen H.-U., Gödecke T., Scheffer M., Lück R. (1996): Philos. Mag. Lett. **74**, 99.
29. Ritsch S., Radulescu O., Beeli C., Warrington D.H., Lück R., Hiraga K. (2000): Philos. Mag. Lett. **80**, 107.
30. Ritsch S., Hiraga K., Beeli C., Gödecke T., Scheffer M., Lück R. (1999): Proc. MRS Fall Meeting, Nov. 30–Dec. 2, 1998, Symp. on Quasicrystals, Boston, Mass., eds. J.-M. Dubois, P.A. Thiel, A.-P. Tsai, K. Urban, MRS, Warrendale, Pennsylvania, p. 171.
31. Ritsch S., Beeli C., Nissen H.-U., Gödecke T., Scheffer M., Lück R. (1998): Philos. Mag. Lett. **78**, 67.
32. Ritsch S., Hiraga K., Gödecke T., Lück R. (1999): Proc. Int. Conf. on Solid-Solid Phase Transformation '99 (JIMIC-3), eds. M. Koiwa, K. Otsuka, T. Miyazaki, The Japan Institute of Metals, Tokyo, 1341
33. Scheffer M., Gödecke T., Lück R. (1998): Proc. 6th Int. Conf. Quasicrystals, Tokyo, 1997, eds. S. Takeuchi, T. Fujiwara), World Scientific, Singapore, 269.
34. Scheffer M., Gödecke T., Lück R., Ritsch S., Beeli C. (1998): Z. Metallkd. **89**, 270 - 278.
35. Steeb S. (1990): *Glassy Metals* (in German), Expert Verlag, Ehningen.

11 Undercooling of Quasicrystal-Forming Liquid Alloys

Dirk Holland-Moritz

Summary. This work gives a review of investigations of the undercooling behavior of melts forming quasicrystalline and polytetrahedral phases. It turns out that these special kinds of solid phases exhibit a lower activation threshold for nucleation than conventional crystalline phases, which can be interpreted in terms of a similarity of the short-range order in undercooled melts and polytetrahedral phases.

11.1 Introduction

As shown by Turnbull [44] in 1950 a great variety of melts of pure metals can be deeply undercooled below their melting point T_{L}. Typical undercoolings of about $\triangle T \approx 0.2 \cdot T_{\mathrm{L}}$ were reported in this work. Frank [8] suggested that these high levels of undercooling might be a result of an icosahedral short-range order (SRO), which should be energetically favored in undercooled melts of systems consisting of atoms of sphere-like geometrical symmetry. Frank's suggestion was based on the fact that the energy of an icosahedral cluster consisting of 13 atoms that is relaxed in a Lennard–Jones potential is 8.4% lower than that of close packed (fcc or hcp) clusters with the same number of atoms. Icosahedral SRO is incompatible with the translational symmetry of crystalline phases. This should give rise to an increase of the nucleation threshold for crystals, because crystal nucleation requires a breakup of the icosahedral SRO.

The assumption of icosahedral SRO existing in undercooled melts was supported by molecular dynamic computer calculations on Lennard–Jones liquids [30,40], which showed an increasing degree of polytetrahedral (icosahedral) SRO with increasing undercooling of the melt.

The question of icosahedral SRO in undercooled melts attracted new attention by the discovery of an icosahedral quasicrystalline I-phase in rapidly quenched Al-Mn alloys [37]. Apart from the I-phases other phases with a more or less pronounced degree of polytetrahedral SRO exist. These are, e.g. the decagonal quasicrystals (D-phase), which are quasiperiodic in two dimensions and periodic in the third dimension, and the Frank–Kasper phases, which are crystalline phases characterized by a large unit cell and polytetrahedral (e.g. icosahedral) symmetry elements inside this cell.

At temperatures above the melting temperature the structure of melts of $Al_{80}Mn_{20}$ was investigated with neutron diffraction by Maret et al. [27]. The

J.-B. Suck et al. (eds.), *Quasicrystals*
© Springer-Verlag Berlin Heidelberg 2002

pair potentials determined from these experiments were used for a molecular dynamic simulation of topological SRO in liquid $Al_{80}Mn_{20}$ alloys which indicated an increasing degree of icosahedral SRO with increasing undercooling [28]. Nevertheless up to now no direct measurements of icosahedral SRO in *undercooled* melts of metals and alloys by e.g. diffraction experiments have been reported. However, the undercoolability of melts is expected to be influenced by similarities of the SRO of liquid and solid provided that disturbing influences by foreign phases are avoided. The larger the similarity of the SRO of the undercooled melt and the solid nucleus is, the lower the interfacial energy and by means of this the undercoolability [29]. Therefore the undercoolability of melts is expected to be smallest for the nucleation of quasicrystalline I-phases, medium for that of quasicrystalline D-phases and the Frank–Kasper phases, and largest for the nucleation of non-polytetrahedral crystalline phases.

11.2 Undercooling and Nucleation

According to equilibrium thermodynamics the phase transition between liquid and solid is governed by the Gibb's free energies of the liquid (G_L) and of the solid (G_S). For temperatures above the melting temperature $\triangle G_V = G_L - G_S$ is negative, which means that the liquid is the energetically favored phase whereas below the melting temperature $\triangle G_V$ is positive and the solid is thermodynamically stable.

Nevertheless, it was already reported in 1724 by Fahrenheit [7] that a liquid can be undercooled below its equilibrium melting point. This phenomenon cannot be described by macroscopic thermodynamic considerations. Obviously the solidification of a liquid is also governed by microscopic processes. In this context nucleation processes are of fundamental importance.

11.2.1 Classical Nucleation Theory

The classical theory of nucleation [4,16,24] is based upon a model by Volmer and Weber [48] that was initially developed for the description of the condensation from a supersaturated vapor. This model was transferred by Turnbull and Fischer [43] to the nucleation of a solid from the undercooled melt. It is assumed that clusters are formed in the melt by statistical fluctuations. When such a cluster is built up, the Gibb's free energy of the system is increased by the surface contribution Ω, which is proportional to the surface of the cluster, and it is decreased by the crystallization energy Φ, which is proportional to the volume of the cluster. Thus, the Gibb's free energy of a spherical cluster of radius r is given by:

$$\triangle G = \Phi + \Omega = -\frac{4}{3}\pi r^3 \triangle G_V + 4\pi r^2 \sigma, \tag{11.1}$$

where σ denotes the solid–liquid interfacial energy, and $\triangle G_{\mathrm{V}}$ the difference of the Gibb's free energy between liquid and solid. $\triangle G$ shows a maximum at the radius

$$r^* = \frac{2\sigma}{\triangle G_{\mathrm{V}}}. \tag{11.2}$$

If a cluster is formed that is smaller than r^* the system can decrease its energy by dissolution of the cluster. Clusters of this type are unstable and are called embryos. If nevertheless a cluster has reached by statistical fluctuations a radius larger than r^*, the system can decrease its energy by further growth of the cluster. These clusters have a tendency to grow and are called nuclei. r^* is the critical radius of a nucleus. For nucleation the activation threshold $\triangle G^*$, given by the height of the maximum $\triangle G\,(r^*)$, has to be overcome:

$$\triangle G^* = \frac{16\pi\sigma^3}{3\triangle G_{\mathrm{V}}^2}. \tag{11.3}$$

This activation barrier is responsible for the undercoolability of melts. Equation (11.3) is valid for the case of homogeneous nucleation, which means that nucleation is an intrinsic process. However, in praxis usually foreign phases such as container walls or impurity sites are in contact with the melt, which leads to a reduction of the activation threshold for nucleation by a catalytic potency factor $f(\vartheta)$ [4,16,24]. This extrinsic process is called heterogeneous nucleation. In this case $\triangle G^*$ has to be multiplied by the catalytic potency factor $f(\vartheta)$ $(0 \leq f(\vartheta) \leq 1)$ of the heterogeneous nucleation site.

Taking $\triangle G^*$, the steady-state nucleation rate I_{SS} is given by

$$I_{\mathrm{SS}} = \frac{k_{\mathrm{B}} T \xi N_{\mathrm{L}}}{3\eta(T) a_0^3} \cdot \exp\left(-\frac{\triangle G^* \cdot f(\vartheta)}{k_{\mathrm{B}} T}\right), \tag{11.4}$$

with $\eta(T)$ being the viscosity of the melt, T the absolute temperature, a_0 the mean interatomic spacing, k_{B} Boltzmann's constant, N_{L} Avogadro's number and ξ the fraction of atoms that can act as a nucleation site [4,16,24]. For homogeneous nucleation $f(\vartheta) = 1$ and $\xi = 1$, for heterogeneous nucleation $f(\vartheta) < 1$ and $\xi \ll 1$. With the exception of σ all parameters mentioned above are either experimentally accessible or at least a good approximation exists.

According to Turnbull the $\triangle G_{\mathrm{V}}$ is roughly approximated by [44]:

$$\triangle G_{\mathrm{V}} = \triangle S_{\mathrm{f}} \triangle T. \tag{11.5}$$

For a better estimation of $\triangle G_{\mathrm{V}}$ the expression

$$\triangle G_{\mathrm{V}} = \triangle S_{\mathrm{f}} \triangle T - \left[\ln\left(\frac{T_{\mathrm{L}}}{T_0}\right)\right]^{-1} \cdot \triangle S_{\mathrm{f}} \cdot \left[\triangle T - T \ln\left(\frac{T_{\mathrm{L}}}{T}\right)\right] \tag{11.6}$$

was suggested [9,14]. $\triangle S_{\mathrm{f}}$ denotes the entropy of fusion and T_0 the ideal glass-transition temperature.

A commonly used expression for the temperature dependence of the viscosity $\eta(T)$ of metallic melts is the Vogel–Fulcher–Tammann ansatz:

$$\eta\,(T) = \eta_0 \exp\left(\frac{A}{T - T_0}\right). \tag{11.7}$$

η_0 and A are free parameters, which have to be determined.

However σ cannot be directly measured, and for a theoretical estimation a model for the structure of the solid–liquid interface is required. The only model available that takes into consideration structural aspects and depends only on parameters that can be experimentally determined is the negentropic model by Spaepen and Thompson [38,39,41]. In this model it is assumed that the entropic contribution to σ is dominant while the enthalpic one is negligible, which leads to the following expression for σ:

$$\sigma = \alpha \frac{\triangle S_\mathrm{f} T}{\left(N_\mathrm{L} V_\mathrm{m}^2\right)^{1/3}}. \tag{11.8}$$

V_m is the molar volume and α a factor that depends on the structure of the solid nucleus. α is given by [38,39,41]

$$\alpha = \frac{N_\mathrm{i}}{N_\mathrm{S}} \cdot \left[\frac{\triangle S_\mathrm{cf}(\mathrm{bulk}) - S_\mathrm{cf}(i)}{\triangle S_\mathrm{f}}\right], \tag{11.9}$$

where N_i denotes the number of atoms in the interface, N_S the number of atoms in the first layer of the solid, $S_\mathrm{cf}(i)$ the configurational entropy of the interface per atom, $\triangle S_\mathrm{cf}(\mathrm{bulk})$ the difference of the configurational entropy between bulk liquid and bulk solid per atom and $\triangle S_\mathrm{f}$ the entropy of fusion per atom. $S_\mathrm{cf}(i)$ is given by $S_\mathrm{cf}(i) = S_\mathrm{cf}(1) \cdot N_1/N_\mathrm{i}$ where $S_\mathrm{cf}(1)$ is the configurational entropy of the first interfacial layer and N_1 the number of atoms in this layer. As a first guess $\triangle S_\mathrm{f}$ and $\triangle S_\mathrm{cf}(\mathrm{bulk})$ are approximated by values typical of most metals ($\triangle S_\mathrm{f} = 1.2 k_\mathrm{B}, \triangle S_\mathrm{cf}(\mathrm{bulk}) = 1 k_\mathrm{B}$). In order to determine the ratio $N_\mathrm{i}/N_\mathrm{S}$ and $S_\mathrm{cf}(1)$, a model for the interface is required. Spaepen and Thompson [38,39,41] constructed the solid–liquid interface by a suitable packing of hard spheres. Assuming that a polytetrahedral SRO prevails in the undercooled melt, the interface is build up by randomly dense packing of hard spheres such that the number of holes with tetrahedral symmetry is maximized, while holes with octahedral symmetry, which are typical for crystals, are forbidden. Moreover the density in the interface is maximized in order to minimize the energy. From this $N_\mathrm{i}/N_\mathrm{S}$ is inferred. $S_\mathrm{cf}(1)$ depends on the number Z of possibilities to build up the interface according to the construction rules ($S_\mathrm{cf}(1) = k_\mathrm{B}/N_1 \cdot \ln(Z)$). It can be estimated from an analysis of the structure of the first interfacial layer as drawn out for fcc, hcp and bcc phases ($S_\mathrm{cf}(1) = 0.096 \cdot k_\mathrm{B}$) [38,39,41]. This delivers $\alpha^{\mathrm{fcc/hcp}} = 0.86$ for fcc or hcp crystals [39] and $\alpha^{\mathrm{bcc}} = 0.71$ for bcc structures [41].

The tetrahedral SRO assumed to prevail in the interface is similar to the SRO in quasicrystals and polytetrahedral phases. Therefore, low numerical

values of α are expected for solids with polytetrahedral SRO in comparison with those of crystalline structures [29]. This purely qualitative argument is confirmed by recent numerical estimations basing on the negentropic model (compare Sect. 11.4). From the experimental side α can be inferred from an analysis of the maximum undercoolability of a melt, which allows a comparison with the theoretical predictions. For this it is assumed that at least one nucleation event is necessary to initiate the solidification of the undercooled melt of volume V during the experiment time t_N:

$$I_{SS}(T_N) \cdot V \cdot t_N \geq 1. \tag{11.10}$$

The nucleation temperature T_N and the experiment time $t_N = (T_L - T_N)/(dT/dt)$ are inferred from the corresponding temperature–time profiles measured during an undercooling experiment.

11.2.2 Experimental Techniques to Undercool Metallic Melts

There exist two completely different approaches to undercool metallic melts: rapid quenching and reduction of heterogeneous nucleation.

The methods of rapid quenching, such as melt spinning, splat cooling or laser melting, are based upon the fact that according to (11.10) at a given nucleation rate some time is required to form a critical nucleus inside the sample of volume V. Thus, if the melts are cooled quickly enough, deep undercoolings can be achieved. In addition to this, (11.4) was derived for a quasistationary cluster-size distribution. For extremely high cooling rates the distribution function is not able to follow the change in temperature rapidly enough to establish steady-state conditions, resulting in high levels of undercooling [16,24].

The methods of rapid quenching are comparatively easy to apply and are already used for the industrial production of metastable materials such as amorphous metals. For meltspinning or splatcooling typically cooling rates in the range of 10^5–10^7 K/s are achievable; for laser melting 10^8–10^{11} K/s. These high cooling rates allow almost no *in situ* diagnostic of the melt. Therefore neither the study of the properties of the undercooled melt nor the direct determination of the maximum level of undercooling reached is possible during the quenching process.

However, by reduction of heterogeneous nucleation high levels of undercooling can be obtained for massive specimens even at low cooling rates, which enables the *in situ* diagnostic of the melt. Since impurities and crucible walls act as heterogeneous nucleation sites, it is necessary to process the melt (quasi)containerlessly under high purity conditions.

The containerless undercooling methods (for a good review see [15]) consist on the one hand of different levitation techniques such as electromagnetic [13,15], electrostatic [32], gas–film [25] or acoustic [26] levitation, in which the specimens are freely suspended, and on the other hand of the methods

of solidification in free fall (atomization and drop-tube experiments [11]). All levitation methods have the advantage that the sample is processed at a fixed position and that the experiment time is in principle not limited, which allows low cooling rates and *in situ* diagnostics.

For containerless solidification in free fall the experiment times are limited by the length of the drop tube, and cooling rates in the range of 10^2–10^6 K/s are accessible. This and the movement of the samples restrict the possibilities for an *in situ* diagnostic during solidification.

Another group of undercooling techniques are quasicontainerless methods such as meltfluxing [1,31] or droplet dispersion [31,45,49]. In these cases the specimens are processed in crucibles but are only in contact with a medium with a low catalytic potency factor $f(\vartheta)$, for instance with glasses or melts.

Alloys forming quasicrystalline phases consist of elements which are highly reactive with respect to oxidation such as Al, Ti, Zr, and/or Mg. For instance, Al forms a very stable metaloxide which acts as a heterogeneous nucleation site of high catalytic potency. Therefore, the quasicontainerless techniques are very difficult to apply in order to obtain reliably and reproducibly large undercoolings of quasicrystal-forming alloys [6]. The special conditions of containerless processing are most favorable to overcome such difficulties, since any reaction between the melt and container is completely avoided [6,15].

11.3 Experimental Studies on the Nucleation Behavior of Quasicrystalline and Polytetrahedral Phases

11.3.1 Atomization Drop-Tube and Splat-Cooling Experiments

The first experiments on the nucleation behavior of quasicrystalline solids were reported by Bendersky and Ridder [3]. Liquid droplets of an $Al_{86}Mn_{14}$ melt with diameters in the range from 20 nm to 2 μm were solidified in free fall in an electrohydrodynamic atomization facility. The droplet size correlates inversely with the cooling rate, which covered a range between 10^4 and 10^6 K/s. An extremely high density of quasicrystalline grains in the order of $10^{24}\,\mathrm{m}^{-3}$ was observed in the smallest droplets [3], which is indicative of a high nucleation rate and a low $\triangle G^*$ for nucleation of the I-phase.

Similar experiments on $Al_{88}Mn_{12}$ droplets of diameters in the range of (50–1000) μm were conducted using a 2.5 m drop tube [14]. The cooling rates ranged from 800 K/s for the largest particles to $3 \cdot 10^5$ K/s for the smallest particles. At small cooling rates exclusively stable crystalline phases solidified whereas with increasing cooling rate also the metastable quasicrystalline phases were formed, the quasicrystalline decagonal T-phase at medium cooling rates, and the quasicrystalline I-phase at the highest cooling rates [14]. For all phases a temperature–time transformation diagram was calculated by employing classical nucleation theory under the assumption of homogeneous nucleation of the quasicrystalline phases. σ was expressed by (11.8). The

structure-dependent factor α was a free parameter. The best fit to the experimental results was achieved with $\alpha^{\mathrm{I}} = 0.36$ for the I-phase and $\alpha^{\mathrm{D}} = 0.45$ for the T-phase. These α-factors are significantly smaller than the theoretical values calculated for crystalline phases with bcc structure [41] ($\alpha^{\mathrm{bcc}} = 0.71$) and for those with fcc or hcp structure [39] ($\alpha^{\mathrm{fcc/hcp}} = 0.86$). This is indicative of a low σ especially for the I-phase.

Also for quasicrystal-forming alloys that were rapidly quenched by splat-cooling with cooling rates in the order of 10^6 K/s, extremely small sizes of the quasicrystalline domains were observed [18,21,35]. For splat-quenched $Al_{62}Cu_{25.5}Fe_{12.5}$ [18,21] and $Al_{72}Pd_{21}Mn_7$ [35] samples, TEM investigations revealed that the specimens consist of grains of the major I-phase with an average diameter of about 200 nm. In splat-quenched $Al_{64}Cu_{22}Co_{14}$ slightly larger grain sizes of the major D-phase of about 300 nm are found [18,21]. These low grain sizes once again indicate a low $\triangle G^*$ for the quasicrystalline phases.

11.3.2 Levitation Undercooling Experiments

While for the above-mentioned investigations on the nucleation behavior of quasicrystalline and polytetrahedral phases the level of undercooling cannot be directly determined, the technique of electromagnetic levitation allows a pyrometric measurement of the temperature of the specimen. First experiments on the maximum undercoolability of droplets of the quasicrystal-forming alloys about 7 mm in diameter by application of this method were reported in [17,18,46] for the I-phase in Al-Cu-Fe and the D-phase in Al-Cu-Co. Meanwhile similar experiments were performed in which the nucleation behavior of the I-phase in Al-Pd-Mn [35], the D-phase in Al-Ni-Co [34], the metastable D-phase in Al-Co [36], the polytetrahedral phases λ–$Al_{13}Fe_4$ [20,21], [35] and μ–Al_5Fe_2 [20,21,35] and – for comparison – the crystalline CsCl-type β-phase in Al-(Cu-)Co [20,21] was investigated. The results of these experiments are compiled in this paragraph.

11.3.2.1 Experimental Results. All undercooling experiments mentioned below were performed in an electromagnetic levitation facility which is described elsewhere [21,22].

As an example in Fig. 11.1 the temperature–time profile of a levitation-processed $Al_{60}Cu_{34}Fe_6$ sample is shown. The sample was first molten and subsequently undercooled below its liquidus temperature T_L. Nucleation sets in at the temperature T_N. The release of the heat of fusion during crystallization leads to a temperature rise (recalescence). After recalescence the sample is cooled to lower temperatures.

For the $Al_{60}Cu_{34}Fe_6$ sample a maximum undercooling of $\triangle T^{\mathrm{I}} = T_{\mathrm{L}}^{\mathrm{I}} - T_{\mathrm{N}} \approx 100\,\mathrm{K}\,(\triangle T^{\mathrm{I}}/T_{\mathrm{L}}^{\mathrm{I}} = 0.09)$ with respect to the melting temperature $T_{\mathrm{L}}^{\mathrm{I}}$ of the I-phase is inferred from the temperature–time profile. A similar level of undercooling was measured for the alloy $Al_{58}Cu_{34}Fe_8$ ($\triangle T^{\mathrm{I}} = 100\,\mathrm{K}$,

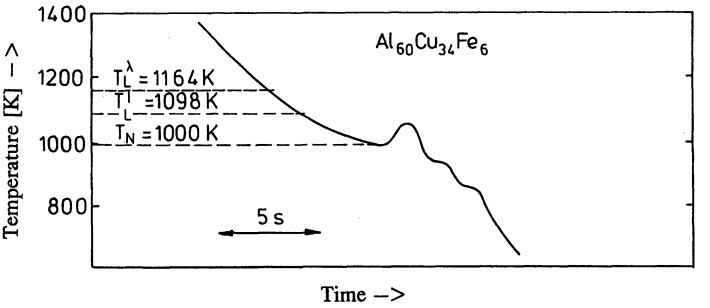

Fig. 11.1. Temperature-time profile of a levitation experiment on a $Al_{60}Cu_{34}Fe_6$ sample where a maximum undercooling was obtained. The sample was molten and subsequently cooled and undercooled. At the nucleation temperature T_N the solidification of the sample starts. Due to the release of heat of fusion during solidification the sample temperature rises (recalescence)

$\triangle T^I/T_L^I = 0.09$) [18,19]. SEM and TEM examinations of the as-solidified specimens showed that in both cases the I-phase nucleated primarily growing with a dendritic morphology [17–19,21]. For example a SEM micrograph of the maximum undercooled $Al_{60}Cu_{34}Fe_6$ specimen is depicted in Fig. 11.2. The measurement of the concentration ratios by EDX allows the identification of the different phases. This indicates the primary solidification of dendritic I-phase (indicated by "1" in Fig. 11.2) followed by the formation of a τ-phase (11.2) with a vacancy ordered CsCl-type structure and the intermetallic phases AlCu (11.3) and Al_2Cu (11.4).

The undercooling behavior of the I-phase in $Al_{72}Pd_{21}Mn_7$ is similar to that of the I-phase in Al-Cu-Fe. A maximum level of undercooling of $\triangle T^I = 125\,K\,(\triangle T^I/T_L^I = 0.11)$ was achieved [35].

For the polytetrahedral phase λ–$Al_{13}Fe_4$ an undercooling of $\triangle T^\lambda = 170$ $K(\triangle T^\lambda/T_L^\lambda = 0.12)$ was observed at its stoichiometric composition[20,21,35]. Even a larger undercooling of $\triangle T^\mu = 205\,K(\triangle T^\mu/T_L^\mu = 0.14)$ is measured on Al_5Fe_2 samples, which primarily solidify as a μ-phase [21,35].

$Al_{74}Ni_{14.5}Co_{10.5}$ melts were undercooled by $\triangle T^D = 190\,K\,(\triangle T^D/T_L^D = 0.14)$ below the melting temperature T_L^D of the D-phase which primarily nucleated from the undercooled melt [34].

Also for several Al-Cu-Co alloys with a low Co content the primary nucleation of the D-phase from the deeply undercooled melt was reported [17] – [19,21,46]. With respect to its melting temperature T_L^D for $Al_{65}Cu_{25}Co_{10}$ maximum levels of undercooling of $\triangle T^D = 204\,K\,(\triangle T^D/T_L^D = 0.16)$ were measured, for $Al_{67}Cu_{21}Co_{12}$ $\triangle T^D = 210\,K\,(\triangle T^D/T_L^D = 0.16)$ [18,19], and for $Al_{64}Cu_{22}Co_{14}$ $\triangle T^D \approx 189\,K\,(\triangle T^D/T_L^D = 0.15)$.

The binary alloy Al-Co forms a metastable D-phase [5,12,42] which has a narrow range of compositions closely around $Al_{73}Co_{27}$ [12]. This phase was observed in thin films produced by rapid quenching. Recently it was reported

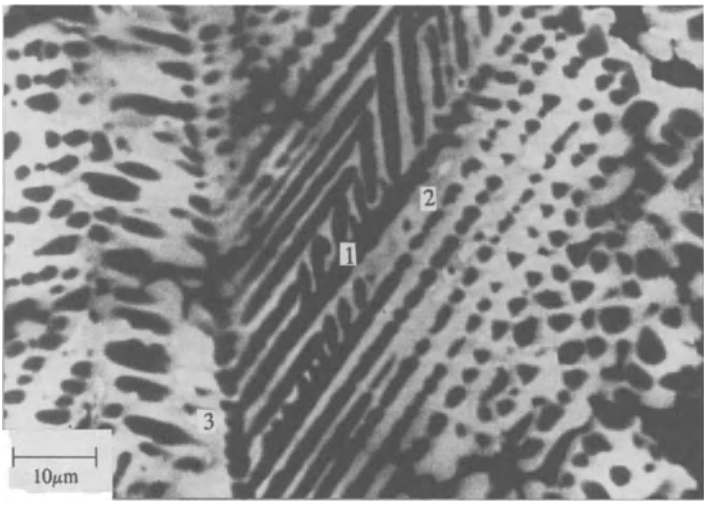

Fig. 11.2. SEM micrograph of the as-solidified $Al_{60}Cu_{34}Fe_6$ sample whose temperature–time profile is shown in Fig. 11.1. The following phases are observed: the I-phase (1) of composition $Al_{64.4}Cu_{22.6}Fe_{13}$, a vacancy-ordered CsCl-type τ-phase of composition $Al_{57.5}Cu_{36.3}Fe_{6.2}$ (2), AlCu (11.3) and Al_2Cu (4)

that massive samples 7 mm in diameter that consist purely of the D-phase can be produced by solidification from the deeply undercooled $Al_{74}Co_{26}$ melt employing the electromagnetic levitation technique [35,36]. The samples were undercooled to about $\triangle T^{\mathrm{D}} \approx 210\,\mathrm{K}\,(\triangle T^{\mathrm{D}}/T_{\mathrm{L}}^{\mathrm{D}} \approx 0.15)$ with respect to the virtual melting temperature of the metastable D-phase $T_{\mathrm{L}}^{\mathrm{D}} \approx 1440\,\mathrm{K}$ [36].

For some of the Al-Cu-Co alloys with a higher Co-content the cubic β-phase nucleates primarily even for the deepest undercoolings [20,21]. The undercoolings related to their liquidus temperatures T_{L}^{β} are much higher and reach values of about $\triangle T^{\beta} = 365\,\mathrm{K}\,(\triangle T^{\beta}/T_{\mathrm{L}}^{\beta} = 0.25)$ for e.g. $Al_{65}Cu_{20}Co_{15}$.

11.3.2.2 Discussion. The maximum relative undercoolings achievable by electromagnetic levitation for the I-phases both in Al-Cu-Fe and Al-Pd-Mn amount to $\triangle T^{\mathrm{I}}/T_{\mathrm{L}}^{\mathrm{I}} \approx 0.1$ while for the D-phases in Al-Cu-Co, Al-Ni-Co and Al-Co values of $\triangle T^{\mathrm{D}}/T_{\mathrm{L}}^{\mathrm{D}} \approx 0.15$ are obtained. For the polytetrahedral crystalline phases in Al(-Cu)-Fe, relative undercoolings were measured of $\triangle T^{\lambda}/T_{\mathrm{L}}^{\lambda} \approx 0.13$ for λ and of $\triangle T^{\mu}/T_{\mathrm{L}}^{\mu} \approx 0.14$ for μ. The undercoolability of the crystalline β-phase in Al-Cu-Co was the largest ($\triangle T^{\beta}/T_{\mathrm{L}}^{\beta} \approx 0.25$). This structure dependence of the undercoolability is described by the relation

$$\triangle T^{\mathrm{I}}/T_{\mathrm{L}}^{\mathrm{I}} < \triangle T^{\lambda}/T_{\mathrm{L}}^{\lambda} < \triangle T^{\mu}/T_{\mathrm{L}}^{\mu} < \triangle T^{\mathrm{D}}/T_{\mathrm{L}}^{\mathrm{D}} < \triangle T^{\beta}/T_{\mathrm{L}}^{\beta}\,. \qquad (11.11)$$

Similar levels of undercooling as observed for the β-phase were also observed for several other pure metals and alloys forming phases with bcc, fcc or

hcp structures by application of the electromagnetic levitation technique. For instance for pure Ni maximum relative undercoolings of $\triangle T/T_{\mathrm{L}} \approx 0.28$ were reported [10], for Co of $\triangle T/T_{\mathrm{L}} \approx 0.2$ [33] or for Co-Pd alloys (fcc structure) of $\triangle T/T_{\mathrm{L}} \approx 0.20$–$0.23$, depending on the composition [47]. Thus the β-phase is representative of crystalline phases with a small unit cell. However, since it occurs in the quasicrystal-forming alloy system Al-Cu-Co at compositions close to those of the D-phase, it is more suiteable for a comparison of its undercooling behavior with that of polytetrahedral phases than other normal crystalline phases from completely different alloy systems.

The interfacial energy σ at the nucleation temperatures T_{N} of the respective phases is estimated from the measured undercoolings employing (11.3), (11.4), (11.6), (11.7) and (11.10). For this homogeneous nucleation ($f(\vartheta) = 1$ and $\xi = 1$) is assumed, and the numerical values of the different parameters compiled in Table 11.1 are employed. For all alloys the molar volumes are

Table 11.1. Energy σ of the interface between nucleus and melt, relative undercoolings $\triangle T/T_{\mathrm{L}}$ and structure-dependent α-factors calculated for the different primarily nucleated phases from the maximum undercoolings observed for the different alloys as well as data used for the calculation. The $\triangle S_{\mathrm{f}}$ values for the I-, D-, λ- and μ-phases were estimated from DTA measurements on single-phase quasicrystalline $Al_{62.5}Cu_{25.5}Fe_{12}$ samples, single-phase quasicrystalline $Al_{64}Cu_{17}Co_{17}$ and $Al_{74}Co_{26}$ samples and on samples of the binary alloys λ-$Al_{13}Fe_4$ and μ-Al_5Fe_2 [23]. For the β-phase it is referred to as an approximation to Richard's rule ($\triangle S_{\mathrm{f}} \approx R$), with R the gas constant

Parameters Primary phase	$Al_{60}Cu_{34}Fe_6$ I-phase	$Al_{72}Pd_{21}Mn_7$ I-phase	$Al_{13}Fe_4$ λ-phase	Al_5Fe_2 μ-phase
T_{L}/K	1098	1137	1420	1430
T_{N}/K	1000	1012	1250	1225
t_{N}/s	5	15	38	25
$\triangle S_{\mathrm{f}}$/(J/ K mol)	11.3	11.3	13.7	13.6
$\triangle T/T_{\mathrm{L}}$	0.09	0.11	0.12	0.14
$\sigma(T_{\mathrm{N}})/(\mathrm{J/m^2})$	0.09±0.01	0.10±0.01	0.16±0.01	0.18±0.02
α	0.28±0.03	0.32±0.03	0.33±0.03	0.37±0.03

Parameters Primary phase	$Al_{74}Ni_{14.5}Co_{10.5}$ D-phase	$Al_{65}Cu_{25}Co_{10}$ D-phase	$Al_{74}Co_{26}$ D-phase	$Al_{65}Cu_{20}Co_{15}$ β-phase
T_{L}/K	1360	1259	1440	1485
T_{N}/K	1169	1055	1230	1120
t_{N}/s	20	8	28	60
$\triangle S_{\mathrm{f}}$/(J/K mol)	7.6	7.6	11.6	8.3
$\triangle T/T_{\mathrm{L}}$	0.14	0.16	0.15	0.25
$\sigma(T_{\mathrm{N}})/(\mathrm{J/m^2})$	0.11±0.01	0.11±0.01	0.16±0.01	0.17±0.02
α	0.44±0.04	0.48±0.04	0.40±0.03	0.63±0.06

approximated by $V_m \approx 8.3\ \mathrm{cm^3\ mol^{-1}}$, the interatomic spacing by $a_0 \approx 0.24$ nm. The sample volumes were $V \approx 0.18\ \mathrm{cm^3}$. For the parameter A the same value as for Al-Mn [2] is used ($A = 2106$ K). As a first estimate the prefactor η_0 is chosen such that the viscosity at the melting temperature equals 1 poise – a typical value for quasicrystal-forming alloys [14]. As a rough approximation for the ideal glass temperature $T_0 \approx 0.5 \cdot T_L$ is assumed. This delivers the following relation of σ for the different phases (units in $\mathrm{J/m^2}$):

$$\begin{aligned}\sigma^I \approx 0.1 \ &< \sigma^D \approx 0.11 \ < \sigma^\lambda \approx 0.15 < \sigma^{D-AC} \\ &\approx 0.16 < \sigma^\beta \approx 0.17 < \sigma^\mu \approx 0.19\,.\end{aligned} \tag{11.12}$$

Relation (11.12) resembles the one given in (11.11), from which it is deduced. There are, however, some differences in the sequence of the various terms and σ inferred for the D-phase in Al-Co (σ^{D-AC}) is larger than that for the D-phases in Al-Ni-Co and Al-Cu-Co (σ^D).

According to most models for the solid–liquid interfacial energy [38,39,41] σ depends on the temperature. The various phases studied in the present work differ in T_L. For an analysis of possible structural effects on nucleation of solid phases in undercooled melts, a parameter should be evaluated that is independent of T_L and other phase-relevant parameters such as e.g. $\triangle S_f$. The only model which enables such an analysis is the negentropic model by Thompson and Spaepen [38] in which the parameter α depends on the solid structure.

Equations (11.8) and (11.12) are used to determine α for the various phases of different degrees of polytetrahedral order (Table 11.1). This delivers:

$$\alpha^I \approx 0.3 < \alpha^\lambda \approx 0.33 < \alpha^\mu \approx 0.37 < \alpha^D \approx 0.45 < \alpha^\beta \approx 0.63\,. \tag{11.13}$$

α is lowest for both I-phases ($\alpha \approx 0.3$) and largest for the crystalline CsCl-type β-phase ($\alpha^\beta \approx 0.63$). The corresponding α-values of the polytetrahedral phases λ–$Al_{13}Fe_4$ and μ–Al_5Fe_2 as well as those of the D-phases are in between. The α-value for λ is lower than that of μ due to the higher degree of polytetrahedral SRO of λ (large unit cell of 102 atoms) than that of μ (unit cell of 15 atoms). For the D-phases in Al-Cu-Co, Al-Co and Al-Ni-Co α-values in the range between 0.40 and 0.48 were obtained. Relation (11.13) reflects the same sequence of α-values as relation (11.11) with respect to $\triangle T/T_L$.

It should be stressed that the α-values obtained for I-phases in both alloy systems are similar. Also the differences in the α-factors obtained for the D-phases out of the three alloy systems Al-Ni-Co, Al-Cu-Co and Al-Co are small. This indicates that the nucleation behavior of the investigated solid phases is mainly governed by the topological structure and only to a minor degree by the chemical composition.

11.4 Estimation of the Energy of the Solid–Liquid Interface

The undercooling experiments presented in the preceding section indicate a systematic variation of σ and α with the structure of the solid phase.

As already mentioned in Sect. 11.2.1, the negentropic model by Spaepen and Thompson [38,39,41] delivers an estimate of σ for crystals with an fcc/hcp [39] and bcc [41] structure by modeling of the interface between liquid and solid using the following three construction principles:

1. The formation of tetrahedra is preferred.
2. Octahedral holes are forbidden.
3. The density is maximized.

Recently in a similar way an estimate for the interfacial energy of the I-phase in Al-Pd-Mn and the polytetrahedral phases λ–$Al_{13}Fe_4$ and μ–Al_5Fe_2 was provided [22]. Because an analytical estimation as performed for fcc/hcp and bcc phases by Spaepen and Thompson appears only to be possible for simple crystalline phases but not for complex crystalline or quasicrystalline phases, the configurational entropy of the interface between a melt and polytetrahedral phases was calculated numerically.

The employed numerical algorithm [22] computes all possibilities to construct the first interfacial layer on top of a section of the most densely packed (quasi)crystal plane following the rules mentioned above. For simplicity we do not distinguish between different atomic species, which means that only the topological structure of the solid is considered. Taking into account the experimentally observed low impact of the chemical composition on the undercoolability, this simplification appears to be justified.

The calculations were performed on a Pentium^{TM}-PC for different numbers N_S of atoms in the solid layer as specified in Table 11.2. From the number Z of different configurations determined by the algorithm and the number N_i of atoms in the constructed interface the configurational entropy $S_{cf}(1)$ per atom in the first interfacial layer is calculated by $S_{cf} = (k_B/N_i)\ln(Z)$, which is valid for systems large enough.

Table 11.2. Numerically estimated α-factors (α_{calc}) as well as data inferred from modeling of the interface for the different phases

Phase	System size	N_i/N_s	$S_{cf}(i)$	α_{calc}
I	$83 \leq N_s \leq 186$	0.50	$0.19 \cdot k_B$	0.34
λ–$Al_{13}Fe_4$	$104 \leq N_s \leq 234$	0.55	$0.15 \cdot k_B$	0.39
μ–Al_5 Fe_2	$72 \leq N_s \leq 128$	0.67	$0.23 \cdot k_B$	0.43
bcc	analytic. est. [41]	0.923 [41]	$0.078 \cdot k_B$ [41]	0.71 [41]
fcc/hcp	analytic. est. [39]	1.10 [38,39]	$0.066 \cdot k_B$ [39]	0.86 [39]

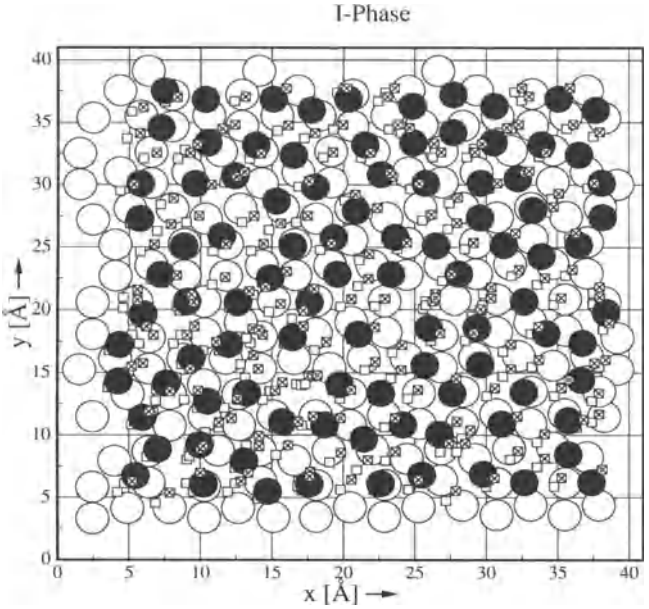

Fig. 11.3. One possibility of constructing the first interfacial layer on top of a section of the five-fold plane of the I-phase in Al-Pd-Mn

As an example one possibility to construct the first interfacial layer on top of a section from a fivefold plane of the I-phase in Al-Pd-Mn is depicted in Fig. 11.3. Unlike fcc, hcp and bcc phases [38,39,41], the density of the first interfacial layer of the λ, μ and I-phase is already so low that a second layer cannot be constructed. Therefore, the interface consists only of one layer ($N_\mathrm{i} = N_1$). From these results $S_\mathrm{cf}(i)$ the α-values (α_calc) for the different phases are calculated by use of (9). The results inferred from this analysis are summarized in Table 11.2 together with those from the analysis by Spaepen and Thompson [39,41] for fcc, hcp and bcc structures. The differences in α_calc are mainly a result of a different number $N_\mathrm{i}(1)$ of atoms in the interface, while the variation of the estimated configurational entropy is less decisive.

The sequence of the α-values obtained for the different phases is the same as that deduced from the undercooling experiments (Sect. 11.3.2). Despite the fact that the model for the interface is very simple (e.g. only the topological structure of the solid is considered) and although the modeled systems consist of only a few hundred atoms, the α-factors inferred from calculations agree qualitatively with the experimental values. This indicates that the modeling assumptions are reasonable and describe the major physical processes that give rise to the energy of the solid–liquid interface.

11.5 Conclusions

Results of different kinds of experiments (droptube, atomization, rapid quenching, levitation undercooling) on the nucleation behavior of quasicrystalline and polytetrahedral phases were reviewed. All these experiments indicate that the activation threshold for the nucleation is lower, the more pronounced the polytetrahedral SRO of the nucleating solid phase.

The energy of the interface between solid and the melt was estimated by a numerical method basing on the negentropic model by Spaepen and Thompson for the I-phase in Al-Pd-Mn and the polytetrahedral phases $Al_{13}Fe_4$ and Al_5Fe_2. Within this model it is assumed that tetrahedral SRO prevails in the solid–liquid interface. The results of the calculations show the same tendency for the structure dependence of the interfacial energy as observed in the undercooling experiments, which supports the model assumption of a polytetrahedral SRO prevailing in undercooled melts.

Acknowledgment

The author is grateful to Dr. J. Schroers, Dr. B. Grushko, T. Schenk and Dr. T. Volkmann for fruitful discussions, to Prof. Dr. D.M. Herlach, Prof. Dr. K. Urban and Prof. Dr. B. Feuerbacher for continuous support, to Dr. G.P. Görler and Dr. G. Wilde for assistance in the DTA measurements and to M. Beyß for sample preparation and to H. Mühlmeyer and H. Grill for technical help. Financial support from the Deutsche Forschungsgemeinschaft (DFG) and DLR-BO (former DARA) is gratefully acknowledged.

References

1. Bardenheuer P. and Bleckmann R. (1939), Mitteilung KWI für Eisenforschung **21**, 201
2. Battezzati L., Antonione C. and Marino F. (1989), J. Mater. Sci **24**, 2324
3. Bendersky L.A. and Ridder S.D. (1986), J. Mater. Res. **1**, 405
4. Christian J.W., *The Theory of Transformation in Metals and Alloys* (Pergamon, Oxford, 1975), p. 418
5. Dong C., Li G.B. and Kou K.H. (1987), J. Phys. **F17**, L189
6. Ebalard S., Spaepen F., Cochrane R.F. and Greer A.L. (1991), Mat. Sci. Eng. A **133**, 569
7. Fahrenheit D.B. (1724), Philos. Trans. R. Soc. **39**, 78
8. Frank F.C. (1952), Proc. R. Soc. London A **215**, 43
9. Gillessen F. and Herlach D.M. (1991), Mater. Sci. Eng. **A134**, 1220
10. Gomersall D.W., Shriraishi S.Y. and Ward R.G. (1965), J. Aust. Inst. Met **10**, 220
11. Greer A.L. (1994), Mat. Sci. Eng. **A178**, 113
12. Grushko B., Holland-Moritz D. and Bickmann K. (1996), J. Alloys Comp. **236**, 243

13. Herlach D.M. (1991), Ann. Rev. Mater. Sci. **21**, 23
14. Herlach D.M., Gillessen F., Volkmann T., Wollgarten M. and Urban K. (1992), Phys. Rev. B **46**, 5203
15. Herlach D.M., Cochrane R.F., Egry I., Fecht H.-J. and Greer A.L. (1993), International Materials Review **38**, 273
16. Herlach D.M. (1994), Mat. Sci. Eng. **R12**, 177
17. Holland-Moritz D., Herlach D.M. and Urban K. (1993), Phys. Rev. Lett. **71**, 1196
18. Holland-Moritz D. (1994), Thesis, RWTH Aachen
19. Holland-Moritz D., Herlach D.M., Grushko B. and Urban K. (1994), Mat. Sci. Eng. A **181/182**, 766
20. Holland-Moritz D., Schroers J., Herlach D.M., Grushko B. and Urban K., *Proceedings of the International Conference on Quasicrystals*, ed. Janot Ch. and Mosseri R. (World Scientific, Singapore, 1995), p. 636
21. Holland-Moritz D., Schroers J., Herlach D.M., Grushko B. and Urban K. (1998), Acta Mater. **46**, 1601
22. Holland-Moritz D. (1998), Int. J. Non-Equil. Process. **11**, 169
23. Holland-Moritz D., Lu I.-R., Wilde G., Schroers J. and Grushko B. (1999), J. Non-Cryst. Sol. **250-252**, 829
24. Kelton K.F., *Solid State Phys.*, ed. H. Ehrenreich, F. Seitz, and D. Turnbull (Academic Press, New York, 1991), Vol. 45, p. 75.
25. Lopez A., Baniel P., Gall P. and Granier J. (1991), *Proc. of the OE Fibers'91 Symp.*, Boston, MA, 3-6. SPIE proc. Vol. 1590-23, p. 191
26. Magill J., Capone F., Beukers R., Werner P. and Ohse R.W. (1987), High Temp.- High Press. **19**, 461
27. Maret M., Pasturel A., Senillou C., Dubois J.M. and Chieux P. (1989), J. Physique **50**, 295
28. Maret M., Lançon F. and Billard L. (1993), J. Phys. I France **3**, 1873
29. Nelson D.R. and Spaepen F., *Solid State Phys.*, ed. H. Ehrenreich, F. Seitz, and D. Turnbull (Academic Press, New York, 1989), Vol. 42, p. 1.
30. Nosé S. and Yonezawa F. (1986), J. Chem. Phys. **84**, 1803
31. Perepezko J.H. (1980), *Proc. of the 2nd Int. conf. on Rapid solidification processing*, ed. R. Mehrabian et al., 56
32. Rhim W.-K., Chung S.K., Barber D., Man K.F., Gutt G., Rulison A. and Spjut R.E. (1993), Rev. Sci. Instrum. **64** (10), 2961
33. Schade J., McLean A. and Miller W.A., *Undercooled alloy phases*, ed. E.W. Collings and C.C. Koch 233, Warrendale, PA, Metallurgical Society of AIME (1986)
34. Schenk T., Holland-Moritz D. and Grushko B.; to be published.
35. Schroers J. (1997), Thesis, RWTH Aachen
36. Schroers J., Holland-Moritz D., Herlach D.M., Grushko B. and Urban K. (1997), Mat. Sci. Eng. **A226-228**, 990
37. Shechtman D., Blech I., Gratias D. and Cahn J. (1984), Phys. Rev. Lett. **53**, 1951
38. Spaepen F. (1975), Acta Metall. **23**, 729
39. Spaepen F. and Meyer R.B. (1976); Scripta Met. **10**, 257
40. Steinhardt P.J., Nelson D.R. and Ronchetti M. (1984), Phys. Rev. B **28**, 784
41. Thompson C.V. (1979), Ph.D. Thesis, Harvard University
42. Tsai A.P., Inoue A. and Masumoto T. (1995), Phil. Mag. Lett. **70**, 303

43. Turnbull D. and Fischer J.C. (1949), J. Chem. Phys. **17**, 71
44. Turnbull D. (1950), J. Appl. Phys. **21**, 1022
45. Turnbull D. (1952), J. Chem. Phys. **20**, 411
46. Urban K., Holland-Moritz D., Herlach D.M. and Grushko B. (1994), Mat. Sci. Eng. A**178**, 293
47. Volkmann T., Wilde G., Willnecker R. and Herlach D.M., J. Appl. Phys. (1998), **83**, 3028
48. Volmer M. and Weber A. (1926), Z. phys. Chem. **119**, 227
49. Vonnegut B. (1948), J. Colloid Sci. **3**, 563

Part IV

Defects and Mechanical Properties

12 Phasons, Dislocations, and Cracks

Hans-Rainer Trebin

Summary. It is shown that the mechanical properties of quasicrystals, such as plasticity and fracture, are strongly influenced by the phason degree of freedom, which is specific for quasiperiodic systems.

12.1 Introduction

The physical properties of an atomic system are determined by two factors: the chemical species of the constituents and the structure. In quasicrystals, the structure appears to be dominant, and the study of structure–property relations is not only of academic interest, but of importance in satisfying the material request by applications. Structure consists of two ingredients: order and its defects. Our interest focuses here on mechanical properties, plasticity and fracture. A major mechanism of plastic deformation is migration of specific defects, the dislocations. These exist in both periodic [5] and quasiperiodic [2] crystals. In the latter, however, they are accompanied by special elementary excitations, the phasons, which exist due to the peculiar quasicrystalline structure. Thus, before illuminating dislocation motion and crack propagation in quasicrystals (Sects. 12.3 and 12.4), we will investigate the structural origin of phasons both in quasiperiodic tilings and in realistic models (Sect. 12.2).

12.2 Phasons

12.2.1 Quasiperiodic Mass Densities as Cuts

A major tool to study the structure of quasicrystals is electron (or X-ray or neutron) diffraction. Icosahedral quasicrystals, such as AlMnPd or AlCuFe, display sharp Bragg peaks, whose scattering wave vectors $\boldsymbol{q}$ are integer linear combinations of the six vertex vectors $\boldsymbol{k}_i, i = 1, \ldots, 6$, of an icosahedron,

$$\boldsymbol{q} = n_1\boldsymbol{k}_1 + n_2\boldsymbol{k}_2 + n_3\boldsymbol{k}_3 + n_4\boldsymbol{k}_4 + n_5\boldsymbol{k}_5 + n_6\boldsymbol{k}_6 \tag{12.1}$$

and, hence, are indexed by the sixtuple $(n_1, n_2, \ldots, n_6) \in \mathbb{Z}^6$. The scattering wave vectors are the fingerprints of the structure, because they represent the *support of the mass density in reciprocal space*, i.e. the set $\{\boldsymbol{q}\}$, where the

J.-B. Suck et al. (eds.), *Quasicrystals*
© Springer-Verlag Berlin Heidelberg 2002

Fourier transform of the mass density can be non-zero. The mass density of periodic crystals contains three basic plane waves. Their three wave vectors $\boldsymbol{k}_1, \boldsymbol{k}_2, \boldsymbol{k}_3$ are linearly independent, and they are supplemented by higher harmonics, whose wave vectors are integer linear combinations

$$\boldsymbol{q} = n_1\boldsymbol{k}_1 + n_2\boldsymbol{k}_2 + n_3\boldsymbol{k}_3. \tag{12.2}$$

Hence the scattering wave vectors of a periodic crystal form a periodic lattice. Three phases φ_1, φ_2 and φ_3 are associated with the basic waves. They can be expressed as $\varphi_j = \boldsymbol{k}_j \cdot \boldsymbol{u}$ and denote a rigid translation of the crystal by the displacement vector $-\boldsymbol{u}$. If $\boldsymbol{u}(\boldsymbol{r}, t)$ is position- and time-dependent, it is a displacement field and describes a deformation of the crystal such as, for example, a sound wave. Hence the phases φ_j are denoted "phonon-like".

The mass density of icosahedral quasicrystals contains *six* basic plane waves [6]:

$$\rho(\boldsymbol{r}) = \sum_{j=1}^{6} \rho_j \exp \mathrm{i}(\boldsymbol{k}_j \cdot \boldsymbol{r} + \varphi_j). \tag{12.3}$$

Their wave vectors, the vertex vectors of the icosahedron, are linearly independent over the integers. Hence the number cannot be reduced. The superposition of basic waves and higher harmonics is quasiperiodic. The wave vectors form a dense set in reciprocal space, and there are now six phases φ_j.

The meaning of these phases becomes evident when we associate with each of the basic reciprocal wave vectors its own, linearly (over the reals) independent direction. Physical reciprocal space is denoted by $E_q^{||}$ and is supplemented by a three-dimensional (3D) orthogonal space $E_q^{\perp}$ such that $E_q^{||} \oplus E_q^{\perp} = \mathbb{R}_q^6$. The basic wave vectors are renamed $\boldsymbol{k}_j^{||}$ and obtain components $\boldsymbol{k}_j^{\perp}$ with the property that $\kappa_j = (\boldsymbol{k}_j^{||}, \boldsymbol{k}_j^{\perp})$ form six orthogonal vectors of the same length. Denoting $\boldsymbol{x}^{||} = \boldsymbol{r}$ and $\xi = (\boldsymbol{x}^{||}, \boldsymbol{x}^{\perp})$, we replace the phases $\boldsymbol{k}_j \cdot \boldsymbol{r} = \boldsymbol{k}_j^{||} \cdot \boldsymbol{x}^{||}$ by their lift $\kappa_j \cdot \xi = \boldsymbol{k}_j^{||} \cdot \boldsymbol{x}^{||} + \boldsymbol{k}_j^{\perp} \cdot \boldsymbol{x}^{\perp}$ to obtain a mass density that is periodic in $E^{||} \oplus E^{\perp} = \mathbb{R}^6$:

$$\rho^6(\xi) = \sum_{j=1}^{6} \rho_j \exp \mathrm{i}(\kappa_j \cdot \xi + \varphi_j). \tag{12.4}$$

$\rho(\boldsymbol{r})$ is retrieved by putting $\boldsymbol{x}^{\perp} = 0$, and hence is the *restriction* of $\rho^6(\xi)$ to $E^{||}$. The phases φ_j can be expressed as

$$\varphi_j = \kappa_j \cdot \gamma = \boldsymbol{k}_j^{||} \cdot \boldsymbol{u} + \boldsymbol{k}_j^{\perp} \cdot \boldsymbol{w} \tag{12.5}$$

with a 6D shift vector γ, which is composed of the phonon-like displacement $\boldsymbol{u}$ and a new type of shift, $\boldsymbol{w}$, denoted the "phason shift".

Such a "lift" of the quasiperiodic mass density into a higher-dimensional periodic crystal actually is being performed when the amplitudes ρ_j are determined from scattering experiments (more exactly, it is the Patterson function, which is constructed from the scattering intensity $|\rho_j|^2$ [6]).

12.2.2 Tiling Vertices from Cuts

Hypercrystallography is also applied in the construction of quasiperiodic tilings of the line, plane or 3D space [1]. For the standard tilings, such as the Fibonacci chain (in one dimension) or the octagonal tiling (in two dimensions), the hypercrystal is 2D and 4D cubic, respectively. Atomic surfaces, resulting from the projection of the hypercubic unit cell onto orthogonal space $E^{\perp}$, are attached to each lattice point (Fig. 12.1). These are line segments, or regular octagons, connected by "steps". The cut with $E^{||}$ yields the vertices of the tiling. The tilings exhibit rich structures. Striking features of the octagonal tilings (Fig. 12.2) are hexagon–square worms, which run horizontally, vertically and along the two diagonals. The hexagons consist of a square and two 45° rhombs and are all oriented (square pointing up or down) identically along the worm.

12.2.3 Phasonic Flips

A uniform change of phase is equivalent to a parallel displacement of the cutting plane by the phason shift $\boldsymbol{w}$ (Fig. 12.1). In the course of the shift, the cutting plane occasionally leaves one atomic surface and enters an adjacent one, causing a vertex to jump within a cage. In the Fibonacci chain, the cage is a long–short segment. In the octagonal tiling (Fig. 12.2) it is a hexagon, and the jump occurs in all hexagons along certain hexagon–square worms. If the phase differs in two halves of the tiling, along the phase boundary the hexagons change orientation, i.e. the boundary acts like a Bloch wall. This boundary can move along the worm by simpleton flips of adjacent hexagons.

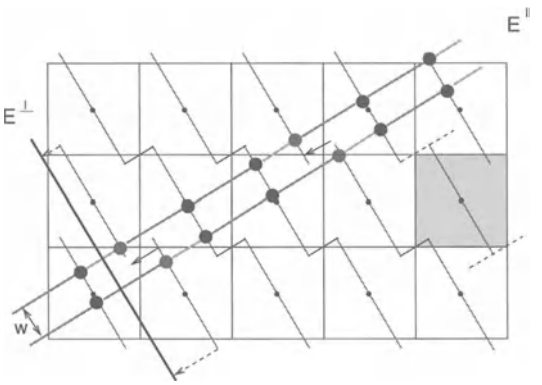

Fig. 12.1. The construction of the Fibonacci chain by a cut through a 2D periodic crystal. An atomic surface is attached to each lattice point. The intersection with physical space $E^{||}$ yields the atoms of the chain. A phason shift amounts to displacing the cut parallel to itself (or, alternatively, the entire crystal). Occasionally, the intersecting line leaves an atomic surface and enters another one. As a consequence, atoms perform a flip motion in a cage, which consists of a long and a short segment

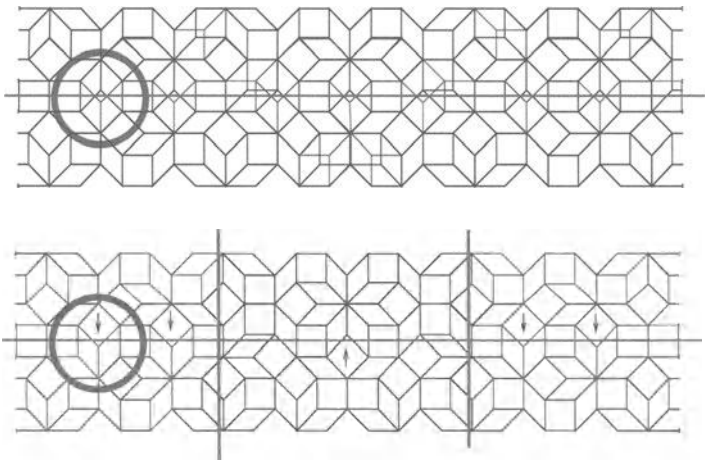

Fig. 12.2. The octagonal tiling consists of squares and 45° rhombs. The cages for phason flip are hexagons (one being encircled), which after the flip have changed orientation. The hexagons are arranged in hexagon–square worms, where they all point in the same direction and all are flipping simultaneously in a homogeneous change of phase. Top: Two tilings differing in phase are superposed. Bottom: Regions of different phase have opposite orientations of the hexagons and are separated by a type of Bloch wall. The wall can move by flip of adjacent hexagons

12.2.4 Realistic Models

Are these phasonic jumps merely tiling properties, or do they also occur in real systems? To obtain quasiperiodic crystals consisting of point-like particles, tiles have to be "decorated" with atoms, in much the same way as the unit cell of a periodic crystal has to be endowed with a basis. For decagonal AlCuCo, which consists of two quasiperiodic layers stacked periodically along the layer normal, the Tübingen triangle tiling has been decorated with the three kinds of atomic species for each layer (Fig. 12.3) [12]. The tiling consists of an acute and a flat triangle. The basic phasonic flips are the "simpleton flips" within a rhomb and the trapezoid flip (Fig. 12.4). The decoration consists of 13 symbols for the acute and eight symbols for the flat triangle. The vertices are centers of ten-rings of atoms. There is, however, an inflation–deflation symmetry, by division of the triangles into congruent subunits, which finally leads to decorations by two and one symbols, respectively. From a slightly different point of view, each of the two layers can by itself be interpreted as a partially filled "binary tiling" (Fig. 12.5). We will make use of a binary tiling later when simulating dislocation and crack motion. It arises if atoms are placed onto all vertices of the Tübingen triangles and into the interior of the acute triangles. For the two layers of the AlCuCo model structure (Fig. 12.5) half of these interior atoms are missing. In this way, the simpleton flip is realized by a very short-ranged jump of two atoms (0.86 Å,

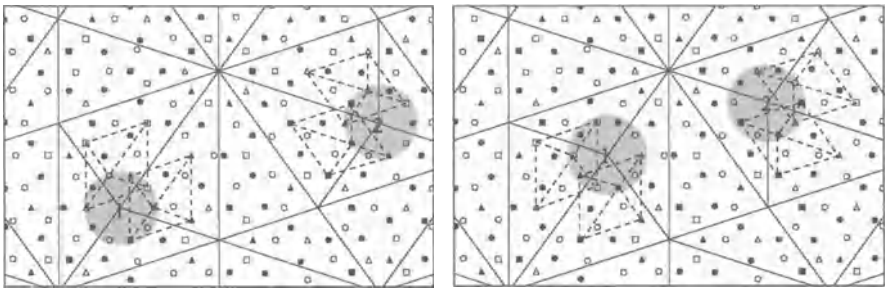

Fig. 12.3. A model of AlCuCo based on the Tübingen triangle tiling [12]. It consists of two layers (one of empty, the other of filled symbols) which are stacked periodically along the paper normal. Circles denote Al, triangles Cu and squares Co. The atomic configuration is obtained by decorating the large triangle with 13 and the small one with eight atoms. There is, however, a deflation symmetry: a simpler decoration (by 5/3, and finally by 2/1 atoms) arises if the triangles are divided into congruent smaller ones. Phason flips of four atoms in the highest deflation step (shown in Figs. 12.4 and 12.5) mimic a phason flip on the lowest deflation step, where a ring of ten atoms is rearranged (right)

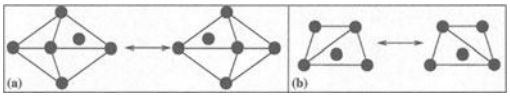

Fig. 12.4. Simpleton flips of the Tübingen triangle tiling and the associated atomic decoration

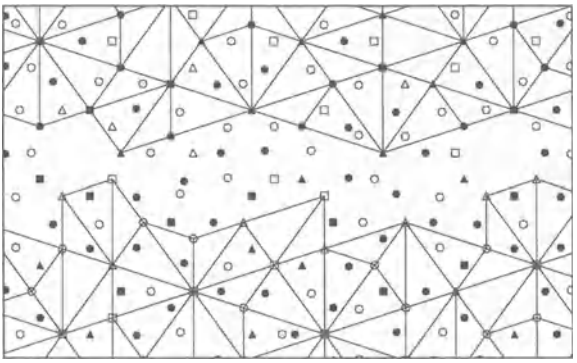

Fig. 12.5. Each layer of the model AlCuCo structure can be interpreted as a partially filled binary tiling [12]. Two correlated simpleton flips, of the type shown in Fig. 12.4, one in each layer, lead to the simpleton flip in the lowest stage of deflation shown in Fig. 12.3

Fig. 12.4). If this twin jump happens simultaneously in the two layers involving a total of four atoms, a ten-ring of the lower stage of deflation dissolves and rearranges at a slightly displaced position (Fig. 12.3). Thus, by phason flips of four atoms, the motion of an entire ten-ring of atoms is simulated, invoking simpleton flips in a tiling of much larger scale. A similar phenomenon occurs in a model structure for i-AlMnPd [4].

12.3 Plasticity

At room temperature, quasicrystals are brittle, i.e. they break when they are deformed beyond a certain limit. At about 80 % of the melting temperature, which is around 700°C, they become plastically deformable *without hardening*. This means that, at a certain critical stress, the deformation is irreversible and, when progressing, requires less and less stress. Experimentally, it has been confirmed that dislocation motion is largely responsible for plastic ductility [11]. In theory, one first must ascertain that the quasiperiodic

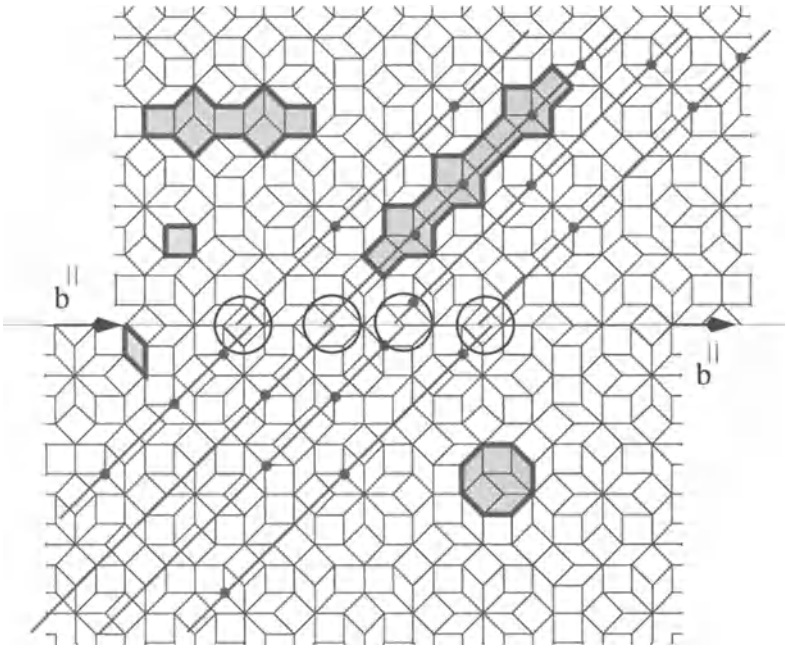

Fig. 12.6. The upper half of the octagonal tiling has been shifted by a lattice vector $\boldsymbol{b}^{\parallel}$ relative to the lower half. The two halves match again, but the hexagon–square worms crossing the glide plane change orientation. Thus the plane has become a phason wall of phase difference $\boldsymbol{b}^{\perp}$. The shift can happen stepwise by motion of a dislocation along the glide plane. The phason wall follows in the wake of the dislocation

structure admits dislocations. Then one must test dislocation dynamics, for example, by numerical simulations.

Periodic crystals are deformed plastically by shear along lattice planes. If the shear distance is a lattice vector $\boldsymbol{b}$ then, due to periodicity, the crystal appears to be undisturbed after the deformation except for surface steps. Dislocations in crystals are elementary topological defects, which perform the shearing step by step and which are characterized by the shearing vector $\boldsymbol{b}$, denoted the Burgers vector. Because of the periodicity in higher-dimensional space, dislocations also exist in quasicrystals [2]. They are connected to a vector $\boldsymbol{b} = (\boldsymbol{b}^{||}, \boldsymbol{b}^{\perp})$ of the hyperlattice. The parallel component $\boldsymbol{b}^{||}$ denotes the relative displacement along the lattice plane that separates the two halves of the quasicrystal. Since there is no periodicity, after the glide phasonic defects are found on this plane (Fig. 12.6). Indeed, the glide plane then represents a phason wall, with phase difference $\boldsymbol{b}^{\perp}$ between the two sides. If the deformation proceeds stepwise via the motion of a dislocation, this wall follows the dislocation line just as a flag follows the pole. The wall can disperse by phason flips.

Numerical simulations of plastic deformation have been performed on the 2D binary tiling (Fig. 12.7) [7,8,10]. Large A-type atoms were placed at the vertices of the Tübingen triangle tiling, and small B-type atoms in

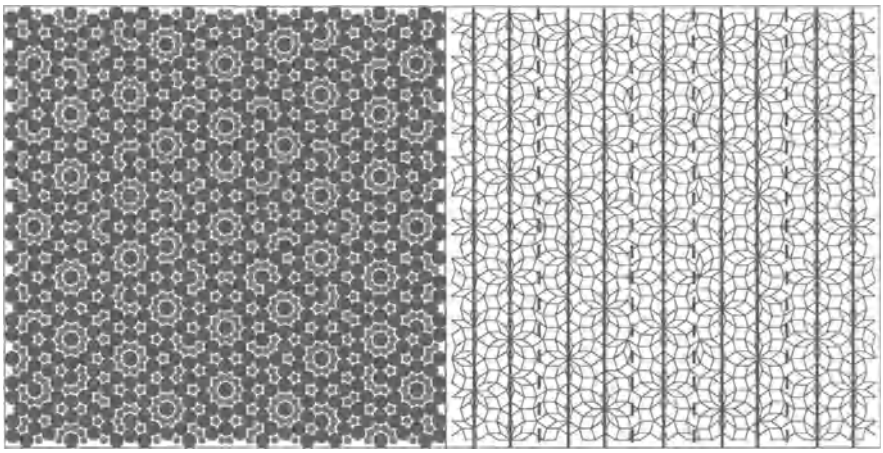

Fig. 12.7. Binary tiling, which was used for molecular dynamics simulations. Left: The atom representation, where large atoms were placed at the vertices of the Tübingen triangle tiling, and small ones in the interior of the large triangles. If neighboring atoms of different types are connected, one obtains the bond representation (right). The atomic ten-rings are represented by ten-pronged stars. They sit on parallel families of lines, inclined by 36° relative to each other (one family being drawn). There are two separations in the golden ratio, forming a Fibonacci sequence. The broken line in the middle of the large separation does not touch the ten-rings, and forms an "easy" line for dislocation motion and crack propagation

the interior of the large triangles. Two-body forces were applied in the form of three Lennard–Jones potentials, V_{AA}, V_{BB} and V_{AB}. The depth of the potential V_{AB} was chosen to be twice that of identical atoms to prevent phase separation. As a consequence, the striking ten-rings, which contain many AB bonds, become tightly bound clusters (Fig. 12.7). Instead of the atomic representation, frequently the bond representation of the binary tiling is applied, where only nearest-neighbor AB bonds are drawn. It is a rhombic tiling, not locally isomorphic to the Penrose pattern. The ten-rings turn into ten-pronged stars. These clusters are arranged along families of parallel lines, separated by two distances in the ratio of the golden number τ. The (broken) line dividing the large distance is an "easy" one. It does not touch any of the clusters and possesses a low surface energy. The different families of parallels are rotated with respect to each other by 36° due to the ten-fold symmetry of the binary tiling.

The shear was applied by different boundary conditions (Lees–Edwards boundaries or fixed strips), and the motion of atoms under the external forces and the internal two-body potentials was pursued by integration of Newton's equations. In these molecular dynamics simulations, it is also possible to control temperature and pressure. Figure 12.8 shows a numerical experiment, where under shear a dislocation dipole was formed in the interior of the sample of about 13 000 atoms, at 59 % of the melting temperature. As the dislocations traversed the sample, they left a phason wall (shaded areas). This wall is sharp and flat and runs exactly along an easy plane. At 90 % of the melting temperature (Fig. 12.9) the phason wall broadened due to strain-induced diffusion. A wide glide zone was formed, on which secondary

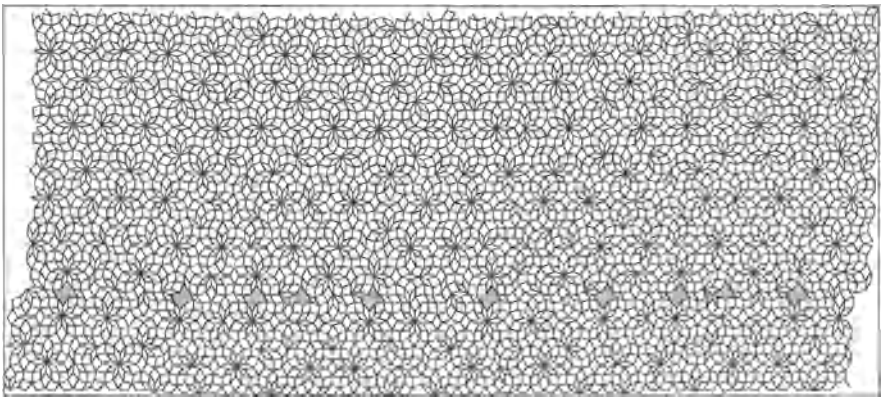

Fig. 12.8. In a molecular dynamics simulation at low temperature, a binary tiling has been sheared (bond representation). A dislocation dipole was formed in the middle of the figure, whose components moved outward and formed a sharp phason wall along an "easy line" [8]

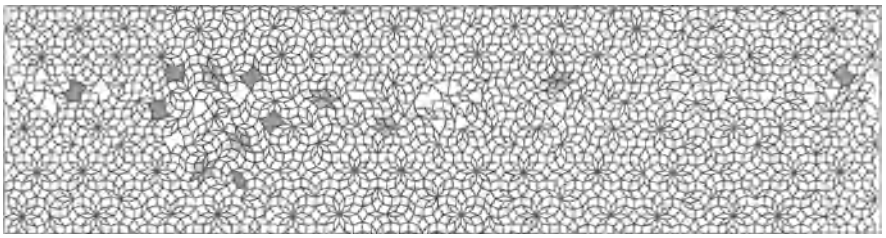

Fig. 12.9. A similar simulation as in Fig. 12.8, but close to the melting temperature. The phason wall has broadened due to strain-induced diffusion. The wide disturbed zone gives rise to secondary dislocations and is a hint for the deformation softening of quasicrystals [8]

dislocations form and plastic flow occurs, which contributes to the softening effects.

12.4 Cracks

On the same binary tiling, crack propagation has been studied [9]. A notch was inserted, and the quasicrystal was dilated by transverse displacement of the boundary strips (each being about four AB separations wide). The crack propagation was monitored at very low temperatures (10^{-4} of the melting temperature) by molecular dynamics simulation (Fig. 12.10). The fracture plane (line in two dimensions) shows two striking features. First, it is rough, strictly avoiding cutting any cluster. Second, it is running zig-zag, with deviations by 36° to the left and the right. Both features are caused by a new fracture mechanism, involving the new phason degree of freedom. Because of the dilative strain, the principle planes of maximum and minimum stress run vertically and horizontally, respectively. The plane of maximum shear stress, bisecting these planes, is inclined by 45° and is very close to the easy planes at 36°. Hence dislocations are being emitted from the crack tip at 36° to the left and the right. They are stopped at obstacles on the easy planes (incomplete ten-rings) and followed by a phason wall. Along the wall the binding energy of the atomic bonds is weakened and the surface energy is so low that the crack is opening along it. Cleavage planes of i-AlMnPd recorded by scanning tunneling microscopy indeed closely resemble this picture [3].

12.5 Conclusion

It has been shown that the mechanical behavior of quasicrystals is strongly influenced by the phason degree of freedom. Dislocation motion is accompanied by phason walls, which broaden at high temperature and give rise to wide glide zones, which support the softening of quasicrystals. At low temperatures these walls remain narrow and sharp. Crack tips emit dislocations,

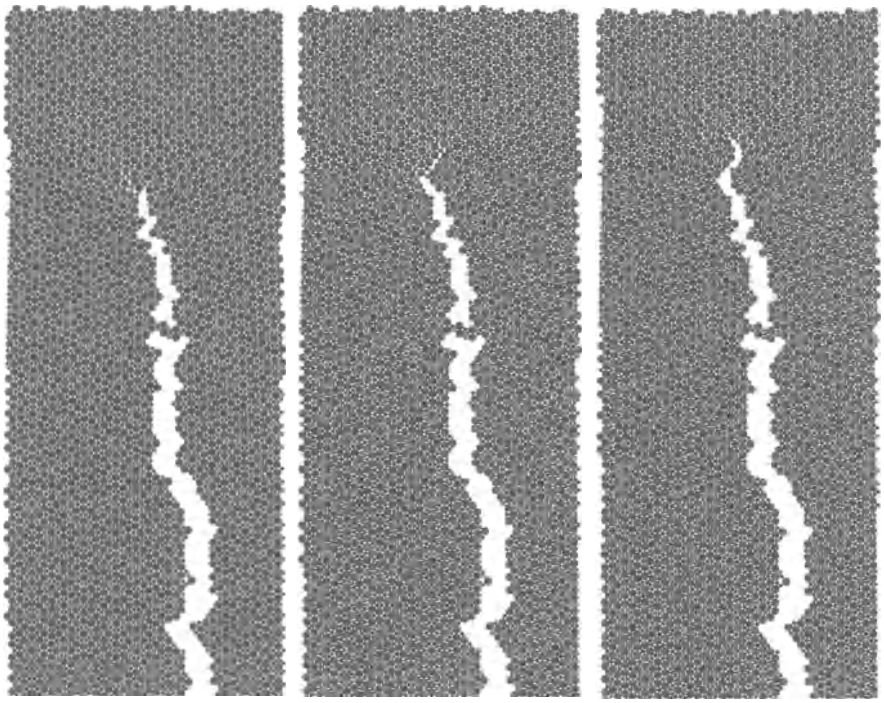

Fig. 12.10. Crack propagation in quasicrystals by the dislocation emission mechanism [9]. The crack tip has stopped (left) and then emits a dislocation (middle), which is followed by a phason wall (similar to Fig. 12.8). The atomic bonds are weakened along the phason wall. The surface energy is reduced along this wall and the crack can open further along it (right). The cleavage plane is rough on the scale of the cluster-like ten-rings, which remain complete due to their large binding energy

which are followed by these walls and guide the propagation of the crack. We have studied the binary tiling as a model system. It contains clusters separated by glue. It will be interesting to perform the same type of simulations in binary tilings with interpenetrating clusters, or in systems where the quasicrystalline order is systematically disturbed by an increasing number of phasons, thus performing the transition from a highly ordered to a random system.

References

1. Bak P. (1986): Scr. Metall. **20**, 1199
2. Bohsung J., Trebin H.-R. (1989): In *Introduction to the Mathematics of Quasicrystals*, ed. M.V. Jarić, volume 2 of *Aperiodicity and Order*, Academic Press, Boston, p. 183
3. Ebert Ph., Feuerbacher M., Tamura N., Wollgarten M., Urban K. (1996): Phys. Rev. Lett. **77**, 3827
4. Elser V. (1996): Phil. Mag. A **73**, 641
5. Hull D., Bacon D.J. (1984): *Introduction to Dislocations*, Pergamon Press, Oxford
6. Janot C. (1992): *Quasicrystals*, Clarendon Press, Oxford
7. Mikulla R., Roth J., Trebin H.-R. (1995): *Proc. 5th Int. Conf. Quasicrystals*, ed. Ch. Janot and R. Mosseri, World Scientific, Singapore, p. 297
8. Mikulla R., Roth J., Trebin H.-R. (1995): Phil. Mag. B **71**, 981
9. Mikulla R., Krul F., Gumbsch P., Trebin H.-R. (1997): In *New Horizons in Quasicrystals: Research and Applications*, ed. A.I. Goldman, D.J. Sordelet, P.A. Thiel, J.M. Dubois, World Scientific, Singapore, p. 200
10. Trebin H.-R., Mikulla R., Roth J. (1993): J. Non-Cryst. Solids **153 & 154**, 272
11. Wollgarten M., Beyss M., Urban K., Liebertz H., Köster U. (1993): Phys. Rev. Lett. **71**, 549
12. Zeger G., Trebin H.R. (1996): Phys. Rev. B **52**, R720

13 Defects

Markus Wollgarten, Volker Franz, Michael Feuerbacher, and Knut Urban

Summary. Defects in quasiperiodic lattices are introduced and described. The observed static and dynamic defects in esp. i-AlPdMn with different methods using electron diffraction and microscopy are analyzed in detail.

13.1 Introduction

As in normal crystalline materials, defects play an important role in quasicrystal research, too. There are direct relations between the structure of a specific material and its possible structural imperfections. Therefore, we will learn something about the perfect structure by the investigation of its defects. In addition, defects have to be considered when physical properties are investigated and discussed. However, as in usual crystalline materials, the *perfect* quasicrystal is not the state of matter which is right at hand for the investigation of physical properties.

The resulting necessity of observation and characterization of defects in quasicrystals is discussed in the following. We first demonstrate how to observe and characterize phason defects. Further, dislocations will be discussed. There, the techniques of diffraction contrast analysis and convergent beam electron diffraction (CBED) are explained. These topics are well investigated and are the basis for the following sections where results of more recent research on the motion and dissociation of dislocations in quasicrystals are presented.

Though defects are observed in various classes of quasicrystals (decagonal, icosahedral), we restrict the discussion to defects in icosahedral quasicrystals and their investigation by means of transmission electron microscopy (TEM).

13.2 Observation and Characterization of Phason Defects

Figure 13.1 shows two systematic rows of diffraction patterns obtained from different Al-Pd-Mn quasicrystals in a transmission electron microscope (for basics about TEM see [13,14,24]). Figure 13.1a was taken with a weakly deformed sample ($\Delta l/l_0 = \epsilon = 0.15\%$) while Fig. 13.1b is from a sample

J.-B. Suck et al. (eds.), *Quasicrystals*
© Springer-Verlag Berlin Heidelberg 2002

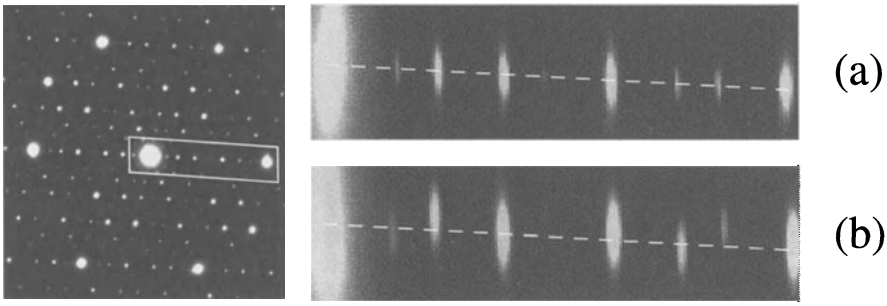

Fig. 13.1. Systematic rows of reflections taken from two-fold diffraction patterns; (**a**) a weakly deformed Al-Pd-Mn quasicrystal ($\epsilon = 0.15\%$); and (**b**) a strongly deformed specimen ($\epsilon = 0.25\%$). A line along which the reflections should align for a perfect quasicrystal has been added

which was deformed to a larger extend ($\epsilon = 0.25\%$). Close inspection of the rows of reflections reveals that for the strongly deformed sample the diffraction spots are shifted away from an ideal straight line which is almost not detectable in the upper image. These shifts can be quantitatively analyzed within the framework of a linear phason strain field analysis. Referring to a paper by Gratias and co-workers [12] we qualitatively demonstrate the action of linear phason strain fields. The argument is based on the construction of an one-dimensional quasicrystal but can be easily extended to the case of three-dimensional icosahedral quasicrystals.

The one-dimensional quasilattice L_{1D} can be described by the function

$$L_{1D} = (((H * \eta) \cdot \mathrm{d}x_{E_c}) * \mathrm{d}x_{E_\perp}) \cdot \mathrm{d}x_{E_\parallel}. \tag{13.1}$$

The construction of L_{1D} is shown graphically in Fig. 13.2 and starts with the quadratic hyperlattice H of nodes indexed by integer numbers (m, n) (Fig. 13.2a). First, H is convoluted with a function η which describes the atomic hypersurfaces. The convolution places one hypersurface on every node of H. η has the value 1 along the hypersurface; outside of it, it equals zero. For the construction of a canonical quasilattice, the length d of the hypersurface is given by the image obtained by projection on a line parallel to η. The orientation of η with respect to the hyperlattice is chosen to be irrational (the slope is $-\tau = -(1+\sqrt{5})/2$). Now, we determine the intersections of the hypersurfaces with a cut space E_c by multiplying with a function $\mathrm{d}x_{E_c}$ which has value 1 along a straight line; elsewhere it is zero. For the construction of an ideal quasilattice, $\mathrm{d}x_{E_c}$ is oriented perpendicular to the hypersurfaces. Now, we have obtained a set of points (Fig. 13.2a) along the cut line which are finally projected into the physical space $E_\parallel$. This is achieved by attaching a straight line, $\mathrm{d}x_{E_\perp}$ at each point of the set by the convolution product $(\ldots * \mathrm{d}x_{E_\perp})$ and cutting through this comb with the physical space $(\ldots \cdot \mathrm{d}x_{E_\parallel})$ (Fig. 13.2b). $\mathrm{d}x_{E_\perp}$ is oriented perpendicular to $\mathrm{d}x_{E_\parallel}$ which in the present

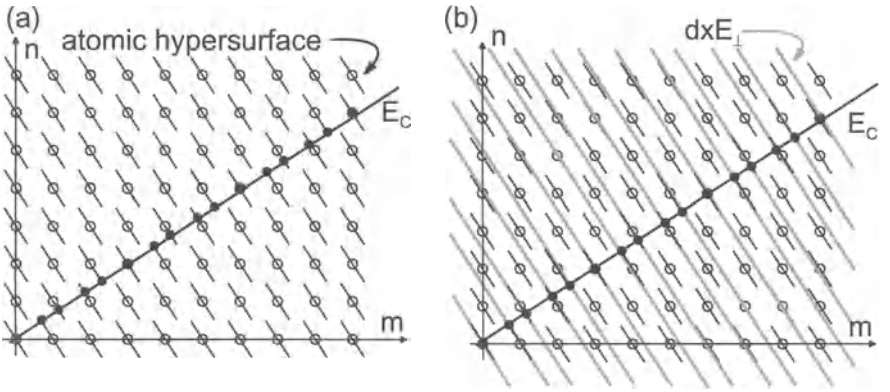

Fig. 13.2a,b. Construction of an ideal, one-dimensional quasilattice. For details see the text

case is identical to $\mathrm{d}x_{E_c}$ in order to construct the canonical one-dimensional quasilattice. As show below this identity has to be given up for constructing a defected quasilattice. However, here the set of points is identical with the sequence already obtained after the first cut with E_c.

In the kinematic approximation of (electron) diffraction the diffraction pattern can be calculated as a planar cut through the squared function describing the reciprocal lattice. This function is obtained by Fourier transformation of the direct lattice [4]. Here, the Fourier transform of $L_{1\mathrm{D}}$ is given by

$$L^*_{1\mathrm{D}} = (((H^* \cdot \eta^*) * \mathrm{d}x_{E_c^{\perp *}}) \cdot \mathrm{d}x_{E^*_{\parallel}}) * \mathrm{d}x_{E^*_{\perp}}, \tag{13.2}$$

where the superscript * denotes the respective Fourier transform. The procedures for the construction of the reciprocal lattice are illustrated in Fig. 13.3. Starting from the reciprocal lattice of the quadratic direct hyperlattice, which again is a quadratic lattice (H^*) with nodes indexed by (m^*, n^*), we first have to multiply by the Fourier transform of η, η^*. For the construction of the canonical quasilattice η and η^* are given by

$$\eta(\xi_{\parallel}, \xi_{\perp}) = \begin{cases} 1; & |\xi_{\perp}| < \frac{d}{2} \text{ and } \xi_{\parallel} = 0 \\ 0; & \text{elsewhere} \end{cases} \quad \text{and} \quad \eta^*(q_{\parallel}, q_{\perp}) = \frac{\sin(d\, q_{\perp})}{d\, q_{\perp}} \tag{13.3}$$

where $\xi_{\parallel}$ and $\xi_{\perp}$ are measured along and perpendicular to the atomic hypersurface, respectively ($q_{\parallel}$ and $q_{\perp}$ are the respective coordinates in reciprocal space). As a consequence the points of H^* become weighted by η^*. The envelope of η^* decays like $1/|q_{\perp}|$ with increasing $q_{\perp}$, therefore the intensity of the individual reflections of the kinematical diffraction pattern will decay like $1/|q_{\perp}|^2$. In Fig. 13.3 we accounted for this by drawing filled circles. Their radii indicate the intensity and decrease with increasing distance from the cut function $\mathrm{d}x_{E_c}$. The multiplication is followed by the projection of *all*

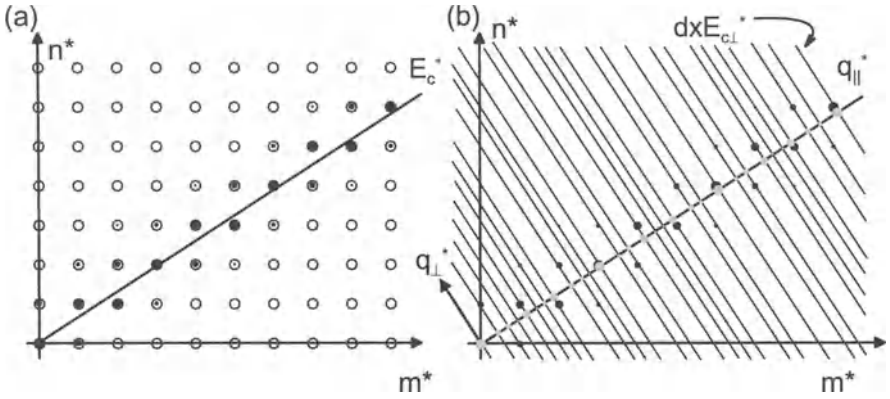

Fig. 13.3a,b. Construction of the reciprocal lattice of a one-dimensional quasicrystal. For details see the text

weighted hyperlattice points into the physical reciprocal space $E_{\parallel}{}^{*}$. This is accomplished by decorating the reciprocal hyperlattice points with straight lines ($\ldots * \mathrm{d}x_{E_c^{\perp *}}$) and cutting through this comb with the reciprocal physical space ($\ldots \cdot \mathrm{d}x_{E_{\parallel}^{*}}$). In Fig. 13.3b this is shown only for the most intense hyperlattice points. The final convolution in (13.2) with $\mathrm{d}x_{E_{\perp}^{*}}$ is a consequence of the Fourier transformation of a one-dimensional object within a two-dimensional space which leads to an extension of the reciprocal object in the direction(s) perpendicular to the direct object. However, in an experiment we observe the set of points obtained before the final convolution.

In principle, the resulting reciprocal lattice is a dense set of points. Nevertheless, the diffraction pattern obtained from this lattice shows a limited number of diffraction spots due to the great variation of the spot intensities in combination with the detection limit of the recording media. It is important to note that reflections which originate from reciprocal hyperlattice points with great distance from the physical space (great $q_{\perp}$ component) show small intensities.

We are now ready to introduce and discuss the action of a linear phason field. It shifts the points of the direct hyperlattice parallel to the hypersurfaces. The parallel component, $\xi_{\parallel}$, remains unchanged,

$$\xi_{\parallel}{}' = \xi_{\parallel} \quad \text{and} \quad \xi_{\perp}{}' = \xi_{\perp} + M^T \xi_{\parallel}. \tag{13.4}$$

M is a scalar (in the 3D case a 3×3 matrix) characterizing the strength (in the 3D case, the directional dependence and direction) of the strain [19]. An example of the action of the linear phason strain field is shown in Fig. 13.4. However, instead of shifting the hyperlattice points due to the action of the strain field it is equivalent to turning the cut function in the opposite direction (Fig. 13.4). This equivalence facilitates the calculation of the new reciprocal lattice. The rotation of $\mathrm{d}x_{E_c}$ leads to a rotation of $\mathrm{d}x_{E_c^{\perp *}}$ which in turn shifts

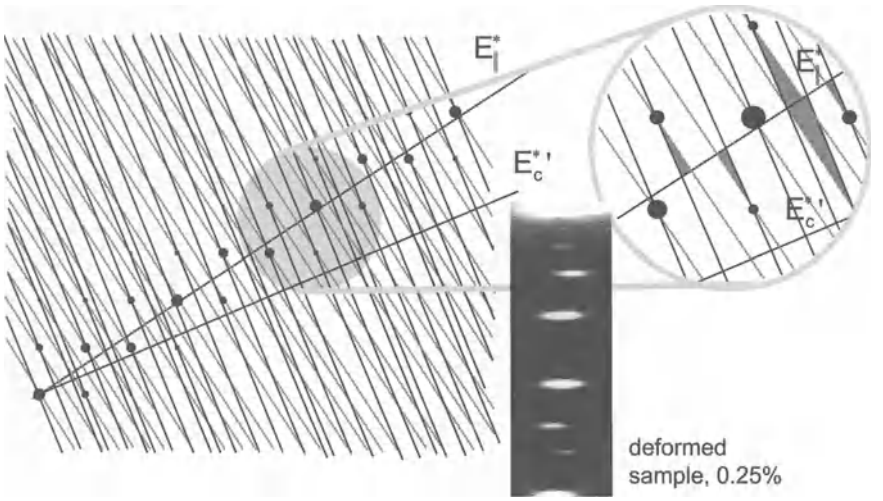

Fig. 13.4. Construction of the reciprocal lattice of a one-dimensional quasicrystal under the action of a linear phason strain field. The rotated cut space $E_c^{*\prime}$ leads to a shift of the reciprocal lattice points indicated by the grey triangle in the circular enlargement (right). These one-dimensional shifts correspond to the shifts in the two-dimensional TEM diffraction pattern

the intersections of $\mathrm{d}x_{E_c^{\perp *}}$ with the physical reciprocal lattice and therefore the positions of the diffraction spots. Moreover, since a copy of $\mathrm{d}x_{E_c^{\perp *}}$ is fixed to (and turns around) each node of the hyperlattice the amount of spot shift increases with increasing distance of the respective hyperlattice node from the physical space. Therefore, the weaker the reflection the stronger its deviation from the ideal position which is indeed the effect observed in the diffraction patterns of deformed Al-Pd-Mn quasicrystals (Fig. 13.4).

A quantitative discussion results in the following equation for the correction of the spot positions in physical space [12]

$$\boldsymbol{q}_{\parallel}{}' = \boldsymbol{q}_{\parallel} - M\,\boldsymbol{q}_{\perp}\,. \tag{13.5}$$

Recently, M has been determined for plastically deformed icosahedral Al-Pd-Mn quasicrystals [10]. For this, diffraction patterns were recorded by TEM. The images were corrected for aberrations of the microscope using standard samples with known positions of the diffraction spots. A number of reflections were indexed ($\boldsymbol{q}_{\parallel}{}^{i,\mathrm{exp}}$) ([2]) and their ideal positions, $\boldsymbol{q}_{\parallel}{}^{i,\mathrm{ideal}}$ and $\boldsymbol{q}_{\perp}{}^{i,\mathrm{ideal}}$, were calculated. Finally, M was determined by minimizing the least square sum

$$S = \sum_i |\boldsymbol{q}_{\parallel}{}^{i,\mathrm{exp}} - (\boldsymbol{q}_{\parallel}{}^{i,\mathrm{ideal}} - M\,\boldsymbol{q}_{\perp}{}^{i,\mathrm{ideal}})|^2. \tag{13.6}$$

Here, a principal problem arises. Specimens for TEM have to be rather thin ($\simeq 100\,\mathrm{nm}$) in order to be transparent for the electron beam. In reciprocal

space, this leads to elongation of the lattice points from diffraction spots into diffraction rods along the direction of the foil normal [13]. In diffraction patterns, it is not possible to determine the center of these rods. Therefore the shift component along the direction of the specimen normal cannot be determined, i.e. the third line of M (the z-direction was chosen to be parallel to the foil normal).

As a result, a single diffraction pattern is sufficient to record all accessible spot shifts. We just have to consider the orientation of this specific pattern with respect to the foil normal in order to account for a shortening of the deviations.

Two typical examples for phason strain matrices are given here:

$$M^{\mathrm{Ref}} = 10^{-3} \begin{pmatrix} 0.0 & -1.0 & -0.8 \\ -0.5 & 1.2 & -1.1 \\ M_{3,1} & M_{3,3} & M_{3,3} \end{pmatrix} \tag{13.7}$$

$$M^{0.25\%} = 10^{-3} \begin{pmatrix} 6.9 & 1.8 & -1.0 \\ 0.9 & -2.4 & 0.5 \\ M_{3,1} & M_{3,3} & M_{3,3} \end{pmatrix} \tag{13.8}$$

The diagrams in Fig. 13.5 show the results graphically. The amount of deviation of diffraction spots from the positions in the corresponding perfect systematic row is depicted as a function of the amplitude of the respective reciprocal lattice vector in $E_\perp$. The lines have been calculated on the basis of the above matrices.

The left diagram (13.7) was determined from spot positions of an undeformed reference sample. The errors of the individual matrix components are about as large as the values of M itself. Therefore, within experimental error there is no spot shift detectable for the reference specimen. The matrix of (13.8) was determined for a sample with a plastic deformation of 0.25%. Compared to the reference, the entries are much larger here. Moreover, the

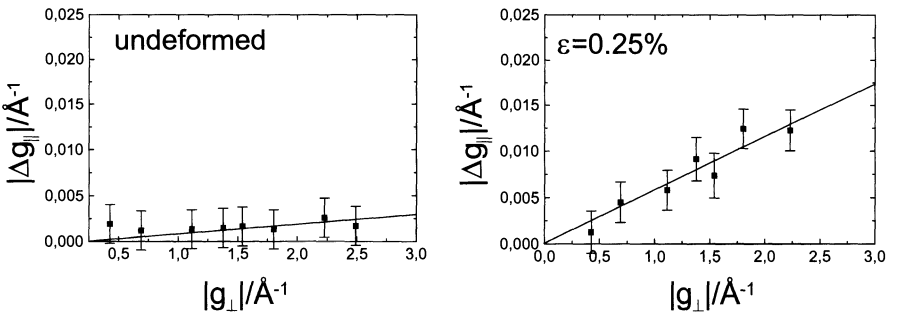

Fig. 13.5. Amount of the reflection shift for diffraction spots within a systematic row as a function of the corresponding reciprocal lattice vector in $E_\perp$. (**a**) Undeformed reference sample. (**b**) Specimen deformed to 0.25% of plastic strain

deviations align quite well to the calculated line justifying the assumption of a linear phason strain field.

A closer inspection of M reveals that $M_{1,1}$ turns out to be larger than all other components of M. This was found not only at other places of the specimen, but also in samples with less plastic strain [10]. This anisotropy results from the geometry of the deformation experiment. The samples were compressed along the z-direction. Nevertheless, it remains unclear why the x-direction is pronounced and a relative small phason shift along the y-direction occurred.

Generally, it was found that the size of the entries of M increases with the amount of plastic strain.

Eventually, it is an interesting question whether the observed phason strain induces a phase transformation to an approximant phase of the Al-Pd-Mn quasicrystal. In such case, M has to show certain symmetry properties according to the symmetry properties of possible approximant phases [12,16]. Such indications are difficult to find since three elements of M are unknown. However, the elements are rather small when compared to phason matrices of known transformations. From high-resolution transmission electron micrographs, Menguy et al. [20] determined phason matrices for the transformation of the icosahedral Al-Cu-Fe phase towards two pentagonal modifications with different periodicities. The elements of M determined there are up to two orders of magnitude larger than the values of M shown in (13.8).

13.3 Observation and Characterization of Dislocations

When imaging and analyzing dislocations and other extended defects by TEM, it is generally operated by employing diffraction contrast [13,14,24]. For this, a so-called *bright field image* is formed with those electrons which pass undiffracted through the specimen. Specimen areas which fulfill the Bragg condition diffract the electrons and therefore appear dark under such imaging conditions. This technique is used to image dislocations. In the microscope, the specimen is oriented such that only one set of lattice planes fulfills the Bragg condition. In the corresponding diffraction pattern, we observe two reflections: the undiffracted electrons and one diffracted beam (the so-called *two-beam condition* (TBC)). Close to a defect the proper orientation of the lattice planes might be distorted and the Bragg condition is no longer fulfilled. Rotating the specimen further allows one to adjust the distorted planes to be in the Bragg condition. Therefore this region of the sample will show up with a dark contrast against the bright surroundings which are now not in TBC.

In the following we will discuss the conditions of image formation quantitatively in the framework of the column approximation and kinematical diffraction. The specimen is illuminated by a parallel electron beam with wave vector $\boldsymbol{k}_0$. For the image contrast at a point P of the specimen it is

only necessary to consider the electrons diffracted by atoms within a narrow column along $\boldsymbol{k}$ at position P. Each atom contributes to the diffracted beam with a wave of amplitude $A_p \propto \exp(-2\pi \mathrm{i}(\boldsymbol{k} - \boldsymbol{k}_0) \cdot \boldsymbol{r}_n)$, where $\boldsymbol{r}_n$ denotes the position of the n-th atom within the column.

The total scattering amplitude A_P of the diffracted wave is proportional to the sum

$$A_P \propto |\sum_{\text{column}} \exp(-2\pi \mathrm{i}(\boldsymbol{k} - \boldsymbol{k}_0) \cdot \boldsymbol{r}_n)|. \tag{13.9}$$

This sum can be visualized graphically by means of an amplitude phase diagram (APD) where each contribution to the sum is shown as a vector within the complex number plane. The total scattering amplitude is determined by the length of a vector resulting from this summation. In Fig. 13.6a as an example of such a column, a single chain of a quasicrystal lattice is depicted. Its width defines the diameter of the column mentioned above. $\boldsymbol{k}_0$ and $\boldsymbol{k}$ are chosen such that their difference $\boldsymbol{k}_0 - \boldsymbol{k}$ points along the chain. In this case we can think of a three-dimensional array of lattice planes normal to $\boldsymbol{k}_0 - \boldsymbol{k}$ at the marked positions of the chain. Figure 13.6c shows the respective APD where the difference $\boldsymbol{k} - \boldsymbol{k}_0 = \boldsymbol{g}_{\|}$ is a vector of the reciprocal lattice. Under such diffraction conditions and for a *periodic* chain, the phase vectors align perfectly parallel and we observe constructive interference of the waves. Here, since quasicrystals have two incommensurate lattice spacings, the phase vectors align *almost* parallel. Nevertheless, the scattering amplitude has a maximum.

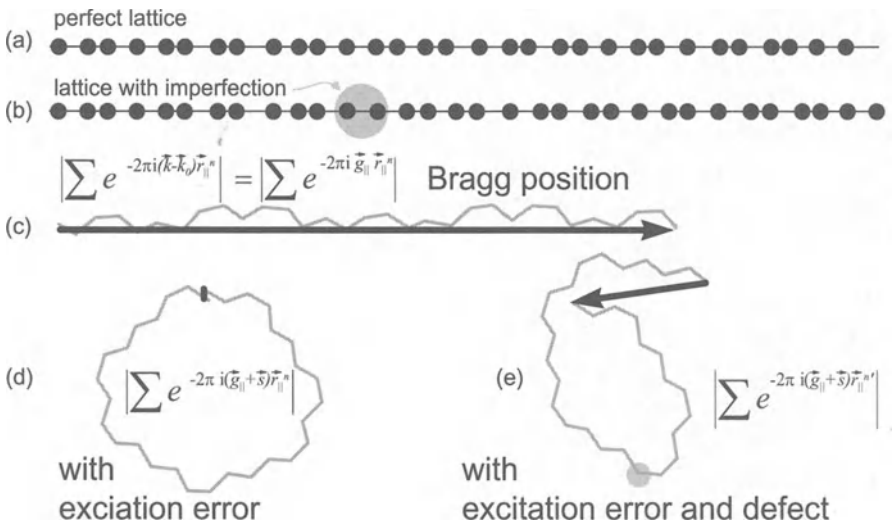

Fig. 13.6a–e. Amplitude phase diagrams for various atom columns. For details see the text

For the case that the Bragg condition is not fulfilled, an additional phase shift has to be added to each phase vector. The deviation from the Bragg condition is characterized by the excitation error $\boldsymbol{s}$, i.e. $\boldsymbol{k} - \boldsymbol{k}_0 = \boldsymbol{g}_\parallel + \boldsymbol{s}$. In Fig. 13.6d $\boldsymbol{s}$ has been adjusted such that the total scattering amplitude just vanishes. No intensity is diffracted in the direction of $\boldsymbol{k}$. Figure 13.6b shows the Fibonacci sequence again but now a defect has been introduced by insertion of an additional long spacing at about the center of the sequence. In the corresponding APD (Fig. 13.6e), this locally results in an additional phase shift increasing the total scattering amplitude and constructive interference occurs. A bright field image (i.e., obtained with the electrons along $\boldsymbol{k}_0$) will show a dark contrast at the position of the defect.

In quasicrystals, dislocations introduce two types of strain which can be distinguished from the directions of the corresponding shifts of the lattice points. The first component, the *phonon strain* $\boldsymbol{u}_\parallel$, results in local shifts of the hyperlattice points within the subspace $E_\parallel$. In the direct lattice, this leads to local variations of the atomic distances. The second component is the *phason strain* $\boldsymbol{u}_\perp$. Its consequences for the reciprocal lattice have been discussed in the previous subsection. In the direct lattice it results in local rearrangements of the unit cells leading to configurations which are forbidden in the ideal quasilattice (matching rule violations [17]).

Calculation of the phase sum (13.9) including these strains in the case of quasicrystals has to be carried out with respect of the hyperlattice. It results in the additional contribution [33]

$$\exp(-2\pi \mathrm{i}(\boldsymbol{g}_\parallel \cdot \boldsymbol{u}_\parallel + \boldsymbol{g}_\perp \cdot \boldsymbol{u}_\perp)). \tag{13.10}$$

This means that for a given TBC no contrast effects occur if $\boldsymbol{g}_\parallel \cdot \boldsymbol{u}_\parallel + \boldsymbol{g}_\perp \cdot \boldsymbol{u}_\perp = 0$.

This extinction condition can be divided into two cases:

$$\text{(a) } \boldsymbol{g}_\parallel \cdot \boldsymbol{u}_\parallel = \boldsymbol{g}_\perp \cdot \boldsymbol{u}_\perp = 0 \quad \text{and} \quad \text{(b) } \boldsymbol{g}_\parallel \cdot \boldsymbol{u}_\parallel = -\boldsymbol{g}_\perp \cdot \boldsymbol{u}_\perp \neq 0. \tag{13.11}$$

(a) is called the *strong extinction condition* (SEC) while (b) is termed the *weak extinction condition* (WEC). In order to distinguish both conditions we carry out the following Gedanken experiment. For a given TBC with reflection $\boldsymbol{g}_\parallel{}^{(1)}$, let a dislocation be out of contrast and suppose (13.11) applies. However, we cannot decide whether (a) or (b) holds. A second observation with a reflection $\boldsymbol{g}_\parallel{}^{(2)} = \tau \boldsymbol{g}_\parallel{}^{(1)}$ should again yield contrast extinction. Thus we can write $\boldsymbol{g}_\parallel{}^{(2)} \cdot \boldsymbol{u}_\parallel + \boldsymbol{g}_\perp{}^{(2)} \cdot \boldsymbol{u}_\perp = 0$. Due to the one-to-one correspondence between the positions of the reciprocal lattice vectors in $E_\parallel$ and $E_\perp$, $\boldsymbol{g}_\perp{}^{(1)}$ scales by $-1/\tau$ if the corresponding parallel component is multiplied by τ [33]. Using this relation, we replace $\boldsymbol{g}_\parallel{}^{(2)}$ and $\boldsymbol{g}_\perp{}^{(2)}$ and obtain two equations:

$$\boldsymbol{g}_\parallel{}^{1} \cdot \boldsymbol{u}_\parallel + \boldsymbol{g}_\perp{}^{1} \cdot \boldsymbol{u}_\perp = 0 \quad \text{and} \quad \boldsymbol{g}_\parallel{}^{1} \cdot \boldsymbol{u}_\parallel - \frac{1}{\tau^2} \boldsymbol{g}_\perp{}^{1} \cdot \boldsymbol{u}_\perp = 0. \tag{13.12}$$

These equations can only be fulfilled if the scalar products $\boldsymbol{g}_{\parallel}{}^{1} \cdot \boldsymbol{u}_{\parallel}$ and $\boldsymbol{g}_{\perp}{}^{1} \cdot \boldsymbol{u}_{\perp}$ *both* vanish, i.e. the SEC is observed. In this case neither the phonon nor the phason strain field adds a phase shift to the electron beam. The direction of the strain fields is orthogonal to the employed reciprocal lattice vectors $\boldsymbol{g}_{\parallel}$ and $\boldsymbol{g}_{\perp}$. Experimentally, no dislocation contrast is observed for any reflection with a reciprocal lattice vector parallel to $\boldsymbol{g}_{\parallel}$ in the case of the SEC. For the WEC, contrast extinction is obtained only for one single reflection.

Now, we introduce the Burgers vectors of the dislocations by the integrals

$$\boldsymbol{b}_{\parallel} = \oint_C \mathrm{d}\boldsymbol{u}_{\parallel} = \boldsymbol{b}_{\parallel} \oint_C \mathrm{d}\Phi_{\parallel} \quad \text{and} \quad \boldsymbol{b}_{\perp} = \oint_C \mathrm{d}\boldsymbol{u}_{\perp} = \boldsymbol{b}_{\perp} \oint_C \mathrm{d}\Phi_{\perp}. \tag{13.13}$$

The integration is carried out around a closed path around the dislocation line with respect to the coordinates in physical space. Further, we assume that the action of the strain is along a specific direction along $\boldsymbol{b}_{\parallel}$ and $\boldsymbol{b}_{\perp}$, respectively. This allows the strain fields to be separated into a constant part defining the direction and magnitude and a scalar component which describes the variation of $\boldsymbol{u}_{\parallel} = \boldsymbol{b}_{\parallel}\Phi_{\parallel}$ and $\boldsymbol{u}_{\perp} = \boldsymbol{b}_{\perp}\Phi_{\perp}$ with varying position in $E_{\parallel}$. $\boldsymbol{b}_{\parallel}$ and $\boldsymbol{b}_{\perp}$ are the three-dimensional Burgers vectors, the projections of a six-dimensional Burgers vector $\boldsymbol{B}$ – defined within the hyperlattice – into the subspaces $E_{\parallel}$ and $E_{\perp}$, respectively. Since $E_{\parallel}$ and $E_{\perp}$ have an irrational orientation to the basis vectors of the hyperlattice, $\boldsymbol{b}_{\parallel}$ and $\boldsymbol{b}_{\perp}$ will never be zero separately. The above separation yields for the WEC

$$\frac{\Phi_{\perp}}{\Phi_{\parallel}} = -\frac{\boldsymbol{g}_{\parallel}{}^{(1)} \cdot \boldsymbol{b}_{\parallel}}{\boldsymbol{g}_{\parallel}{}^{(1)} \cdot \boldsymbol{b}_{\parallel}} = \text{const.} \tag{13.14}$$

Therefore, the functions $\Phi_{\parallel}$ and $\Phi_{\perp}$ are related by a constant factor. This factor can be included into the Burgers vectors and the scalar functions be removed from (13.11). The general extinction condition for dislocations in icosahedral quasicrystals now reads

$$\boldsymbol{g}_{\parallel} \cdot \boldsymbol{b}_{\parallel} + \boldsymbol{g}_{\perp} \cdot \boldsymbol{b}_{\perp} = 0. \tag{13.15}$$

Using this condition it is possible to determine the direction of the Burgers vector in the subspaces $E_{\parallel}$ and $E_{\perp}$ by observing the SEC twice. If additionally the WEC can be observed, the orientation of the dislocation Burgers vector can be fixed within the six-dimensional hyperlattice.

Applications of the method can be found in [1,11,28,34–36]. A similar derivation for dislocations in decagonal quasicrystals was given by [31].

While the SEC is analogous to the necessary extinction criterion for dislocations in normal crystals [14], i.e. $\boldsymbol{g} \cdot \boldsymbol{b} = 0$, the WEC is a new contrast effect. Here, the phase shift induced by the phonon strain field is just canceled by the shift due to the corresponding phason strain field. Therefore, the contrast behavior of dislocations directly reflects the quasiperiodic nature of quasicrystalline alloys.

Diffraction contrast analysis of dislocations allows the investigation of several defects at the same time. Nevertheless, experiments show that the functions describing the strain fields may be more complicated leading in some cases to dislocation contrast where the theory just presented predicts contrast extinction and *vice versa* [29].

Employing diffraction contrast analysis, it is not possible to determine the magnitude of the strain fields characterized by the lengths of the respective Burgers vectors. For this, we have to use CBED.

Here, instead of parallel illumination, the electron beam is converged such that the focus of the beam is just above or below the specimen and a small, circular region is illuminated (Fig. 13.7). As a consequence, reflections of the

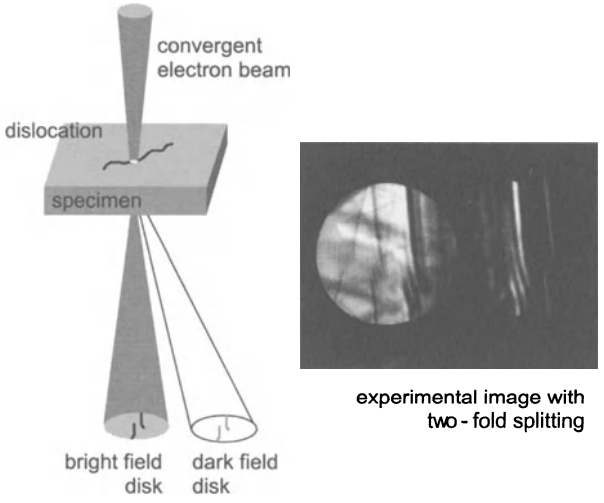

Fig. 13.7. Left: geometry of the illumination for CBED. Right: typical CBED pattern showing a two-fold splitting of the deficiency and excess line

diffraction pattern are enlarged to disks. Their sizes are proportional to the opening angle of the illuminating cone. If the sample is properly oriented there is now a set of beams within this cone which can fulfill a specific Bragg condition. All these beams point along the outside of a cone which is defined by the wave vectors $\boldsymbol{k}_0$ and $\boldsymbol{k}$ fulfilling the Bragg condition and the reciprocal lattice $\boldsymbol{g} = \boldsymbol{k} - \boldsymbol{k}_0$ defining the cone's symmetry axis (Fig. 13.7). In the diffraction pattern, the set of diffracted beams is seen as a bright line. In the bright zero-disk we observe a dark deficiency line. Since the cross-over of the illumination is placed outside the specimen foil each beam direction belongs to a different position in the sample plane. Therefore, the diffraction disk provides a mapping of Bragg plane orientations. A defect can distort orientations locally shifting the places where the Bragg condition is fulfilled and in turn the deficiency line and the corresponding excess line will be distorted and split. In the case of dislocations in normal crystals the number

of splittings, n, can be calculated by the generalized Cherns–Preston rule [3] which was extended to quasicrystals by Dai [5,37]:

$$\boldsymbol{g}_{\parallel} \cdot \boldsymbol{b}_{\parallel} + \boldsymbol{g}_{\perp} \cdot \boldsymbol{b}_{\perp} = n. \tag{13.16}$$

An experimental diffraction pattern showing the case $n = 2$ is displayed in Fig. 13.7. To determine all components of the Burgers vector one has to observe six lines for which the corresponding reciprocal lattice vectors have to be linearly independent.

Table 13.1 shows the results from numerous analyzes which were carried out in Al-Pd-Mn quasicrystals in its as-grown and plastically deformed state. In addition, results from dislocations in Al-Cu-Fe quasicrystals are also listed. Several types of Burgers vectors for a certain symmetry direction exist. They

Table 13.1. List of dislocations observed in Al-Pd-Mn and Al-Cu-Fe icosahedral alloys. a_0 denotes the six-dimensional lattice parameter and $a_0 = a_0/\sqrt{4+2\tau} \approx 2.4$ Å(p2-fold denotes a $< 0/0, 0/1, 1/0 >$ direction). We use the indexing system described in [8].

alloys [Ref.]	Dir.	$\boldsymbol{B}/a_0$	$\lvert\boldsymbol{b}_{\parallel}\rvert/a_0'$	$\lvert\boldsymbol{b}_{\perp}\rvert/\lvert\boldsymbol{b}_{\parallel}\rvert$
AlCuFe [5,30,37], AlPdMn [6,21,26]		$< \bar{1}, 1, 1, 0, 0, \bar{1} >$	1.24	$\tau^3 \approx 4.2$
AlPdMn [7,21,26]	2-fold	$< 2, \bar{1}, \bar{1}, 0, 0, 2 >$	0.76	$\tau^5 \approx 11.1$
AlPdMn [21,26]		$< \bar{3}, 2, 2, 0, 0, \bar{3} >$	0.47	$\tau^7 \approx 29.0$
AlPdMn [21,26]		$< \bar{5}, 3, 3, 0, 0, \bar{3} >$	0.29	$\tau^9 \approx 76.0$
AlCuFe [8]	3-fold	$< 0, 0, 0, 2, 2, 2 >$	2.14	$\tau^3 \approx 4.2$
AlPdMn [21,26]		$\frac{1}{2} < \bar{5}, 5, \bar{1}, 5, 1, \bar{1} >$	0.41	$\tau^7 \approx 29.0$
AlPdMn [21,26]		$\frac{1}{2} < 1, 1, \bar{1}, \bar{1}, \bar{3}, \bar{1} >$	0.73	$\tau^4 \approx 6.9$
AlCuFe [8] AlPdMn [21,26]	5-fold	$\frac{1}{2} < 2, \bar{4}, 2, \bar{2}, 2, 2 >$	0.45	$\tau^6 \approx 17.9$
AlCuFe [8] AlPdMn [21,26]		$< 2, \bar{4}, 2, \bar{2}, 2, 2 >$	0.90	$\tau^6 \approx 17.9$
AlPdMn [21,26]		$\frac{1}{2} < 3, \bar{3}, 3, \bar{7}, \bar{3}, \bar{3} >$	0.28	$\tau^8 \approx 47.0$
AlPdMn [21,26]	p2-fold	$\frac{1}{2} < 3, \bar{1}, \bar{3}, \bar{1}, \bar{1}, 3 >$	0.18	$\tau^6 \approx 17.9$
AlPdMn [21,26]	-	$\frac{1}{2} < 7, \bar{3}, 1, \bar{9}, \bar{7}, \bar{3} >$	0.55	32.4
AlPdMn [21,26]	-	$\frac{1}{2} < 2, 6, \bar{8}, 4, \bar{4}, 2 >$	0.65	24.2
AlPdMn [21,26]	-	$\frac{1}{2} < 2, 2, 0, \bar{4}, \bar{6}, \bar{4} >$	0.33	13.2

are characterized by the ratio of the amplitudes of their Burgers vectors in the subspaces $E_{\parallel}$ and $E_{\perp}$, respectively. For the main symmetry axes it is possible to express this *strain accommodation parameter* (SAP) in powers of τ. It is noted that as the SAP increases, $|\boldsymbol{b}_{\parallel}|$ decreases and $|\boldsymbol{b}_{\perp}|$ increases at the same time.

Moreover, we observe both perfect and partial dislocations whereas with perfect we want to refer to Burgers vectors that are vectors of the F-type hyperlattice [2,25]. Partial dislocations are mainly observed in plastically deformed samples [21,26]. In Table 13.1, they can be recognized by the pre-factor 1/2.

What is the physical meaning of the Burgers vector component in orthogonal space? In principle, we are free to choose a scale within the subspace $E_{\perp}$. But as soon as this length scale is fixed, the sizes of the atomic hypersurfaces have to be set accordingly in order to correctly describe the structure. Therefore, the proper interpretation of the Burgers vector component $\boldsymbol{b}_{\perp}$ implies a comparison of the sizes of the various observed $\boldsymbol{b}_{\perp}$ and the extension of the atomic hypersurfaces. For Al-Pd-Mn, but also for Al-Cu-Fe, quasicrystals the typical size of the atomic hypersurface is of the order 10 Å. Most of the Burgers vectors in $E_{\perp}$ surpass this size which indicates that the dislocations are accompanied by a large number of phason defects. In addition, when dislocations move (see below) they leave phason defects in their wake. This is confirmed by microstructural analyzes of plastically deformed Al-Mn-Pd quasicrystals [21,26]. Figure 13.8 shows the development of the frequency curve of various SAPs of dislocations with Burgers vectors along two-fold directions for different amounts of sample deformation. For undeformed reference specimens we observed less Burgers vectors with large SAPs in favor of Burgers

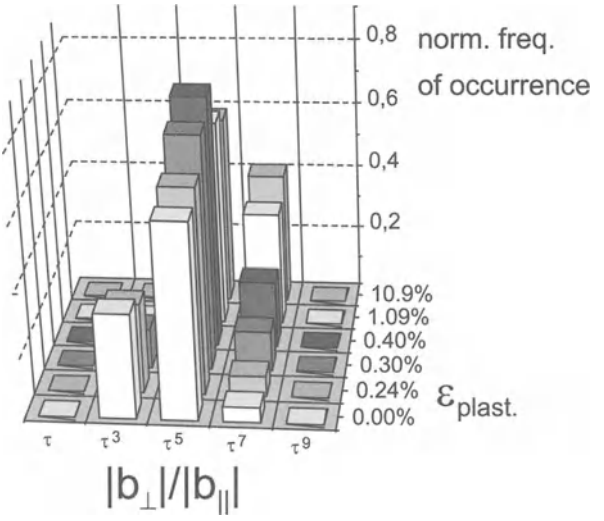

Fig. 13.8. Statistic of SAP development with increasing strain during plastic deformation of Al-Pd-Mn quasicrystals

vectors with small SAP. This distribution is reversed when the plastic strain on the samples is increased and the center of weight of the distribution shifts to higher values of the SAP. An explanation for this effect will be given in the following subsection.

13.4 Dislocation Motion and Dissociation

Up to this point, we have discussed dislocations in quasicrystals as static objects. Nevertheless, the mobility of dislocations becomes a quite important point when plastic deformation of quasicrystals is considered. *A priori*, the mobility of dislocations in quasicrystals cannot be taken for granted due to their complicated structure. Indeed, it was for a long time presumed that dislocations are immobile or at least only partial "phonon dislocations" move whereas the remaining phason part is not mobile [23].

In this respect, we have deformed single quasicrystalline Al-Pd-Mn *in situ* at 750 °C and continuously recorded the bright field image of the microstructure by video TEM [38]. An example for such a movie can be found in reference [22]. Resultsfrom these experiments can be summarized as follows. Dislocations move during the high-temperature plastic deformation of quasicrystals. The motion of dislocations is confined to special planes which can be identified as being perpendicular to low-indexed symmetry directions of the icosahedral quasicrystal. The same planes have been found in the glide system analysis of dislocations in samples deformed under similar conditions in an ordinary testing machine [21,26].

Interaction of dislocations was observed and quantitatively analyzed using the model of an isotropic solid with elastic dislocation interaction [40]. Dislocation sources and the dissociation of dislocations have been observed during *in situ* experiments. In particular, the dissociation of dislocations is an interesting observation, since such events allow one to compare the energy costs for the introduction of a dislocation with respect to the accompanying phonon and phason strain fields.

Dislocations distort the ideal configuration of the lattice thus leading to an increased free energy of the system. As in usual periodic crystals also the quasicrystal tries to minimize its free energy. This can be accomplished by the dissociation of one dislocation into two, whereas the sum of the dislocation energies is lower than the energy of the initial defect.

For dislocations in quasicrystals there are two contributions to the dislocation energy. The first stems from the elastic distortion of the lattice introduced by the phonon strain field and characterized by the Burgers vector $\boldsymbol{b}_{\|}$. The stress is elastic, thus we expect the energy to be proportional to the squared modulus of $|\boldsymbol{b}_{\|}|$ as in usual periodic crystals [27]. The second contribution takes account of the phason defects introduced by the dislocations. Presently, there are two models discussed. The first assumes that each phason defect requires a certain amount of energy. In addition, the number of phason

defects is proportional to the modulus of $\boldsymbol{b}_\perp$. Therefore it is expected that the phason energy increases linearly with the modulus of $\boldsymbol{b}_\perp$ [18,39]. This interpretation is based on the deterministic description of quasicrystal lattices. The second model considers the density wave picture of quasicrystals [17]. With this description it turns out that $|\boldsymbol{b}_\perp|^2$ determines the phason part of the dislocation energy [15].

Therefore the dislocation energy E is

$$E \propto |\boldsymbol{b}_\parallel|^2 + c\,|\boldsymbol{b}_\perp|^\delta. \tag{13.17}$$

Depending on the model, we adopt either 1 or 2 for δ. c is called the *strain energy ratio* and describes the ratio between the proportionality constants of the phonon and phason parts of the dislocation energy, respectively.

By generalizing Frank's rule ([9]) to the case of quasicrystals we expect dislocation dissociation if

$$|\boldsymbol{b}_\parallel{}^{(i)}|^2 + c\,|\boldsymbol{b}_\perp{}^{(i)}|^\delta > |\boldsymbol{b}_\parallel{}^{(r_1)}|^2 + c\,|\boldsymbol{b}_\perp{}^{(r_1)}|^\delta + |\boldsymbol{b}_\parallel{}^{(r_2)}|^2 + c\,|\boldsymbol{b}_\perp{}^{(r_2)}|^\delta. \tag{13.18}$$

The exponent (i) denotes the initial dislocation while (r_1) and (r_2), respectively, indicate the resulting dislocations. Effects due to a change of the dislocation line direction have been neglected here and are discussed elsewhere [39].

For quantitative estimates of c and possible reactions we have to introduce reasonable Burgers vectors into (13.18).

In usual periodic crystals, dislocations possessing Burgers vectors which are multiples of lattice vectors dissociate instantly until their Burgers vectors become simple vectors of the lattice. This follows directly from Frank's rule. In addition, such a perfect dislocation may separate into partial dislocations and the energy gain is used to create a stacking fault. The stacking fault energy determines the separation of the partial dislocations.

These arguments can be used for quasicrystals. However, a large number of additional possibilities arises from the aperiodic structure of quasicrystals. Consider the lattice of an icosahedral quasicrystal with a face centered hypercubic parent lattice in 6D hyperspace. Here, for each lattice vector characterized by $\boldsymbol{b}_\parallel$ there exists a second vector $\boldsymbol{b}_\parallel{}'$ which exceeds the first by a factor τ but characterizes a vector of the 6D lattice, too. The respective vectors, $\boldsymbol{b}_\perp$ and $\boldsymbol{b}_\perp{}'$, of the orthogonal space scale by $-1/\tau$.

As a consequence

$$\boldsymbol{b}_\parallel{}'' = \boldsymbol{b}_\parallel + \boldsymbol{b}_\parallel{}' \Leftrightarrow \boldsymbol{b}_\parallel + \tau\,\boldsymbol{b}_\parallel = \tau^2\,\boldsymbol{b}_\parallel \tag{13.19}$$

is a relation among lattice vectors. More generally, we construct a dissociation starting from a Burgers vector $\boldsymbol{b}_\parallel(\boldsymbol{b}_\perp)$ which splits into components $(m + n\tau)\boldsymbol{b}_\parallel$ $((m - 1/\tau)\boldsymbol{b}_\perp)$ and $(1 - m - n\tau)\boldsymbol{b}_\parallel$ $((1 - m + 1/\tau)\boldsymbol{b}_\perp)$, respectively. m and n are integer numbers which label a specific dissociation. The important point to note is that these vectors describe a reaction between lattice vectors

which all point along the same direction of the 3D physical (orthogonal) space.

Now, these vectors can be introduced into (13.18) and combinations of m, n and c searched for which dislocation dissociation is favorable. Details of this calculation can be found in [32,39]. One reaction turns out to be quite favorable and shall be discussed here. This specific case involves the dissociation of a dislocation with Burgers vector along a two-fold direction and strain accommodation parameter τ^3, into two dislocations with the same Burgers vector direction in physical space but strain accommodation parameters τ^5 and τ^7, respectively. It turns out that c (13.18) has to be smaller than $0.1\,\text{Å}(\delta = 1)$ or $c < 3 \times 10^{-3}$ $(\delta = 2)$, respectively. c has to be positive in both cases. This reaction is remarkable since it has the highest limits for c. For all other reactions, i.e. all combinations of m and n, respectively, we find smaller values for c. Assuming that realistic c's are about half of these values, we calculate the ratio between the phason part of the dislocation energy and the total dislocation energy. For the initial dislocation about 5% of the total dislocation energy is stored in the phason defects whereas after the dissociation it is about 40–50% of the total energy. The exact values are determined by the actual value of δ and the line directions of the dislocations involved [39].

Investigation of the other dissociation possibilities shows that almost always the phason part of the energy is increased and the elastic part is decreased. Nevertheless, it has to be stressed that the total free energy is reduced. Since the products of this type of dissociation are perfect dislocations no stacking fault is created which might have consumed part of the energy gain.

Therefore, this type of dissociation might explain the phenomenon that during increasing plastic deformation more dislocations with large strain accommodation parameter are observed (Fig. 13.8).

Acknowledgment

The authors gratefully acknowledge enlightening discussions with D. Gratias.

References

1. Baluc N., Yu D.P., and Kleman M. *Phil. Mag. Lett.*, 72:1–9, 1995.
2. Cahn J.W., Shechtman D., and Gratias D. *J. Mat. Res.*, 1:13–26, 1986.
3. Cherns D. and Preston A.R. In *Proc. XIth Int. Congr. on Electron Microsc.*, page 721. Kyoto, 1986.
4. Cowley J.M. *Diffraction Physics.* North-Holland, Amsterdam, Oxford, New York, Tokyo, 1984.
5. Dai M.X. *Phil. Mag. Lett.*, 66:235–240, 1992.
6. Dai M.X. *Phil. Mag.*, A67:789–796, 1993.
7. Feng J., Wang R., and Wang Z. *Phil. Mag. Lett.*, 68:321–326, 1993.

8. Feng J. and Wang R. *Phil. Mag. Lett.*, 69:309–315, 1994.
9. Frank F.C. *Physica*, 15:131, 1949.
10. Franz V. Diploma thesis, RWTH Aachen, IFF Forschungszentrum Jülich GmbH, 1997.
11. Gastaldi J.,Reinier E., Grange G., Jourdan C., and Smolsky I. In Chr. Janot and R. Mosseri, editors, *Proc. 5th Int. Conf. on Quasicrystals*, pages 287–293. World Scientific, 1995.
12. Gratias D., Katz A., and Quiquandon M. *J. Phys.: Cond. Matter*, 7:9101–25, 1995.
13. Heimendahl M. von *Einführung in die Elektronenmikroskopie. Verfahren zur Untersuchung von Werkstoffen und anderen Festkörpern.* Friedr. Vieweg & Sohn, Braunschweig, 1970.
14. Hirsch P.B., Howie A., and Whelan M.J. *Phil. Trans. Roy. Soc.*, A252:499–529, 1960.
15. Horn P.M., Malzfeldt W., DiVincenzo D.P., Toner J., and Gambino R. *Phys. Rev. Lett.*, 57:1444–1447, 1986.
16. Ishii Y. *Phys. Rev. B*, 39:11862–11871, 1989.
17. Levine D., Lubensky T.C., Ostlund S., Ramaswamy S., Steinhardt P.J., and Toner J. *Phys. Rev. Lett.*, 54:1520, 1985.
18. Levitov L. and Gratias D. 1995. Personal communication.
19. Mai Z., Tao S., Zeng L., and Zhang B. *Phys. Rev. B*, 38:12913–16, 1988.
20. Menguy M., Audier M., Guyot P., and Vacher M. *Phil. Mag. B*, 68:595–606, 1993.
21. Metzmacher Chr. Diploma thesis, RWTH Aachen, IFF Forschungszentrum Jülich GmbH, 1995.
22. movie, see www–server of the Institute of Microstructure Research, URL: `http://www.kfa-juelich.de/iff/mik/quasid.html`.
23. Ovid'ko I.A. *Mater. Sci. Engn. A*, 154:29–33, 1992.
24. Reimer L. *Transmission electron microscopy. Physics of Image Formation and Microanalysis.* Springer-Verlag, Berlin, Heidelberg, New York, Tokyo, 1989.
25. Rokhsar D.S., Mermin N.D., and Wright D.C. *Phys. Rev. B*, 35:5487–5495, 1987.
26. Rosenfeld R., Feuerbacher M., Baufeld B., Bartsch M., Wollgarten M., Hanke G., Beyss M., Messerschmidt U., and Urban K. *Phil. Mag. Lett.*, 72:375–384, 1995.
27. Schöck G. In F. R. N. Nabarro, editor, *Dislocations in Solids*, volume 3, pages 63–163. North Holland Pub. Comp., New York, Tokyo, 1980.
28. Wang R., Yang X., Zou W., and Wang Z. *J. Phys.: Cond. Matt.*, 6:9009–9016, 1994.
29. Wang Z.G., Wang R., and Feng J.L. *Phil. Mag.*, A69:577–590, 1994.
30. Wang R., Yang X., Zou W., Wang Z., Gui J., and Jiang J. *J. Phys.: Condens. Matter*, 6:9009–9016, 1994.
31. Wittmann R. *Phil. Mag. Lett.*, 72:87–91, 1995.
32. Wang R., Feuerbacher M., Wollgarten M., and Urban K. *Phil. Mag. A*, 77:523–540, 1998.
33. Wollgarten M., Gratias D., Zhang Z., and Urban K. *Phil. Mag.*, A64:819–833, 1991.
34. Wollgarten M., Zhang M., and Urban K. *Phil. Mag. Lett.*, 65:1–6, 1992.
35. Wollgarten M., Lakner H., and Urban K. *Phil. Mag. Lett.*, 67:9–18, 1993.

36. Wollgarten M., Beyss M., Urban K., Liebertz H., and Köster U. *Phys. Rev. Lett.*, 71:549–552, 1993.
37. Wollgarten M. and Urban K. *Phil. Mag. Lett.*, 68:273–277, 1993.
38. Wollgarten M., Bartsch M., Messerschmidt U., Feuerbacher M., Rosenfeld R., Beyss M., and Urban K. *Phil. Mag. Lett.*, 71:99–105, 1995.
39. Wollgarten M., Metzmacher Chr., Rosenfeld R., and Feuerbacher M. *Phil. Mag. A*, 76:455–470, 1997.
40. Wollgarten M., Takeuchi S., Messerschmidt U., and Bartsch M. In S. Takeuchi and T. Fujiwara, editors, *Proc. of the 6th Int. Conf. on Quasicrystals*, pages 549–552. World Scientific, Singapore, 1998.

14 Ion Channeling in Quasicrystals

Dieter Plachke and Heinz Dieter Carstanjen

Summary. It is the aim of this chapter to outline the principles of ion chapter in quasicrystals and to give an overview of the potential applications of this technique. We will see that in quasicrystals there exist rows and planes of atoms which are the prerequisite for channeling in ordered structures. In contrast to periodic lattices in quasicrystals these rows and planes exhibit a wide distribution of densities. This causes problems, in part, but does not render channeling impossible.

While the first ion channeling investigations in quasicrystals were almost exclusively concerned with proving its existence, it was subsequently found that ion channeling is particularly useful for the investigation of the decoration of the quasicrystalline lattice by the different atom species present in these materials. Examples are shown for d-AlCuCoSi and i-AlPdMn. According to this work there still exist considerable discrepancies between the results of these experiments and of channeling calculations performed for the presently available structure models. The discrepancies are particularly strong for i-AlPdMn and indicate that Boudard's model and related models still require major changes. Suggestions for solving this problem are given.

In the final section it is shown how ion channeling may be used to determine the interstitial positions of small amounts of impurities in quasicrystals. It is a powerful technique and has been frequently used in the case of periodic crystals.

14.1 Introduction

Shortly after the discovery of the first quasicrystals in 1982 and the development of the concept of the quasicrystalline structure, the question arose in the ion channeling community of whether ion channeling was feasible in quasicrystals. At that time it was not clear whether densely packed rows or planes of lattice atoms exist in these crystals, a necessary prerequisite for channeling. In those days many scientists tried to find channeling in these new materials – and failed. Mostly, this was because the samples were too small or had poor quality. Many quasicrystals also are very sensitive to radiation damage and thus did not survive the channeling experiment.

It was Kupke et al. [11] who showed in 1991 that such atom rows and planes necessary for channeling exist in an icosahedral Ammann tiling. By decorating this tiling with atoms they could, in addition, demonstrate via computer simulation, that ion channeling should be feasible in quasicrystals.

J.-B. Suck et al. (eds.), *Quasicrystals*
© Springer-Verlag Berlin Heidelberg 2002

One year later Carstanjen et al. [7] for d-AlCuCoSi and du Marchie van Voorthuysen et al. [15] for i-AlCuFe proved experimentally that ion channeling is indeed possible in these materials.

These first papers were primarily concerned with the feasibility of channeling in quasicrystals and with the investigation of the quasicrystalline symmetry by the use of channeling. As was pointed out by Carstanjen and Plachke in subequent work in the following years (see for, example, [21]) by measuring element-specific channeling yield profiles, ion channeling is particularly useful for the investigation of the decoration of the quasicrystalline structure by the different atom species present in these materials. Such information is not easily obtainable by other techniques. Additionally, ion channeling may be used to determine the lattice positions of low concentration impurities in quasicrystals.

This chapter deals first with the principles of ion channeling (Sect. 14.2), followed by a short outline of Lindhard's analytical theory of channeling (Sect. 14.3). In Sect. 14.4 the basic experimental techniques are described. The final section gives various examples of applications. It starts with a subsection on atom rows and planes in quasicrystals (Sect.14.5.1), the prerequisite for channeling, followed by a sub-section on the use of channeling to study symmetries in quasicrystals (Sect. 14.5.2). Section 14.5.3 deals with the investigation of the decoration of quasicrystalline structures by different atom species – the examples pertain to the analysis of d-AlCuCoSi and of i-AlPdMn. The paper ends with a short section (Sect. 14.5.4) on the use of channeling to locate Si atoms in d-AlCuCoSi.

14.2 Basics of Channeling

14.2.1 Principles

In a periodic crystal the atoms are well arranged in linear and planar arrays, so-called atom rows and planes. Figure 14.1a demonstrates this in a perspective view of a cubic crystal along a [100] direction and a (100) plane. When a well collimated beam of fast ions is incident on a crystal parallel to low-index crystal axes or planes, the ions feel the regular arrangement of the atoms. The repulsive potentials of the crystal atoms exert strong steering forces on the incident ions, and, as a consequence, the ions move in a so-called channel through the crystal being scattered in a series of small-angle collisions by the atoms forming the channel walls: they are *channeled.* This correlated scattering is shown in Fig. 14.1b for the case of an ion scattered by a single atom row.

On continuing their way through the crystal the ions are reflected by the channel walls, as shown in Fig. 14.1c. They perform a kind of oscillatory motion, being in phase at the crystal surface but losing their phase coherence during penetration. Accordingly, they mainly dwell in the more open parts of the crystal, thus avoiding close contact with the atom cores. This particular

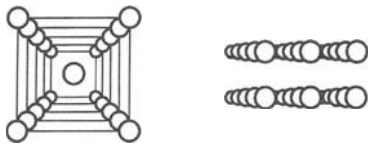

a)

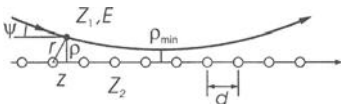

b)

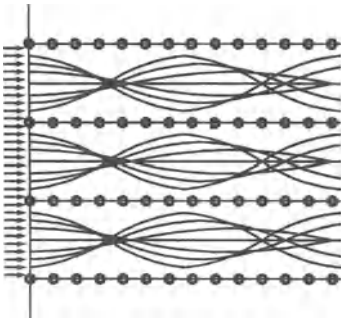

c)

Fig. 14.1. (**a**) Perspective view of a cubic crystal along a [100] direction and a (100) plane. (**b**) Correlated scattering of a fast particle of charge Z_1e and energy E by a row of atoms of charge Z_2e. r: instantaneous position vector of the fast particle, ρ: distance from the row. (**c**) Oscillatory motion of channeled ions, getting out of phase with penetration depth

behavior of channeled ions causes several effects which can be seen experimentally. Here we give some examples. Since close encounters between ions and lattice atoms are very rare under channeling conditions, effects such as Rutherford backscattering (RBS) of the primary ions, nuclear reactions with the lattice atoms or excitations as well as ionization of the lattice atoms which then may lead to X-ray emission are strongly reduced. It is this reduction of the interaction yield which leads to the famous channeling minima known from RBS experiments (see Sect. 14.2.2).

Another effect is connected with the slowing down of channeled ions. The slowing down of fast ions in matter is caused by two effects: by energy transfer to the atom cores which is the dominant effect at low energy (typically a few keV) and by energy transfer to electrons which are, at least partially, located around the atom cores (dominant at high energies). Since under channeling conditions any interaction with the lattice atoms is strongly reduced, the slowing down of channeled ions is less effective, leading to large penetration depths of channeled ions. In fact, channeling was first seen in an investigation of ion ranges by computer simulation of ion trajectories at low energies by Robinson and Oen [23]: when the authors started their simulations in the evening by shooting keV Cu ions in a Cu crystal along a low-index lattice direction, the computer was still running the following morning, while it had finished after only a few hours for non-low index directions. The reason was

the prolonged ion ranges due to channeling. Such increased ion ranges were later found experimentally [14,18,19].

The channeling effect disappears for oblique ion incidence, i.e. if the angle between the particular channel and the incidence direction of the ion beam exceeds a certain *critical angle* ψ_c. For axial channeling, Lindhard, who has developed the theoretical basis of most of the channeling effects in his famous paper of 1965 [13], derived the following expression:

$$\psi_c = \sqrt{\frac{2Z_1 Z_2 e^2}{E\,d}}\,. \tag{14.1}$$

This was derived under the premiss that a channeled ion during its collision with a single atom row, has to interact with several atoms of the row. Here Z_1 and E are the nuclear charge and the energy of the incident ion, Z_2 the nuclear charge of the lattice atoms, d the spacing between atoms in the considered lattice row and e the elementary charge. For 1-MeV He^+ ions incident on a Cu crystal along a [100] lattice direction ψ_c is about 1.2°. It is worth noting that according to (14.1) the critical angle varies with the square root of Z_1, the charge density Z_2/d of the atom rows, and as $1/E$. For planar channeling the critical angles are typically smaller by a factor of 3 than for axial channeling. The disappearance of channeling at larger incidence angles results from the fact that the ions can now approach the lattice atoms closer than before, which leads to occasional large-angle collisions and thereby to the loss of correlated scattering.

14.2.2 Channeling Minima

As stated in the previous section, ion backscattering is strongly reduced under channeling conditions. This effect can easily be measured by counting the rate of backscattered ions and analyzing their energies with an energy-sensitive detector, e.g. a silicon surface barrier detector. Figure 14.2a shows the energy spectrum of He^+ ions backscattered from a single crystal for perfect alignment of a low-index crystal axis with the ion beam and for random incidence, i.e. if the ion beam is not aligned with a low-index crystal direction. The figure indicates the strong reduction of the scattering rate at high energies, i.e. close to the crystal surface. The reduction levels off towards lower energies due to *dechanneling* (see below). Besides, one recognizes a small peak in the aligned spectrum at the highest energies: this peak is due to the fact that the ion beam can not distinguish between the surface of an aligned and a not-aligned crystal, since channeling develops inside the crystal. So the first few layers (about three) scatter ions in the same way as a not-aligned crystal, in this way causing the surface peak.

If one sets an energy window directly behind this surface peak and counts all backscattered particles in this window as a function of the angle ψ of ion incidence, one obtains the famous channeling minimum (see Fig. 14.2b). At

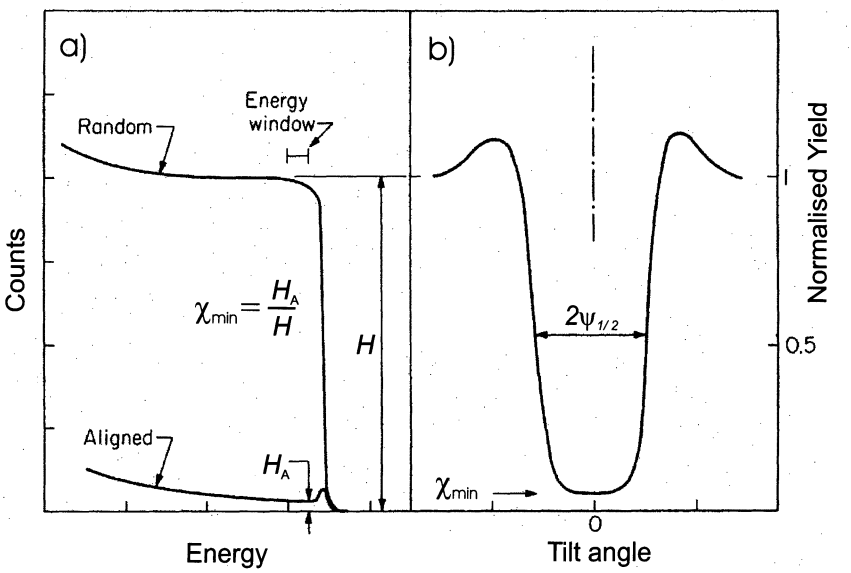

Fig. 14.2. (**a**) Energy spectra of backscattered ions for aligned and random incidence (schematic). (**b**) Angular yield profile of backscattered ions of energies in the window as marked in (**a**) (schematic)

the angle $\psi = 0$ the crystal axis is in perfect alignment with the ion beam. Similar yield profiles are also obtained for planar channeling. The channeling minima can be characterized by two parameters: the angular half-width $\psi_{1/2}$ (=HWHM) and the minimum yield $\chi_{\min}$. The angular half-width is typically smaller by a factor of $\sqrt{2}$ than ψ_c. More precise expressions for axial as well as planar angular half-widths have been derived by Barrett [1] and are given in the following. They in particular include the influence of thermal lattice vibrations which tend to narrow the minima.

$$\psi_{1/2}^{(\text{axial})} = 0.8\, F_{\text{RS}}(1.2\, u_1/a_{\text{TF}})\psi_c\,, \tag{14.2}$$

$$\psi_{1/2}^{(\text{planar})} = 0.72\, F_{\text{PS}}(1.6\, u_1/a_{\text{TF}}, d_p/a_{\text{TF}})\psi_p\,. \tag{14.3}$$

Here u_1 is the 1-dimensional root-mean-square thermal-vibration amplitude of the lattice atoms, a_{TF} the Thomas–Fermi screening radius, F_{RS} the square root of the row potential using Moilière's screening function (see Sect. 14.3.1), F_{PS} the square root of the mean planar potential, d_p the distance between planes and ψ_p the critical angle for planar channeling. The Thomas–Fermi screening radius is given by

$$a_{\text{TF}} = 0.8853\, a_0 \left(Z_1^{1/2} + Z_2^{1/2}\right)^{-2/3}\,, \tag{14.4}$$

where a_0 denotes the Bohr radius. The critical angle for planar channeling is given by

$$\psi_p = \sqrt{\frac{2\pi Z_1 Z_2 e^2 N d_p a_{TF}}{E}} , \tag{14.5}$$

where N is the volume atom density of the crystal.

The minimum yield in a channeling experiment is primarily determined by the fraction of non-channeled ions, since only these ions have the chance to interact with the lattice atoms and to contribute to the backscattering yield. At a short distance below the first surface layers the fraction of non-channeled ions, at axial channeling in a perfect crystal, is determined by the fraction of ions hitting the heads of the atom rows at the surface, since these ions are scattered by larger angles than ψ_c. Their fraction is, to a good approximation, given by the ratio of the area A_r describing the range of the influence of one atom row and the Wigner–Seitz area A_0 of one atom row. A_r is approximately given by $\pi(a_{TF}^2 + \rho_{th}^2)$ and A_0 by $1/(Nd)$; so one arrives at:

$$\chi_{min} = A_r/A_0 = \pi(a_{TF}^2 + \rho_{th}^2)\, N\, d , \tag{14.6}$$

where ρ_{th} denotes the two-dimensional mean thermal amplitude of the atoms and N the atom number density. Similarly, one finds for planar channeling:

$$\chi_{min} = 2(a_{TF} + y_{th})/d_p , \tag{14.7}$$

where d_p is the interplanar distance and y_{th} the one-dimensional mean thermal vibration amplitude of the lattice atoms perpendicular to the plane.

Also, for the axial minimum yield Barrett [1] has derived a more elaborate formula which reads:

$$\chi_{min} = 18.8\, N\, d\, u_1^2 \sqrt{1 + \left(\frac{\psi_{1/2}\, d}{126\, u_1}\right)^2} , \tag{14.8}$$

where $\psi_{1/2}$ is given in degrees.

A minimum yield for good crystals ranges at room temperature from 3 to 5 % for axial channeling and from 20 to 30 % for planar channeling. For crystals containing larger concentrations of defects considerably higher minimum yields are observed. Noticeable effects start at defect concentrations of 1 %.

14.2.3 Blocking

Up to now we have only considered the influence of the lattice steering on a well-collimated beam of particles *entering* the crystal. This steering caused the channeling minima of the previous section. Now we want to discuss the inverse problem (Fig. 14.3), namely the *emission* of particles by the lattice atoms. After emission by the atoms the particles penetrate and finally leave

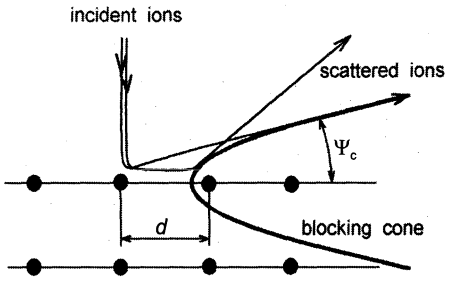

Fig. 14.3. Formation of a blocking cone along an atomic row for ions backscattered from lattice atoms

the crystal to be recorded at a large distance as a function of the emission angle. As the figure shows, the emission of these particles is blocked along major crystal directions, since the particles are deflected by the neighboring lattice atoms. Due to the reversibility of particle trajectories in electrostatic fields the angular profiles obtained in such measurements are the same as those obtained in the channeling experiment described above. This is the so-called *rule of reversibility* between channeling and blocking, first pointed out by Lindhard [13]. Commonly, blocking patterns are obtained by shooting a beam of particles on a single crystal along a random direction (Fig. 14.3) and recording large-angle scattered particles with a film. During large-angle scattering the particles approach the atom cores very closely, so the scattered particles can be considered as being emitted by the atoms. Blocking patterns of quasicrystals are shown in Sect. 14.5.2.

14.2.4 Flux-Density Distribution of Channeled Ions

Ions channeled in a single crystal exhibit a particular flux-density distribution. This is illustrated in Fig. 14.4, which shows under (a) the flux-density distribution (averaged over a penetration depth of several hundred nm) of 750-keV $^3He^+$ ions in a (110) planar channel of a Ta crystal for various angles of ion incidence. The data were obtained from Monte Carlo simulations of ion channeling. As the figure shows, for $\psi = 0°$ (ion incidence exactly parallel to the (100) plane) the particle flux is strongly reduced in the region of the atom planes (at $y = 0$), but peaked in the center between neighboring planes (at $y = d_p/2$). This is due to the fact mentioned above that channeled particles avoid the region around rows or planes and spend most of the time in the most open regions of the channel. On the other hand, all particles have to pass the channel center which causes the observed flux peak. With increasing angle of particle incidence the flux peak moves towards the channel walls, simultaneously decreasing its height. For large angles of incidence one finally finds an almost homogenous flux-density distribution.

This peculiar change of particle flux with the angle of ion incidence provides an excellent ion-flux probe which is fine tunable over atomic distances by the variation of the incidence angle. In fact, it provides – in combination

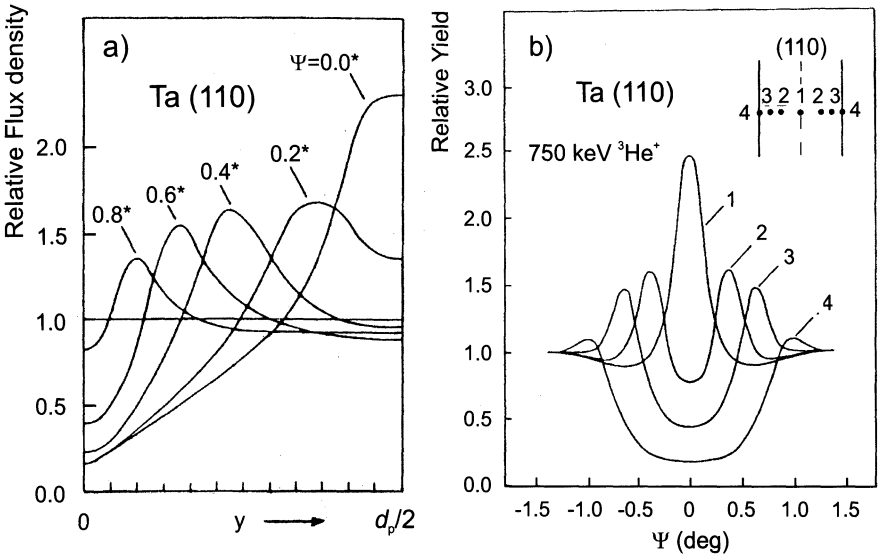

Fig. 14.4. (**a**) Calculated flux-density distribution of 750-keV $^3He^+$-ions in a planar (110) channel of Ta as a function of the angle of ion incidence ψ. The atomic plane is located at $y = 0$, the center of the channel at $y = d_p/2$. (**b**) Angular profiles of the reaction yield of 750-keV $^3He^+$-ions for planar channeling in a (110) channel of Ta. The profiles correspond to the positions 1–4 in the planar channel shown in the inset

with appropriate reactions with the atoms under consideration – a tool which is widely used for locating the impurities in crystals [4]. Appropriate reactions are ion backscattering, X-ray excitation or nuclear reactions. Figure 14.4b shows angular-yield profiles obtained from the flux distributions shown under (a) for atoms located at different positions in the planar channel shown on the left (inset). It shows, in particular, that one obtains a peak in the angular-yield profile for atoms located in the channel center, an off-center peak for atoms at off-center sites, and a pronounced minimum for atoms located in the channel walls. An application of this technique to quasicrystals will be given in Sect. 14.5.4. Finally we would like to note that the minimum obtained for atoms located at positions in the channel walls is identical with the channeling minimum obtained by recording backscattering from the lattice atoms, provided they exhibit the same thermal amplitudes.

At the end of this section we would like to recommend the reader to a few monographies on channeling. Besides the article by Lindhard [13] which gives an introduction to the principles and the theory of channeling, in particular we recommend the book by Morgan [17] and the article by Gemmell [9] which, besides chapters about principles and theoretical aspects, gives many examples of applications.

14.3 Lindhard's Theory of Channeling

14.3.1 Principles

In his paper of 1965 [13] Lindhard presented an analytical theory for ion channeling which describes most of the features inherent to channeling phenomena. The underlying principles will be outlined in the following. In his approach Lindhard replaces the individual interaction potentials $V(r)$ between the incident ions and the atoms of an atom row by an average potential, averaged along the extension z of the row which is an appropriate description for ion scattering under channeling conditions. This average potential $U(\rho)$ then reads:

$$U_{\mathrm{a}}(\rho) = \frac{1}{d}\int_{-\infty}^{+\infty} V(\sqrt{\rho^2 + z^2})\,\mathrm{d}z\,, \tag{14.9}$$

where ρ is the radial distance perpendicular to the row and d the spacing between neighboring atoms within the row. Similarly, one defines the average interaction potential with a plane of atoms by:

$$U_{\mathrm{p}}(y) = N d_{\mathrm{p}} \int_{-\infty}^{+\infty}\int_{-\infty}^{+\infty} V(\sqrt{y^2 + x^2 + z^2})\,\mathrm{d}x\mathrm{d}z\,, \tag{14.10}$$

where N and d_{p} are defined as above and y is the distance perpendicular to the plane. For the atomic potential, $V(r)$, commonly a screened Coulomb–potential of the form $V(r) = Z_1 Z_2 \mathrm{e}^2/r\,\exp(-a/r)$ or a sum of such potentials are used, exhibiting different pre-exponential factors and screening lengths. The above-mentioned Moilière-potential and the so-called krypton-carbon-potential by Biersack and Ziegler are of this type [8]. Thermal displacements of the lattice atoms can be taken into account by folding the potentials with an appropriate Gaussian distribution. The potential of an array of rows or planes, as found in a crystal, is then obtained by a summation over neighboring rows or planes.

If an ion is incident on the crystal along the direction z, then the so-called transverse energy $E_\perp$ of the particle moving in the direction perpendicular to z is conserved. $E_\perp$ is the sum of the potential energy U and the kinetic energy $E{\cdot}\sin^2\psi$. For small angles ψ the latter is approximately given by $E{\cdot}\psi^2$ where E is the total kinetic energy of the particle and ψ the momentary angle between the particle velocity and the extension of the row or plane under consideration. At the crystal surface the initial transverse energy $E_{\perp 0}$ is determined by the position ρ_0 (or y_0), where the ion enters the crystal, and the angle of ion incidence ψ_0. $E_{\perp 0}$ thus reads

$$E_{\perp 0} = U_a(\rho_0) + E\cdot\psi_0^2\,, \tag{14.11}$$

for the axial case and

$$E_{\perp 0} = U_p(y_0) + E\cdot\psi_0^2\,, \tag{14.12}$$

for the planar case. When the particle leaves the surface and penetrates into the crystal the position in the potential changes and so does ψ. Under the condition that $E_{\perp 0}$ is conserved we thus have the relations:

$$E_{\perp 0} = U_a(\rho) + E \cdot \psi^2 \tag{14.13}$$

and

$$E_{\perp 0} = U_p(y) + E \cdot \psi^2 \,, \tag{14.14}$$

for the axial and planar cases, respectively. The distance of closest approach of a particle with transverse energy $E_{\perp 0}$ to a row or plane is obtained by setting the transverse kinetic energy to zero which gives $U_{\mathrm{a}}(\rho_{\min}) = E_{\perp 0}$ for the axial and $U_{\mathrm{p}}(y_{\min}) = E_{\perp 0}$ for the planar case.

The motion of channeled particles in an axial potential is illustrated in Fig. 14.5. The figure shows equipotential lines with the minimum at its center. If a particle enters this potential with a certain transverse energy $E_{\perp 0}$, then the particle has access to all parts of the channel with $U_{\mathrm{a}}(\rho)$ smaller than $E_{\perp 0}$, indicated in Fig. 14.5 by hatching. One further recognizes that the channel center is accessible to all particles which leads to the enhanced flux density at this position as mentioned before (flux peaking). On the other hand, only particles with the highest transverse energies are able to reach the area of the atom rows and to interact with the lattice atoms. This leads to, for example, the reduced backscattering rate in RBS experiments under channeling conditions. The critical distances of approach ρ_{c} and y_{c}, i.e. the distances where channeling becomes impossible, are obtained by setting $U_{\mathrm{a}}(\rho_{\mathrm{c}})$ or $U_{\mathrm{p}}(\mathrm{y_c})$ equal to $E \cdot \psi_{\mathrm{c}}^2$. The corresponding transverse energy $E_{\perp c} = E \cdot \psi_c^2$ is called the critical transverse energy. The critical area around the atom rows is indicated in Fig. 14.5 by cross hatching.

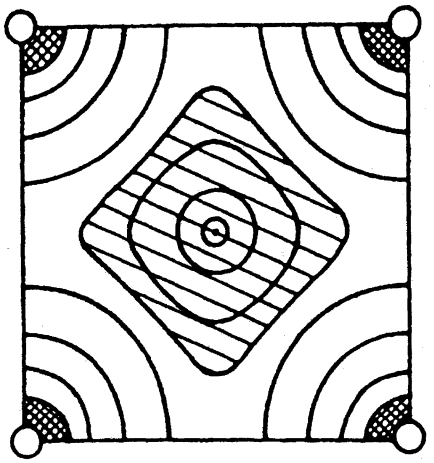

Fig. 14.5. Schematic contour diagram of the continuum potential $U_{\mathrm{a}}(\rho)$ for axial channeling in a cubic crystal along [100]. The potential minimum is located in the center. The *open circles* at the corners represent the [100] atom rows, the *cross-hatched area* around the "forbidden" regions of radius ρ_{c}. The motion of a channeled particle of transverse energy $E_{\perp 0}$ is restricted to the *hatched area* in the center, with the contour $U(\rho) = E_{\perp 0}$ as boundary

If the angle of incidence is zero, the ion motion is restricted to the area inside the potential contour U_0, i.e. the region with lower potential, where the ion started at the surface. With increasing angle of incidence the particles are able to extend the accessible area up to the line $U = U_0 + E \cdot \psi_0^2$, until finally the whole transverse area becomes accessible, even for particles which entered the crystal in the channel center. Channeling effects then disappear.

14.3.2 Angular and Spatial Distributions

Lindhard's theory also allows us to calculate the angular and spatial distributions of channeled ions. Angular distributions are observed, for instance, in transmission experiments through thin single crystals. Spatial distributions, synonymous with flux densities, play an important role for atom-location experiments, as mentioned in Sect. 14.2.4. However, since the integrations, required to obtain quantitative and realistic results, have to be done numerically, channeling Monte-Carlo calculations are preferred instead. In addition, these calculations allow us to use more realistic models than analytic calculations. Nevertheless, the principles of Lindhard's analytic treatment will be outlined in the following. Lindhard starts from the assumption that the channeled ions of a given transverse energy $E_\perp$ – having penetrated the crystal to a certain depth – are distributed homogeneously in the corresponding position-momentum transverse space, i.e. transverse phase space, which has the dimension 4 for axial and 2 for planar channeling, respectively. This procedure is well known from, for example, thermostatistics. By integration over the position-coordinates one obtains the transverse momentum and, hence, the angular distribution of the channeled particles, by integration over the transverse momenta the spatial distribution in transverse space. Finally, in order to obtain the distribution of all ions of all transverse energies, one has to weight these distributions by the distribution of transverse energies, which is determined by the incidence conditions, and integrate over all transverse energies. A short outline of this theory can be found in Lindhard's article [13], a more detailed description may be found in [5,17]. To give at last one example, it turns out that in the case of axial channeling the spatial distribution inside of a given equipotential contour line is homogeneous and proportional to $1/A_\mathrm{a}$, where A_a is the accessible area. This allows a simple calculation of the flux distributions. By integration over all transverse energies, i.e. accessible areas, one obtains a logarithmic divergence of the flux density in the channel center.

14.3.3 Dechanneling

Up to this point, a given transverse energy of a particle was considered to be constant while the particle penetrates into the crystal. In general, the transverse energy of a particle is not exactly constant, but changes slightly, either due to changes of the energy or due to angular straggling. Changes of

the energy are primarily due to slowing down processes. Angular straggling, i.e. scattering of the particles, may arise from various sources such as thermal displacements of the lattice atoms or impurities or intrinsic defects. In quasicrystals there are new sources for angular straggling: besides phasons, which do not exist in periodic crystals, one has in particular the quasiperiodic structure itself which causes a considerable amount of scattering. As shown in Sect. 14.5.1, the occupation density of equivalent crystal rows or planes by atoms is by no means constant – as is the case in periodic crystals. Some rows have a very low occupation density (for instance 1 atom per 3 nm), thus acting like isolated scattering centers.

Most of these effects cause a broadening of the transverse energy distribution and dechanneling: the particles that have surmounted the critical transverse energy $E_{\perp c} = E \cdot \psi_c^2$ are no longer channeled and have therefore a high probability of interaction with lattice atoms. It should be noted that already at the surface a certain fraction of the incident ions is dechanneled, even at incidence exactly parallel to the crystal axis or planes. It is that part that enters the crystal in a circular area with radius ρ_c around atom rows, or within strips of width $2y_c$ along the atom planes. These particles have a high chance for interaction with the lattice atoms and provide the minimum yield χ_{min} mentioned in Sect. 14.2.2. Also, an amorphous surface layer causes dechanneling, thus increasing the minimum yield. For a more detailed description of dechanneling the reader is referred to [5,17].

14.4 Experimental

14.4.1 Basic Set-Up and Crystal Orientation

The basic set-up for a channeling experiment is quite simple. A scattering chamber (vacuum vessel) equipped with a two-axes goniometer and the detector will be enough (Fig. 14.6). Typically, ion beams in the few MeV range are used for the analysis, e.g. 2-MeV He^+ ions for RBS and 3-MeV H^+ or He^+ for PIXE (particle induced X-ray emission) measurements. For the energy-dispersive registration of particles, commonly silicon surface-barrier detectors are used, for the measurement of X-rays either Li-drifted silicon or intrinsic germanium detectors. In channeling experiments the count rate of the particles or X-rays in question is recorded as a function of the angle between the crystal axis and the ion beam. Commonly, the entire energy spectra are recorded as obtained, and appropriate windows are set afterwards during the data analysis.

Before the actual channeling measurement can be started the desired crystal axis has to be aligned with the ion beam. This is usually done by orienting the crystal by the ion beam itself by means of channeling in combination with RBS. For this purpose the crystal is tilted into a certain angular position α_1 (Fig. 14.6b) and the backscattering yield recorded while the crystal is rotated around a second axis, perpendicular to the first (angle ψ). Whenever the

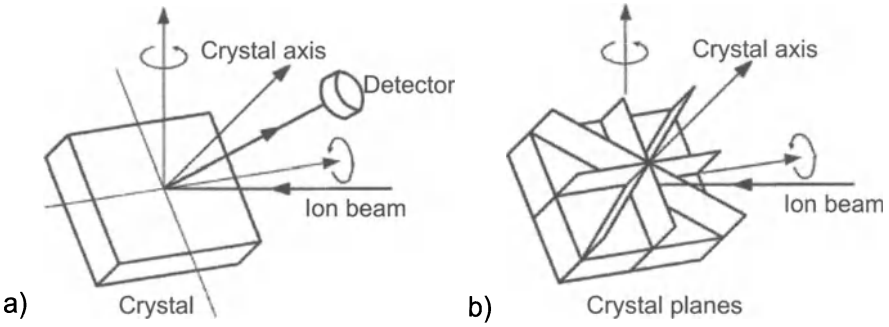

Fig. 14.6. (**a**) Set-up for a channeling experiment: the single crystal is mounted on a goniometer with at least two axes (angles ψ and α). (**b**) Alignment of a crystal with the beam: during rotation of the crystal (tilted to a certain angle α) around a vertical axis (angle ψ) the backscattering yield is reduced whenever the beam direction coincidences with a lattice plane

beam direction coincides with one of the planes merging in the common crystal axis (Fig. 14.6b) the backscattering yield is reduced due to channeling. Figure 14.10 of Sect. 14.5.1 shows such an angular yield profile for channeling in a decagonal quasicrystal. The minima in these profiles indicate the angular positions of various planes. After such a scan the crystal is tilted to new positions α_2, α_3 etc. and the measurement repeated. Plotting the angular positions of the observed minima in a ψ–α diagram (the so-called orientation diagram, Fig. 14.14 in Sect. 14.5.2) allows us to find the desired crystal axis.

14.4.2 Rutherford Backscattering and Particle-Induced X-Ray Excitation

In many cases one is not only interested in the interaction rate of the ion beam with the crystal atoms in general, but one also wants to know from which atom species the recorded signal may come. This is particularly interesting in the case of quasicrystals, since all known quasicrystals are alloys. Two techniques used in the following paragraphs which allow such an identification will be described in the following. For more detailed information the reader is refered to, for example, the Ion Beam Handbook by Mayer and Rimini [16].

The first technique described is RBS. If an ion is backscattered by a lattice atom, it transfers energy to the scattering atom. The amount depends on the ratio of the masses of the incident ions and the scattering atoms: m_1/m_2. According to the kinematics of scattering only a little energy can be transferred to heavy atoms by the light ions typically used in these investigations, but in collisions with light atoms this can be a considerable amount. The amount of energy left to the scattered ion, E_1, also depends on the scattering angle θ. For 180° backscattering it amounts to: $E_1 = (m_2 - m_1)^2/(m_2 + m_1)^2 \cdot E_0$,

where E_0 is the kinetic energy of the incident ions. For example, for He^+ scattered by Au-atoms the ratio $k = E_1/E_0$, called the kinematic factor, amounts to 0.92, while for scattering by C it is only 0.25. This fact is used for the identification of atoms. The steps seen in the RBS spectrum from an icosahedral AlPdMn quasicrystal (Fig. 14.7) correspond to the atom species present in this alloy and allow a clear identification. Besides being scatte-

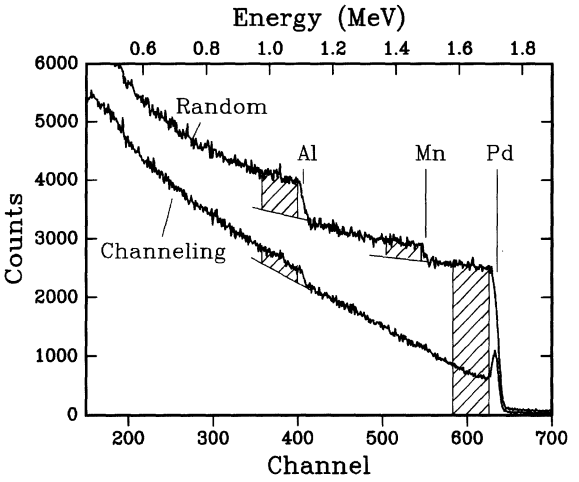

Fig. 14.7. Rutherford backscattering spectra of 2-MeV He ions obtained from i-$Al_{72}Pd_{19}Mn_9$ for ion incidence along a random direction and along the 5-fold axis. For channeling experiments the marked energy windows corresponding to a depth interval of 200 nm in the sample were used to obtain the Pd, Mn and Al yield. For the recording of Mn and Al profiles the Pd and the Pd/Mn background, respectively, as obtained from the extrapolation of the high-energy scattering data, was subtracted

red and losing energy in this large-angle collision, the ions lose an additional amount of energy on their way in and out of the target. Since this amount depends on the depth where the collision has occurred, a continuous band of scattered particles extends from the maximum scattering energy $E_1 = k \cdot E_0$ down towards lower energies, which allows additional depth information to be extracted.

The second technique described is PIXE. Similarly as in X-ray tubes by impinging electrons, X-rays can also be excited by fast ions, e.g. H^+ or He^+ ions. However, since the cross sections scale with the particle velocities, high ion energies in the 3–4 MeV range are required. Due to the higher mass of the ions, compared with the mass of the electrons, the X-ray spectra are almost free of Bremsstrahlung and mainly exhibit characteristic lines, different from those produced from X-ray tubes. The measurement of these characteristic X-rays is an ideal means for atom identification. Figure 14.8 shows a PIXE spectrum from a decagonal AlCuCoSi quasicrystal. The characteristic

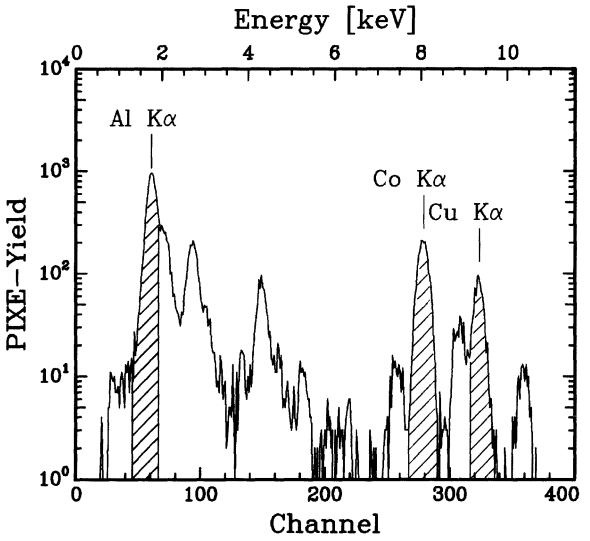

Fig. 14.8. PIXE spectrum as obtained from a T-phase $Al_{62}Cu_{20}Co_{15}Si_3$ quasicrystal with 3-MeV $^4He^+$-ions. The windows set on the different X-ray peaks were used for the channeling measurements presented in Fig. 14.17

Kα-lines for the elements Al, Co, and Cu are indicated. With the detectors available at present it is even possible to differentiate between neighboring elements. This, commonly, is not possible by ion backscattering. Because X-rays are primarily emitted in close encounters between the incident ions and the atoms under consideration, PIXE can very well be combined with ion channeling in atom-location experiments.

14.5 Ion Channeling in Quasicrystals

14.5.1 Rows and Planes in Quasicrystals

Over a period of several years after the discovery of quasicrystals in 1982 by Shechtman et al. [25] it was not clear if ion channeling is possible also in quasicrystals, since it was unknown whether quasicrystals contain the prerequisites for channeling, namely *rows and planes of atoms*. It was Kupke et al. [11] who showed for the first time that also quasicrystals contain such elements (Fig. 14.9) and demonstrated in a computer simulation that icosahedral quasicrystals should show channeling effects. The first experimental evidence was found one year later by Carstanjen et al. [7] who performed channeling experiments with 2-MeV He^+ ions on decagonal AlCuCoSi (Fig. 14.10) and by van Voorthuysen et al. [15] who used 1-MeV He^+ ions to study channeling on icosahedral AlCuFe (Fig. 14.11). The structure of atomic rows and planes in quasicrystals is, however, different from that of periodic crystals [10,12].

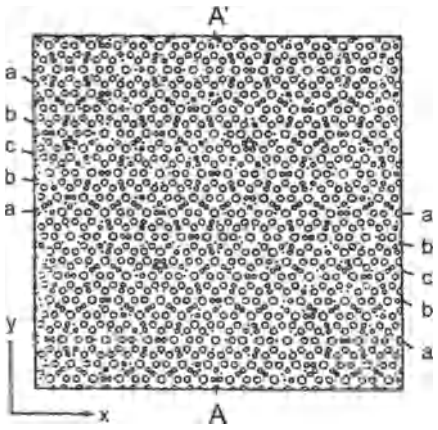

Fig. 14.9. Projections of the vertices of an icosahedral Ammann tiling along a 5-fold axis. The letters a, b, c indicate different planes [11]

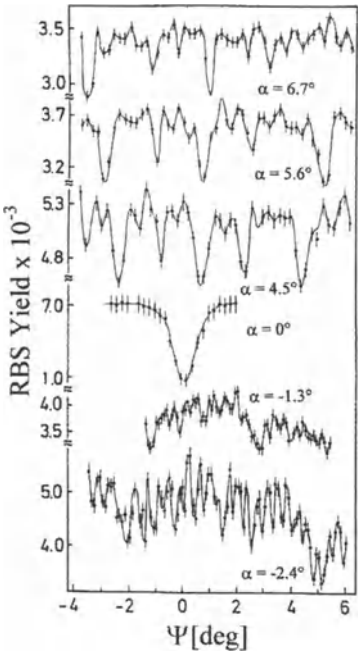

Fig. 14.10. Rutherford backscattering yield profiles (Co/Cu scattering) as obtained from angular scans in the (angular) neighborhood of the decagonal axis of a T-phase $Al_{62}Cu_{20}Co_{15}Si_3$ quasicrystal. During the scans (rotation about a vertical axis, angle: ψ) the quasicrystal was kept at various fixed tilting positions α. Channeling in the decagonal axial channel (at $\psi = 0$, $\alpha = 0$) and in various planar channels is clearly visible

(i) Atom rows as well as planes are arranged quasiperiodically (Figs. 14.9 and 14.13). For instance in an icosahedral Ammann tiling the planes parallel to the icosahedral axes show two different interplanar distances which are arranged quasiperiodically and which are interlaced by a third interplanar distance (Fig. 14.13). (ii) In periodic crystals all parallel atom rows exhibit the same number density. This is different in quasicrystals. Here one has a

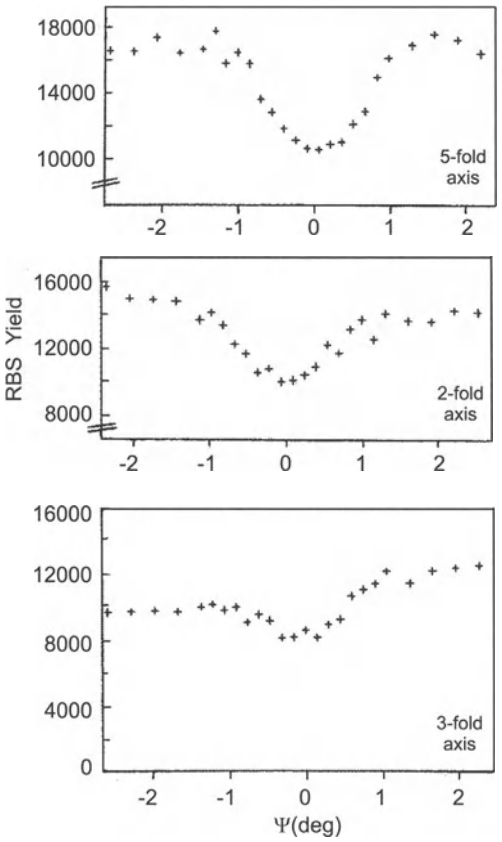

Fig. 14.11. Rutherford backscattering yield profiles (1-MeV $^4He^+$-ions, Fe/Cu-scattering) from angular scans across the 5-, 3- and 2-fold axes of an icosahedral AlCuFe quasicrystal (after du Marchie van Voorthuysen et al. [15])

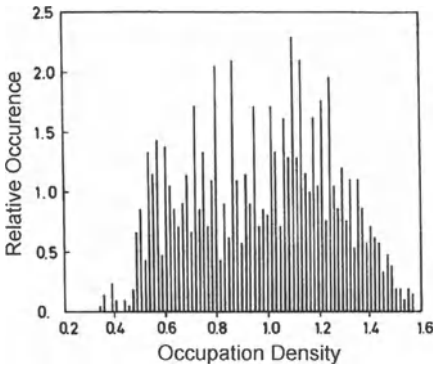

Fig. 14.12. Distribution of occupation densities (atoms/nm) of atomic rows of the Ammann tiling of Fig. 14.9

distribution of number densities which varies over a wide range. Figure 14.12 shows the density distribution of an icosahedral Ammann tiling.

Density distributions for atom planes in this lattice show similar features (Fig. 14.13). The quasiperiodic arrangement of the atom rows and planes is less disturbing. In periodic crystals one also finds various arrangements of rows exhibiting different symmetries; as long as the occupation density of the rows does not change, one obtains – according to (14.1) and (14.2) – identical critical angles for channeling. Only the symmetry of the orientation diagram changes; similarly for atom planes. Also in periodic crystals one encounters different interplanar distances (for instance neighboring (111)-planes in Si show two different interplanar distances). Since in channeling experiments the steering forces are due to the atom rows and planes and their occupation by atoms, the critical angles do not, to first order, depend on the distance between neighboring rows or planes.

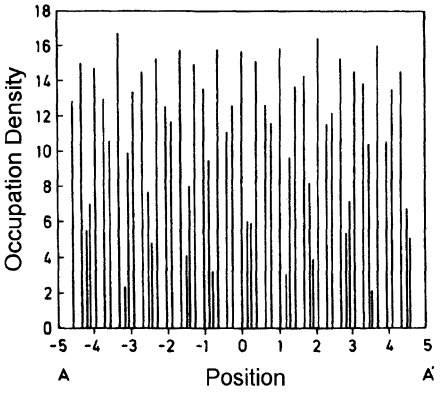

Fig. 14.13. Occupation densities (atoms/nm^2) of the planes along the path AA′ in Fig. 14.9

It is the non-uniform occupation of the rows and planes by atoms which causes problems in the analytical interpretation of the data. Since channeling works with the distribution of occupation densities, in quasicrystals every row or plane has its own scattering strength. An adjusted theory has not yet been developed. All that can be derived at present by, for example, angular half-widths are mean occupation densities of rows or planes. In order to be able to relate the experimental data to crystal models, one has to perform Monte-Carlo simulations of channeling in the model structure. Such a computer code, based on an early program by Carstanjen and Sizmann [6] has been set up for RBS on decagonal quasicrystals by Kupke and Peschke [11] and extended to RBS and PIXE on decagonal and icosahedral quasicrystals by Plachke [22]. Finally it can be noted that the non-uniform occupation densities are the source for increased dechanneling effects, as described in more detail in Sect. 14.3.3.

On the other hand, the sensitivity of the critical angles against changes in the occupation densities of rows and planes may be used to investigate the presence of the thermal formation of phason flips. As simulations of such

flips on a computer have shown, new rows and also planes are created by these flips. This implies that the already existing rows or planes are then less densely populated by the atoms than before, while the new rows and planes primarily act as scattering Centrex, thus increasing dechanneling. This of course influences the size of the critical angles; changes as small as 1 % should be detectable. Additionally, the influence of phasons should also be seen by changes of the minimum yield, since this quantity also sensitively depends on the number density of rows or planes and on dechanneling. Up to now the influence of phason flips has not unambiguously been seen experimentally, since the effect is obscured by the effect of phonons which have a similar influence on critical angles and minimum yields. Possibly, the large differences in the minimum yields of quasicrystals taken from different charges are due to the presence of different amounts of phasons.

Since its first demonstration, channeling in quasicrystals has been shown to be a valuable tool in structural studies. There are currently essentially three fields where channeling can provide valuable information: (i) in symmetry studies: channeling images the structure of a crystal in real space, (ii) in investigations of the decoration of a quasicrystalline lattice by the different atom species, since the ion-beam techniques used are able to differentiate between different atom species, and (iii) in lattice-location studies of impurities. These three techniques will be discussed in the following paragraphs.

14.5.2 Symmetries

As described in detail in Sect. 14.4.1, channeling is able to provide the orientation diagram of a quasicrystal, i.e. it allows us to obtain the symmetry of a crystal in real space. Figure 14.10 shows the measurement of the backscattering rate from a d-AlCuCoSi quasicrystal (Cu/Co-yield only) during six angular scans (rotation around a vertical axis) in the angular neighborhood of the decagonal axis [7]. Each scan corresponds to a different tilt angle around a horizontal axis. The deep minimum corresponds to the scan through the decagonal axis. By plotting the minima in an α–ψ diagram one obtains the orientation diagram shown in Fig. 14.14. One clearly sees that the different planes intersect at the position of the decagonal axis, thus providing the ten-fold symmetry of the decagonal structure.

A different technique is the blocking technique, described in detail in Sect. 14.2.3. Here, the ion beam is incident on the crystal along a random direction and the angular distribution of the scattered ions is recorded by a position-sensitive device. Figure 14.15 shows a blocking pattern from an i-AlPdMn single crystal [22]. The scattered particles were recorded photographically. Besides an axis of 5-fold symmetry one is able to see an axis of 3-fold and an axis of 2-fold symmetry.

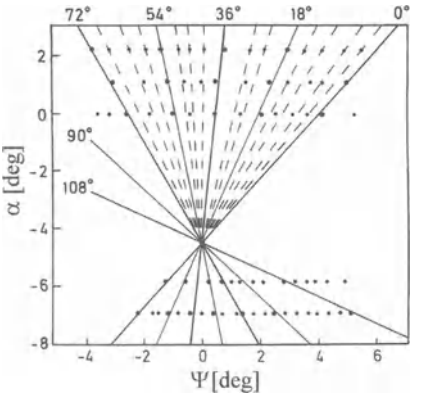

Fig. 14.14. Orientation diagram of a T-phase quasicrystal as obtained from the channeling results of Fig. 14.10. Besides the decagonal axis at $\psi = 0$, $\alpha = 0$ various strong and weak planes (*thick, thin* and *dashed lines*, respectively) are indicated which show the ten-fold symmetry of the quasicrystal

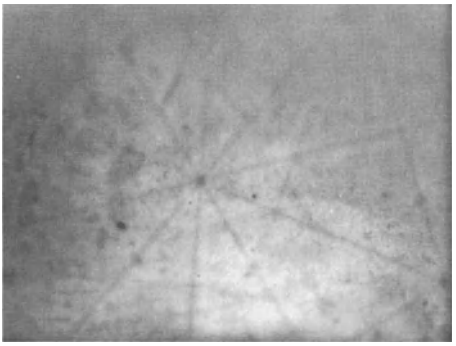

Fig. 14.15. Blocking pattern of an i-AlPdMn quasicrystal obtained by Rutherford backscattering of 1.3-MeV He ions

14.5.3 Test of Structure Models

14.5.3.1 Decagonal AlCuCoSi. In a detailed study the structure and decoration of d-$Al_{62}Cu_{20}Co_{15}Si_3$ has been investigated by Plachke et al. [20]. Plachke performed channeling experiments in combination with RBS employing 2-MeV He^+ ions on these crystals and compared the results with computer simulations for the structure model by Steurer and Kuo [26]. Element-resolved channeling profiles (by RBS only Al and Cu/Co can be distinguished) were taken for the decagonal axis (Fig. 14.16a) and two planar systems having the decagonal axis in common (Fig. 14.16b). As the figure shows, one obtains fair agreement between experiment and model calculations for the decagonal axis and the major planar channel (at 0° in Fig. 14.16b) for both groups of atoms, Al and Cu/Co. This is not the case for the minor planar channel (at 1.6° in Fig. 14.16b) where the minimum yields of both groups of atoms are opposite in experiment and calculation. This indicates that some modifications have to be applied to Steurer's model [26]. The same calculations have also been performed on a more recent model by Steurer et al. [27] and models by Burkov [3] and by Tsuda [28]. There were small quantitative differences from the

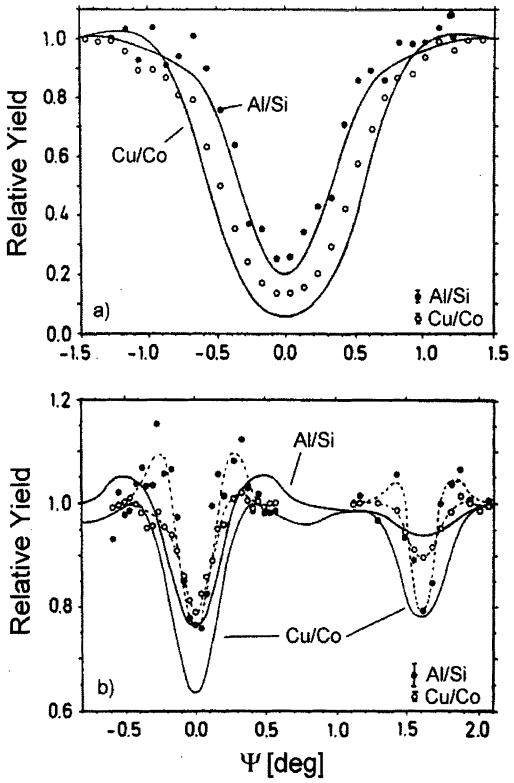

Fig. 14.16. Comparison of experimental (*symbols*) and calculated (*full lines*) Rutherford backscattering profiles from angular scans across the decagonal axis (**a**) and the two major planar systems containing this axis (**b**) of a T-phase $Al_{62}Cu_{20}Co_{15}Si_3$ quasicrystal for scattering by Co/Cu and Al/Si atoms, respectively. The *dashed lines* through the experimental data are drawn to guide the eye

previous calculations, but the main discrepancies for the minor planar channel still remained, indicating that there are still some discrepancies between the proposed crystal models and the real crystal used in the experiments.

In a PIXE-channeling study employing 3-MeV He^+ ions Plachke [20] also investigated differences in the occupation of the decagonal lattice by Cu and Co by measuring the Cu-Kα and Co-Kα-yields (Fig. 14.17). As the figure shows, the Cu and Co profiles are of almost equal shape for channeling along the decagonal axis, indicating that Cu and Co sit on equivalent sites along the decagonal axis. In contrast, the channeling profiles for the major planar channel show that along this plane the atoms occupy sites which are not equivalent, since the Co profile is much deeper than the Cu profile. Plachke also performed the corresponding PIXE-channeling calculations for the model of Burkov [3]. The results are shown in the lower part of Fig. 14.17 [22]. They show fair agreement with the experiment for the decagonal axis, but almost no agreement for the planar case.

14.5.3.2 Icosahedral AlPdMn. The other system studied by Plachke was i-Al_{72} $Pd_{19}Mn_9$ [21] by employing an ion beam of 2-MeV He^+ ions. The results of an element-resolved RBS-channeling study are shown in Fig. 14.18

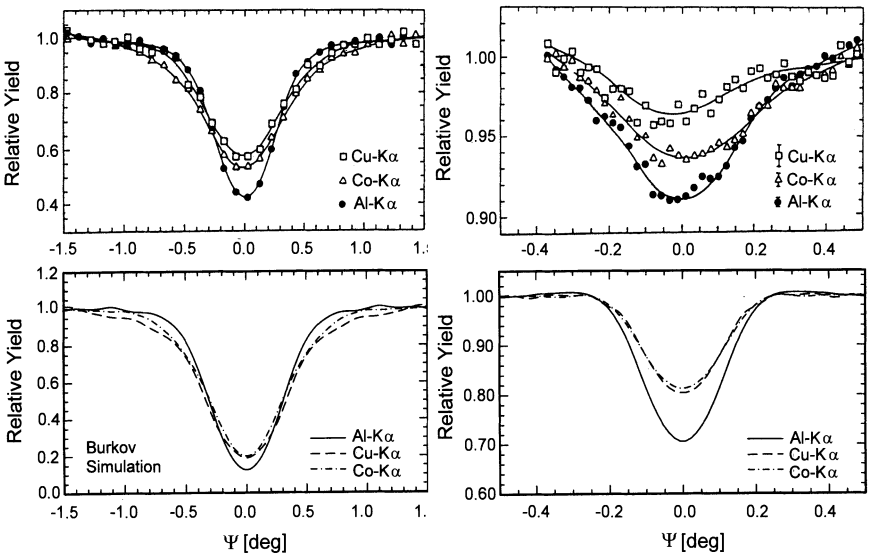

Fig. 14.17. Comparison of experimental (*upper part*) and calculated (*lower part*) PIXE profiles from angular scans across the decagonal axis (*left*) and the major planar system containing this axis (*right*) of a T-phase $Al_{62}Cu_{20}Co_{15}Si_3$ quasicrystal for Al, Cu and Co Kα X-rays, respectively. The *lines* through the experimental data are drawn to guide the eye

together with the results of computer simulations for the structure model of Boudard [2] for ion incidence along axes of 5-fold, 3-fold and 2-fold symmetries. The channeling profiles show deep minima along all three axes, but in the experimental profiles the Al and Pd profiles are equal and much shallower than the Mn profiles, this is different in the calculations: here the Pd and Mn profiles are about equal and much deeper than the Al profile. These large discrepancies have to be taken into account by future models. The results indicate in particular that in the real crystal only the Mn atoms sit in the most densely packed atom rows, while in the model by Boudard the Pd atoms also occupy sites in these rows. Seeger tried to take these experimental findings into account and modified Boudard's model by putting the Pd atoms to the outside of the atomic hypersurfaces [24]. The results of a calculation for this model are shown in Fig. 14.19 and demonstrate that this procedure, in fact, improves the agreement considerably, although full agreement is not yet obtained.

14.5.4 Lattice Location of Silicon in Decagonal AlCuCoSi

The presence of an amount of about 3 % Si seems to stabilize d-AlCuCo quasicrystals. It is therefore interesting to know where the Si is located in the decagonal structure, which may help to reveal its role in the stabilization.

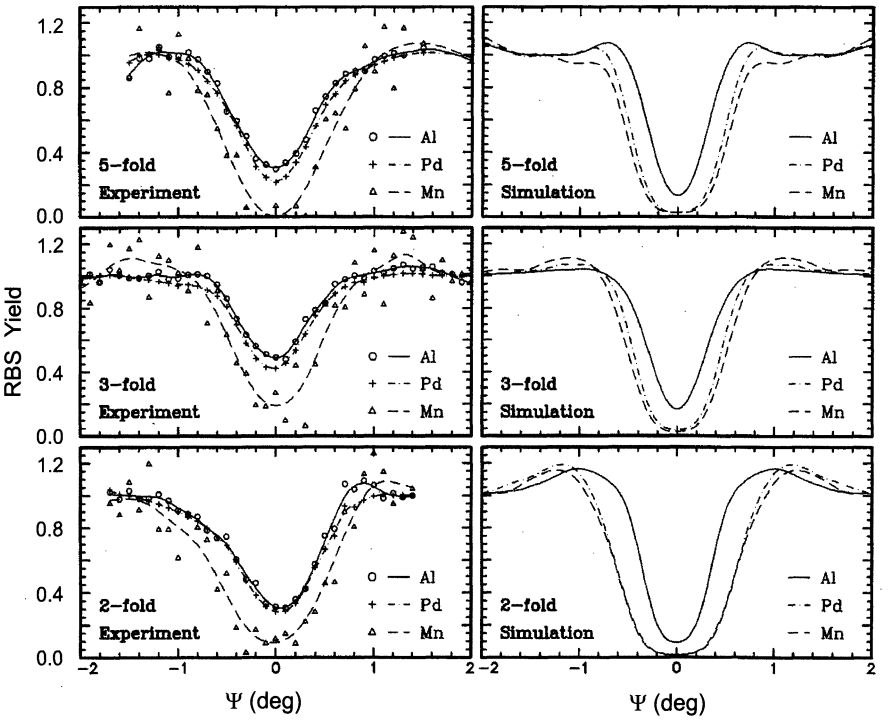

Fig. 14.18. Comparison of experimental (*left*) Rutherford backscattering profiles from angular scans across 5-fold, 3-fold and 2-fold axes of an i-phase AlPdMn quasicrystal for scattering by Al, Pd and Mn atoms, respectively, with simulated profiles for the Boudard model. The fit *curves* through the experimental data are drawn to guide the eye

Since it is possible also to locate small amounts of an impurity in the matrix of a host material by channeling ([4] and Sect. 14.2.4), Plachke measured the Si Kα-profiles in a PIXE study in the planes perpendicular to the decagonal axis [22]. For these planes the situation is rather simple, since they are periodic, which simplifies the interpretation. The results are shown in Fig. 14.20 and depict a Si profile with a minimum, containing a small peak in the center.

The shape of this profile already indicates that the Si occupies sites i) close to the planar channel walls and ii) in the middle between two neighboring planes. Plachke has deconvoluted the Si profiles (this is possible due to the periodicity of these planes) on the basis of flux-density distributions calculated in Monte-Carlo simulations [22]. The Si distribution obtained is shown in the right part of Fig. 14.20 and indicates that about 11 % of the Si atoms are located in the center between neighboring planes, while the rest (89 %) is located at positions at a distance of 0.02 nm from these planes. The Si-channeling profile obtained on the basis of this distribution is included in the left part of the figure.

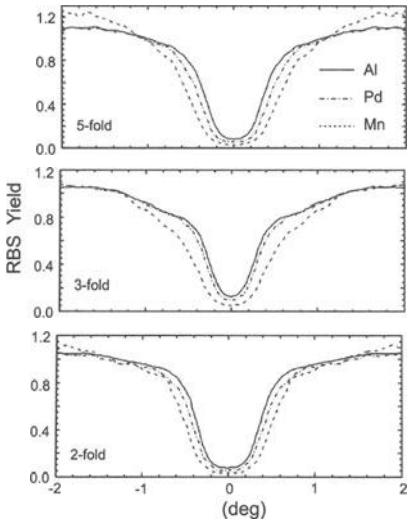

Fig. 14.19. Simulated Rutherford backscattering profiles for the structure model of i-AlPdMn modified by Seeger

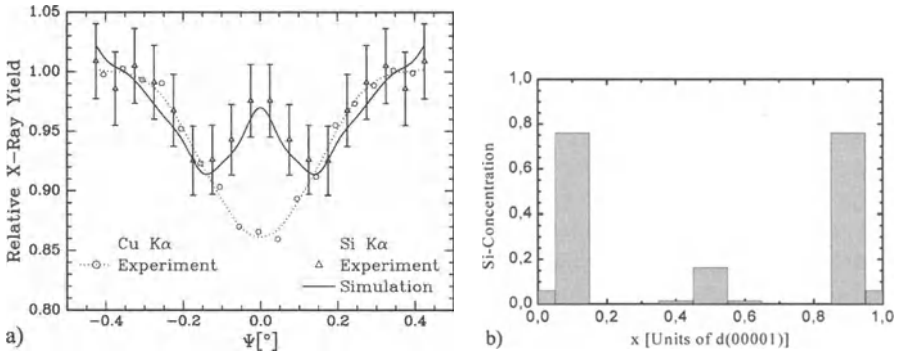

Fig. 14.20. (**a**) Experimental PIXE-channeling profiles for Cu (*circles*) and Si (*triangles*) and the profile simulated for the Si-distribution of Fig. 14.20b (*full line*). The *dotted line* through the experimental data for Cu is drawn to guide the eye. (**b**) Si distribution between adjacent periodic planes in d-AlCuCoSi as derived from a deconvolution of measured PIXE-channeling profiles shown under (**a**)

Finally, we want to mention that ion channeling is particularly sensitive to the presence of phasons, as discussed in Sect. 14.5.1, and was very recently demonstrated in the work of Zeger et al. [29].

References

1. Barrett J.H. (1971): Phys. Rev. **B 3**, 1527
2. Boudard M., de Boissieu M., Janot C., Heger G., Beeli C., Nissen H.-U., Vincent H., Ibberson R., Audier M., Dubois J.M. (1992): J. Phys. Condens. Matter **4**, 10149
3. Burkov S.E. (1993): Phys. Rev. **B 47**, 12325
4. Carstanjen H.D. (1976): In: Ion Beam Surface Layer Analysis, Vol. 2, eds. O. Meyer, G. Linker, F. Käppeler, Plenum Press, New York, pp. 497–515
5. Carstanjen H.D., Seeger A. (1984): In: Muons and Pions in Materials Research, eds. J. Chappert and R.I. Grynszpan, North Holland, Amsterdam, pp. 293–362
6. Carstanjen H.D., Sizmann R. (1972): Radiat. Eff. **12**, 211
7. Carstanjen H.D., Emrick R.M., Grunwald R., Plachke D., Wittmann R. (1992): Phys. Rev. **B 45**, 10822
8. Eckstein W. (1991): Computer Simulation of Ion Solid Interactions, Springer, Berlin
9. Gemmell D.F. (1974): Rev. Mod. Phys. **46**, 129
10. Hoffmann S., Trebin H.-R. (1992): Phys. Status Solidi **B 174**, 309
11. Kupke T., Peschke U., Carstanjen H.D., Trebin H.-R. (1991): Phys. Rev. **B 43**, 13758
12. Kupke T., Trebin H.-R. (1993): J. Phys. I France **3**, 1629
13. Lindhard J. (1965): K. Dan. Vidensk. Selsk. Mat. Fys. Medd. **34** No. 14
14. Lutz H., Sizmann R., (1963): Phys. Lett. **5**, 113
15. du Marchie van Voorthuysen E.H., Smulders P.J.M., Werkman R.D., de Boer J.L., van Smaalen S. (1992): Nucl. Instrum. Methods **B 64**, 261
16. Mayer J.W., Rimini E. (eds.) (1977): Ion Beam Handbook for Materials Analysis, Academic Press, New York
17. Morgan D.V. (ed.) (1973): Channeling: Theory, Observations and Applications. Wiley, New York
18. Nelson R.S., Thompson M.W. (1963): Philos. Mag. **8**, 1677
19. Piercy G.R., Brown F., Davies J.A., McCargo M. (1963): Phys. Rev. Lett. **10**, 399
20. Plachke D., Kupke T., Carstanjen H.D., Emrick R.M. (1993): J. Non-Crystalline Solids **153&154**, 72
21. Plachke D., Carstanjen H.D. (1995): Proc. 5th Int. Conf. on Quasicrystals, Avignon, eds. C. Janot and R. Mosseri, World Scientific, Singapore, 148
22. Plachke D. (1999): Ph.D. Thesis, Univ. Stuttgart
23. Robinson M.T., Oen O.S. (1963): Appl. Phys. Lett. **2**, 30; Phys. Rev. **132**, 2385
24. Seeger, K.: unpublished
25. Shechtman D., Blech I., Gratias D., Cahn W. (1984): Phys. Rev. Lett. **53**, 1951
26. Steurer W., Kuo K.H. (1990): Philos. Mag. Lett. **62**, 175
27. Steurer W., Haibach T., Zhang B., Kek S., Lück R. (1993): Acta Crystallogr. **B 49**, 661
28. Tsuda K., Nishida Y., Saitoh K., Tanaka M. (1996): Philos. Mag. **A 74**, 697
29. Zeger G., Plachke D., Carstanjen H.D., Trebin H.-R. (1999): Phys. Rev. Lett. **82**, 5273

15 Mechanical Properties of Quasicrystals

Knut Urban, Michael Feuerbacher, and Markus Wollgarten

Summary. Quasicrystals show mechanical properties which distinctly differ from those of crystals, particularly of metals. The plasticity of these materials shows a brittle-to-ductile transition at very high temperatures and a lack of work hardening. A review of the experimental work, mainly performed on icosahedral Al-Pd-Mn will be presented in this chapter. This includes results of macroscopic deformation experiments as well as microstructural characterizations of deformed samples in a transmission electron microscope. The interpretation of the results is presented in terms of a cluster-friction model, which assumes the Mackay-type clusters as rate controlling obstacles for moving dislocations.

15.1 Introduction

The mechanical properties, i.e. the response of a material to an externally applied mechanical load, is of basic importance for any kind of structural application. This wide field can be separated into some subdivisions: elastic properties (reversible response to small strains according to Hooke's law), anelastic properties (time dependence of elastic behavior), fracture and failure, and plastic properties. The latter describe the irreversible response of materials at higher strains, leading to shape changes of bodies under applied mechanical load.

In the present chapter we will restrict ourselves to the plastic properties of quasicrystals. Macroscopically, these properties can be expressed in terms of materials parameters, which can usually be measured without detailed knowledge of their microscopic origin. Microscopically, they are related to processes on a scale ranging from atomic dimensions to the typical dimensions of the morphology of the material. In single crystals (and quasicrystals) it has been shown that the most prominent microscopic mechanism of plastic deformation is provided by the motion of dislocations (see the chapter on "Defects" by M. Wollgarten et al. in this volume) on densely packed crystallographic slip planes. The key concepts of crystal plasticity are described e.g. in [13,16,24].

The plastic properties of quasicrystalline materials had already been studied quite early [3,30–32] on a number of poly-quasicrystalline alloys. Later studies were performed on single-quasicrystals of high structural quality [7,26,34,35], providing information on the intrinsic plastic properties. Based on these results, which are not affected by the presence of grain boundaries,

J.-B. Suck et al. (eds.), *Quasicrystals*
© Springer-Verlag Berlin Heidelberg 2002

second phases, etc. first attempts can be made to identify the microscopic processes governing plastic deformation in quasicrystals [8,22].

In the present chapter, we will describe the experimental procedures, the thermodynamic description of the activation processes, and the interpretation of the results in terms of a structure-related model of the deformation mechanism. The description will be based on the studies performed on single quasicrystalline (in the following abbreviated to sq) icosahedral Al-Pd-Mn.

15.2 High-Temperature Plastic Deformation

15.2.1 Theoretical

A material's plastic response to mechanical loading can be investigated by means of tension or compression tests. In such a test the material is stretched or compressed at a given strain rate $\dot{\varepsilon} = \mathrm{d}\epsilon/\mathrm{d}\,t$ (*dynamic* testing), i.e. the relative length change per unit time, and the force to be exerted by the testing machine in order to maintain this strain rate is measured. The force divided by the specimen cross-section, the stress σ, is then plotted as a function of the relative length change, the strain ε, already achieved.

In crystals, dislocations provide the most prominent plastic deformation mechanism. Dislocations are one-dimensional crystal defects, which can move through the structure driven by an applied load, thereby leading to permanent shape change. In quasicrystals dislocations also exist (see "Defects" by M. Wollgarten et al. in this volume) and it has been shown that plastic flow is mediated by dislocation motion.

The following brief treatment of the theory of plasticity serves as a more quantitative description of the plastic behavior of a material (for a review see reference [5]). It was developed for the description of crystal plasticity and is adopted here for quasicrystals. The dislocation Burgers vector $\mathbf{b}$ occurring in the relations derived in this section is taken to be identical with $\mathbf{b}_{\|}$, i.e. the component of the six-dimensional Burgers vector in physical space (see "Guide to Mathematical Quasicrystals" by M. Baake in this volume).

The contribution of a dislocation to slip depends on the slip plane and the slip direction which together characterize the *slip system* . In a uniaxial test, the resolved shear stress τ is related to the axial stress σ by

$$\tau = m_{\mathrm{S}}\sigma, \tag{15.1}$$

where the *Schmid factor* is given by $m_{\mathrm{S}} = \cos\phi\cos\lambda$. Here ϕ is the angle between the load axis and the normal to the slip plane and λ the angle between the load axis and the slip direction, $0 \leq m_{\mathrm{S}} \leq 0.5$. For a given $\dot{\varepsilon}$ there is a corresponding *slip velocity* $\dot{a}$ in the slip plane. If slip is induced by the movement of dislocations occurring at a density ρ and moving at a velocity v the slip velocity is given by the *Orowan relation*

$$\dot{a} = \rho b v, \tag{15.2}$$

where b is the modulus of the Burgers vector.

The effective shear stress τ^* acting on the dislocation [24] is given by

$$\tau^* = \tau - |\tau_i| \tag{15.3}$$

where τ_i originates from the *internal stresses* resulting from the superposition of the stress fields of the dislocations present in the material. The effective shear stress induces a perpendicular force K acting on a line element of length l of the dislocation of magnitude $K = \tau^* lb$. This is counteracted by a friction force $K_f = \tau_f lb$, where τ_f, the line glide resistance, is the shear stress equivalent to friction. The dislocation can move through the lattice if $\tau^* > \tau_f$. If the dislocation encounters an obstacle (Fig. 15.1a) for which, locally, $\tau^* < \tau_f$ the running dislocation is stopped by the obstacle at a stable position x_1. At finite temperatures the dislocation can be released by thermal fluctuations and overcome the obstacle, provided that a Gibbs free energy ΔG of activation is supplied. The part of the work done by the effective shear stress, the work term ΔW, is given by

$$\Delta W = \tau^* lb \Delta x, \tag{15.4}$$

where $\Delta x = x_2 - x_1$ is the activation distance given in Fig. 15.1a.

For plastic deformation controlled by thermally activated processes, the temperature dependence of the plastic strain rate is given by the Arrhenius expression

$$\dot{\varepsilon} = \dot{\varepsilon}_0 \exp\left(-\frac{\Delta G(\tau)}{k_B T}\right), \tag{15.5}$$

where Boltzmann's constant is denoted k_B, T is the absolute temperature, and the pre-exponential factor $\dot{\varepsilon}_0$ is assumed to be constant.

Since ΔG depends on temperature and on the effective shear stress, we can write the Gibbs equation as $\mathrm{d}(\Delta G) = -\Delta S \mathrm{d}T - V_a \mathrm{d}\tau^*$ with

$$\Delta S \equiv -\left.\frac{\partial(\Delta G)}{\partial T}\right|_{\varepsilon^*} \tag{15.6}$$

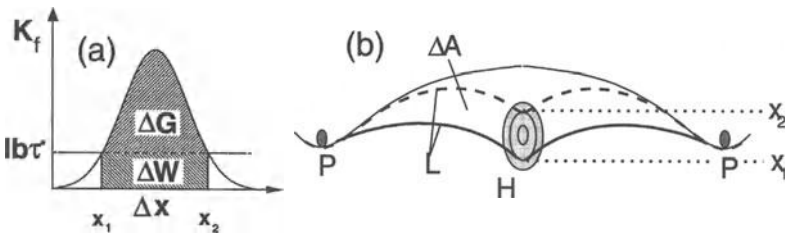

Fig. 15.1. (**a**) Force–distance diagram visualizing the quantities ΔG and ΔW. (**b**) Schematic representation of the activation process. The dislocation line L pinned at points P overcomes the obstacle H by movement from x_1 (full line) to x_2 (dashed)

and

$$V_{\mathrm{a}} \equiv -\left.\frac{\partial(\Delta G)}{\partial \tau^*}\right|_T . \tag{15.7}$$

ΔS denotes the activation entropy related to ΔG by $\Delta G = \Delta H - T\Delta S$, where ΔH is the activation enthalpy. V_{a} is the activation volume.

The activation volume can be written as [16]

$$V_{\mathrm{a}} = lb\Delta x = b\Delta A, \tag{15.8}$$

where ΔA is the activation area which, for the case of the interaction of a dislocation with a localized obstacle, is illustrated by means of Fig. 15.1b. The values of the thermodynamic parameters defined are characteristic of the active microscopic deformation mechanisms. They can be measured by the application of e.g. stress relaxation experiments and/or incremental changes of experimental parameters such as temperature or strain rate.

The activation volume can be determined by means of *stress-relaxation* experiments. In these the testing machine is abruptly stopped and, while the sample is held at constant total strain ε_{t} the stress is measured as a function of time. The total strain consists of an elastic part ε_{e} and the plastic part ε (the latter was the subject of the definitions in the previous paragraphs), i.e. $\varepsilon_{\mathrm{t}} = \varepsilon_{\mathrm{e}} + \varepsilon$. During stress relaxation the elastic part is transformed into additional plastic strain. Since $\varepsilon_{\mathrm{t}} = \text{const.}$

$$\dot{\varepsilon_{\mathrm{t}}} = \dot{\varepsilon} + \dot{\varepsilon_{\mathrm{e}}} = 0. \tag{15.9}$$

According to Hooke's law $\dot{\varepsilon_{\mathrm{e}}} = C\dot{\sigma}$, where C is the total elastic compliance of the specimen and the testing machine. With (15.9)

$$\dot{\varepsilon} = -C\dot{\sigma}. \tag{15.10}$$

Taking the logarithm of (15.5), differentiating with respect to τ and taking into account (15.1) and (15.10) we obtain

$$V_{\mathrm{ex}} = \frac{k_{\mathrm{B}}T}{m_{\mathrm{S}}} \left.\frac{\partial \ln(-\dot{\sigma})}{\partial \sigma}\right|_T , \tag{15.11}$$

which allows the *experimental* activation volume V_{ex} to be derived from plots of the negative time derivative of the observed stress as a function of stress. It is important to differentiate between the experimental activation volume V_{ex} and the theoretical activation volume V_{a} [5,11]. An important prerequisite for $V_{\mathrm{ex}} \approx V_{\mathrm{a}}$ is that, during the experiment, the microstructure remains unchanged.

We note that the Gibbs free energy of thermal activation cannot be measured directly. This can be shown considering the temperature dependence of

the strain rate. Taking the logarithm and differentiating (15.5) with respect to T yields

$$\left.\frac{\partial \ln \dot{\varepsilon}}{\partial T}\right|_T = -\left.\frac{\partial \ln \dot{\varepsilon}}{\partial \sigma}\right|_T \left.\frac{\partial \sigma}{\partial T}\right|_{\dot{\varepsilon}} = -\frac{1}{k_B T}\left.\frac{\partial(\Delta G)}{\partial T}\right|_\tau + \frac{\Delta G}{k_B T^2}$$
$$= \frac{T\Delta S + \Delta G}{k_B T^2} = \frac{\Delta H}{k_B T^2}. \tag{15.12}$$

With (15.11)

$$\Delta H = -m_S T V_{ex} \left.\frac{\partial \sigma}{\partial T}\right|_{\dot{\varepsilon}} \tag{15.13}$$

is obtained. Thus, the activation *enthalpy* can be determined by the combination of stress relaxations and temperature changes. The determination of the Gibbs free energy requires additional information on the nature of the entropy terms which likewise is not directly available from experiments (see below).

15.2.2 Results of Mechanical Testing

Figure 15.2 shows the stress/strain curve for sq icosahedral $Al_{70.5}Pd_{21}Mn_{8.5}$ samples deformed in compression along a twofold direction at 1033 K and 1073 K at a strain rate of 10^{-5} s^{-1}. At 1033 K, after a region of Hooke-type linear elastic behavior, the sample yields plastically at about 180 MPa. There is an *upper yield point* at 270 MPa and 0.6% strain and a *lower yield point* at 220 MPa and a strain of 1%. From there on, the stress decreases continuously with increasing strain. This behavior was observed up to 20% plastic strain

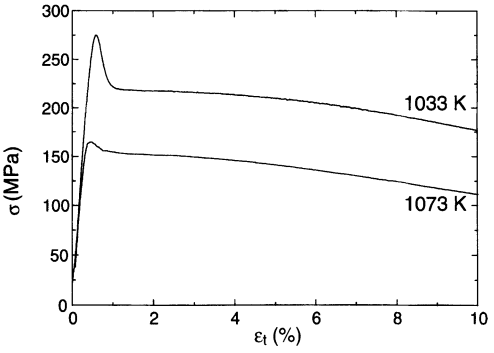

Fig. 15.2. Stress/strain curve for sq icosahedral $Al_{70.5}Pd_{21}Mn_{8.5}$ samples deformed in compression along the twofold [0/0, 0/0, 0/2] direction at 1033 K and 1073 K at a strain rate of 10^{-5} s^{-1}. The samples were about 7 mm in length, $2 \times 2\,mm^2$ in cross-section and oriented with the long axis (compression axis) parallel to the twofold direction. From [8]

without any evidence for saturation. This means that *the more the material has already been deformed the easier it will be to compress it further.* This demonstrates the most prominent salient feature of quasicrystal plasticity, the phenomenon of *deformation softening.*

Figure 15.3 shows the temperature dependence of the maximum flow stress $\sigma_{\max}$. It decreases from about 750 MPa at 953 K to 120 MPa at 1073 K. At temperatures below about 873 K brittle fracture occurs and no plastic deformation is possible.

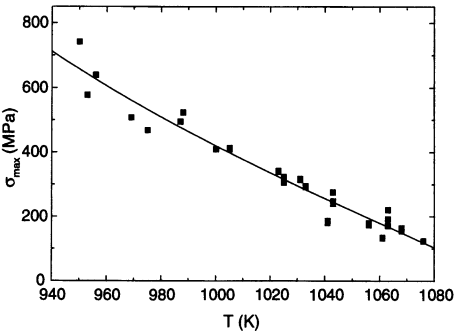

Fig. 15.3. Temperature dependence of the maximum flow stress $\sigma_{\max}$ for deformation along a twofold direction. The line is a guide to the eye. From [6]

Figure 15.4 shows an example of the determination of the experimental activation volume V_{ex} by means of (15.11) and data obtained in stress relaxation experiments carried out at 1033 K. A value of $m_{\mathrm{S}} = 0.5$ is employed, an assumption justified by the high isotropy of the icosahedral lattice. The result is $V_{\mathrm{ex}} = 0.56\ \mathrm{nm}^3$. In order to express the activation volume in terms of the modulus of the Burgers vector we take the value of $b_{\|} = 0.183$ nm, a typical value most frequently found in plastically deformed $Al_{70.5}Pd_{21}Mn_{8.5}$ (see below). We find $V_{\mathrm{ex}} = 92\, b_{\|}^3$.

The stress dependence of the activation volume is depicted in Fig. 15.5. The values of the activation volume range from 0.2 to 1.2 nm^3. This means that it is larger by about two orders of magnitude than $b_{\|}^3$. The stress dependence approximately follows a hyperbolic function.

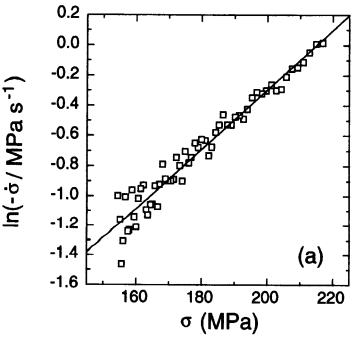

Fig. 15.4. Plot of $\ln(-\dot{\sigma})$ vs σ for the determination of the experimental activation volume on the basis of the data obtained in a stress-relaxation experiment at 1033 K. Before, the sample was deformed at $\dot{\varepsilon} = 10^{-5}$ to $\varepsilon \approx 0.6\%$ total strain corresponding to the stress maximum. From [6]

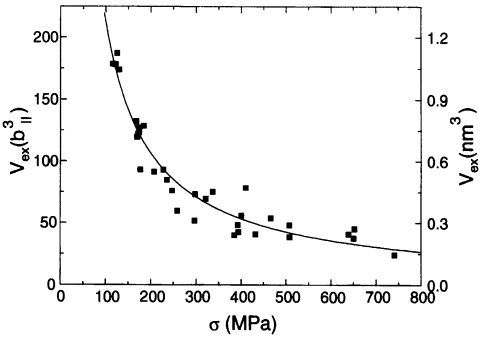

Fig. 15.5. The activation volume as a function of stress determined by stress relaxation experiments. V_{ex} shows a hyperbolic stress dependence (solid line). From [8]

The results of a series of temperature change experiments, obtained employing (15.13), are depicted in Fig. 15.6. The activation enthalpy is rather high, about 7 eV. The work term also shown in Fig. 15.6 was calculated according to (15.1), (15.4) and (15.8).

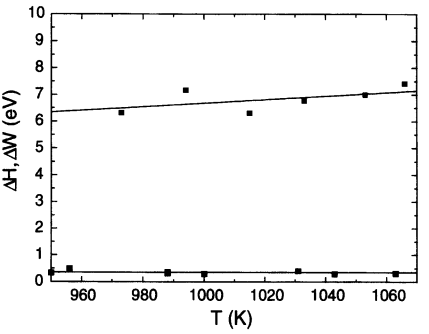

Fig. 15.6. The activation enthalpy ΔH and the work term ΔW as a function of temperature. The solid lines depict the linear and constant temperature behavior of ΔH and ΔW, respectively. From [8]

In order to obtain the effective shear stress τ^*, according to (15.3), the internal stress level τ_i has to be determined. This can be done by the technique of *stress-transient dip tests* [20]. For icosaheadral Al-PdMn a value of $\tau_i = 33$ MPa was found [6]. This means that the internal stress level amounts to about 25% of the maximum shear stress at 1033 K. We note that the measured τ_i in (15.3) enters at a negative sign. This means that, apart from special cases, the long-range stress field resulting from the entire dislocation structure of the sample reduces the effective shear stress [12,24].

15.2.3 Microscopic Observations

15.2.3.1 Dislocation Density. At the present state of the art of $Al_{70.5}Pd_{21}Mn_{8.5}$ single-quasicrystal growth by the Czochralski technique, the density of grown-in dislocations is of the order of a few 10^7 cm^{-2}. During plastic deformation in the high-temperature region the density increases typically by about two orders of magnitude. Figure 15.7 shows the dislocation

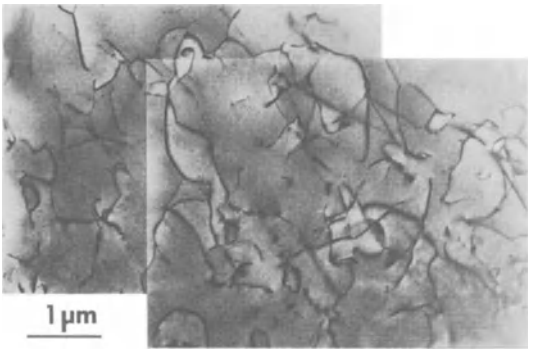

Fig. 15.7. Dislocation arrangement in a sample after deformation at 1033 K to a total strain of 6%. The electron-microscopic sample was prepared in such a way that the (0/0,0/1,1/0) slip plane is parallel to the sample plane. The line is a fit according to (15.11) [6]

arrangement in a sample after deformation at 1033 K to a total strain of 6%. The long dislocation segments lie in the (0/0,0/1,1/0) slip plane. The fact that the dislocations are indeed mobile during deformation was demonstrated during straining *in situ* in a high-voltage electron microscope at 1023 K. These experiments indicate a viscous, i.e. a smooth and spatially uniform motion of the dislocation lines.

Measurements of the dislocation density in sq $Al_{70.5}Pd_{21}Mn_{8.5}$ as a function of temperature and strain were carried out by Schall [27]. The temperature dependence at the lower yield point, i.e. at constant plastic strain of about 1.2%, is shown in Fig. 15.8 a for temperatures between 968 K and 1093 K. Figure 15.8b shows the strain evolution of the dislocation density at constant deformation temperature of 1003 K. A maximum value of 1.2×10^9 cm^{-2} is observed at a plastic strain of 6% after which it drops to about 6×10^8 cm^{-2} at 12% plastic strain.

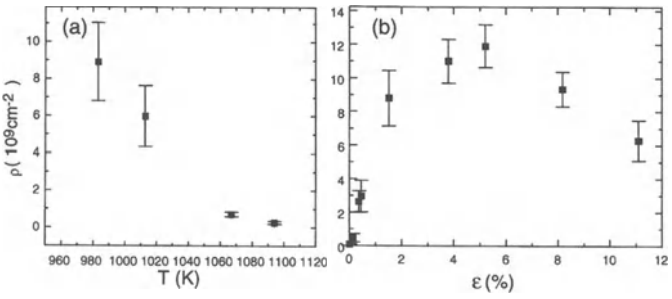

Fig. 15.8. Temperature dependence at the lower yield point (**a**) and plastic-strain dependence at constant temperature of 1003 K (**b**) of the dislocation density in sq $Al_{70.5}Pd_{21}Mn_{8.5}$

It was already noted by Wollgarten et al. [35] that dislocations anneal out at temperatures in the range used in the plastic deformation experiments. This effect was investigated in detail by Schall [27]. Figure 15.9 depicts the results of annealing experiments carried out at 1003 K in samples which were predeformed at the same temperature and then quenched to room temperature. Within 30 min the dislocation density falls by about 60% of the original value.

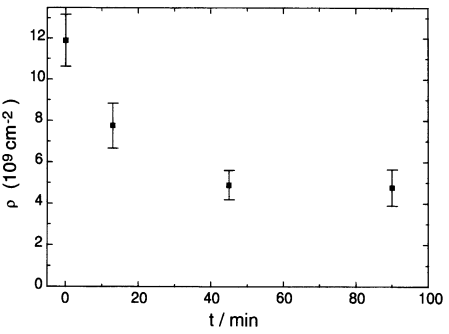

Fig. 15.9. Reduction of the dislocation density during annealing at 1003 K of an $Al_{70.5}Pd_{21}Mn_{8.5}$ sample which was predeformed at the same temperature and quenched to room temperature. From [27]

15.2.3.2 Burgers Vectors. A detailed analysis of dislocations with respect to their Burgers vector and slip system was carried out by Rosenfeld [25], Metzmacher [23] and Rosenfeld et al. [26] in sq $Al_{70.5}Pd_{21}Mn_{8.5}$ deformed at 1033 K. The authors used the d-CBED technique for Burgers vector determination (see the chapter on "Defects" by M. Wollgarten et al. in this volume) and stereo analysis for determination of the dislocation line direction. For a given symmetry direction several types of Burgers vectors exist. These are characterized by different values of the strain accommodation parameter ζ [8], describing the ratio of the moduli of phason and phonon components of a dislocation:

$$\zeta = \frac{|\mathbf{b}_\perp|}{|\mathbf{b}_\parallel|} \tag{15.14}$$

This parameter can be expressed in powers of the value of the golden mean ($\tau = (1+\sqrt{5})/2$), i.e.

$$\zeta = \tau^n. \tag{15.15}$$

A complete list of Burgers vector directions and magnitudes is presented in the chapter on defects. Let us briefly summarize the results of the Burgers vector determinations: the major proportion of dislocations possesses Burgers vector components in physical space parallel to twofold quasicrystal lattice directions (referred to as *twofold* Burgers vectors). Among these the frequency of the type of dislocation characterized by $\mathbf{B} = \mathrm{A} < \bar{2}\,1\,1\,0\,0\,\bar{2} >$, $\mathbf{b}_\parallel = \mathrm{a} <$

$\bar{2}/1, 3/\bar{2}, 1/\bar{1} >$, $|\mathbf{b}_{\|}| = 0.183$ nm, and $\zeta = \tau^5$ is by far the highest, i.e. 61% (a, the component of the hyperlattice constant A parallel to physical space, is given for an icosahedral quasicrystal by $a = A/\sqrt{4+2\tau}$). However, the character of the dislocations changes with strain: at higher strains, the fraction of dislocations exhibiting larger strain accommodation parameters ζ increases [8].

Correlating the measured direction of the Burgers vector with the line direction $\mathbf{l}$ obtained by stereo analysis yielded angles between $\mathbf{b}_{\|}$ and $\mathbf{l}$ between close to zero and 90°. The dislocations predominantly exhibit a mixed character between screw and edge type [26].

The dislocation slip-plane normals $\mathbf{n}$ can be calculated according to $\mathbf{n} = \mathbf{l} \times \mathbf{b}_{\|}$. It is found that slip occurs on low-index planes. Data of an analysis of the slip systems are compiled in Table 15.1. At a twofold $[0/0, 0/0, 0/2]$ sample compression direction the slip systems most frequently observed consist of a fivefold $\{0/0,1/0,0/1\}$ slip plane with a twofold $< 1/0, \bar{1}/\bar{1}, 0/1 >$ slip direction and a fivefold $\{0/1,0/0,1/0\}$ slip plane with a twofold $< 0/\bar{1}, 1/0, 1/1 >$ slip direction, both exhibiting a Schmid factor of 0.43. Other slip systems with twofold and threefold slip planes, having smaller Schmid factors, are found less frequently [6,23,26].

Table 15.1. Slip systems observed in sq $Al_{70.5}Pd_{21}Mn_{8.5}$ deformed along the twofold $[0/0, 0/0, 0/2]$ direction at 1033 K. Ψ denotes the direction in physical space to which the slip-plane normal is parallel. m_S is the Schmid factor. f gives the frequency of occurrence. After [6]

Ψ	slip plane	slip direction	m_S	f(%)
5-fold	$\{0/0, 1/0, 0/1\}$	$< 1/0, \bar{1}/\bar{1}, 0/1 >$	0.43	11.7
5-fold	$\{0/1, 0/0, 1/0\}$	$< 0/\bar{1}, 1/0, 1/1 >$	0.43	11.7
5-fold	$\{0/0, 1/0, 0/1\}$	$< 1/1, 0/\bar{1}, 1/0 >$	0.26	13.3
5-fold	$\{0/1, 0/0, 1/0\}$	$< \bar{1}/0, 1/1, 0/1 >$	0.26	1.7
2-fold	$\{0/1, 1/0, 1/1\}$	$< \bar{1}/0, \bar{1}/\bar{1}, 0, 1 >$	0.41	16.7
2-fold	$\{0/1, 1/0, 1/1\}$	$< \bar{1}/\bar{1}, 0/1, 1/0 >$	0.25	8.3
3-fold	$\{0/1, 0/0, 1/2\}$	$< \bar{1}/\bar{1}, 0/1, 1/0 >$	0.30	13.3
3-fold	$\{0/0, 1/2, 0/1\}$	$< 0/1, \bar{1}/0, 1/1 >$	0.30	6.7
3-fold	$\{1/1, 1/1, 1/1\}$	$< 1/0, \bar{1}/\bar{1}, 0/1 >$	0.29	3.3

The presence of phason strain in plastically deformed material can be studied by means of quantitative electron diffraction experiments in the transmission electron microscope. In the diffraction pattern, the presence of phason defects leads to deviations of the diffraction peaks from their ideal positions for a perfect lattice [1,9,36].

15.3 Discussion

From the observations on sq icosahedral $Al_{70.5}Pd_{21}Mn_{8.5}$ it can be directly inferred that plastic deformation in the ductile temperature regime above 900 K is based on thermally activated dislocation motion. As in conventional crystals, dislocations move on low-index planes of the quasicrystal lattice (see below). These are fivefold, twofold and threefold planes which, in this order, also correspond to the densest planes in the Al-Pd-Mn structure.

First hints on the nature of the microscopic rate-controlling mechanism can be obtained discussing the values measured for the experimental activation volume. For a simple Peierls-type lattice friction mechanism, an activation volume comprising a few atomic volumes, i.e. a few $|\mathbf{b}_{\|}|^3$, is expected (e.g. [17]). In contrast, the experimental results (Fig. 15.5) range from 1.2 nm^3 to 0.15 nm^3, i.e. from 200 to 25 $|\mathbf{b}_{\|}|^3$ depending on stress. This indicates that dislocation motion is not controlled by a Peierls mechanism but by the interaction with obstacles.

The activation enthalpy of 7 eV determined experimentally is a rather high value. Since it is not ΔH but ΔG which determines the temperature dependence of the deformation rate, the contribution of the deformation entropy has to be estimated. For this, an approach suggested for crystals by Schöck [29] can be employed. Assuming that the entropy term arises solely from the temperature dependence of the elastic shear modulus, Schöck [29] derived the following expression

$$\Delta G = \frac{\Delta H + C\tau V_a}{1 - C}, \tag{15.16}$$

where

$$C = \frac{T}{\mu}\frac{\partial \mu}{\partial T} \tag{15.17}$$

and μ denotes the shear modulus. With the data for $\mu(T)$ of Tanaka et al. [33] we arrive for, e.g., 1003 K at $\Delta G \approx 4$ eV which is still a relatively high value. However, the homologous temperatures, 0.7 to $0.8\,T_m$, at which plastic behavior of quasicrystals is observed, are very high and, as shown by Schall et al. [28], dislocation annihilation takes place at a high rate. This influences the measurements of the thermodynamic activation parameters, since the initial assumption, of the structure to be constant, is violated. Advanced techniques for the determination of the thermodynamic activation parameters such as repeated relaxations, have to be applied in this case.

Employing this technique, Geyer et al. [10] obtained lower values for the activation enthalpy of about 4.5 eV for temperatures between 953 K and 1073 K. Using (15.16) yields $\Delta G = 2.3$ eV at 1008 K.

The direct interpretation of the macroscopic and microscopic investigations thus give us a first view on the mechanism of plastic deformation in icosahedral quasicrystals. Summarizing, we find that plastic deformation is

mediated by dislocations moving through the material on the densest planes, driven by the applied stress. The dislocations thermally activated overcome rate controlling obstacles. During dislocation motion, phason defects are introduced and accumulated in the material, leading to an increase of the strain accumulation parameter and peak shifts in electron diffractograms with increasing plastic strain.

15.3.1 Cluster Friction in Quasicrystals

Let us now describe the plasticity of icosahedral quasicrystals in terms of a structure-based model. This will give us the possibility to develop a semi-quantitative understanding of the rate-controlling processes on a microscopic scale.

According to the structure model of Boudard et al. [2] for icosahedral Al-Pd-Mn the structure can be described by a hierarchical arrangement of two types of Mackay-type clusters [21] comprising about 60% of the atoms. These clusters of 52 atoms exhibit icosahedral symmetry and consist of a central Mn atom, a core consisting of Al atoms surrounded by an inner icosahedron of either Mn and Al atoms or Mn and Pd and an outer icosidodecahedron of either Pd and Al atoms or Al atoms only. Their diameter amounts to about 1 nm. The physical properties of this cluster-based structure have been discussed by Janot and de Boissieu [15] and Janot [14] who arrived at the conclusion that, due to their particular electronic properties, the Mackay-type clusters have to be considered as energetically very stable entities. This is corroborated by the results of the investigation of cleavage surfaces of *sq* $Al_{70.5}Pd_{21}Mn_{8.5}$ [4]. Complete clusters are preserved at the surface which indicates that cracks circumvent the Mackay-type clusters. This demonstrates that they are mechanically strong entities capable of deflecting the propagating cracks.

It was suggested by Feuerbacher et al. [8] that the Mackay-type clusters act as obstacles to the dislocation motion, and that the resulting friction controls the plastic deformation. The main argument in favor of this *cluster-friction model* is based on the value of the activation volume which is larger by one to two orders of magnitude than the few atomic volumes expected for a simple Peierls model in which dislocation motion would be controlled by double-kink formation (e.g. [13]). Indeed, the mutual distance as well as the volume of the Mackay-type clusters fit this length scale. The clusters limit the mean dislocation velocity since they represent localized regions of higher mechanical strength. These must either be cut or circumvented by moving dislocations in the course of plastic deformation. On the average, a decrease in the density of obstacles in the course of plastic deformation is expected. This is not only due to the destruction of obstacles by cut processes but also results directly from the introduction of structural and chemical disorder by moving dislocations. Due to the aperiodicity of the quasilattice any shear is unavoidably connected with the introduction of matching-rule violations. Thus, in the wake of a moving dislocation a layer of high phason

density is left behind. Since the cluster structure is characteristic of the ideal quasicrystal, the introduction of phason disorder on the average causes a reduction of obstacles. This means that the structure is weakened in the sense that dislocation motion becomes easier. Therefore a reduced force is needed to maintain a given dislocation velocity. According to the Orowan equation (15.2), in experiments at constant strain rate this will lead to a decrease of the flow stress with increasing plastic strain, a behavior we have detected to be a salient feature of quasicrystal plastic deformation.

The qualitative cluster-friction model has been worked out in more detail by Messerschmidt et al. [22] applying the Labusch-theory for extended obstacles [18,19]. This is necessary due to the high density of clusters in the structure. Due to the resulting small intercluster distances and the rigidity of the dislocation line, not single clusters but rather several clusters, simultaneously acting as one extended obstacle, are overcome in a single activation step. Within the framework of the Labusch-theory the discrepancy between the experimental activation volume and that expected for a single-obstacle process can be lifted. Furthermore, the Mackay-type clusters can be regarded as weak obstacles, yielding individually an activation barrier of about 0.9 eV. The simultaneous overcoming of a number of clusters leads to the measured value for ΔG of 2.3 eV determined at 1008 K by Geyer et al. [10]

Acknowledgments

The authors are grateful to Prof. U. Messerschmidt and Dr. M. Bartsch as well as V. Franz, B. Geyer, C. Metzmacher, R. Rosenfeld and Dr. N. Tamura for stimulating discussions.

References

1. Bancel, P. and Heiney, P., *J. de Phys. Coll.*, **47**(C-3), 341–50, 1986
2. Boudard, M., de Boissieu, M., Janot, C., Heger, G., Beeli, C., Nissen, H.-U., Vincent, H., Ibberson, R., Audier, M., and Dubois, J., *J. Phys.: Cond. Mat.*, **4**(50), 10149–68, 1992
3. Bresson, L. and Gratias, D., *J. Non Cryst. Sol.*, **153**, 468–72, 1993
4. Ebert, P., Feuerbacher, M., Tamura, N., Wollgarten, M., and Urban, K., *Phys. Rev. Lett.*, **77**(18), 3827–30, 1993
5. Evans, A. and Rawlings, R., *Phys. Stat. Sol.*, **34**(1), 9–31, 1969
6. Feuerbacher, M., PhD thesis, RWTH Aachen, IFF Forschungszentrum Jülich GmbH, 1996
7. Feuerbacher, M., Baufeld, B., Rosenfeld, R., Bartsch, M., Hanke, G., Beyss, M., Wollgarten, M., Messerschmidt, U., and Urban, K., *Phil. Mag. Lett.*, **71**(2), 91–8, 1995
8. Feuerbacher, M., Metzmacher, C., Wollgarten, M., Urban, K., Baufeld, B., Bartsch, M., and Messerschmidt, U., *Mater. Sci. Eng. A*, **A226**, 943–9, 1997

9. Franz, V., Feuerbacher, M., Wollgarten, M., and Urban, K., *Phil. Mag. Lett.*, **79**, 333, 1999
10. Geyer, B., Bartsch, M., Feuerbacher, M., Urban, K. and Messerschmidt, U., *Phil. Mag.* A **80**, 1151, 2000
11. Gibbs, G., *Phil. Mag.*, **16**, 97, 1967
12. Haasen, P., *Physical Metallurgy*, Cambridge Univ. Press, Cambridge, 1986
13. Hirth, J. and Lothe, J., *Theory of Dislocations*, Wiley, New York, 1982
14. Janot, C., *Phys. Rev. B*, **53**(1), 181–91, 1996
15. Janot, C. and de Boissieu, M., *Phys. Rev. Lett.*, **72**(11), 1674–7, 1994
16. Kocks, U., Argon, A., and Ashby, M., *Prog. in Mater. Sci.*, **19**, 1, 1975
17. Krausz, A. and Eyring, H., *Deformation Kinetics*, Wiley, New York, 1975
18. Labusch, R., *Czech. J. Phys. B*, **B38**(5), 474–81, 1988
19. Freund, Labusch, R. and Schwarz, R., In *Proc. 9th Int. Conference on the Strength of Metals and Alloys*, page 47, London, 1992
20. MacEwen, S., Kupcis, O., and Ramaswami, B., *Scripta Met.*, **3**(7), 441–8, 1969
21. Mackay, A., *Acta Cryst.*, **15**, 916–918, 1962
22. 2 Messerschmidt, U., Bartsch, M., Geyer, B., Feuerbacher, M. and Urban, K., *Phil. Mag.*, A **80**, 1165, 2000
23. Metzmacher, C., PhD thesis, RWTH Aachen, IFF Forschungszentrum Jülich GmbH, 1995
24. Mughrabi, H., In Mughrabi, H., editor, *Materials Science and Technology*, page 1. VCH, Weinheim, 1993
25. Rosenfeld, R., PhD thesis, RWTH Aachen, Institut für Festkörperforschung, 1995
26. Rosenfeld, R., Feuerbacher, M., Baufeld, B., Bartsch, M., Wollgarten, M., Hanke, G., Beyss, M., Messerschmidt, U., and Urban, K., *Phil. Mag. Lett.*, **72**(6), 375–84, 1995
27. Schall, P., PhD thesis, RWTH Aachen, IFF Forschungszentrum Jülich GmbH, 1998
28. Schall, P., Feuerbacher, M., Messerschmidt, U., and Urban, K., Phil. Mag. Lett. **79**, 785, 1999
29. Schöck, G., *Phys. Stat. Sol.*, **8**, 499, 1965
30. Shibuya, T., Hashimoto, T., and Takeuchi, S., *J. Phys. Soc. Japan*, **59**(6), 1917–20, 1990
31. Song-Seng-Kang and Dubois, J., *Phil. Mag. A*, **66**(1), 151–63, 1992
32. Takeuchi, S. and Hashimoto, T., *Japn. J. Appl. Phys., Part. 1*, **32**(5A), 2063–6, 1993
33. Tanaka, K., Mitarai, Y., and Koiwa, M., *Phil. Mag. A*, **73**(6), 1715–23, 1996
34. Wollgarten, M., Bartsch, M., Messerschmidt, U., Feuerbacher, M., Rosenfeld, R., Beyss, M., and Urban, K., *Phil. Mag. Lett.*, **71**(2), 99–105, 1995
35. Wollgarten, M., Beyss, M., Urban, K., Liebertz, H., and Koster, U., *Phys. Rev. Lett.*, **71**(4), 549–52, 1993
36. Zhang, H. and Kuo, K., *Phys. Rev. B*, **42**(14), 8907–14, 1990

Part V

Electronic Properties

16 Electronic Conductivity of Quasicrystals and Approximants

Stephan Roche, Claire Berger, and Didier Mayou

Summary. From rigorous mathematical developments to extensive numerical calculations in realistic models of periodic approximants or 3D quasiperiodic systems, anomalous diffusion has been clearly connected either with quasiperiodic correlations, or with geometrical and chemical features of realistic models in which atomic species and their local environment have been shown to be fundamental.

Criticality in 1D quasiperiodic systems is related to algebraic localization of the eigenstates, singular continuous spectra, and peculiar transport scaling of the conductance. In higher dimension, an analytical analysis of critical states turned out to be rather difficult, but systematic numerical calculations gradually gives a better understanding of this kind of localization due to quasiperiodic order. On the other hand, periodic approximants give an accurate description of the geometrical local environments that electrons may encounter while propagating. They also may conserve, to some extent, the peculiar order-induces-quantum interference leading to localization. Electron-electron interactions may play an important role in i-phases of AlPdRe. It is suggested that a Coulomb gap may occur as a consequence of the quasiperiodic potential.

16.1 Introduction

Since the discovery of quasicrystals (QC) the question of how quasiperiodic order affects electronic properties has attracted much attention. Experimentally, systems of high structural quality reveal singular properties and, in particular, the proximity to a metal-insulator transition. Theoretically there are indications that a quasiperiodic potential tends to localize electrons. However many questions remain about the transport mechanism, such as the role of disorder, and the role of electron-electron interactions. In this chapter we present a short review of experimental and theoretical works.

On the experimental side we restrict our attention to properties of icosahedral (i-)phases of high structural quality, such as i-AlCuFe, i-AlPdMn, i-AlPdRe, and their approximants. Indeed, those systems have the most singular electronic properties, among known quasicrystals, and seem to be close to a metal-insulator transition. The relation between transport properties and quasiperiodic order has thus generated a great deal of interest and excitement.

On the theoretical side, we focus our attention on the band structure of approximants and quasicrystals, in the independent electron scheme. Then

J.-B. Suck et al. (eds.), *Quasicrystals*
© Springer-Verlag Berlin Heidelberg 2002

we discuss various possible mechanisms for electron transport and how to interpret experimental results on dc-conductivity.

16.2 Electronic Conductivity of Quasicrystals

The conductivity of i-phases of high structural quality such as i-AlCuFe or i-AlPdMn alloys is very low, of the order of 100-300 $(\Omega\text{cm})^{-1}$ at zero temperature. Figure 16.1 shows anomalous transport in quasicrystals. Indeed, after

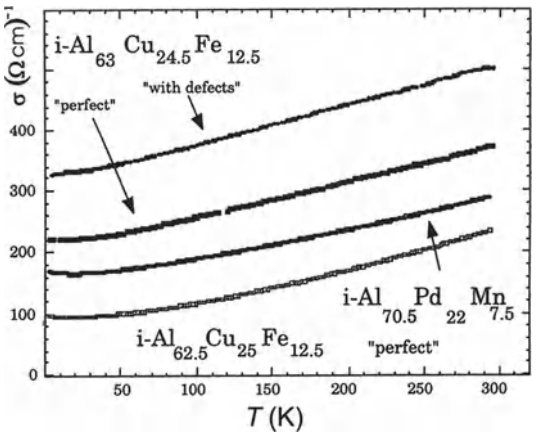

Fig. 16.1. Electronic conductivity for different quasicrystalline phases as a function of temperature and structural quality

annealing treatments to clean the material, conductivities of the samples are found to decrease [12,27]. This tendency is somehow unexpected since these phases are composed of good metals for which an increase of conductivity is usually associated with an improvement of order. Furthermore, the curves $\sigma(T)$ are nearly parallel (Fig. 16.1). This last point suggests that we should write $\sigma(T) = \sigma_{4\,\mathrm{K}} + \delta\sigma(T)$ with $\sigma_{4\,\mathrm{K}}$ as a measure of conductivity at T=4 K and $\delta\sigma(T)$ the variation as a function of temperature that is nearly independent of the alloy. This is a general behavior of all the icosahedral quasicrystals of high structural quality and corresponds to an "inverse Matthiessen rule". We will comment on this rule later.

Generally, the phase diagram of quasicrystals along the composition and temperature is rather complex and the range of existence of quasiperiodic order is narrow. Around the quasicrystalline phase, slightly different compositions will lead to periodic phases grown with a similar local order. These so-called approximant phases possess a common local order with quasicrystals and appear to belong to the same universality class. This is the case for alloys such as (AlCuFe, AlMnSi, AlPdMn) which are associated with families of crystalline approximants like α-AlMnSi, α-AlCuFe, R-AlCuFe, whose smallest unit cell may still have $\sim$ 130 atoms [4].

Recent results of the conductivity of a small cubic approximant α-AlSiCuFe (with a unit cell parameter $a = 12.33$ Å), compared to that of i-AlCuFe, are shown in Fig. 16.2 [33]. The difference of the absolute conducti-

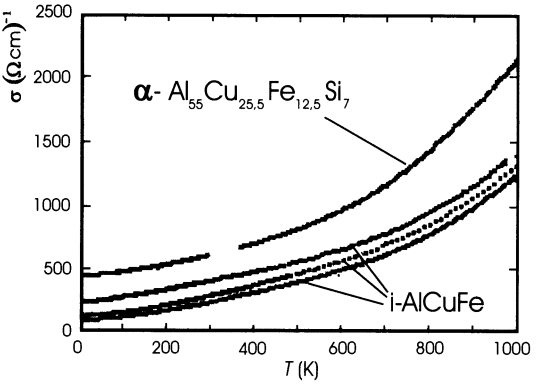

Fig. 16.2. Comparison of the $\sigma(T)$ between i-phases and an approximant alloy of unit cell parameter $a = 12.33$ Å

vity is very small and in addition, $\delta\sigma(T) > 0$ is nearly the same. In contrast, a crystalline "non-approximant" phase of similar stoichiometry (tetragonal ω-Al_7Cu_2Fe phase) with cell parameters $a = 6.34$ Å and $c = 14.87$ Å, has a conductivity of the order of $10^4\ (\Omega\text{cm})^{-1}$ between 0 and 300 K, with a temperature dependence $\delta\sigma(T)/\delta T < 0$ of metallic-type. Recent theoretical studies on the Fermi surfaces of these materials revealed the origin of such a behavior [35].

Another interesting experimental result is the crossover between metallic and anomalous behavior among the approximants of the cubic phase Al-GaMgZn. Indeed, the 1/1 approximant ($a = 14.2$ Å) has a low resistivity $\varrho_{4\,\mathrm{K}} = 58\,\mu\Omega$cm and follows a metallic regime $\delta\varrho(T)/\delta T > 0$. On the contrary, the 2/1 approximant ($a = 23$ Å) with a resistivity close to that of the i-phase $\varrho_{4\,\mathrm{K}} = 120\,\mu\Omega$cm follows an inverse rule $\delta\varrho(T)/\delta T < 0$, i.e. resistivity decreases with temperature [5]. This obviously suggests that a minimal size of the unit cell is required to observe characteristic effects of anomalous transport.

Icosahedral AlPdRe is even more resistive with a behavior as a function of temperature different from the other quasicrystals [10]. Typically at T=4 K, the resistivity of (i-$Al_{62.5}Pd_{22}Mn_{7.5}$) is about 10 000 $\mu\Omega$cm whereas (i-$Al_{70.5}Pd_{21}Re_{8.5}$) shows $\sim$ 1 500 000 $\mu\Omega$cm which is of the same order of that of doped semiconductors. Thus, although both i-phases are defined by the same long-range order, and show close atomic composition, the conductivity differs by several orders of magnitude. With regard to the densities of states at the Fermi level, alloys like AlCuFe, AlPdMn differ by about 1/3 from that of free electrons, and by about 1/10, for AlPdRe, respectively. Consequently, the reduction of conductivity between i-AlPdMn and i-AlPdRe is

not only due to a lower density of states, but also depends substantially on localization of states.

The resistivity of i-AlPdRe at T=4 K is similar to that of resistive materials like doped semiconductors [32]. It seems therefore natural to compare the temperature dependence of their conduction mechanisms (Fig. 16.3). Actually, it is found that $\sigma(T) = 1/\varrho(T)$ follows neither an exponential law of $\exp(-E/k_{\mathrm{B}}T)$, characteristic of activated processes, nor a $\exp(-AT^{-1/4})$ law of variable-range hopping mechanisms at low temperature [30]. On the contrary, the conductivity of AlPdRe follows, over a large range of temperature 4-800 K, a power-law $\sigma(T) \sim T^{\beta}$ with $1 < \beta < 1.5$ [10] which remains unexplained. As a comparison, we show the conductivity of Al_2Ru whose behavior is typical of a thermally activated process of semiconductors. The behavior

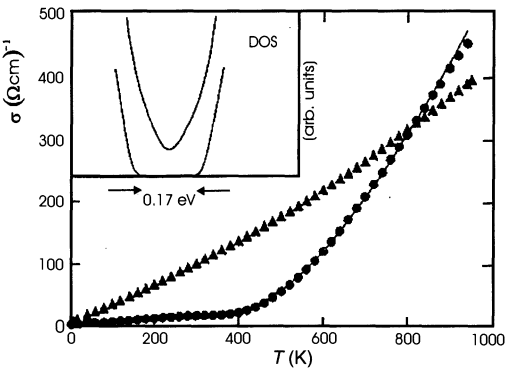

Fig. 16.3. Conductivity $\sigma(T)$ for i-$Al_{70}Pd_{20}Re_{10}$ and Al_2Ru (•). The density of states around the Fermi energy is shown in the inset (courtesy of J. Poon)

of $\sigma(T)$ is described by $\exp(-\Delta/k_{\mathrm{B}}T)$ (Δ=0.17 eV is the gap width). The i-AlPdRe is shown to follow $\sigma(T) \sim T^{\alpha}$ [32].

At low temperature, quantum interference effects (QIE) have been clearly identified [27,32,42], for the class of quasicrystals located on the metallic side, and over a large range of temperature (0.3-100 K) and magnetic field (0-20 T). These phenomena of localization were expected in disordered systems of lower resistivity. However, the dependence $\delta\sigma(T)$ at low temperature and $\delta\sigma(H)$ in magnetic field were analyzed convincingly by means of the theories of QIE (weak localization, electron-electron interaction), even for the approximant cubic phase of AlCuFeSi with small parameter $a = 12.33$ Å [4]. The i-AlPdRe phase remains an exception, and the description of $\sigma(T, H)$ by means of QIE is not possible [4,10]. These materials are seemingly on the insulating side of a new kind of metal-insulator transition.

16.3 Localization in Quasiperiodic Systems

16.3.1 Critical States and Scaling of Bands

In order to study the spectral properties of independent electrons in a quasiperiodic potential, one often uses a tight-binding model where the vertices of a given tiling are chosen as atomic sites $\mid n >$. The Hamiltonian is

$$\mathcal{H} = \sum_{<n,m>\in\mathcal{V}_T} |n > t_{nm} < m| + \sum_n \varepsilon_n |n >< n| \,, \tag{16.1}$$

where quasiperiodicity is introduced either geometrically (respective positions of atomic sites), or through a modulation of energy sites or hopping term on a periodic lattice. One of the main results concerning electronic localization in Fibonacci chains is the power-law behavior of the envelope of the wave function $|\psi_N| \sim N^{-\alpha}$, first studied by Kohmoto et al. [15], and refered to as *critical states* [16,19,24]. For 2D quasiperiodic Penrose lattices, spectral exponents are given typically by $3/8 < \alpha < 5/8$, depending on the eigenstates and the physical parameters [44]. Spectral properties of quasiperiodic Hamiltonians in 1 D are mainly characterized by the *gap-labeling* theorem [1,2], which gives the value of integrated density of states (IDOS) within each gap of the electronic structure. For a Fibonacci chain, the heights of the plateaus of IDOS are given by $j\tau/(\tau+1)$ mod1 where j is an integer.

In higher dimensions, several numerical studies on discrete models (octogonal tiling [39] and Penrose tiling [6]) have enlarged the understanding of critical states. It is worth noting that critical localization can be studied either in quasiperiodic systems, at the price of increasing difficulty in higher dimensions, or by investigating the scaling properties of consecutive periodic approximants [7,22]. Indeed, the golden mean $\tau = 1/2 \cdot (1+\sqrt{5})$ (Fibonacci chain) may be approximated by $1/1, 2/1, 3/2, 5/2, \ldots$, the rational approximations $\tau_n = F_{n+1}/F_n$ (F_n the Fibonacci numbers) of the continuous fraction development of τ. The periodicity of the approximant $\lambda = 2(F_n + \tau F_{n+1})/\sqrt{\tau+2}$ may be used as a suitable measure of their linear system size. This serves as a scaling procedure.

A critical state may be pictorially described as follows. Suppose that a given state Ψ_L has a strong weight in a region of characteristic length L. Then "mesoscopic homogeneity" [41] found in these systems implies that a similar region exists at a distance $\leq 2L$. For sufficiently large L, quantum tunneling between both regions may take place from state Ψ_L to $\Psi_{2L} = z\Psi_L$, where z is the damping amplitude of this tunneling event. The limiting case $z = 0$ corresponds to strictly localized states, whereas $|z| = 1$ will concern extended states. Intermediate cases will take place as soon as $|\Psi_L| \sim L^{-\ln|z|/\ln 2} \sim L^{-\alpha}$. For instance, in a perfect quasicrystal one may find $|z| \neq 1$ generally, depending on the parameters of the model [36,40].

The nature of critical states can also be related to the scaling properties of bandwidths of approximants [22,43]. If we consider an initial cube of length

L in nD, the spectrum of the infinite periodic system of unit cell L with L^n atoms will be composed by L^n bands. The typical bandwidth is then related to the average overlap between two states Φ and Ψ localized in adjacent blocks of length L, that is to say $\Delta\varepsilon \sim | < \Psi|\mathcal{H}|\Phi > |$.

For Bloch states, $|\phi(x)| \sim 1/L^{n/2}$ and t, an average hopping amplitude from one site to another, gives $\Delta\varepsilon \sim t/L$ and the mean velocity is $v \sim \Delta\varepsilon/L^{-1}$ and is independent of L. The same argument holds for a disordered system but involves a localization length ξ. The bandwidth is then $\Delta\varepsilon \sim tL^{n-1}\exp(-L/\xi)$, which leads to a pure point spectrum as $L \to \infty$. For algebraic band scaling $|\phi(x)| \sim 1/L^{\alpha(x)}$, bandwidths scale as $\Delta\varepsilon \sim t/L^{\beta}$ with $\beta > 1$ an exponent related to the distribution of α. The mean group velocity as a function of L is thus $v \sim \Delta\varepsilon/L^{-1} \sim t/L^{\beta-1} \to 0$ when $L \to \infty$. These states are referred to as critical states and may occur either in quasiperiodic systems, or disordered systems close to a metal-insulator transition. The β exponents have been studied for 1D and 2D and confirm this general argument [8].

16.3.2 Transport and Critical States

The possibility of two different unconventional transport mechanisms specific of these materials has been proposed [8,27,36]. Transport may be dominated, for short relaxation times τ (defined by elastic or inelastic scattering mechanisms) by hopping between critical states, whereas for long time τ the regime could be dominated by non-ballistic propagation of wave packets.

A possible interpretation of conductivity in quasicrystals is based on numerical results of anomalous diffusion of wave packets in perfect quasiperiodic structures [27,39,45]. Indeed, for sufficiently long scattering time τ, the propagation of wave packets typically follows a law such that $L(t) = At^{\beta}$ with $\beta < 1$ which defines a sub-ballistic regime. Given the Einstein formula $\sigma = e^2 N(E_{\mathrm{F}})D(\tau)$ and the diffusivity $D(\tau) = L^2(\tau)/3\tau$, where $N(E_{\mathrm{F}})$ is the density of states at the Fermi energy, the dependence of conductivity with τ becomes $\sigma(\tau) \sim A\tau^{2\beta-1}$. Provided that $\beta \leq 0.5$, the conductivity will decrease with τ, that is to say with the increase of elastic or inelastic scattering frequency. The limit with $\beta \sim 0$ leads to $\sigma \sim 1/\tau$. Bellissard and Schulz-Baldes [3] have recently developed a rigorous formulation of the Kubo–Greenwood formula in the context of anomalous transport. In particular, they have shown that for a long relaxation time, $\tau \longrightarrow \infty$, the transport law gives $\sigma \sim \tau^{2\beta-1}$ where the β exponent is linked to the anomalous quantum diffusion regime.

The electronic structure of realistic models of quasicrystalline approximants have been intensively investigated by means of the development of ab-initio calculations. The main features of the electronic structure of quasicrystals are the existence of a deep pseudo-gap at the Fermi level and the spiky structure of the total density of states (TDOS) associated with a high concentration of bands with small dispersion [7,8]. The presence of the pseudo-gap

at E_F has been confirmed experimentally by X-ray emission or absorption spectroscopy for i-phases.

16.3.3 How Anomalous Transport Relates to Multifractality

Quasicrystalline materials are intermetallic long-ranged alloys with very low conductivities. Furthermore, the transport mechanisms are unconventional and do not fit at all within the classical framework. For instance, as mentioned previously, Matthiessen's rule is broken, or more precisely turns out to be opposite. Conventional metals have been shown to obey Matthiessen's rule, in the sense that scattering rates, caused by dissipative mechanisms, can be separable. From the usual Drude formula $\sigma(E_F) = e^2 N(E_F) D$, the diffusivity $D = 1/3 \int_0^\infty < \mathbf{v}(t) \cdot \mathbf{v}(0) > \mathrm{d}t$ reduces to $D = v_F^2 \tau/3$ as soon as averaged velocity-velocity correlations are exponentially screened for times longer that τ (typical elastic mean free time), that is to say $< \mathbf{v}(t)s \cdot \mathbf{v}(0) > \sim v_F^2 \mathrm{e}^{-t/\tau}$. Time-reversal symmetry paths will further lead to quantum corrections for $t > \tau$, decreasing conductivity without modification of the following fact. The additivity rule for the transition amplitude reads $1/\tau = 1/\tau_{\text{elastic}} + 1/\tau_{\text{inelastic}}$, and since $\sigma = 1/\varrho$ then Matthiessen's rule follows $\varrho(T) = \varrho_{\text{elastic}} + \varrho_{\text{inelastic}}(T)$.

The "inverse Matthiessen rule" observed in quasicrystals means that, instead of the resistivity, the conductivity splits into two contributions $\sigma = \sigma_{\text{elastic}} + \sigma_{\text{inelastic}}(T)$ where σ_{elastic} is the residual conductivity depending only on quenched (or static) disorder in the material (dislocation, impurity atoms, phason, etc.) whereas the other part accounts for temperature-dependent scattering mechanisms induced by thermal fluctuations or Coulomb interactions.

To explain this fact and the anomalously high resistivity at low temperature, it was suggested that electronic propagation may be driven by "multifractal" states [8,27,40]. Indeed, from a band-scaling argument, one can understand how critical states will lead to slow propagation, and a group velocity approaching zero in the scaling analysis [8,40]. However, unlike the situation in disordered systems close to an Anderson MIT, the criticality in quasiperiodic systems or quasicrystals may be due to topological complications in the electronic spectrum linked with atomic structure. The major feature of criticality in quasiperiodic systems leading to a power law conductivity $\sigma \sim 1/\tau^\alpha$ (with $\alpha \simeq 1$), relates to non-ballistic diffusion. On the other hand, a hopping mechanism could be expected in these materials, and the hopping distance has indeed been estimated to be of the order of a typical distance between relevant clusters (~10-20 Å).

At this point, one may notice that in other situations where multifractal states dominate a critical regime [14], no length scale prevails by definition. It seems then rather difficult to reconcile a power-law of the conductivity caused by multifractal states in quasicrystals with the concept of mean free path, allowed in usual intermetallics. In conclusion, one should avoid mapping

directly the problem of electronic localization into the pathological case of a real metal-insulator transition.

To overcome the difficulty of transport in these materials, one may consider properly atomic structure. Indeed, these materials can be described as clusters of atoms packed in a quasiperiodic manner. The importance of these clusters seems to be crucial for explaining physical measurements. Janot and de Boissieu [13] proposed that the hierarchical package of pseudo-Mackay icosahedra will ensure electronic and chemical stability. A subsequent power-law behavior of the temperature-dependent conductivity was deduced.

From a different approach, Trambly de Laissardiere et al. [20] have recently shown that when a cluster of d-states impurities is considered in a matrix of conduction s-electrons, the concept of Friedel's virtual-bound states turns out to be generalized to a "cluster virtual-bound states" deeply dependent on geometry. In this model, an icosahedral cluster of manganese atoms is embedded in a metallic matrix of aluminium. When the Fermi energy of itinerant electrons is close to the d-orbital energy of manganese (as is frequently encountered in real quasicrystals), then the scattering potential is strong and generates multiple scattering interference effects. In addition, the icosahedral geometry was shown to be the most efficient in "trapping" electrons through sp-d hybridization effects.

16.4 Kubo–Greenwood Conductivity

From ab-initio calculations of band structure, it has been shown that the Bloch–Boltzmann conductivity in periodic approximants is weak, in good qualitative agreement with experiments [8]. However, in order to study transport phenomena in quasicrystals properly, one clearly needs to go beyond the semi-classical approximation. For instance, the heuristic arguments presented previously suggest that the Bloch–Boltzmann picture of ballistic propagation between scattering events breaks down. A natural starting point for a study of transport is then given by the Kubo–Greenwood linear-response theory of transport coefficients [3,9,18], which makes no prior assumptions on the nature of states. By scaling analysis on periodic approximants of quasicrystals, Fujiwara et al. [7] have recently investigated the relation between the participation ratio of eigenstates (localization) and the diffusion constant. Within an approach beyond Boltzman's approximation, their study revealed how localization in quasicrystals may be connected to anomalous diffusion, in the asymptotic limit. Introducing a finite lifetime $\tau = \hbar/\gamma$, the averaged diffusion constant was shown to follow $< D > \sim \gamma^{0.25}$ for eigenstates in the vicinity of the Fermi level. Therefore, increasing the electronic lifetime by 10 000 will reduce the diffusion constant by a factor of 10. This scaling approach of approximants has consequently unveiled a real specific transport mechanism in these systems. Recent studies starting from an exact Kubo–Greenwood formula reformulated in a proper mathematical framework [3] or

new real-space derivations [36,37] may lead to a better understanding of anomalous transport in quasicrystals. In the following, we present an alternative approach for the numerical evaluation of Kubo–Greenwood in 3D systems. The major asset of this method is to integrate the quantum effects due to disorder or quasiperiodic potential without any prior assumption with respect to the nature of eigenstates, whereas the scaling approach of approximants may assume that extended states carry most of the itinerant electrons. The real part of the conductivity is written as :

$$\Re\mathrm{e}\sigma(\omega) = \frac{2\pi e^2\hbar}{\Omega}\int_{-\infty}^{+\infty} \mathrm{d}E\ \frac{f(E) - f(E+\hbar\omega)}{\hbar\omega}\ \mathrm{Tr}\big[\mathrm{A}\big]\,, \tag{16.2}$$

where $\mathrm{A} = \hat{V}_x\ \delta(E-\mathcal{H})\ \hat{V}_x\ \delta(E+\hbar\omega-\mathcal{H})$.

We have shown [37,38] that a suitable development of the spectral measure in a basis of orthogonal polynomials may further lead to an efficient algorithm. For independent electrons in a given static potential at T=0 K, Kubo–Greenwood reduces to :

$$\sigma_{\mathrm{DC}}(E) = \frac{2\hbar e^2\pi}{\Omega}\mathrm{Tr}\big[\hat{V}_x\ \delta(E-\mathcal{H})\ \hat{V}_x\ \delta(E-\mathcal{H})\big]\,, \tag{16.3}$$

where $\hat{V}_x$ is the component of the velocity operator along direction x, $\delta(E-\mathcal{H})$ is the projector on the eigenstates of $\mathcal{H}$ at energy E, and Ω is the volume of the system. By means of a recursion method and the formalism of orthogonal polynomials, one can complete such a calculation in 3D for weak disorder or quasiperiodic systems [26]. First, simple algebra leads to $\sigma_{\mathrm{DC}}(E) = \lim_{t\to\infty} F(E,t)$ with

$$F(E,t) = \frac{2\hbar e^2\pi}{\Omega}\mathrm{Tr}\left[\frac{1}{t}\big(\hat{\mathcal{X}}(t)-\hat{\mathcal{X}}\big)\ \delta(E-\mathcal{H})\ \big(\hat{\mathcal{X}}(t)-\hat{\mathcal{X}}\big)\right], \tag{16.4}$$

$\hat{\mathcal{X}}(t) = \mathrm{e}^{\mathrm{i}\mathcal{H}t/\hbar}\hat{\mathcal{X}}\mathrm{e}^{-\mathrm{i}\mathcal{H}t/\hbar}$, and $\hat{\mathcal{X}}$ is the component along the direction x of the position operator. At this stage, we define for each orbital $\mid j >$, $\mid \Phi_j(t) > = \hat{X}\mathrm{e}^{-\mathrm{i}\mathcal{H}t/\hbar}\mid j >$ and $\mid \widetilde{\Phi}_j(t) >$ the normalized state. The calculation of conductivity then turns out to be

$$\frac{2\hbar e^2\pi}{\Omega}\sum_j \mathcal{D}_j(t) \times < \widetilde{\Phi}_j(t) \mid \delta(E-\mathcal{H}) \mid \widetilde{\Phi}_j(t) > \ . \tag{16.5}$$

For each initial state at $\mid j >= \mid \Psi(t=0) >$, we can take the origin at j. This means that $< j \mid \hat{\mathcal{X}} \mid j >= 0$. Then $\mathcal{D}_j(t)$ is given by

$$\mathcal{D}_j(t) = \frac{< \Psi_j(t) \mid \hat{\mathcal{X}}^2 \mid \Psi_j(t) >}{t}\,, \tag{16.6}$$

which are clearly related to wave-packet dynamics. The conductivity can thus be calculated from $\mathcal{D}_j(t)$ and the spectral quantity related to $\mid \widetilde{\Phi}_j(t) >$. The

spectral quantity is calculated by the recursion method [11]. The calculations of $\mid \Phi_j(t) >$ are based on the development of $\delta(E-\mathcal{H}) = N(E)\sum_n P_n(E)$ $P_n(\mathcal{H})$ with $N(E)$ a function associated with the polynomials ($N(E)$ being non-zero on the spectrum of $\mathcal{H}$). The unitary operator $\mathrm{e}^{-\mathrm{i}\mathcal{H}t/\hbar}$ admits a corresponding expansion on orthogonal polynomials, allowing a quick calculation of quantum dynamics. Hereafter, we will use Chebyshev polynomials of the first kind associated to the weight $\varrho(E) = 1/(\pi\sqrt{4b_\infty^2 - (E-a_\infty)^2})$ and will define, via the recursive scheme

$$\begin{aligned} Q_0(E) &= 1\,, \\ Q_1(E) &= \frac{E-a_\infty}{2b_\infty}\,, \\ Q_{n+1}(E) &= \left(\frac{E-a_\infty}{b_\infty}\right)Q_n(E) - Q_{n-1}(E)\,, \end{aligned} \tag{16.7}$$

where a_∞ and b_∞ are chosen as band parameters in accordance with those of the true density of states. Then, the time-dependent quantum state is related to

$$\mathrm{e}^{-\mathrm{i}\mathcal{H}t/\hbar} \mid j > = \sum_n h_n \Big(\int \mathrm{d}E\, \varrho(E) Q_n(E) \mathrm{e}^{-\mathrm{i}Et/\hbar} \Big) Q_n(\mathcal{H}) \mid j > \tag{16.8}$$

$$= \sum_n h_n \mathrm{i}^n J_n\Big(\frac{-2b_\infty t}{\hbar}\Big)\, \mathrm{e}^{-\mathrm{i}a_\infty t/\hbar} Q_n(\mathcal{H}) \mid j >\,, \tag{16.9}$$

$h_0 = 1$ and $h_n = 1/2$ for other n. As usual with orthogonal polynomials, the $Q_n(\mathcal{H}) \mid j >$ are evaluated via the recurrence property [11]. Amplitudes of $\mathrm{e}^{-\mathrm{i}\mathcal{H}t/\hbar} \mid j >$ on this basis have a rather simple form connected to Bessel functions. The consequent interest is to obtain asymptotic behaviors for these coefficients which converge very quickly as $n \to \infty$, since $\lim_{n\to\infty} J_n(z) \sim 1/\sqrt{2\pi n} \cdot (ez/2n)^n$.

We performed calculations of quantum diffusion and Kubo-Greenwood conductivity at T=0 K. We consider a s-band tight-binding model on a simple cubic lattice with nearest-neighbor hopping which has already been studied by several authors [40,45]. The hopping integral is the energy unit ($t = 1$) and the on-site energies are given by $\varepsilon_j = \varepsilon_{x_j} + \varepsilon_{y_j} + \varepsilon_{z_j} + \varepsilon_{\mathrm{dis}}$. Randomness is given by $\varepsilon_{\mathrm{dis}}$ = as a random number $\in [-W/2, +W/2]$ with strength W whereas the quasiperiodic potential is introduced via $\varepsilon_{j_\alpha} = \pm V_{\mathrm{qp}}$ constraints to Fibonacci sequences. This model allows a direct comparison between a quasiperiodic system and a periodic one since for $V_{\mathrm{qp}} = 0$ one recovers the classical Anderson model with diagonal disorder. One notes that Rieth and Schreiber have recently identified, in a 3D quasiperiodic tight-binding model, a metal-insulator transition for critical disorder $W_{\mathrm{c}} \simeq 21$ [34].

For finite V_{qp} and no randomness, Zhong and Mosseri [45] have studied quantum diffusion by means of the temporal autocorrelation function

$$C(t) = \frac{1}{t}\int_0^t \mathrm{d}t \mid < \Psi_0 \mid \mathrm{e}^{-\frac{\mathrm{i}}{\hbar}\mathcal{H}t} \mid \Psi_0 > \mid^2 . \tag{16.10}$$

They found, as quasiperiodic potential increases, a crossover between diffusive and anomalous regime. Indeed, for $V_{\rm qp} \leq 0.9$, the asymptotic behavior of $C(t) \sim 1/t$ turns out to be conventional whereas $C(t) \sim t^{\gamma-1}$ with $0 < \gamma < 1$ for $V_{\rm qp} > 0.9$ is referred as anomalous (γ is $V_{\rm qp}$-dependent). Hereafter, we will present calculations for different values of quasiperiodic potential $V_{\rm qp} = 0.7, 0.9, 1.1, 2.5$. One may notice that for $W = 0$ the Hamiltonian is separable in the sense that each eigenstate $\Psi(x, y, z)$ can be written as the product of eigenstates of the chains along each direction $\Psi(x, y, z) = \Psi_1(x) \times \Psi_2(y) \times \Psi_3(z)$, the energy being the sum of the three energies $E = E_1 + E_2 + E_3$. This means also that for a state that is initially localized on a site j one gets $\Psi_j(x, y, z, t) = \Psi_1(x, t) \times \Psi_2(y, t) \times \Psi_3(z, t)$ with $\Psi_1(x, t = 0) = \delta(x - x_j)$ and similarly for y and z. Obviously the Hamiltonian is no longer separable when $W \neq 0$.

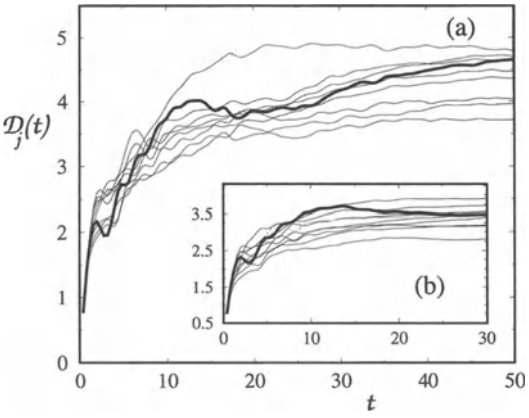

Fig. 16.4. $\mathcal{D}_j(t)$ represented for several initial sites j and $V_{\rm qp} = 0.9$. Time is in units of $2\hbar/W$ where W is the bandwidth. Lengths are in units of the nearest-neighbors distance. **(a)** $W = 2$, **(b)** $W = 2\sqrt{2}$. The *thick line* is an aid to visualize one of the curves

We have studied quantum diffusion through $\mathcal{D}_j(t)$. For $W = 0$ the above relation shows that $\mathcal{D}_j(t)$ is the same as for a 1D model [31]. In this study, we paid attention to the effect of randomness on transport. In Fig. 16.4 and Fig. 16.5, conduction modes undergo a transition from a non-ballistic to a diffusive regime (i.e. $\mathcal{D}_j(t)$ is independent of t at large time) for two different values of quasiperiodic and randomness strengths ($V_{\rm qp} = 0.9, 1.1$ and $W = 2, 2\sqrt{2}$).

When the disorder increases, the crossover to the diffusive regime occurs at shorter times and the asymptotic value of $\mathcal{D}_j(t)$ tends to decrease. We note also that the fluctuations of $\mathcal{D}_j(t)$ within the non-ballistic regime are less important when the disorder increases.

Kubo–Greenwood conductivities $\sigma_{\rm DC}(E)$ and their variations with the strength of disorder are plotted in Fig. 16.6 and Fig. 16.7 for $V_{\rm qp} = 1.1, 2.5$. In a metal one expects a law of the form $\sigma = \sigma_0/W^2$ (σ_0 being independent of disorder). Indeed this is what we find for $V_{\rm qp} = 0$ [38]. In addition, for suf-

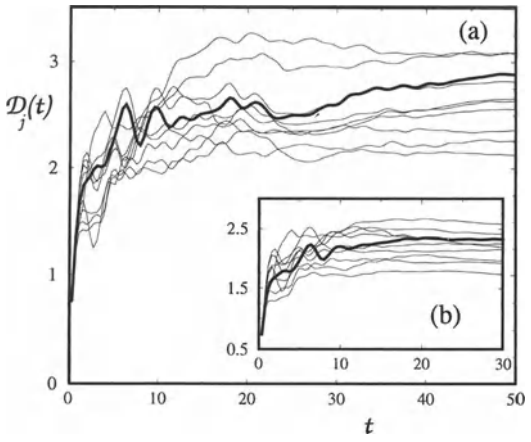

Fig. 16.5. $\mathcal{D}_j(t)$ represented for several initial sites j and $V_{\rm qp} = 1.1$. **(a)** $W = 2$, **(b)** $W = 2\sqrt{2}$. The *thick line* is an aid to visualize one of the curves

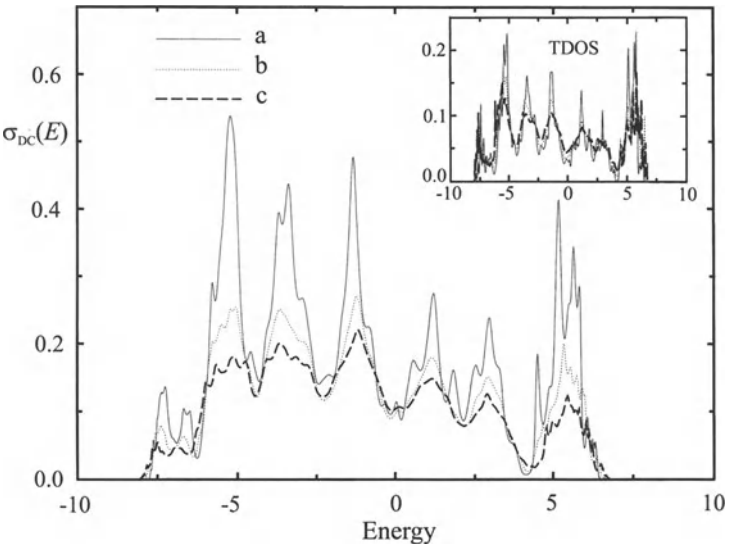

Fig. 16.6. Conductivity $\sigma_{\rm DC}(E)$ for $V_{\rm qp} = 1.1$ as a function of $E_{\rm F}$ for different values of the disorder parameter. Inset: TDOS. **(a)** $W = 1/\sqrt{2}$, **(b)** $W = 2\sqrt{2}$

ficiently small values of disorder our numerical results are in good agreement with the expectation from Bloch–Boltzmann's approximation. However, the enhancement of disorder in a quasiperiodic system clearly leads to a different law. For instance, in the case illustrated on Fig. 16.6, the conductivity decreases when the disorder increases but does not follow the law $\sigma = \sigma_0/W^2$ (note that the TDOS is nearly independent of disorder in this parameter range). Instead, we get approximately for each energy E a law of the form

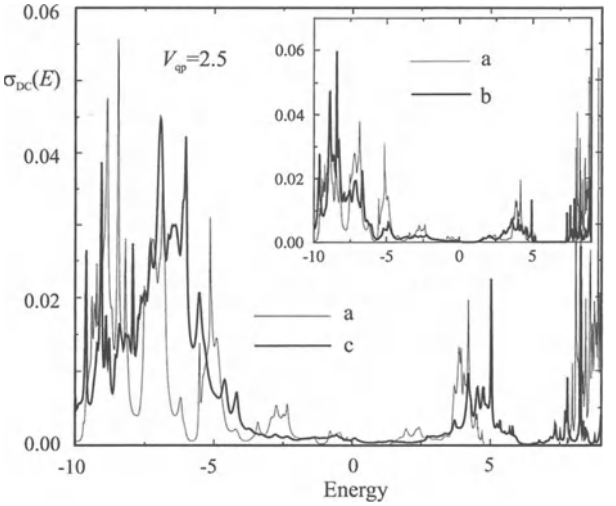

Fig. 16.7. Conductivity $\sigma_{\mathrm{DC}}(E)$ for 3D Fibonacci cube $V_{\mathrm{qp}} = 2.5$ as a function of E_{F} for different values of the disorder parameter. Inset: TDOS. **(a)** $W = 2$, **(b)** $W = 4\sqrt{2}$

$\sigma = \sigma_0/W^{\alpha}$. We can produce an estimation of α by calculating ($\Sigma_{\mathcal{H}}$ the spectrum base of the Hamiltonian $\mathcal{H}$)

$$\int_{\Sigma_{\mathcal{H}}} \sigma_{\mathrm{DC}}(E)\,\mathrm{d}E = \frac{1}{N} \lim_{t\to\infty} \sum_{j=1} \mathcal{D}_j(t)\,. \tag{16.11}$$

Depending on the energy E we find qualitatively $\alpha \sim 0.4$-0.8 [38].

Now we will discuss our results in detail. In Fig. 16.6, the conductivity for a quasiperiodic modulation $V_{\mathrm{qp}} = 1.1$ is shown. We note the presence of particular zones, identified by pseudo-gaps which seem relatively insensitive to a significant increase of randomness (a factor of 16 for W^2). The inset in Fig. 16.6 shows the related TDOS, which increases slightly with disorder in the pseudo-gaps. This enhancement compensates for the decrease of diffusivity leading to a nearly constant conductivity. In regions of high TDOS, which correspond also to higher conductivity, both density and diffusivity decrease. For $V_{\mathrm{qp}} = 2.5$ and different values of W, the variation of the conductivity with E is rather complex. We note, however, that the conductivity increases with W for some energies that correspond to pseudo-gaps. In contrast to the previous cases there is substantial change in the TDOS. It increases where the conductivity increases. This means that the electronic localization has been broken up by randomness, which is reminiscent of the idea of hopping previously discussed [36].

We have also studied the anisotropy of the conductivity between quasiperiodic and periodic directions. Indeed, d-phases of quasicrystals present

such a feature experimentally [25]. If i-phases present a 3D quasiperiodic order, d-phases, such as d-AlCuCo, confine quasiperiodicity in two-dimensional space. In our model, we can easily design such a situation by restriction of the quasiperiodic potential to, e.g. Y–Z planes. We estimate the anisotropy ratio of the case plotted on Fig. 16.8, which is roughly given by

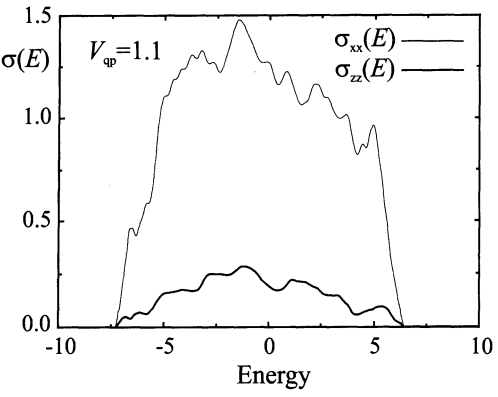

Fig. 16.8. Conductivity $\sigma_{xx}(E)$ in the periodic direction, and $\sigma_{zz}(E)$ in a quasiperiodic direction for $V_{\rm qp} = 1.1$ ($W = 2$)

$$\frac{\int_{\Sigma_{\mathcal{H}}} \sigma_{xx}(E)\,\mathrm{d}E}{\int_{\Sigma_{\mathcal{H}}} \sigma_{zz}(E)\,\mathrm{d}E} \sim \frac{\int_{\Sigma_{\mathcal{H}}} \sigma_{xx}(E)\,\mathrm{d}E}{\int_{\Sigma_{\mathcal{H}}} \sigma_{yy}(E)\,\mathrm{d}E} \sim 5\,, \tag{16.12}$$

which is in very good qualitative agreement with the experiments (note that parameters are $V_{qp} = 1.1, W = 2$ in units of hopping integral).

16.5 Conclusion

To conclude, we note that recent studies have made our understanding of critical states in quasicrystals more accurate. From rigorous mathematical developments to extensive numerical calculations in realistic models of periodic approximants or in 3D quasiperiodic systems, anomalous diffusion in these systems has been more clearly connected either with quasiperiodic correlations (introduced on an one-site potential), or with geometrical and chemical features of realistic models in which atomic species and their local environment have been shown to be fundamental.

Criticality in 1D quasiperiodic systems, as described by the pioneering work of M. Kohmoto, was related to algebraic localization of the eigenstates, singular continuous spectra and peculiar transport scaling of the conductance [15,17]. Recent studies on critical states in 1D have properly revealed unexpected relations between localization and transport [19,21,23,24,29]. In

higher dimension, an analytical analysis of critical states turned out to be rather difficult, but systematic numerical calculations gradually brought a better understanding of this kind of "pathological localization" due to quasiperiodic order (pathological for the usual interpretation of localization in conventional disordered systems). On the other hand, periodic approximants allow us to make an accurate description of the geometrical local environments that electrons may encounter while propagating throughout the sample. They also may conserve, to some extent, the peculiar order-induces-quantum interference leading to localization. Recent scaling studies in realistic periodic models support this latter statement.

To finish, we note that recent experiments now suggest that *electron-electron* interactions could play an important role in i-phases of AlPdRe [10]. It has been suggested that a Coulomb gap may occur as a consequence of the quasiperiodic potential [28]. In the light of the progress that has been made so far to investigate localization and transport in quasicrystals, further studies in this new direction certainly deserves particular attention.

Acknowledgment

S. Roche is very indebted to the European Commission and the Japanese Society of the Promotion of Science for financial support under contract ERB IC17 CT960010. The Department of Applied Physics of the University of Tokyo is also warmly acknowledged for its kind hospitality. We wish to thank T. Fujiwara, J. Bellissard, G. Trambly de Laissardiere and C. Sire for stimulating discussions.

References

1. Bellissard J. (1991): in *From number theory to physics*, eds. M. Waldschmidt, P. Moussa, J. Luck, C. Itzykson, Springer-Verlag, Berlin, 1991
2. Bellissard J., Iochum B., Testard D. (1991): Comm. Math. Phys. **141**, 353
3. Bellissard J., Schulz-Baldes H., to appear in Rep. Math. Phys.; Schulz-Baldes H. (1997): Phys. Rev. Lett. **78**, 2176
4. Berger C., *Seminar 3*, Akkermans E., Montambaux G., Pichard J.L., Zinn-Justin J. (1994): eds. Les Houches, Session LXI, *Mesoscopic Quantum Physics*
5. Biggs B.D., Pierce F.S., Poon S.J. (1992): Europhys. Lett. **19 92**, 415; Edagawa K., Naito N., Takeuchi T., (1993): Philos. Mag. B **65**, 1011
6. Fujiwara T., Tsunetsugu H. (1991): *Quasicrystals : The states of the art*, p. 343, eds. D.P. Di Vincenzo and P.J. Steinhart, World Scintific, 1991
7. Fujiwara T. (1996): in *Physical properties of Quasicrystals* Springer-Verlag, Springer Series in Solid-States Sciences, and references therein. Fujiwara, T., Mitsui, T., and Yamamoto, S. (1996): Phys. Rev. B **53**, R2910
8. Fujiwara T. (1992): Phys. Rev. B **40**, 942 Fujiwara T., Yamamoto S., Trambly de Laissardiere G. (1993): Phys. Rev. Lett. **71**, 4166.
9. Greenwood D.A. (1958): Proc. Phys. Soc. Lond., **71**, 585

10. Gignoux C. et al. (1997): Europhys. Lett. **39** (2), 171
11. Haydock R. (1980): in *Solid. State. Physics*, eds. F. Seitz, D. Turnbull and H. Ehrenreich, Academic, New York **35**
12. Honda Y., Edagawa K., Yoshioka A., Hashimoto T., Takeuchi S. (1994): Jpn. J. Appl. Phys. **33**, pp. 1929–1935
13. Janot, C., de Boissieu M. (1994): Phys. Rev. Lett. **72**, 1674; Janot C. (1996): Phys. Rev. B **53**, 181; ibid. (1997): J. Phys.: Condens. Matter **9**, 1493
14. Janssen M. (1994): Int. J. Mod. Phys. B **8**, 943
15. Kohmoto M., Kadanoff L.P., Tang Ch. (1983): Phys. Rev. Lett. **50**, 1870; Ostlund S., Petit R., Ret D., Schellnhuber H.J., Siggia E.D. (1983): ibid. **50**, 1873.
16. Kohmoto M. (1986): Int. J. Mod. Phys. B **1**, 31
17. Kohmoto M. (1986): Phys. Rev. B **34**, 5043
18. Kubo R. (1957): J. Phys. Soc. Jpn. **12**, 570
19. Kubo H. and Goda M. (1993): J. Phys. Soc. Jpn. **62** pp. 2601–2611
20. Trambly de Laissardière G., Mayou D. (1997): Phys. Rev. B **55**, 2890, Trambly de Laissardière G., Roche S., Mayou D. (1997): Mater. Sci. Eng. **A 226–228**, 986–989
21. Lopez J.C., Naumis G., Aragon J.L (1993): Phys. Rev. B **48**, 12459
22. Levitov L.S. (1989): J. Phys. France **50**, 707
23. Maciá E., Domínguez-Adame F., Sánchez A. (1994): Phys. Rev. B **49**, 9503, Roy C.L., Basu C., Domínguez-Adame F., Maciá E. (1995): Phys. Status Solidi (B) **189**, 193
24. Maciá E.,Dominguez-Adame F. (1996): Phys. Rev. Lett. **76**; ibid., *Semicond. Science and Technol.* **11**, 1041
25. Martin S., Hebard A.F., Kortan A.R., Thiel F.A. (1991): Phys. Rev. Lett. **67**, 719
26. Mayou D. (1988): Europhys. Lett. **6**, pp. 549–554; Mayou D., Khanna S. (1995): J. Phys. I France **5**, pp. 1199–1211
27. Mayou D., Berger C., Cyrot-Lackmann F., Klein T., Lanco P. (1993): Phys. Rev. Lett. **70** 3915
28. Mayou D., Roche S., Trambly de Laissardiere G., Berger C., Gignoux C. (1997): Proc. Int. Conf. *Quasicrystals 6*, eds. T. Fujiwara, S. Takeuchi, World Scientific, Singapore
29. Moulopoulos K., Roche S. (1996): Phys. Rev. B **53**, 212; ibid. (1995): J. Condens. Matter **7**, 8883
30. Mott N. (1990): *Metal-insulator transition*, 2 edn, Taylor & Francis Group, London, New York, Philadelphia, Singapore
31. Piéchon F. (1996): Phys. Rev. Lett. **76**, 4372
32. Pierce F.S., Guo Q., Poon S.J. (1994): Phys. Rev. Lett. **73**, 2220 Biggs B.D., Poon S.J., Munirathnan N. (1990): Phys. Rev. Lett. **65**, 2700 (1990), Poon S.J. (1992): Adv. in Phys. **41**, 303
33. Quivy, A., Quiquandon, M., Calvayrac, Y., Faudot, F., Gratias, D., Berger C., Brand R.A., Simonet V., Hippert F. (1996): J. Phys.: Condens. Matter **8**, pp. 4223–4234
34. Rieth T., Schreiber M. (1997): Z. Phys. B **104**, 99
35. Roche S., Fujiwara T. *Proceeding of Aperiodic 97.*
36. Roche S., Trambly de Laissardière G., Mayou D. (1997): J. Math. Phys., Special issues on Quantum Problems in Condensed Matter Physics **38**, 1794
37. Roche S., Mayou D. (1997): Phys. Rev. Lett. **79**, 2518

38. Roche S. Ph.D. thesis, Université Joseph Fourier Grenoble 1996 (unpublished).
39. Sire C., Passaro B., Benza V.G. (1993): J. Non-Cryst. Solids **153&154**, pp. 420–424
40. Sire C. (1994): in *Lectures On Quasicrystals*, eds. F. Hippert and D. Gratias (Les Editions de Physique Les Ulis, 1994); and *Proceedings of the 5th International Conference on Quasicrystals*, eds. C. Janot, R. Mosseri, World Scientific, Singapore, 1995.
41. *Quasicrystals, the state of the art* eds. D.P DiVicenzo and P.J. Steinhardt, Directions in Condensed Matter Physics, Vol. 11, World Scientific 1991
42. Takeuchi S., Akiyama H., Naito N., Shibuya T., Hashimoto T. (1993): J. Non-Cryst. Solids **153–154**, 353
43. Thouless D. (1983): Phys. Rev. B **28**, 4272
44. Tsunetsugu H., Fujiwara T., Ueda K., Tokihiro T. (1991): Phys. Rev. B **43**, 8879
45. Zhong J. X., Mosseri R. (1995): J. Phys. C. **7**, 8383

17 Electron Densities of States in Quasicrystals and Approximants

Esther Belin-Ferré

Summary. Bulk electronic properties of quasicrystals, such as the very high resistivity, are especially manifest at low temperatures. Thus, for a meaningful understanding, it is necessary to measure the electronic density of states within the same temperature ranges. Similarly, at high temperature, the ductility of quasicrystals and/or the fast atomic movements pointed out by inelastic neutron scattering or atomic transport measurements are indications that density of states studies should also be relevant. Therefore, it appears essential to continue experimentations and, indeed, it might be profitable to use various complementary spectroscopy techniques to investigate the same series of samples.

17.1 Introduction

The knowledge of the electronic structure and nature of bonding in a solid is of interest to understand its properties. For such a purpose, experimental means that involve various spectroscopic techniques are relevant [5,42]. They investigate the transitions between two different quantum states of the solid, each characterized by its energy and life time. Thus, they most often provide direct information about the electronic energy distributions. Many of these techniques have already been used to analyze quasicrystals (QC) and related crystalline alloys [12,42]. The aim was not only to improve our knowledge of the respective electronic structures but also to seek for a possible signature attached to the lack of translational periodicity displayed by QC in comparison to the crystalline counterparts.

In this chapter I will briefly present the principles of various commonly used spectroscopy techniques, namely photoemission, X-ray emission, X-ray photoabsorption, electron-energy loss and optical studies which involve occupied or unoccupied states of the solid or both. I will report on several among the most relevant results which these spectroscopies have allowed us to achieve for QC and approximants, and discuss them comparatively.

17.2 Photoemission Spectroscopies

Integrated *photoemission spectroscopy* (PES) scans the kinetic energies E_K of photoelectrons emitted from inner levels as well as from the valence band

J.-B. Suck et al. (eds.), *Quasicrystals*
© Springer-Verlag Berlin Heidelberg 2002

(VB) of a solid following its interaction with an X-ray (X-ray photoelectron spectroscopy, labeled XPS) or ultra-violet (ultra-violet photoelectron spectroscopy, labeled UPS) incident radiation of energy $h\nu$ [42]. The photoemission process involves three steps: the excitation of the photoelectron, its travel through the solid which gives rise to inelastic interactions and its ejection into the vacuum from the surface (Fig. 17.1). Assuming no perturbation

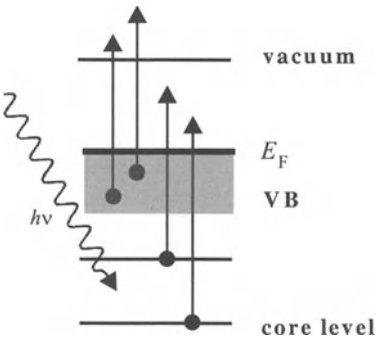

Fig. 17.1. Principle of photoelectron spectroscopy

is induced by the remaining hole in the final state, the binding energy E_B of the photoelectron is related to its kinetic energy by:

$$E_K = h\nu - E_B - \Phi \tag{17.1}$$

where Φ is the difference between the work functions of the spectrometer and the sample. In a usual PES experiment, it is not necessary to know Φ exactly provided the E_B scale is properly calibrated, for example by taking E_B of the 1s level of contaminating carbon (that is always present at the surface) equal to 285.0 eV. Nevertheless, inelastic scattering events always take place, resulting in some asymmetry in the shape of the photoemission peaks. Also, characteristic energy losses, shake-up and shake-off processes as well as plasmon excitations and final state effects may give rise to satellite peaks which usually do not dominate the spectra.

The important features of PES are two-fold. First, whereas the binding energies of the inner levels are obtained separately, those of the electrons of the VB are achieved altogether. Second, the probed depth of the sample is connected to the mean free path of the photoelectrons in the sample, which makes XPS and UPS spectra basically surface sensitive. This imposes a very careful preparation and characterization of the surface of a sample, especially when investigating the valence band. Note that the energy resolution is generally 0.4–0.6 eV in XPS but can be as good as a few tens of a meV in the case of UPS.

The spectral intensities in the binding-energy scale depend upon the number of ejected electrons modulated by photoemission cross sections which significantly favor d- and f-states with respect to p or s. This is why PES tech-

niques are not able to provide any information on the energy distributions of s- and p-valence-band states in alloys containing both sp- and transition metals (TM) or rare earths. Note that as a result of tuning the energy of the incident photons across an absorption edge (*resonant photoemission*), some site selectivity is obtained which allows us to distinguish between the individual contributions to the VB of the components of a binary alloy provided their E_B are different enough. For Al-(Co,Ni)-alloys, the contributions from each of the two TM are at 0.8 ± 0.1 and 1.3 ± 0.1 eV, respectively and therefore cannot be distinguished. Accordingly, a single broad peak is observed in the VB spectrum [58].

The density of states (DOS) in the VB of Al-(Cu, Pd)–(Fe, Mn, Co, Ni, Ru, Re, etc.) icosahedral (i-) or decagonal (d-) QCs as well as related crystalline alloys has been investigated with PES techniques [18,19,45–47,55–60,72]. The VB displays generally two peaks corresponding to Cu, Pd d-states with a maximum at about 4 eV below the Fermi level (E_F) on the one hand and to TM (Fe, Mn, Ru, Re, ...)d-states located between 1–2 eV below E_F on the other hand (Fig. 17.2) [47]. It shows no contribution from the Al states. As

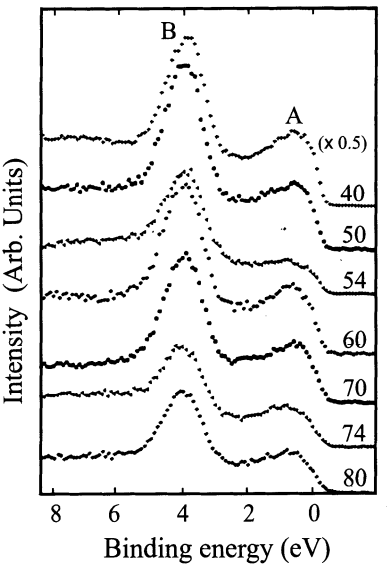

Fig. 17.2. Valence-band spectra for i-Al-Cu-Fe measured for several incident photon energies [47]. The intensity of the spectrum for 40 eV photon energy is scaled by 0.5. (A: Fe d-states, B: Cu d-states, see text)

just mentioned, when the alloy contains no Cu, Pd and two TM, like Ni and Co, the VB spectrum consists of a single peak (Fig. 17.3) [58]. The spectra of i-$Al_{65}Cu_{20}Fe_{15}$ and crystalline $Al_{70}Cu_{20}Fe_{10}$ (the tetragonal ω-compound) were taken with the same experimental conditions. The corresponding PES spectra were found to be essentially identical (Fig. 17.4) [55]. This is rather surprising because the physical properties of the two phases are very different (e.g. the electrical conductivity of the ω-compound is larger than that of the

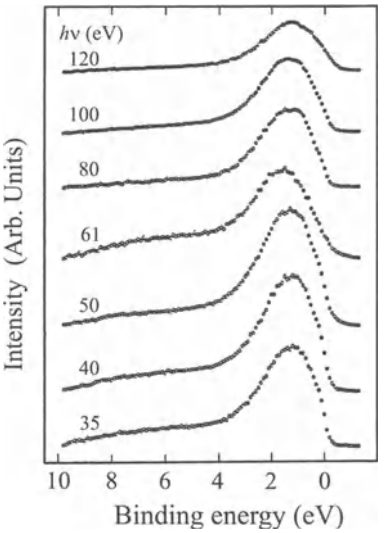

Fig. 17.3. Valence-band spectra of d-$Al_{70}Co_{15}Ni_{15}$ measured at different photon energies [58]

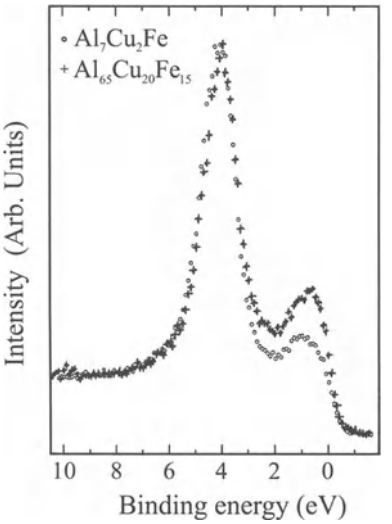

Fig. 17.4. Valence-band spectra of i-$Al_{65}Cu_{20}Fe_{15}$ and $Al_{70}Cu_{20}Fe_{10}$ measured at photon energy of 100 eV [55]

icosahedral phase by four orders of magnitude [15]). The preparation of the sample surface, which was scratched to remove any surface oxide, might be responsible for this effect as this technique induces strong disorder at the surface layers [16]. However, one expects that the positions of the features corresponding to Cu, Pd and TM do not significantly differ in QCs and in crystalline alloys of similar composition since they correspond to localized states which are therefore not so sensitive to modifications of the local topological order around the probe atoms.

Most attention was paid to the sharp decrease of intensity near E_F, as observed in the VB spectra for all alloys. Generally, the slope of the Fermi edge is less straight for the QCs than for metals [47,59,60]. Consequently, the intensity is lowered at E_F which is interpreted as evidence of the presence of a pseudo-gap, in agreement with total DOS calculations for crystalline approximants of QC [28,31,38,39,64,65]. These DOS exhibit a much more spiky structure with very narrow dense spikes than displayed by usual intermetallics [67,68]. Such spikes should be visible in high resolution PES spectra of QCs. Until now, the too-low resolution of the XPS experiments was unable to establish the presence of such spikes in all samples examined. More recently, ultra-high energy resolution valence band UPS measurements, with a far better energy resolution of the order of 5 meV, were performed for a large number of QC as well as for two crystalline phases [59]. They confirmed the previous XPS and UPS results but could not detect any spikes. Note, however, that the surface of the samples was repeatedly scraped, as already mentioned, to eliminate oxide contaminations. Therefore, the case of the existence or not of spikes in the experimental DOSs has not been investigated in the better experimental conditions. However, today, theoretical DOS calculations performed for a Penrose tiling [75] also did not achieve such a spiky structure as in [28]. Therefore this question still remains open.

The XPS technique has also been used to study inner levels. The Al $2p_{3/2}$ spectra of samples to which no cleaning procedure was applied, present two peaks that correspond to the Al $2p_{3/2}$ levels of the surface oxide and in the sample, respectively. As compared to pure fcc-Al, shifts between 0.2 and 0.6 eV have been found for crystalline intermetallics and QCs. The spectra for TM (Fe, Mn, Ni, Co, Ru, Re...) inner levels show no significant difference with respect to the pure metals whereas shifts as large as 1 to 2 eV are noticed for Cu $2p_{3/2}$ and Pd $3d_{5/2}$ inner levels respectively [7,9,35,45,73].

An investigation of core levels was carried out to study the effect of oxygen or water on a single grain of $Al_{70}Pd_{21}Mn_9$ QC at a five-fold surface [50]. It has been shown that, contrary to Al, the two other metals, Pd and Mn, are not oxidized in the absence of water. This no longer remains true in immersion into H_2O or in the presence of H_2O vapor [18,50,65,70]. Recently, it has been pointed out for a single grain of i-$Al_{70}Pd_{21}Mn_9$ that a convenient signature of the occurrence of quasicrystalline order at the surface is supplied by the remarkable sharpness of the Mn $2p_{3/2}$ line. Indeed, in comparison with pure Mn or with the cubic β-phase of composition $Al_{60}Pd_{25}Mn_{15}$, this line is narrower by more than 1 eV [35]. This clearly indicates differences between the PES spectra of QCs and their crystalline counterparts from well prepared and characterized surfaces.

The energy distribution of VB photoelectrons can be probed from samples of well-characterized surfaces as a function of the emission angle. Using this so-called *angular resolved photoemission spectroscopy* technique, dispersion energy curves are obtained which makes it possible to map the variation

of the energy of the valence electrons according to their wave vectors. Such experiments have been performed for the five-fold surface of a single grain of i-$Al_{70}Pd_{21.5}Mn_{8.5}$ whose structure was checked in-situ using *low energy electron diffraction* (LEED) and *Auger electron spectroscopy* (AES) [71]. For incident photons of 13 eV, a very flat dispersion curve was observed, in agreement with DOS calculations for higher order Al-Pd-Mn approximants [30]. The presence of a dip-like pseudo-gap was also detected.

17.3 X-Ray Emission and Photoabsorption Spectroscopies

When a hole is created in a core level of a solid, the ionized or excited system may reorganize from either a more external level or the VB, by emitting a discrete X-ray radiation (Fig. 17.5) [5]. This leaves a remaining hole in

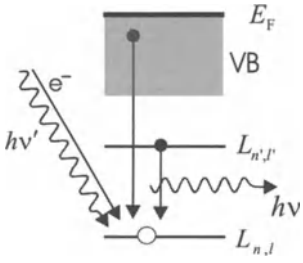

Fig. 17.5. Principle of X-ray emission spectroscopy

the final state. Within the framework of the one-electron approximation, thus neglecting relaxation-energy terms due in part to the remaining hole, X-ray emission (denoted XES) is a two-step process: first, creation of the inner hole and second, reorganization of the electronic cloud. The first step may be achieved subsequently to the irradiation by photons or electrons. Electron irradiation easily produces multiple interactions so that satellite emissions corresponding to the X-ray transition in the multiply ionized or excited system may also be observed.

For an X-ray emission to occur, it is necessary that the radiative transition probability which depends upon the overlap between the initial and final wave functions of the system, each characterized by the quantum numbers ℓ and $j(j = \ell + s)$, differs from 0. This is achieved if dipole selection rules are fulfilled, namely: $\Delta\ell = \pm 1, \Delta j = 0, \pm 1$. Accordingly, an s-hole can be filled from p-states whereas a p-hole involves simultaneously s- and d-states; note that transitions d $\rightarrow$ p are largely dominant with respect to s $\rightarrow$ p. Only the fraction of the final wave function which is in the region of the core hole significantly contributes to the transition probability. Thus, XES probes occupied partial local DOS because the inner hole is on a given atom of the

sample. The contributions of the various components to the VB of a solid can be achieved separately, whatever they are. The XES technique is applicable to any kind of material: crystalline, amorphous, powder, etc. According to the experimental conditions it can inform either about the bulk or about a thin layer under the surface of the sample.

Furthermore, an incoming photon can deliver its energy to a core electron of a solid which can be promoted to a normally unoccupied state provided the energy of the incident photon is equal to or higher than the ionization threshold (Fig. 17.6) [5]. The (photo)absorption spectrum then describes the

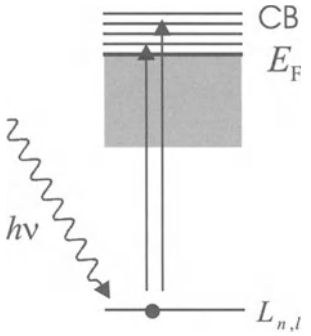

Fig. 17.6. Principle of X-ray photoabsorption spectroscopy

sum of all the transitions from the core level into the continuum states of the appropriate symmetry. If I_0 is the intensity of the incident photon beam, the intensity I, after transmission through a thickness x of the sample is given by the Beer–Lambert law:

$$I = I_0 \mathrm{e}^{-\mu x} \tag{17.2}$$

where μ can be taken as the linear photoabsorption coefficient. Depending on the solid, the incident photon beam is totally absorbed through a thickness that can vary from tens of nm to 1 µm. The photoabsorption coefficient can also be determined from the measurement of the current associated with the electrons that escaped from the sample owing to the photoabsorption process. Then, the photoyield current Y connected to I_0 and to the intensity I absorbed at a depth x into the sample is given by:

$$Y = (I_0 - I)/I_0 = \gamma\left(1 - \mathrm{e}^{-\mu x}\right) \simeq \gamma \mu x\,, \tag{17.3}$$

where γ is a constant. Y is dependent on the mean free path of the escaping electrons. Consequently, the transmission technique gives information mainly related to the bulk solid (although in some cases films with a thickness of a few tens of nm are required for good experimental contrast), whereas the photoyield is more surface sensitive.

The coefficient μ is a function of the photoabsorption cross section σ of the different elements of the sample. The variation of σ is proportional

to both the wave functions describing, in the one-electron approximation, the inner electron and the electron ejected in the conduction state, and to the DOS of the conduction band (CB). So, here again, the photoabsorption transition is forced to follow the dipole selection rules and its probability depends upon the overlap between an extended state and a more localized one. This makes photoabsorption spectroscopy (hereafter denoted XAS) site and symmetry selective. The lifetime τ of a core hole involves all the possible decay processes whether they are radiative or not. The full width at half maximum intensity of the Lorentzian-like energy distribution $\mathrm{L}_{n,l,j}$, which is associated with the core hole, and τ are connected via:

$$\Delta E_{n,l,j} = \hbar\tau^{-1} \quad . \tag{17.4}$$

$\Delta E_{n,l,j}$ is the natural width of the inner level [37]. Thus, the energy distributions of an XES transition involving VB states and of an XAS transition involving CB states, result from the convolution of the energy distribution of the core level and the valence or conduction DOS respectively, weighted by the corresponding transition probabilities. The spectral energy distributions are then written as:

$$I_{(h\nu)} \propto |M_{f\to i}|^2 \cdot N(\varepsilon)_{\mathrm{VB}} \cdot \mathrm{L}_{n,l,j} \,, \tag{17.5}$$

and

$$I_{(h\nu)} \propto |M_{f\to i}|^2 \cdot N(\varepsilon)_{\mathrm{CB}} \cdot \mathrm{L}_{n,l,j} \,, \tag{17.6}$$

for XES and XAS, respectively.

Finally, since the matrix element of the transition probability is constant, or varies very slowly against energy, XES and XAS spectra are directly related to the valence and conduction DOS. However, no absolute values can be derived from the experiments. The total energy resolution results from the instrumental function and the natural width of the inner level $\mathrm{L}_{n,l,j}$. The width of the energy distribution $\Delta E_{n,l,j}$ varies from less than 0.01 to a few eV according to the atomic number of the element considered [37].

XES and XAS techniques have been used to probe Al-(Cu, Pd)-(Fe, Mn, Ni, Co, Ru, Re, etc.) QCs as well as related crystalline intermetallics [7,9–12,14,17,24,25,46,60,69,72]. For the TM of the first series and for Cu, the total resolutions are within the range 0.45 to 0.6 eV, but they increase to more than 2 eV, for Pd, Ru or Re metals, because the transitions which could be probed with the available spectrometers, involve inner levels as large as 2.0, 2.25 and 5.0 eV, respectively [37]. However, a comparison of spectra for all these elements in various alloys is possible. For Al the natural widths of the 1s and $2p_{3/2}$-levels are 0.4 and $\ll 0.1$ eV, respectively [37]. Thus the total resolution is less than 0.4–0.5 eV for the study of s,d- and p-states respectively, i.e. it is comparable to the energy resolution of XPS measurements. Consequently, the investigation of Al electronic distributions using the X-ray spectroscopy techniques can be very informative since, in addition, s- and p-states are

of extended character. They are, accordingly, more sensitive than localized states (i.e. TM d-states) to modifications of atomic surroundings.

Nevertheless, the partial DOS are obtained each one in its own X-ray transition energy scale. The description of the VB and the CB imposes an adjustment of the various spectral curves on an absolute energy scale, namely the binding energy scale. This can be achieved by locating E_F on the X-ray transition energy scales thanks to complementary measurements of X-ray transitions between core levels and of inner level binding energies [69]. No cleaning procedure is applied to the samples that, although kept in glove boxes under argon atmosphere, have been for some time in air. Al is always oxidized but the XPS Al $2p_{3/2}$-level spectra displays two peaks separated from each other by more than 2 eV. They correspond to the oxide and to the alloy, respectively. Finally, E_F is obtained within ± 0.1 to ± 0.2 eV accuracy. For Cu, Pd and TM, because of possible oxidation and also since their concentrations are generally 25 % or less in the alloys, the experimental uncertainty in determining E_F is of the order of ± 0.3 eV and can reach about ± 0.5 eV in the worse situations.

The data obtained using XES and XAS techniques, complemented by core level XPS measurements, give direct insight into the VB and CB. For the sake of illustration, let us first recall data for pure fcc-Al (Fig. 17.7). The VB distributions are parabolic like, with a narrow peak near E_F for the

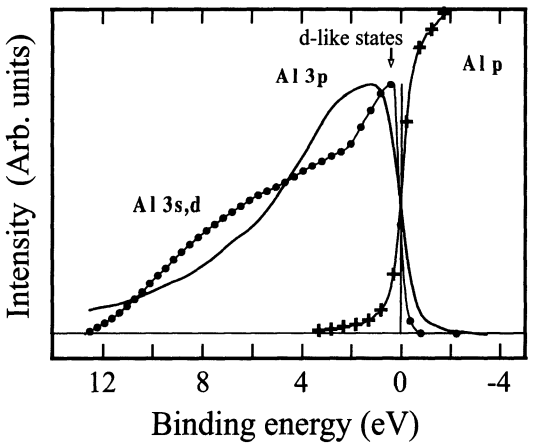

Fig. 17.7. Valence band (3p, 3s, d)- and CB (p)-states in fcc-Al. The VB-curves are normalized to their maximum intensities. Al 3p- and Al p-curves are adjusted to the same intensity at E_F

partial 3s,d-contribution. It is due to both the presence of the infra-red catastrophe (generation of electron-hole pairs of very low energy accompanying the creation of the core hole in a nearly free-electron system) [49] and of states with some d-character [41]. The 3p- and 3s,d-distributions overlap on the entire VB, the states are thus sp-hybridized with some d-character close to E_F. The straight Al 3p-edge cuts E_F at half the maximum intensity of the Al 3p sub-band. The Al p-edge displays an abrupt arctangent shape. As

expected for a free-electron metal, it cuts E_F at half the maximum intensity of the absorption edge.

The results for QC and crystalline alloys are summarized in the following subsections.

17.3.1 Occupied States

Within the VB there are TM-states, essentially of d-character, present in the close vicinity of E_F whereas Cu, Pd d-states are around 4 eV below E_F (Figs. 17.8 and 17.9). Within the experimental uncertainties in setting E_F, consistency is found between the XES results and valence-band XPS data. Indeed, Cu and Fe 3d states in crystalline $Al_{70}Cu_{20}Fe_{10}$ are at 4.0 and 1.3 ± 0.3 eV, respectively, in the XES measurements [6] against 4.0 and 0.7 eV in XPS spectra [55]. For i-$Al_{65}Cu_{20}Ru_{15}$, Cu *d*- and Ru *d*-states are at 3.9 and 1.2 ± 0.3 eV, respectively [10], against 3.8 and 1.8 eV from XPS [56]; Pd- and Mn-states in i-$Al_{71}Pd_{19}Mn_{10}$ are at 3.4 and 1.1 ± 0.3 eV, respectively [7], whereas they are at 3.8 and 1.8 eV in XPS measurements of i-$Al_{70}Pd_{20}Mn_{10}$

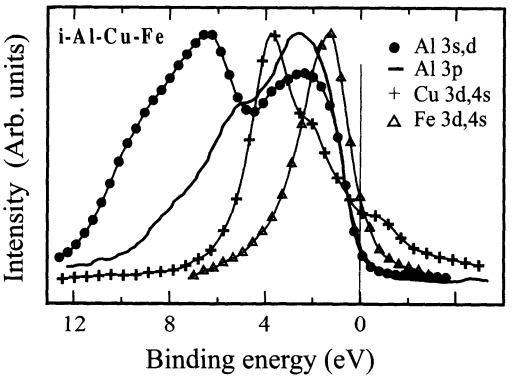

Fig. 17.8. Valence-band distribution curves in i-$Al_{62}Cu_{25.5}Fe_{12.5}$. All curves are normalized to their maximum intensity

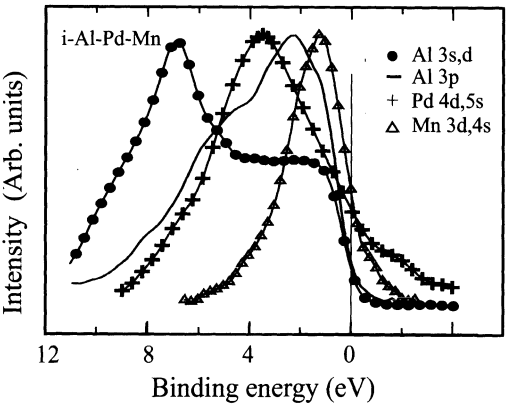

Fig. 17.9. Valence-band distribution curves in i-$Al_{71}Pd_{19}Mn_{10}$. All curves are normalized to their maximum intensity

[57]. The shapes of the occupied TM, Cu or Pd d distributions are like those in the pure metals. There is only a narrowing by about 0.5–1 eV which is observed, consistent with the difference of local order in the alloys with respect to the pure metals. The TM and Cu or Pd distributions are found to be similar in QC and related crystalline intermetallics, in agreement with the fact that d-states are of localized character and therefore, are not very sensitive to modifications of their atomic environment.

On the contrary, Al-state distributions are significantly modified with respect to the same distributions in pure fcc-Al. In the alloys, quasicrystalline or not, the Al distributions display a marked minimum in the energy range of the Cu, Pd d-states. The Al 3s,d-intensity is greatly enhanced in the higher binding energy region of the Cu, Pd d-band and reduced in the lower binding-energy region. Therefore, the bottom of the band has an almost pure s-character whereas states of d-character are observed between +1 and +2 eV below E_F. The Al 3p-distribution is also split into two parts, the most intense being in the low energy region of the VB. This asymmetric distortion is a common feature observed in TM - simple-metal alloys [62]. It results from the interaction between a relatively narrow TM d-band and a broad s-band which induces the formation of a hybridization gap and the splitting of the s-states into bonding and antibonding parts [1]. Note that for concentrated alloys, the maximum of the d-states does not necessarily coincide with the minimum of the hybridization gap. Consequently, due to this kind of interaction between Al sp-states and Cu d-states far from E_F, there is a pronounced dip in the middle of the VB of Al-Cu-TM alloys. Due to the same type of interaction with the TM d-states, the Al-states are pushed far away from E_F, thus displaying a low intensity at E_F and a marked bending of the Al VB edges. This causes the formation of a pseudo-gap at E_F in the VB of Al-based crystalline alloys as well as of QCs, whatever they are, icosahedral or decagonal [7–12,14,25,46,60,61,68,69,72]. Note that the XES results are in agreement with existing partial DOS calculations for approximants and intermetallic alloys [28,31,38,39,48,64–68]. Comparison with these calculations allows us to confirm that the high binding energy Al s,d-states are in fact s-pure in character whereas those of lower binding energy are d-like and hybridized to the 3p-states. However, the resolution of the measurements is not good enough to ascertain the predicted spikyness of the calculated DOSs.

An investigation of a series of Al-Cu-Fe approximants has shown faint differences in the intensities of the various features of the VB with respect to the icosahedral QC. The pseudo-gap is more marked in the QC than in the related crystalline alloys [8,10–12,14,25,37,46,60,61,72] with a slight tendency to shift the Al 3p-edge and to reduce the Al 3p-intensity at E_F when going from the 1/1 cubic approximant [52] to the orthorhombic and rhombohedral compounds [51] and finally to the QC, respectively. In the Al 3s,d-distributions, the role of the periodicity is revealed by changes in the ratio between the intensities of the d-like peak and the minimum between the

d- and s-states. This ratio is 1.23 for the QC alloy and 1.30, 1.33 and 1.34 for the rhombohedral, orthorhombic and 1/1 cubic approximants, respectively. In the Al 3p-distribution, the relative minimum, present in the energy range of the hybridization gap in the middle of the VB, is more marked when going again from the icosahedral alloy to the rhombohedral, orthorhombic and 1/1 cubic approximants, respectively [13]. These results suggest that the lack of periodicity in QCs smoothes out the contrast of the hybridization gap of the middle of the VB and induces a slight increase of the hybridization gap close to E_F. Both effects are connected with the interaction between extended states and localized states, thus indicating that in the QC phases, Al-states behave somewhat differently from the crystalline approximants.

17.3.2 Unoccupied States

Within a short energy range of the conduction band above E_F, TM d-states are present although less localized than in pure metals [53]. Indeed, the intensity curves for the alloys are much less sharp and are broader than in the pure metals (Fig. 17.10) [10]. This broadening might be ascribed either to a charge transfer from Al-states resulting in a filling of the TM d-orbitals, or to an intra d-band reorganization leading to some hybridization with s-states, or to both processes.

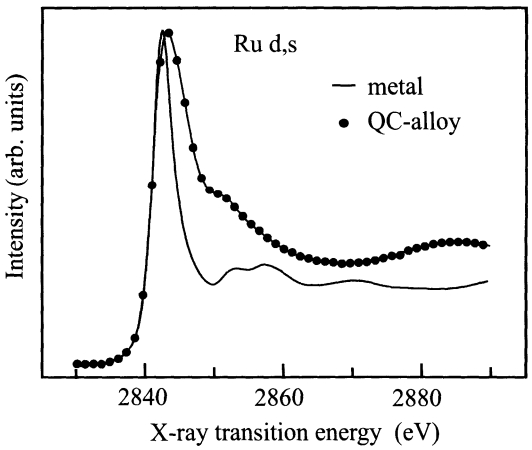

Fig. 17.10. Ru d CB states in pure metal (*full line*) and QC (*dotted line*). Note the less sharp line of QC alloy

About 2 eV above E_F, Cu, Pd-states with a faint d-like character are also present which become strongly hybridized to s-states at larger energies. The Al p-distribution curves for the alloys reveal a less abrupt edge than in fcc-Al and a noticeable depletion over about 5 eV above the edge, especially in the energy range where TM and Cu- or Pd d,s-states are present [11,53]. The overlap between all these partial distribution curves emphasizes the strong

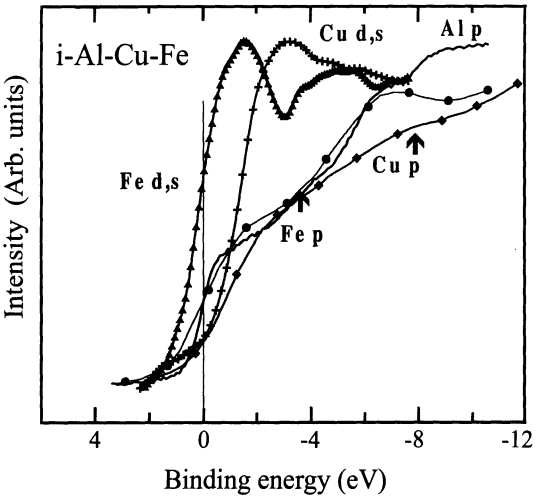

Fig. 17.11. Conduction band distribution curves in i-Al-Cu-Fe. All curves are normalized to their maximum intensity

mixing of the corresponding states. Figure 17.11 shows the CB-distribution curves for i-Al-Cu-Fe.

Thus, with respect to pure metals, the XES and XAS experiments point out new hybridizations. On both sides of E_F, the valence and conduction bands are somewhat localized. Indeed, they contain transition-metal states of partial d-character in interaction with the Al p,d-states whereas s-states, pure or hybridized to d-states, are pushed away from E_F (Fig. 17.12) [7].

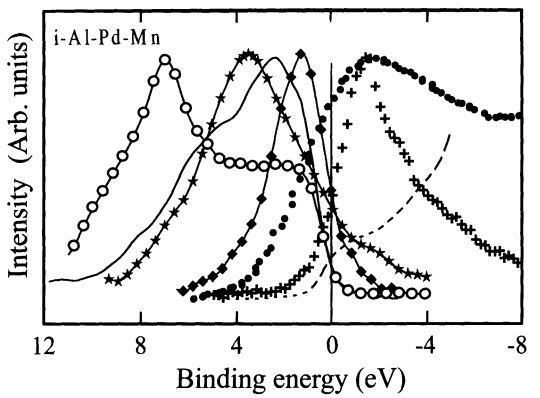

Fig. 17.12. Valence-band curves and CB-curves in i-Al-Pd-Mn. Al $3s,d$: *open circles*, Al $3p$: *full line*, Pd $4d$: *stars*, Mn $3d$: *squares*, Pd d,s: *dots*, Mn d,s: *crosses*, Al p: *dashed line*. All curves are normalised to their maximum intensity

The intensities of the Al p distribution curves at E_F have been adjusted to the occupied Al 3p counterparts assuming that the distribution of p-states is a continuous function of the energy. This implies that the transition probabilities between the Al 1s-wave function and the wave functions describing either the final Al 3p-valence or the Al p-conduction states can be considered as equal, at least in the energy range where the amplitude of the wave functi-

ons associated with the final states, in the region of the Al-core, contribute to the transition matrix element. Within this adjustment scheme, the Al 3p- and Al p-sub-bands cross each other at the Fermi level and give a clear picture of the pseudo-gap in the Al p-states distribution (Fig. 17.13) [10].

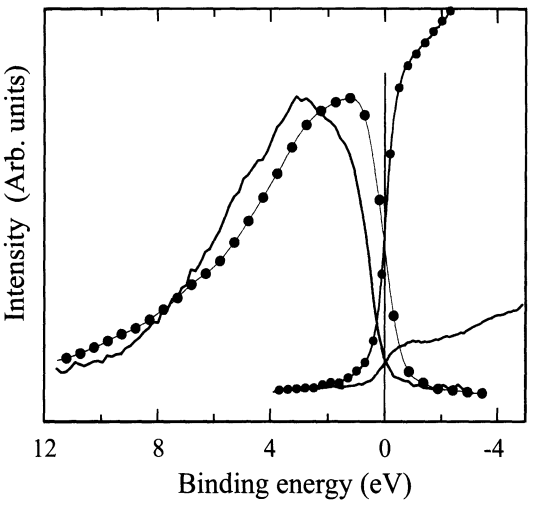

Fig. 17.13. Valence band Al 3p- and conduction band Al p-distribution curves adjusted to the same intensity at E_F. *Full line*: i-Al-Cu-Ru, *dotted line*: fcc-Al

Figure 17.14 shows the Al p-sub-bands in fcc-Al (top curves), tetragonal $Al_{70}Cu_{20}Fe_{10}$ (a), monoclinic $Al_{13}Fe_4$ (b), rhombohedral $Al_{62.5}Cu_{26.5}Fe_{11}$ (c), and four icosahedral QC alloys namely $Al_{71}Pd_{19}Mn_{10}$ (d), $Al_{65}Cu_{20}Ru_{15}$ (e), $Al_{62}Cu_{25.5}Fe_{12.5}$ (f), and $Al_{70.5}Pd_{21}Re_{8.5}$ (g). For clarity, the Al 3p-counterparts are not drawn in Fig. 17.14. Only Al 3p-states in fcc-Al are shown. Within the adjustment of the Al p-bands, this figure points out that over 4 eV above E_F, the Al p-conduction band noticeably flattens as compared to that of pure Al but slightly less in the approximant than in the quasicrystalline phases above 4 eV, some oxide concentrations can modify the shape and intensity of the curves. They are flatter for the more resistive QC alloys as indicated by the values of the resistivity at room temperature given in $\mu\Omega$cm on the right side of the figure. This emphasizes the progressive loss of free-electron-like metallic character of the Al p-conduction states from fcc-Al to usual intermetallics, approximants and QCs [11].

For icosahedral QC, the XES and XAS results altogether are consistent with the hierarchy of quantum wells proposed to describe their electronic structure [33]. In this model, the electronic structure tends to acquire a (recurrent) localized character and states are concentrated into the occupied band, leaving a very flat free-electron-like conduction band [34].

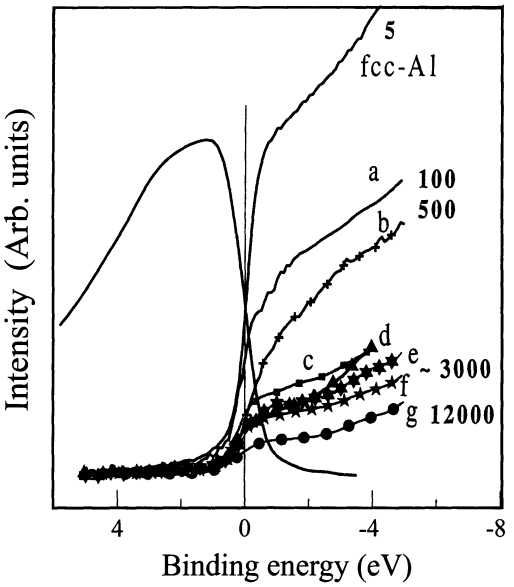

Fig. 17.14. Valence band Al 3p- and conduction band Al p-states adjusted to the same intensity at E_F in various Al-based alloys crystalline and quasicrystalline alloys (see text). The numbers indicate resistivity values in $\mu\Omega$cm, at room temperature

17.3.3 Stability of Quasicrystalline Lattices

In many intermetallics, the structural stability is mainly due to the interaction of free electrons with scattering atomic planes [32]. This mechanism was extended to amorphous metals [29,44] as well as to quasicrystals [44]. Taking usual valences such as +3 for Al, +1 for Cu, 0 for Pd, −2 for Fe or −3 for Mn (a negative effective valence accounts for the tendency to trap electrons from the Fermi sea via hybridization of TM d-states with sp-neighbors), leads to an average electron density $\langle e/a \rangle$ of 1.86 electrons per atom in the Al-TM-TM phases. This correlation holds true also for many other compounds of these systems, including a few which do not show any icosahedral order.

The Hume-Rothery (H-R) mechanism takes place when the moving electronic waves satisfy Bragg's law, i.e. when the Fermi surface (FS) comes into contact with facets of the Brillouin zone (BZ). The definition of the BZ is straightforward in crystals with short lattice parameters. It may be extended to approximants, in principle, but may have little relevance if the unit cell is too large. In QCs, a unique BZ does not exist in physical space. It is, however, possible to define a pseudo-BZ by considering only a restricted set of the most intense Fourier components of the scattering potential [26]. On practical grounds, these components may be identified with the most intense X-ray or electron diffraction peaks. In the case of Al-Pd-Mn icosahedral phases, such a pseudo-BZ (hereafter labeled also BZ for simplicity) is constructed on the $N = 18$ and 20 and M=29 and 32 peaks and forms a polyhedron of 54 facets. Figure 17.15 shows the location of the Fermi vector $2k_F$ with respect to the position K_P of the intense Bragg peaks in several Al-Cu-Fe compounds: λ-$Al_{13}Fe_4$, ω-Al_7Cu_2Fe, i-$Al_{62}Cu_{25.5}Fe_{12.5}$, θ-Al_2Cu,

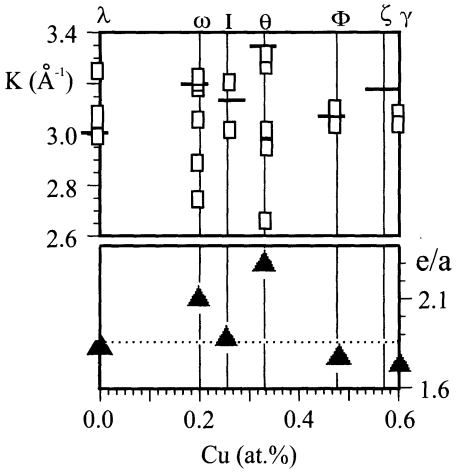

Fig. 17.15. Positions of the intense peaks (*open squares*) of several phases of the Al-Cu-Fe system (see text) and corresponding diameter of the Fermi sphere (*short horizontal lines*). Peak positions for ζ-phase are missing due to lack of structural data. Ratio e/a is given in the lower part of the figure. The *broken horizontal line* corresponds to the ratio $e/a = 1.86$ [22]

ϕ-$Al_{10}Cu_{10}Fe$, ζ-Al_3Cu_4 and γ-Al_2Cu_3. Clearly, the coincidence between $2k_F$ and K_P, i.e. a FS contacting the BZ, is not the specificity of the icosahedral phase [22].

The combined XES, XAS and XPS methodology has been applied to a series of H-R alloys with the aim to determine possible spectral characteristics induced by the H-R condition as a function of increasing isotropy of the BZ [12]. A set of binary Al-Cu-alloys has been used because the Cu d-band lies far enough from E_F so that it does not affect the FS-BZ interaction. For comparison, we have also analyzed two alloys containing Fe atoms, namely tetragonal $Al_{70}Cu_{20}Fe_{10}$ and hexagonal $Al_{10}Cu_{10}Fe$ (Φ-phase). All these H-R alloys display various atomic structures (cubic, hexagonal, rhombohedral, tetragonal and monoclinic) and e/a ratios (electron per atom ratio) ranging from 1.7 to 2.1. For these alloys, the number of contact points between the FS and the BZ varies from 56 to 16 depending on the symmetry of the structure. For each alloy, the pseudo-gap at E_F has been established, thus confirming its H-R character. The pseudo-gap is labeled by the intensity (I_{E_F}) of the Al 3p-distribution at E_F and by the energy interval Δ between the Al 3p-valence and Al p-conduction-band edges taken at half the maximum intensity of the Al 3p-sub-band. Let us recall that this energy distance is by definition 0 in pure fcc Al (and $I_{E_F} = 50\,\%$). Within the experimental uncertainties, it was found that irrespective of the composition and structural complexity of the alloy: $I_{E_F} = 37 \pm 1\,\%$ and Δ ranging between 0.5 and 0.8 eV (± 0.1 eV), except for $Al_{35}Cu_{65}$ and for $Al_{70}Cu_{20}Fe_{10}$ for which $I_{E_F} = 37$ and $34\,\%$ and $\Delta = 1.5 \pm 0.1$ and 0.9 ± 0.1 eV, respectively. For this latter alloy, the increase of the pseudo-gap width can be connected to the Al-Fe interaction near E_F. For comparison, several approximants for which the number of contact points between the FS and the BZ varies from 30 to 72 were also probed. It was found that $I_{E_F} = 16 \pm 1\,\%$ and $\Delta = 2.8 \pm 0.1$ eV for monoclinic $Al_{13}Fe_4$ and

$I_{E_F} = 27, 21, 18$ and 16 ± 1 and $\Delta = 2.5, 5.7, 6.1$, and 6.7 ± 0.1 eV for the 1/1 cubic, orthorhombic, rhombohedral and pentagonal Al-Cu-Fe approximants, respectively. Within the intensity-normalization scheme at E_F, because the maximum intensity of the Al p-sub-bands of QC is usually less than 50 %, Δ could not be measured for these samples. As to the values for I_{E_F}, they are 14, 12, 18 and 7 ± 1 % for $Al_{62}Cu_{25.5}Fe_{12.5}$, $Al_{65}Cu_{20}Ru_{15}$, $Al_{71}Pd_{19}Mn_{10}$ and $Al_{70.5}Pd_{21}Re_{8.5}$, respectively. Note that in the Al-Li-Cu system, a significant Al p-pseudo-gap also exists with $I_{E_F} = 15 \pm 1$ % for i-Al_6CuLi_3 and 18 ± 1 % for its 1/1 approximant.

Thus, the H-R and usual Al-TM-hybridization effects are not sufficient to explain the formation of the pseudo-gaps in approximants and QC. The model of recurrent localization examines this issue from its own stand-point (see Chapter 8 in this book).

17.4 Electron Energy Loss Spectroscopy

A mono energetic incident beam on a solid can be slowed down due to either elastic or inelastic collisions. When the incident energy is high enough, ionizations and excitations of the electrons of the solid may occur and inner shell electrons can be promoted to unoccupied states of appropriate symmetry. Thus, *electron energy loss spectroscopy* (EELS) allows us to explore the distribution of unoccupied states (Fig. 17.16). In addition, this spectroscopy is site selective. The energy loss is measured with respect to the elastic peak in the reflection or the transmission mode. In the transmission mode, the spectra are equivalent to those obtained using transmission photoabsorption. The spectra in the reflection mode are dominated by the mean free path of the electrons and are therefore surface sensitive. They are analogous to yield

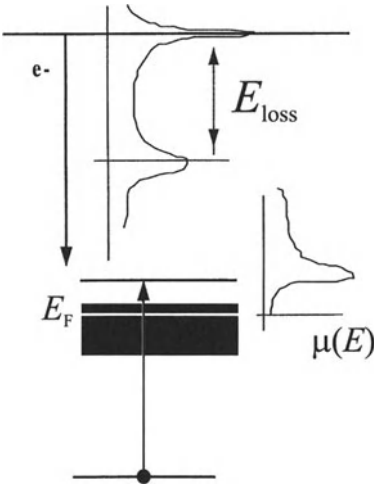

Fig. 17.16. Principle of electron energy loss spectroscopy

photoabsorption spectra. Note that when the incident electron energy is close to the energy edge, extra features may appear due to non-dipolar transitions. Note also that as for XAS, no absolute DOS values are achieved thanks to EELS measurements.

Features due to energy losses are commonly observed in XPS spectra. These are due to interactions between the outcoming electrons and the electron cloud. As a consequence, the electronic cloud oscillates which gives rise generally to a broad peak towards high binding energies of the spectra. Investigations of such plasmon features may give information about the free character of the oscillating electrons.

The EELS technique was first used with a scanning transmission microscope to study Mn L edges of quasicrystalline and crystalline $Al_{86}Mn_{14}$ alloys [26]. The Mn L spectra were rather similar except just beyond the edge (Fig. 17.17) [2]. Indeed, the intense and narrow peak in the QC came out with

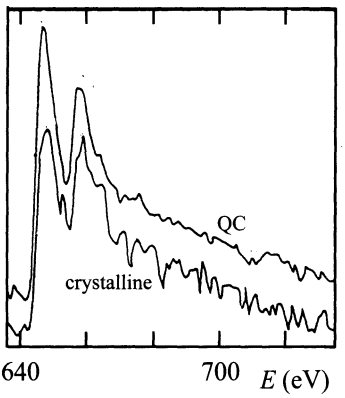

Fig. 17.17. EELS spectra around the Mn $M_{2,3}$-edge in QC and crystalline $Al_{86}Mn_{14}$ [2]

less intensity and was broader in the crystalline alloy. The authors assumed that different charge transfers from Al to Mn may have occurred in both samples, so that the d-occupancy was lower in the icosahedral phase than in the crystalline alloy.

Recently, Al s,d unoccupied states (Al L-edges) have been probed comparatively in fcc-Al, i-$Al_{65}Cu_{20}Ru_{15}$, d-$Al_{70}Ni_{15}Co_{15}$ and $Al_{70}Ni_{20}Rh_{10}$ [63] with an energy resolution of 0.12 eV. The alloys were characterized by high-resolution microscopy imaging and electron-diffraction patterns. The EELS spectra for the alloys differ noticeably from that of the pure metal (Fig. 17.18) [63]. For fcc-Al, the steep and intense L_I-edge is followed by L_{II} and then by a rather smooth, monotonous increase of intensity with small wavy features. In the QCs, the edge is also straight but of low intensity. It is followed by a series of oscillations and exhibits a marked maximum at about 2 V from the edge. The authors concluded the presence of a pseudo-gap at E_F. The comparison between fcc-Al and alloys indicates an important depletion of Al-

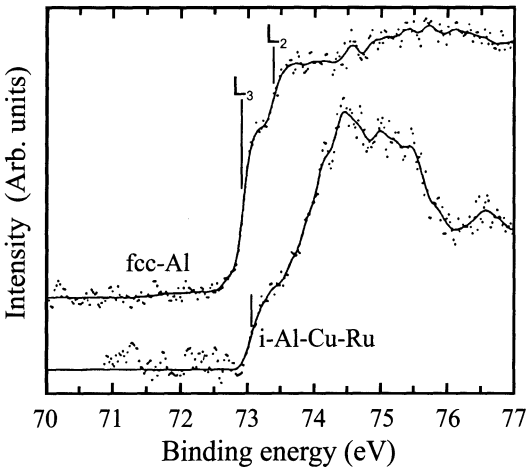

Fig. 17.18. Al EELS-spectra of $Al_{65}Cu_{20}Ru_{15}$ and of fcc-Al in the energy range 70-77 eV [63]

conduction states just beyond the edge [63]. These data, which correspond to Al s,d-conduction states, are fully in line with the XAS results presented in the previous section for Al p CB states.

The electronic structure of crystalline AlPd (CsCl-structure) and of i-$Al_{70}Pd_{20}Mn_{10}$ has been investigated by XPS and EELS measurements [74]. These show very clear similarities. Therefore, the Al-Pd interaction appears essential in these alloys. Although the Al-Mn interaction causes minor changes in the VB structure, the role of Mn 3d electrons could be important to stabilise the icosahedral structure. On the other hand, plasmon energy losses due to the excitation of Al s,p electrons have been observed to be very weak. Therefore, this indicates that Al-states in the alloys have lost the nearly free electron character they have in fcc-Al, being thus more localised in both AlPd and the quasicrystal (Fig. 17.19) [74].

17.5 Optical Measurements

It is not the purpose of this chapter to deal with details of optical spectroscopy. Valuable information can be found in many text books (see, for example, [70]). Nevertheless, optical measurements are developing nowadays which are worth summarizing here.

Optical investigations of solids use photons of energies up to tens of eV. The measurements are carried out in transmission or in reflection mode so that the sampled depth is of the order of a few nm, depending on the material. The experimental data allow us to determine the complex dielectric constant $\varepsilon(\omega)$ of the sample by appropriate treatments such as the classical Kramers–Kronig analysis [40]. The complex dielectric constant accounts for the response of the sample to the electromagnetic field to which it is subjected. Thus, investigations over a wide range of frequencies may provide data

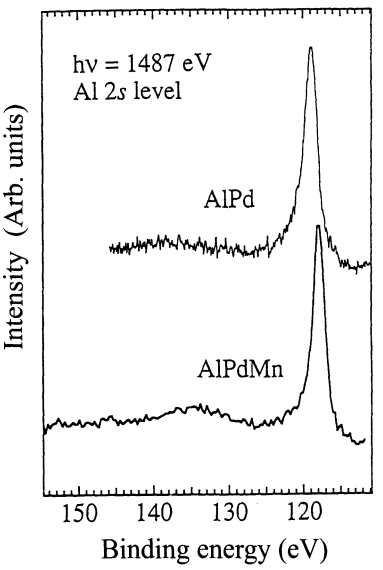

Fig. 17.19. Plasmon losses in the XPS Al 2s-core-level spectra of AlPd (*top*) and $Al_{70}Pd_{20}Mn_{10}$ (*bottom*) [74]

about the excitation spectrum of the solid (phonons, electronic transitions, etc). Two important contributions are involved in $\varepsilon(\omega)$. One is due to intraband transitions of conduction electrons which can be analyzed using the Drude model for free electrons [23]. This depends on the plasma frequency associated with the conduction electrons. The second contribution is due to transitions involving both VB and CB. No direct information about the occupied or unoccupied DOS is obtained. Analysis of the spectra requires some modeling to carefully compare with the experimental data. Note that for energies lower than the limit of intraband transitions to happen, only interband transitions can be investigated.

Preliminary results were obtained in the energy range 0.5 to 6 eV for Al-Mn alloys prepared by ion beam mixing of Al/Mn multilayers with 19 at.% and 24 at.% Mn. The spectra showed dominant Mn d states and suggested an asymmetrical narrowing of the Mn d distribution with respect to the pure metal [27]. The infra-red properties of quasicrystalline Al-Mn films and of the i-$Al_{64}Cu_{22}Fe_{14}$ sample which contained 5 to 6 % of residual crystalline phase, were interpreted in terms of a low DOS at E_F in relation to a tendency to localization of these states [43]. The electrodynamic response of bulk single-phase samples of i-Al-Cu-Fe, Al-Mn-Si and i-Al-Pd-Mn as well as d-Al-Co-Cu and i-Al-Co-Cu-Si quasicrystals within a broad energy range, corresponding to frequencies between few cm^{-1} up to 105 cm^{-1} [3,21] (Figs. 17.20 and 17.21).

Unlike in disordered metals or semiconductors, the spectra of the icosahedral phases display low optical conductivity in the infra-red energy range and a marked absorption in the visible (around 104 cm^{-1}). This strong absorption is connected to electronic interband transitions and has been ascribed to

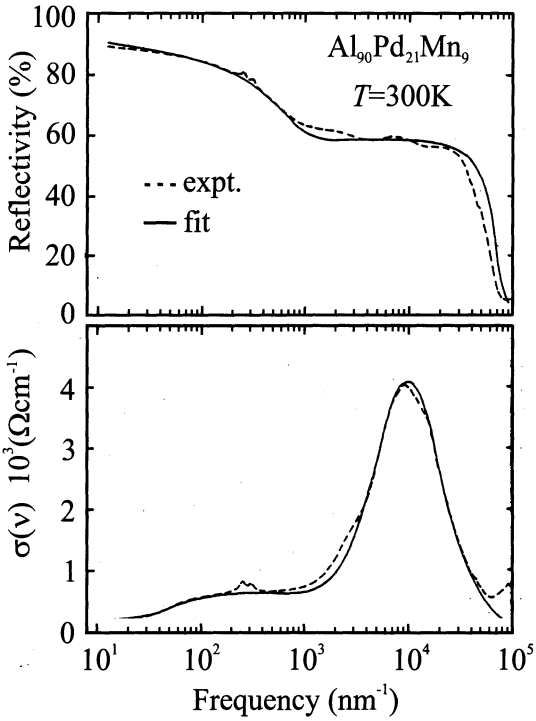

Fig. 17.20. (**a**) The reflectivity spectrum $R(\nu)$ of i-Al-Pd-Mn at 300 K in the frequency range up to $105\,\mathrm{cm}^{-1}$, (**b**) the optical conductivity obtained by Kramers–Kronig transformation [27]

excitations across the pseudo-gap at E_F. These measurements suggest for instance that i-$Al_{70}Pd_{21}Mn_9$ resembles other materials which actually present a real energy gap.

On the other hand, results for highly ordered i-$Al_{70}Pd_{20}Re_{10}$ and Al_2Ru [4] show strong similarities; in the high-frequency range, their behavior is reminiscent of semiconductors.

However, remarkable differences appear between both alloys in the low-frequency (thus low-temperature) properties. This is interpreted by arguing that electronic states are localized deep into the band gap of the quasicrystal in spite of the free-carrier density. Note that XES measurements on both alloys have also shown strong similarities of the Al 3p electronic distributions and have pointed out the occurrence of an extremely low intensity in the vicinity of E_F [25]. For the decagonal phases [3], differences are clearly established between the quasicrystalline and the periodic directions. It is suggested that this is due to the dense filling of reciprocal space in the quasiperiodic planes. In some respect, the conductivity resembles that of disordered and amorphous metals. The analysis of the optical data shows that contrary to the icosahedral quasicrystals, there is no clear evidence for the presence of a marked pseudo-gap at E_F. Finally, comparison between icosahedral and decagonal QC and amorphous alloys suggests that localization of the electronic

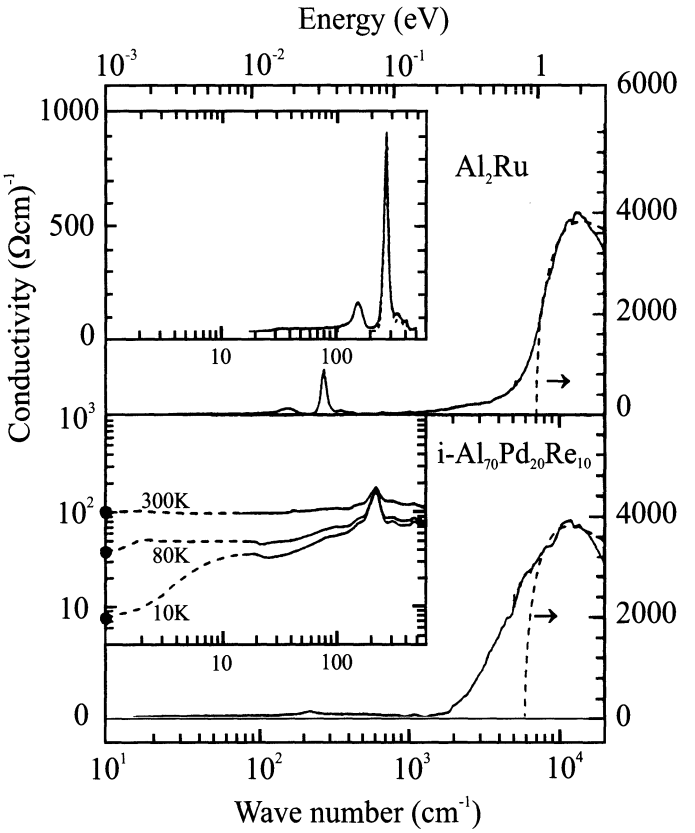

Fig. 17.21. *Top panel*: Optical conductivity of Al_2Ru. *Inset*: far infra-red conductivity at room temperature (*solid line*) and 10 K (*dashed line*). *Bottom panel*: optical conductivity of i-Al-Pd-Re. *Inset*: far infra-red conductivity. *Dashed lines*: regions of Kramers–Kronig interpolations [3]

states in QC is the most obvious in the highly ordered QC and disappears in the amorphous state.

17.6 Conclusion

In this chapter, I have concentrated on various spectroscopies that have been extensively used to investigate QC since their discovery [54]. There is a consensus nowadays on the results: the occurrence of a pseudo-gap at E_F as well as the tendency to weak electron localization. As mentioned in the introduction, all such studies of quasicrystalline alloys aimed at improving our knowledge of the electronic structure but also sought a specific signature of the quasicrytalline order. Thus, comparison with crystalline alloys was mandatory. In this respect the occurrence of a pseudogap at E_F as well as the

tendency to weak electron localization have been reported for crystalline alloys as well.

To go a step further, it is still essential to investigate systematically not only quasicrystals and their elemental constituents but also the many compounds belonging to the same system, including binary alloys and amorphous samples. Only such methodic studies will allow us to ascertain in which aspects quasicrystals may have any specificity that differentiates them from other intermetallics.

Bulk electronic properties of quasicrystals, such as the very high resistivity, are especially manifest at low temperatures. Thus, for a meaningful understanding, it is necessary to perform the DOS investigations within the same temperature ranges. Similarly, at high temperature, the ductility of QC and/or the fast atomic movements pointed out by inelastic neutron scattering or atomic transport measurements [20,36] are indications that DOS studies should also be relevant. Therefore, it appears essential to continue experimentations and, indeed, it might be profitable to use various complementary spectroscopy techniques to investigate the same series of samples.

Acknowledgment

I am indebted to J.M. Dubois, D. Mayou, U. Mizutani and G. Trambly de Laissardière for stimulating discussions. I thank Z. Dankhazi, V. Fournée and A. Sadoc for participating to the SXS measurements. This work has been supported in part by the Austrian Ministry of Research, East West Co-operation programme, under the title "Soft X-ray Emission Spectroscopy of Metallic Systems". I gratefully acknowledge Professor H. Kirchmayr's and Doctor H. Müller's hospitality at the Technical University in Vienna.

This paper is dedicated to Hans-Ude Nissen on the occasion of his 65th birthday.

References

1. Acker J.F. van, Lindeyer E.W., Fuggle J.C. (1991): J. Phys.: Condens. Matter **3**, 9579
2. Bahadur D., Gaskell P.H., Imeson D. (1987): Phys. Lett. A **120**, 417
3. Basov D.N., Timusk T., Barakat F., Greedan J., Grushko B. (1994): Phys. Rev. Lett. **72**, 1937
4. Basov D.N., Pierce F.S., Volkov P., Poon S.J., Timusk T. (1994): Phys. Rev. Lett. **73**, 1865
5. Bonnelle C. (1987): *X-ray Spectroscopy. Annual Report C, The Royal Society of Chemistry.* London, pp. 201–272, Agrawal, B. K. (1979): *X-ray Spectroscopy. An Introduction.* Springer Verlag, Berlin
6. Belin E., Dankhazi Z., Sadoc A., Calvayrac Y., Klein T., Dubois J.M. (1992): J. Phys.: Condens. Matter **4**, 4459, Belin E., Dankhazi Z. (1993): J. Non-Cryst. Solids. **153&154**, 298

7. Belin E., Dankhazi Z., Sadoc A., Dubois J.M. (1994): J. Phys.: Condens. Matter **6**, 8771
8. Belin E., Miyoshi Y., Yamada Y., Ishikawa T., Matsuda T., Mizutani U. (1994): Mater. Sci. Eng. A **181&182**, 730
9. Belin-Ferré E., Dankhazi Z., Fournée V., Sadoc A., Berger C., Müller H. Kirchmayr H. (1996): J. Phys.: Condens. Matter **8**, 6213
10. Belin-Ferré E., Dankhazi Z., Sadoc A., Berger C., Müller H., Kirchmayr H. (1996): J. Phys.: Condens. Matter **8**, 3513
11. Belin-Ferré E., Dubois J.M. (1996): J. Phys.: Condens. Matter **8**, L717–23 and references therein
12. Belin-Ferré E., Fournée V., Dubois J.M. (1997): In *New Horizons in Quasicrystals: Research and Applications*, eds. A.I. Goldman, D.J. Sordelet, P.A. Thiel, J.M. Dubois. World Scientific, Singapore, p. 9
13. Belin-Ferré E., Fournée V. Y., Dubois J.M. *submitted to J. Phys.: Condens. Matter*
14. Berger C., Belin E., Mayou D. (1993): Annales de Chimie Fr., **18**, 485
15. Berger C. (1994): *Electronic properties of quasicrystals. Experimental Lectures on quasicrystals*, eds. F. Hippert, D. Gratias, Les Editions de Physique, les Ulis p. 463
16. Boudard M., Boissieu M. de, Simon J.P., Berar J.F., Doisneau B. (1996): Philos. Mag. Lett. 74, 429
17. Bruhwiller P.A., Wagner J.L., Biggs B.D., Shen Y., Wong K.M., Schnatterly S.E., Poon S.J. (1988): Phys. Rev. B **37**, 6529
18. Chang S-L., Chin W. B., Zhang C-M., Jenks C.J., Thiel P.A. (1995): Surf. Sci. **337**, 135
19. Chang S-L., Anderegg J.W., Thiel P.A. (1996): J. Non-Cryst. Solids **195**, 95
20. Coddens G. (1993) Ann. Chim. Fr. **18**, 513
21. Degiorgi L., Chernikov M.A., Beeli C., Ott H.R. (1993): Solid State Commun. **87**, 721
22. Dong C., Perrot A., Dubois J.M., Belin E. (1994): in *Quasicrystals and Imperfectly Ordered Crystals*, eds. K.H. Kuo, S. Takeuchi, Trans. Tech. Publications Switzerland, Germany, UK, USA, p. 403
23. Drude P. (1900): Annalen der Physik **1**, 566 and **3**, 369
24. Ederer D.L., Schaefer R., Tsang K.L., Zhang C.H., Calcott T.A., Arakawa E.T. (1988): Phys. Rev. B **37**, 8594
25. Fournée V., Belin-Ferré E., Trambly de Laissardière G., Sadoc A., Volkov P., Poon S.J. (1997): J. Phys.: Condens. Matter, **9**, 7999
26. Friedel J. Dénoyer F. (1987): C. R. Acad Sci. série II. **305**, 171, Friedel, J. (1988): Helvetica Acta. **61**, 538
27. Frigerio J.M. Meddour A. (1988): Mater. Sci. Eng. **99**, 361
28. Fujiwara T.(1989): Phys. Rev. B **40**, 942
29. Häussler P. (1992): Phys. Rep. **222**, 68
30. Hafner J., Krajci M. (1992): Phys. Rev. Lett. **68**, 2321
31. Hafner J., Krajci M. (1993): Phys. Rev. B **47**, 11795
32. Hume-Rothery W. (1926) J. Inst. Met. 35, 295, Hume-Rothery, W., Raynor, GV, (1954) *The Structure of Metals and Alloys.* The Institute of Metals. London, Jones H. (1937) in Proc. Phys. Soc. A 49, 250 and (1960) *Theory of Brillouin Zones and Electronic States in Crystals.* North Holland, Amsterdam
33. Janot C. Boissieu M. de (1994): Phys. Rev. Lett. **72**, 1674

34. Janot C. (1997): J. Phys.: Condens. Matter. **9**, 1493
35. Jenks C.J, Chang S-L., Anderegg J.W., Thiel P.A., Lynch D.W. (1996): Phys. Rev. B **54**, 6301
36. Joulaud J.L., Bernardini J., Gas P., Dubois J.M., Calvayrac Y., Gratias D. (1997): Philos. Mag. A **75**, 1287
37. Krause M.O., Oliver J.H. (1979): J. Phys. Chem. Ref. Data **8**, 329.
38. Krajci M., Hafner J., Mihalkovic M. (1997): Phys. Rev. B **55**, 843
39. Krajci M., Windisch M., Hafner J., Kresse G., Mihalkovic M. (1995): Phys. Rev. B **51**, 17355
40. Landau L.D., Lifshitz E.M. (1960): *Electrodynamics of Continuous Media.* Addison-Wesley, Reading, Mass.
41. Léonard P. (1978): J. Phys. F **8**, 467, Papaconstantopoulos D.A. (1986): *Handbook of the Band Structure of Elemental Solids,* Plenum Press, New York
42. Ley L., Cardona M. (1979): *Topics on Applied Physics, Photoemission in solids I and II.* Springer Verlag, Berlin
43. Macko D. Kasparova M. (1993): Philos. Mag. Lett. **67**, 307
44. Massalki T.B. Mizutani U. (1978): Prog. Mater. Sci. *22*, 152
45. Matsubara H., Ogawa S., Kinoshita K. Kishi K., Takeuchi S., Kimura K., Suga S. (1991): Jpn. J. Appl. Phys. **30**, L 389
46. Mizutani U., Yamada Y., Takeuchi T., Belin E., Sadoc A., Yamauchi M. Matsuda T. (1994): J. Phys.: Condens. Matter **6**, 7335 and references therein
47. Mori M., Matsuo S., Ishimasa T., Matsuura T, Kamiya K., Inokuchi H., Matsukawa T. (1991): J. Phys.: Condens. Matter **3**, L767
48. Nguyen Mahn D., Trambly de Laissardière G., Julien J.P., Mayou D., Cyrot–Lackmann F. (1992): Solid State Commun. **82**, 329
49. Nozières P., de Dominicis C.T. (1969): Phys. Rev. **178**, 6105
50. Pinheiro P.J., Chang S-L., Anderegg J.W., Thiel P.A. (1997): Philos. Mag. B **75**, 271
51. Quiquandon M., Quivy A.J., Faudot F., Säadi N., Calvayrac Y., Lefebvre S., Bessière M. (1995): in *Proc. 5th Int. Conf. Quasicrystals*, eds. C. Janot, R. Mosseri, World Scientific, Singapore 152
52. Quiquandon M., Quivy A., Devaud J., Faudot F., Lefebvre S., Bessière M., Calvayrac Y. (1996): J. Phys.: Condens. Matter **8**, 2487
53. Sadoc A., Belin E., Dankhazi Z., Flank A.M. (1993): J. Non-Cryst. Solids **153&154**, 338
54. Shechtman D., Blech I., Gratias D., Cahn J.W. (1984): Phys. Rev. Lett. **53**, 1951
55. Stadnik Z.M., Stroink G. (1993): Phys. Rev. B **47**, 100
56. Stadnik Z.M., Zhang G.W., Tsai A.P., Inoue A. (1994): J. Phys.: Condens. Matter **6**, 6885
57. Stadnik Z.M., Zhang G.W., Tsai A.P., Inoue A. (1994): Phys. Rev. B **50**, 6696 and references therein
58. Stadnik Z.M., Zhang G.W., Tsai A.P., Inoue A. (1995): Phys. Rev. B **51**, 11358
59. Stadnik Z.M., Purdie D., Garnier M., Baer Y., Tsai A.P., Inoue A., Edagawa K., Takeuchi S., Buschow K.H.J. (1997): Phys. Rev. B **55**, 10938
60. Takeuchi T., Mizutani U. (1995): Phys. Rev. B **52**, 9300 and references therein
61. Takeuchi T., Yamada Y., Mizutani U., Honda Y., Edagawa K., Takeuchi S., (1995): in *Proc. 5th Int. Conf. Quasicrystals*, eds. C. Janot, and R. Mosseri, World Scientific, Singapore, 534

62. Terakura K. (1977): J. Phys. F: Metal Phys. **7**, 1773
63. Terauchi M., Tanaka M., Tsai A.P., Inoue A., Masumoto T. (1996): Philos. Mag. Let. **74**, 107, Terauchi M., Ueda H., Tanaka M., Tsai A.P., Inoue A., Masumoto T. (1997): Quasicrystals, Yamada Conference XLVII, *Proc. 6th Int. Conf. on Quasicrystals*, eds. S. Takeuchi and T. Fujiwara, World Scientific, Singapore, 587
64. Trambly de Laissardière G., Fujiwara T. (1994): Phys. Rev. B **50**, 5999
65. Trambly de Laissardière G., Fujiwara T. (1994): Phys. Rev. B **50**, 9843
66. Trambly de Laissardière G., Fujiwara T. (1994): Mater. Sci. Eng. A **181&182**, 722
67. Trambly de Laissardière G., Nguyen Mahn D., Magaud L., Julien J.P., Cyrot-Lackmann F., Mayou D. (1995): Phys. Rev. B **52**, 7920
68. Trambly de Laissardière G., Dankhazi Z., Belin E., Sadoc A., Nguyen Mahn D., Mayou D., Keegan M.K., Papaconstantopoulos D.A. (1995): Phys. Rev. B **51**, 14035
69. Traverse A., Dumoulin L., Belin E., Sénémaud C. (1988): in *Quasicrystalline Materials*, eds. C. Janot and J.M. Dubois, World Scientific, Singapore, 399
70. Wooten, F., (1972): *Optical Properties of Solids*, Academic Press, London New York
71. Wu X., Kycia S.W., Olson C.G., Benning P.J., Goldman A.I., Lynch D.W. (1995): Phys. Rev. Lett. **75**, 4540
72. Yamaguchi, S., Takeuchi, T., Yamada, Y., Mizutani U., Nakashima T., Matsuda T. (1995): *in Proc. 5th Int. Conf. on Quasicrystals*, eds C. Janot, R. Mosseri, World Scientific, Singapore, 548
73. Zurkirch M., Atrei A., Hochstrasser M., Erbudak M., Kortan A.R. (1996): J. Electron Spectrosc. Relat. Phenom. **77**, 233
74. Zurkirch M., Atrei A., Hochstrasser M., Erbudak M., Kortan A.R. (1996): J. Electron Spectrosc. Relat. Phenom. **77**, 233, Zurkirch M., De Crescenzi M., Erbudak M., Hochstrasser M., Kortan A.R. (1997), Phys. Rev. B **55**, 8808
75. Zijlstra E.S, Janssen T. (2000): Communications at the joint Colloqium CINQ and SPQK. Quasicrystals, Jülich, 2000

18 Electronic Transport Properties of Quasicrystalline Thin Films

Roland Haberkern

Summary. Quasicrystals are assumed to be electronically stabilized by a Hume-Rothery type mechanism. This explains most of the peculiar properties of quasicrystals. The stabilization is investigated by electronic transport properties, as they depend sensitively on the stabilizing interaction between the static structure and the conduction electrons.
Thin-film techniques provide samples which are well suited for systematic investigations as a function of composition and structural quality for Al-Cu-Fe and Al-Pd-Re *i*-phases. For a narrow range of composition, large transport anomalies occur, reaching a metal-insulator transition in thin films of *i*-Al-Pd-Re. We discuss this in the framework of a resonant scattering of the conduction electrons with the quasicrystalline structure, leading to a reduced electronic mobility and density of states (DOS) at the Fermi energy E_{F}.

18.1 Introduction

Electronic transport properties (see also [24,29]) as for example the electrical conductivity, the thermopower, as well as the Hall effect, are of particular interest due to their sensitivity to the interrelation between the atomic structure and electronic system. As described in more detail in [14], a correspondence between the wavelength of the conduction electrons at E_{F} and a frequently occurring distance in the atomic system leads to resonance-like interaction, causing an energy-lowering of the electronic system. This behavior can, on one hand, stabilize an atomic structure like the quasicrystalline one and, on the other, it modifies the electronic system so that transport anomalies arise. Stable quasicrystals can exhibit transport properties which can neither be described as metallic nor as semiconducting (activated behavior) as shown in Fig. 18.9. The anomalies can be strong enough to cause a metal-insulator transition (MIT) in icosahedral Al-Pd-Re [23].

First investigations on quasicrystalline thin films were performed in order to investigate properties which could be relevant for technical applications, as for example mechanical, tribological and corrosion properties [21,28]. Additionally, thin films were used to measure transport properties, because of two reasons: first of all, thin films show a much higher electrical resistance than bulk samples and allow a much easier and more precise determination of the resistivity. Films were used to determine the very small magnetoresistance at

J.-B. Suck et al. (eds.), *Quasicrystals*
© Springer-Verlag Berlin Heidelberg 2002

low magnetic fields, which is useful to interpret some transport anomalies in the framework of quantum corrections [19]. Secondly, some work was performed to investigate the transition from three to two-dimensional behavior as a function of film thickness [30].

We want to show here that thin quasicrystalline films do not differ substantially from bulk materials, but offer many advantages with respect to the preparation as well as to measuring electronic transport properties. Additionally, thin films can be prepared in the amorphous phase (a-phase) and crystallized afterwards into the icosahedral phase (i-phase) without the intermediate formation of crystalline counterparts. Accordingly, one sample allows the comparison of the quasicrystalline with the amorphous phase as well as the investigation of the transition between both.

Thin-film techniques provide samples which are well suited for systematic investigations as a function of composition and structural quality. We show that for a narrow range of composition large transport anomalies occur, up to insulating films for i-Al-Pd-Re. We discuss this in the framework of resonant scattering of the conduction electrons with the quasicrystalline structure, causing a reduced electronic mobility and DOS at E_{F}.

We should address the question of which films are denoted as thin. The thickness should be compared to the length scales of structural units or relevant physical lengths. The smallest structural units, namely the building clusters of quasicrystals are of order 1 nm [17]. As clusters are self-similar, an upper limit for cluster sizes is not easy to specify, but 20 nm is a value of a quite large cluster shown in [16,17]. Most of the relevant length scales of physical mechanisms are much shorter. The electronic scattering length for example is in the order of some atomic distances in the case of elastic scattering (intrinsic to good quasicrystals), while the inelastic scattering length increases with decreasing temperature and can reach $l_{\mathrm{i}} = 10^2\mathrm{nm}$ at $T = 1\,\mathrm{K}$ [7]. From this it can be concluded that the thickness of a typical film is well inside the regime where three-dimensional behavior can be expected. A film may be called "thin" when it is prepared by a deposition process from the vapor phase.

Very thin films with a thickness starting at about $d = 10$ nm were produced as selective solar absorbers [4]. It is not clear if films of such a thickness are homogeneous or behave more like a percolating network. Therefore, samples for electronic transport measurements cover the thickness range $30 < d < 1000$ nm. The thickness of coatings for technical applications is much higher, up to 200 μm [21].

18.2 Preparation of Thin Quasicrystalline Films

The films considered here are prepared by evaporation or sputtering from one or more sources onto substrates at different temperatures. Two routes are possible: homogeneous samples may be prepared directly, or crystalline

multilayers of the different components may be prepared first, followed by extensive heat treatment. While the first technique can lead directly to quasicrystalline (qc) films (if deposited at a sufficiently high temperature), the second needs interdiffusion between the layers and a solid state reaction to form a qc film. The first films for conductivity measurements were fabricated with the second technique by a sequential sputtering technique of Al, Fe, and Cu. As the thickness of each layer could be controlled by a quartz oscillator with high accuracy, the overall composition has been adjusted such that the narrow range of the i-phase in the phase diagram was reached [6,19]. Some groups have prepared thin films of Al-Cu-Fe by sputtering from a composite or area-sectional target [3,4]. This results in samples with homogeneous composition and can lead to amorphous films if the substrate temperature is held below $T \approx 500\,\mathrm{K}$ and to qc films for $T > 750\,\mathrm{K}$. The amorphous films could be transformed to the qc state (780 K) via a cubic phase (T_{cryst}=580 K) by an appropriate heat treatment [3]. A problem of this technique in order to gain samples with systematically varying compositions is the need of an individual target for each composition desired.

The evaporation of a master alloy by an electron beam is another method which has been used [30]. Here the films have compositions which are different from the master alloy and have to be determined afterwards.

In the present chapter we report on a sequential flash-evaporation technique (Fig. 18.1) in order to prepare amorphous Al-Cu-Fe samples with an exactly defined stochiometry as a precursor for the qc phase. Grains of a premolten master alloy of the correct composition are fed to a hot tungsten filament where they flash evaporate. As each grain contributes one monolayer or less to the film thickness, even a complete segregation finally ends up with a homogeneous film of the nominal composition. As a second technique for Al-Pd-Re we use co-sputtering with two magnetron sources (Fig. 18.2a). Due to the positions of the two sources with respect to the substrate a de-

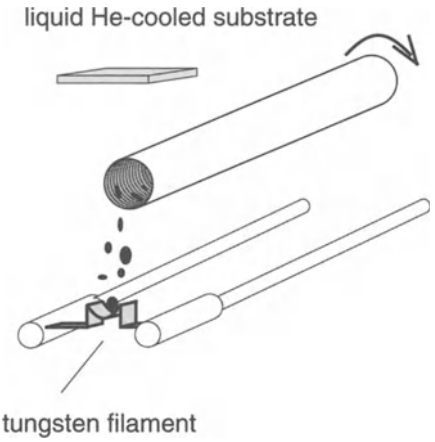

Fig. 18.1. Sketch of sequential flash evaporation

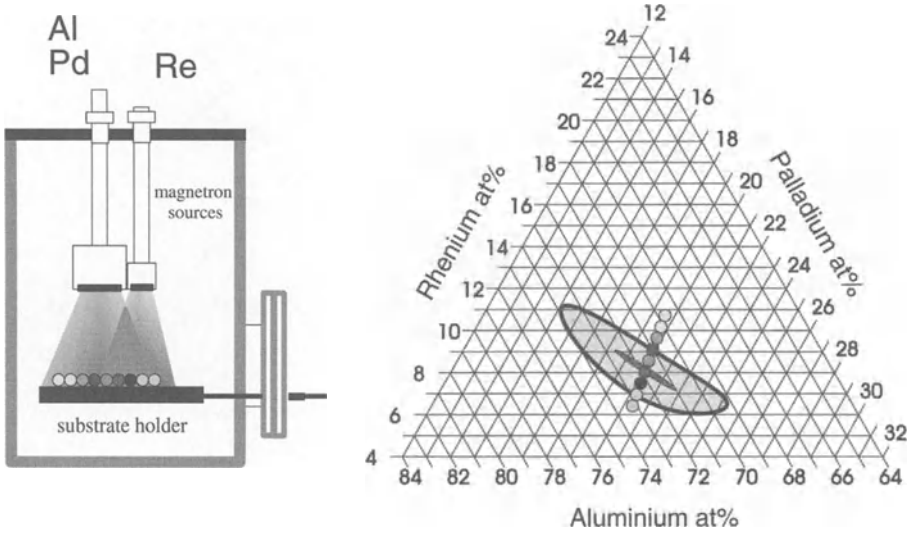

Fig. 18.2. Sketch of the co-sputtering device **(a)** and a part of the ternary phase diagram **(b)** showing the presumed area of the *i*-phase (shadowed) and a sequence of samples co-sputtered in one deposition step

fined composition gradient can be achieved along the substrate. With the latter technique in one preparation process a set of amorphous samples can be produced consisting of about 20 samples with a composition, slightly and systematically changing from one sample to the next, cutting the ternary phase diagram at, or close to the optimal composition (Fig. 18.2b). A defined shape of the evaporated or sputtered samples can be achieved by applying a mask or a structuring technique using microelectronic technologies, respectively. This allows one to determine the absolute resistivity, which is difficult for most bulk samples because of their irregular shape and brittleness.

18.3 Amorphous to Quasicrystalline Transition

The amorphous state prepared by quenching of the vapor phase onto a cooled substrate is structurally similar to the liquid phase. Therefore, a direct transition from the amorphous to the qc phase is possible for films at appropriate composition. In contrast to the transition from the liquid to the quasicrystal, the transition from the amorphous to the qc state is irreversible and occurs at much lower temperatures. Figure 18.3a shows the resistivity of a thin film of Al-Cu-Fe deposited by sequential flash evaporation onto a substrate cooled down to $T = 4.2\,\mathrm{K}$. The resistivity of the amorphous state at this temperature is $\rho(4.2\,K) = 300\,\mu\Omega\mathrm{cm}$ and increases to a value of $\rho(4.2\,K) = 470\mu\Omega\mathrm{cm}$ after annealing up to $T = 550\,\mathrm{K}$. This behavior is discussed later. Besides

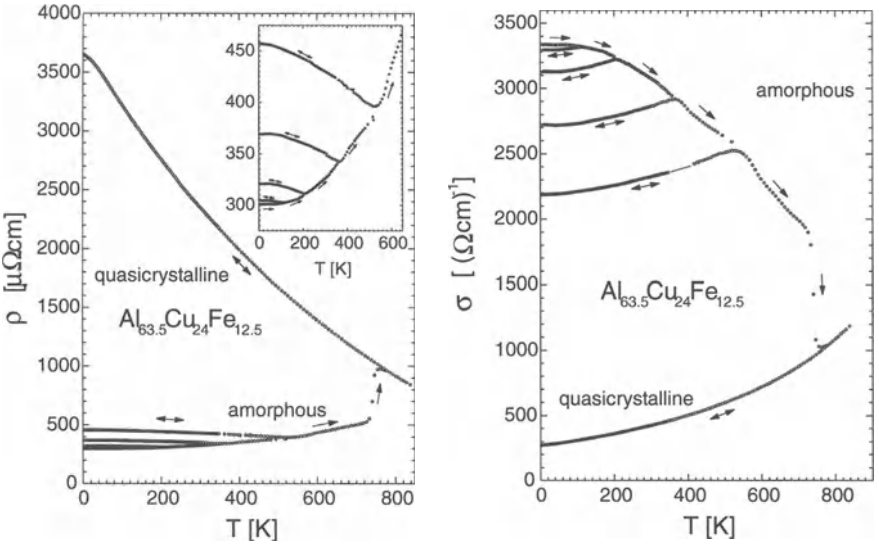

Fig. 18.3. Electrical resistivity **(a)** and conductivity **(b)** of a thin film of Al-Cu-Fe prepared at $T = 4\,\mathrm{K}$ in the amorphous state. After some annealing steps in the still amorphous sample (enlarged in the inset) the crystallization to the i-phase occurs at $T = 760\,\mathrm{K}$ [9]

the quite small and continuous irreversible increase of the resistivity and its temperature coefficient, a distinct increase related to the direct transition from the a- to the i-phase can be seen at $T \approx 740\,\mathrm{K}$. Above, the sample is icosahedral as shown by electron diffraction [11]. The transition temperature is about 350 K lower than the solidus temperature of the same system. This offers new possibilities. First, the transition happens within the solid phase and allows the measurement of electronic transport properties at the transition (Fig. 18.4). Second, the transition plotted in Fig. 18.3 shows no indication of the formation of crystalline phases like the cubic β- or τ-phases which occur whenever an Al-Cu-Fe melt is cooled down from the liquid state by melt-spinning or conventional casting. Therefore, in films produced via the amorphous route no long-term annealing treatments (typically some hours at $T = 1050\,\mathrm{K}$ for bulk samples) are necessary for removing crystalline phases. Third, the transition from the a- to the qc-phase happens not only at low T but also on short time scales in the order of minutes. Figure 18.4 shows this transition of $Al_{63.5}Cu_{24}Fe_{12.5}$ films for different heating rates. Together with a low surface roughness achieved by this preparation, this may have consequences for technical applications of qc coatings.

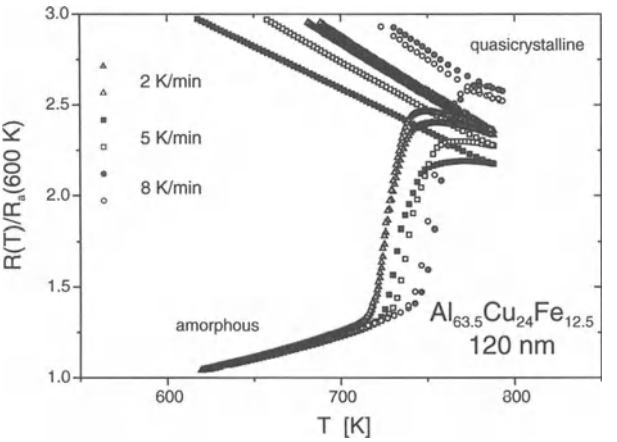

Fig. 18.4. Normalized electrical resistivity of Al-Cu-Fe as a function of the heating rate for the transition from the amorphous to the icosahedral phase [11]

18.4 Comparing the a- with the i-Phase – The Scattering Approach

The preparation of qc thin films via the route of the *a*-phase offers the possibility of comparing directly the electronic system of the isotropic amorphous with the nearly isotropic quasicrystalline phase in one and the same sample.

The conductivity of very different quasicrystals, stable ones with strong transport anomalies like *i*-Al-Cu-Fe, *i*-Al-Pd-Mn, or *i*-Al-Pd-Re, as well as simple ones (without *d*-states at the Fermi level) with much smaller transport anomalies like *i*-Al-Mg-Zn have often been described by an inverse Matthiessen rule. That means that their T-dependencies of the conductivity $\sigma(T)$ are claimed to be the sum of the conductivity σ_0 at $T \rightarrow 0\,\mathrm{K}$ which depends on the particular system, its composition and structural quality, and on a temperature-dependent increase $\Delta\sigma(T)$ which is very similar for all qc phases and samples:

$$\sigma(T) = \sigma_0 + \Delta\sigma(T).$$

This behavior is inverse to that of ordinary metals, where the electrical resistivity instead of the conductivity shows a comparable behavior. Astonishingly, Fig. 18.3b (conductivity) shows a parallel behavior of the curves belonging to the amorphous and the icosahedral phases. Accordingly, also the behavior of the *a*-phase can be described by the inverse Matthiessen rule, suggesting a strong similarity between the amorphous and the quasicrystalline phases.

For quasicrystals theories exist which are based on the particular features of the quasicrystalline structure and its relation to the electronic system; for example, a scattering-induced electronic hopping between badly propagating

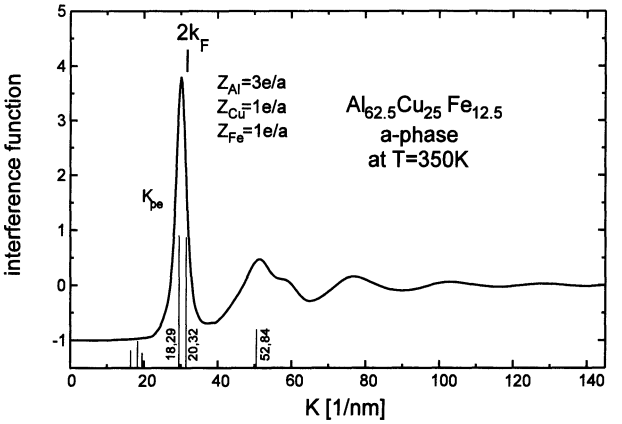

Fig. 18.5. Electron diffraction of an amorphous $Al_{62.5}Cu_{25}Fe_{12.5}$ film (20 nm) in comparison with the position of major *i*-Al-Cu-Fe peaks [9]

electronic states [22], the localization tendency of electrons in self-similar clusters [16,17] or a temperature dependent change of the band structure due to the decrease of elastic Bragg scattering at higher temperatures [8]. These models can explain only a few aspects of electronic transport as for example the inverse Matthiessen rule. A different approach to understand the unexpected properties of quasicrystals is motivated by the electronic stabilization of their peculiar structure. This is due to the interaction between the electrons at the Fermi level (characterized by $2k_F$) and the structure (characterized by the Jones zone diameter k_{pe}). Such behavior corresponds to the Hume-Rothery mechanism in periodic crystals [18,15] and was first discussed for quasicrystals by Smith and Ashcroft [27] and Friedel [5]. This description is obvious as the Jones zone of a quasicrystal (Fig. 18.6b) consists of many flat areas and hence can interact with a spherical Fermi surface in many directions. Figure 18.5 shows that the strongest peaks of the *i*-phase are at the position of the electronically induced peak of the *a*-phase [9]. This suggests that the size of the Jones zone as well as its shape (see Fig. 18.6) is very similar for the *a*- and the *i*-phase. It has been shown [13] that the stability and many other properties of a large class of amorphous systems can be understood by such an interaction. Thin films are well suited to investigate this aspect because they allow the comparison of the amorphous with the quasicrystalline state in one sample. Electronic transport properties of films can be measured in situ up to elevated temperatures due to easy preparation techniques and high contact stability.

The interaction between the electronic and atomic systems is based on the elastic scattering of electrons with the Fermi wavenumber ($k = k_F$) at a pronounced peak in the structure factor $S(2k_F)$ describing the atomic structure. The elastic (Bragg-like) scattering of electrons not only reduces the mean

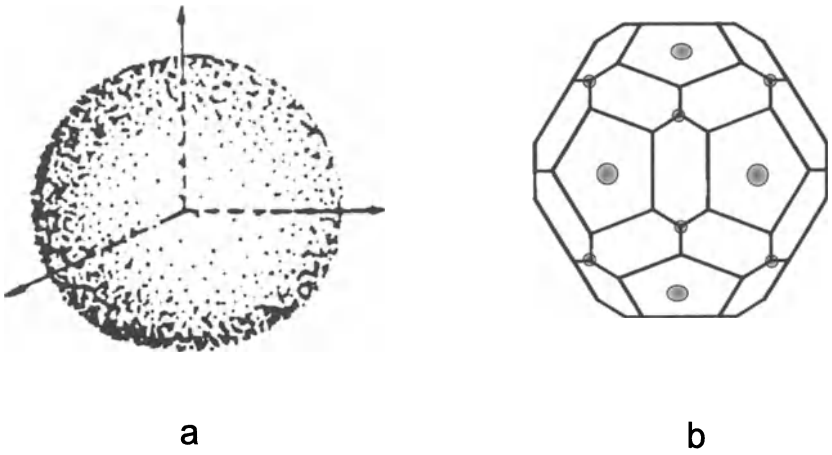

Fig. 18.6. Jones zone for the amorphous **(a)** and the icosahedral phase **(b)** constructed from the peak at K_{pe} (Fig. 18.5) and the 20, 32 and 18, 29 peaks for the a- and i-phase, respectively

free path; the main effect may be the depression of the DOS at E_{F}. If the matching of the k-vectors of the electronic and the atomic system is good, this results in a resonant-like scattering of electrons. The previously freely propagating electrons change partially to standing waves because of resonant scattering, resulting in a tendency of localization of the electrons at E_{F}. As a consequence, the electronic DOS at E_{F} is reduced, the stability of the system increases and electronic transport anomalies arise. This aspect of stability is discussed in [14], while the consequences for electronic transport in amorphous and quasicrystalline films will be briefly discussed in the following. In the case of a weak scattering approach the Ziman formula

$$\rho_z = \frac{1}{\sigma_z} \propto \int_0^{2k_{\mathrm{F}}} S(K)|v(K)|^2 K^3 \mathrm{d}k$$

[31] has been used to describe the resistivity and its temperature dependence for liquid and amorphous systems. K represents the scattering vector, $v(K)$ the pseudopotential and $S(K)$ the static structure factor. This formula cannot strictly be applied to systems with strong scattering as in some amorphous systems or quasicrystals. But this relatively simple formula can be helpful to follow up the trends to stronger scattering. Due to the weighting with K^3 the elastic scattering strongly depends on $S(2k_{\mathrm{F}})$, the structural weight at the upper limit of the integral. Thus, a pronounced peak in the structure factor at $2k_{\mathrm{F}}$ leads to strong elastic scattering and low conductivity. As the temperature increases, the portion of the elastic scattering at $K = 2k_{\mathrm{F}}$ is reduced in favor of inelastic scattering. The latter is less effective on reducing the conductivity than the diffuse umklapp scattering. Thus, the conductivity increases with increasing inelastic scattering due to rising temperature.

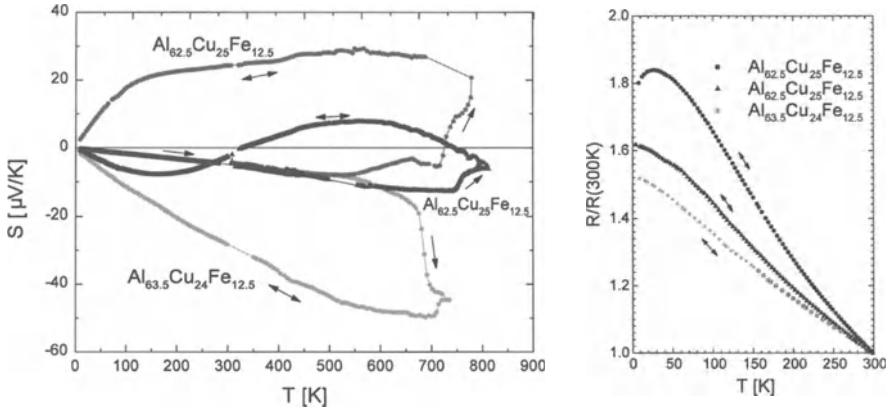

Fig. 18.7. Thermopower **(a)** and normalized resistance **(b)** for three Al-Cu-Fe films of slightly different composition [26]

Additionally, the resonant-like elastic scattering due to the coincidence of the electronic wavelength with structural distances opens a gap or a pseudogap at E_F. This is similar to the case of periodic crystals where matching of the wavelength of the electron waves at E_F with the wavelength of a reciprocal lattice vector causes a gap due to the energy difference for the two solutions of standing electron waves. In quasicrystals the matching may be slightly different. A resonance-like interaction is most effective, if not only the wavelength but also the waveforms of both systems are identical. In quasicrystals and especially in amorphous alloys, it is well known that the atoms are onionshell-like located around ad-atoms. The distance between neighboring shells λ_P is in agreement with the Friedel wavelength $\lambda_F = 2\pi/2k_F$. Each atom is surrounded by "mirror spheres" analogous to the equidistant separation of mirror planes in the crystalline case. The electrons should be treated as spherical waves in coincidence with the onion shell-like static structure. Under resonance, any plane wave which once may have been formed will by scattering immediately fall apart into spherical waves which are strongly localized due to the phase-coherent backscattering from all the neighboring onion shells. The resonance-like coupling causes localization of the electrons at any site and hence a short mean-free path which itself helps to enhance the role of the spherical waves at medium range. In the electronic DOS pseudogaps arise. The onion shell-like position of the neighboring atoms around any ad-atom may also be seen as a cluster-model with strongly interpenetrating clusters. Whereas in the amorphous phase the location of the atoms on the onion shells is still strongly random and in addition angular correlations are weak or absent, this is no longer the case in the qc phase. The distances of the individual atoms to the ad-atoms are much better defined and strong angular correlations exist. The phase coherence of the backscattered

spherical waves is better fulfilled and therefore the interference effects are even stronger. Accordingly the localization of the electron waves should be stronger and the pseudogap should become deep. As the temperature rises the portion of the resonant elastic scattering is decreased in favor of inelastic scattering reducing the pseudogap both for amorphous and quasicrystalline systems. We mention that this behavior is simply ruled by the Debye-Waller factor which describes the ratio of the elastic to inelastic scattering for the relevant peaks building up the Jones zone. This can be seen in Fig. 18.3b. The conductivity for all reversible parts (marked by $\leftrightarrow$) of the amorphous states and also for the quasicrystalline state increases with temperature in exactly the same manner. The conductivity irreversibly decreases (marked by $\searrow$) with every annealing step reaching its smallest value in the qc-phase with its strong radial and angular correlation of atoms. The temperature dependence of the conductivity is discussed in detail in the Al-Pd-Re system as this icosahedral system shows even larger transport anomalies (reaching insulating behavior) and has a much smaller contribution of low-temperature effects from spin-orbit scattering.

The effect of resonance in amorphous and quasicrystalline samples can also be seen in the thermopower. For amorphous systems it is well known that a stronger resonance between static structure and electronic system causes a deviation from the free-electron value of the thermopower S_0 to positive values [13]. Figure 18.7 shows the same behavior for the icosahedral phase. The samples show a transition from a large negative to a large positive thermopower. This correlates with the increase of the resistance ratio $\rho(4\,\mathrm{K})/\rho(300\,\mathrm{K})$, which is an indication of the enhanced resonance effect between the static structure and the electronic system. Note that the i-phases show thermopowers which are much larger than the free-electron value. This can be attributed to a deep pseudogap which reduces the effective number of charge carriers at the Fermi-level.

18.5 The Al-Pd-Re System

The icosahedral Al-Pd-Re system shows the largest transport anomalies amongst all the quasicrystals, up to a metal-insulator transition (MIT) [23]. Thus it is interesting to check the concept of resonant interaction between the static structure and the conduction electrons on this alloy. Due to the extremely different vapor pressures of the constituents it is difficult to produce homogeneous bulk samples of a defined composition in a reproducible way. With the co-sputtering technique mentioned before, systematic and slightly different samples can be fabricated as thin films. As an example, Fig. 18.8a shows the conductivity of such a sequence as a function of the rhenium content for a constant aluminium to palladium ratio. There exists a systematic variation of the low-T conductivity with a minimum around $Al_{72.3}Pd_{20.2}Re_{7.5}$. Simultaneously, some of the samples seem to be insulating [12]; that means

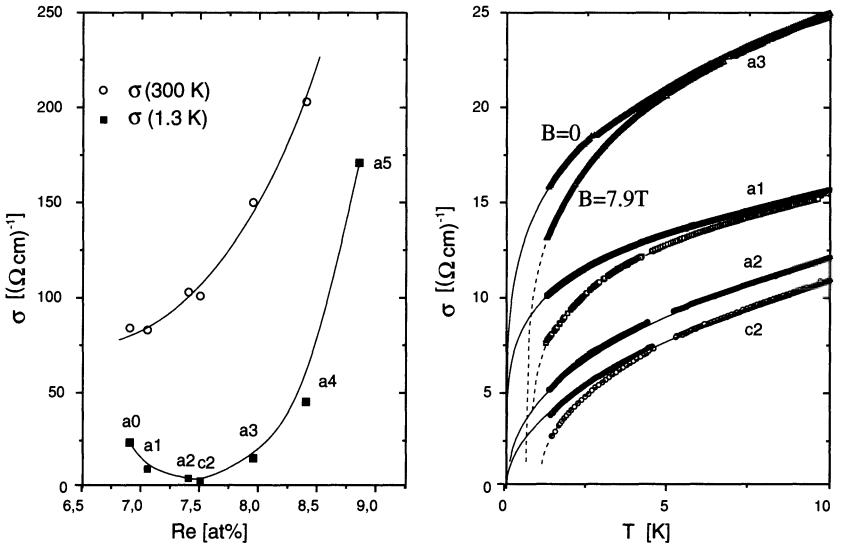

Fig. 18.8. Conductivity for a sequence of Al-Pd-Re films of constant Al/Pd ratio **(a)** and their low-temperature conductivity **(b)** with a magnetic field of $B = 7.9\,\mathrm{T}$ (open symbols) and without field (solid symbols)

the conductivity vanishes for $T \to 0\,\mathrm{K}$ (Fig. 18.8b). A magnetic field enhances this behavior and apparently leads to a vanishing conductivity at a small but finite temperature.

Thereby, the transport properties of *i*-Al-Pd-Re match into the common behavior of stable quasicrystals mentioned before in the *i*-Al-Cu-Fe system. Fig. 18.10b shows again the validity of the inverse Matthiessen rule for the conductivity of the *a*- and *i*-phases of different structural qualities. In contrast to all other qc systems, the Al-Pd-Re system offers two exciting aspects. First, the conductivity vanishes at $T \to 0\,\mathrm{K}$, which may be due to a stronger resonant scattering because of heavier elements in the case of Al-Pd-Re. Second, at low-T, there is no increase of conductivity, as for high-quality *i*-Al-Cu-Fe (Fig. 18.7b) or for other stable quasicrystals like *i*-Al-Pd-Mn. Such a low-T increase of conductivity (attributed to strong spin-orbit scattering and electron-electron interaction [7]) makes a MIT unlikely and complicates interpretation. The model of a resonant-like interaction of the electronic and the static structure is able to explain the transport properties also for the insulating samples. Fig. 18.9 shows a fit to the conductivity data in a quite large temperature range. The fit is indirectly proportional to a function of the Debye-Waller factor $exp(-cP(\frac{T}{\Theta}))$, with the Debeye-temperature Θ and a constant c which describes the temperature-dependent decrease of the elastic scattering of the electrons at $2k_\mathrm{F}$ at the Jones zone. There has been only one parameter (c_3 in the expression written in Fig. 18.9) added which is related to the size of the gap between electron- and hole-like charge carriers and is

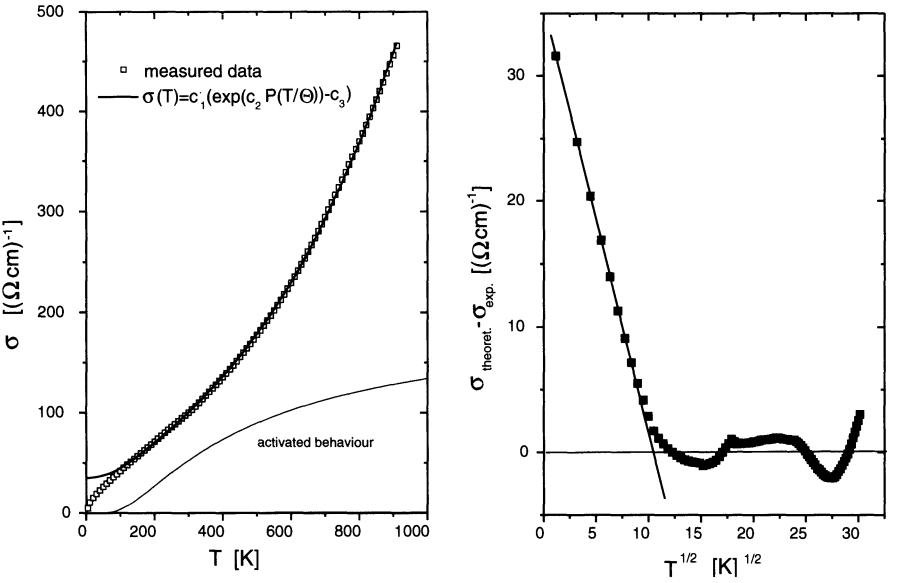

Fig. 18.9. Conductivity of a $Al_{72.3}Pd_{20.2}Re_{7.5}$ film in comparison with a fit according to a function of the Debye-Waller factor **(a)** and the difference between fit and experimental values **(b)**

related to the effective pseudopotential. A significant difference between fit and measured data occurs only at temperatures below 100 K. Figure 18.9b shows that this difference is proportional to $\sqrt{T}$ which can be attributed to the electron-electron interaction (EEI). In systems of strong elastic scattering, electrons are less able to screen charge variations and EEI is enhanced, leading to a small dip in the electronic density of states at E_F [1]. In the case of amorphous alloys this behavior can be computed quantitatively as a function of temperature and magnetic field [2,20]. In weakly insulating icosahedral systems the MIT seems to have two origins. First, the resonance-like interaction between the static structure leads to a deep pseudogap in the electronic DOS at E_F and the localization tendency of the conduction electrons due to standing spherical waves in some structural clusters. Second, the EEI lowers the small DOS at E_F additionally. The sum of both effects leads to a vanishing conductivity at $T \rightarrow 0\,K$. A magnetic field dephases the electronic wavefunction enlarging the EEI by a further decreased screening. The MIT occurs at a finite temperature.

The thermopower of *i*-Al-Pd-Re can be described in the resonance-model mentioned before. As shown in Fig. 18.10, the thermopower increases to large positive values as the structural quality increases from the amorphous to the defective and finally the good icosahedral state. The conductivity of the same sample reduces in the same manner as the resonance effect increases.

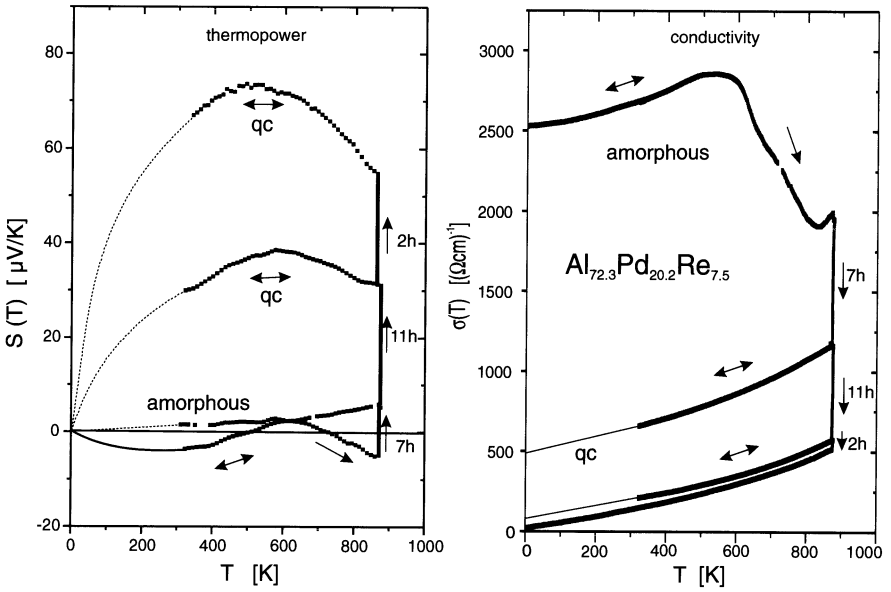

Fig. 18.10. Thermopower **(a)** and conductivity **(b)** for a Al-Pd-Re film during annealing and in steps of different structural quality

18.6 Conclusion

Quasicrystalline thin films can be produced with high structural quality. The low-temperature electrical conductivity, which is very sensitive to the structure quality, reaches values which are comparable to that of bulk materials. A MIT is achieved in both the bulk samples as well as in thin films of *i*-Al-Pd-Re. Thin films provide the possibility of making systematic investigations as a function of composition and structural quality. Further understanding in the interpretation of the peculiar transport anomalies of quasicrystals could be achieved by comparison to the isotropic amorphous phase. This has been done on different annealing states of the same sample. Astonishingly, the temperature dependence of the conductivity is qualitatively very similar for both phases; the inverse Matthiessen rule which is thought to be peculiar to quasicrystals is also valid for amorphous samples of the same composition. We discussed this in the framework of resonant scattering between the conduction electrons and the static structure. Hereby, the mechanism is the same for amorphous as well as for qc systems. Due to the sharp distance distributions and angular correlations in quasicrystals the quantity of scattering is much larger in the quasicrystalline case, leading to a deeper pseudogap and a stronger localization tendency of the conduction electrons. The temperature dependence of the conductivity could be fitted due to the scattering approach by a simple function of the Debye-Waller factor for the temperature range from 100 to 900 K. At low-temperatures the conductivity of *i*-Al-Pd-Re is

additionally influenced by strong electron-electron interaction. This leads to an additional dip of the electronical DOS at E_F and finally to the metal-insulator-transition. The thermopower increases to large positive values as the conductivity vanishes for high-quality qc samples. Again, this is typical behavior of electronically stabilized systems, which can be described by a strong interaction between the conduction electrons and the static structure.

Acknowledgments

Support of this work by DFG under contracts Ha2359/1, Ha1627/8 and Ha1627/9 is gratefully acknowledged.

References

1. Altshuler B.L., Aronov A.G., *Solid State Comm.* **30** (1979) 115
2. Altshuler B.L., Aronov A.G., *Solid State Comm.* **46** (1983) 429
3. Chien C.L., Lu M. *Phys. Rev. B* **45** (1992) 12793
4. Eisenhammer T., Mahr A., Haugeneder A., Reichelt T., Assmann W., Proceeddings of the 5th Int. Conf. on Quasicrystals. Eds. C. Janot, R. Mosseri, World Scientific (1996) 758
5. Friedel J., *Helv. Phys. Acta* **61** (1988) 538
6. Giroud F., Grenet T., Schaub T.M., Berger C., Barna B.P., Radi Z., Proceeddings of the 6th Int. Conf. on Quasicrystals. Eds. Takeuchi S., Fujiwara T., World Scientific (1998) 712
7. Haberkern R., Fritsch G., Schilling J., *Z. Phys. B* **92** (1993) 383
8. Haberkern R., Fritsch G., Proceedings of the 5th Int. Conf. on Quasicrystals. Eds. Janot C., Mosseri R., World Scientific (1996) 460
9. Haberkern R., Roth C., Knöfler R., Zavaliche F., Häussler P., Proceedings of the 6th Int. Conf. on Quasicrystals. Eds. S. Takeuchi, T. Fujiwara, World Scientific (1998) 643
10. Haberkern R., Roth C., Knöfler R., Zavaliche F., Häussler P., Proceedings of the 6th Int. Conf. on Quasicrystals. Eds. Takeuchi S., Fujiwara T., World Scientific (1998) 716
11. Haberkern R., Roth C., Knöfler R., Schulze S., Häussler P. in: Quasicrystals, MRS-Proceedings Vol. 553 (1999), eds. Dubois J.-M., Thiel P. A., Tsai P.-A., Urban K.
12. Rosenbaum R., Haberkern R., Häussler P., Palm E., Murphy T., Hannahs S., Brandt R., J. Phys. Condens. Matter. **12** (2000) 9735
13. Häussler P. in: Glassy Metals III, eds Beck H., Günterodt H.-J. Topics in Applied Physics (Springer), Vol. 72 (1994) 163
14. Häussler P., Nowak H., Haberkern R., Mat. Sci. Eng. **294–296** (2000) 283
15. Hume-Rothery W., *J. Inst. Met.* **35** (1926) 295
16. Janot C., J. Phys.: *Condens. Matter* **9** (1997) 1493
17. Janot C., Dubois J.-M. (2002): See Chapter 8 of this book
18. Jones H., *Proc. Phys. Soc.* **49** (1937) 250
19. Klein T, Symko O.G., *Appl Phys. Lett.* **64** (1994) 431

20. Lee P.A., Ramakrishnan T.V., *Phys. Rev. B* **26** (1982) 4009
21. Massiani Y., Ait Yaazza S., Dubois J.-M., Proceedings of the 5th Int. Conf. on Quasicrystals. Eds. Janot C., Mosseri R., World Scientific (1996) 790
22. Mayou D., Berger C., Cyrot-Lackmann F., Klein T., Lanco P., *Phys. Rev. Lett.* **70** (1993) 3915
23. Pierce F.S., Poon S.J., Guo Q., *Science* **261** (1993) 737
24. Roche S., Berger C., Mayou D. (2002): See Chapter 16 of this book
25. Rodmar M., Ahlgren M., Rapp Ö., Proceedings of the 5th Int. Conf. on Quasicrystals. Eds. Janot C., Mosseri R., World Scientific (1996) 518
26. Roth C., Schwalbe G., Knöfler, Zavaliche F., Madel O., Haberkern R., Häussler P., *J. of Non-cryst. Solids* **250-252** (1999) 869
27. Smith A.P., Ashcroft N.W., *Phys. Rev. Lett.* **59** (1987) 1365
28. Sordelet D.J., Kramer M.J., Anderson I.E., Besser M.F., Proceedings of the 5th Int. Conf. on Quasicrystals. Eds. Janot C., Mosseri R., World Scientific (1996) 778
29. Trambly de Laissardière G., Mayou D. (2002): See Chapter 25 of this book
30. Yoshioka A., Edagawa K., Kimura K., Takeuchi S., *Jpn. J. Appl. Phys.* **34** (1995) 1606
31. Ziman J.M., *Proc. Roy. Soc. , Ser. A* **318** (1970) 401

19 Electron Transport in a Magnetic Field: A Landauer-Formula Approach

Gerald Kasner, Holger Wegmann, and Harald Böttger

Summary. The density of states as a function of a magnetic field and the magnetoconductance of two- and three-dimensional quasicrystalline model systems are calculated in a simple tight-binding description. The zero-field spectra are known to show a very complicated spiky structure with many small gaps. A magnetic field leads to a more uniform distribution of the states. Correspondingly, the energy regions that show finite values for the magnetoconductance as a function of the Fermi energy become larger with a growing field. The investigation of the high-field behavior uncovers an interesting structure of the spectra that is quasiperiodic with the field. This quasiperiod can be explained as a simple interference of periods in the incommensurate ratio of the areas perpendicular to the flux contained in the cluster.

19.1 Introduction

Since the discovery of quasicrystals, many authors have found experimentally very exotic behavior of some of their physical properties [7,13]. The results show, for instance, a very low electrical conductance that depends strongly on the composition [14]. In theoretical studies, simple model systems have been used to find the origin of these properties in the quasicrystalline structure [8,11,12,15–19,21]. A well investigated one-dimensional (1D) model – the Fibonacci chain – has a singular continuous spectrum and the corresponding wave functions are neither exponentially localized nor extended, but critical [17]. The Penrose lattice serves as an example of a 2D quasicrystal. Most of the wave functions are believed to be critical too, but some highly degenerate strongly localized states, so-called confined states, have been found [1,5,8,12,15–17]. In a tight-binding picture, the conductance as a function of the Fermi energy shows very strong fluctuations and even energy ranges that have zero conductance [18]. This can be explained by a very irregular distribution of the states that contribute to the conductance. First calculations for a 3D icosahedral model system exhibit qualitatively the same behavior [12]. Some work has been done on introducing a magnetic field to quasicrystalline model systems [1,9]. Very interesting properties have been found, for instance, a quasiperiodic structure in the magnetic-field dependence of the spectrum for the Penrose lattice [9].

J.-B. Suck et al. (eds.), *Quasicrystals*
© Springer-Verlag Berlin Heidelberg 2002

We want to present some more systematic theoretical investigations of electronic properties of 2D and 3D quasicrystals in a magnetic field, to compare the results of a few simple but significant example models. First, we introduce the model systems. The next sections give an overview of our results for the magnetoconductance based on the density of states (DOS). A further section deals with a detailed investigation of the spectra as a function of the magnetic field. The quasiperiodic repetition of significant structure elements in the spectra with an increasing field can be explained as a simple interference of periods in the ratio of the areas perpendicular to the flux contained in the cluster. To show this, we perform a Fourier analysis for the plots of some selected eigenvalues as a function of the magnetic field. We find only very few frequencies in the positions of the areas in the cluster. Finally, we draw some conclusions.

19.2 The Model

We use a very simple standard model that describes only the quasicrystalline structure but no other physical effects of real materials (see, for instance, [17]). The main features are to use mesoscopic clusters at zero temperature, which are small enough to avoid inelastic scattering, lattices in a tight-binding approximation with s-like atomic wave functions localized at the lattice sites and open boundary conditions. To calculate the conductance we have to add an external electric field in the linear-response approximation [18]. The charged particles are spinless and non-interacting electrons. Two leads of undisturbed material, which are infinitely long but of finite width and outside of the magnetic field, serve as electronic reservoirs. The calculation is carried out via the Landauer formula $\Gamma = \frac{e^2}{h}\hat{t}\hat{t}^{+}$, where $\hat{t}$ is the transmission matrix of states of the undisturbed lead, scattered elastically at the quasicrystalline cluster.

19.2.1 The Hamiltonian in a Magnetic Field

The Hamiltonian H that describes a quasicrystalline cluster reads, in tight-binding representation,

$$H = \sum_{ij}^{\text{n.n.}} V_{ij}|i\rangle\langle j| \quad , \tag{19.1}$$

with the transfer integrals between the nearest-neighbor (n.n.) sites i and j without a magnetic field

$$V_{ij} = \int \mathrm{d}\boldsymbol{r}\ \phi_i^*(\boldsymbol{r} - \boldsymbol{R}_i) H \phi_j(\boldsymbol{r} - \boldsymbol{R}_j) \equiv V_{ij}(0) = 1, \tag{19.2}$$

where $\phi_j(\boldsymbol{r} - \boldsymbol{R}_j)$ denotes the s-like atomic wave function at lattice site j.

The introduction of a magnetic field is carried out by $H(\boldsymbol{p}) \longrightarrow H(\boldsymbol{p}-e\boldsymbol{A})$, where the vector potential $\boldsymbol{A}$ belongs to the magnetic field $\boldsymbol{B} = B\boldsymbol{e}_z$. The wave function at site i in the magnetic field is [3]

$$\begin{aligned} \phi_i(\boldsymbol{r}, \boldsymbol{R}_i, B) &= \chi_i(\boldsymbol{r} - \boldsymbol{R}_i, B) \mathrm{e}^{\mathrm{i}\boldsymbol{A}(\boldsymbol{r})\boldsymbol{R}_i e/\hbar} \,, \\ \chi_i(\boldsymbol{r} - \boldsymbol{R}_i, B) &\approx \chi_i(\boldsymbol{r} - \boldsymbol{R}_i) \,, \end{aligned} \tag{19.3}$$

with elementary charge e and Planck's constant $\hbar$. The approximation neglects the shrinking of the wave function in very strong magnetic fields. The integrals of the transfer energy (19.2) in the field take the form

$$\begin{aligned} V_{ij}(B) &= \int \mathrm{d}\boldsymbol{r} \; \mathrm{e}^{\mathrm{i}\boldsymbol{A}(\boldsymbol{r})(\boldsymbol{R}_j - \boldsymbol{R}_i)e/\hbar} \chi_i^*(\boldsymbol{r} - \boldsymbol{R}_i) H \chi_j(\boldsymbol{r} - \boldsymbol{R}_j) \\ &\approx \mathrm{e}^{\mathrm{i}\boldsymbol{A}(\boldsymbol{R}_i + \boldsymbol{R}_j)(\boldsymbol{R}_j - \boldsymbol{R}_i)e/2\hbar} . \end{aligned} \tag{19.4}$$

This approximation is valid for functions $\chi_i^*(\boldsymbol{r} - \boldsymbol{R}_i) H \chi_j(\boldsymbol{r} - \boldsymbol{R}_j)$ that are localized in the middle between sites i and j.

In what follows, we use the Landau gauge $\boldsymbol{A}(\boldsymbol{r}) = -yB\boldsymbol{e}_x$. Then the transfer energy (19.4) becomes

$$V_{ij}(B) = \mathrm{e}^{\mathrm{i}b(x_i - x_j)(y_i + y_j)}, \qquad b \equiv \frac{eB}{2\hbar} \quad \longrightarrow \quad b a_0^2 = \frac{\Phi}{2\Phi_0}. \tag{19.5}$$

Here $\Phi_0 = \frac{h}{2e}$ is the flux quantum and $\Phi = \pi a_0^2 B$ is the flux at the field B through an area πa_0^2, with $a_0 \equiv 1$ being the lattice constant. Therefore, b denotes the value of the magnetic flux through the elementary cells of the lattice in units of Φ_0; that is, b measures the strength of the magnetic field in a dimensionless form.

19.2.2 2D and 3D Quasicrystalline Clusters

The most investigated 2D quasiperiodic structure is the Penrose lattice. Its proto-tiles are two sorts of rhombs. We use the lattice in two ways. The first one is to set an atom at every vertex point to obtain the so-called vertex model (PVM). The second model is the center model (PCM), with one atom in the center of each rhomb. Both models have several interesting opposite features, which are well summarized in [17]. The coordination number of the PVM varies from 3 to 7 for the different vertex stars and the model is bipartite. As a consequence, the DOS has to be symmetric around $E = 0$ in a band of $-7 < E < 7$. The PCM has an uniform coordination number of 4 and is not bipartite, which leads to an asymmetric DOS.

A 3D model with similar features is that described in [6], which may serve as a model for real icosahedral quasicrystals of high quality such as AlPdMn or AlCuFe. It has several tetrahedra as proto-tiles. Again, we can define a vertex model (IVM) with atoms at the corners of the tetrahedra and a center model (ICM) with an atom situated in the middle of each tetrahedron [12].

Also, for the icosahedral system the center model has an uniform coordination number of 4, while for the IVM this varies up to 62. Contrary to the Penrose lattice, the ICM is bipartite but not the IVM.

We have calculated some electronic properties for one example of each of these four models. Specifically, we used a piece of a Penrose 8/5 approximant that has 473 sites for the PVM and 378 sites for the PCM for the 2D calculations, and a triacontahedron-shaped cluster of the Danzer model in the third deflation level, having 1069 sites for the IVM and 4320 sites for the ICM, for the 3D one. In the following sections, we show the results and compare them for the four models.

19.3 Density of States and Magnetoconductance

The DOS in quasicrystalline systems is known to show a very irregular structure, with energy regions containing clusters of discrete states and other regions having no or just a few isolated states. This behavior is proven even analytically for the 1D quasicrystalline Fibonacci chain, where the DOS forms a Cantor-set-like fractal structure [17]. The DOS for 2D [8,17] and 3D [12] quasicrystalline models seems to be more complicated, but of fractal structure. Calculating the conductance of the same systems as a function of the Fermi energy, one finds that the complicated structure of the DOS is recovered. That is, the system shows conductivity only in a small region surrounding each state. If there is another state in this region, a conducting band arises. Certainly, the width of this region depends on the size of the finite cluster. It becomes smaller with increasing size. However, computational results suggest that the additional states of a larger system are also arranged in many small clusters, rather than showing an uniform distribution over the whole energy range, leading to very spiky DOS and conductance plots. The formation of wide energy bands, as in periodic systems, cannot be observed.

Now we introduce a magnetic field to our quasicrystalline models and calculate the DOS and the conductance again. We find that an increasing strength of the magnetic field leads to a more uniform distribution of states. In Fig. 19.1 the integrated DOS in a magnetic field of strength $b = 0.5$ is compared to that without a field for some of our model systems. Generally, the curves in the field are much smoother, more linear and show smaller steps. Additionally, for the PVM it is seen that the high degeneracy of the confined states at $E = 0$ also occurs in the field. This is not the case for the PCM at $E = 2$ and, although it cannot be seen so clearly, for the IVM at $E = 0$. We will return to this point later.

Corresponding to the uniform distribution of states, we also find much smoother conductance plots. That is, the absolute values of the highest peaks in the plot become lower but larger conducting energy regions arise. As an example of the development of the conductance in a magnetic field, we show the plot for the IVM in Fig. 19.2, without and with a magnetic field. The

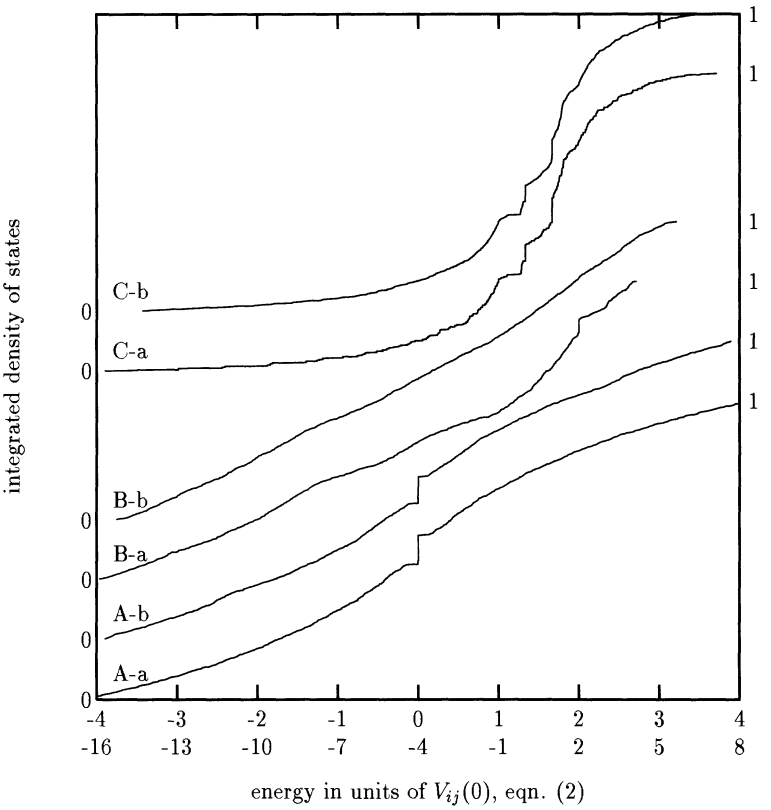

Fig. 19.1. Integrated DOS of (A) PVM, (B) PCM and (C) IVM: **(a)** without a magnetic field $b = 0$ and **(b)** in a field $b = 0.5$. The lower labels of the energy axis are valid for (A) and (B), and the upper for (C)

behavior of the DOS and the conductance in a magnetic field can be regarded as being very similar to the behavior of eigenstates in fractal lattices [20]. There, a magnetic field leads to a spreading of highly degenerate localized states to new extended states, because of the broken structural symmetry due to the field.

In the case of our models, we do not have degenerate states but some clusters of very densely distributed states at several energy regions without a field. Some exceptions are the highly degenerate so-called confined states that are strongly localized at distinct local environments in the quasilattice. We found them in three of our four models at integer energy values, but not in the ICM. The total number of states is fixed, so a "spreading" means a more uniform distribution here, rather than new states. Whether the states are localized or extended cannot be determined, because of the small size of the cluster. That is, there is no well-defined localization length. An interesting

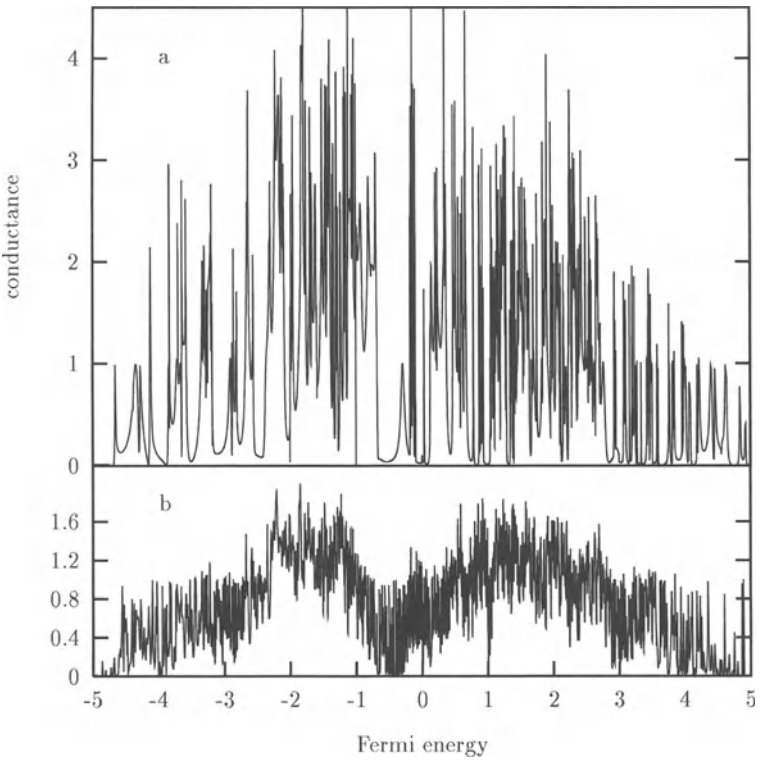

Fig. 19.2. Conductance as a function of the Fermi energy for the IVM: **(a)** without a magnetic field $b = 0$ and **(b)** in a field of strength $b = 0.5$

fact is that we observed a spreading mechanism for the confined states as expected, but not in the bipartite PVM. In this model, the confined states turned out to be absolutely stable against even very high magnetic fields, in the sense that their amplitudes remain zero at the sites that are not yet occupied without a field. It follows that a field does not cause a breaking of any structural symmetry in this case. Generally, confined states in bipartite models are reported as being stable [9,12,15–17], while those in the non-bipartite models vanish quickly with any disturbance of the structure or in a field [1,15].

19.4 Spectra in a Magnetic Field

A very interesting development of the spectrum of the PVM for a growing magnetic field is reported in [9]. Let us define "plot a spectrum" as meaning to make a point at an energy value if there is a state. Then a plot of the calculated spectrum versus the magnetic field strength b uncovers a compli-

cated structure similar to the fractal butterfly-shaped graph introduced by Hofstadter [10] for the square lattice, but showing a quasiperiodic repetition of structure elements, that form a Fibonacci chain for the PVM. A similar form of behavior has been found for the superconducting transition temperature as a function of the applied magnetic field in artificial quasiperiodically arranged systems [2]. The interpretation of the clear structure in [9] was the assumption of Landau band formation in the PVM, as is known for the square lattice. We found a somewhat different form of behavior when investigating the other models and discovered a quasiperiodic structure for the width of the band for the ICM too. However, for our non-bipartite models it is the position of the band rather than its width that changes quasiperiodically. Additionally, a clear structure within the band could be seen only for the PVM. Here, we denote a band as the region between the lowest and the highest eigenvalues.

To analyze this behavior, we limit our investigations to the eigenvalues at the band edge. Let us start with the PVM. Because this model is bipartite, we only have to look at the lowest eigenvalue $\epsilon(b)$. It is plotted as a function of the magnetic field in Fig. 19.3. One can see the typical quasiperiodic Fibonacci chain structure in the repetition of peaks and dips, as reported in [15]. Because the highest eigenvalue is mirror symmetric with the lowest one, this means that the width of the band changes quasiperiodically with the magnetic field. As is shown by the plot of the simple function $f_{\mathrm{PVM}}(b) = [A\cos(2Ab) + B\cos(2Bb)]/(A + B)$ in Fig. 19.3, this structure can be explained by the incommensurate ratios of the areas A and B of closed loops perpendicular to the flux in the PVM. Here $A = \sin(2\pi/5)$ and

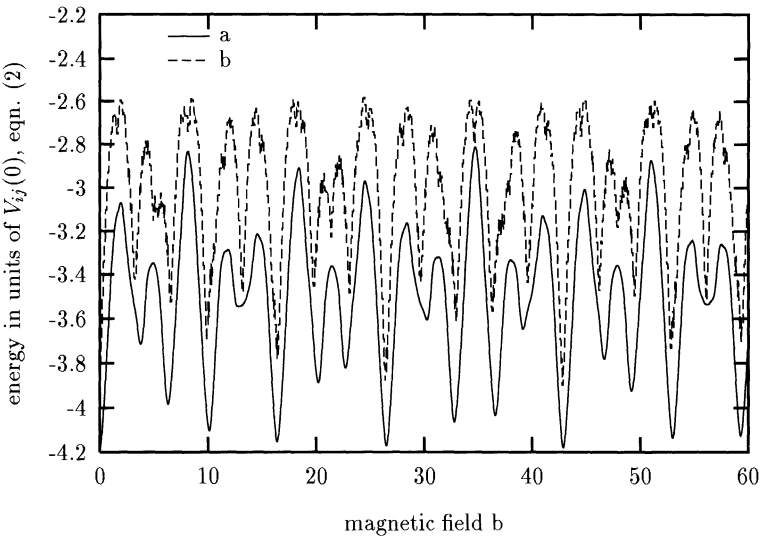

Fig. 19.3. **(a)** The lowest eigenvalue of the finite PVM as function of the magnetic field; **(b)** $f_{\mathrm{PVM}}(b) = [A\cos(2Ab) + B\cos(2Bb)]/(A + B)$

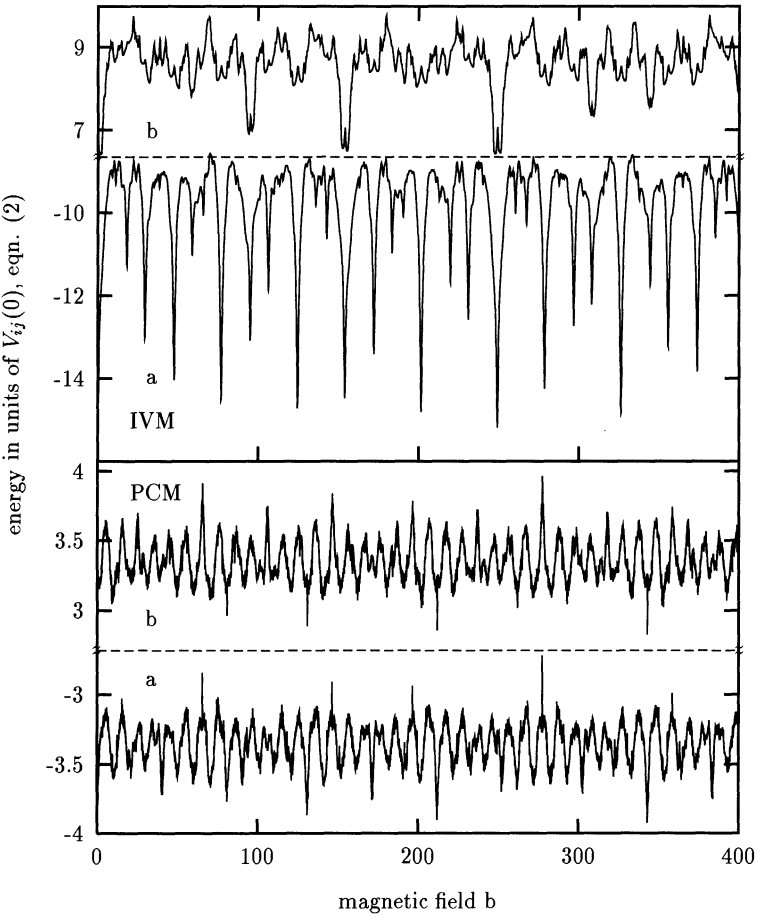

Fig. 19.4. The **(a)** lowest and **(b)** highest eigenvalues of the non-bipartite models PCM and IVM as a function of the magnetic field b

$B = \sin(\pi/5)$ are the areas of thick and thin rhombs in the PVM that have the golden ratio $A/B = \tau = (\sqrt{5}+1)/2$. Also, the ratio of the number of rhombs is τ. This simple interference function of the cosines of both areas in the weighted ratio of their occurrence in the model is astonishingly similar to the curve of $\epsilon(b)$.

A more complicated structure was found for the plot of the lowest eigenvalue as a function of the magnetic field for the PCM. Additionally, we found a very similar appearance of the plot for the lowest and the highest eigenvalues in this non-bipartite model; that is, peaks of the highest eigenvalue corresponded to peaks of the lowest one. For the band a shift follows that changes quasiperiodically with the magnetic field, while the width of the band is nearly fixed. This is plotted in Fig. 19.4.

A similar form of behavior could be found for the IVM, which is also not bipartite. However, only the main dips in the lowest eigenvalue have corresponding dips in the highest one and the amplitude is smaller, as can be seen in Fig. 19.4. That is, the picture of a fixed bandwidth is only valid as a rough approximation. We have to leave the explanation of the special behavior of non-bipartite models for later investigations.

As suggested by the strong similarity of the curves in Fig. 19.3 for the PVM, which was described above, we extend this approach to other quasicrystalline systems by calculating the Fourier transforms of the functions $\epsilon(b)$, which are the lowest or highest eigenvalues, as

$$\tilde{\epsilon}(K) = \left| \int_0^\infty \mathrm{d}b \; \epsilon(b) \exp(\mathrm{i}Kb) \right| . \tag{19.6}$$

If $\epsilon(b)$ contains only some discrete frequencies K, we must find delta-function-like peaks in the plot of $\tilde{\epsilon}(K)$ at these values.

To explain this method, we start with a simple finite cluster of a square lattice, applying open boundary conditions in a magnetic field with the lattice constant $a_0 = 1$. Solving the arising Harper equation

$$[\epsilon_\gamma + 2\cos(2yb + k_\gamma)]\chi_\gamma(y) + \chi_\gamma(y+1) + \chi_\gamma(y-1) = 0 \tag{19.7}$$

and plotting the eigenenergy $\epsilon_\gamma(b)$ of this model in the way described above, one obtains the well-known butterfly introduced in [10]. Again, we only want to investigate the development of the smallest eigenvalue in the magnetic field. The graph is periodic in the magnetic field b with a period of 2π. This can easily be understood by noticing that b enters the Harper equation via the phase of the transfer energy (19.5) multiplied by A, which is the size of the areas contained in the cluster. Therefore a period of 2π divided by the area size is expected in the graph. These areas are uniform in the square lattice and of size $A = 1$. The physical meaning of this behavior is the quantization of the flux through an area in a cluster. With open boundaries it is not necessary to choose only distinct magnetic field values b. Nevertheless, we find peaks in the graph of the eigenvalues as a function of the magnetic field at values that satisfy the condition of integer flux quanta per area. It can easily be understood that magnetic field values of, for example, half of that size also satisfy such a condition. Then the flux through the area of two squares of the lattice has an integer value. Therefore, we also find peaks also at $2\pi/2$, $2\pi/3$, $2\pi * 2/3$ and so on.

Only the period of 2π and all its subharmonics $2\pi n$ are contained in the Fourier transform (19.6), which we calculated as an example for a cluster of 20×20 atoms. It is suggested by the amplitude that rectangular areas are preferred by the "resonance" of the flux at the lattice areas. The largest peak is the one at the smallest possible area, the elementary square of the lattice. The amplitudes of areas formed by linear chains of squares decrease with increasing length. The peak at $n = 5$ already has hardly any amplitude.

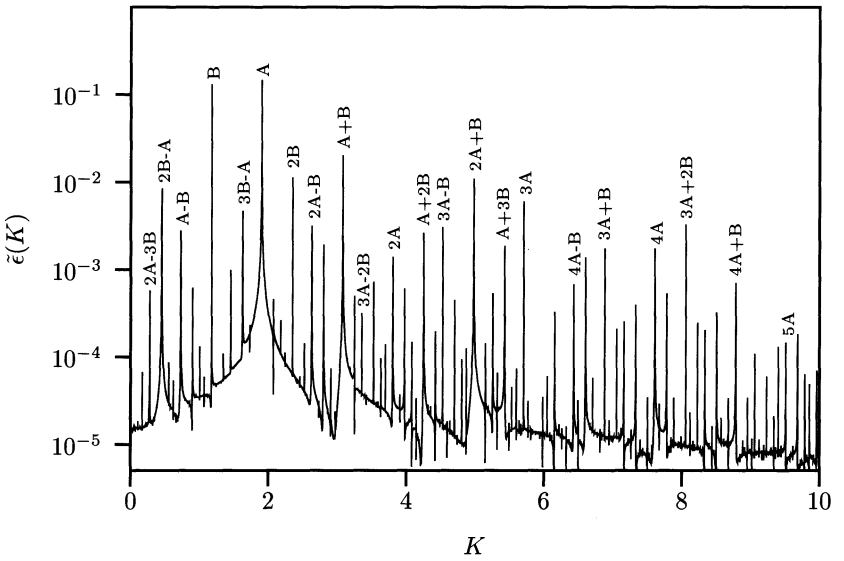

Fig. 19.5. The Fourier transform $\tilde{\epsilon}(K)$ of the lowest eigenvalue as a function of the magnetic field in the PVM in logarithmic representation. The main peaks are labeled with the areas of resonance

However, there seem to be additional contributions to the amplitude values by rectangular arrangements of squares. Therefore, there are relatively high peaks at $n = 4 \equiv 2 * 2$, $n = 6 \equiv 2 * 3$, $n = 8 \equiv 2 * 4$ and especially at $n = 12 \equiv 2 * 6 = 3 * 4$, because of two possible rectangular areas both of which contribute "resonances".

As already shown in the graph $\epsilon(b)$ for the PVM, it can be nearly recovered in a manner similar to that described for the square lattice, by interference of only two simple cosine waves of the two frequencies belonging to the areas of fat and thin rhombs A and B in the ratio of their relative distribution in the lattice. Indeed, we find that the corresponding peaks are clearly the largest and in the correct ratio in the Fourier transform (19.6) for the PVM, Fig. 19.5. However, additionally, there are smaller peaks at sums and also differences of the areas A and/or B as in the square lattice. Note that difference peaks are not to be distinguished in the square lattice. Again, the magnitude of the subharmonic peaks decreases with the number of included areas in the sum, that is, with higher indices. But some peaks are unexpectedly small – as for instance is $2A$ compared to the series $3A, 4A, 5A$. We suppose that these area combinations are rare in the cluster or that there are other reasons why they are not very important.

Because of the incommensurate ratio of A and B, peaks are densely distributed on the K-axis. In particular, peaks with higher indices do not necessarily lie at higher values of K, in contrast to the case of the square lattice.

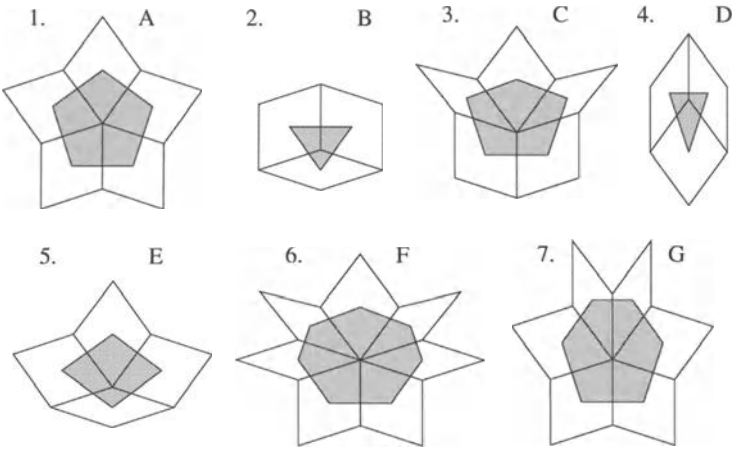

Fig. 19.6. The allowed vertex stars in the Penrose lattice. The areas assigned in the PCM are shaded

Instead, the distribution of high and low peaks shows a form of behavior like that of a fractal. Because the PVM is bipartite, the highest eigenvalue as a function of the magnetic field must be the negative of the smallest one, and so the absolute value of the Fourier transform has to be identical.

The very dominant magnitude of the main peaks that belong to the basic rhombs of the Penrose lattice suggests that the subharmonics do not play such an important role in this case. We assume that this magnitude preserves the formation of Landau bands in the PVM as a nearly undisturbed interference of only two periodic systems with lattice constants A and B, respectively. This behavior cannot be found for the other model systems, to which we now turn.

We will test the behavior of the non-bipartite PCM. First, we need to know the areas that occur and their relative distribution in the Penrose lattice. The lattice consists of seven vertex stars [15], every one of which is related to a distinct polygonal area of the PCM, as shown in Fig. 19.6. The number of edges is equal to the coordination number of the vertex star. In Table 19.1 it is listed together with the relative distribution D_j in the Penrose lattice and the size A_j of the related areas. Note that the vertex star A here is the sum of the five-fold vertex stars S and S5 [4] both of which occur in the Penrose lattice, arising from different vertex classes but having the same shape and size. Here only geometric properties enter our investigation.

The Fourier spectrum of the function $f_{\mathrm{PCM}}(b) = \sum_{j=1}^{7} D_j \cos(A_j b)$, defined by analogy with $f_{\mathrm{PVM}}(b)$, is plotted in Fig. 19.7. The comparison with the Fourier analysis of the smallest eigenvalue of the PCM shows that the resonances D and B of the two smallest areas are recovered exactly in the correct magnitude and ratio. The third largest area leads to a peak E of

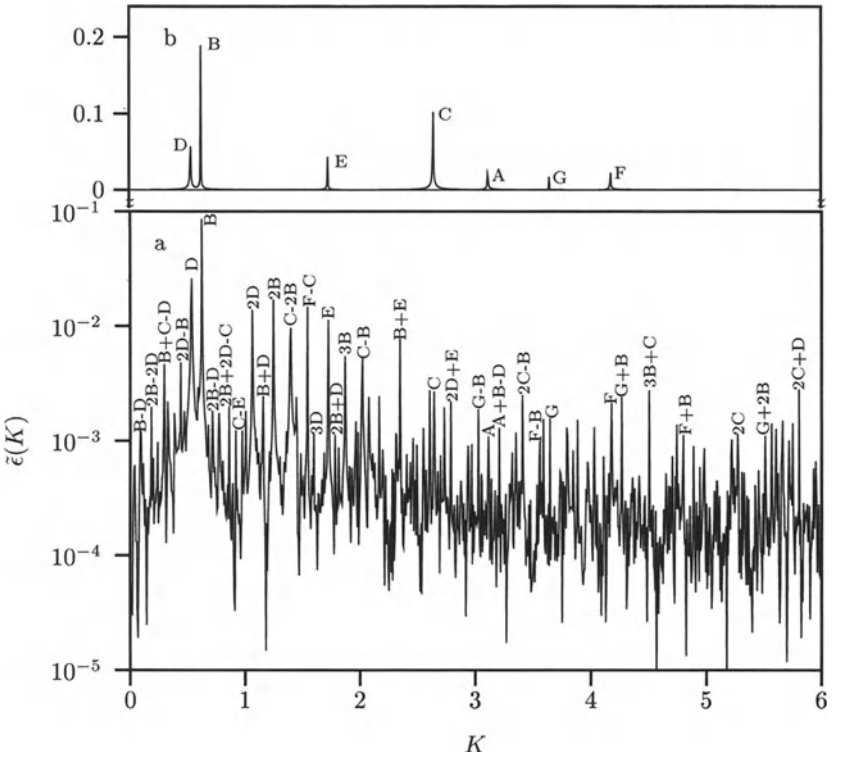

Fig. 19.7. **(a)** The Fourier transform $\tilde{\epsilon}(K)$ of the lowest eigenvalue as a function of the magnetic field in the PCM in logarithmic representation: main peaks are labeled with the areas of resonance. **(b)** The Fourier transform of $f_{\mathrm{PCM}}(b) = \sum_{j=1}^{7} D_j \cos(A_j b)$

Table 19.1. The distribution [15] of the allowed vertex stars in the Penrose lattice and the corresponding areas in the PCM (Fig. 19.6)

Label of the vertex star	A	B	C	D	E	F	G
Coordination number	5	3	5	3	4	7	6
Distribution in the lattice	τ^{-6}	τ^{-2}	τ^{-3}	τ^{-4}	τ^{-5}	τ^{-6}	τ^{-7}
Distribution in %	5.57	38.20	23.61	14.59	9.02	5.57	3.44
Corresponding area in PCM	3.11	0.62	2.64	0.53	1.72	4.18	3.64
Area in % of the smallest	585	117	496	100	324	785	685

around 50 % of the amplitude, as suggested by its relative distribution in the lattice. The most remarkable behavior has the peak C. The amplitude does not even reach 5 % of its distribution, although with about 24 % it is the

second most frequent vertex star in the lattice. The peaks of the larger vertex stars A, F and G can be found in the Fourier spectrum with about 20 % of the expected amplitude. However, all of these areas are relatively rare in the lattice. This means that the resonances of the large areas in a magnetic field do not play any important role here.

Again, subharmonics at sums and differences of the main peaks can be found in the spectrum. Because of the seven basic areas in the cluster, there are many more possibilities of obtaining resonant areas compared to the case of the PVM. Indeed, some peaks at K values corresponding to sums of even more than two areas are higher than other basic area peaks, e.g. B + C − D. This indicates strong mixing of states. The formation of clear Landau bands should be prevented in this case.

Note that the Fourier analyzes of the lowest and the largest eigenvalues for this model are almost identical although the model is not bipartite, in correspondence with the similarity of the $\epsilon(b)$ curves in Fig. 19.4. Our second non-bipartite system is the IVM. Remember that we also found very similar functions for the lowest and the highest eigenvalues as a function of the magnetic field. However, in contrast to the PCM, only the main peaks for the lowest eigenvalue could also be found for the highest one. Investigating the Fourier transforms of both functions, this behavior is underlined. There are some peaks in $\tilde{\epsilon}(K)$ for the lowest eigenvalue which cannot be found for the highest one. On the other hand, all of the peaks of $\tilde{\epsilon}(K)$ for the highest eigenvalue also exist for the lowest one.

The investigation of whether the structure of the peaks conforms with areas in the cluster is omitted for the 3D IVM. There is a very large number of various areas in the Danzer model. Moreover, because several angles occur between each area and the direction of the magnetic field vector, the number of effective areas perpendicular to the magnetic flux is even larger. Here we will only mention that we again find only some discrete frequencies that have significant amplitudes, suggesting a fixed set of resonant areas in the cluster.

19.5 Conclusions

We have investigated magnetic spectra and the magnetoconductance of finite 2D and 3D quasicrystalline model systems in a tight-binding description. Generally, there is a trend of the eigenstates to develop a more uniform distribution over the whole energy band with an increasing magnetic field. Correspondingly, the very small Fermi energy regions of the clusters showing finite conductance without a field become wider in an increasing field. The width of the band in the bipartite models and its position in the non-bipartite models change quasiperiodically with the magnetic field strength. This is due to incommensurate ratios of areas perpendicular to the flux inside the quasicrystalline lattice. We can find a clear structure of the spectra inside the band only for the PVM. That means the formation of Landau bands

described in [9] seems to be due to the fact that the PVM consists only of two types of area perpendicular to the flux. Therefore, it can be regarded as an ideal binary lattice that is not disturbed enough to destroy the Landau bands of the square lattice. With every additional structural unit, they vanish more and more. Because the band limits the region of the Fermi energy in which the cluster can show finite conductance, the magnetoconductance near the band edge has to be sensitive to the structure of the quasicrystal.

References

1. Arai M., Tokihiro T., Fujiwara T. (1987): J. Phys. Soc. Jpn. **56**, 1642
2. Behrooz A., Burns M.J., Deckman H., Levine D., Whitehead B., Chaikin P.M. (1986): Phys. Rev. Lett. **57**, 386
3. Böttger H., Bryksin V.V. (1985): *Hopping Conduction in Solids*, Akademie Verlag, Berlin
4. de Bruijn N.G. (1981): Mathematics A **84**, 39
5. Choy T.C. (1987): Phys. Rev. B **35**, 1456
6. Danzer L. (1989): Discr. Math. **76**, 1
7. DiVincenco D.P., Steinhardt P.J. (1991): *Quasicrystals: The State of the Art*, World Scientific, Singapore
8. Fujiwara T.: In [13], p. 294
9. Hatakeyama T., Kamimura H. (1989): J. Phys. Soc. Jpn. **58**, 260
10. Hofstadter D.R. (1976): Phys. Rev. B **14**, 2239
11. Jian Y. (1992): Z. Phys. B **88**, 141
12. Kasner G., Schwabe H., Böttger H. (1995): Phys. Rev. B **51**, 10454
13. Kuo K.H., Ninomiya T. (1991): *Quasicrystals*, World Scientific, Singapore
14. Lindqvist P., Lanco P., Berger C., Jansen A.G.M., Cyrot-Lackmann F. (1995): Phys. Rev B **51**, 4796
15. Odagaki T. (1986): Solid State Commun. **60**, 693
16. Rieth T., Schreiber M. (1995): Phys. Rev. B **51**, 15827
17. Tsunetsugu H., Fujiwara T., Ueda K., Tokihiro T. (1991): Phys. Rev. B **43**, 8879
18. Tsunetsugu H., Ueda K. (1991): Phys. Rev. B **43**, 8892
19. Ueda K., Tsunetsugu H. (1987): Phys. Rev. Lett. **58**, 1272
20. Wang X.R. (1996): Phys. Rev. B **53**, 12035
21. Yamamoto S., Fujiwara T. (1995): Phys. Rev. B 51, 8841

20 Phonons and Electrons in Quasicrystals

Marián Krajčí and Jürgen Hafner

Summary. We present methods for *ab initio* calculations of phonon and electron spectra of quasicrystals and their approximants. The phonon and electron spectra of smaller approximants are calculated by the exact diagonalization of the dynamical matrix and the tight-binding-linear-muffin-tin-orbital (TB-LMTO) Hamiltonian, respectively. The eigenvalue spectra of bigger approximants are calculated by the recursion method. We discuss the results obtained for realistic models of icosahedral and decagonal quasicrystals. We show that the nature of the phonon and electron eigenvalue spectra is closely related to the diffraction pattern of quasicrystals. We investigate the character of propagated and localized phonon states in icosahedral and decagonal approximants. We discuss the formation of the pseudo-gap in the electronic spectrum and its contribution to the structural stability of quasicrystals. We show that highly anomalous transport properties of quasicrystals are related to the almost dispersionless character of the electron-eigenvalue spectrum.

20.1 Introduction

Spectra of elementary excitations (phonons, electrons, etc.) may be classified as point spectra, absolutely continuous and singular continuous, corresponding to localized, extended and critical eigenstates. Absolutely continuous and point spectra are characteristic for periodic and random systems, respectively. For one-dimensional (1D) quasiperiodic chains, renormalization group studies [61] have shown that the spectrum is singular continuous and the corresponding eigenstates are critical, i.e. they have a complex structure that is characterized by a power-law decay of the amplitudes. The existence of critical eigenstates is related to the self-similarity of quasiperiodic structures: according to Conway's theorem (see, e.g., [15]), a given pattern of a quasiperiodic tiling of diameter d repeats in the tiling within a distance less than $2d$ from the original pattern. Hence an eigenstate localized on one of this patterns can easily tunnel to the next pattern, where it assumes an identical form, except for a finite damping factor. Overlapping localized eigenstates form an extended state. While the spectrum of localized eigenstates is discrete, extended states are characterized by a continuous spectrum. The contradiction between the singularity and continuity of the spectrum leads to criticality of the eigenstates of quasiperiodic structures: they are neither singular nor continuous. The criticality of the eigenstates of quasiperiodic structures has been

J.-B. Suck et al. (eds.), *Quasicrystals*
© Springer-Verlag Berlin Heidelberg 2002

confirmed by numerical studies on 1D and 2D quasiperiodic systems [3,14]. There are suggestions that the 3D quasicrystalline structures may have also singular-continuous spectra [30]. However, according to [54] this question still remains open.

Knowledge of the character of the spectrum of quasicrystals is important not only from the theoretical point of view. It is generally believed that the peculiar character of the spectrum of elementary excitations is also responsible for the highly unusual physical properties of quasicrystals: a very low electrical conductivity, a very low thermal conductivity, a negative temperature coefficient for the resistivity, an increasing resistivity with improved structural perfection and a low electronic contribution to the specific heat. Non-icosahedral quasicrystals are in addition characterized by very strong anisotropies: the electronic transport may even be metallic along the periodic direction and non-metallic in the quasiperiodic plane. For more details see, e.g., [47,52].

In Sect. 20.2, we introduce some theoretical notions that are important for the interpretation of the character of spectra of elementary excitations. In Sect. 20.3, we discuss numerical techniques for the investigation of phonon and electron spectra in realistic models of quasicrystals. Numerical studies are always performed on finite samples – approximants to quasicrystals. A sequence of approximants of increasing size can be constructed. Small approximants can be treated numerically as ordinary crystals. For large approximants, special numerical techniques must be used. The essential results obtained for phonons and electrons in quasicrystals are summarized in Sects. 20.4 and 20.5, respectively.

20.2 Reciprocal Quasilattice, Quasi-Brillouin Zone

For the description of phonons or electrons in periodic crystals, the concept of Brillouin zones (BZs) in reciprocal space is very important. For quasiperiodic systems BZs, and hence dispersion relations, in the usual sense do not exist. In the quasiperiodic limit, the BZ reduces to a point. However, this is a formal statement, as is that stating that Bragg reflections are dense everywhere. In practice, interference leads to a modulation of the intensity of Bragg peaks, so that in practice the diffraction pattern is quasi-discrete. The same happens to the spectrum of elementary excitations in an extended zone scheme.

It has been shown that the characterization of the quasiperiodic crystals in terms of the Fourier spectrum of their density does not only allow the description of their symmetry in terms of operations of their point and space groups [5,48], but also leads to a generalization of the concept of BZ that is very fruitful for understanding the properties of elementary excitations.

The Fourier transform of the density of periodic or quasiperiodic structures consists of δ-peaks (Bragg peaks) at the positions of a vector module of finite rank n (= number of independent basis vectors $\boldsymbol{a}_i^\star$):

$$\boldsymbol{k} = \sum_{i=1}^{n} h_i \boldsymbol{a}_i^\star, \tag{20.1}$$

where the h_i are integers. A crystal is periodic if and only if the rank of its reciprocal lattice $L^\star$ (= the set of all integer linear combinations of the $\boldsymbol{a}_i^\star$ vectors) is equal to the physical dimension d. Hence, for ordinary crystals, $n = d = 3$. For an icosahedral quasicrystal we have $n = 6$, $d = 3$, for a decagonal lattice in the plane $n = 5$, $d = 2$. The symmetry of a lattice may be described as the set of proper or improper rotations about the origin of wavenumber space which leave the positions of the Bragg peaks invariant [5]. For a periodic crystal this has the consequence that the rotations leave the density in real space invariant under a translation. No such symmetry exists for quasicrystals. However, the density of the rotated quasicrystal is indistinguishable from that of the unrotated quasicrystal in a statistical sense, i.e. any bounded substructure of the rotated quasicrystal can be found in the unrotated quasicrystal, albeit at distances that increase with the diameter of this region (see Conway's theorem). The precise mathematical definition of two densities being indistinguishable is that they have the same positionally averaged m-point autocorrelation functions for all m. This generalized notion of indistinguishability (or invariance) is the key to the definition of the symmetry group of a quasicrystal [48,55].

The lattice $L^\star$ is dense in wavenumber space – in contrast to the case of periodic crystals there is no requirement of a minimal distance between wave vectors. The amplitude of the Fourier components $\rho(\boldsymbol{k})$ of the density ($\sim$ the intensity of the Bragg peaks) is modulated because of the symmetry. There may even be lattice vectors for which $\rho(\boldsymbol{k})$ is required to vanish because of symmetry (extinction rules). The set of lattice vectors for which $\rho(\boldsymbol{k})$ exceeds experimentally measured values is essentially discrete – in this sense quasicrystals meet the International Union of Crystallography's new definition of a crystal as a solid "with an essentially discrete diffraction pattern" [28].

The reciprocal lattice $L_3^\star$ may also be viewed as the projection of a regular reciprocal lattice $L_6^\star$ in $n = 6$ dimensions on to 3D space. This forms the basis for the generalization of the concept of BZs. Each Bragg peak may be considered as the projection of the center of a BZ of the nD reciprocal lattice. Similarly, the projection of high-symmetry points corresponding to the corners and midpoints of faces and edges of the nD BZ is defined in wavenumber space [50]. For an icosahedral lattice, for example, there exist seven types of special points, denoted as Γ, R, X_5, M_5, X_3, X_2 and M_2, corresponding to the 6D wavevectors (h = 1/2) (000000), (hhhhhh), (h00000), (0hhhhh), (hhh000), (hh0000) and (00hhhh). Like the Bragg points, the projection of these special points are dense everywhere in wavenumber space, but their

intensities are described by a generalized structure factor that accounts for the symmetry of the quasiperiodic structure. R points, for example, have intensities on the five- and three-fold symmetry axes, but vanish on the two-fold symmetry axes. X_2 and M_2 points have intensities on the two-fold axes, but vanish on the other symmetry axes. Again, the most important special points defining "quasi-BZ boundaries" form an essentially discrete set in wavenumber space. One of the important results to emerge from the work of recent years is that the spectrum of elementary excitations is determined very strongly by these "quasi-BZ" structures of wavenumber space: free-particle dispersion relations are found around the most intense Γ points, whereas the most intense "quasi-BZ boundaries" lead to stationary states.

20.3 Numerical Techniques for the Calculation of Spectra of Elementary Excitations in Quasicrystals

The prerequisite for the numerical investigation of elementary excitations in quasicrystals is a proper structural model of the quasicrystal. There are two major approaches to the construction of the structural models of quasicrystals. The first one is based on the decoration of proper, quasiperiodically arranged structural units by atoms. For instance, the structural models of icosahedral quasicrystals of the AlCuLi class are based on the decoration of golden rhombohedra and a composed unit – a rhombic dodecahedron (Henley–Elser decoration [26]). The underlying Penrose tiling is constructed by the projection method. In the second approach, for each chemical species there exists one or more acceptance domains (or atomic motifs, in other terminology) in the the higher-dimensional hyperspace. The structural model is then obtained by a projection from the hyperspace. A typical example of such a model is the 6D model of icosahedral (i-)AlPdMn proposed originally by Katz and Gratias (see, e.g., [12]). While great progress has been made in understanding the structure of icosahedral quasicrystals, the situation with the decagonal quasicrystals is not so optimistic. Although high-resolution electron microscopy helps significantly in revealing the medium-scale structure (10–20 Å) [27], for most of the decagonal quasicrystals the detailed arrangement of atoms remains unclear. In such cases the calculation of the phonon or electronic density of states (DOS) for several tentative structural models and their comparison with the experimental data can significantly help in establishing the correct structural model. For instance, for the decagonal (d-)AlCuCo, Burkov [7] proposed a model based on a binary tiling. Later, he proposed, for the same system, a new model based on a triangle tiling [8]. X-ray spectroscopic measurements did not prefer any of these models. The calculation of the electronic structure of both models [41] clearly favors the latter.

We shall not discuss the details of the construction of a model for a particular system. We refer the reader to other chapters of this book, or to [23,31,41,44,62] and the references therein.

Numerical studies must always be performed on finite samples. A very important notion is the possibility of constructing approximant structures. Rational or periodic approximants may be constructed by deforming the subspace of the higher-dimensional hyperspace perpendicular to the physical space in such a way that the projected lattice is periodic. For icosahedral quasicrystals, each approximant may be characterized by a rational approximant $\tau_n = F_{n+1}/F_n$ (F_n is a Fibonacci number) to the golden mean τ. As $\tau_n \to \tau$, the lattice constants and the number of atoms contained in a unit cell tend to infinity. The lattice constant of an nth order cubic approximant to an icosahedral quasicrystal may be expressed as $d_n \doteq 1.701\tau^n a_{qc}$, where a_{qc} is a quasilattice constant – the edge of the golden rhombohedral tile. Each next approximant therefore has a lattice constant that is $\tau \approx 1.62$ times larger. The volume of the next approximant, and correspondingly also the number of atoms in the unit cell, increase by a factor of $\tau^3 \approx 4.24$. In practice, a third or fourth generation approximant is essentially indistinguishable from the infinite quasicrystal (see Table 20.1). Some approximants also exist as stable or metastable phases. In addition to quasicrystalline approximants, some crystals have a structure that is more or less directly related to quasicrystals. Comparison of elementary excitations of such crystals with elementary excitations of quasicrystals is often very interesting.

Table 20.1. The unit cell lattice constant d_n, number of atoms N_{atom} and chemical composition c (in at. %) of the rational approximants to i-AlPdMn

n	Approximant	d_n (Å)	N_{atom}	c_{Al}	c_{Pd}	c_{Mn}
1	1/1	12.45	128	68.8	15.6	15.6
2	2/1	20.15	544	68.4	22.8	8.8
3	3/2	32.60	2 292	70.3	20.6	9.1
4	5/3	52.75	9 700	70.6	20.7	8.7
5	8/5	85.36	41 068	70.7	20.6	8.6
6	13/8	138.11	173 936	70.8	20.6	8.6

The physically relevant information about phonons and electrons is contained in the eigenvalue spectrum and the eigenvectors of the dynamical and Hamiltonian matrices, respectively. As the quasicrystalline approximants are periodic systems, it is legitimate to apply the Bloch theorem. A complete spectrum of elementary excitations is therefore obtained by integration over all $\boldsymbol{k}$ vectors in the BZ of the periodic approximant. The eigenvalue problem for each $\boldsymbol{k}$ of the BZ may be formulated for phonons as

$$[\, \boldsymbol{D}(\boldsymbol{k}) - \omega_\alpha^2(\boldsymbol{k})\boldsymbol{I} \,]\, \boldsymbol{u}_\alpha(\boldsymbol{k}) = \boldsymbol{0}, \tag{20.2}$$

where $\boldsymbol{D}(\boldsymbol{k})$ is the dynamical matrix, and $\omega_\alpha^2(\boldsymbol{k})$ and $\boldsymbol{u}_\alpha(\boldsymbol{k})$ are eigenvalues and eigenvectors of vibrational eigenstates. $\boldsymbol{I}$ is an identity matrix. For electrons, the eigenvalue problem may be formulated as

$$[\, \boldsymbol{H}(\boldsymbol{k}) - E_\alpha(\boldsymbol{k})\boldsymbol{I} \,]\, \boldsymbol{w}_\alpha(\boldsymbol{k}) = \boldsymbol{0}, \tag{20.3}$$

where $\boldsymbol{H}(\boldsymbol{k})$ is the Hamiltonian, and $E_\alpha(\boldsymbol{k})$ and $\boldsymbol{w}_\alpha(\boldsymbol{k})$ are again eigenvalues and eigenvectors. From the viewpoint of the numerical techniques, both types of elementary excitations – phonons and electrons – may be treated by the same numerical methods.

The main difference between the calculation of spectra of elementary excitation of quasicrystalline approximants and the calculation of the corresponding spectra of ordinary crystals consists of the size of the structural model and consequently the size of the matrix describing the problem. Even the lowest order 1/1-approximant to an icosahedral quasicrystal has more than 100 atoms in the elementary cell. Large approximants can contain many thousands of atoms. The size of the corresponding matrices is $3N_a \times 3N_a$ and $9N_a \times 9N_a$ (N_a is number of atoms in the elementary cell) for phonons and electrons, respectively. Treatment of such large matrices requires special numerical techniques, which are discussed in Sect. 20.3.2.

20.3.1 Direct Diagonalization

The eigenvalue spectrum of phonons or electrons is obtained by diagonalization of the dynamical or Hamiltonian matrix, respectively. Small quasicrystalline approximants can be treated as ordinary crystals. The corresponding matrix is diagonalized by a standard library routine for diagonalization of Hermitian matrices; it usually implements the Householder method. The size of the approximant is severely limited by the available core memory. For instance, to store the Hamiltonian matrix of 2/1-approximant to i-AlCuLi (680 atoms in the unit cell, minimal s,p,d-basis, i.e. nine basis functions per atom) requires 600 MB of core memory. Each next approximant requires $\tau^6 \approx 18$ times more core memory. Calculation of the eigenvalue spectrum of large approximants using the standard methods therefore quickly exceeds available computer resources. Fortunately, for large approximants some further simplifications may be adopted. As the linear size of the BZ is inversely proportional to the real-space lattice constant of an approximant for large approximants (larger than 2/1-approximant), the size of the BZ is so small that the $\boldsymbol{k}$ dependence of the excitation spectrum inside the BZ may be neglected. In this case one can restrict the calculation of the spectrum to the Γ point (center of the BZ, $\boldsymbol{k} = 0$) only. Elements of matrices become real numbers. The calculation can be performed fully in real space. Moreover, as the radius of interaction of atoms is usually restricted to the second or third neighbor shell, the matrix of large approximants becomes sparse. Only non-zero matrix elements of sparse matrices have to be stored. This greatly reduces the

demands on the core memory. In the following sections, we consider the case of large approximants only, i.e. the case of the Γ point.

The quasicrystalline approximants with proper centering of the acceptance domains in the perpendicular space can possess some space-group symmetries. For instance, the quasicrystalline approximants of the i-AlCuLi class possess $Pa\bar{3}$ symmetry, and the approximants of the i-AlPdMn possess $P2_13$ symmetry. The symmetry of the lattice is also reflected in the symmetry properties of the matrices. The symmetry is the highest just in the case of the Γ point. The point-group subgroups T_h and T, respectively, of the above space-group symmetries can be used for the block diagonalization of the Hamiltonian or the dynamical matrix. The maximal size of the eigenvalue problem is then reduced by factors of eight and four, respectively. The symmetry also allows very compact and efficient storage of the matrix elements.

20.3.2 The Recursion Method

The eigenvalue spectrum of large sparse matrices can be efficiently calculated by the recursion method [25]. From the numerical point of view, the recursion method is essentially a method for transforming a symmetric matrix into a tridiagonal form. In this section we shall consider the case of the Hamiltonian matrix. After the replacement $\boldsymbol{H} \rightarrow \boldsymbol{D}$, $E \rightarrow \omega^2$, the formalism for the dynamical matrix is the same. The recursion method is a real-space method. The calculation is performed fully in the real space, i.e. for the Γ point only. Let $\boldsymbol{u}_0$ be a starting vector of the tridiagonalization. The starting vector has an important physical meaning and the choice of the starting vector is discussed in the next section. Using the recurrence relation

$$\boldsymbol{u}_{n+1} = \boldsymbol{H}\boldsymbol{u}_n - a_n\boldsymbol{u}_n - b_{n-1}\boldsymbol{u}_{n-1}, \tag{20.4}$$

a sequence of vectors $\boldsymbol{u}_n$, $n = 0, 1, 2, ...$, is generated. The coefficients a_n and b_n are determined at the each recursion level from the orthonormality condition for $\boldsymbol{u}_n$ vectors, $\boldsymbol{u}_n^+ \cdot \boldsymbol{u}_m = \delta_{mn}$ for all $m \leq n$, with the initial condition $b_{-1} = 0$, resulting in

$$a_n = \boldsymbol{u}_n^+ \boldsymbol{H}\boldsymbol{u}_n, \tag{20.5}$$

$$b_n = \boldsymbol{u}_n^+ \boldsymbol{H}\boldsymbol{u}_{n+1}. \tag{20.6}$$

The coefficients a_n and b_n represent the diagonal and off-diagonal matrix elements of the tridiagonal matrix $\boldsymbol{J}$, which may be formally expressed as

$$\boldsymbol{J} = \boldsymbol{U}^+ \boldsymbol{H}\boldsymbol{U}, \tag{20.7}$$

where the transformation matrix $\boldsymbol{U}$ consists of vectors $\boldsymbol{u}_n$, $n = 0, 1, 2, ..., L$.

The efficiency of the recursion method lies in the possibility of terminating the recursion process at a level L that is much smaller than the size N of the Hamiltonian matrix. L is usually of order of tens, while N is of order of

thousands. Altogether, only L multiplications of the sparse matrix $\boldsymbol{H}$ times a vector $\boldsymbol{u}_n$ are necessary. As only the last two vectors of the sequence $\boldsymbol{u}_n$ must be stored at each time, the method also has only modest core memory requirements.

It is possible to show that the set of coefficients a_n, b_n, $n = 0, 1, 2, ..., L$, contains the information about the eigenvalue spectrum equivalent to $2L$ moments of the DOS. A diagonal matrix element of the Green function

$$G_0(z) = \boldsymbol{u}_0^+ (z - \boldsymbol{H})^{-1} \boldsymbol{u}_0 \tag{20.8}$$

can be expressed as the continued fraction

$$\begin{aligned} G_0(z) = 1/(z - a_0 - b_1^2/(z - a_1 - b_2^2/(z - a_2 \\ - b_3^2/(z - ... - a_{L-2} - b_{L-1}^2/T_L(z)...)))), \end{aligned} \tag{20.9}$$

where $T_L(z)$ is a terminator. The proper termination of the continued fraction is a non-trivial task. Several sophisticated terminators have been proposed. In our calculations we have obtained satisfactory results with the terminator proposed in [45]. A different approach to the termination of the continued fraction is based on the Gaussian quadrature [49].

The imaginary part of the Green function $G_0(E + i0^+)$ gives the DOS $n_0(E)$ projected on to the state $\boldsymbol{u}_0$:

$$n_0(E) = -\frac{1}{\pi} \operatorname{Im} G_0(E + i0^+). \tag{20.10}$$

With a proper terminator one can obtain a smooth DOS that represents the DOS of an asymptotically large model.

The recursion method is an efficient method of providing information about the eigenvalue spectrum of large matrices. The physically relevant information takes the form of a projected DOS $n_0(E)$. We note that, in the present formulation, the method does not provide information about the individual eigenvalues or eigenvectors. The recursion method has limited energy resolution. The energy resolution of the recursion method is given by the number of recursion levels, L. The resolution may be estimated as $\Delta E = W/L$, where W is the width of the band. As the recursion method is a real-space method (calculation for the Γ point only), to increase the energy resolution one also has to increase the size of the model. Otherwise, finite-size effects (sharp spikes near the edges of the band) become significant. A satisfactory accuracy can be therefore obtained only for large models, typically with several thousands atoms in the unit cell. Smaller models must be treated within a supercell, i.e. the unit cell is periodically repeated in each direction several times in order to give a supercell containing several thousands of atoms.

20.3.3 Calculation of the DOS and Spectral Functions

The recursion method is a real-space method for the calculation of a diagonal element of the Green function: the imaginary part of this matrix element gives the DOS $n_\psi(E)$ projected on an arbitrarily chosen state $|\psi\rangle$. Let the state $|\psi\rangle$ be represented in a tight-binding (TB) basis by a vector $\boldsymbol{u}_0$. The projected DOS may be formally expressed as

$$n_0(E) = \sum_\alpha |\boldsymbol{u}_0^+ \boldsymbol{w}_\alpha|^2 \delta(E - E_\alpha), \tag{20.11}$$

where E_α and $\boldsymbol{w}_\alpha$ are the eigenvalues and eigenvectors of the tridiagonal matrix $\boldsymbol{J}$; see (20.7). Let the components of $\boldsymbol{u}_0$ be u_0^i, $i = 1, 2, ..., N$, where $i = (l, m, \boldsymbol{R}_l)$ is a shorthand for an orbital (l, m) located on an atom at $\boldsymbol{R}_l$.

If we choose the initial vector $\boldsymbol{u}_0$ as

$$u_0^i = \delta_{ik}, \tag{20.12}$$

then $n_0(E)$ is the DOS projected on an orbital k. Repeating the calculation for all orbitals k, $k = 1, 2, ..., N$, one can obtain the total DOS $n(E)$ as a sum of orbital contributions. For large models this procedure can become very time-consuming. A more efficient method for the calculation of the total DOS is the approach based on randomly phased vectors. If we choose the initial vector $\boldsymbol{u}_0$ as

$$u_0^i = C \exp(2\pi \mathrm{i} \eta_i), \tag{20.13}$$

where the η_i are uniformly distributed random numbers from the interval $[0, 1)$, the resulting DOS converges for large N to the total DOS $n(E)$. C is a normalization constant that normalizes the $\boldsymbol{u}_0$ vector to unity. A possible statistical error introduced by this random sampling may be minimized by averaging over several randomly phased vectors.

If $\boldsymbol{u}_0$ is chosen as a plane wave propagating in a direction $\boldsymbol{k}$,

$$u_0^i = C \exp(\mathrm{i} \boldsymbol{k} \boldsymbol{R}_l), \tag{20.14}$$

the resulting projected DOS is the Bloch spectral function $f(\boldsymbol{k}, E)$. The $\boldsymbol{k}$ vectors can take any values that are compatible with the periodic boundary conditions of the model. In practice, we calculate the spectral function for the Γ points in the repeated-zone scheme. The projection may also be restricted to a particular orbital, atom or to a polarization direction in the case of electrons or phonons, respectively.

As noted above, the Green function and the projected DOS may be expressed in a continued-fraction representation. The continued fraction may be terminated at the level $L \ll N$, which is much smaller than the dimension N of the Hamiltonian matrix. For most applications, $L \sim 20$–80 is sufficient, and a smooth DOS or spectral function may be obtained using a proper terminator. Increasing the number of recursion levels L over a certain limit does not improve the resolution, as problems with boundary conditions arise.

20.4 Phonons in Quasicrystals

From the viewpoint of a numerical calculation, phonons are the easier case: given the inter-atomic forces and the structure of an approximant, it is sufficient to construct and to diagonalize the dynamical matrix. For approximants that are too large to allow direct diagonalization, projected DOS and Bloch spectral functions may be calculated using the real-space recursion method discussed in Sect. 20.3.2. On the other hand, inelastic neutron scattering experiments [16] allow determination of the dynamical structure factor, and hence the dispersion relations and lifetimes of propagating dynamical excitations (whether the term "phonon" is really legitimate remains to be seen), rather than only their spectral distributions.

In order to reduce the complexity of the calculations, one has to adopt certain approximations concerning the physical picture of the elementary excitations in quasicrystals. It is convenient to restrict the physical picture of phonons to the harmonic approximation and the one-phonon approximation only. The "physics" of phonons is then contained in the dynamical matrix. If the interatomic potentials are known, the construction of the dynamical matrix is straightforward. The main difficulty just lies in the construction of proper interatomic potentials. A satisfactory general theory of interatomic potentials exists only for simple metals, where the pseudopotential theory is applicable [18,24]. Quasicrystals are typically binary or ternary alloys consisting of Al and one or two transition metals (TM). Construction of Al-TM interatomic potentials is a non-trivial task, and we refer the reader to [9] and the references therein.

The harmonic approximation assumes that the potential energy may be expanded around the equilibrium positions of atoms. The structural model must therefore first be statically relaxed using the same set of interatomic potentials as that used for the calculation of the dynamical matrix.

20.4.1 The Dynamical Matrix

The normal modes of vibration of a solid material (crystal, quasicrystal or glass) are given in the harmonic approximation in terms of the eigenvalues ω_ν and eigenvectors $\boldsymbol{u}_\nu(i)$ of the real-space dynamical matrix (i, j label atomic sites; α, β are Cartesian coordinates)

$$D_{\alpha\beta}(ij) = m_i^{-1/2}\, \Phi_{\alpha\beta}(ij) m_j^{-1/2}, \tag{20.15}$$

where m_i is the mass of the atom and $\Phi_{\alpha\beta}(ij)$ are force constants, defined as

$$\Phi_{\alpha\beta}(ij) = \frac{\partial^2}{\partial u_{i\alpha} \partial u_{i\beta}} U. \tag{20.16}$$

Let the total potential energy U of the system be written as a sum of interatomic pair potentials $V_{ij}(r)$:

$$U = \tfrac{1}{2} \sum_{ij, i \neq j} V_{ij}(|\boldsymbol{R}_i - \boldsymbol{R}_j|). \tag{20.17}$$

Then the force constants may be determined by the first and second derivatives of the interatomic pair potentials. For $i \neq j$,

$$\Phi_{\alpha\beta}(ij) = \left[\frac{1}{r}\frac{\partial V_{ij}}{\partial r} - \frac{\partial^2 V_{ij}}{\partial r^2}\right]\frac{r_\alpha r_\beta}{r^2} - \frac{1}{r}\frac{\partial V_{ij}}{\partial r}\delta_{\alpha\beta}, \tag{20.18}$$

where $\boldsymbol{r} = \boldsymbol{R}_i - \boldsymbol{R}_j$. For $i = j$, we have

$$\Phi_{\alpha\beta}(ii) = -\sum_{j, j \neq i} \Phi_{\alpha\beta}(ij). \tag{20.19}$$

Once the dynamical matrix is diagonalized, the vibrational spectrum (or "phonon" DOS) $g(\omega)$ may be expressed in terms of the eigenvalues ω_ν^2:

$$g(\omega) = 2\omega G(\omega^2) = \frac{2\omega}{3N_a}\sum_\nu \delta(\omega^2 - \omega_\nu^2). \tag{20.20}$$

If negative eigenvalues ω_ν^2 appear in the eigenvalue spectrum, this indicates that the model has not been correctly relaxed.

The Bloch spectral function $f_{\boldsymbol{e}}(\boldsymbol{k}, \omega)$ for propagating collective excitations with wave vector $\boldsymbol{k}$ and polarization $\boldsymbol{e}$ is given by the projection of the atomic displacements (described by the eigenvectors $\boldsymbol{u}_\nu(i)$) on to a plane wave $\boldsymbol{e}\, \mathrm{e}^{\mathrm{i}\boldsymbol{k}\boldsymbol{R}_i}$:

$$f_{\boldsymbol{e}}(\boldsymbol{k}, \omega) = 2\omega \sum_\nu \sum_{i,j} \boldsymbol{e} \cdot \boldsymbol{u}_\nu(i)\, \mathrm{e}^{-\mathrm{i}\boldsymbol{k}\boldsymbol{R}_i}\, \boldsymbol{e} \cdot \boldsymbol{u}_\nu(j)\, \mathrm{e}^{\mathrm{i}\boldsymbol{k}\boldsymbol{R}_j}\, \delta(\omega^2 - \omega_\nu^2)\,. \tag{20.21}$$

In order to obtain smooth functions, it is necessary to apply, for example, a Gaussian broadening of the δ-functions.

Localization of vibrational eigenmodes is characterized by the participation ratio P_ν:

$$P_\nu = \left(\sum_j \frac{\sum_\alpha |u_{\alpha\nu}(j)|^2}{m_j}\right)^2 \left(N_a \sum_j \frac{(\sum_\alpha |u_{\alpha\nu}(j)|^2)^2}{m_j^2}\right)^{-1}. \tag{20.22}$$

For extended modes in crystals one has $P \sim 0.6$, whereas for a mode localized on a single atom, $P_\nu \sim 1/N_a$. The dynamical matrix has always a three-fold degenerate eigenvalue at $\omega_0 = 0$ corresponding to an uniform translation of the system. In this case, the participation ratio is $P_0 = 1$.

Calculation of the vibrational eigenmodes by direct diagonalization is limited by computer capacity. In practice, the limit is $N_a \sim 1000$ atoms. For larger systems, approximate techniques for the calculation of the vibrational spectrum must be used.

20.4.2 The Dynamical Structure Factor

Experimentally, the information on the vibrational eigenmodes is contained in the double-differential scattering cross-section for neutrons per solid angle and energy. The coherent cross-section is proportional to the dynamical structure factor $S(\boldsymbol{k},\omega)$,

$$\frac{\mathrm{d}^2\sigma}{\mathrm{d}\Omega \mathrm{d}\omega} = \langle b \rangle^2 \left| \frac{k_{out}}{k_{in}} \right| S(\boldsymbol{k},\omega), \tag{20.23}$$

where $\boldsymbol{k} = \boldsymbol{k}_{in} - \boldsymbol{k}_{out}$ is the wave vector difference between the incoming and scattered neutrons and b is the scattering length of the atomic nucleus. $S(\boldsymbol{k},\omega)$ may be expressed in terms of the vibrational Green function $G_{\alpha\beta}(ij,\omega)$, defined as the resolvent operator

$$G_{\alpha\beta}(ij,\omega^2) = \left[\omega^2 \delta_{ij} \cdot \delta_{\alpha\beta} - D_{\alpha\beta}(ij)\right]^{-1}. \tag{20.24}$$

In a one-phonon approximation, one has

$$S(\boldsymbol{k},\omega) = -2\hbar \left[n(\omega)+1\right] \mathrm{e}^{-2W(\boldsymbol{k})} \times \\ \times \sum_{ij} \mathrm{e}^{-\mathrm{i}\boldsymbol{k}(\boldsymbol{R}_i - \boldsymbol{R}_j)} \sum_{\alpha,\beta} k_\alpha \, \mathrm{Im}\, G_{\alpha\beta}\left[ij, (\omega + \mathrm{i}0^+)^2\right] k_\beta, \tag{20.25}$$

where $W(\boldsymbol{k})$ is the Debye–Waller factor and $n(\omega)$ the Bose–Einstein occupation function. Expressing the Bloch spectral function as a diagonal matrix element of the Green function between plane waves, cf. (20.14),

$$f_{\boldsymbol{e}}(\boldsymbol{k},\omega) = -\frac{2\omega}{\pi} \sum_{i,j} \sum_{\alpha,\beta} e_\alpha \, \mathrm{e}^{-\mathrm{i}\boldsymbol{k}\boldsymbol{R}_i} \, \mathrm{Im}\, G_{\alpha\beta}\left[ij, (\omega + \mathrm{i}0^+)^2\right] \, e_\beta \, \mathrm{e}^{\mathrm{i}\boldsymbol{k}\boldsymbol{R}_j}, \tag{20.26}$$

we find that the dynamical structure factor $S(\boldsymbol{k},\omega)$ is given in a one-phonon approximation in terms of the spectral function for longitudinal polarization $(\boldsymbol{e} \| \boldsymbol{k})$ as

$$S(\boldsymbol{k},\omega) = \frac{\hbar}{m} \frac{n(\omega)+1}{\omega} \mathrm{e}^{-2W(\boldsymbol{k})} (\boldsymbol{e} \cdot \boldsymbol{k})^2 \, f_{\boldsymbol{e}}(\boldsymbol{k},\omega). \tag{20.27}$$

For simplicity, the previous equations have been formulated for a monoatomic material. For a binary system, partial vibrational spectral functions $f_{\boldsymbol{e}}^{IJ}(\boldsymbol{k},\omega)$ $(I,J = A,B)$ may be defined by restricting the atomic displacements to the sites occupied by one atomic species. Partial dynamical structure factors $S_{IJ}(\boldsymbol{k},\omega)$ are obtained by multiplying the $f_{\boldsymbol{e}}^{IJ}(\boldsymbol{k},\omega)$ for longitudinal polarization by the thermal occupation and Debye–Waller factors:

$$S_{IJ}(\boldsymbol{k},\omega) = \hbar \frac{n(\omega)+1}{\omega} \frac{\mathrm{e}^{-W_I(\boldsymbol{k})}}{{m_I}^{1/2}} \frac{\mathrm{e}^{-W_J(\boldsymbol{k})}}{{m_J}^{1/2}} (\boldsymbol{e} \cdot \boldsymbol{k})^2 \, f_{\boldsymbol{e}}^{IJ}(\boldsymbol{k},\omega). \tag{20.28}$$

The total dynamical structure factor is given in terms of a weighted average over the partials:

$$\langle b\rangle^2 S(\boldsymbol{k},\omega) = c_A b_A^2 S_{AA}(\boldsymbol{k},\omega) + c_B b_B^2 S_{BB}(\boldsymbol{k},\omega) + 2\sqrt{c_A c_B}\; b_A b_B S_{AB}(\boldsymbol{k},\omega), \tag{20.29}$$

with $\langle b\rangle = c_A b_A + c_B b_B$. Alternatively, the partial dynamical structure factors relating to dynamical fluctuations in the number density $S_{NN}(\boldsymbol{k},\omega)$, the concentration $S_{CC}(\boldsymbol{k},\omega)$ and their cross-correlations $S_{NC}(\boldsymbol{k},\omega)$ may be used [17]. In practice, the "diagonal" spectral functions $f_{\boldsymbol{e}}^{AA}, f_{\boldsymbol{e}}^{BB}$ and $f_{\boldsymbol{e}}^{NN}$ are calculated using the recursion method, and the off-diagonal terms are given by linear combinations of the diagonal terms. The partial Debye–Waller factors $W_I(\boldsymbol{k})$ may be calculated in terms of the partial vibrational DOS $g_I(\omega)$:

$$W_I(k) = \frac{\hbar k^2}{m_I} \int_0^\infty g_I(\omega)\, \frac{n(\omega)+\frac{1}{2}}{\omega}\, \mathrm{d}\omega. \tag{20.30}$$

This completes the information necessary for the determination of $S_{IJ}(\boldsymbol{k},\omega)$.

20.4.3 Phonons in Icosahedral Quasicrystals

Figure 20.1 shows the Bloch spectral function $f_L^{NN}(\boldsymbol{k},\omega)$ for longitudinal density fluctuations propagating along a two-fold symmetry axis of an icosahedral quasicrystal. The calculation has been performed using the recursion method for the 5/3-approximant to i-AlCuLi. The lattice parameter of the model measures $a = 59.6$ Å and the cell contains 12 232 atoms. Interatomic forces have been constructed via pseudopotential theory. For more details of the calculation, see [62].

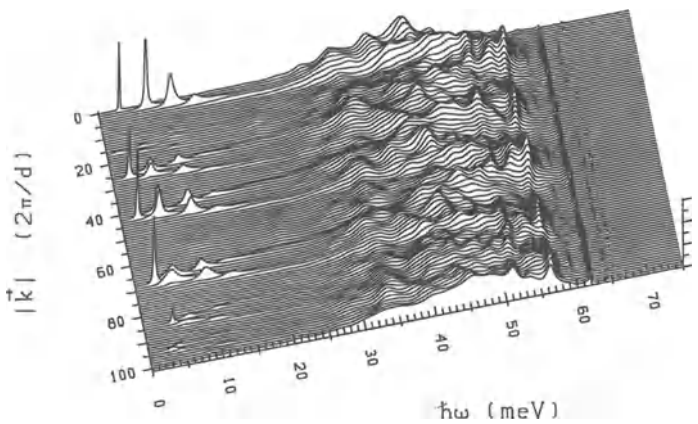

Fig. 20.1. The vibrational spectral function $f_L^{\mathrm{LiLi}}(\boldsymbol{k},\omega)$ for longitudinal density fluctuations propagating along a two-fold symmetry direction in i-(AlCu)Li, calculated by the recursion method

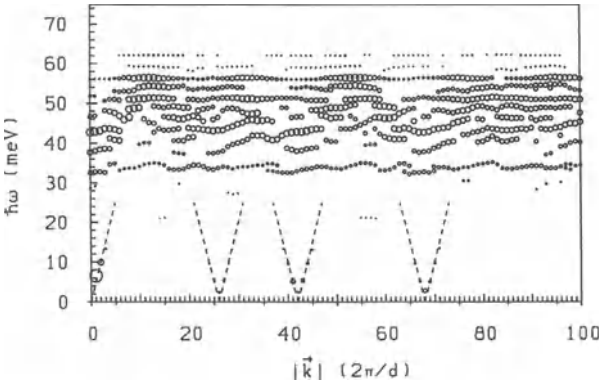

Fig. 20.2. Dispersion relations for longitudinal phonons defined in terms of the positions of the peaks in the spectral function $f_L^{\mathrm{LiLi}}(\boldsymbol{k},\omega)$

The essential results obtained for icosahedral quasicrystals can be summarized as follows. (a) In the spectral function a series of sharp peaks with linear dispersion relations are found around the most intense Bragg peaks (Γ points of 6D reciprocal lattice). These peaks represent acoustic modes propagating with the sound velocity c, $\omega = c|\boldsymbol{k}|$. The maxima of these peaks define dispersion relations (see Fig. 20.2). These long-wavelength acoustic excitations are accessible to neutron scattering. (b) Close to "quasi-BZ boundaries" the dispersion relations become stationary. The lowest-energy stationary modes have also been detected in neutron experiments on i-AlPdMn [6]. (c) At higher frequencies one finds a series of rather broad peaks, again with very little dispersion. These quasistationary modes determine the structure of the vibrational DOS, similar to the van Hove singularities in a crystal. (d) In the spectrum, localized modes exist. These modes exist not only at high and low frequencies, but certain discrete groups of localized modes also exist at intermediate frequencies. Each of these groups can be associated with certain topological features of the supporting quasicrystalline structure [19].

20.4.4 Phonons in Decagonal Quasicrystals

In decagonal quasicrystals, quasiperiodicity is restricted to the plane perpendicular to the non-crystallographic ten-fold axis, while along this axis the structure is periodic. Model studies have shown that the singular features of spectra of quasiperiodic Hamiltonians are more pronounced in lower dimensions. Our recent studies [23] of phonons in approximants to d-AlMn alloys (854 atoms in the unit cell) confirm this conjecture. In the comparison with i-AlMn alloys, the striking differences are that (a) the eigenvalue spectrum is broader (70 meV in comparison to 50 meV for i-AlMn) and (b) the DOS has rather a spiky structure (see Fig. 20.3). The analysis of the dispersion relations shows that around the most intense Γ points we again find propagating

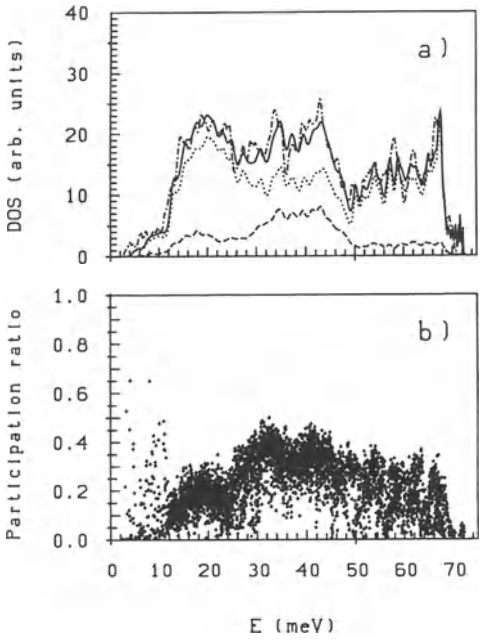

Fig. 20.3. **(a)** Vibrational DOS in d-AlMn. Full lines – total DOS; dotted – partial Al-DOS; dashed – partial Mn DOS, all calculated via the recursion method. Dash-dotted line – total DOS via exact diagonalization for Γ and X points. **(b)** The participation ratio $P(\omega_\nu)$ of eigenstates

acoustic modes, but with very strong anisotropies in the velocities of sound for modes traveling along periodic and quasiperiodic directions. We also find a striking difference between transverse modes propagating in the quasiperiodic plane and polarization vectors in the quasiperiodic plane and along the periodic axis, respectively. Whereas transverse modes with in-plane polarization vectors (and also longitudinal modes) are stationary only in a narrow region around the "BZ-boundary" points, modes with polarization along the periodic axis are stationary almost everywhere in $\boldsymbol{k}$ space. The tendency to localization is stronger in decagonal than in icosahedral quasicrystals. This illustrates the fact that the reduced dimensionality of the quasiperiodicity favors the confinement of eigenstates.

Another interesting phenomenon found in the phonon spectra of decagonal quasicrystals is the existence of optical modes at very low (3–6 meV) energies. These modes have also been observed in the AlMn T-phase – an approximant phase to the decagonal quasicrystal. The structure of the phase has been resolved in [27]. Figure 20.4 shows phonon dispersion relations of the $Al_{77}Mn_{23}$ T-phase (156 atoms in the orthorhombic unit cell) along the Cartesian directions. Acoustic modes are hybridized with low-lying optical modes. Several of these modes exhibit very weak dispersion and the calculated participation ratio indicates their localization. These low-energy modes are also seen as a small peak in the DOS. The low-energy optical modes have their origin in the existence of less dense regions in the atomic structure, which may occur in such complex structures. This conjecture also supports the fre-

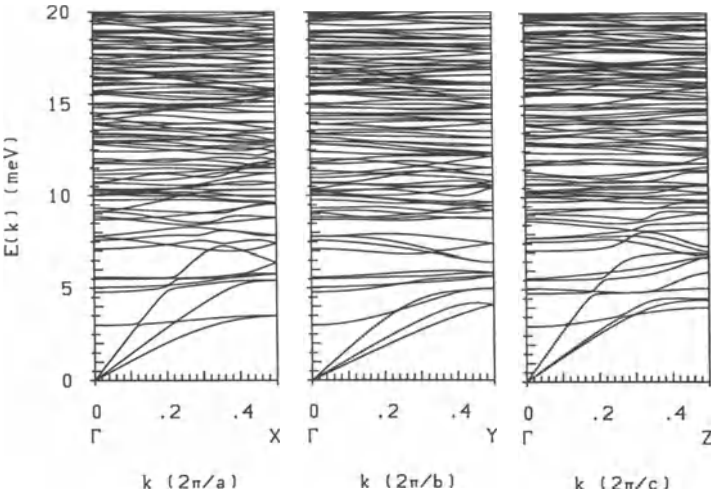

Fig. 20.4. Phonon dispersion relations in orthorhombic AlMn T-phase calculated along Cartesian directions. Low-lying optical modes hybridized with the acoustic modes indicate the existence of loosely packed regions in the structure. Calculated by exact diagonalization for the reduced BZ

quent occurrence of crystallographic sites with fractional occupations [27], experimentally observed in many crystalline approximants to the decagonal quasicrystals. We assume that such regions are not specific to the decagonal quasicrystals only and they may also exist in icosahedral quasicrystals.

20.5 Electrons in Quasicrystals

Electrons in quasicrystals are treated within the density functional formalisms (see, e.g., [46]). The electronic eigenstates are economically calculated in the basis of "linear muffin-tin orbitals" (LMTO) [1]. The formalism of muffin-tin orbitals (MTO) allows one to treat separately the dependence of the electronic structure on the topological structure of the system represented by a matrix of structure constants and the chemical individuality of atoms represented by a potential function. The price to pay for this simplification is the dependence of the MTO basis on energy. In the LMTO formalism, the MTO energy dependence is linearized around properly chosen energies ϵ_ν, where ν is the principal quantum number. The reference energy is defined for each muffin-tin sphere and for each angular momentum l. For instance, for an Al atom we have three reference energies: one for $3s$, one for $3p$ and one for $3d$ orbitals. Although the electronic structure is sufficiently accurate only in the vicinity of the center of expansion, this accuracy is usually satisfactory for the whole interval of energies of interest – for the occupied valence band. In the LMTO method, the potential function is parametrized in terms of

four potential parameters per atom. These potential parameters have to be determined self-consistently. The main advantage of the LMTO method over other methods (LCAO, APW, etc.) and the key of the success of the method is the minimal size of the MTO basis. The size of the basis determines the size of the matrix to be diagonalized. In the LMTO method nine orbitals (one s, three p and five d orbitals) per atom are usually sufficient to form a base for the expansion of a wave function. The size of the basis of other methods is usually much larger. For details of the LMTO method, we refer the reader to [56] and to the references therein.

With the LMTO method one can calculate the electronic structure of a system with up to 200 atoms per unit cell. The LMTO method is therefore suitable for the investigation of the electronic structure of lowest quasicrystalline approximants or of crystals related to quasicrystals. For larger quasicrystalline approximants, we have to adopt further simplifications. The LMTO method leads to a generalized eigenvalue problem, i.e. in addition to the Hamiltonian matrix one also has to treat an overlap matrix. This is a consequence of the fact that MTOs, particularly s and p orbitals, are long-ranged. An important simplification is introduced by the concept of screening. This concept allows one to define a basis of screened most localized MTOs. However, the Hamiltonian defined in this most localized screened basis turns out to be accurate only up to first order in energy $(E - \epsilon_\nu)$. Such a Hamiltonian describes only narrow d bands of transition metals with sufficient accuracy. A more accurate Hamiltonian can be obtained by a canonical transformation which allows one to factorize the overlap matrix and perform the Löwdin orthonormalization. As a consequence, the overlap matrix disappears from the calculation and the transformed Hamiltonian becomes accurate up to the second order in $(E - \epsilon_\nu)$. This formalism represents a simplified version of the LMTO method – the TB-LMTO method [2]. This method is described in more detail in the next section. The advantage of the TB-LMTO method over the standard LMTO method is its simplicity and the possibility of performing the calculation in real space. We have to treat only one matrix – the Hamiltonian matrix. If the potential parameters are known, the construction of the Hamiltonian matrix is straightforward.

20.5.1 The Tight-Binding LMTO Hamiltonian

The two-center TB Hamiltonian in the Löwdin-orthonormal representation may be written as (a superscript γ defines quantities calculated in a nearly orthonormal basis)

$$\boldsymbol{H}^\gamma = \boldsymbol{\epsilon}_\nu + \boldsymbol{h}^\gamma, \tag{20.31}$$

where $\boldsymbol{\epsilon}_\nu$ is a diagonal matrix with components ϵ_ν that represent the reference energies for the linearization of the MTOs. The subscript ν indicates the dependence on the principal quantum number of the orbital, the subscript i,

$i = (l, m, \boldsymbol{R}_l)$, labeling orbitals and atomic sites is suppressed for simplicity. The Hamiltonian (20.31) is accurate up to the second order in $(E - \epsilon_\nu)$. The Hamiltonian matrix $\boldsymbol{h}^\gamma$ may be determined from the expansion (a superscript α defines quantities calculated in the screened, most localized TB basis)

$$\boldsymbol{h}^\gamma = \boldsymbol{h}^\alpha - \boldsymbol{h}^\alpha \boldsymbol{o}^\alpha \boldsymbol{h}^\alpha + \boldsymbol{h}^\alpha \boldsymbol{o}^\alpha \boldsymbol{h}^\alpha \boldsymbol{o}^\alpha \boldsymbol{h}^\alpha - \ldots, \tag{20.32}$$

where $\boldsymbol{o}^\alpha$ is a diagonal matrix of overlap parameters. The Hamiltonian $\boldsymbol{h}^\alpha$ satisfies the relation

$$\boldsymbol{H}^\alpha = \epsilon_\nu + \boldsymbol{h}^\alpha = \boldsymbol{c}^\alpha + \sqrt{\boldsymbol{d}^\alpha}\boldsymbol{S}^\alpha\sqrt{\boldsymbol{d}^\alpha}, \tag{20.33}$$

where $\boldsymbol{c}^\alpha$ and $\boldsymbol{d}^\alpha$ are diagonal matrices of screened potential parameters describing the center of gravity and the width of each band, respectively, and $\boldsymbol{S}^\alpha$ is a matrix of screened structure constants determined by the screening constants $\boldsymbol{\alpha}$. $\boldsymbol{H}^\alpha$ is accurate to first order in $(E - \epsilon_\nu)$. The screened structure constants are given in terms of conventional LMTO structure constants $\boldsymbol{S}^0$ by the relation

$$\boldsymbol{S}^\alpha = \boldsymbol{S}^0(\boldsymbol{I} - \boldsymbol{\alpha}\boldsymbol{S}^0)^{-1}. \tag{20.34}$$

Values of the screening constants that provide the most localized structure constants were found from numerical studies [2] as $\boldsymbol{\alpha} = (0.34848, 0.053030, 0.010714)$ for s, p and d orbitals. When the potential parameters $C \equiv c^\gamma$, $\Delta \equiv d^\gamma$ and γ are known, the screened potential parameters c^α and d^α, and the overlap parameters o^α, can be obtained using the expression

$$\frac{c^\alpha - \epsilon_\nu}{c^\gamma - \epsilon_\nu} = \left(\frac{d^\alpha}{d^\gamma}\right)^{1/2} = \frac{\alpha - \gamma}{o^\alpha d^\gamma} = 1 + \frac{\alpha - \gamma}{d^\gamma}(c^\gamma - \epsilon_\nu). \tag{20.35}$$

More details of the TB-LMTO method can be found, for example, in [51] and in the references therein. The explicit formulas for $\boldsymbol{S}_0$ are given also in [56]. The inversion (20.34) may be performed approximately [51]. There also exists an approximative explicit formula for the screened matrix constants $\boldsymbol{S}^\alpha$ [51]. The accuracy obtained by the truncation of the expansion (20.32) after the second term is, in practice, sufficient. As the recursion method requires only the result of a multiplication of the Hamiltonian $\boldsymbol{H}^\gamma$ and the vector $\boldsymbol{u}_n$, but not the Hamiltonian matrix itself, it is possible to avoid the matrix multiplications in (20.32).

For each topologically non-equivalent muffin-tin sphere, the potential parameters C, Δ and γ should be determined self-consistently. The initial values of the potential parameters may be chosen as the potential parameters of the pure elements. These potential parameters have been tabulated for most elements. Once the Hamiltonian is diagonalized it is possible to calculate the charge density inside each muffin-tin sphere. The charge density determines the new intra-sphere potential. New potential parameters can be calculated

from a solution of the radial Schrödinger (or scalar-relativistic Dirac) equation, solved for each muffin-tin sphere. This procedure is iteratively repeated. Although the self-consistent iterations substantially complicate the electronic structure calculations, the self-consistency has proven to be essential, particularly for ternary alloys with two TM elements.

The exact self-consistent calculation of the electronic structure of large quasicrystalline approximants becomes a formidable task. A simplification is made possible by considering only the nearest neighbors in the definition of equivalency of topological sites. Then one can distinguish only a limited number (of the order of tens) of topologically inequivalent sites, even in an infinite quasicrystal. A further simplification consists of transferring the potential parameters calculated self-consistently for a small approximant to larger approximants.

20.5.2 The Structure-Induced Pseudo-Gap in the DOS and Stability of Quasicrystals

For the quasicrystals of the i-Al(Mg,Li)(Zn,Cu) class, the electronic spectrum has been analyzed for a series of even quite large approximants [20,63]. The results may be summarized as follows. (a) Nearly-free-electron (NFE) dispersion relations are found around the most intense Γ points, leading to a parabolic DOS near the bottom of the band. (b) Close to the "quasi-BZ-boundary" points, a series of strongly degenerate free-electron states exist that are close to the Fermi level. Lifting the degeneracy leads to the formation of a Hume–Rothery-like minimum in the electronic DOS [57]. (c) The depth of this pseudo-gap varies only insignificantly in the hierarchy of the approximants (see Fig. 20.5). (d) The pseudo-gap is significant for the stability of quasicrystals. In an amorphous or liquid phase of the same composition, the pseudo-gap is much shallower or disappears [20].

The situation is slightly different for the thermodynamically stable i-AlPdMn alloys. A detailed investigation of the electronic structure of 1/1 to 8/5 approximants [44] shows that a structure-induced DOS minimum at the Fermi level exists in higher approximants, but not in the lowest order approximants that are destabilized by conflicting requirements from local topology and local chemical order (see Fig. 20.6). In Al–TM alloys, the structure-induced pseudo-gap is enhanced by the anti-resonance arising from the hybridization between the s,p band and the more localized TM d states [60]. Hence band-gap stabilization is here an important, but not the only decisive, factor in understanding the formation of quasicrystals.

In Fig. 20.7 a Bloch spectral function $f(\boldsymbol{k}, E)$ of the 5/3-approximant to i-AlCuLi calculated for $\boldsymbol{k}$ vectors in the direction along the two-fold symmetry axis is presented. Around the Bragg peaks at positions 0, 26, 42, 54, 68, ... (in units of $[2\pi/a]$) parabolic-like excitations are observed (see Fig. 20.8). These nearly-free-electron excitations are analogous to the acoustic excitations observed around the strong Bragg peaks in the phonon spectrum.

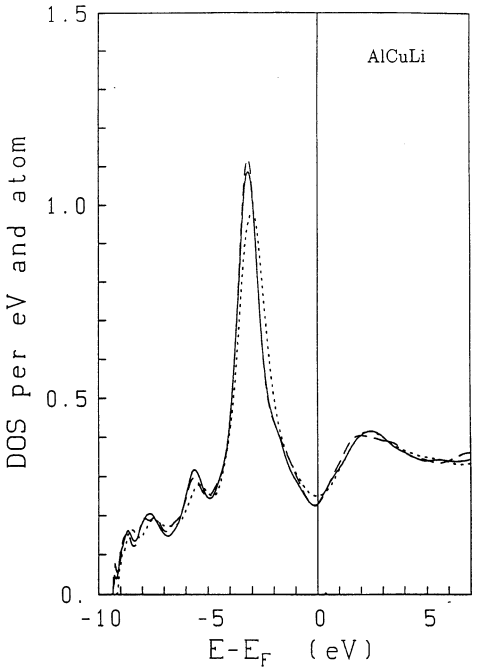

Fig. 20.5. The total electronic DOS of approximants to i-AlCuLi. Dotted line – 3/2-approximant, dashed line – 5/3-approximant, full line – 8/5-approximant

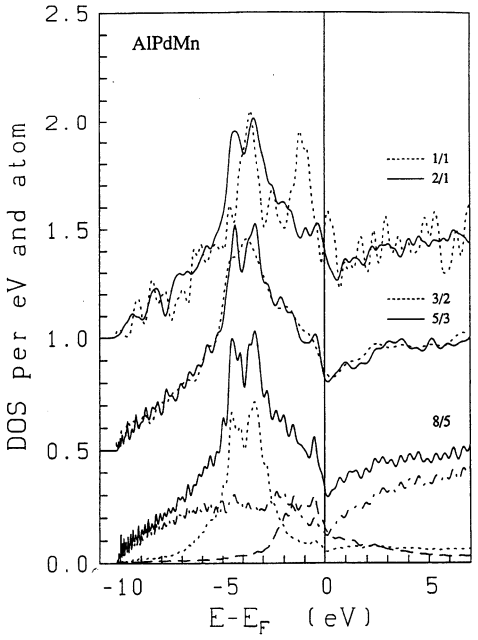

Fig. 20.6. Electronic DOS of 1/1 (dashed line), 2/1 (full line), 3/2 (dashed line), 5/3 (full line) and 8/5 (full line) approximants to i-AlPdMn. For the 8/5-approximant, the partial (dotted line – Pd, dashed line – Mn, dot-dashed line – Al) electronic DOS is also presented. The structural model of the 8/5-approximant consists of 41 068 atoms. Calculated using the recursion method

The possible importance of a Hume–Rothery stabilization mechanism is currently the subject of lively debate for decagonal quasicrystals [39,58,59].

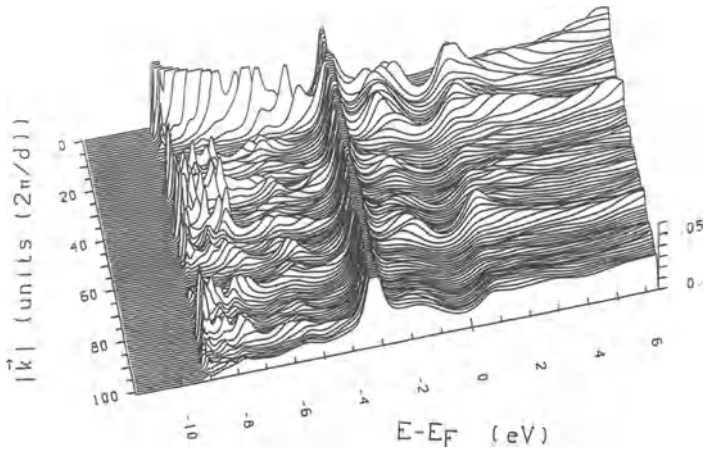

Fig. 20.7. The Bloch spectral function $f(\boldsymbol{k}, E)$ of the 5/3-approximant to i-AlCuLi, calculated for $\boldsymbol{k}$ vectors in the direction along the two-fold symmetry axis

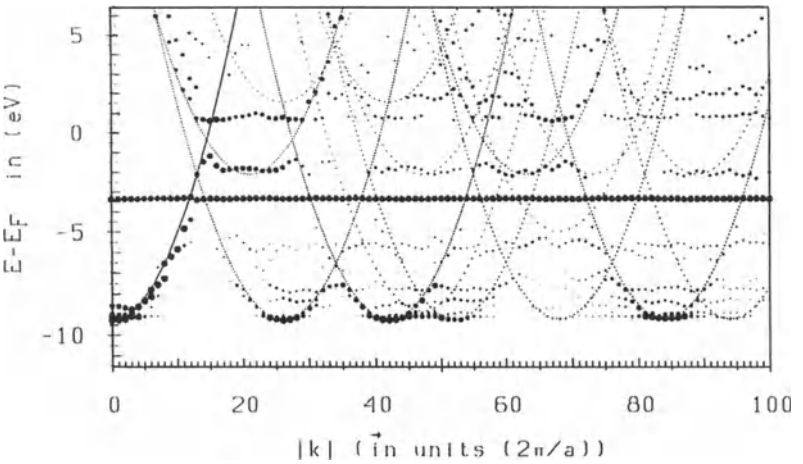

Fig. 20.8. Dispersion relations defined in terms of maxima of the Bloch spectral function $f(\boldsymbol{k}, E)$ of the 5/3-approximant to i-AlCuLi, calculated for $\boldsymbol{k}$ vectors in the direction along the two-fold symmetry axis

Part of the controversy is certainly due to the fact that the structural models for the decagonal phases are not yet as reliable in their details as those for icosahedral alloys. Recently, we have presented detailed studies of the electronic structure of d-$Al_{0.70}Pd_{0.13}Mn_{0.17}$ and d-$Al_{0.62}Cu_{0.19}Co_{0.19}$ alloys [40,41]. Due to the higher content of Mn (Co), the *d* band is broadened and partially covers the structure-induced minimum present in the Al-*sp* band (see Fig. 20.9). This structure-induced pseudo-gap in the Al band is shallower in

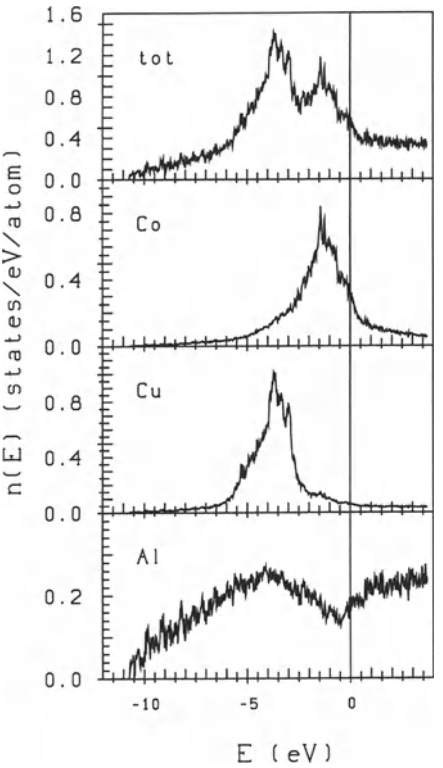

Fig. 20.9. The total and partial electronic DOS of an orthorhombic approximant to d-AlCuCo. The approximant has 356 atoms in the unit cell. Calculated via exact diagonalization of the Hamiltonian and integration over 32 $\boldsymbol{k}$ points in the irreducible part of the BZ

comparison with icosahedral quasicrystals and hence the decagonal quasicrystals receive less bandgap stabilization. A more substantial contribution to the stability here comes from the interaction of the TM atoms with a fully occupied d band (Pd, Cu) with the TM atoms with a partially occupied d band (Mn, Co). During self-consistent iterations the d bands of both metals in the alloy are repelling each other. Both the shift of the fully occupied (Pd, Cu)-d band to lower energies and the broadening of the partially occupied (Mn, Co)-d band can stabilize the alloy. Both effects are well confirmed by photoelectron (see Fig. 20.10) and soft X-ray spectroscopies [41].

20.5.3 Spiky Structure, Deep Pseudo-Gaps, and Real Gaps in the DOS

A spiky structure of the DOS is a characteristic feature of quasicrystals. The spikes may be interpreted as van Hove singularities, which arise from topological characteristics of the energy surfaces. If the number of atoms in the elementary cell increases, the topological structure of the energy surfaces becomes more complicated and the frequency of the singularities increases. Large approximants to quasicrystals contain huge number of atoms in the

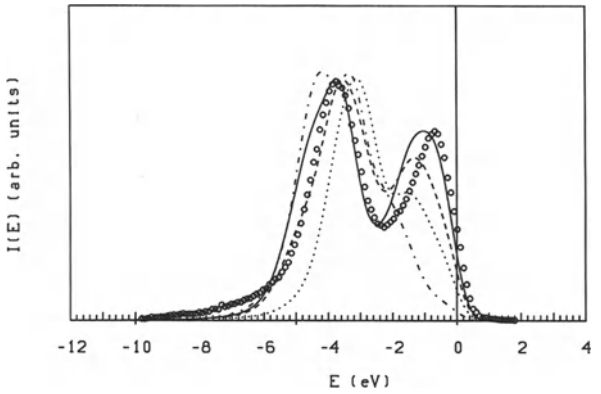

Fig. 20.10. A comparison of the photoemission spectrum of d-AlCuCo (dots) with the results of the electronic structure calculation for three variants of the Burkov model: B2Cu (full line), B2 (dashed line) and B2Co (dotted line); see the text

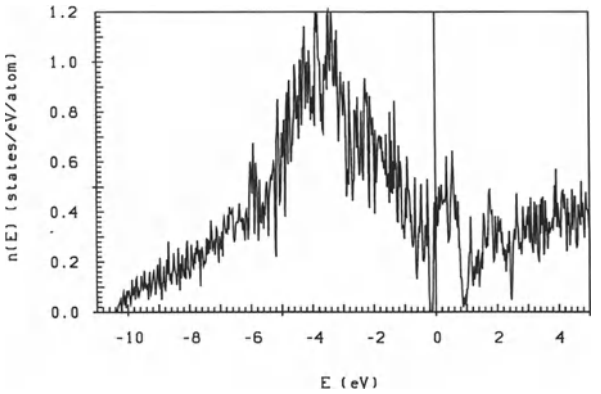

Fig. 20.11. The electronic DOS of an AlPdRe 1/1-approximant (128 atoms in the unit cell). The spectrum has a characteristic spiky structure. A gap of 0.15 eV is opened in the spectrum near the Fermi level. Calculated by exact diagonalization of the Hamiltonian and integration over 172 $\boldsymbol{k}$ points in the irreducible part of the BZ

unit cell and hence the corresponding DOS is strongly modulated by the van Hove singularities. For an infinite quasicrystal the spectrum is expected to become singular almost everywhere. An alternative view of the character of the spectrum is provided by the results of calculations of the electronic structure of 1D and 2D Fibonacci quasilattices. These results demonstrate a "singular continuous" character of the spectrum. The significance of the spiky character of the spectrum for the interpretation of the anomalous transport properties has been discussed many times. However, the experimental results on transport properties indicate the existence of very deep and narrow pseudo-gaps

or even real gaps in the spectrum, which cannot be identified with the relatively broad (of order 1 eV) and shallow structure-induced pseudo-gaps. These deep pseudo-gaps also seem to be clearly unattainable by the statistics of the discussed spiky structure of the DOS.

Figure 20.11 presents the DOS of the 1/1-approximant to AlPdRe. The structural model is a 6D model based on the Katz–Gratias model for AlPdMn. Although 128 atoms in the unit cell is not yet representative for a quasicrystal, the spiky character of the spectrum is already well demonstrated here. The most significant feature of this result is a gap in the spectrum very close (–0.09 eV) to the Fermi level. The width of the gap is 0.15 eV. The composition of the approximant is $Al_{68.75}Pd_{15.6}Re_{15.6}$. We note that a direct gap of 0.2 eV in the electronic spectrum of quasicrystalline $Al_{70}Pd_{20}Re_{10}$ has been experimentally observed in optical conductivity measurements [4]. Another interesting feature of the calculated spectrum is a very deep pseudo-gap about 0.9 eV above the Fermi level. The pseudo-gap is 0.25 eV wide and the DOS in the minimum reaches only about 10 % of the free-electron value. The origin of the gap and of the deep pseudo-gap is not yet completely clear. Similar deep pseudo-gaps have also been observed in AlMn approximants to the decagonal quasicrystals – T-phase and R-phase [32]. We have observed that the gap and the deep pseudo-gaps are very sensitive to changes in the local atomic structure. Although the presence of the gap or deep pseudo-gap means that *all* local DOS of all atomic sites possess the gap or deep pseudo-gap at the same energy, replacement of the occupation of one topological atomic site by a different chemical species can destroy the gap or the pseudo-gap. This indicates a strong hybridization of all orbitals.

20.5.4 Stationary States and Transport Properties

It has been shown that the electronic transport properties in quasicrystals can be characterized as marginally metallic (as in i-AlPdMn), insulating (as in i-AlPdRe) and extremely anisotropic (as in d-AlCuCo). The case of the decagonal quasicrystals is particularly intriguing, because their relatively high DOS at the Fermi level shows that the low conductivity cannot be attributed to a low number of carriers, but must be explained in terms of the character of the wave functions. The calculation of the participation ratio shows that, for example, in d-AlCuCo the eigenstates tend to be rather localized in the region of the d bands, with discrete groups of strongly localized states. However, as relatively extended eigenstates also exist in the same energy range, this is not sufficient to explain the observed transport behavior. Within the framework of Boltzmann transport theory, the electrical conductivity,

$$\sigma_{\alpha\beta} = \frac{e^2\tau}{\Omega_0} \sum_{n\boldsymbol{k}} v_{n\alpha}(\boldsymbol{k}) v_{n\beta}(\boldsymbol{k}) \left(- \frac{\partial f}{\partial E_n(\boldsymbol{k})} \right), \tag{20.36}$$

can be given in terms of the relaxation time τ and the velocities of the electrons $\boldsymbol{v}_n(\boldsymbol{k}) = \nabla_{\boldsymbol{k}} E_n(\boldsymbol{k})/\hbar$ determined by the dispersion of the bands $E_n(\boldsymbol{k})$,

where Ω_0 is a volume per atom. Although Boltzmann transport theory cannot be considered as a satisfactory theory to explain the observed anomalous transport properties of quasicrystals, the quantity $\sigma_{\alpha\beta}$ has proved to be a convenient quantity for characterizing the anisotropy in the electronic structure of decagonal quasicrystals.

We have considered two structural models of d-AlCuCo [7,8]. For the latter one (B2), we proposed two modifications that differ in their chemical ordering. We have denoted these as B2Cu and B2Co. The modification B2Cu excludes short Cu–Cu distances and allows Co atoms as nearest neighbors. In the B2Co modification, the situation is vice versa [41]. Figure 20.10 shows a comparison of the experimental photoemission spectrum [58] with the results of our theoretical calculations. The calculated partial DOS are truncated by the Fermi function, weighted by corresponding cross-sections and convoluted with a Gaussian function that simulates the instrumental resolution.

Figure 20.12 shows the diagonal elements of the energy-dependent conductivity tensor $\sigma_{\alpha\beta}$, calculated for a 352-atom model (B2) of d-AlCuCo. We find that around the Fermi level the conductivities σ_{xx} and σ_{yy} in the quasiperiodic plane are much smaller than the conductivity σ_{zz} along the periodic direction, with an anisotropy ratio of ~ 50 for a perfect decagonal structure. Experimentally, anisotropy ratios of the order of ten have been found at the lowest temperatures, depending strongly on quasicrystalline perfection and decreasing with higher temperature. The effect of disorder has been studied

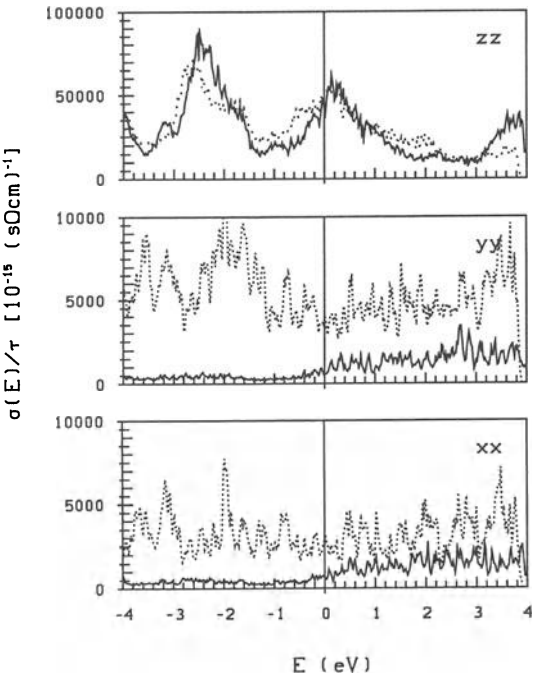

Fig. 20.12. The electronic conductivity tensor $\sigma_{\alpha\beta}(E)$ calculated along the Cartesian direction of an orthorhombic approximant to d-AlCuCo. Full lines show the conductivity for the ideal lattice, and broken lines that for a structure perturbed by random atomic displacements with a root-mean-square displacement of 0.15 Å

on a randomized structure. If we randomly shift atoms from their ideal positions with mean-square displacements of about 0.15 Å, the anisotropy ratio decreases dramatically by about one order of magnitude (Fig. 20.12). This demonstrates that the observed low conductivity values depend crucially on the coherence of the wave function. Random perturbations break the coherence of the eigenstates and lead to an increase in the conductivity [41].

20.6 Conclusion

We have shown that the nature of the eigenvalue spectrum is closely related to the diffraction pattern of quasicrystals. As a consequence of quasiperiodicity, Bragg peaks – "quasi-BZ centers" – are dense everywhere in wavenumber space, with intensities that are modulated by interference of radiation scattered from different atoms. As a consequence, the eigenvalue spectrum of a quasicrystal is characterized by a hierarchy of large and small "pseudo-gaps" (= minima in the DOS), arising from the more or less intense quasi-BZ centers and quasi-BZ boundaries. Larger gaps at the Fermi level are responsible for the Hume–Rothery-like mechanism for energetic stabilization of icosahedral quasicrystals, the narrower gaps being important for an understanding of the unusual physical properties. Propagating acoustic phonons and free-electron states have been found at low energies close to the most intense quasi-BZ centers, while stationary states have been identified at higher energies close to the quasi-BZ boundaries. These densely distributed stationary states are responsible for the characteristic spiky structure of the phonon and electron DOS in quasicrystals.

Recent Developments

The reader can find further information in our recent papers. A study of the electronic structure of a free-electron quasicrystal i-AlCuLi [13] shows that transition metals that are usual in the composition of most quasicrystals are not a prerequisite for formation of the characteristic pseudo-gap in the density of states near the Fermi level. A similar study of another non-traditional rare-earth–ZnMg quasicrystal [36] demonstrated that aluminum that is the dominant component in the majority of quasicrystals is not necessary for the formation of a deep pseudogap at the Fermi level. Conditions for formation of magnetic moments in quasicrystalline AlMn and AlPdMn systems were studied in [21,33]. It has been demonstrated that although most of manganese sites have zero magnetic moments, there exist some special sites in the structure where manganese atoms have large magnetic moments. The large anisotropy of the electronic structure and its consequences for the transport properties were investigated in [32]. Electronic structure, Fermi surfaces and transport properties of icosahedral AlPdRe was studied in detail in our recent papers [35,37]. Although the atomic structure of decagonal AlNiCo has not

been satisfactorily resolved so far, the electronic structure calculations [42,43] can contribute to understanding the short range ordering of aluminum and transition metal atoms. Some of our recent results are summarized also in review articles [22,29].

Recently, Conrad et al. [10,11,53] have resolved the structure of three different approximants to the dodecagonal $Ta_{1.6}Te$. The structure is based on a rectangle–triangle tiling decorated by large $Ta_{151}Te_{74}$ clusters whose nucleus is formed by distorted icosahedral Ta clusters. This is the first example of an atomic structure model of a dodecagonal quasicrystal. Detailed calculations of the electronic structure have been performed [38].

References

1. Andersen O.K. (1975): Phys. Rev. B **12**, 3060
2. Andersen O.K., Jepsen D., Sob M. (1987): In *Electronic Band Structure and its Applications*, ed. M. Youssouff, Springer, Berlin
3. Arai M., Tokihiro T., Fujiwara T., Kohomoto M. (1988): Phys. Rev. B **38**, 1621
4. Basov D.N., Pierce F.S., Volkov P., Poon S.J., Timusk T. (1994): Phys. Rev. Lett. **73**, 1865
5. Bienenstock A., Ewald P.P. (1962): Acta Crystall. **15**, 1253
6. Boissieu M. de, Boudard M., Moudden M., Quilichini M., Bellisent R., Hennion B., Currat R., Janot Ch. (1993): J. Non-Cryst. Solids, **153 & 154**, 552
7. Burkov S.E. (1991): Phys. Rev. Lett. **67**, 614
8. Burkov S.E. (1991): Phys. Rev. **47**, 12 325
9. Carlsson J.C. (1993): Phys. Rev. B **47**, 2515
10. Conrad M. (1997): *Tantalreiche Telluride*, Thesis, Universität Dortmund (unpublished)
11. Conrad M., Krumreich F., Harbrecht B. (1998): Angew. Chemie Int. Ed. **37**, 1383
12. Cornier-Quinandon M., Qivy A., Lefebvre S., Elkaim E., Heger G., Katz A., Gratias D. (1991): Phys. Rev. B **44**, 2071
13. Dall'Acqua G., Krajčí M., Hafner J. (1997): J. Phys. Cond. Matt. **9**, 10725
14. Fujiwara T., Arai M., Tokihiro T., Kohomoto M. (1988): Phys. Rev. B **37**, 2797
15. Gardner M. (1977): Sci. Am. **236**(1), 110
16. Goldmann A.I., Stassis C., Boissieu M. de, Currat R., Janot Ch., Bellisent R., Moudden M., Gayle F.W. (1992): Phys. Rev. B **45**, 10 280
17. Hafner J. (1983): J. Phys. C **16**, 5773
18. Hafner J. (1987): *From Hamiltonians to Phase Diagrams*, Springer, Berlin
19. Hafner J., Krajčí M. (1993): Phys. Rev. B **47**, 1084
20. Hafner J., Krajčí M. (1993): Phys. Rev. B **47**, 11 795
21. Hafner J., Krajčí M. (1998): Phys. Rev. B **57**, 2849
22. Hafner J., Krajčí M. (1999): In *Physical Properties of Quasicrystals*, ed. Z. M. Stadnik, Springer Series in Solid State Physics Vol. 126, Springer, Berlin, p. 209
23. Hafner J., Krajčí M., Mihalkovič M. (1996): Phys. Rev. Lett. **76**, 2738
24. Harrison W.A. (1989): *Electronic Structure and the Properties of Solids*, Dover, New York, p. 359

25. Haydock R. (1980): In *Solid State Physics*, ed. H. Ehrenreich, F. Seitz, D. Turnbull, Academic Press, New York, Vol. **35**, 215
26. Henley C.L., Elser V. (1986): Phil. Mag. B **53**, L59
27. Hiraga K., Sun W. (1993): Phil. Mag. Lett. **7**, 11
28. IUC, International Union of Crystallography (1992): Acta Crystall. A **48**, 928
29. Krajčí M. (1997): Mat. Sci. Eng. A **226-228**, 950
30. Krajčí M., Fujiwara T. (1988): Phys. Rev. B **38**, 12 903
31. Krajčí M., Hafner J. (1992): Phys. Rev. B **46**, 10 669
32. Krajčí M., Hafner J. (1998): Phys. Rev. B **58**, 5378
33. Krajčí M., Hafner J. (1998): Phys. Rev. B **58**, 14110
34. Krajčí M., Hafner J. (1998): In *Aperiodic 97*, ed. M. de Boissieu, J.-L. Verger-Gaugry, R. Currat, World Scientific, Singapore, p. 619
35. Krajčí M., Hafner J. (1999): Phys. Rev. B **59**, 8347
36. Krajčí M., Hafner J. (2000): J. Phys. Cond. Matt. **12**, 5831
37. Krajčí M., Hafner J. (2001): J. Phys. Cond. Matt. **13**, 3817
38. Krajčí M., Hafner J. (2001): to be published
39. Krajčí M., Hafner J., Mihalkovič M. (1996): Europhys. Lett. **34**, 207
40. Krajčí M., Hafner J., Mihalkovič M. (1997): Phys. Rev. B **55**, 843
41. Krajčí M., Hafner J., Mihalkovič M. (1997): Phys. Rev. B **56**, 3072
42. Krajčí M., Hafner J., Mihalkovič M. (2000): Phys. Rev. B **62**, 243
43. Krajčí M., Hafner J., Mihalkovič M. (2000): Mat. Sci. Eng. A **294-296**, 548
44. Krajčí M., Windisch M., Hafner J., Kresse G., Mihalkovič M. (1995): Phys. Rev. B **51**, 17 355
45. Lucchini M.U., Nex C.M.M. (1987): J. Phys. C **20**, 3125
46. Lundqvist S., March N.H. (1983): *Theory of the Inhomogeneous Electron Gas*, Plenum Press, New York
47. Martin S., Hebard A.E., Kortan A.R., Thiel F.A. (1991): Phys. Rev. Lett. **67**, 719
48. Mermin N.D. (1992): Rev. Mod. Phys. **63**, 3
49. Nex C.M.M. (1978): J. Phys. A **11**, 653
50. Niizeki K. (1990): J. Phys. A **22**, 4295
51. Novak H.J., Andersen, O.K., Fujiwara T., Jepsen O., Vargas P. (1991): Phys. Rev. B **44**, 3577
52. Pierce F.S., Poon S.J., Guo Q. (1994): Phys. Rev. Lett. **73**, 2220
53. Reich C., Conrad M., Krumreich F., Harbrecht B. (1999): Mat. Res. Soc. Symp. Proc. **553**, 83
54. Rieth T., Schreiber M. (1997): Z. Phys. B **104**, 99
55. Rokhhsar D.S., Wright D.C., Mermin N.D. (1988): Phys. Rev. B **37**, 8145
56. Skriver H.L. (1984): *The LMTO Method*, Springer, Berlin
57. Smith A.P., Ashcroft N.W. (1987): Phys. Rev. Lett. **59**, 1356
58. Stadnik Z.M., Zhang G.W., Tsai A.P., Inoue A. (1995): Phys. Rev. B **51**, 11 358
59. Trambly de Laissardière G., Fujiwara T. (1994): Phys. Rev. B **50**, 9843
60. Trambly de Laissardière G., Nguyen Manh D., Magaud L., Julien J.P., Cyrot-Lackmann F, Mayou D. (1995): Phys. Rev. B **52**, 7920
61. Tsunetsugu H., Fujiwara T., Ueda K., Tokihiro T. (1986): J. Phys. Soc. Jpn. **55**, 1420; see also Sire C. (1994): In *Lectures on Quasicrystals*, ed. F. Hippert, D. Gratias, Les Editions de Physique, Les Ulis
62. Windisch M., Hafner J., Krajčí M., Mihalkovič M. (1994): Phys. Rev. B **49**, 8701
63. Windisch M., Krajčí M., Hafner J. (1994): J. Phys. Cond. Mat. **6**, 6977

Part VI

Atomic Dynamics and Thermodynamics

21 Computer Simulations of Lattice Dynamics in Quasicrystals

Ted Janssen

Summary. Determination of the phonons in a quasicrystal is made complicated by the absence of lattice periodicity. Nevertheless, there are propagating phonon modes. In general, however, the eigenvectors are not Bloch functions. The spectra show a rich structure, and eigenvectors can be extended, localized and pseudo-localized.

21.1 Introduction

We shall consider here ideal quasiperiodic structures which are supposed to be in thermodynamic equilibrium. The problem that we want to discuss here is that of small oscillations around the equilibrium positions.

The systems are quasiperiodic and aperiodic. From the definition of quasiperiodicity it follows that a lattice-periodic structure is a special case of a quasiperiodic structure, but here we shall suppose that the quasiperiodic structure is not lattice-periodic. Furthermore, we suppose that the harmonic approximation is valid. Then it is allowable to use classical equations of motion. The problem is to find the spectrum and the eigenvectors (if they exist) of the dynamical matrix which follows from the equations of motion

$$m_j \ddot{\boldsymbol{u}}_j = \sum_k \boldsymbol{\Phi}_{jk} \boldsymbol{u}_k. \tag{21.1}$$

Here $\boldsymbol{\Phi}_{jk}$ is the second derivative of the potential energy with respect to the displacements $\boldsymbol{u}_j$ and $\boldsymbol{u}_k$ of the jth and kth particles. The indices j and k run over all atoms of the structure. As a consequence of the lack of lattice periodicity, there is no Brillouin zone and the usual procedure cannot be applied.

Quasiperiodic structures can be seen as the intersection of a periodic structure in a higher-dimensional space with the physical space. The periodic structure is a lattice-periodic array of atomic surfaces. The lattice of translations of the structure does not have three independent vectors in physical space. Otherwise, the physical structure would be lattice-periodic. This means that there are symmetry translations that bring the physical space to another point in internal space V_I. The set of these points is dense in V_I. Therefore, these points just label different realizations of the same quasiperiodic structure.

J.-B. Suck et al. (eds.), *Quasicrystals*
© Springer-Verlag Berlin Heidelberg 2002

We consider here the case in which the intersections of the atomic surfaces correspond to atomic equilibrium positions. This means that the derivative of the potential energy of the quasiperiodic structure with respect to each atomic coordinate vanishes: $\partial\Phi/\partial\boldsymbol{r}_j = 0$ for every atom j. The small oscillations around the equilibria are time-dependent displacements. Because these refer to displacements of atomic positions, these displacements can be taken along the physical space V_E. Furthermore, the displacement field depends on the internal coordinate t_I. Finally, we take the usual harmonic approximation. Then the potential energy can be written as

$$\Phi(t) = \sum_{njn'j'} \boldsymbol{u}_{njt} \cdot \Phi^{(2)}(nj, n'j', t) \cdot \boldsymbol{u}_{n'j't}\, C(nj,t)C(n'j',t)\,, \tag{21.2}$$

where t is the internal coordinate, the sum is over all atomic surfaces and all unit cells in n-dimensional (nD) space, and C is the characteristic function of the atomic surface, which is equal to 1 if $t-(\boldsymbol{n}+\boldsymbol{r}_j)_I$ belongs to the atomic surface, and equal to zero otherwise. The equations of motion are then

$$m_j\omega^2\boldsymbol{u}_{njt} = \sum_{n'j'} \Phi^{(2)}(nj, n'j', t) \cdot \boldsymbol{u}_{n'j't}. \tag{21.3}$$

These are linear equations with translation symmetry. Therefore, in nD space the solutions can be written in terms of Bloch functions:

$$\boldsymbol{u}_{njt} = \exp[\mathrm{i}\boldsymbol{k}_s \cdot \boldsymbol{r}_{njt}]\boldsymbol{U}(\boldsymbol{r}_{njt}). \tag{21.4}$$

It is easily shown that the factor $\exp[\mathrm{i}\boldsymbol{k}_I \cdot \boldsymbol{r}_I]$ drops out of the equations of motion. Therefore, one may choose $\boldsymbol{k}_s$ in V_E. This means that $\boldsymbol{u}_{njt}$ is the product of a phase factor $\exp(\mathrm{i}\boldsymbol{k}_E \cdot \boldsymbol{r})$ and a quasiperiodic function $\boldsymbol{U}$. This is the generalization of Bloch's theorem to quasiperiodic structures. The function $\boldsymbol{U}$ is determined by its value on the jth atomic surface, with the internal coordinate t as argument.

21.2 Phonons in IC-Modulated Phases and IC Composites

21.2.1 The Modulated Chain Model

The first class of quasiperiodic systems studied was that of the incommensurate (IC) modulated crystal phases. If the modulation is displacive, each atom is changed in position. That means that, in principle, the interactions lose lattice periodicity as well. A discussion of phonons in IC phases is given in [2].

A very simple 1D model is the following. Take a linear chain with harmonic interactions such that the potential energy is given in terms of the deviations u_n from the equilibrium positions by

$$V(t) = \tfrac{1}{2}\sum_n \alpha_n[u_n(t) - u_{n-1}(t)]^2, \tag{21.5}$$

where the spring constants are position-dependent with a period L. For example, one can simply take

$$\alpha_n = \alpha[1 + \Delta\cos(Qn + \phi)], \quad Q = 2\pi/L. \tag{21.6}$$

This was called the modulated spring model [3]. The corresponding equations of motion for $u_n(t) = u_n \exp(\mathrm{i}\omega t)$ are

$$m\omega^2 u_n = \alpha_n(u_n - u_{n-1}) + \alpha_{n+1}(u_n - u_{n+1}). \tag{21.7}$$

For $\Delta = 0$ the solution is simply given by the dispersion $\omega^2 = 4\alpha \sin(k/2)^2/m$, but in the presence of modulation the phonons of the unmodulated chain are coupled to an infinite set of equations. Each phonon with wave vector k in the Brillouin zone is coupled to the phonons with wave vector $k \pm Q$ (modulo the reciprocal lattice). The aperiodicity is the reason why the phonon problem does not fully decouple.

If L is an irrational number, a possible way to attack the problem is to approximate it with a rational number. A systematic method for that is the use of the continued fraction expansion. One writes

$$Q/(2\pi) = \cfrac{1}{m_1 + \cfrac{1}{m_2 + \cfrac{1}{m_3 + \ldots}}}, \quad m_i \in \mathbb{Z}. \tag{21.8}$$

By truncation one obtains a better and better commensurate approximation. For each commensurate approximation one has a finite number of particles in the unit cell, and the problem becomes finite-dimensional. If the periodicity is N ($1/L \approx M/N$), one has to determine the eigenvalues of an $N \times N$ matrix for every wave vector k in the Brillouin zone $-\pi/N < k < \pi/N$. This implies that there are N bands in the spectrum, that fully consists of bands. The eigenvectors are Bloch waves. For $M/N \to 1/L$, the number of bands and the number of gaps tend to infinity. One obtains a good picture of the limiting case by comparing the spectra at the different approximations, at which the length of the unit cell is N_n in the nth step. The sum of all the bandwidths goes to zero. A striking observation is that there is a self-similar character. If one takes the case $1/L = \tau = (\sqrt{5} - 1)/2$, the numbers m_i in the continued fraction expansion are all equal to unity, and the length of the unit cell grows as $N_n \sim (1 + \tau)^n$. The self-similar character can best be seen if one plots the eigenvalues for each value of $M/N \approx 1/L$ in the plane $1/L \leftrightarrow \omega^2$, for example, for all values of N up to 100. Every pattern in this picture comes back an infinite number of times on different scales, albeit slightly deformed [3]. This is very similar to the phenomenon found by Hofstadter [8] for a Bloch electron in an external magnetic field. In fact, the Hamiltonians of the two systems have much in common. There is, however, an important difference. The spectrum for the Hofstadter problem arising from a magnetic field on a square lattice has measure zero in the limit. For the modulated chain model that is only the case when $\Delta = 1$.

21.2.2 Phasons and Amplitudons

The modulated spring model gives an insight into the consequences of the coupling between phonon modes induced by the modulation, but cannot describe possible new types of excitations. A slightly more general 1D model has this possibility and can in principle explain the origin of the modulation. Suppose that the linear chain has positions n and is attached to those degrees of freedom x_n, for example, a local displacement or rotation. Suppose that the potential energy is given by

$$V = \sum_n \left[\alpha x_n^2/2 + x_n^4/4 + \beta x_n x_{n-1} + \delta x_n x_{n-2}\right]. \tag{21.9}$$

The equilibrium state satisfies

$$\alpha x_n + x_n^3 + \beta(x_{n-1} + x_{n+2}) + \delta(x_{n-2} + x_{n+2}) = 0. \tag{21.10}$$

These form an infinite set of coupled non-linear equations. An obvious solution is $x_n = 0$. The stability of this solution follows from a linear stability analysis. The small oscillations around the trivial solution have frequency ω, with

$$m\omega^2 = \alpha + 2\beta\cos(k) + \delta\cos(2k). \tag{21.11}$$

Notice that this corresponds to an optic branch, because the frequency goes to a constant ($\neq 0$) at $k = 0$. Moreover, the minimum of the curve is either at $k_c = 0$, or $k_c = \pi$ or $k_c = \cos^{-1}(-\beta/4\delta)$, depending on whether or not the modulus of $\beta/4\delta$ is smaller than unity. If α is small enough this means that for decreasing α values there is an instability at k_c. Because, generally, this is an arbitrary point in the Brillouin zone, the instability gives rise to an aperiodic structure. Variation of α as a function of temperature corresponds to that of the coefficient of the quadratic term in the Landau theory of phase transitions. The movement of the dispersion curve towards the instability is called a soft mode. Actually, both modes at $\pm k_c$ become soft.

Below the phase transition, a modulated phase appears with wave vector k_c. One has $x_n = A\cos(k_c n + \phi)$. The phonons in such a structure are obtained as the oscillations around the equilibrium positions. There are two new types of excitations. If one replaces the phase ϕ by $\phi + k_c m$, the total potential energy will remain the same. Because the values of $k_c m$ (modulo 2π) are dense on the interval $(-\pi, \pi)$, there is a dense set of shifts that leave the energy unchanged. Such a shift is therefore a zero-frequency excitation. In addition to this, oscillations in the amplitude A can occur. These two new excitations are known as phasons and amplitudons. They are special new excitations in quasiperiodic structures. The phason corresponds to a uniform phase shift, and this can be seen as well as a uniform shift in the internal space.

21.2.3 The Sliding Mode in IC Composites

A different type of phason occurs in IC composite structures. Such a structure consists of two or more subsystems which are modulated structures with a mutually IC basic structure. Each atom in the composite is assigned to one of the subsystems. The modulation of each subsystem is caused by the interaction with the other subsystems. Without this interaction, each subsystem would have phonon excitations characterized by a wave vector in its Brillouin zone. By the interaction, the different phonon modes become coupled.

In particular, without the interaction each subsystem would have three acoustic branches. The interaction couples these modes. There remain at least three acoustic modes with frequencies that are tending to zero. For the same reason as one can shift the modulation wave with respect to the underlying lattice, one can shift the subsystems with respect to each other. If one embeds the IC composite in a higher-dimensional space, such a shift can correspond to the global shift of the internal coordinates, a motion that connects configurations with the same energy. Whether the corresponding mode has zero-frequency depends on the modulation induced by the various subsystems in each other. There remains a zero frequency phason if the modulation functions are smooth. The phason is also called "sliding mode".

21.3 Models for Phonons in Quasicrystals

A model for studying phonons in a quasicrystal requires a structural model and an interaction model. Structural models run from 1D tilings to 3D structures based on real structure analysis. Very often, a tiling model already gives insight into the special new features of quasicrystals with respect to lattice-periodic structures.

A simple model is based on the Fibonacci chain. It is the intersection of physical space $(x,0)$ with a periodic array based on a lattice generated by $(1,-\tau)$ and $(\tau,1)$, consisting of atomic surfaces made of lines of length $1+\tau$ parallel to internal space $(0,y)$. It is a chain of atoms at positions $m+n\tau$ with intervals of length 1 or τ.

A 3D model is the 3D version of the Penrose tiling. It is the intersection of physical space $(V_E,0)$ with a periodic array of atomic surfaces. The lattice in 6D space is generated by

$$(\tau,1,0,\tau,1,0)\quad(-\tau,1,0,\tau,-1,0)\quad(0,\tau,1,-1,0,-\tau)$$
$$(1,0,\tau,0,-\tau,1)\,(1,0,-\tau,0,-\tau,-1)\,(0,\tau,-1,-1,0,\tau).$$

The atomic surfaces consist of rhombic triacontahedra, the projection of the unit cell on V_I. The structure consists of a quasiperiodic atomic set on a so-called Bravais module, the span of six vectors that are given by the first three components of the 6D basis. The atoms are on vertices of a tiling with two types of tiles: rhombohedra with a volume ratio of τ.

The interactions are given in terms of pair potentials. The potential $V = \sum_{ij} V(\boldsymbol{r}_i, \boldsymbol{r}_j)$ leads to a dynamical matrix in the harmonic approximation:

$$D_{ij} = \frac{\partial^2}{\partial \boldsymbol{u}_i \partial \boldsymbol{u}_j} \sum_{mn} V(\{\boldsymbol{r}_m + \boldsymbol{u}_m, \boldsymbol{r}_n + \boldsymbol{u}_n\}) \,|_0 / \sqrt{m_i m_j} \,. \tag{21.12}$$

Here $|_0$ indicates that the second derivative should be evaluated in the equilibrium positions. The squares of the eigenfrequencies are the eigenvalues of the operator D_{ij}. For a lattice-periodic structure this operator can be transformed into a sum of finite-dimensional operators by a Fourier transform. Due to the lack of lattice periodicity, this is not the case for a quasicrystal.

Specific examples of dynamical matrices are

$$D_{mn} = (\alpha_n + \alpha_{n+1})\delta_{mn} - \alpha_n \delta_{m,n-1} - \alpha_{n+1}\delta_{m,n+1}, \tag{21.13}$$

where α_n is A or B according to whether the nth interval in the Fibonacci chain is long or short, and the second derivatives of

$$V = \tfrac{1}{4} \sum_{ij} \alpha_{ij} u_{ij\parallel}^2 \,, \qquad u_{ij\parallel} = (\boldsymbol{u}_i - \boldsymbol{u}_j) \cdot (\boldsymbol{r}_i - \boldsymbol{r}_j)/|\boldsymbol{r}_i - \boldsymbol{r}_j|, \tag{21.14}$$

or

$$V = \tfrac{1}{4} \sum_{ij} \left(\alpha_{ij} u_{ij\parallel}^2 + \beta_{ij} u_{ij\perp}^2 \right). \tag{21.15}$$

The eigenvalues of the infinite-dimensional dynamical matrices cannot simply be obtained by a Fourier transformation. One possible approach is to consider clusters of increasing size. The tiling models often can be obtained by inflation rules: one starts with a seed, expands it with a certain factor, and fills the enlarged tiles with copies of the original tiles. A simple 1D example is the Fibonacci chain. One starts with a seed consisting of a number of intervals A or B, with length ratio τ. Then each A is replaced by AB and each B by A and the result is enlarged with a factor $1+\tau$. Iteration of this procedure yields an infinite Fibonacci chain, but this is approached via a series of finite chains. For each finite chain, the phonon problem comes down to the determination of the eigenvalues of a finite matrix.

Another approach is that via commensurate approximants. The embedding of a quasiperiodic tiling has points arbitrarily close to the physical space V_E. By a small strain, i.e. a small change in the basis vectors of the nD lattice, one can bring three independent points into V_E. This can be done by changing the internal coordinates only. Again, we take the Fibonacci chain as an example. The number τ has a continued fraction expansion, for which the successive truncations are F_m/F_{m+1}, where the Fibonacci numbers F_m are defined by $F_{m+1} = F_m + F_{m-1}$ with $F_0 = 1, F_1 = 1$. If one puts a strain on the lattice with basis vectors $(1, -\tau), (\tau, 1)$ such that the new basis is $(1, -F_m/F_{m+1}), (\tau, 1)$, the resulting chain is periodic. In the latter case, one can apply the usual theory, although the number of atoms in the unit cell

grows exponentially with m. In many cases an analysis of the influence of the size of the unit cell on the spectrum gives an insight into the spectrum of the infinite quasiperiodic system.

Other techniques are the use of the so-called trace map, and renormalization methods. A review of these, and of the relation with experiments, is given in [12].

21.4 Model Calculations

21.4.1 One-Dimensional Models

A 1D quasiperiodic chain can always continuously be deformed into a lattice-periodic chain. Therefore, such a chain is always an IC-modulated chain. It is not surprising that the properties of phonons in quasicrystalline models are very similar to those in the modulated spring model. The main difference is that the modulation function describing a quasicrystal is discontinuous. For the Fibonacci chain, for example, it is a saw-tooth function.

Consider that Fibonacci chain. The dynamical matrix is given by (21.13) with two spring constants, one for the long and one for the short interval. The series of commensurate approximants tends to the quasiperiodic chain. The length of the unit cell goes as the Fibonacci number F_m, i.e. as $(1+\tau)^m$. The number of bands is F_m and the total width of the spectrum goes exponentially to zero:

$$\sum_{i=1}^{F_m} \Delta_i \;=\; B_m \;\sim \exp(-m\alpha).$$

The density of states (DOS) is not a very nice function in 1D, because there is a divergence at the borders of the bands. The integrated DOS $I(\omega)$, which is the fraction of all states with frequency smaller than ω, is constant in a gap, and increases by an amount $1/F_m$ over each band. This function has $F_m - 1$ plateaus and is monotonically non-decreasing. It runs from $I(0) = 0$ to $I(\omega_{\max}) = 1$. In the limit it becomes a Cantor function, a monotonically non-decreasing function with a derivative that is zero almost everywhere. The bigger gaps stem from the lowest approximants, i.e. they reflect the structure of the smallest units, such as AB and ABA.

A first question is whether propagating waves still exist in a quasicrystal. This can be concluded from the dynamical structure factor. For a commensurate approximant, it is

$$S(q,\omega)_{L/N} \;\sim\; \sum_{k\nu} \left| \sum_{j=1}^{N} \mathrm{e}^{\mathrm{i}qr_j}\, q \cdot \epsilon_j(k,\nu) \right|^2 \Delta(q-k)\delta(\omega - \omega_{k\nu}), \qquad (21.16)$$

where the sum is over the vectors k in the Brillouin zone and over the modes ν for each k. The vector $\epsilon(k,\nu)$ is the eigenvector for the mode (k,ν). In a

lattice-periodic system there are N sharp peaks along a line k = constant. The position of this peak grows linearly for small k along the lowest branch, then flattens to a stationary point at the Brillouin zone boundary and finally goes to zero in the inverse way. The zero is reached at the first reciprocal lattice vector.

For the Fibonacci chain, the behavior is as follows (cf. Fig. 21.1).

1. For low frequency there is a sharp peak at a position that grows linearly with q. This indicates an acoustic mode of propagating waves.
2. The frequency of this peak reaches a maximum at a position that is halfway towards the position of the first strong Bragg peak in the static structure factor. This is a pseudo-Brillouin zone boundary.
3. For higher frequencies the peak broadens. Because the calculations were made in the harmonic approximation, this is not a lifetime effect, but it reflects the pseudo-localized character of the eigenvector.
4. There is an infinite number of gaps, with a hierarchical order. The bigger gaps are those already found for the lowest commensurate approximants.

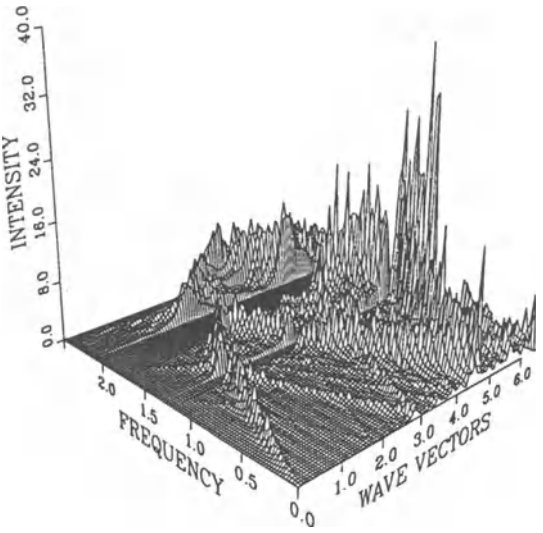

Fig. 21.1. The dynamical structure factor: the cross-section as function of wave vector and frequency for the Fibonacci chain. One may observe the linear dispersion for low frequencies, the broadening at higher frequencies, the gaps in the spectrum and the pseudo-zone boundary between the origin and the strong Bragg peak near 4.5

21.4.2 Models in Higher Dimensions

The treatment of models in higher dimensions is very similar. Two models are the 2D octagonal tiling and the 3D icosahedral tiling [4–6,9,10]. It turns out that, qualitatively, it makes no difference whether or not one makes all spring constants equal. For a short-range interaction the coordination is the important factor. Not all atoms have the same environment, and this topological difference is responsible for the difference with a periodic crystal. Both the octagonal tiling and the 3D icosahedral tiling can be constructed via an inflation rule. For the octagonal tiling each square is divided into four rhombs and three squares, each rhomb into three rhombs and two squares, and then the new structure is inflated by a factor $1 + \sqrt{2}$. A similar construction is available for the 3D icosahedral tiling. This means that one can again use either the cluster or the approximant approach. Approximants are obtained by replacing $\sqrt{2}/2$ and τ in the internal coordinates by the values of the truncated continued fraction expansion.

A possible further simplification is the use of "scalar" phonons. This means that for each site only one degree of freedom is considered and the potential energy is expressed in terms of these degrees of freedom only. This leads to a dynamical matrix with a dimension equal to the number of particles. For vector phonons this number has to be multiplied by the dimension of the physical space.

The DOS for (vector) phonons shows much structure in these models. There are many peaks, corresponding to van Hove singularities: for low frequencies the behavior is as ω^{d-1}, if d is the dimension of physical space. Also, in these cases the dynamical structure factor has peaks for constant q, and the position of this peak is, for low frequencies, linear in q. There the maximum is sharp. In the low-frequency region there are several pseudo-gaps, sharp minima in the DOS. The positions of these pseudo-gaps form a geometrical series towards the origin, but at the same time their depths decrease. For higher frequencies, the peaks broaden.

For the approximants one can determine the dispersion curves, which are functions on the Brillouin zone of the approximant. Comparing the various approximants (square for the 2D octagonal tiling and cubic for the 3D icosahedral tiling), the following interesting observation can be made. If one plots the dispersion curves for various approximants along a closed path in the Brillouin zone (e.g. $\Gamma - X - W - \Gamma$ in the square 2D zone) they become more and more the same if one scales the frequency with a constant factor. This means that in principle optic branches occur at arbitrarily low frequencies. This does influence physical measurements only up to a certain degree. For example, in the dynamical structure factor there are low-lying branches of peaks, but their intensity becomes very low (cf. Fig. 21.2). One can understand this in the following way. For low frequencies the zeroth order waves are the elastic waves. They are coupled by perturbation terms with Fourier components in the Fourier module of the quasicrystal. The admixing of other

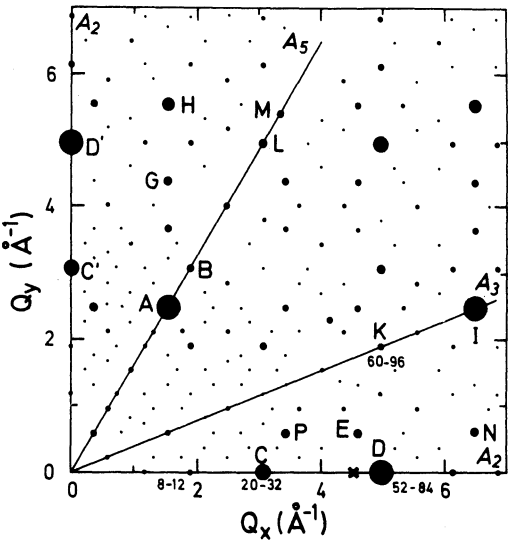

Fig. 21.2. A plane perpendicular to a two-fold axis for the icosahedral phase. There are two two-fold, a three-fold and a five-fold axis. The intensity of the elastic scattering is represented by the diameter of the circles. In going from one strong peak to another (e.g. from A to D), there is a narrow peak in the inelastic scattering which starts with a linear dispersion. Half-way between two strong static peaks, the inelastic peak goes down again and ends with zero frequency at the other strong Bragg peak

waves is very small if this interaction term is weak, which occurs when the static structure component with the coupling wave vector is very weak.

The conclusions from the simple models are to a high degree confirmed by more sophisticated calculations, where one takes a more realistic atomic interaction term, e.g. one of the known pseudo-potentials, and where one uses as structure a model closely related to the structure as determined by X-rays or neutrons [11].

21.5 The Character of Spectra and Eigenvectors

The vibration eigenvectors in a lattice-periodic structure are in the form of Bloch functions:

$$\boldsymbol{u}_{\boldsymbol{n},j} = \epsilon(\boldsymbol{k}, \nu|j) \exp(\mathrm{i}\boldsymbol{k} \cdot \boldsymbol{n}). \tag{21.17}$$

Here $\epsilon(\boldsymbol{k}, \nu)$ is a $3s$-dimensional vector, if s is the number of particles in the unit cell, and 3 is the dimension of physical space. The direct consequence is that all states are extended: the absolute value of displacements of atoms that are equivalent via the translations is the same. For aperiodic crystals this is no longer the case.

Another property that quasicrystals do not necessarily share with periodic crystals is the continuous character of the spectrum. For lattice-periodic crystals, the spectrum consists of bands, and is absolutely continuous. In general, the spectrum of a Hermitian operator consists of three parts: a discrete part, an absolutely continuous part and a singular continuous part. An indication of the character can be obtained from a multifractal analysis. To that end, consider a series of commensurate approximants. For each approximant, the frequencies are multivalued functions of the wave vector. The label for the discrete values is the branch label ν. Each branch has a width Δ_ν, the difference between the minimum and the maximum of branch ν. In the series labeled by m, the number of bands increases. In the mth step it is N_m. Following the splitting up of a certain band, its number is approximately $\nu = xN_m$. The width of the band scales as

$$\Delta_{xN_m} \sim \exp[-m\epsilon(x)]. \tag{21.18}$$

For an absolutely continuous or discrete spectrum, the exponents ϵ tend to one common value. For a singular continuous spectrum there is a distribution of values. The distribution function can be constructed [7] from the quantity $F_m(\beta)$:

$$F_m(\beta) = \left(\log \sum_\nu \Delta_\nu^\beta\right)/m. \tag{21.19}$$

The sum is taken over all ν for which $\Delta_\nu \neq 0$. If the density of bands with scaling exponent ϵ is $\Omega(\epsilon) \sim \exp[mS(\epsilon)]$, the function S is given by

$$S_m(\epsilon) = F_m + \beta\epsilon\,, \qquad \epsilon = -\frac{\mathrm{d}F_m}{\mathrm{d}\beta}. \tag{21.20}$$

If this function tends to a smooth limit function, this is an indication that the spectrum has a singular continuous part.

In that case, the eigenvectors also have a special character. They are neither localized in the usual sense of exponential decay towards infinity, nor are they extended. The modulus of the displacement differs strongly in the system. Very often, there is a self-similar character (cf. Fig. 21.3). These states are called "critical". As the name indicates, one expects that they will lose this character under very small perturbation. For a number of 1D model systems, usually tight-binding models on substitutional chains, it has rigorously been proven that the spectrum is singular continuous [1].

21.6 Surface Phonons in Quasicrystals

Surfaces may change the character of eigenstates strongly. It is well known that near the surface of a lattice-periodic crystal localized surface states may occur, although in the bulk only extended states are possible, at least if

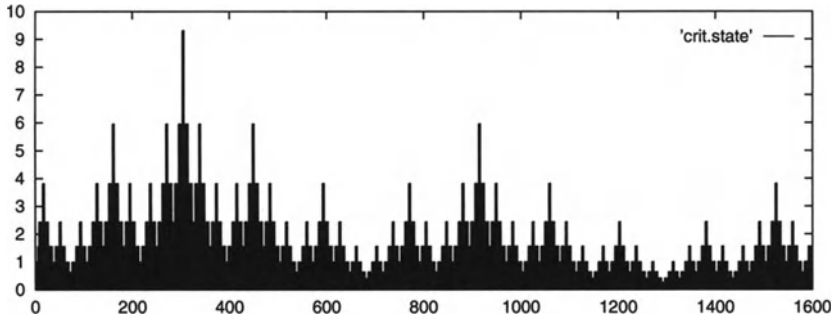

Fig. 21.3. A self-similar wave function for a tight-binding model based on a Fibonacci chain. On the vertical axis is plotted $|c_i|$ along a chain ($i = 1, N_m$) for the approximant with $N_m = 1597$

one considers an ideal crystal without defects. One may expect that this phenomenon is even stronger for quasiperiodic structures, because there non-extended states already appear in the bulk. In particular, a critical state could be changed into a localized state.

In a lattice-periodic structure a surface is characterized by a reciprocal lattice vector $[h, k, \ell]$. The distance $d_{hk\ell}$ between parallel net planes perpendicular to this wave vector is easily calculated. For a quasiperiodic structure the nD netplanes also intersect physical space in a family of parallel planes. If $\boldsymbol{H}$ is an nD reciprocal lattice vector, the plane $\boldsymbol{H} \cdot \boldsymbol{x} = m$ intersects physical space along lines $\boldsymbol{H}_E \cdot \boldsymbol{x}_E = m$. The distance between the planes is $|\boldsymbol{H}_E|^{-1}$. The vector $\boldsymbol{H}_E$ belongs to the Fourier module.

The phonon DOS can be decomposed in a sum over local DOS for the various slabs, where a slab is the collection of points $\boldsymbol{x}_E$ with $m < \boldsymbol{H}_E \cdot \boldsymbol{x}_E \leq m + 1$. In each slab, only states with eigenvectors with non-vanishing components on the atoms of the slab contribute.

Also, for quasicrystals it has been found that additional states appear. One should distinguish between two types of surface-induced phonons. First, there are those for which the modulus of the displacement goes exponentially to zero with the distance to the surface and which are concentrated in the first few atomic layers. Second, there are states that are different from those in the bulk, which also decay exponentially, but with a maximum that is not near the surface. These states may grow out of critical states if the boundary conditions are changed.

References

1. Bovier A., Ghez J.M. (1995): J. Phys. A **28**, 2313
2. Currat R., Janssen T. (1988): In *Solid State Physics*, ed. H. Ehrenreich, D. Turnbull, **41**, 202

3. de Lange C., Janssen T. (1989): J. Phys. C **14**, 5269
4. Hafner J., Krajčí M. (1990): Europhys. Lett. **13**, 335
5. Hafner J., Krajčí M. (1993): J. Phys. Cond. Mat. **5**, 2489
6. Hafner J., Krajčí M. (1993): Phys. Rev. **B47**, 11795
7. Hiramoto H., Kohmoto M. (1992): Int. J. Mod. Phys. **B6**, 281
8. Hofstadter D. (1976): Phys. Rev. **B14**, 2239
9. Los J., Janssen T. (1990): J. Phys. Cond. Mat. **2**, 9553
10. Los J., Janssen T., Gähler F. (1993): Int. J. Mod. Phys. **B7**, 1505
11. Poussigue J.P., Benoit C., de Boissieu M., Currat R. (1994): J. Phys. Cond. Mat. **6**, 659
12. Quilichini M., Janssen T. (1997): Rev. Mod. Phys. **69**, 277

22 Experimental Determination of the Dispersion of Vibrations in Monodomain Quasicrystalline Alloys

Bernard Hennion and Marguerite Quilichini

Summary. Inelastic neutron scattering on monodomain crystals is the only technique giving access to a detailed study of vibrational properties of quasicrystalline alloys. Several experiments, performed on different icosahedral phases, are now available in the literature. In this chapter the basis of the experimental determination of phonon dispersion curves by three-axis spectrometry is recalled. Experimental results on monodomain quasicrystalline alloys are presented and discussed in order to point out their specific vibrational properties compared to those of periodic lattices.

22.1 Introduction

Dynamical properties of quasicrystals are expected to differ from the usual behavior of 3D periodic crystals. Their specific long-range order, with no translational invariance, exclude Bloch wave expansion and the classical concept of Brillouin zones to describe collective lattice excitations, phonons, which are the basis of dynamical properties of periodic lattices. Theoretical aspects of the specific dynamics of quasicrystals are detailed in other contributions (see the chapters by T. Janssen and M. Krajčí in this volume). The purpose of this chapter is to give an overview of the experimental information which has been obtained so far on several monodomain quasicrystalline samples. As most of the experimental results on the lattice dynamics have been obtained by means of inelastic neutron scattering on a three-axis spectrometer, that technique and the usual approach to measure phonon dispersion in periodic crystalline samples will be presented in Sect. 22.2. After a brief summary of the experimental results obtained by other techniques in Sect. 22.3, Sect. 22.4 will be devoted to the presentation and discussion of the main experimental data obtained on monodomain icosahedral quasicrystals by inelastic neutron scattering on a three-axis spectrometer[1].

[1] Most of the results reviewed hereinafter, together with theoretical considerations, may be found in the paper of M. Quilichini and T. Janssen, *Rev. Mod. Phys.* **69** (1997) 277

J.-B. Suck et al. (eds.), *Quasicrystals*
© Springer-Verlag Berlin Heidelberg 2002

22.2 Inelastic Neutron Scattering on Three-Axis Spectrometer

22.2.1 Principle of the Measurement

The principle of a three-axis spectrometer is quite simple, and is displayed in Fig. 22.1: a monochromatic neutron beam is selected from a neutron source by using Bragg reflection on a single crystal (monochromator), with $\lambda_\mathrm{i} = \frac{2\pi}{k_\mathrm{i}} = 2d_\mathrm{m}\sin(\theta_\mathrm{m})$; this beam is sent to a sample; in a selected direction another single crystal (analyzer) is positioned in such a way that only a selected wavelength ($\lambda_\mathrm{f} = \frac{2\pi}{k_\mathrm{f}}$) can be reflected; a neutron detector is placed behind this analyzer. If neutrons are counted in the detector, that means that there has been some process in the sample which has induced the changes of trajectory and wavelength of the incident neutrons.

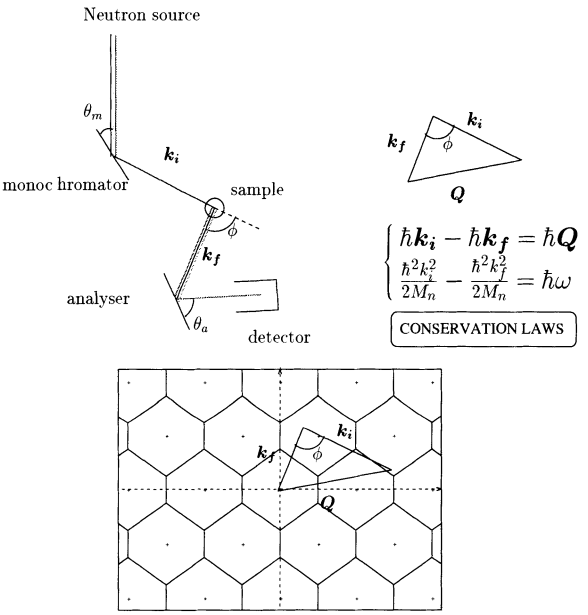

Fig. 22.1. Principle of a triple-axis spectrometer: a single $(\boldsymbol{Q}, \omega)$ point corresponds to a given configuration of the spectrometer. For a periodic lattice, the projection in the reciprocal space of the sample yields a single $(\boldsymbol{Q}, \omega)$ point, with $\boldsymbol{Q} = \boldsymbol{\tau} + \boldsymbol{q}$

The conservation rules of the energy and momentum of the total system may be written as

$$\begin{cases} \hbar \boldsymbol{k}_\mathrm{i} - \hbar \boldsymbol{k}_\mathrm{f} = \hbar \boldsymbol{Q} \\ \frac{\hbar^2 k_\mathrm{i}^2}{2M_\mathrm{n}} - \frac{\hbar^2 k_\mathrm{f}^2}{2M_\mathrm{n}} = \hbar\omega \end{cases} \tag{22.1}$$

where $\hbar\boldsymbol{Q}$ and $\hbar\omega$ are the momentum and energy of the process (or quasiparticle). The important point is that each selected configuration of the spectrometer corresponds to a single $(\boldsymbol{Q},\omega)$ point. Changing step by step either k_i or k_f, the sample rotation and the scattering angle allows one to cover a large part of the $(\boldsymbol{Q},\boldsymbol{\omega})$ space and to detect all possible scattering processes corresponding to the physics of the sample. Furthermore, it may easily be checked that a given $(\boldsymbol{Q},\omega)$ point may be obtained in different ways (varying for instance k_i or k_f). This provides the experimentalist with the possibility of adjusting the experimental conditions to the specific requirements of a specific problem.

The intensity of the scattering is governed by the neutron scattering cross-section, which depends on the nature of the process giving rise to the scattering. Actually the cross-section is proportional to the space and time Fourier transforms of the correlation function of the atomic positions, for nuclear scattering, or of the magnetic moments, for magnetic scattering. This correlation function describes the thermal average of the response of the studied system at position $\boldsymbol{r}'$ and time t', when a point-like perturbation has been given at position $\boldsymbol{r}$ and time t. This is indeed the relevant function to describe the space and time evolution of a system, which is directly related to the microscopic quantities which are responsible for the properties of the system.

When $\omega = 0$, there is no energy transfer between neutron and sample, and this corresponds to **elastic scattering**: this also means that the response concerns the correlations at $t = \infty$, i.e. the structural properties of the system. On the other hand, if the scattered intensity is integrated over energy (no energy analysis), the measurement yields the instantaneous $(t = 0)$ correlation function, which gives information on the spatial average of atomic positions (or density correlations). These two kinds of measurements are commonly used to study the structural properties of a system. The three-axis spectrometry is devoted to the intermediate range, which corresponds to neutron **inelastic scattering** as a function of $\boldsymbol{Q}$ and involves the dynamical properties.

Due to the interaction between neutrons and matter, many processes may give rise to inelastic neutron scattering, either from nuclear origin (phonons, molecular relaxations, atomic diffusions, for instance) or from magnetic origin (spin waves, critical scattering, electronic transitions due to the crystalline electric field, for instance). We shall see below what is more specific for nuclear vibrations. But just notice that, when working on periodic crystals the momentum of the quasiparticle giving rise to the neutron scattering has to be decomposed as $\boldsymbol{Q} = \boldsymbol{\tau} + \boldsymbol{q}$, where $\boldsymbol{\tau}$ is a vector of the reciprocal lattice and $\boldsymbol{q}$ is a vector of the first Brillouin zone. This is due to translational invariance.

Before going into the details of the inelastic neutron cross-section let us have a look at the experimental aspects which have a direct incidence on the accuracy of the measurements.

22.2.2 Experimental Resolution of a Three-Axis Spectrometer

Measuring on a three-axis spectrometer means scanning step by step the $(\boldsymbol{Q},\omega)$ space, counting at each step, to get the scattering law of the sample. Each step corresponds to a configuration of the spectrometer. The determination of the scattering law would be ideal if all the elements of the spectrometer were perfectly defined: perfect single crystals for monochromator and analyzer, parallel trajectories for all neutrons in the beam. Of course, monochromator and analyzer are mosaic crystals and the neutron beam has angular divergencies. This means that for a given configuration of the spectrometer, centered on $(\boldsymbol{Q_0},\omega_0)$, a whole set of values $(\boldsymbol{Q},\omega)$ contributes to the scattered intensity. The function which gives the weight of this distribution is the resolution function of the three-axis spectrometer, written $R(\boldsymbol{Q}-\boldsymbol{Q_0},\omega-\omega_0)$. The measured intensity is then given by integration over $\boldsymbol{Q}$ and ω of this function, weighted by the scattering law of the sample:

$$I(\boldsymbol{Q_0},\omega_0)=\int \partial\boldsymbol{Q}\partial\omega S(\boldsymbol{Q},\omega)R(\boldsymbol{Q}-\boldsymbol{Q_0},\omega-\omega_0) \tag{22.2}$$

The use of Gaussian approximations to account for crystal mosaic spreads and angular divergences yields a 4D Gaussian function to describe the three-axis resolution, and constant probability cuts have ellipsoidal shape (see [16]). It is difficult to give general ideas on the lineshapes of the measurements, which depend on the $\boldsymbol{Q}$-dependence of the scattering, but it is important to have in mind that the accuracy and the intensity of a measurement will depend essentially on the choice of k_f (or k_i). The accuracy is improved by a decrease of k_f (or k_i), roughly as $k^2\cot(\theta)$, where k is the largest of k_i and k_f and θ the corresponding Bragg angle, but the intensity per unit of time is then decreasing as $k^3\cot(\theta)$ [11], and the range of accessible Q values is reduced. Thus a compromise is always to be made between accuracy and intensity. The choice obviously depends on the sample size, which explains the strong evolution of the neutron results with the increase of available sample sizes as will be shown below. To give an order of magnitude of the energy resolution of a measurement, a useful formula to get the full width at half maximum (FWHM) is :

$$\Delta(\mathrm{Thz})=\frac{\beta(\mathrm{radian})}{2}\left(k_\mathrm{i}^4\cot^2(\theta_m)+k_\mathrm{f}^4\cot^2(\theta_\mathrm{a})\right)^{1/2} \tag{22.3}$$

where β is the mean horizontal divergence (FWHM) of the beam. The frequency of the mode is given by $k_\mathrm{i}^2-k_\mathrm{f}^2\approx 2\nu$ (a frequency of 1 THz corresponds to an energy of 4.13 meV). For instance, using PG002 (d_m=3.354 Å) as monochromator and analyzer with 40′ collimations (0.0116 radian) and constant k_f of 2.662 $\mathrm{Å}^{-1}$ (final energy of 14.7 meV) to measure a non-dispersive mode at 1 THz (transfer energy of 4.13 meV), the instrumental linewidth (FWHM) will be 0.245 THz, that is $\approx$ 1meV.

22.2.3 Inelastic Neutron Scattering Cross-Section for Lattice Vibrations

As we are concerned with lattice vibrations, it is useful to have a detailed look at the cross-section corresponding to these processes in periodic lattices. In an ordered system, the reaction to a perturbation is a vibration of the whole system according to its eigenmodes. These eigenmodes are related to the short-range force constants and long-range electronic forces, if present, and are classically derived from the dynamical matrix of the system, yielding $3r$ modes if there are r atoms in the primitive unit cell of the lattice. This scattering is called **one-phonon coherent inelastic scattering**. When the system is disordered (including isotopic and nuclear spin disorder), there exists a second kind of signal, given by the self-correlation function, the intensity of which depends on the disorder itself. In periodic crystals, this signal is related to the phonon density of states of the system, and is called **incoherent inelastic scattering**. In the following we shall consider this signal as incorporated in the background noise.

The master formula of the one-phonon coherent inelastic scattering law for a harmonic phonon process is:

$$\begin{array}{l} S(\boldsymbol{Q},\omega) = \frac{k_\mathrm{f}}{k_\mathrm{i}} \frac{(2\pi)^3}{v_0} \sum_{\boldsymbol{\tau}} \sum_{j\boldsymbol{q}} \delta(\boldsymbol{Q}+\boldsymbol{q}-\boldsymbol{\tau}) |F_{\boldsymbol{q}}^{j}(\boldsymbol{Q})|^2 \\ beq2ex] \quad \times \frac{1}{2\omega_j(\boldsymbol{q})} [n_j(\boldsymbol{q})\delta\{\omega+\omega_j(\boldsymbol{q})\} + \{1+n_j(\boldsymbol{q})\}\delta\{\omega-\omega_j(\boldsymbol{q})\} \end{array} \tag{22.4}$$

where $|F_{\boldsymbol{q}}^{j}(\boldsymbol{Q})|^2$ is the dynamical structure factor , with:

$$F_{\boldsymbol{q}}^{j}(\boldsymbol{Q}) = \sum_{d} \bar{b}_d \exp(-W_d(\boldsymbol{Q})) \exp(-\mathrm{i}\boldsymbol{Q}\cdot\boldsymbol{d}) \{\boldsymbol{Q}\cdot\boldsymbol{\xi}_d^j(\boldsymbol{q})\} M_d^{-1/2} \tag{22.5}$$

where d is the index of the different atoms of the primitive cell of volume v_0, $\bar{b}_d$ are the coherent scattering lengths and $W_d(\boldsymbol{Q})$ are the partial Debye–Waller coefficients. j is the index of the different eigenstates of the dynamical matrix of energy $\omega_j(\boldsymbol{q})$, $\boldsymbol{\xi}^j(\boldsymbol{q})$ the corresponding eigenvectors and $n_j(\boldsymbol{q})$ are the Bose thermal factors, namely $1/(\exp(\frac{\hbar|\omega_j|}{k_\mathrm{B}T}) - 1)$. The δ functions are for phonon creation or annihilation, which means that the neutron loses or gains energy.

When the phonon is no longer harmonic, a damping appears and the δ function is replaced by a normalized spectral weight function, which is usually written as a damped harmonic oscillator:

$$\frac{1}{\pi} \frac{\omega_j^2(\boldsymbol{q})\Gamma_j(\boldsymbol{q})}{(\omega^2 - \omega_j^2(\boldsymbol{q}))^2 + \omega^2\Gamma_j^2(\boldsymbol{q})} \tag{22.6}$$

where $\Gamma_j(\boldsymbol{q})$ characterizes the damping of the mode. But according to the microscopic mechanism which is responsible for the attenuation of the vibrations of the lattice, different spectral weight functions may be defined.

The main features to keep in mind are the following:

- The dynamical structure factor includes a scalar product of the momentum transfer and the polarization of the measured phonon. When the symmetry is such that the polarization may be simply related to the propagation vector, this provides a selection rule to measure transverse or longitudinal phonons. This is mostly the case when the $\boldsymbol{q}$ of the phonon is small enough.
- The scattering intensity depends on $|\boldsymbol{Q}|^2$, which means that, when several equivalent positions are accessible in the reciprocal space, the larger Q gives the higher intensity.
- The dynamical structure factor also depends on $\boldsymbol{\tau}$, the Brillouin zone where the measurement is performed, via the phase factors which depend on the positions of the atoms in the primitive cell. For acoustic phonons at small q values, the vibration consists essentially of an in-phase displacement of all the atoms. That means that the intensity of acoustic phonons is directly correlated with the intensity of the Bragg peak around which the measurement is performed (with a weighting in $1/\sqrt{M_j}$ of the scattering lengths).

22.2.4 Vibrations in Quasicrystals

The inappropriateness of a Bloch wave representation for a non-periodic structure implies that the spectral weight function of a quasicrystal is not a standard one. There is no longer a first Brillouin zone to define the $\boldsymbol{q}$ values [17]. Localized modes are also predicted which could interact with propagative excitations. Moreover, in the dispersion of the propagating modes, an infinite number of gaps is predicted. These gaps may be seen as the analog of the gaps induced by a structural phase transition when a doubling of the cell yields a folding of the Brillouin zone. Actually, there is no inelastic neutron scattering cross-section that can be used as a standard reference to analyze the experimental data. As one can see in the chapters related to estimations by approximant periodic lattices or to numerical simulations [17,18], what is generally expected is the existence of propagating excitations starting from the intense Bragg reflections and of bands of optic-like phonons, the broadening and intensities of which are model dependent. A pseudo-Brillouin-zone behavior is generally referred to [17], using an intensity criterion of the $\boldsymbol{Q}$-dependence of the dynamical susceptibility.

As a first approximation, we shall keep the usual one-phonon cross-section to analyze the experimental data on the vibrations of quasicrystals. The data will be reported using $\boldsymbol{q}$ defined as the difference ($\boldsymbol{q} = \boldsymbol{Q} - \boldsymbol{\tau}$) between the momentum transfer and the nearest intense Bragg position $\boldsymbol{\tau}$. This will allow us to determine the position, the intrinsic linewidth and the intensity of the modes which have been measured. Similarities and/or differences between observations in quasicrystalline samples and the behavior of phonons in periodic lattices will be used to determine the specific properties of the vibrations

in quasicrystals, for instance to check the concept of pseudo-Brillouin zones. As long as the linewidth is small compared to the energy of the mode, the modeling of the scattering cross-section would not affect the determination of the peak position very much and therefore of the dispersion curve. But the meaning of the linewidth should be considered with caution, because in many cases we shall be unable to decide whether a broad structure is due to the damping of a single mode or to the overlap of several modes that cannot be separated by the measurement.

22.3 Experimental Results with Ultrasonic and Brillouin Measurements

Before describing neutron scattering results, let us briefly review what has been obtained by ultrasonic and Brillouin measurements which are classically used to get access to sound velocities in the low-frequency regimes. Ultrasonic measurements have been performed on AlCuLi [26] and on AlMnPd [1] and came to the same conclusion, namely that the measurements could be accounted for by two elastic coefficients, C_{11} and C_{44}. Anisotropy of ultrasonic attenuation has also been studied and the observations are in accordance with theoretical predictions for icosahedral quasicrystals [2,20,21]. Because of the opacity of the material, light scattering experiments are rather difficult and very scarce. They provide informations on surface phonons and allow an indirect determination of the bulk sound velocity. The only Brillouin measurements published so far in the literature concern AlFeCu [29].

22.4 Neutron Scattering Measurements on Monodomain Quasicrystals

Up to now, three monodomain quasicrystals have been investigated by inelastic neutron scattering. The main difficulty was to obtain a large enough volume to get a sizeable scattered intensity. AlFeCu, with a sample of about 7 mm^3, and AlLiCu, with about 200 mm^3, were the first candidates. As the scattered intensity depends on the coherent neutron scattering lengths of the constituents and on the absorption of the sample, these two samples gave comparable intensities despite the difference in volume. Fortunately AlPdMn soon provided larger samples, up to several cm^3 and thus allowed the experimentalists to improve considerably the pioneer results. The three samples were icosahedral phases, so that the comparison of experimental results is relevant. Quite recently, a monodomain sample of a decagonal phase (AlNiCo), which is a 2D quasicrystal, has been obtained and the first measurements have begun [12]. This should provide, in the near future, quite interesting information on this kind of system.

22.4.1 Results for $Al_{63}Cu_{25}Fe_{12}$

This compound has been investigated by Quilichini et al. [24]. A structural investigation ascertained the very high quality of the sample, with a mosaicity of less than 10′. Inelastic neutron scattering measurements have been performed at the Orphée reactor of the Laboratoire Léon Brillouin in Saclay, France, on the three-axis spectrometer 1T, installed on a thermal beam.

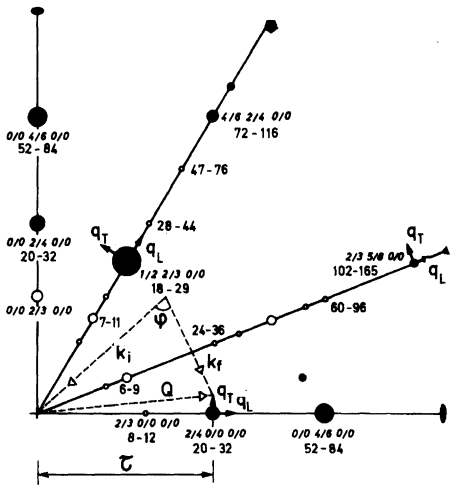

Fig. 22.2. The two-fold scattering plane of AlFeCu. The intensity of a Bragg peak is proportional to the surface of the dark circle. Labeling follows the indexing method of icosahedral quasiperiodic crystals by Cahn et al. [8]

The scattering plane was a two-fold plane, displayed in Fig. 22.2, to get access to the main symmetry directions of the icosahedral phase. The strongest Bragg reflections have been selected and acoustic phonons have been investigated in transverse and longitudinal configurations, as illustrated in the figure, where $\boldsymbol{q}_T$ and $\boldsymbol{q}_L$ indicate the polarization which would have been selected in a periodic lattice. Due to the small size of the sample, the resolution has been relaxed to gain intensity (k_f=3.85 or 4.25 Å^{-1}). In Fig. 22.3 some of the measurements are reported. Well-defined peaks are observed, but the signal-to-background ratio is low and prevents a detailed study.

The results have been analyzed by applying the scattering cross-section of the damped phonon model, and the main features, illustrated in Fig. 22.4, may be summarized as follows:

- Propagating modes are indeed observed in a q range which is far beyond the long-wavelength limit, in transverse as well as in longitudinal configurations, yielding two dispersion curves, starting linearly from intense Bragg peaks.

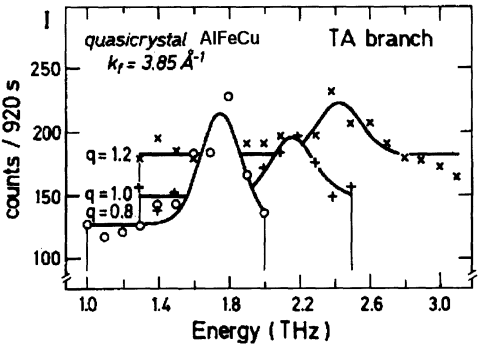

Fig. 22.3. Examples of raw data obtained in AlFeCu along a twofold axis in constant Q scans. q values are in reduced units with q (r.u.)=q (Å^{-1})$\times a/2\pi$ where a is a pseudocubic lattice parameter, a= 16.944 Å [24]

- In the range of observation, there is no anisotropy of the dispersion.
- On the transverse acoustic branches, an intrinsic linewidth is detected, which is increasing with the modulus of q, for q values larger than about 0.4 Å^{-1}.
- The longitudinal acoustic modes also showed an intrinsic broadening, but the experimental accuracy did not allow a precise determination of its q-dependence.
- Heating the sample up to 400 °C does not affect the dynamics of the system. The Bose thermal factor just enhances the scattered intensities.

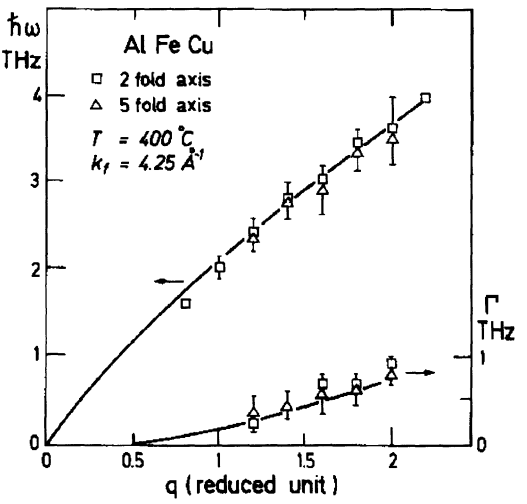

Fig. 22.4. Dispersion curve and broadening of the unique transverse acoustic mode in icosahedral $Al_{63}Cu_{25}Fe_{12}$ [25]

22.4.2 Results for $Al_{60.3}Cu_{10.5}Li_{29.2}$

This compound has been investigated by Goldman et al. [13,14]. Although the sample was characterized as a single grain, its mosaicity was approximately

1.2°. Measurements have been performed on the H-7 three-axis spectrometer at the High Flux Beam Reactor at Brookhaven National Laboratory and on the 2T three-axis spectrometer at the Orphée reactor at the Laboratoire Léon Brillouin in Saclay. The results obtained with this sample are in very good agreement with those obtained with AlFeCu. In the small q range, up to about 0.2 $Å^{-1}$, the dispersions of transverse and longitudinal acoustic modes are isotropic. A broadening of the phonon peaks is observed when q is increasing, but the determination of the q-dependence of this broadening is strongly hampered by the large mosaic spread of the sample. In addition, there is some hint of a dispersionless excitation in the two-fold direction, at about 10 meV, which could be an optic or a localized mode. The authors have also checked that the integrated intensity of the phonons, normalized to Q^2, scaled with the integrated intensity of the zone-center Bragg peaks, behaves in a similar manner as is expected for acoustic phonons in periodic lattices. This is illustrated on Figure 5a.

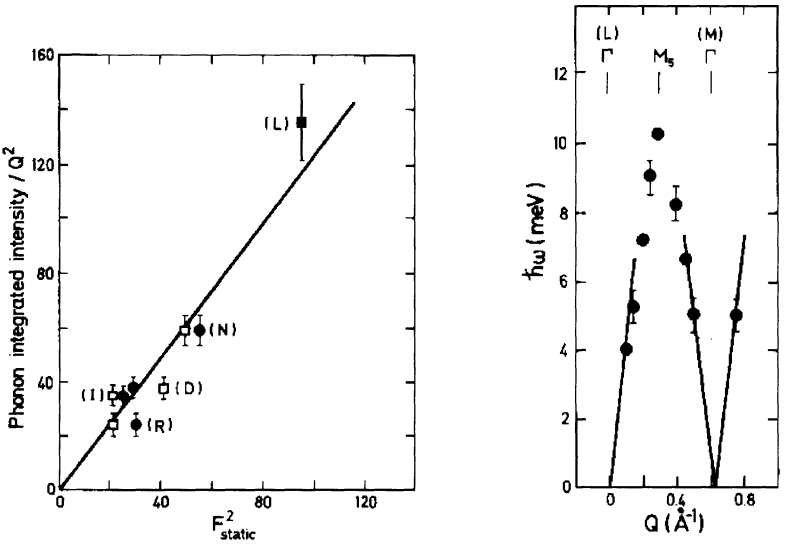

Fig. 22.5. (**a**) Integrated phonon intensity, normalized to Q^2 versus intensity of the zone-center Bragg peaks. (**b**) Longitudinal modes along the five-fold axis between points L and M of the icosahedral AlLiCu phase [13]

Along the five-fold direction, measurements have been performed between Bragg peaks labeled L and M in Fig. 22.6, which are very near intense Bragg reflections. The results, reported in Fig. 22.5b, show that the branch starting from one Bragg peak increases and then decreases to zero energy when arriving at the other Bragg peak, which is analogous to what is observed in

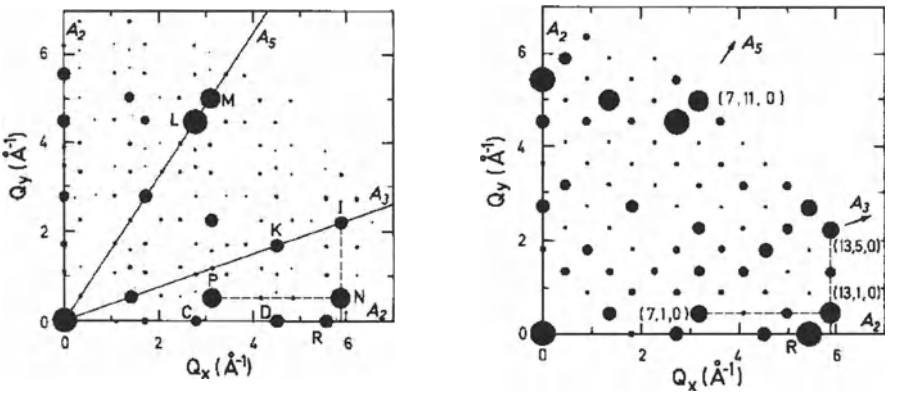

Fig. 22.6. Two-fold planes of AlLiCu. Left side: icosahedral phase; right side: R phase. The dashed lines denote the directions of inelastic scans for the two-fold longitudinal and transverse modes. The arrows in the R-phase plane denote the three-fold and five-fold axes of the icosahedral phase for comparison [14]

periodic lattices, when there is a zone boundary between adjacent zones. This supports the pseudo-Brillouin zone concept.

The AlLiCu system also gave the opportunity to go a step further, as it has been possible to get a sample of the approximant cubic R phase and thus to compare inelastic results for icosahedral and cubic phases. Measurements have been performed on the IN8 three-axis spectrometer at the Institute Laue–Langevin in Grenoble and on 2T at the LLB. Longitudinal and transverse phonons have been measured near intense Bragg peaks which are clearly related in both phases, as can be seen in Fig. 22.6. As exemplified in Fig. 22.7 the results are very similar. The only small difference is observed in the optic regime (see Fig. 22.7b), where the optic-like phonon in the icosahedral phase looks less dispersive than in the cubic R phase. This could point to a tendency towards localization of optic modes, as predicted by theory. But the modest accuracy of the measurement prevents a definite conclusion. The strong similarity of the lattice dynamics of i- and R-AlLiCu had also been observed in the measurements of the generalized vibrational density of states (GVDOS) [28].

22.4.3 Results for $Al_{68.7}Pd_{21.7}Mn_{9.6}$

This compound has been investigated by M. de Boissieu, M. Boudard et al. [9,3]. Several samples of increasing size and quality have been used. The large available size (more than 1 cm^3) allowed much more accurate measurements and many of the aspects revealed by the previous measurements could thus be made more precise and new interesting features could be detected. Again a two-fold plane was chosen as the scattering plane, which is reported in Fig. 22.8.

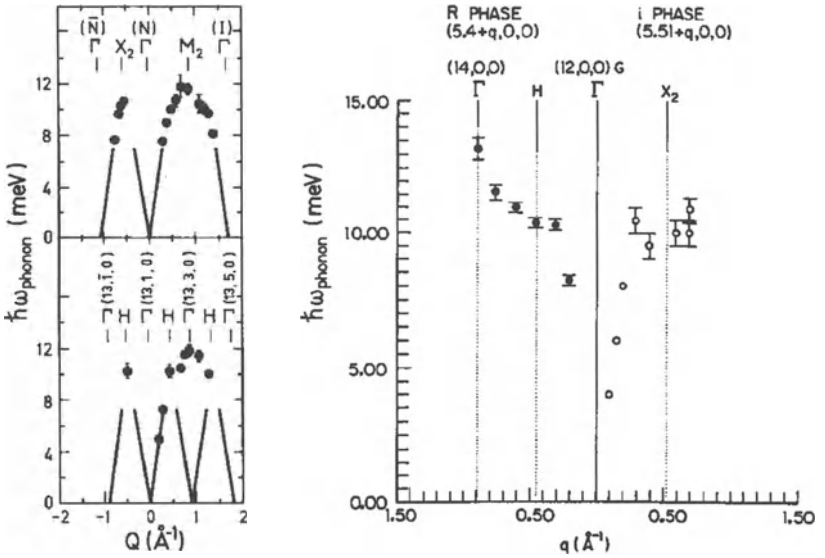

Fig. 22.7. Phonon dispersions along a two-fold direction. (**a**) Transverse phonons of the icosahedral (top panel) and the cubic R phase (bottom panel). (**b**) Longitudinal phonons of the icosahedral phase measured from point R (right side) and of the cubic R phase from the (12, 0, 0) (left side), where H is a zone boundary and the mode between H and Γ (14, 0, 0) is a low-lying dispersive optical branch [14]

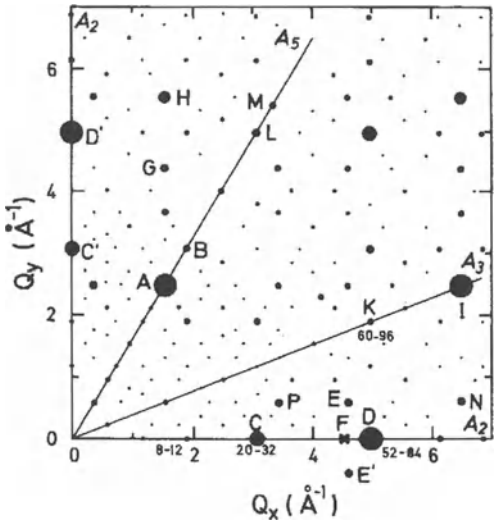

Fig. 22.8. The two-fold reciprocal plane of icosahedral AlPdMn

All the measurements have been carried out at the Orphée reactor at the LLB either on a thermal source (three-axis spectrometer 1T) or on a cold source (three-axis spectrometer 4F2). The main results are as follows.

22.4.3.1 Acoustic Regime. An example of the quality of this new set of measurements is given in Fig. 22.9a, where raw data are reported, which were collected near the point D along the transverse two-fold direction. The counting rate is now quite good, allowing a more precise data analysis and providing a deeper insight into finer details of the scattering law.

The isotropy of the longitudinal and transverse acoustic branch has been again evidenced. But the possibility of using a better resolution (k_f=2.662 Å^{-1} on 1T and k_f=1.64 Å^{-1} on 4F2) allowed the authors to get a more accurate determination of the width of the transverse mode. This is illustrated in Fig. 22.9 for several directions in the lattice.

Clearly there is a jump in the q dependence of the phonon width: below q = 0.4 Å^{-1} no intrinsic linewidth is observed, while above this q value modes broaden rapidly. We may note (Fig. 22.9) that the transverse modes propagating along a twofold axis do not have the same dispersion with increasing energy if they are measured from point D or from point D′. This could seem abnormal, but indeed, even if D and D′ are equivalent two-fold Bragg peaks, there is no symmetry requirement that the dispersion relation starting from these points should be equivalent.

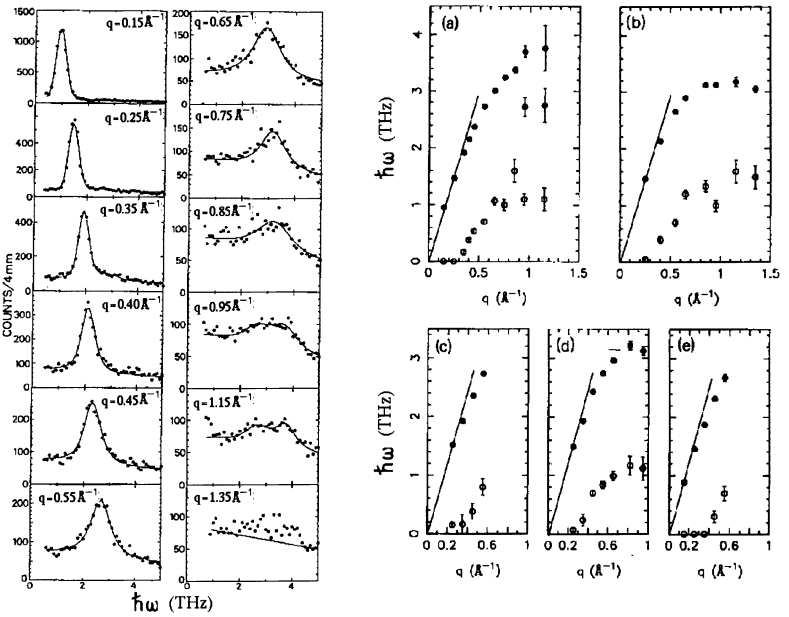

Fig. 22.9. (**a**) Raw data of the transverse acoustic branch measured along a two-fold direction in AlPdMn. (**b**) Measurements along a five-fold direction, in a longitudinal configuration between points A and B After de Boissieu et al. [9]

22.4.3.2 Pseudo-Brillouin Zones and Gap Openings. An infinite number of gap openings is predicted in the dispersion curves of a quasicrystal. But the observability of such a gap depends on the intensity expected for the dispersive mode where the gap is located and to the ratio of its energy width to that of the energy resolution of the measurement. Gaps are expected at points which are midpoints between Bragg peaks, that is pseudo-Brillouin zone boundaries. An estimation of an appropriate structure factor has been performed by de Boissieu et al. [9] and the results for the two-fold plane are reported in Fig. 22.10. Using the strongest structure factors, this gives a hierarchy of the most relevant Brillouin-zone boundaries, which may be placed around each strong Bragg reflection of the scattering planes. This provides an adequate criterion for the choice of $\boldsymbol{q}$ values where gap openings should be observable.

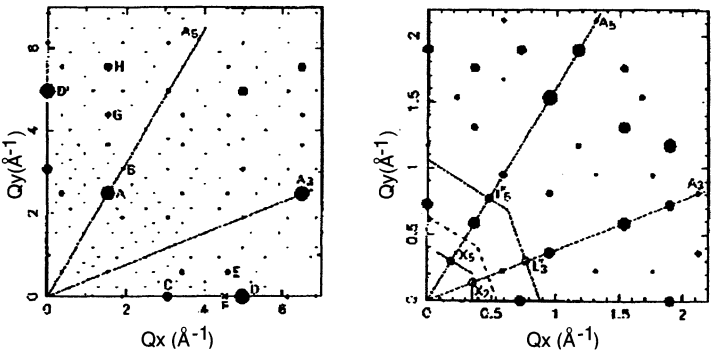

Fig. 22.10. The reciprocal plane of AlPdMn, with the weighting calculated from the inelastic structure factor in order to determine gap openings [9]

Therefore careful measurements between points such as D and E, where a gap is expected at the pseudo-zone boundary point X_5 have been performed. But no evidence of a gap opening has been found so far.

The best resolution which could be achieved leads to an estimate of about 0.2 meV for the smallest gap that could have been observed. But the limited q-resolution could also have hampered the determination of the gap. To get a more precise idea of the continuity of the dispersion of the phonon modes, measurements have been performed on several paths in the vicinity of points D and E. This led to the dispersions reported in Fig. 22.11, from D to E, via an X_5 point; from E to F, which is an X_2 point; as well as from F to X_5 and from F to D. The data analysis leads to a description where transverse and longitudinal dispersive modes originate from D and E and cross without any interaction at the pseudo-zone boundaries. Besides these dispersive modes, evidence of optic modes is also found as reported on Figures 11b, c and d.

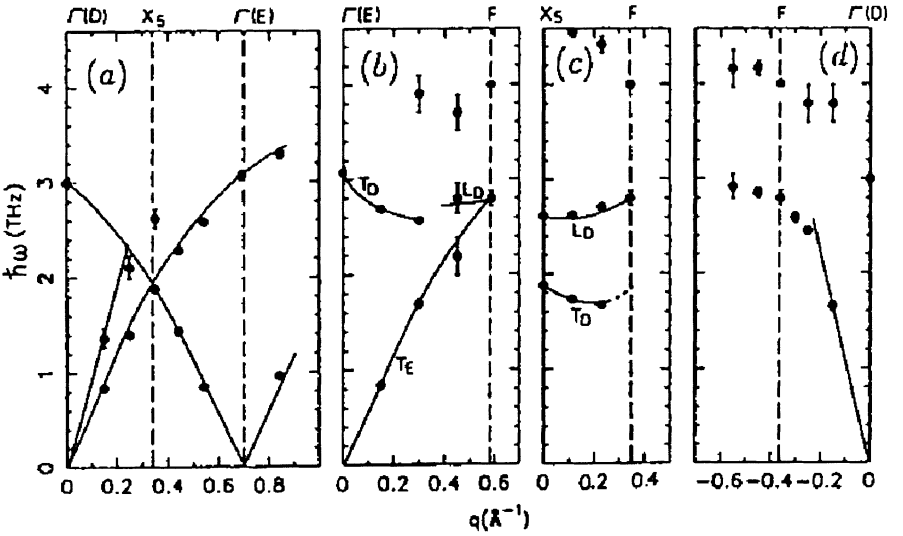

Fig. 22.11. Measurements between D-E(**a**), E-F(**b**), F-X_5(**c**) and F-D(**d**) [9]

22.4.3.3 Optic Modes. Centimeter-size monodomain crystals allowed a more detailed examination of optic modes [4]. Indeed a series of dispersion modes have been found at energies close to 1.8, 3, 4 and 5.5 THz. They are broad ($\approx$ 1 THz) and present intensity variations in reciprocal space. Fig. 22.12 displays the results which have been obtained along different paths in reciprocal space. These results should be considered with care. Indeed, in contrast to acoustic modes where the use of small $\boldsymbol{q}$ values was rather straight-

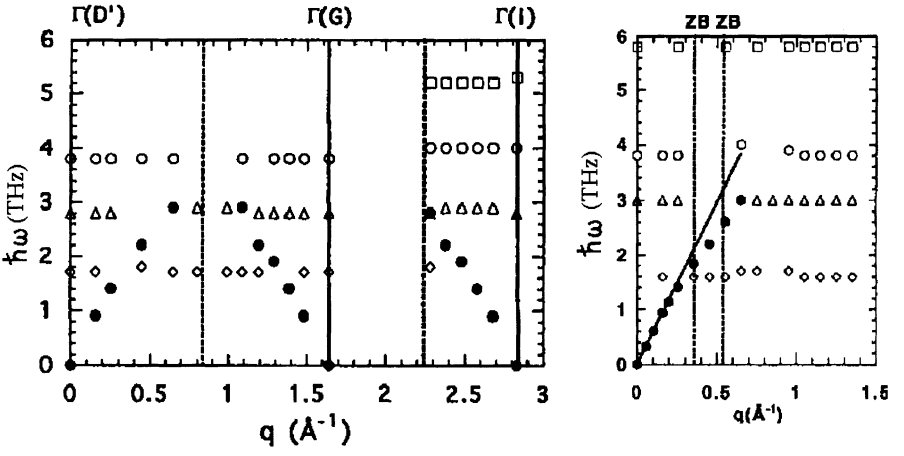

Fig. 22.12. Optic modes. Measured along the line D′ GI (left side) and in transverse configuration from point D (right side) in AlPdMn. [4]

forward, there is no way of attributing unambiguously a mode to a particular Bragg reflection. Moreover the observed broadening may merely result from a distribution of modes having close energies. Nevertheless the coincidence between the energies of some of these modes and the energy where acoustic modes cross pseudo-Brillouin zone boundaries must be emphasized. This kind of behavior has indeed been predicted by several theoretical approaches [15,23]. Finally the observation of such optic modes is in agreement with the general vibrational density of states which has been measured on a powder sample [27].

22.4.3.4 Temperature Dependence. Measurements have been carried out up to 800 °C, i.e. 60 °C below the melting point. At this temperature, other measurements devoted to diffuse scattering [10] or to phason hopping [6,22] have revealed significant changes which are thought to be specific for the quasicrystalline state. The connection between these results and the evolution of the vibrational properties was appealing. Unfortunately, nothing was found to substantiate such a connection. The sound velocities slightly decrease with increasing temperature as is usually observed and all the checked scatterings just scale according to the thermal Bose factor. Of course this must not be considered as a definite answer. But it means that the determination of any connection between vibrational properties and high-temperature peculiarities, such as phason hopping, if it exists, requires new careful measurements. But this could also be due to the indirect correlation between these properties, which could explain the absence of sizeable effects for measurements such as point-like inelastic neutron scattering performed on a three-axis spectrometer.

22.5 Conclusion

The experiments reported above provide very valuable experimental material to check theoretical predictions. Agreement between experiment and theory has been pointed out in this chapter. Very important points still remain to be clarified. One point concerns the gap openings: with the continuous increase of the sample size, progress may still be made and new measurements with a better energy and q-resolution would be very useful. A more general question concerns the specific nature of the vibrations of quasiperiodic lattices compared to those of periodic crystals. This concerns the q-dependence of the broadening of the acoustic phonons and the localization of optic modes. To answer that question, there is a strong need for equivalent measurements on the approximant phase of AlPdMn, but we are still waiting for samples. On the other hand, all the results obtained so far by inelastic neutron scattering concern the icosahedral phase. Other phases, the decagonal one for instance, should provide a very interesting comparison.

Finally we must not forget that there is now a considerable amount of experimental data, including a lot of neutron scattering measurements. The measurements which have been reviewed herein should be compared with all other neutron scattering measurements, four-circle measurements, diffuse scattering, quasielastic scattering on monodomain samples as well as on powder and phonon density of states measurements. The specific nature of the quasicrystalline state implies a subtle balance between long-range properties and local rearrangements. This implies a very large range of energy and time scales, which are now nearly covered by these various experiments. The understanding of the very nature of the quasicrystalline state implies a global use of all this experimental information.

References

1. Amazit Y., de Boissieu M., Zarembovitch A., Europhys. Lett. **20** (1992) 703
2. Bak P., Phys. Rev. Lett. **54** (1985) 1517; Bak P., Phys. Rev. B**32** (1986) 5764
3. Boudard M., de Boissieu M., Goldman A.I., Hennion B., Bellissent R., Quilichini M., Currat R., Janot C., *Proceedings of Euroconference 94 Neutrons in disordered Materials*, Stockholm 1994
4. Boudard M., de Boissieu M., Kycia S., Goldman A.I., Hennion B., Bellissent R., Quilichini M., Currat R., Janot C., J. Phys.: Condens. Matter **7** (1995) 7299
5. Boudard M., de Boissieu M., Letoublon A., Hennion B., Bellissent R., Janot C., Europhys. Lett. **20** (1996) 703
6. Coddens G, Lyonnard S., Calvayrac Y., Phys. Rev. Lett. **78** (1997) 4209
7. Cooper M.J. Nathans R., Acta Cryst. **23** (1967) 357
8. Cahn J.M., D. Shechtman, D. Gratias, J Mater. Res. **1** (1986) 13
9. de Boissieu M., Boudard M., Bellissent R., Quilichini M., Hennion B., Currat R., Goldman A.I., Janot C., J. Phys.: Condens. Matter **5** (1993) 4945
10. de Boissieu M., Boudard M., Hennion B., Bellissent R., Kycia S., Goldman A.I., Janot C., Audier M., Phys. Rev. Lett. **75** (1995) 89
11. Dorner B., Acta Cryst. A**28** (1972) 344
12. Dugain F., de Boissieu M., Hradil K., Shibata K., Currat R., Kortan A.R., Tsai A.P., Suck J.-B., Frey F., International Conference on Aperiodic Crystals "Aperiodic'97" (1997)
13. Goldman A.I., Stassis C., Bellissent R., Moudden H., Pyka N., Gayle F.W., Phys. Rev. B **43** (1991) 8763
14. Goldman A.I., Stassis C., de Boissieu M., Currat R., Janot C., Bellissent R., Moudden H., Gayle F.W., Phys. Rev. B **45** (1992) 10280
15. Hafner J., Krajči M., Phys. Rev. B **47** (1993) 11795
16. Hennion B., "Introduction à la Spectroscopie Neutronique" Lecture in Saclay (1974) p. 61
17. Janssen, T. (2002): See Chapter 4 of this book
18. Janssen, T. (2002): See Chapter 21 of this book
19. Krajčí, M., Hafner, J. (2002): See Chapter 20 of this book
20. Lubensky T.C., Ramaswamy S., Toner J., Phys. Rev. B **32** (1985) 7444
21. Lubensky T.C. in *Aperiodicity and Order*, edited by M.V. Jaric (Academic Press, Orlando FL 1988) p. 99

22. Lyonnard S., Coddens G., Phys. Rev. B **53** (1996) 3150
23. Poussigue G., Benoit C., de Boissieu M., Currat R., J. Phys. Cond. Mat. **6** (1994) 659
24. Quilichini M., Heger G., Hennion B., Lefebvre S., Quivy A., J. Phys. France **51** (1990) 1785
25. Quilichini M., Hennion B., Heger G., Lefebvre S., Quivy A., J. Phys. France **I 2** (1992) 1785
26. Reynolds G.A.M., Golding B., Kortan A.R., Parsey J.M., Phys. Rev. B**41** (1990) 1194.
27. Suck J-B., J. Non-Cryst. Solids **156&158** (1993) 872
28. Suck, J.-B. (2002): See Chapter 23 of this book
29. Vanderwal J. J., Zhao P., Walton D., Phys. Rev. B**46** (1992) 501

23 Vibrational Density of States of Stable and Metastable Quasicrystalline Alloys

Jens-Boie Suck

Summary. The generalized vibrational density of states (GVDOS) of metastable and especially stable quasicrystalline alloys as determined in neutron inelastic scattering experiments is briefly presented. It is shown that the GVDOS gives the most complete information on the atomic dynamics of quasicrystals, that it is a much smoother function than originally expected from theoretical calculations and that quasicrystalline alloys and their rational approximants can hardly be distinguished on the basis of their GVDOS because of the high similarity in their atomic short-range order. The temperature dependence of the GVDOS is very similar for a quasicrystal and its approximant and also similar compared to other alloys which expand with temperature. For decagonal quasicrystals a nearly quantitative description of the GVDOS can be obtained and even the development of the GVDOS with temperature can be accounted for very satisfactorily.

23.1 Introduction

In a very general manner, having in mind more realistic systems than perfectly ordered periodic and harmonic crystals, one can define the normalized vibrational density of states (VDOS) $G(\omega)$ as the relative probability for the occurrence of a frequency when taking all existing atomic vibrations with frequency ω_i of a condensed matter system into account (excluding multiexcitations)

$$G(\omega) = (1/A) \sum \delta(\omega - \omega_i)\,, \tag{23.1}$$

where A is the normalizing constant. $G(\omega)$ defined in this way thus reflects a single particle property, just the frequency of vibration of a particle, independent of whether or not this vibration is related to the movement of neighboring atoms, belongs to a propagating vibrational excitation, etc. The density of states (DOS) therefore does not give the most detailed information on atomic movements, but – as it contains *all* existing frequencies – it gives the *most complete* information on the atomic vibrations in condensed matter. And this is exactly what is needed if one wants to calculate all properties of a material for which their vibrational properties intervene and cannot be approximated by a guessed Einstein frequency or Debye spectrum: thermodynamic properties like the specific heat, the vibrational entropy, the Debye–Waller

J.-B. Suck et al. (eds.), *Quasicrystals*
© Springer-Verlag Berlin Heidelberg 2002

factor, the mean force constant, the mean square amplitude of the vibration, the thermal conductivity, optical properties, the electron–phonon interaction in superconductivity, etc.

Equation (23.1) gives a definition, not a recipe of how to calculate $G(\omega)$, which may be rather difficult depending on the types of atomic movement possible in the sample investigated. In most cases, however, phonons, i.e. collective lattice vibrations, will dominate the atomic motions, and in this case we have at least a recipe of how to calculate the phonon density of states (PDOS) , which can also be related to the slope $\Delta\omega_j(q)$ of the different phonon dispersion branches $\omega_j(q)$, where $\boldsymbol{q}$ is the wavevector of the phonon with frequency ω in the branch labeled j

$$F(\omega) = \frac{1}{2}\pi^3 \sum_j \int \delta(\omega - \omega_j(q))\mathrm{d}q = \frac{1}{2}\pi^3 \sum_j \int \frac{\mathrm{d}S}{|\Delta\omega_j(q)|}\,, \tag{23.2}$$

where S is that surface in the irreducible part of the first Brillouin zone (BZ) of a periodic crystal where $\omega_j(q) = \omega$ [1]. In this definition of the PDOS the relation between the more detailed information on the lattice vibrations, the dispersion branches, and the PDOS is especially clear: for a linear dispersion $F(\omega)$ will be proportional to ω^2 as in the case of the Debye model ($D(\omega) = [3/(2\pi^2 v_s^3)\omega^2)$ and if the slope of the dispersion approaches zero, i.e. the same ω appears for many q-values, the PDOS will have a maximum or a singularity, a van Hove singularity [24]. Equation (23.2) only holds if *all* dispersion branches relevant to the PDOS are known, and then the PDOS is just a reduction of the more detailed information on frequencies, amplitude and direction of motion contained in the complete set of dispersion branches. However, this normally is not the case, as dispersion branches are usually only measured in high symmetry directions in reciprocal space of the single crystal and thus frequencies, which may give important contributions to the PDOS, remain unknown. Phonon dispersions are measured in order to deduce the forces acting between the atoms, and a different way of expressing the same facts is to say that one has to know these interatomic forces or the potentials from which they are deduced, to a high degree of accuracy in order to be able to calculate the PDOS reliably. This calculation, in a simple approach, is done by dividing the irreducible part of the BZ of periodic crystals into very small volumes and then calculating the contribution of each of these volumes to the PDOS via the dynamical matrix [19]. Thus the accuracy of the calculated PDOS *crucially* depends on the completeness of the information obtained for the phonon dispersions or the interatomic potentials. In the case of the more generally defined VDOS (23.1) other atomic motions like rotation of molecular groups, phason motion in incommensurate systems, localized vibrations in amorphous solids, fractons in fractal systems, etc. have to be taken into account also – as is necessarily done in the experimental determination of $G(\omega)$ – and thus even more knowledge is needed beforehand to get the complete information of the atomic motions as they are reflected in a measured VDOS.

Besides the interatomic potentials, from which the acting forces are deduced, the relative positions of the interacting atoms, i.e. the atomic structure, strongly influence the shape of the resulting PDOS. For elemental crystals with a simple structure like fcc or bcc $F(\omega)$ therefore has a characteristic shape [40]. This is partly due to the (logarithmic) van Hove singularities at special points of the BZ and are therefore related to long-range order (LRO) in the system. The strongest influence on the shape of the VDOS however is given by the atomic short-range order (SRO) in the system [63]. The more complicated a structure gets, the less obvious a fingerprint from the LRO of the underlying structure is reflected in the VDOS. The influence from the SRO should remain, but so far no classification of this kind has been attempted for $G(\omega)$ of different quasicrystalline (qc) structures.

For many systems only few or no dispersion branches can be measured at all and the density of states is not only the *most* complete information on the atomic motions but the *only* complete one. Examples of this kind are amorphous solids, for which only two dispersion branches could be measured up to now [47,56], which are insufficient to deduce the complete $G(\omega)$, and also quasicrystals (qc), for which we know that the VDOS extend out to $E_m = 50$ or 60 meV [42] for different alloys, but dispersion branches even in highly ordered monograins could only be determined up to 1/3 of E_m for icosahedral (i-) monograins [42] and up to 2/5 of E_m for a dispersion measured in the periodic direction of a decagonal (d-) monograin [12].

Theoretical calculations of the PDOS of qc are presented in two different contributions in this volume [27,30]. In addition, an excellent and complete review on phonons in QC has appeared most recently [42]. Thus we shall not summarize theoretical approaches here again [57] but turn directly to the experimental determination of the GVDOS.

23.2 Determination of the Generalized Vibrational Density of States by Neutron Inelastic Scattering

Experimentally, inelastic scattering of different probes (or IR-absorption) can be used to determine the VDOS. The resulting inelastic scattering or absorption spectra are not only related to the VDOS, but contain – apart from constants – the *coupling function* of the probe to the vibrating atoms. In the case of light, Raman scattering or IR absorption, selection rules restrict the information further to Raman and IR active modes. Thus one obtains a partial VDOS for these modes, if the energy-dependent coupling function can reliably be separated out. Most recently inelastic nuclear scattering with synchrotron radiation has been used to determine the partial VDOS of the Fe atoms in α-Fe and also in an qc alloy, i-AlCuFe [6], resolving the energy spectrum of the recoil fraction of the resonant absorption of synchrotron γ-radiation by the ^{57}Fe-nuclei. By detuning the energy E_0 of the incident synchrotron radiation from the resonance energy E_R (14.4 keV) by the energy

one wants to investigate in the DOS of the sample, i.e. in the meV range, only nuclei which vibrate with a frequency which subtracts or adds the additional or missing energy $\pm\hbar\omega = E_R - E_0$ are able to absorb the incident photon. The observed intensity of e.g. the X-ray fluorescence radiation (nuclear inelastic absorption which leads to incoherent scattering) is then proportional to the relative probability of this vibration in the sample. As the energy width of the absorbing nuclear level is in the neV range the energy resolution of the experiment is determined by the resolution of the monochromator (meV range up to now). The coupling function reduces to a constant in this case and the resulting VDOS can be determined from the measured X-ray intensity by separating the inelastic part of the spectrum and by subtracting the calculated multiphonon contribution to the measured intensity [8].

Thermal neutrons are an especially advantageous probe for investigating the atomic dynamics, as the coupling function to a scattering element is a constant, energy transfers can be measured with high spectral resolution and the method is especially and mainly sensitive to the SRO of the sample. In neutron inelastic scattering (NIS) results the one-phonon part of the incoherent double differential scattering cross-section $\mathrm{d}^2\sigma_{\mathrm{inc}}/\mathrm{d}\Omega\mathrm{d}E$ measured in these experiments [31] is directly proportional to the density of states $f(\omega)$ and in the case of cubic crystals consisting of one element one has

$$f(\omega) = \frac{4\pi}{\sigma_{\mathrm{inc}}}\frac{k_0}{k}\hbar\omega(1-\mathrm{e}^{-\beta})\frac{2M}{\hbar^2Q^2}\mathrm{e}^{2W}\frac{\mathrm{d}^2\sigma_{\mathrm{inc}}}{\mathrm{d}\Omega\mathrm{d}E}_{1\mathrm{phon}}, \tag{23.3}$$

where Ω is the solid angle of the detector seen from the center of the sample, σ_{inc} the scattering cross-section for incoherent neutron scattering, k_0 and k are the moduli of the wavevector of the neutron before and after scattering, $\hbar\omega$ is the energy transfer in the inelastic scattering process ($\hbar\omega = E_0 - E$) with E_0 and E the incident and the final energy of the neutron, $\hbar Q$ is the modulus of the corresponding momentum transfer ($\boldsymbol{Q} = \boldsymbol{k}_0 - \boldsymbol{k}$), M is the mass of the scattering unit, e^{-2W} is the Debye–Waller factor and $\beta = \hbar\omega/k_{\mathrm{B}}T$, with k_{B} the Boltzmann constant and T the temperature in K. For coherent scattering elements a similar relations holds for $g(\omega)$ except that it is valid only within the approximation that a mean value of $\mathrm{d}^2\sigma_{\mathrm{sc}}/\mathrm{d}\Omega\mathrm{d}E$ is taken in a sufficiently large part of reciprocal space

$$g(\omega) = \frac{4\pi}{\sigma_{\mathrm{sc}}}\frac{k_0}{k}\hbar\omega(1-\mathrm{e}^{-\beta})\frac{8Mk_0k}{\hbar^2(Q^4_{\max}-Q^4_{\min})} \int \mathrm{e}^{2W}\frac{\mathrm{d}^2\sigma_{\mathrm{sc}}}{\mathrm{d}\Omega\mathrm{d}E}_{1\mathrm{phon}}\sin(\Theta)\mathrm{d}\Theta \tag{23.4}$$

Here $Q_{\min} = Q(\Theta_{\min})$ and $Q_{\max} = Q(\Theta_{\max})$ where $\Theta_{\min}$ and $\Theta_{\max}$ are the smallest and largest scattering angles used in the experiment and the weighting of the one-phonon part of $\mathrm{d}^2\sigma_{\mathrm{sc}}/\mathrm{d}\Omega\mathrm{d}E$ transforms the intensities measured in equal steps in scattering angle into intensities measured in equal steps in Q-space [39]; i.e. the coherent scattering effects have to be averaged

out in a good approximation [48] (avoiding partial double counting of contributions to the density of states [58]). This requires a directional averaging in reciprocal crystals are *necessarily* needed to determine the VDOS. All of the quasicrystalline alloys discussed below are predominantly coherent neutron scatterers and thus (23.4) applies to them.

A generalization is required if the sample is composed of several different scattering elements, because then the coupling of the probe to the vibration is different for each of the elements, depending on the scattering cross-section σ_{sc}^{i}, the Debye–Waller factor e^{-2W_i}, the concentration of the element c_i in the sample and on the mass M_i of the element i which influences the amplitude of the vibrations:

$$G(\omega) = \frac{\sum w_i g_i(\omega)}{\sum w_i} \tag{23.5}$$

$$w_i = \frac{\mathrm{e}^{-2W_i} c_i \sigma_{\mathrm{sc}}^{i}}{M_i} \,. \tag{23.6}$$

The $g_i(\omega)$ are the partial density of states of the element i in the sample under investigation. This generalization of the density of states, which is a good approximation to the true density of states if the weighting factors w_i are not too different from each other [21], is called the Generalized Vibrational Density of States (GVDOS) . It is this quantity which will be discussed here for qc alloys. All GVDOS presented below have been determined by inelastic scattering of thermal and cold neutrons using the time-of-flight (TOF) technique, which is especially advantageous for the determination of density of states of coherent scatterers. The weighted sum of all TOF spectra guarantees a good average over the coherence effects if the spectra were measured in a large range of scattering angles and with not too low an incident energy (here E_0 was always ≥ 4.75 meV). Then a sufficiently large shell between Q_{min} and Q_{max} is covered in reciprocal space, sufficient to average out the different intensities from the coherent inelastic scattering. At the same time, effects due to collecting intensities from only part of a BZ are avoided, i.e. this mistake is made so often that "too much" and "not enough" compensate to zero [58].

Depending on the temperature of the sample, in real experiments not only do single excitations contribute to the measured spectra but also *multiexcitations* like multiphonons. As the density of states is defined only by all single excitations, corrections for multiexcitations have to be calculated and subtracted from the measured intensities. For multiphonons this is done in the harmonic and incoherent approximation [48] using the multiphonon expansion of the incoherent part of the double differential scattering cross-section [46]. Depending on the type of scatterer the zeroth approximation $G_0(\omega)$ to the density of states is calculated from (23.3) or (23.4) and with this the multiphonon contributions to the scattered intensities are calculated and subtracted. This process is repeated until self-consistency is obtained

[58]. For other excitations no corrections are normally done assuming that the multiphonons present the major contribution of the multiexcitations.

Due to the finite resolution of the spectrometers, the foot of the huge peak of the elastically scattered probes extends into the inelastic spectrum. This part at lowest energies of the inelastic spectrum has therefore to be replaced by a model DOS. In the case of qc, nearly always a Debye type of model DOS ($\sim \omega^2$) was *fitted* to the measured intensity. The GVDOS are then normalized to 1 after choosing an appropriate cut-off energy.

The resulting GVDOS is still convoluted with the resolution function of the spectrometer. In all cases discussed below, this was not removed as this procedure often leads to changes of the DOS which are difficult to control. Therefore the theoretical results have been convoluted with a function simulating the finite energy resolution of the spectrometer. In most cases presented below, the resolution of the spectrometer used was 0.2–0.4 meV at energies below approximately 10 meV and became increasingly worse for higher energy transfers measured in neutron energy gain. The high-energy part of the GVDOS therefore is not very well resolved in most cases and it suffers from less good statistical accuracy due to the fact that the neutron inelastic scattering cross-section is approximately proportional to ω^{-2}.

Due to their aperiodic structure one expects for qc alloys some rather specific properties in connection with the atomic dynamics. In principle, due to the fact that the Bragg peaks are dense in the Fourier space, one is dealing with an infinite number of overlapping BZ, of which however only those belonging to strong reflections at the Γ-point can be realized as such in measurements of the atomic dynamics [3]. We do not expect any influence from this on the measured GVDOS, but there is no rigorous proof up to now. Leaving the phason-related elastic constants aside, the high symmetry of the (i-) structure reduces the number of elastic constants to two [32]. This has been proved in different experiments, where the same slope of the dispersion for all longitudinal acoustic modes independent of the symmetry axis, and the same slope for the degenerated transverse acoustic modes was found [42]. Thus rather high isotropy is expected for all acoustic contributions to the GVDOS. In these systems, up to now, acoustic dispersion branches could never been measured to higher energies than 4 THz approximately. Above this energy region, broad nearly dispersionless branches have been measured [5,29,57]. For two-dimensional qc, e.g. decagonal ones, some anisotropy could be expected on the basis of the investigation of other than vibrational properties [16,70], but has been found most recently to be rather small for heat conduction and dispersions of acoustic phonons [7,13] . Besides the translational degrees of freedom in parallel or external space which lead to the phonon modes, aperiodic crystals have additional degrees of freedom corresponding to translations in perpendicular or internal space leading to phasons [32]. In fact the dispersion of phasons could be determined for incommensurate phases [61] but not yet for qc where they are expected to be pinned [32] up

to temperatures of approximately 200–300 K below the liquidus temperature of the alloy. Presently the only possible contribution from phason modes to the GVDOS of qc alloys is expected at high temperatures in the region of quasielastic scattering, i.e. in he low-energy region [9].

23.3 Results for Metastable Quasicrystalline Alloys

The majority of all known qc alloys are metastable, i.e. on heating they make a transition to one ore more periodic crystalline phases. All of the qc alloys known soon after their discovery [45] were metastable and some of them were investigated first. Practically all methods used to produce amorphous alloys can also be used for the production of qc alloys, melt-spinning being used most often. In contrast to stable qc alloys, these samples cannot be annealed at the high temperatures needed to improve the qc order and thus these samples have to be used as produced or after annealing at a few hundred K only, i.e. with all imperfections of the lattice. From the qc alloys of which the GVDOS was studied first and which were all produced by the melt spinning techniques [34,53] therefore only two examples will be discussed.

23.3.1 Quasicrystalline and Amorphous Alloys of the Same Chemical Composition

Some metastable qc alloys can be obtained from a metallic glass of the same chemical composition by annealing. In this polymorphous transition the static structure factor changes drastically from the continuous $S(Q)$ of a metallic glass to an $S(Q)$ which is dominated by Bragg peaks, which however, measured with high resolution, show a finite width [15], pointing to a qc lattice with considerable phason strain [54] or defects. In addition, qc samples obtained by a short (to avoid crystallization of the metastable qc phase) annealing from a metallic glass tend to be nano-quasicrystalline which was obviously also the case for $Pd_{58.8}Si_{20.6}U_{20.6}$ [38]. This was one of the first icosahedral alloys of which different physical properties including the GVDOS [49] and the dynamic structure factor $S(Q,\omega)$ [50] have been measured. The basic question of this investigation was: if $S(Q)$ changes so drastically will one observe similar changes in the atomic dynamics? The answer to this question is negative: the GVDOS of the i-sample is very similar to that of the metallic glass. It is in fact like that of a very well relaxed metallic glass, and both are very different from that of the fully crystallized sample which consists of a mixture of crystalline UPd_3, UPd_2Si_2 and a third phase (see Fig. 23.1). This difference is especially obvious in the low-energy region of the GVDOS where the glass shows low-energy modes (LEM) which are typical for topologically disordered systems [48], and so does, even though in a reduced amount, the GVDOS of i-$Pd_{58.8}Si_{20.6}U_{20.6}$. The lattice part of the specific heat at low temperature, which was calculated using the experimentally determined GVDOS, is especially sensitive to the low-energy part of the GVDOS. As this

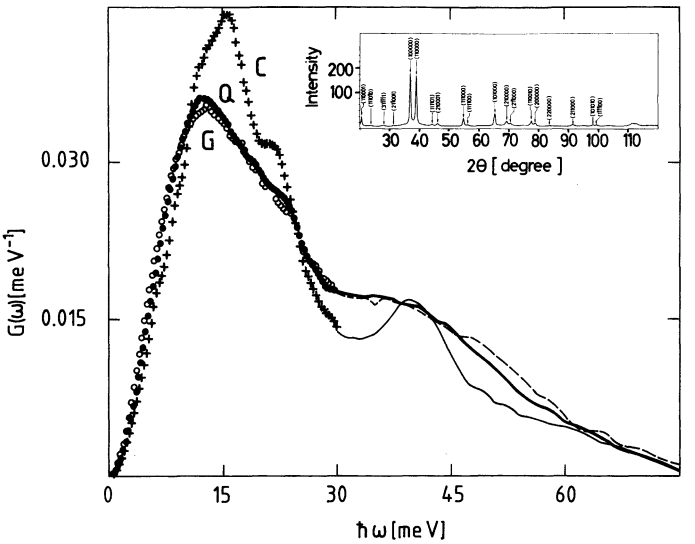

Fig. 23.1. GVDOS of amorphous (o) and icosahedral $Pd_{58.8}Si_{20.6}U_{20.6}$ and of the crystallized sample (+) (three periodic crystal phases) measured at 297 K

is slightly different for the amorphous and the icosahedral alloy, the specific heats calculated from the GVDOS (instead of the unknown VDOS) for the two alloys have the same temperature dependence but different absolute values. This finding was confirmed later by a careful direct measurement of the total specific heat with and without the application of a magnetic field [69]. As the VDOS is mainly sensitive to the SRO in the sample, it was concluded from the strong similarity of the very simple and smooth structure of the GVDOS that the SRO in the metallic glass and in the i-sample must be very similar. The main conclusion of this investigation therefore concerned the structure of the *metallic glass*: as one has to expect quite some icosahedral local symmetry in the i-alloy, this should therefore also be true for metallic glasses. This had been suggested before from computer simulations [61] but there had been no experimental results supporting this view. This similarity of the GVDOS, which in this case has a smooth and broad double peak structure, of the as-quenched metallic glass and of the i-alloy obtained from this by annealing and this strong difference to the GVDOS of the fully crystallized sample has been confirmed later for the case of $Al_{70}Cu_{20}V_{10}$ [52].

23.3.2 Low-Energy Modes and Structural Imperfections

The LEM which, though reduced in intensity, are observed in the GVDOS and $S(Q,\omega)$ of metastable qc alloys, raised the question of whether these modes are intrinsic to qc measured at room temperature, at which phasons where expected to be pinned [32], or whether they are a consequence of the production technique, i.e. melt-spinning in most cases. This question was in-

vestigated for the example of i-$Al_{74}Mn_{20}Si_6$ produced by melt spinning. This alloy, without Si, had been investigated before using a triple-axis spectrometer (TAS) [34]. Si was added in order to enhance the formation of the i-phase with respect to fcc-Al which contaminated the first samples [25,46]. Even though the i-phase of $Al_{74}Mn_{20}Si_6$ is metastable, the as-quenched sample can be carefully annealed at 600 K for 1 h without further crystallization and this slight annealing was sufficient to show that quite an amount of the LEM observed in the GVDOS and in $S(Q,\omega)$ of the as-quenched alloy could be removed and therefore were most likely caused by imperfections of the icosahedral lattice after the rapid quench [51]. As soon as stable i-alloys had been discovered, which stayed icosahedral on annealing in a certain temperature region, it could be shown that the largest part of these LEM in the melt-spun samples could be annealed out quantitatively [53]. However one has to keep in mind that obviously LEM do contribute to the VDOS of some or all qc, as the intensity of the VDOS in the low-energy region is proportional to ω^2 but the prefactor of the Debye model is higher than expected from the sound velocities alone [17]. At that time the smooth GVDOS found experimentally caused quite some discussion, because one had expected a strongly structured density of states for quasicrystals on the basis of the arguments given above, supported by the results of first calculations [26]. Up to now the existence of fine structure in the GVDOS remains an open questions [27,41].

23.4 Stable Quasicrystalline Alloys

Even though metastable qc alloys form the majority of all qc alloys, most of them do not belong to those which have been investigated in detail, because experimentalists turned to the few stable icosahedral and decagonal alloys as soon as they had been discovered by the end of the 1980s and the beginning of the 1990s. Stable here just means that in a certain – in most cases rather small – region of temperature and element composition the qc alloy will be formed as the only or as the preferred solid phase. For the determination of the GVDOS the advantage of these alloys compared to the metastable ones is the fact that polydomain samples can be kept at high temperature for very long times, this way annealing out the defects and favoring the formation of the qc phase with respect to crystalline impurities introduced by different production techniques. In fact many of the alloys investigated have been produced by melt-spinning (to homogenize the element distribution in the alloys) and subsequent annealing next to the melting temperature. Besides the GVDOS, in all cases $S(Q,\omega)$ has also been determined, from which angular averaged dispersion curves (in reciprocal space) have been obtained mainly for the optic branches in all but one case, while such dispersion curves could not be obtained for any of the metastable qc alloys investigated so far. The most important advantage of stable qc alloys is the fact that *monodomain* samples can be drawn from the melt by Bridgeman or Czochralski techniques

and thus the dispersion branches of acoustic and some optic phonons could be measured [23,42]. As this chapter is devoted to the density of states, no comparison of the angular averaged dispersions and the dispersion branches obtained for the same alloys will be made here.

23.4.1 Quasicrystalline Alloys and Their Rational Approximants

Is it possible to distinguish a quasicrystalline alloy from its rational approximant of low order on the basis of its lattice dynamics? This question was investigated in some detail for one of the stable i-alloy as well via the GVDOS [55] as also via the dispersion relations [20,23,42] (after monodomain samples had been grown) and also for a d-alloy via the GVDOS this time in a large temperature range [14]. In these TOF and TAS experiments, the lattice dynamics of i-$Al_{57}Li_{32.2}Cu_{10.8}$ (the T2-phase [22]), and of cubic $Al_{56}Li_{32}Cu_{12}$ (the R-phase, a bcc crystal with 160 atoms per unit cell) was compared. These alloys have practically the same composition and density, and therefore forces and distances will hardly determine the difference in the GVDOS but mainly the difference in their short-range order. The result of this investigation was that the GVDOS of the i-phase and its approximant only differ in small details. While the peak positions are essentially the same, the peak intensities differ slightly especially in the energy region from 10 to 20 meV. This strong similarity in the atomic dynamics of a thermodynamically stable qc alloy and of its low-order approximant, which was also found in the investigation of the monodomain sample [20], reflects the fact that both crystals are built up of essentially the same building units [2] and that the GVDOS is mainly determined by the SRO in the sample, the small differences in peak intensity reflecting slightly different connections between the building units in the i- and the bcc structure. Again the atomic dynamics of this alloy has also been calculated [68]. Most of the structure of the GVDOS has been reproduced by the calculations, even though the most prominent maxima between 10 and 20 meV are not well reproduced. Instead one observes an intense peak just below this energy region. This example demonstrates that *the atomic dynamics is more sensitive to the perfectness of the chosen potential* (here especially the Al(Cu) potentials) *than to the atomic structure*, which was very well reproduced in this calculation as judged from $g(r)$. From all the i-alloys of which the GVDOS was investigated so far, this one is the first example of the Bergman or Franck–Kasper type of i-structure [62] of which up to now only a second one, i- $Zn_{63}Mg_{26.3}Y_{10.7}$, was investigated most recently [43]. The GVDOS of i-alloys based on more or less complete Mackay icosahedra (MI) investigated so far essentially show a two-band structure (see below). This is not the case for AlLiCu nor for ZnMgY except one would interpret for AlLiCu the two maxima between 10 and 20 meV and for ZnMgY the 3 maxima between 10 and 25 meV (see Fig. 23.2) as substructures of the first band, an interpretation which would not be supported by the calculated partial density of states for AlLiCu [68]. It seems to be characteristic for the Bergman type of

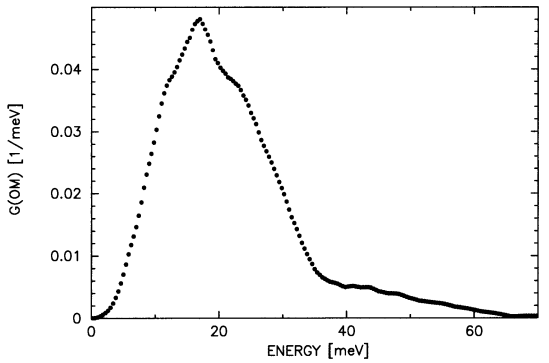

Fig. 23.2. GVDOS of i-$Zn_{63}Mg_{26.3}Y_{10.7}$ measured at 297 K. The richer structure of the main band between 10 and 25 meV compared to the Mackay type i-alloys is obvious

i-alloys that the GVDOS shows a stronger separation into energy bands than for the i-phase, the structure of which is dominated by more or less complete Mackay icosahedra. All presently available experimental [43,44,55] and theoretical results [18,30] support this finding, which can be understood on the basis of the rather different local vibrational density of states (LVDOS) for the latter structures and the grouping of more similar partial (element dependent) LVDOS in the case of the Frank–Kasper type of icosahedral qc. We assume that also the newly found types of qc, the binary CdYb qc with a Cd-tetraeder in the center of the building units, which otherwise – except for the 3^{rd} shell – are very similar to those of the Frank–Kasper type of qc, and the similar $Zn_{80}Mg_5Sc_{15}$ qc with an empty second shell, will show an atomic dynamics similar to the Frank–Kasper type of qc. First results obtained in NIS–experiments also suggest that the atomic dynamics of decagonal ZnMgY falls into this latter class [60].

Most recently it has been shown that this high similarity of the GVDOS of the qc phase and of an approximant phase is not limited to the i-structure – the only 3D qc structure and the one with the highest point symmetry – but has also been observed for a 2D case, d-$Al_{71.5}Co_{13.5}Ni_{15}$ and its metastable rational approximant $Al_{71.5}Co_{15.5}Ni_{13}$ [14] in a very large temperature range. As is demonstrated in Fig. 23.3, the two GVDOS of these samples are identical within experimental error at 300 K (which is true also at 1100 K, i.e. nearly up to the melting temperature of these alloys). This experiment also shows that the pronounced change of the GVDOS on expansion of the alloy with increasing temperature is the same for the d-crystal and for its rational approximant.

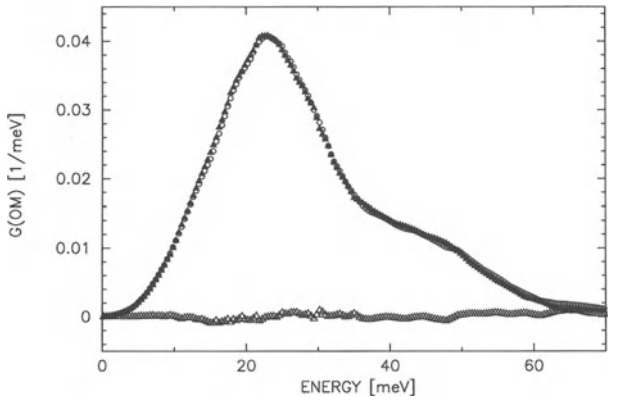

Fig. 23.3. GVDOS of d-$Al_{71.5}Co_{13.5}Ni_{15}$ (o) and the modulated approximant $Al_{71.5}Co_{15.5}Ni_{13}$ measured at 300 K. The small difference (△) (open triangles at the bottom) shows that the two GVDOS agree within experimental error

23.4.2 Quasicrystal versus Non-Approximant

Is this observed similarity between the lattice dynamics of a qc alloy and of its approximant also true for any other periodic crystal as long as it has the same or nearly the same chemical composition and a large unit cell? This question was behind the investigation of the GVDOS and the dynamic structure factor of i- $Al_{62}Cu_{25.5}Fe_{12.5}$ and tetragonal $Al_{70}Cu_{20}Fe_{10}$ [29]. The tetragonal crystal has 62 atoms in the unit cell. Figure 23.4 demonstrates that the GVDOS of the well-characterized i-alloy has a rather smooth two-band structure while that of the tetragonal crystal with very similar chemical composition spans essentially the same energy region covered by that of the qc

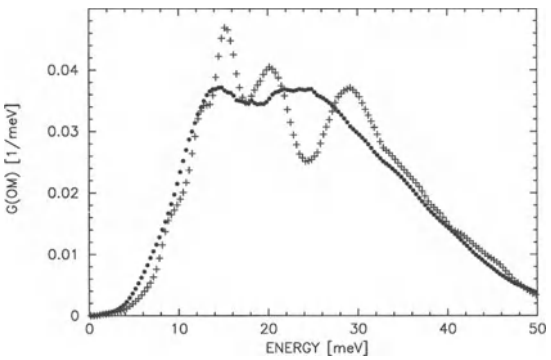

Fig. 23.4. GVDOS of i-$Al_{62}Cu_{25.5}Fe_{12.5}$ and t-Al_7Cu_2Fe (+) measured at 280 K. The strong difference between the GVDOS of the i-phase and the non-approximant with very similar chemical composition is clearly demonstrated

alloy, but has at least a three-band structure with very clear substructures on each of these bands. This GVDOS also demonstrates the fine structure which could be easily resolved in these experiments if it existed in the GVDOS of the quasicrystals. The answer to the question at the beginning of this section therefore is: crystals which are *not* approximants, even though they may have a very similar chemical composition and a large unit cell, can easily be distinguished from a corresponding quasicrystal via their GVDOS, because – as non-approximants – they have a different local atomic structure.

23.5 Temperature Dependence of the GVDOS

How does the GVDOS develop with temperature? As long as the harmonic approximation is valid, it should not change at all [1], but when approaching the liquidus of the alloy, one has to take into account the deviations from the harmonic approximation – the latter being applicable anyhow only at temperatures well below the Debye temperature (normally around 400 K for the Al-dominated alloys). The investigation described here for i-$Al_{71}Pd_{19}Mn_{10}$ [59,67] was done in parallel with the same investigation of d-$Al_{70}Co_{15}Ni_{15}$ [11] in order to study the changes of the lattice dynamics with temperature.

23.5.1 Temperature Dependence of the GVDOS of i-AlPdMn

The DOS of i-AlPdMn, measured at 297 K, has been discussed in detail before [57,58]. It consists of two broad bands centered at 13 and 33 meV approximately, of which the one at lower energy contains 1/3 of the total intensity and shows an indication of a small pseudogap within the first band at 13 meV when measured with high resolution [57]. In addition it had been shown that the GVDOS follows a Debye-like spectrum (ω^2) between 7 (the lowest energy accessible in that experiment) and 13 meV [58], however with a larger slope than expected from the known sound velocities. This energy region was masked by the disorder related LEM in the GVDOS of the metastable i-samples produced by meltspinning and the Debye spectrum behavior could therefore only be demonstrated with the advent of stable qc alloys. The main structure of the GVDOS has been quite well reproduced in a computer simulation using a structural model based on the model of Boudard et al. [4] and a Born–van Karman model for the interatomic forces in a pseudobinary alloy [10]. According to these calculations, the band at lower energies can be attributed mainly to the vibration of the heavy Pd-atoms and the upper band to that of the light Al-atoms.

In the investigation of the temperature dependence, the GVDOS was determined at seven temperatures between 293 and 1100 K. In the differences of the GVDOS $\Delta G(\omega) = G(\omega, T) - G(\omega,\ 297\ \mathrm{K})$ mainly the change of the first band was studied quantitatively by integration of $\Delta G(\omega)$ between 0 and 16 meV. As shown in Fig. 23.5 one observes a strong shift of intensity

into this energy region (0–25 meV). For temperatures up to about 1000 K the intensity increases linearly with temperature and it can be correlated with the mean expansion of the alloy, which has been measured separately in a high-resolution neutron diffraction experiment on the same sample, the Bragg peaks shifting essentially linearly with temperature up to the highest temperature investigated [67]. Up to 1000 K the observed shift of the GVDOS

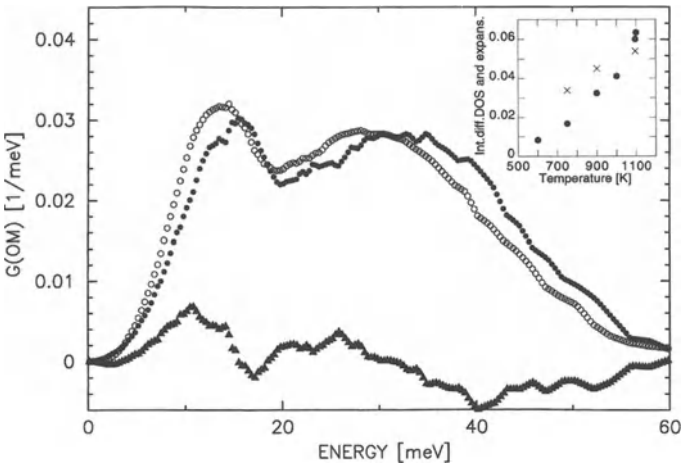

Fig. 23.5. T-dependence of the GVDOS of i-$Al_{71}Pd_{19}Mn_{10}$ measured at 300 and at 1000 K. The strong shift of the GVDOS to lower energies with increasing T is seen from the difference of the GVDOS. The insert shows the integrated positive part of $\Delta G(\omega)$ in comparison with the mean expansion of the alloy

to lower energies can therefore reasonably be related to the expansion of the alloy which is an anharmonic process. For higher temperatures one observes a steplike increase of the shifted intensity (see insert in Fig. 23.5) which is partly due to the onset of a new type of atomic movement in the very low energy region, which is observed as an additional intensity in the quasielastic region in the dynamic structure factor [33,66] and has a strong intensity contribution to the measured spectra only at Q-values above 22 nm^{-1} [65,66]. Whether or not this quasielastic intensity in the low-energy region of the GVDOS is due to the much discussed phason flips of the atoms [9] is presently an open question.

23.5.2 Temperature Dependence of the GVDOS of d-AlCoNi and Its Approximant

In contrast to the GVDOS of the i-alloys investigated so far, the GVDOS of d-AlCoNi and d-AlCoCu consists of one dominant band centered around 24 meV (values for AlCoNi) which contains 80% of the weight of the GVDOS

and a second centered around 47 meV which appears as a pronounced shoulder on the high-energy slope of the first band (see Fig. 23.3). The GVDOS extends to surprisingly high cut-off energies of about 60 meV (for fcc-Al it is only 2/3 of this value!). As in the case of i-AlPdMn one observes a considerable shift of the GVDOS with increasing T to lower energies. Integrating $\Delta G(\omega)$ (as defined above) between 0 and 25 meV one gets again a quantitative measure of the intensity shifted into this energy region with increasing temperature. As in the case of i-AlPdMn also in the case of d-AlCoNi this integrated intensity shift is linear with temperature and correlates perfectly up to 1100 K with the mean expansion of the alloy as obtained from the shift of a Bragg peak – measured in a high-resolution neutron diffraction experiment – which contained contributions from the qc-plane as well as from the periodic direction. Thus for d-AlCoNi the observed anharmonic shift of the GVDOS can reasonably be related to the thermal expansion of the alloy. This result obtained for d- $Al_{71.5}Co_{13.5}Ni_{15}$ agrees perfectly well with the results obtained in an earlier experiment on an $Al_{70}Co_{15}Ni_{15}$ sample, which proved – again in a high-resolution neutron diffraction experiment – to have a structure between the pure decagonal phase and a rational approximant. This agreement is not surprising in view of the practically identical result obtained for the d-phase and the approximant, which according to the electron diffraction pattern obtained for the two samples had a modulated periodic structure.

For this decagonal alloy detailed calculations have been performed using a decorated tiling [37], *ab initio* Al-Al, Al-Co and Co-Co pair potentials and the recursion technique [35,36]. The resulting GVDOS convoluted with the resolution function of the spectrometer agrees semiquantitatively with the experimentally determined GVDOS, which in view of the complicated structure and pair potentials is very impressive. More important, the calculation explains the origin of the two-band structure, the intensity distribution and the high cut-off energies of the experimental result: the dominant band at lower energies is largely due to the vibrations of the TM atoms, which appear enhanced in the GVDOS due to the strong weighting factors in favor of the Ni atoms, while the upper shoulder is mainly due to the vibrations of the Al atoms, which however also contribute to the lower energy band. This explains also why about 70% of the vibrations are concentrated in this latter band of the VDOS. Likewise the calculations show that the surprisingly large cut-off energies are mainly due to Al atom vibrations in the narrow and deep Al-TM pair potentials. The temperature dependence of this GVDOS has been investigated in the quasiharmonic approximation most recently. In this theoretical investigation it has been shown that the observed changes of the GVDOS with temperature can be accounted for by a frequency shift related to the expansion of the structure and to the temperature dependence of the weighting factors in (23.5), i.e. the Debey–Waller factor which is the only temperature dependent-term in (23.6) [17]. In addition, these theoreti-

cal investigations have lead to the determination of the VDOS, starting from the calculated partial $g(\omega)$ and determining the partials in an iterative and self-consistent way until they are in accordance with the measured GVDOS. This now opens the way to determine the thermodynamic and other dynamic properties of solids from the real VDOS instead in the GVDOS approximation!

Summing up this brief review on the GVDOS of qc alloys it was shown here that the GVDOS of qc alloys as investigated experimentally so far show a rather smooth shape. If the GVDOS of icosahedral alloys can be compared with that of the metallic glass from which they were obtained by a careful annealing, then the GVDOS of the icosahedral alloy has the appearance of that of a fully relaxed glass. The largest part of the LEM seems to be due to a disordered or defective quasiperiodic lattice and can be annealed out for stable quasicrystalline alloys. If the GVDOS of qc alloys are compared with that of periodic crystalline alloys of essentially the same chemical composition, the GVDOS of the periodic crystal is very similar to that of the qc alloy only if the periodic crystal is a rational approximant (only then is the atomic SRO alike) and it is very different for non-approximants. Finally the temperature dependence of the GVDOS can largely be related to the mean expansion of the alloy for icosahedral and for decagonal qc, even though at temperatures near melting new excitations may contribute to the observed intensity. For d-quasicrystals a semiquantitative description of the VDOS has been achieved so far and the temperature dependence can satisfactorily be described using a linear shift of the vibrational frequencies and taking proper account of the Debye–Waller factors in the weighting factors of the partial density of states.

Acknowledgment

It is a pleasure to acknowledge critical comments on this article by Ted Janssen.

References

1. Ashcroft N.W., Mermin N.D. "Solid State Physics" (Saunders College Publishing 1976) p. 464
2. Audier M., Janot C., de Boissieu M., Dubost B., Phil Mag. B 60 (1989) 437
3. Benoit C., Poussigue G., Azougarh A., J. Phys.: Condensed Matter 2 (1990) 2519
4. Boudard M., de Boissieu M., Janot C., Heger G., Beeli C., Nissen H.-U., Vincent H., Ibberson R., Audier M., Dubois J.-M., J. Phys.: Condens. Matter 4 (1992) 10149
5. Boudard M., de Boissieu M., Kycia S., Goldman A.I., Hennion B., Bellissent R., Quilichini M., Currat R., Janot C., J. Phys.: Condens. Matter 7 (1995) 7299

6. Brand R.A., Coddens G., Chumakov A.I., Calvayrac Y., Phys. Rev. B 59 (1999) R14145
7. Chernikov M.A., Ott H.R., Bianchi A., Migliori A., Darling T.W., Phys. Rev. Lett. 80 (1998) 321
8. Chumakov A., Rüffer R., Hyperfine Interactions 113 (1998) 59
9. Coddens G., Lyonnard S., Calvayrac Y., Phys. Rev. Lett. 78 (1997) 4209
10. Cordelli A., Gallo P., J. Phys.: Condens. Matter 7 (1995) 1245
11. Dugain F., Mihalkovič M., Suck J.-B., Mat. Science & Engineer. A226-228 (1997) 967
12. Dugain F., de Boissieu M., Hradil K., Shibata K., Currat R., Kortan A.R., Tsai A.P., Suck J.-B., Frey F., in "Aperiodics 97" ed. by M. de Boissieu, J.-L. Verger-Gaugry, R. Currat (World Scientific, Singapore 1998) p. 651
13. Dugain F., de Boissieu M., Shibata K., Currat R., Sato T.J., Kortan A.R., Suck J.-B., Hradil K., Frey F., Tsai A. P., Eur. Phys. J. B 7 (1999) 513
14. Dugain F., Mihalkovič M., Suck J.-B., J. Non-Cryst. Solids 250-252 (1999) 860
15. e.g. Edagawa K., Phil Mag. Lett. 61 (1990) 107
16. Edagawa K., Chernikov M.A., Bianchi A.D., Felder E., Gubler U., Ott H.R., Phys. Rev. Lett. 77 (1996) 1071
17. El Hor H., Mihalkovič M., Suck J.-B., Mat. Sci. & Eng. in print
18. El Hor H., thesis TU Chemnitz, Chemnitz (2002)
19. Gilat G., Raubenheimer L.J., Phys. Rev. 144 (1966) 390
20. Goldman A. I., Stassis C., de Boissieu M., Currat R., Janot C., Bellissent R., Moudden H., Gayle F.W., Phys. Rev. B 45 (1992) 10280
21. Hafner J., Phys. Rev. B 27 (1983) 678
22. Hardy K.H., Silcock J.M., J. Inst. Metals 84 (1955) 423
23. Hennion B., Quilichini M. (2002): See Chapter 22 of this book
24. van Hove L., Phys. Rev. 89 (1953) 1189
25. Janot C., Dubois J.-M., J. Phys. F: Met. Phys. 18 (1988) 2303
26. Janssen T. in "Quasicrystalline Materials" ed. C. Janot, J.-M. Dubois (World Scientific Singapore 1988) p. 327
27. Janssen T. (2002): See Chapter 21 of this book
28. Kaneko Y., Arichika Y., Ishimasa T., Phil. Mag. Lett. 81 (2001) 777
29. Klein T., Pares G., Suck J.-B., Fourcandot G., Cyrot-Lackmann F., J. Non-cryst. Solids 153-154 (1993) 562
30. Krajci M., Hafner J. (2002): See Chapter 20 of this book
31. Lovesey S.W. "Theory of Neutron Scattering from Condensed Matter" (Oxford Univ. Press, Oxford 1986)
32. Lubensky T.C., Ramaswamy S., Toner J., Phys. Rev. B 32 (1985) 7444
33. Lyonnard S., Coddens G., Calvayrac Y., Gratias D., Phys. Rev. B 53 (1996) 31
34. Miceli P.F., Youngquist S.E., Neumann D.A., Zabel H., Rush J.J., Rowe J.M., Phys. Rev. B 34 (1986) 8977
35. Mihalkovič M., Dugain F., Suck J.-B., J. Non-cryst. Solids 205 (1996) 701
36. Mihalkovič M., Elhor H., Suck J.-B., Mat. Sci. & Eng.A, in print
37. Mihalkovič M. (2002): See Chapter 7 of this book
38. Nissen H.-U., private communication 1987
39. Oskotskii V.S., Sov. Phys.-Solid State 9 (1967) 420
40. e.g. all PDOS of the bcc structures of the alkali metals look alike (mainly the energy scales are different due to the different masses) and likewise the PDOS of fcc-crystals with such different interactions as Al, Ne and Cu are most similar in shape (and considerably different from those of the bcc-crystals) to each other.

41. Poussigue G., Benoit C., de Boissieu M., Currat R., J. Phys.: Condensed Matter 6 (1994) 656
42. Quilichini M., Janssen T., Rev. Mod. Phys. 69 (1997) 277
43. Rouijaa M., Suck J.-B., Sterzel, R., J. Alloys & Comp. (2002) in print
44. Rouijaa M., Suck J.-B., Sterzel, R., Petrenko O.A., J. Alloys & Comp. (2002) in print
45. Shechtman D., Blech I., Gratias D., Cahn J.W., Phys. Rev. Lett. 53 (1984) 1951
46. Sjölander A., Ark. Fys. 14 (1958) 315
47. Suck J.-B., Rudin H., Güntherodt H.-J., Beck H., Phys.Rev.Lett. 50 (1983) 49
48. Suck J.-B., Rudin H. in "Glassy Metals II", ed. H. Beck, H.-J. Güntherodt, Topics in Applied Physics 53 (Springer, Berlin Heidelberg 1983) p. 217
49. Suck J.-B., Bretscher H., Rudin H., Grütter P., Güntherodt H.-J., Phys. Rev. Letters 59 (1987) 102
50. Suck J.-B., Bretscher H., Güntherodt H.-J., Z. Phys. B 68 (1987) 285
51. Suck J.-B. in "Quasicrystalline Materials" ed. C. Janot, J.-M. Dubois (World Scientific Singapore 1988) p. 337
52. Suck J.-B., Güntherodt H.-J. in "Phonons 89" ed. S. Hunklinger, W. Ludwig, G. Weiss (World Scientific Singapore 1990) p. 573
53. Suck J.-B. in ref. [50] p. 397
54. for the sample discussed here this was shown by: Suck J.-B. in "Basic Features of the Glassy State" ed. by Colmenero, J. and Alegria, A. (World Scientific, Singapore, 1990) p. 41
55. Suck J.-B., Janot C., de Boissieu M., Dubost B. ref. [48] p. 576
56. Suck J.-B., Egelstaff, P.A., Robinson, R.A., Sivia, D.S., Taylor, A.D.: Europhys. Letters 19 (1992) 207
57. Suck J.-B., J. Non-cryst. Solids 153-154 (1993) 573
58. Suck J.-B., J. Non-cryst. Solids 156-158 (1993) 872
59. Suck J.-B. in "Rapidly Quenched and Metastable Materials" ed. P. Duhaj, P. Mrafko, P.Svec (Elsevier Amsterdam 1997) p. 410
60. Suck J.-B., Scheffer M., Sterzel R., ICQ8 submitted
61. For references see Suck J.-B. (2002): See Chapter 1 of this book
62. Tamura N., Phil. Mag. A 76 (1997) 337
63. Thorpe M.F., Phys. Rev. B 8 (1973) 5352
64. Tsai A.P., Guo J.Q., Abe E., Takakura H., Sato T.J., Nature 408 (2000) 537
65. Uhlig H., Suck J.-B. in "Aperiodics 97" ed. by M. de Boissieu, J.-L. Verger-Gaugry, R. Currat (World Scientific, Singapore 1998) p. 657
66. Uhlig H., Rouijaa M., Suck J.-B., J. Non-Cryst. Solids 250-252 (1999) 855
67. Uhlig H., Suck J.-B., J. Phys.: Condens. Matter submitted
68. Windisch, Hafner J., Krajci M., Mihalkovič M., Phys. Rev. B 49 (1994) 8701
69. Wosnitza J., van den Berg R., v. Löhneysen H., Poon S.J., Z. Phys. B 70 (1988) 31
70. Zhang Dian-Linet, Cao Shao-chun, Wang Yun-ping, Lu Li, Ang Xue-mei, Phys. Rev. Lett. 66 (1991) 2778

24 Thermodynamics of Quasicrystals

Reinhard Lück

Summary. An overview of experimental methods for the determination of thermodynamic data of alloys is given. The significance of thermodynamic and kinetic data is outlined for stable and metastable states with respect to quasicrystalline alloys. The information on the stability of quasicrystals is summarized on the basis of the competitive formation of quasicrystals and of crystals with translation symmetry.

24.1 Introduction

In the sense of thermodynamics, quasicrystals have to be considered as intermetallic compounds; these compounds are formed of at least two chemical elements, all being metals, or metals and metalloids; however, at least one metallic species is included. Intermetallics are usually stable phases, but metastable intermetallics have also been observed. The first quasicrystals [53] to be prepared were metastable. Stable quasicrystals were detected a few years later. The main difference between quasicrystals and other intermetallics is the lack of periodicity of their lattice. As amorphous alloys have no crystal structure and hence no periodicity, some relationships with quasicrystals have been assumed. Amorphous alloys are metastable as are several quasicrystals. The thermodynamic investigation of quasicrystals is partly related to that of intermetallics with periodic structure and on the other hand partly related to the study of amorphous alloys.

What can we learn by thermodynamics of quasicrystals? Hopefully we will understand the stability of quasicrystals. It is intended to distinguish between stable and metastable quasicrystals by thermodynamical considerations. Subsequently it is necessary to discover whether quasicrystallinity may be considered thermodynamically as a ground state.

Thermodynamic data are needed for the calculation of phase diagrams, which in turn are necessary for the production of high-quality quasicrystals. The metastable formation of quasicrystalline alloys in the Al-Mn system has been calculated [16]. No calculation of the formation of a stable quasicrystal is known.

J.-B. Suck et al. (eds.), *Quasicrystals*
© Springer-Verlag Berlin Heidelberg 2002

24.2 Molar Heat

Specific heat is the heat capacity referred to mass whereas molar heat is referred to mole or g-atom. The determination of the molar heat, C_p, and its dependence on temperature, gives further information on the thermodynamic functions: enthalpy, $H(T)$, entropy, $S(T)$, and Gibbs energy (formerly termed free energy or Gibbs free energy) $G(T)$:

$$H(T) = \int_0^T C_p(\Theta)\mathrm{d}\Theta, \tag{24.1}$$

$$S(T) = \int_0^T \frac{C_p(\Theta)}{\Theta}\mathrm{d}\Theta, \tag{24.2}$$

$$G(T) = \int_0^T C_p(\Theta)\mathrm{d}\Theta - T\int_0^T \frac{C_p(\Theta)}{\Theta}\mathrm{d}\Theta, \tag{24.3}$$

Integration beginning at 0 K assumes that the enthalpy at 0 K does not affect further computations and that no entropy is involved at 0 K [24]. This implies that the alloy is composed of phases in their ground state. This condition is generally not fulfilled; therefore another integration is often used in thermodynamic considerations:

$$H_\mathrm{s}(T) = \int_{298.15}^T C_p(\Theta)\mathrm{d}\Theta, \tag{24.4}$$

$$S_\mathrm{s}(T) = \int_{298.15}^T \frac{C_p(\Theta)}{\Theta}\mathrm{d}\Theta, \tag{24.5}$$

These data are termed standard functions. The determination of G again follows $G = H - TS$, and the entropy at 298.15 K enters this formula. The data of metals and alloys do not differ appreciably. The main difference stems from different Debye temperatures. At low temperatures C_p is influenced by the electronic density of states for metallic systems.

C_p has to be determined experimentally. Usually, a calorimeter is applied. A commercial differential scanning calorimeter can be used [25]. Another possibility is the determination of C_p via lattice vibration data; for the vibrational density of states reference should be made to [55] and [56]; this gives the lattice part of the density of states and allows us to separate the lattice and the electronic part of the total measured C_p. At low temperatures the lattice part is approximated by $c_p \sim T^3$.

The first data on metastable icosahedral Al-Mn alloys were published by Wosnitza et al. [57]; these data are restricted to low temperatures (0.1–15 K). For comparison with thermodynamic data high-temperature C_p values are necessary. Inaba et al. [19] have measured the heat capacity of Al-Cu-Ru icosahedral quasicrystals. The measurements have been performed on three different samples: a 'phasonless perfect' quasicrystal $Al_{65}Cu_{20}Ru_{15}$, an $Al_{65}Cu_{20}Ru_{15}$ quasicrystal with phason disorder, and an approximant

$Al_{70}Cu_{20}Ru_{10}$. A low-temperature plot C_p/T vs. T^2 showed that the electronic heat capacity of the perfect quasicrystal was essentially zero. The authors concluded that the perfect quasicrystal is an insulator. An extra contribution in heat capacity above 150 K was detected for the quasicrystal with phason disorder, which was attributed to phasonic defects. The vibrational properties of quasicrystals have been found to be distinctly different from those of the crystal approximant in the region below one tenth of the Debye temperature [[19].

Bianchi et al. [4] report on data of C_p of decagonal Al-Co-Ni. The investigated composition was $Al_{70}Co_{15}Ni_{15}$. In this case C_p/T vs T^2 gives a straight line; fitting with $C_p(T) = \gamma T + \beta T^3$ results in $\gamma T = 0.63\ T$ mJ mol^{-1} K^{-1}, in that there is definitely an electronic contribution. Wang et al. [60] measured the low-temperature molar heat of $Al_{62}Cu_{25.5}$ $Fe_{12.5}$ and $Al_{63}Cu_{24.5}Fe_{12.5}$ using an ac method. They investigated samples with different heat treatment and found that electronic contribution had the lowest contribution after heat treatment at 800 °C.

The determination of molar heat can be affected by further latent heats. Heats of transformation – such as the heat of melting – can be reversible if the transformation is in equilibrium. Also latent heats of irreversible processes can be observed in such experiments. An example is the heat of transformation of metastable quasicrystalline alloys which will be discussed in another section. Such processes make it difficult to measure the molar heat. Early C_p measurements up to the transformation temperature on metastable Al-Mn showed slightly higher C_p values for the quasicrystalline state than for the transformed state [39]. It could not be excluded that this result was an artifact caused by latent heats of relaxation processes.

The discussion of stability needs enthalpy and entropy versus temperature, but these data do not refer to the pure components. Quantities which refer to the components will be discussed in the next section.

24.3 Thermodynamic Functions of Formation

Quasicrystals are only formed in alloy systems with a pronounced negative enthalpy of formation in the solid and in the liquid state. Thermodynamic data of binary systems have been collected in [18] and [45]. As stable quasicrystals are formed in ternaries further data are needed.

24.3.1 Enthalpy of Formation in the Solid State

The enthalpy of formation of the $Al_{63}Cu_{25}Fe_{12}$ icosahedral phase has been determined by Saâdi et al. [49,50] (see Table 24.1). For this determination solution calorimetry was applied. For this method well-prepared alloys – in the present case quasicrystals and competing intermetallics – are brought into a liquid metal, liquid Al in the present case. The heat of reaction is recorded.

For $Al_{63}Cu_{25}Fe_{12}$ it seemed to be difficult to come to a definitive conclusion about whether the icosahedral phase is a ground state of the Al-Cu-Fe system.

However, in their second paper [50] the authors conclude that the icosahedral phase of the Al-Cu-Fe phase diagram is an equilibrium phase with an enthalpy of formation which is comparable to those of the surrounding phases in the ternary system. No particularly high entropy of formation is necessary for stabilization. The authors stress the fact that the icosahedral phase can be the ground state, since the values of G vs concentration form a convex configurational polyhedron. They state that "the 'random tiling' hypothesis should be used with great caution when applied to practical cases".

Table 24.1. Formation enthalpies for compounds of the Al-Cu-Fe system [50]

Phase	$\Delta_{\mathrm{sol}} H_{\mathrm{f}}$ J/g-atom
λ(AlFe)	−30245
β	−24235
Φ	−23935
ω	−24085
λ(AlCuFe)	−28425
R	−24670
i	−25250

In the Al-Co-Ni system solution calorimetry measurements have been performed on the β phase (CsCl structure) [14]. They infer that the enthalpy of formation in the ternary system is 5% lower than the weighted average of the data for AlCo and AlNi. An enhanced concentration of defects in the ternary β (Co, Ni) Al compounds is evaluated.

24.3.2 Entropy of Formation

The simplest manner to determine the entropy of configuration is the application of the ideal solution model. This renders the equation:

$$S = -R(x_{\mathrm{A}} \ln x_{\mathrm{A}} + x_{\mathrm{B}} \ln x_{\mathrm{B}} + x_{\mathrm{C}} \ln x_{\mathrm{C}} + \cdots) \tag{24.6}$$

This equation is applied in the solid as well as in the liquid state. In the liquid state some modifications are necessary if the atomic sizes of the constituents are different [40]. In the case of chemical order, the equation will no longer hold and the entropy will be smaller.

The entropy of formation depends on temperature. It is influenced by the ordering of the compound formed at the considered temperature. Disorder would enhance the entropy and therefore stabilize the compound at high temperatures. Generally, some modeling is necessary to determine the formation entropy from other measured thermodynamic data.

A more sophisticated method to determine the entropy is the cluster variation method (CVM) [6]. This method gives more reliable results, but it needs more computation and knowledge on next-neighbor interactions. No applications to quasicrystals are known.

24.3.3 Mixing Enthalpy in the Liquid State

The melt of the composition of quasicrystals possesses a high degree of chemical short-range ordering, so chemically ordered icosahedral clusters can be assumed in the melt [17]. This fact must be taken into account in a thermodynamic description of the melt. The determination of the mixing enthalpy in the liquid state is generally difficult: it has to be performed at high temperatures because of the high melting temperature of two components (Pd and Mn or Co and Ni); at these temperatures the components with a low melting temperature (Al, Mg) have a high vapor pressure. The evaporation of one component produces systematic errors and can destroy the calorimeter equipment. Magnetic measurements of quasicrystalline alloys in the liquid state confirmed a chemical short-range ordering in the liquid which decreases with increasing temperature; this is indicated by an anomalous increase of the magnetic susceptibility with increasing temperature (compare for instance [42,51].

Estimated data in the ternary liquid are available [58,59] for the case of the newly detected stable Ni-Zr-Ti quasicrystal [28]. The data have been calculated from experimental data of the enthalpy of mixing in the Ni-Zr [1] and the Ni-Ti [38] systems. No ternary interactions have been taken into account. The Ni-Zr system has the highest negative heats of mixing of transition metal–transition metal systems. Even the heats of formation have exceptionally high negative values in these binary systems. No ternary data of heat of formation are available for the Ni-Zr-Ti system.

The thermodynamic data of the important quasicrystal-forming systems Al-Pd-Mn and Al-Co-Ni in the liquid state can be interpolated from collected binary data [18,45] neglecting ternary interactions. For liquid binary Al-Ni alloys, new calorimetric data have been published [54]. For liquid Al-Mn alloys, the Gibbs energy of mixing of the liquid state was measured using Knudsen cell mass spectroscopy by Bergman et al. [3]. This method is based on the evaporation of atoms from a heated container through a small orifice. In the case of combination of Knudsen cell evaporation with a mass spectrometer the amount of evaporating species is measured. In the cited work, the so-called intensity ratio method was applied. This method is based on measuring the ratio of ionic intensities $I(^{27}\mathrm{Al})$ and $I(^{55}\mathrm{Mn})$ of the isotopes at the same temperature for different molar fractions. The data indicate a moderate ordering effect due to attractive interactions between aluminium and manganese atoms and the entropy of formation was slightly positive. The authors [3] compare the results with several other data of Al-based binary alloys and come to the conclusion that moderate ordering and a positive entropy of formation could

be a significant feature of quasicrystal-forming alloys. The Gibbs energy can also be determined by EMF (electro-motoric force) methods; this method has been applied to binary boundary systems [45] of quasicrystal-forming systems, but no application to quasicrystal-forming alloys is known.

24.3.4 Entropy of Mixing

The entropy of mixing in the liquid state cannot be measured directly. It is generally determined by modeling the dependence of mixing enthalpy on concentration and temperature. If the Gibbs energy of mixing and the enthalpy of mixing are measured independently, the entropy of mixing can be calculated. The entropy of mixing exhibits a minimum if a strong cluster-forming tendency with chemical interactions of constituents is found for a special chemical composition. For chemical compositions of stable quasicrystals such a minimum cannot be supposed, since several other competing intermetallics have similar compositions.

24.4 Metastable Quasicrystals and Heat of Transformation

The transformation from the metastable state is a thermally activated process and can be investigated in a similar manner to the crystallization of amorphous alloys. DSC (differential scanning calorimetry) scans yield an exothermic peak with a peak temperature and a peak area. The peak area can be tentatively attributed to the transformation enthalpy [29]. There is an uncertainty due to amounts of the second phase of supersaturated aluminium. For the quasicrystalline Al-Mn alloys it turned out that the peak temperature depends on the preparation process [41]. At lower temperatures than the peak temperature, a reaction with a small exothermic energy is found for splat quenched alloys in the DSC scan. This process is similar to the relaxation of melt-spun or splat-quenched amorphous alloys; in both cases it is a kind of recovery in a temperature range where no long-range diffusion is possible. However, there should be a difference on the atomic scale considering the different atomic structure (see also [55] where these relaxation experiments and there influence on the phonon density of states are described).

The peak temperature depends not only on the preparation process but also on the heating rate. This dependence can be used to determine the activation enthalpy of the transformation process [36] in a Kissinger plot [30]. To extend the range of heating rates the measurement with stepwise heating can be applied [25]. This peak temperature can also be determined by measuring physical properties; use of the inflection point of the magnetic susceptibility vs temperature curve [39] is a successful method.

The measurement of the released energy in an isothermal experiment can yield the reaction order as an Avrami exponent according to the Johnson–Mehl–Avrami (JMA) theory [5]. Lu et al. [36] determined this exponent to

be $n = 3$ for the crystallization of quasicrystalline Al-Mn alloys, and the exponent is explained by volume growth. Köster and Schumacher [33] reported that this transformation is of peritectic type with a $\sqrt{t}$ law, t being the time. For that case a lower n is required [5].

Isothermal experiments for the long periods necessary for low-temperature observations can be performed by magnetic measurements. The change of the magnetic susceptibility can be easily monitored and this change can be evaluated according to the JMA theory. The transformation of melt-spun Al-Mn has been investigated extensively [31]. Generally, the transformation of quasicrystalline Al-Mn has been found to be of the $\sqrt{t}$ type; from this time law generally a diffusion controlled process is concluded.

Even in stable quasicrystals activation energies can be determined. For this purpose thermal defects should be quenched in from high temperatures. These defects are metastable at low temperatures. The annealing-out can be monitored in a similar manner by magnetic measurements, the activation energy determined using the Kissinger plot amounts to 1.7 eV [52].

24.5 Stability Arguments

The main aim of thermodynamic considerations is to find explanations of why some phases are stable and others are not. On the other hand, several phases are not stable in the sense of thermodynamics; however, they can exist for very long times; they are kinetically stabilized. In the case of quasicrystals it is an often discussed problem whether quasicrystals are stable and if so why. There are several arguments for the stability of quasicrystals, which should be briefly summarized. In any case, there must be a compound-forming interaction of the constituent atoms as for any intermetallic compound. There are additional arguments. These are not very specific, so that only empirical rules can be used for searching. Quasicrystals might be stabilized by a special ratio of the different atomic or ionic radii, and in that a special stoichiometry is preferred. The Hume–Rothery argument requires special values of the valence electron concentration. Phasons can cause a contribution to entropy and so enhance the stability at high temperatures.

24.5.1 Experimental Evidence

The liquid–solid transition has been found for several ternary quasicrystalline alloys also for low cooling rates. Therefore, it is assumed that these quasicrystals are stable in the thermodynamic sense. Long heat treatment does not disturb the quasicrystallinity, hence stabilization from kinetics could be excluded.

24.5.2 Atomic Size Influence

It is generally accepted that the known quasicrystalline structures are composed of clusters or parts of clusters with icosahedral symmetry and that the formation of these clusters is favored by special ratios of the atomic diameters of their constituents. So far, there is a strong relationship to Frank–Kasper phases [7,8]. A similar relationship may be constructed for Laves phases [35]; stable icosahedral quasicrystals have been found in Zn-Mg-RE (RE=rare earth metal) systems. The difference in the atomic radii for Zn and Mg is responsible for the formation of the hexagonal Laves phase Zn_2Mg. The clusters forming eightfold and twelvefold quasicrystals should be slightly different; in the case of 12-fold $Ta_{1.6}Te$ clusters of other compounds found in this binary system are taken into account [34].

24.5.3 Electronic Influence

At room temperature the magnetic susceptibility of most investigated quasicrystals with ideal composition after heat treatment was found to be negative [42], [51]. From this fact it can be concluded that the number of electrons and of holes per atom is very low. This can be understood if the Fermi surface is cut quite often by important Bragg planes; it is known that the Fermi energy is lowered by this fact. A pseudo-Brillouin zone can be constructed of these Bragg planes based on the strongest Bragg peaks. The term "pseudo" is used to distinguish these from the Brillouin zones of periodic lattices; the pseudo-Brillouin zone does not have the translational and repetitive properties of the Brillouin zone. This first pseudo-zone approaches a spherical shape. From this fact the existence of a narrow electronic density of states is confirmed. The same fact is concluded from electronic specific heat data. The conclusion is that the different quasicrystalline structures are related to special electronic concentrations. The evaluation of these numbers depends on the model for the number of electrons per atom (e/a) of the components. Often the noninteger values given by Raynor [46] are used for the transition metals. Nevertheless, a strong correlation between the quasicrystalline structure and the number of electrons per atom in the alloy seems to be independent of the model. According to this point of view, the quasicrystals can be regarded as Hume–Rothery alloys. If the Hume–Rothery argument holds for quasicrystals, the existence regions in ternaries should follow loci with constant e/a values in the Gibbs triangle, which are straight lines. A detailed discussion of stability arguments for Hume–Rothery alloys is given in [15].

Cluster formation and packing of clusters is another approach to describe stable quasicrystals. The starting point is the assumption of localized electronic states which lead to chemical (ionic) bonding forming stable clusters, which in turn have charges and will form larger clusters [22,23]. Janot determines with this cluster model the ideal composition of icosahedral AlPdMn as:

$$x_{\mathrm{Al}} = 0.702666.. \qquad x_{\mathrm{Pd}} = 0.214666.. \qquad x_{\mathrm{Mn}} = 0.082666..,$$

which is close to the experimentally determined ideal composition [10,11]:

$$x_{\mathrm{Al}} = 0.71 \qquad x_{\mathrm{Pd}} = 0.21 \qquad x_{\mathrm{Mn}} = 0.08.$$

24.5.4 Closeness Condition and Stoichiometry

The quasilattice is often derived by the cut-and-project method [27]. The decoration of the periodic lattice in hyperspace by atomic surfaces in a "complementary space" yields the quasilattice after appropriate projection in physical space. (For more details on tiling theory see the chapter by M. Baake in this book [2]). The atomic surface cannot be taken with an arbitrary shape, as this shape has to fulfill the so-called closeness condition. In ordered quasicrystals the same holds for the atomic surfaces of the different elements [37]. This means, a phason flip (Sect. 24.5.6) should not produce or destroy atoms and it should not interchange chemical elements. The consequence of this is that a well-defined stoichiometry of an ideal quasicrystal exists. This closeness condition must strongly be fulfilled for the ground state, but even at high temperatures the deviation should not be too large.

24.5.5 Pair Potentials

There are several theoretical calculations using different kinds of potentials (compare for instance [44]). Such computations do not result in all cases in quasilattices, which remain stable under relaxation with the applied pair potentials.

24.5.6 Entropic Stabilization

It is well known that high-temperature phases can be stabilized by disorder which enhances the entropy [see (24.3)]. The shrinking of the existence region at low temperatures gives an indication of the influence of entropy. Some quasicrystals seem to be stable at low temperatures, and these samples are more or less perfect. The entropy in quasicrystals has attracted appreciable attention. Whereas in periodic crystals point defects like vacancies and antisite atoms are mainly responsible for the entropy, in quasicrystals an additional type of defect has to be considered. This type is related to the phason strain, briefly called phasons. Phasons are, in three-dimensional quasiperiodic lattices, lines of defects which can move, shrink and annihilate by phason flipping, but which are in contrast to dislocation lines fixed on a plane [32]. It is known that some of the investigated alloys have a high concentration of phasons. Phasons may be quenched in and can be annealed out during heat treatment. That means that the mentioned reaction similar to a relaxation might be an annealing-out of phasons. The kinetics of the annealing-out of

defects has been investigated [31,52] and modeled for two-dimensional tilings [20]. Even thermal vacancies will exist in quasicrystals as in related periodic intermetallic compounds [52] and they can contribute to entropy.

A model which favors the role of the entropy in the stabilization is that of random tiling. Mosseri et al. [43] determined the configurational entropy in random tiling models. It is believed that the derived formula is valid in the thermodynamic limit. Gähler [9] has described the thermodynamics of random tiling quasicrystals. He studied matching rule interactions by Monte Carlo simulation for octagonal and icosahedral quasilattices. The phasonic influence on the entropy has been evaluated and the specific heat has been computed from the entropy. He found a maximum in the specific heat for both investigated tilings (compare the phasonic contribution to C_p in Al-Cu-Ru, Sect. 24.2 and [19]). Gähler concluded that his results in the icosahedral case "consistently suggest the existence of a phason unlocking transition at a unique, finite temperature". Joseph and Elser [26] modeled a square and triangle tiling; they studied nucleation and growth at limited temperatures. They found that the formation of tears depends on temperature. They came to the conclusion that slow growth is enough to model thermodynamic equilibrium (see also [13]).

Another approach to the entropy is the computation of the fluctuation of the cut in hyperspace, which is discussed in the next section.

24.5.7 Thermodynamics of Modifications and Approximants

The phasons can also be distributed homogeneously. In that case new related structures can be formed. If the cut in the hyperspace is oriented in an orientation which slightly deviates from an irrational cut, which would lead to a quasiperiodic lattice in physical space, a periodic structure with an elementary cell composed of motifs of the quasicrystal can be formed. That means, phases with similar periodic structures can occur with nearly the same composition as the quasicrystal; these structures are called approximants. In other words: a small deviation from the ideal composition can result in new phases especially at low temperatures. Therefore the investigation of phase diagrams of quasicrystal-forming systems can be a very difficult and tedious work program, where the combination of different thermal analyzes with optical metallography and scanning, transmission and high-resolution electron microscopy is necessary. It seems to be impossible to distinguish between quasicrystals and their approximant phases by thermodynamic methods; the electronic specific heat might be an exception [19]. The enthalpy of formation is the same, the difference in the entropy will be lower than the change caused by the alteration of temperature. In Al-Cu-Fe [12], Al-Pd-Mn [21] and Al-Co-Ni [47,48] several modifications within the phase region of quasicrystalline phases have been found; there is little chance to separate them by thermodynamics. Up to now first-order as well as second-order transformations seem to be present. A mixture of motifs and a high density of phasons will be

produced by a fluctuation of the slope of the cut, which in turn contributes to the entropy.

24.6 Conclusion

Thermodynamics of quasicrystals is an interesting but not in every case simple field of research. Important investigations have been done; others might be done in the near future. A deep understanding of the reason for the formation of quasiperiodic crystals seems to be lacking. Several factors leading to stability can be listed. Most of them also hold for periodic crystals. These are:

(i) the ideal ratio of atomic radii of constituents for dense packing,
(ii) the compound-forming tendency due to pronounced negative enthalpy of formation in the solid and in the liquid state with formation of chemically ordered clusters in the melt,
(iii) special valence electron concentration in the sense of Hume–Rothery alloys,
(iv) additional entropy contribution from phasonic defects.

If the quasicrystalline state is the ground state of matter, the quasicrystal is a low-temperature phase. There should be no entropic stabilization, as no entropy is allowed.

Thermodynamics support the calculation of phase diagrams. The calculation for quasicrystal-forming alloy systems is difficult for several reasons:

(i) There are still only little thermodynamic data of quasicrystals available.
(ii) Quasicrystalline phases and similar crystalline phases (e.g. 'approximants') generally compete in formation and will have very similar heats of formation.
(iii) The significance of entropy is not clear; an entropic stabilization by phasons has been proposed. Random tiling models do not in all cases produce stable configurations in the sense of thermodynamic equilibrium.

Calculation of phase diagrams containing stable quasicrystals is a formidable (but important and interesting) task made all the more difficult by the necessary consideration of the factors of quasicrystal modifications, the existence of their approximant competing phases and chemical ordering in the melt. Calculation of metastable phase diagrams containing quasicrystals and metastable extensions of stable diagrams may be facilitated in binaries but will generally also be difficult for the same reasons.

Acknowledgment

Part of this work has been supported by the Deutsche Forschungsgemeinschaft (DFG), which is gratefully acknowledged. I am indebted to several

colleagues for helpful discussions and important information on thermodynamics as well as on quasicrystals; an inexhaustive list would contain at least: I. Arpshofen, M. Baake, C. Beeli, C. Bergman, A.D. Bianchi, J.-M. Dubois, F. Gähler, T. Gödecke, M. Harmelin, D. Joseph, K. Lu, H.-U. Nissen, B. Predel, S. Ritsch, M. Scheffer, J.F. Smith, J.-B. Suck, J. Tomiska, A.P. Tsai and D.H. Warrington.

References

1. Arpshofen I., Lück R., Predel B., Smith J.F., J. Phase Equilibria **12** (1991) 141
2. Baake M., (2002), see Chapter 2 of this book
3. Bergman C., Saito M., Chastel R., Mater. Sci. Eng. **A178** (1994) 89
4. Bianchi A.D., Felder E., Kenzelmann M., Chernikov M.A., Ott H.R., Edagawa K., Proc. 6th Int. Conf. Quasicrystals, Tokyo, 1997, Eds. S. Takeuchi, T. Fujiwara, World Scientific, Singapore, 1998, p 471
5. Christian J. W., "The Theory of Transformation in Metals and Alloys", Part 1, Second Edition, Pergamon Press, Oxford, 1975
6. de Fontaine D., Solid State Physics, **34** (1979) 73
7. Frank F.C., Kasper J.S., Acta Cryst. **11** (1958) 184
8. Frank F.C., Kasper J.S., Acta Cryst. **12** (1959) 483
9. Gähler F., Proc. 5th Int. Conf. Quasicrystals, Avignon, 22–26 May 1995, Eds. Ch. Janot, R. Mosseri, World Scientific, Singapore (1995) p. 235
10. Gödecke T., Lück R., Z. Metallkd. **86** (1995) 109
11. Gödecke T., Lück R., Beeli C., as Ref. 9, p. 644
12. Gratias D., Calvarac Y., Devaud-Rzepski J., Faudot F., Harmelin M., Quivy A., Bancel P.A., J. Non-Cryst. Sol. **153/154** (1993) 482
13. Grimm U., Joseph D. (2002), see Chapter 9 of this book
14. Grün A., Dissertation, Stuttgart, 1996
15. Hafner J., "From Hamiltonians to Phase Diagrams", Springer, Berlin, 1997
16. Harmelin M., Maârmar S., Fries S.G., Lukas H.L., Z. Metallkd. **85** (1994) 12
17. Holland-Moritz D. (2002), see Chapter 11 of this book
18. Hultgren R., Desai P.D., Hawkins D.T., Gleiser M., Kelley K.K., "Selected Values of the Thermodynic Properties of Binary Alloys", ASM, Metals Park, Ohio 44073, 1973
19. Inaba A., Ishida S., Matsuo T., Shibata K., Tsai A.P., Phil. Mag. Lett. **74** (1996) 381
20. Ishii Y., J. Non-Cryst. Sol. **153/154** (1993) 645
21. Ishimasa T., as Ref. 9, p. 648
22. Janot C., J. Phys.: Condens. Matter **9** (1997) 1493
23. Janot C., Dubois J.-M. (2002), see Chapter 8 of this book
24. Jiang Q., Lück R., Predel B., Z. Metallkd. **81** (1990) 214
25. Jiang Q., Lück R., Predel B., Z. Metallkd. **81** (1990) 94
26. Joseph, D., Elser V., preprint (1997)
27. Katz A., Duneau M., J. Physique **47** (1986) 181
28. Kelton K.F., Viano A.M., Stroud R.M., Kim J.Y., Gibbons P.C., as Ref. 4, p. 261
29. Kelton K.F., Wu T.W., Appl. Phys. Lett. **46** (1985) 1059
30. Kissinger H.E., Anal. Chem., **29** (1957) 1702

31. Knoll S., unpublished results (1994)
32. Knoll S., Lück R., Mater. Sci. Eng. **A181/A182** (1994) 749
33. Köster U., Schumacher B., Mater. Science Forum **22-24** (1987) 505
34. Krumeich F., Conrad M., Nissen H.-U., Harbrecht B., Phil. Mag. Letts. **78** (1998) 357
35. Laves, F., "Factors Governing Crystal Structure" in J.H. Westbrook (ed.) Intermetallic Compounds (1967) 129; Theory of Alloy Phases, ASM, Cleveland (1956) 124
36. Lu K., Hu T.B., Wang J.T., Scripta metall. **21** (1987) 793
37. Lück R., Mater. Science Forum **150–151** (1994) 145
38. Lück R., Arpshofen I., Predel B., Smith J.F., Thermochim. Acta **131** (1988) 171
39. Lück R., Bahle J., Mater. Sci. Eng. **A134** (1991) 1208
40. Lück R., Gerling U., Predel B., Z. Metallkd. **77** (1986) 442
41. Lück R., Haas H., Sommer F., Predel B., Scripta metall. **20** (1986) 667
42. Lück R., Kek S., J. Non-Cryst. Sol. **153/154** (1993) 329
43. Mossery R., Bailly F., Sire C., J. Non-Cryst. Sol. **153/154** (1993) 201
44. Phillips R., Widom M., J. Non-Cryst. Sol. **153/154** (1993) 416
45. Predel B., Landolt-Börnstein, New Series, Group IV, Volume 5, "Phase Equilibria, Crystallographic and Thermodynamic Data of Binary Alloys", Springer-Verlag, Berlin, 1991 etc
46. Raynor G.V., Prog. Metal Phys. **1** (1949) 1
47. Ritsch S., Ph.D. thesis, ETH Zürich, Zurich, 1996
48. Ritsch S., Beeli C., Nissen H.-U., as Ref. 4, p. 367
49. Saâdi N., Harmelin M., Faudot F., Legendre B., J. Non-Cryst. Sol. **153/154** (1993) 500
50. Saâdi N., Faudot F., Gratias D., Legendre B., as Ref. 9, p. 656
51. Scheffer M., Gödecke T., Lück R., as Ref. 4, p. 269
52. Scheffer M., Lück R., Proc. of Aperiodic'97, Eds. M. de Boissieu, J.-L. Verger-Gaugry, R. Currat World Scientific, Singapore, 1998, 57
53. Shechtman D., Blech I., Cahn J.W., Gratias D., Phys. Rev. Lett. **53** (1984) 1951
54. Stolz U.K., Arpshofen I., Sommer F., Predel B., J. Phase Equilibria **14** (1993) 473
55. Suck J.-B. (2002), see Chapter 23 of this book
56. Suck J.-B., J. Non-Cryst. Sol. **153-154** (1993) 573
57. Wosnitza J., Löhneysen H. v., Compans E., Proc. ILL/CODEST Workshop Quasicrystalline Materials, Grenoble, 21–25 March 1988, Eds. Ch. Janot, J.M. Dubois, World Scientific, Singapore (1988) 381
58. Wang H., Dissertation Stuttgart, 1992
59. Wang H., Lück R., J. Non-Cryst. Sol. **205–207** (1996) 417
60. Wang K., Scheidt C., Garoche P., Calvarac Y., J. Non-cryst. Alloys **153/154** (1993) 357

Part VII

Magnetic Properties

Part VIII

Surfaces and Applications

25 Magnetic Properties of Quasicrystals and Approximants

Guy Trambly de Laissardière* and Didier Mayou

Summary. In this chapter we discuss the localized magnetism of quasicrystals and approximants. We focus in particular on the conditions for occurrence of local moments carried by the transition atoms. The systems which are the most interesting in this context are those containing Mn. We recall first the basic model concerning TM impurities in free-electron metals like Al, Cu, Ag, ... Yet there is good evidence that this classical model (virtual bound state of Friedel and Anderson) is not applicable to quasicrystals and approximants and more generally to many Hume–Rothery-type alloys that are stabilized by a pronounced pseudo-gap close to the Fermi energy. We then develop two types of model that allow an analysis of the occurrence of local magnetic moments. The pseudo-gap at the Fermi energy is shown to have a deep effect on the conditions for the appearance of moments and the theoretical analyzes are consistent both with *ab initio* calculations and with experimental results.

25.1 Introduction

The magnetic properties of quasicrystals have been studied since the discovery of the icosahedral AlMn phase. A question which has attracted much attention, which also is the main focus of this chapter, is the existence of local moments carried by the transition elements (Mn in AlPdMn, AlMn; Fe in AlCuFe, ...), their concentration and position in the quasiperiodic structure.

The existence and characterization of local magnetic moments in quasicrystals has been investigated in much detail in systems like AlMn AlPdMn or AlCuFe. The local magnetic moments are due to the d states of the transition metal (TM) atoms. In the following a TM atom on which there is a local magnetic moment m ($m \neq 0$) is called *"magnetic"*, otherwise it is called *"non-magnetic"*.

It is now well established that the bulk of the thermodynamically stable Al-Cu-Fe systems do not contain local moments. Yet it may be that some samples contain magnetic moments but in that case they probably result from the elaboration technique and are located for example in grain boundaries [29]. The systems that have the most interesting properties are the systems containing manganese atoms. In crystals (Al_6Mn, $Al_{12}Mn$, ...) and

* Present address: Laboratoire de Physique Théorique et Modélisation (LPTM), Universtié de Cergy-Pontoise, 95308 Cergy-Pontoise Cedex.

J.-B. Suck et al. (eds.), *Quasicrystals*
© Springer-Verlag Berlin Heidelberg 2002

approximants (α-AlMnSi, ...) Mn atoms are non-magnetic (see [40] and references therein). In quasicrystals icosahedral (i-) AlMn, decagonal (d-) AlMn, i-AlPdMn and most of their approximants [29] very few Mn atoms are magnetic. Their behavior is rather similar although some systems are stable and have a high structural quality (AlPdMn) and some are metastable and are more similar to glasses (AlMn ...). However in liquid AlPdMn and AlMn local moments are found in a much higher concentration [22,34]. This clearly shows the effect of the atomic order on the occurrence of magnetic moments. Thus the following sections are concerned with this question: why are most of the Mn atoms non-magnetic in AlMn crystals and quasicrystals whereas they are magnetic in liquids?

Many other aspects of magnetism that cannot be discussed here are surprising in these systems. For example the RKKY interaction is unexpectedly strong in AlPdMn systems [29] for which a theoretical explanation based on the role of the local environment has been proposed [31]. The RKKY interaction can induce a spin order at sufficiently low temperature. In some systems one observes a spin glass state at low temperature [29].

The magnetic moments can also affect transport properties. For example the so-called anomalous Hall effect coefficient has a huge value in several quasicrystalline phases [29]. The conductivity can also be sensitive to local magnetic moments through quantum interferences effects [33].

The magnetic properties of nuclei (NMR) can also be used to probe the local atomic environment of some elements [21] or the band structure close to the Fermi energy. Very recently this led several groups to conclude that there is a narrow pseudo-gap at the Fermi energy, in agreement with observation based on tunneling microscopy [37]. Nevertheless, this fine structure, that is superposed to the Hume–Rothery pseudo-gap discussed in the following, has no significant effect on the magnetic moment of electrons.

Finally the diamagnetism observed in some systems seems characteristic of samples with the best structural quality [6]. This surprising behavior has been discussed recently [9]. It seems that the particular electronic structure of quasicrystals increases the Landau diamagnetism in respect of the Pauli paramagnetism. But the disorder destroys the particular electronic structure of quasicrystals, therefore as the disorder increases as the diamagnetism decreases.

The following parts of this section are concerned with the analysis of the conditions of the occurrence of localized magnetic moments in AlTM crystals, quasicrystals and liquids. In these alloys there are delocalized sp states. Moreover the strong potential of the TM atoms creates d resonances of the wave function. In Sect. 25.2, the notion of *"virtual bound state"*, which describes the physics of one d impurity (TM impurity) in a metal host, is presented. But the virtual bound state fails to explain the fact that Mn atoms are not magnetic in AlMn crystals and quasicrystals. In Sect. 25.3, we propose an extension of the Anderson model Hamiltonian to analyze the

electronic structure and the magnetism of one d impurity in these AlMn alloys. In Sect. 25.4, we focus on the effect of the long-range Mn–Mn effective interaction (up to 10–12Å), which seems to be determinant for stability and magnetism.

Model results are compared with linear muffin-tin orbital (LMTO) simulations in the atomic sphere approximation (ASA) [1]. This *ab initio* method performs self-consistent calculations of the electronic structure for crystals.

25.2 Localized Moments on Transition Metal Impurity

25.2.1 Anderson Hamiltonian for d States in Aluminium

We consider a Friedel–Anderson model [12,2] including sp states which are represented by linear combinations of plane waves $\mathbf{k}$, and d atomic orbitals of the TM atoms. The Hamiltonian is written [2],

$$\mathcal{H} = \sum_{id} E_{id}|id\rangle\langle id| + \sum_{n\mathbf{k}} E_n(\mathbf{k})|n(\mathbf{k})\rangle\langle n(\mathbf{k})| + \sum_{id,n\mathbf{k}} V_{id,n\mathbf{k}}|id\rangle\langle n(\mathbf{k})| + \text{h.c.} + UN_{d\downarrow}N_{d\uparrow} \tag{25.1}$$

when i is a TM site index, E_{id} and E_n are the on-site d energy and the energy of the n^{th} sp band, respectively. The third term represents the sp-d interaction with is essential in this context. This Hamiltonian does not contain hopping between the d orbitals of two different atoms. This is justified if there are very few nearest neighbor TM atoms as it is the case in many alloys discussed here. In many AlTM alloys, the local environment of the TM atoms is close to an icosahedral environment. Therefore in the following, we consider five degenerate d orbitals per TM atom since the icosahedral environment leads to large degeneracy or approximate degeneracy. The last term in (25.1) is the Coulomb interaction between d electrons. The interaction between sp electrons is neglected. The partial densities of states (partial DOS) are given by the equations:

$$n_{\mathrm{d}}(\epsilon) = \sum_{\alpha,d} |\langle id|\alpha\rangle|^2 \delta(\epsilon - E(\alpha)) \ , \ n_{\mathrm{sp}}(\epsilon) = \sum_{\alpha,\mathbf{k}} |\langle \mathbf{k}|\alpha\rangle|^2 \delta(\epsilon - E(\alpha)) \tag{25.2}$$

where $|\alpha\rangle$ are the eigenstates of the Hamiltonian and $E(\alpha)$ is the energy of $|\alpha\rangle$.

25.2.2 The Virtual Bound State Model

We now consider only one TM atom in a matrix of sp elements (Al, Ga, Cu, ...). Following a classical assumption the sp electrons are treated as free electrons [12,2]. In the model Hamiltonian (25.1), $|n(\mathbf{k})\rangle$ are plane waves.

25.2.2.1 Non-Magnetic Case. We assume first that there is no magnetic moment ($m = 0$) on the TM atoms. The partial d DOS is a Lorentzian [2] as represented in Fig. 25.1. The half width of the Lorentzian is Γ,

$$2\Gamma = \pi |\langle d|\mathbf{k}\rangle|^2 n^0_{\rm sp}(E_{\rm F}), \tag{25.3}$$

where $n^0_{\rm sp}$ is the sp DOS without sp-d interaction.

It is centered at the energy $E_{\rm d}$ obtained, in the Hartree approximation, by the self-consistent relation:

$$E_{{\rm d},\sigma} = E^0_{\rm d} + U(N_{{\rm d},-\sigma} - N^0_{{\rm d},-\sigma})\,. \tag{25.4}$$

$N_{{\rm d}\sigma}$, and $N^0_{{\rm d}\sigma}$ are the number of d electrons for a TM atom with spin σ in the alloys, and for an isolated TM atom, respectively. In the non-magnetic case, $N_{{\rm d},\sigma} = N_{{\rm d},-\sigma}$; $N^0_{{\rm d},\sigma} = N^0_{{\rm d},-\sigma}$ and $E_{{\rm d}\uparrow} = E_{{\rm d},\downarrow}$. The total sp DOS is not modified by the sp-d hybridization (compensation theorem).

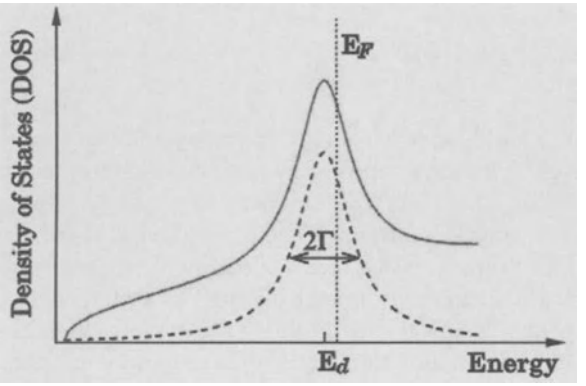

Fig. 25.1. Density of states (DOS) of the virtual bound state without magnetic moment ($m = 0$). The partial sp DOS $n_{\rm sp}(\epsilon)$ is parabolic and the partial d DOS $n_{\rm d}(\epsilon)$ (dashed line) is a Lorentzian

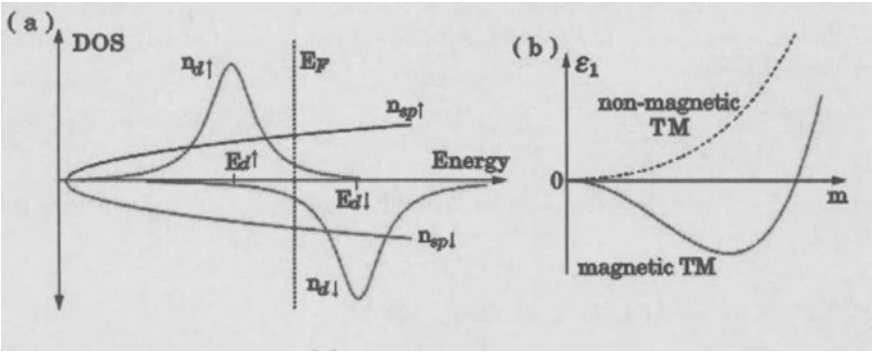

Fig. 25.2. Density of states (**a**) of the virtual bound state with magnetic moment ($m \neq 0$). Schematic representation (**b**) of the energy $\mathcal{E}_1(m)$ for one TM impurity in a metal host

25.2.2.2 Magnetic Case. The origin of the local magnetic moment on the TM atom is a competition between the Coulomb energy and the kinetic energy of the d electrons. In the Hartree–Fock approximation, the Coulomb energy for one d orbital is given by the relation

$$\mathcal{E}_{\text{int}} = UN_{\text{d}\downarrow}N_{\text{d}\uparrow} = \frac{U}{4}(N^2 - m^2) \,, \tag{25.5}$$

where N, $N = N_{\text{d}\uparrow} + N_{\text{d}\downarrow}$, is the total number of d electrons. m, $m = N_{\text{d}\uparrow} - N_{\text{d}\downarrow}$, is the local magnetic moment on the impurity. The Coulomb energy decreases when m increases, so it favors the occurrence of a magnetic moment ($m \neq 0$). The kinetic energy (or band energy) of the d electrons is written:

$$\Delta_\sigma \sim \int (\epsilon - E_{\text{d}}^0) n_{\text{d},\sigma}(\epsilon) \text{d}\epsilon \,. \tag{25.6}$$

This energy is negative, it decreases when the width 2Γ of the d resonance increases and it increases when m increases. Roughly speaking Δ_σ is proportional to Γ. The total electronic energy of the d impurity is $\mathcal{E}_{\text{int}} + \Delta_\sigma$. It is useful to define the energy $\mathcal{E}_1$,

$$\mathcal{E}_1(m) = (\mathcal{E}_{\text{int}} + \Delta_\sigma)(m) - (\mathcal{E}_{\text{int}} + \Delta_\sigma)(m = 0) \,, \tag{25.7}$$

which represents the energy gain between one non-magnetic impurity and one magnetic impurity. $\mathcal{E}_1$(m) is represented schematically in Fig. 25.2.

Assuming a rigid band model for the partial d DOS, the criterion of the appearance of a localized moment is easy to calculate by writing the self-consistent Hartree–Fock equation (25.4) for spin up and spin down. It follows [2] that a localized moment exists if

$$Un_{\text{d}}(E_{\text{F}}) \geq 1 \,, \tag{25.8}$$

where n_{d} is the d DOS per spin in the non-magnetic case ($m = 0$). In the case of the virtual bound state, n_{d} is a Lorentzian and the criterion (25.8) is equivalent to:

$$\frac{U}{\Gamma} \geq \frac{\pi}{\sin^2 \pi N_{\text{d}}} \,. \tag{25.9}$$

In this last expression, the competition between the Coulomb energy (U) and the kinetic energy ($\Delta_\sigma \sim \Gamma$) is obvious.

For TM atoms in a metallic host we have to consider five degenerate d orbitals per TM impurity. In that case, the exchange integral J between two electrons, localized on two different orbitals of the same TM impurity, is taken into account by changing U to $(U - 4J)$ in criteria (25.8) and (25.9) [19].

25.2.2.3 Application of the Virtual Bound State Model to Dilute Alloys. The virtual bound state model has been successfully applied to understand the existence of localized magnetic moments on TM impurities

in the non-magnetic hosts Au, Cu and Ag (examples: **Cu**Cr, **Cu**Mn, **Cu**Fe, **Ag**Cr, **Ag**Mn) [3,19]. Cr, Fe and Co are non-magnetic in Al [3]. But in spite of extensive experimental studies [11,8,18] the case of Mn impurities in Al host is still an open question. It seems that in dilute **Al**Mn, Mn is magnetic and its moment is about $3.2\,\mu_B$. Moreover this moment appears to be screened by sp electrons up to very high temperatures, suggesting surprisingly high values of the Kondo temperature, $T_K \simeq 600\,K$ [8]. From the theoretical side, there are contradicting results [10,24,26,38]. In [10] the Mn is magnetic in Al, whereas all atoms are found to be non-magnetic in [24]. We performed LMTO calculations of Mn impurities substituting Al atoms in the f.c.c. Al lattice. For the concentration $Al_{31}Mn$, Mn is magnetic with a moment $m \simeq 2\,\mu_B$ and the variation of the energy between magnetic and non-magnetic Mn is $\mathcal{E}_1(m=2) \simeq -0.05\,eV$ per Mn.

25.2.3 Effect of the Expansion and the Local Symmetry on the Localized Moment

The thermal expansion can modify the spin of the TM impurities. Indeed when the atomic density decreases, the overlap between orbitals of neighboring atoms decreases and the kinetic energy of d states decreases too. It follows that the d states of the impurity are more and more localized and the occurrence of a magnetic moment is favored. When the moments exist, it increases with the expansion. This effect is illustrated in Fig. 25.3 for a $Al_{12}Mn$ crystal and a hypothetical $Al_{10}Mn$ crystal.

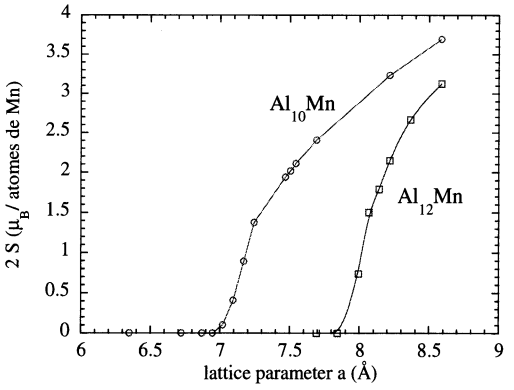

Fig. 25.3. Local magnetic moment m ($m = 2S$) versus the cell parameter a, for $Al_{12}Mn$ and $Al_{10}Mn$ crystals calculated by the LMTO method. $Al_{12}Mn$ (Im3) is composed of Al icosahedra centered by one Mn atom. The Mn atoms are located on the vertex of a b.c.c. lattice [2]. The hypothetical $Al_{10}Mn$ crystal is constructed from $Al_{12}Mn$ with two Al vacancies per Al icosahedron. The vacancies are sited in opposite positions and they are not first neighbors to each other

The local symmetry around a TM atom may also have some effects on the criterion of the appearance of a localized moment and on its value [26]. Particular local symmetries can reinforce the DOS locally around the TM atom. Moreover the number of atoms around the TM atom may have an important effect too. Nevertheless, it is rather difficult to deduce the effect of the local symmetry. It will depend on the TM nature and the nature of the host. As explained in the previous section, the case of **Al**Mn alloys is the most ambiguous. An Mn impurity in an Al host seems to be at the limit between the magnetic case and the non-magnetic case. In that case, the local symmetry around the Mn should have a strong effect on the occurrence of a magnetic moment. But for alloys in finite concentration (crystal and quasicrystals) the occurrence of magnetic moments is controlled by effects that take into account the middle-range and the long-range order of the atomic structure. This effect is analyzed in Sects. 25.3 and 25.4.

25.2.4 Is the Virtual Bound State Relevant for Crystalline and Quasicrystalline AlTM?

For crystalline and quasicrystalline AlTM with TM concentrations 7–20% of atoms, the virtual bound state cannot be applied. Indeed, the sp electrons for the host are not free-electron-like but they are nearly free-electron-like. The main characteristic of the electronic structure is a deep valley in the DOS at the Fermi level, called the *"pseudo-gap"*. This has been shown from *ab initio* calculations for crystals [40] and quasicrystals [15–17,23,39]. In Fig. 25.4, the total DOS of the crystal Al_6Mn and of the approximant α-AlMnSi to the i-quasicrystal are presented. The pseudo-gap is clearly seen in the two cases, but, as expected [36], it is deeper for the approximant. Specific heat measurements also give a weak total DOS at the Fermi level, of the order $\sim 1/3$ of the free-electron values for i-AlCuFe, i-AlPdMn and α-AlMnSi, and $\sim 1/10$ for i-AlCuRu and i-AlPdRe [6]. From photoemission spectroscopy the pseudo-gap is observed in the partial Al p DOS for crystals, approximants and quasicrystals [5].

The presence of a pseudo-gap is expected for alloys of Hume–Rothery type [25]. The band energy is minimized by an interaction between the Bragg planes of a particular Brillouin zone, called the "*pseudo-Brillouin zone*", and the electrons at the Fermi level (for details see [3,32]). This mechanism has been successfully applied to several crystals (Al_6Mn, Al_3Ni, Al_9Co_2, Al_5Co_2, ...) [27] and quasicrystals (i-AlLiCu, i-AlCuFe, ...) [4,5,13,14,16,36].

The *ab initio* calculations also show that the partial d DOS of the transition metal deviates strongly from the Lorentzian shape of the virtual bound states Fig. 25.4 because of the presence of the pseudo-gap in the sp band and the strong sp-d hybridization [15,23,38,40]. Therefore one cannot use the virtual bound state to describe the DOS of TM atom in crystals, quasicrystals and approximant AlMn phases.

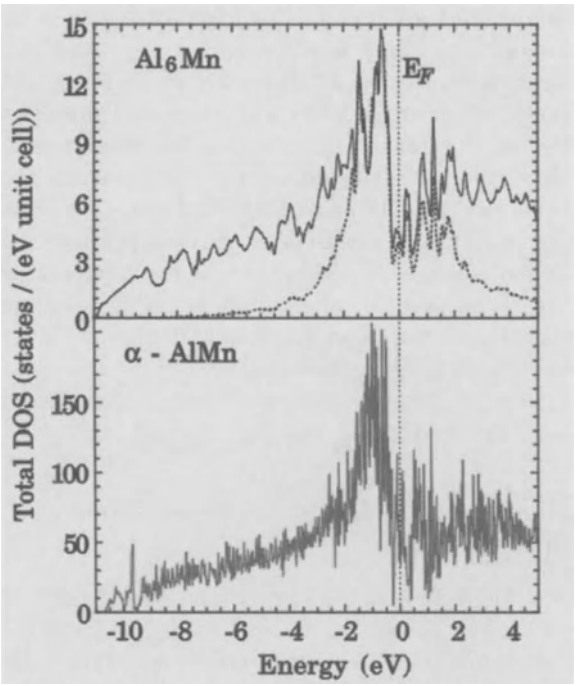

Fig. 25.4. Total DOS for a Al_6Mn crystal [40] (the dashed line is the partial d DOS of Mn) and $\alpha-$AlMnSi approximant [15], calculated by the LMTO method

25.3 One Transition Atom in a Realistic Effective Metallic Medium

25.3.1 Description of the Model

We now consider the Hamiltonian (25.1) to treat one TM impurity embedded in a realistic effective medium [38]. The difference from the classical virtual bound state is that we take into account the diffraction of the conduction electrons (sp) by the Bragg planes (potential $V_B(\mathbf{K})$). As shown in [38], the partial d and sp DOS are entirely determined by the quantity, $g(\epsilon) = n^0_{sp}(\epsilon)\ \langle V^2_{sp-d}(\epsilon)\rangle$, which is the effective coupling strength between the d orbitals and the conduction sp states with the energy ϵ. $n^0_{sp}(\epsilon)$ is the DOS of the conduction states without the sp-d coupling, and $\langle V^2_{sp-d}\rangle(\epsilon)$ is the mean square of the matrix element of the sp-d coupling between the d orbital and the conduction sp states with the energy ϵ.

In the case of the virtual bound state, $g(\epsilon)$ is nearly constant, and it is related to the half width Γ of the d resonance, $g(\epsilon)= \Gamma/\pi$. Thus $g(\epsilon)$ is independent of the position $\mathbf{r}_d$ of the TM atom in the alloys.

But if diffraction by Bragg planes takes place ($V_B \neq 0$), $g(\epsilon)$ varies strongly on an energy scale of V_B. We consider the Bragg planes of the pseudo-Brillouin

zone which create the deep pseudo-gap at E_F [33].[1] A realistic value for V_B is 0.4 eV [36]. The pseudo-Brillouin zone of i-AlCuFe leads to an sp DOS at E_F equal to one-half of the free-electron value [38]. The diffraction by Bragg planes splits the conduction sp states into bonding and antibonding states. Consequently, there is no translational invariance of the conduction states; whereas in the case of virtual bound states ($V_B = 0$) the conduction states are free-electron states with a constant amplitude in space. Therefore in the context of diffraction by Bragg planes, the effect of the hybridization depends on the positions $\mathbf{r}_d$ of the d orbital. Schematically, one finds that there are two extreme cases depending on $\mathbf{r}_d$ via the parameter $\langle\cos(\mathbf{K}\cdot\mathbf{r}_d+\Phi)\rangle$. Here $\mathbf{K}$ are the wave vectors of the reciprocal lattice that define the Bragg plane from which the pseudo-Brillouin zone is constructed, and Φ is a phase depending on the lattice. When $\langle\cos(\mathbf{K}\cdot\mathbf{r}_d + \Phi)\rangle = 1$, the amplitude of the bonding sp states is minimized at $\mathbf{r} = \mathbf{r}_d$, and the amplitude of the antibonding sp states is maximized at $\mathbf{r} = \mathbf{r}_d$. Thus the d orbital is more coupled with the antibonding sp states. On the other hand, when $\langle\cos(\mathbf{K}\cdot\mathbf{r}_d + \Phi)\rangle = -1$, the d orbital is more coupled with the bonding sp states.

The electronic structure, the energy and the magnetic behavior, calculated within this model, are now presented. To analyze the effect of the diffraction from Bragg planes, these quantities are calculated with ($V_B \neq 0$) and without ($V_B = 0$) diffraction from Bragg planes.

25.3.2 Electronic Structure of Transition Atoms in Hume–Rothery Alloys

The partial d DOS calculated for one Ti impurity and one Fe impurity are shown in Fig. 25.5. The d DOS calculated with diffraction by Bragg planes deviates from the Lorentzian shape of the virtual bound state. Moreover, it depends on the position $\mathbf{r}_d$ of the TM atoms in the unit cell. Following the argument of Jones [25] for the stability of the Hume–Rothery alloys, one expects that the more stable system is obtained when E_F is located at a local minimum of the DOS. In the present calculation, the d DOS $n_d(E_F)$ varies with $\mathbf{r}_d$, therefore the stability of the impurities depends on its position. Schematically we can distinguish two cases: the d orbitals of V and Ti impurity are preferentially coupled with sp bonding states ($\langle\cos(\mathbf{K}\cdot\mathbf{r}_d + \Phi)\rangle \simeq -1$); and the d orbitals of Cr, Mn, Fe and Co are preferentially coupled with antibonding sp states ($\langle\cos(\mathbf{K}\cdot\mathbf{r}_d + \Phi)\rangle \simeq 1$). This analysis is confirmed by the comparison between model DOS and LMTO DOS for Ti and Fe in Al_3Ti and Al_7Cu_2Fe crystals (Fig. 25.5).

Another difference with the classical virtual bound state is the strong variation Δn_{sp} of the partial sp DOS between the DOS n_{sp} with sp-d hybridization and n^0_{sp} without the sp-d hybridization: $n_{sp}(\epsilon) = n^0_{sp}(\epsilon) + \Delta n_{sp}(\epsilon)$. In the case of the virtual bound state ($V_B = 0$): $\Delta n_{sp} = 0$ (Sect. 25.2).

[1] For alloys with a finite concentration of TM atoms, the potential V_B includes qualitatively the effect of other TM atoms [40,41].

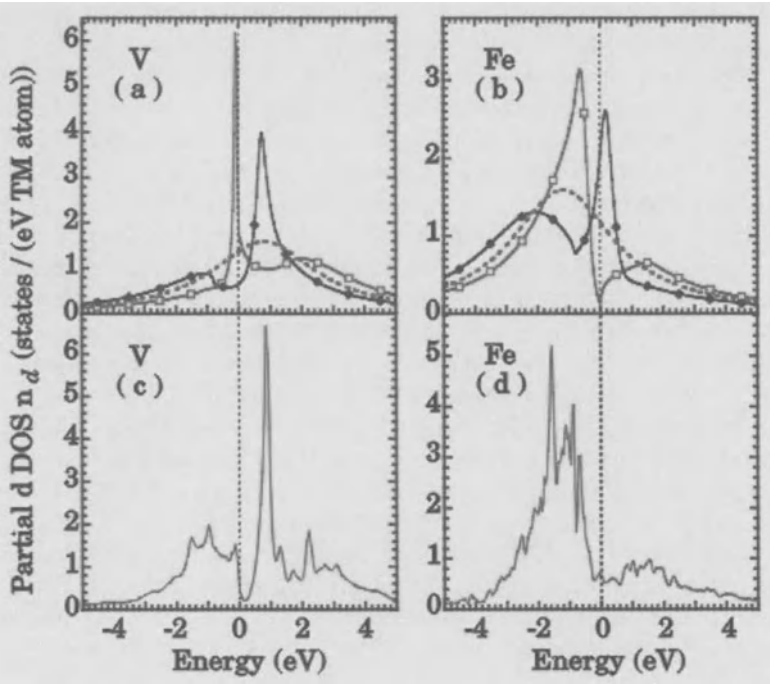

Fig. 25.5. Partial d DOS n_{d} for one V impurity and one Fe impurity. Upper curves, model results for (**a**) V and (**b**) Fe: lines with black points for d orbital coupled with bonding sp states ($\langle\cos(\mathbf{K}\cdot\mathbf{r}_{\mathrm{d}}+\Phi)\rangle = -1$ and $V_{\mathrm{B}} = 0.4\,\mathrm{eV}$); lines with squares for d orbital coupled with antibonding sp states ($\langle\cos(\mathbf{K}\cdot\mathbf{r}_{\mathrm{d}}+\Phi)\rangle = 1$ and $V_{\mathrm{B}} = 0.4\,\mathrm{eV}$); dashed lines for the virtual bound state ($V_{\mathrm{B}} = 0$). LMTO d DOS of (**c**) V and (**d**) Fe in Al_3V and Al_7Cu_2Fe crystals, respectively. $E_{\mathrm{F}} = 0$. From [38]

25.3.3 Energy of One d Impurity

Considering one d orbital in an effective metallic medium (with or without diffraction by Bragg planes). The total band energy $\mathcal{E}_{\mathrm{B}}$ is decomposed into two terms:

$$\mathcal{E}_{\mathrm{B}} = \mathcal{E}_{\mathrm{impurity}} + \mathcal{E}_{\mathrm{medium\ without\ impurity}},\ \mathcal{E}_{\mathrm{impurity}} = \int^{\mathrm{E_F}} \epsilon \Delta n(\epsilon) \mathrm{d}\epsilon. \quad (25.10)$$

where $\mathcal{E}_{\mathrm{impurity}}$ is the variation of band energy due to the d orbital. Δn, $\Delta n = n_{\mathrm{d}} + \Delta n_{\mathrm{sp}}$, is the variation of the total DOS due to the d orbital. $\mathcal{E}_{\mathrm{impurity}}$ is a function of Γ, E_{d} ($E_{\mathrm{d}} = (E_{\mathrm{d}\uparrow} + E_{\mathrm{d}\downarrow})/2$), $\mathbf{r}_{\mathrm{d}}$, E_{F}, m and V_{B}. E_{F} and V_{B} are fixed by the effective medium. We use $E_{\mathrm{F}} = 11$ eV, which is close to the value calculated for AlTM alloys [15,23,40]. Γ, E_{d}, are fixed by the nature of the TM impurity. When we neglect the effect of diffraction by Bragg planes ($V_{\mathrm{B}} = 0$), $\mathcal{E}_{\mathrm{impurity}}$ is the same as for the virtual bound state. In this case, $\mathcal{E}_{\mathrm{impurity}}$ is independent of $\mathbf{r}_{\mathrm{d}}$ as the electronic structure of the virtual bound

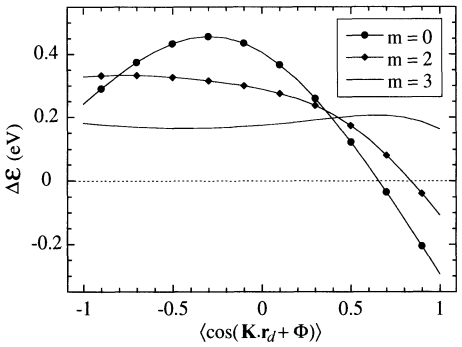

Fig. 25.6. Variation $\Delta\mathcal{E}$ of the energy due to one Mn d impurity in a metal host. Full line, with diffraction by Bragg planes $V_B = 0.4$ eV; dashed line, without diffraction by Bragg planes $V_B = 0$. ($2\Gamma = 2.7$ eV, $E_F = 11$ eV)

state does not depend on $\mathbf{r}_d$. Considering now the diffraction by Bragg planes, we calculate the quantity:

$$\Delta\mathcal{E}(\mathbf{r}_d, m) = \mathcal{E}_{\text{impurity}}(V_B, \mathbf{r}_d, m) - \mathcal{E}_{\text{impurity}}(V_B = 0, m)$$
$$= \int^{E_F} (\epsilon - E_F)(\Delta n(V_B, \mathbf{r}_d, m, \epsilon) - \Delta n(V_B = 0, m, \epsilon))d\epsilon \,. \tag{25.11}$$

Following a classical approximation, the on-site energy E_d is assumed to be independent of $\mathbf{r}_d$ [38]. $\Delta\mathcal{E}(\mathbf{r}_d)$ of one Mn d impurity is drawn in Fig. 25.6.

The total electronic energy of the impurity is $\mathcal{E}(m) = \mathcal{E}_1(m) + \Delta\mathcal{E}(\mathbf{r}_d, m)$, where $\mathcal{E}_1(m)$, given by (25.7), is the gain in energy between a non-magnetic impurity and a magnetic impurity in the case of the virtual bound state ($V_B = 0$).

25.3.3.1 Non-magnetic Case ($m = 0$). In the realistic case (i.e. with diffraction by Bragg planes, $V_B \neq 0$), the energy $\Delta\mathcal{E}$ of the d Mn impurity varies with the Mn position on an energy scale of $\sim$ 0.8 eV. This variation is strong, and one can conclude that the positions of the impurity that lead to high $\Delta\epsilon$ are not stable. Thus the values of $\langle\cos(\mathbf{K}\cdot\mathbf{r}_d + \Phi)\rangle$ leading to the most stable position is $\langle\cos(\mathbf{K}\cdot\mathbf{r}_d + \Phi)\rangle = -1$ for Ti and V impurities, and $\langle\cos(\mathbf{K}\cdot\mathbf{r}_d + \Phi)\rangle = 1$ for Mn, Fe, Co and Ni impurities. For a Cr impurity it seems that these two extreme values of $\langle\cos(\mathbf{K}\cdot\mathbf{r}_d + \Phi)\rangle$ are equivalent. This calculation of the energy confirms the qualitative argument given in Sect. 25.3.2 for the effect of $\mathbf{r}_d$ on the local stability of the TM atom.

25.3.3.2 Magnetic Case ($m \neq 0$). We now consider one magnetic Mn impurity in a non-magnetic metallic host. Its energy is $\mathcal{E}$, $\mathcal{E}(m) = \mathcal{E}_1(m) + \Delta\mathcal{E}(\mathbf{r}_d, m)$. The band energy $\Delta\mathcal{E}$ is drawn in Fig. 25.6 for $m = 2\,\mu_B$ and $m = 3\,\mu_B$. For a magnetic Mn impurity in Al, we find that $|\mathcal{E}_1|$ is about 0.05 eV per Mn atom (Sect. 25.2.2.3). Therefore it is possible to discuss the magnetic state of the impurity as follows. For the positions $\mathbf{r}_d$ of the impurity

such as $\langle\cos(\mathbf{K}\cdot\mathbf{r}_\mathrm{d}+\Phi)\rangle > 0.5$, the Mn impurity is non-magnetic. Indeed, if $\langle\cos(\mathbf{K}\cdot\mathbf{r}_\mathrm{d}+\Phi)\rangle > 0.5$, $\mathcal{E}$ is minimized in the non-magnetic case. For the positions $\mathbf{r}_\mathrm{d}$ such as $\langle\cos(\mathbf{K}\cdot\mathbf{r}_\mathrm{d}+\Phi)\rangle < 0.3$, the Mn impurity is magnetic. These positions are unstable with respected to the cases $\langle\cos(\mathbf{K}\cdot\mathbf{r}_\mathrm{d}+\Phi)\rangle > 0.5$. In crystals (quasicrystals) they should correspond to defects or particular sites of the crystalline (quasicrystallines) structure.

To conclude, our analysis of the extended Anderson Hamiltonian (25.1) shows that the magnetic states of the Mn atom in a metallic medium vary with its position in the alloy. The most stable positions lead to a non-magnetic impurity whereas the unstable positions lead to a magnetic impurity.

25.3.4 Criterion for the Appearance of a Localized Moment

In the previous section the magnetic state of a Mn impurity was discussed by analyzing its energy. Another approach is to determine a new criterion of the appearance of the magnetic moment, by considering the stability of the self-consistent Hartree–Fock equation as in Sect. 25.2.2.2. This approach is in the spirit of the original paper of Anderson [2] for a TM impurity in free electrons. The difference compared with this original approach is that we include the diffraction of sp electrons by Bragg planes. In the Hartree–Fock approximation, the on–site energy of the d states with spin up and the one–site energy of the d states with spin down are given by (25.4). It is easy to show that this system has a stable non–magnetic solution (i.e. $E_{\mathrm{d}\sigma} = E_{\mathrm{d},-\sigma}$) if [38]:

$$-U\,\frac{\partial N_\mathrm{d}}{\partial E_\mathrm{d}} > 1\,. \tag{25.12}$$

This criterion differs from the criterion of the virtual bound state (without diffraction by Bragg planes) because the rigid band approximation is no longer valid if diffraction by Bragg planes is important. But without diffraction from Bragg planes ($V_\mathrm{B} = 0$), (25.12) is equivalent to the criterion in the case of the virtual bound state (25.8). The analysis of the criterion (25.12) leads to the same conclusion as the calculation of the energy presented in the previous section.

25.4 Interaction Between Transition Metal Atoms

25.4.1 Electron Diffraction by the d Orbitals Lattice

In the previous sections, we have shown that the electronic structure, the local stability and the magnetism of TM atom in Hume–Rothery alloys and quasicrystals depends strongly on the presence of a pseudo-gap in the DOS at E_F. It is now interesting to analyze the exact origin of this pseudo-gap.

It is commonly admitted that the pseudo-gap in the DOS of Hume–Rothery alloys is due to the diffraction of conduction electrons by the Bragg

planes corresponding to the intense peaks in the diffraction pattern [13,25,36]. If the potential of the ions is weak (Al, Ga, or Cu atoms, ...) the sp electrons are diffracted by a pseudo-potential V which is almost energy independent. But in the Hume–Rothery alloys containing TM atoms, the potential of the TM atoms is strong and creates d resonances of the wave function. This TM potential varies rapidly with energy and it is large for energies ϵ such that $\mathrm{E_d} - \Gamma \leq \epsilon \leq \mathrm{E_d} + \Gamma$. In this energy range, the TM atoms can be considered, in a first approximation, as hard spheres with a radius of the order of the size of the d orbitals (i.e. about 0.4 Å) [42]. Thus the coherent scattering of sp electrons by the network of the TM atoms via sp-d hybridization should be strong in these alloys.

Schematically, the sp conduction states are like free states $|\mathbf{k}\rangle$ diffracted by an effective pseudo-potential V_{eff}. V_{eff} is due to the diffraction by the d orbital lattice via the sp-d hybridization. In previous work [40,41], we have shown that V_{eff} can be decomposed in two parts:

$$V_{\mathrm{eff}}(\mathbf{r}) = \sum_{\mathbf{K}} \left(V_{\mathrm{B}}(\mathbf{K}) + \frac{|V_{\mathrm{d}}|^2}{\epsilon - E_{\mathrm{d}}} \sum_i \mathrm{e}^{-\mathrm{i}\mathbf{K}\cdot\mathbf{r}_{\mathrm{di}}} \right) \mathrm{e}^{\mathrm{i}\mathbf{K}\cdot\mathbf{r}} , \tag{25.13}$$

where i is a TM site index. V_{d} is the matrix element that couples the states $|\mathbf{k}\rangle$ and $|\mathbf{k}-\mathbf{K}\rangle$ via the sp-d hybridization. As the states $|\mathbf{k}\rangle$ and $|\mathbf{k}-\mathbf{K}\rangle$ are plane waves, their amplitudes are constant in the space, and we neglect the dependence of V_{d} on $|\mathbf{k}\rangle$ and $|\mathbf{k}-\mathbf{K}\rangle$. The first term in (25.13) is the usual diffraction by Bragg planes for the nearly free electrons. The second term is the diffraction of the sp electrons by the network of d orbitals. This term is controlled by $\sum_i \mathrm{e}^{-\mathrm{i}\mathbf{K}\cdot\mathbf{r}_{\mathrm{di}}}$, which is a structure factor of the sublattice of TM atoms. If $\epsilon \simeq E_{\mathrm{d}}$, it is the most important term. For AlTM crystals and quasicrystals containing TM atoms from the middle of the d series (Cr, Mn and Fe), $E_{\mathrm{F}} \simeq E_{\mathrm{d}}$. Consequently, their pseudo-gap at E_{F} is mainly due to the diffraction of sp electrons by the sublattice of TM atoms. This analysis is confirmed by a series of LMTO calculations for AlTM crystals [38]. In the following we analyze the physics of the sublattice of TM atoms embedded in a metallic medium, typically an aluminium matrix.

25.4.2 Effective Potential Between Two Transition Atoms in Aluminium

A model pair potential for TM-TM in the aluminium host has been calculated by Zou and Carlsson [44] from an Anderson model Hamiltonian with two impurities, using a Green's function method. They show the existence of a characteristic preferred spacing of 4.7 Å between two Mn atoms in AlMn crystals and quasicrystals [44]. The effective Mn-Mn interaction is larger than the Al-Mn interaction and the Al-Al interaction, thus it should have a major effect on the electronic energy. Moreover, this interaction has a long-range nature. As expected [3] because of the sharp Fermi surface of Al, at a large

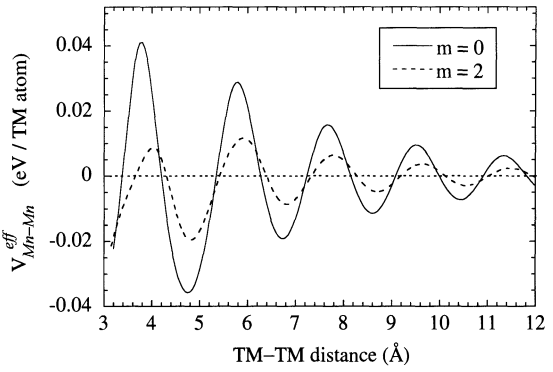

Fig. 25.7. Effective potential between two Mn atoms in an Al host: non-magnetic case ($m = 0$), and magnetic case ($m = 2\,\mu_B$) with ferromagnetic spin interaction

distance d this pair potential has the following form (Friedel oscillations of the charge density):

$$V^{\text{eff}}_{\text{Mn-Mn}}(d) \propto \frac{\cos(2k_F d - \delta)}{d^3}\,, \tag{25.14}$$

where k_F is the Fermi wave vector and the phase shift δ is determined by the nature of the TM atom. δ varies from 2π to 0 as the d band fills.

We also calculated the effective pair potential between two TM atoms as follows [42]. We focus on the *"structural energy"* $\mathcal{E}_S$ of an assembly of n_{at} TM atoms in an Al host. $\mathcal{E}_S$ is defined as the energy needed to build the system from isolated Mn atoms in the Al host:

$$\mathcal{E}_S = \int^{E_F} (\epsilon - E_F)(\Delta n(\epsilon) - n_{at}\Delta n_0(\epsilon))\mathrm{d}\epsilon\,. \tag{25.15}$$

Δn and Δn_0 are the variation of the DOS due to the assembly of the n_{at} Mn atoms, and the variation of the DOS due to one Mn atom (virtual bound state), respectively. Δn is calculated using the Lloyd formula from the transfer matrix $\mathbf{T}$ of the assembly of Mn atoms [42]. If $n_{at} = 2$, $\mathcal{E}_S$ is equal to $V^{eff}_{\text{Mn-Mn}}$.

Our calculation Fig. 25.7 confirms the result of Zou and Carlsson. The potential is strong up to ~ 12 Å for the TM of the middle of the d series, whereas it is small for Cu-Cu, Al-Al and Al-Mn [44,42]. Therefore the long-range TM-TM interaction for atoms of the middle of the series (Cr, Mn, Fe) has a strong effect on the total energy of the alloys. Indeed the minima of this potential correspond to the maxima of the Mn-Mn pair distribution function in many AlTM crystals, approximants and quasicrystals [28,43,44]. It also determines the magnetic behavior, as we discuss now.

In Fig. 25.7, $V^{\text{eff}}_{\text{Mn-Mn}}$ is drawn for Mn without a magnetic moment and Mn with a magnetic moment, $m = 2\,\mu_B$. The spin alignment is ferromagnetic. The amplitude of the Mn-Mn pair potential is smaller in the magnetic case. This is mainly due to the difference between the phases $\delta_\uparrow$ and $\delta_\downarrow$ in (25.14). Thus, the magnetic Mn atoms are less sensitive to the long-range order than are the non-magnetic Mn atoms.

25.4.3 Structural Energy of the Sublattice of Transition Atoms

The structural energy of the sublattice of Mn atoms is calculated as the sum of Mn-Mn pair interactions. Indeed, the Hume–Rothery stabilization is expected if the structural energy is given by the sum of pair interaction [14]. For quasicrystals and approximants, because of their particular electronic localization [33], this assumption has to be checked. This has been done as far as the local structure is concerned. In [42], we calculated the structural energy of one icosahedron of 12 Mn atoms that is actually found in several approximants and quasicrystals. It appears that the main contribution to the structural energy is the sum of pair interactions. Therefore in spite of the original electron localization observed in quasicrystals, their energy can be decomposed into a sum of pair interactions.

25.4.3.1 Free Energy Calculation. Let us consider an assembly of Mn atoms with moments m_i in an Al host. The free energy of this systems is

$$\mathcal{E} = \sum_i \mathcal{E}_1(m_i) + \underbrace{\sum_{i,j} \mathcal{E}_2(m_i, m_j, |\mathbf{r}_j - \mathbf{r}_i|)}_{\mathcal{E}_{\text{Mn lattice}}} + \cdots \tag{25.16}$$

where $\mathcal{E}_1(m_i)$ is the energy of one Mn impurity in an Al host, (25.7) that includes the Coulomb interaction $\mathcal{E}_{\text{int}}$ and the kinetic energy Δ_σ. In Sect. 25.2.2.2, we have shown that a realistic value of $\mathcal{E}_1(m_i)$ for a magnetic Mn impurity is $\mathcal{E}_1(m_i = 2\,\mu_B) \simeq -0.05\,\text{eV}$. For a non-magnetic Mn impurity, $\mathcal{E}_1(m_i = 0) = 0$. The second term in (25.17) is the doublet interaction. It is calculated from the effective pair potential presented in the previous section, $\mathcal{E}_2 = V^{\text{eff}}_{\text{Mn-Mn}}$. The triplet and higher terms are neglected.

The energies $\mathcal{E}_{\text{Mn lattice}}$ for an AlMn crystal, an approximant and a liquid, are given in Table 25.1. Calculations are done using the effective Mn-Mn potential drawn in Fig. 25.7.

Table 25.1. Energy of the sublattice of Mn-Mn atoms (unity: eV/Mn atom)

Alloys	Structure Ref.	$\mathcal{E}_{\text{Mn lattice}}$ $m_i = m_j = 0$ Zou et al. [44]	Present work	$m_i = m_j = 2\mu_B$ Ferromagnetic
Al_6Mn	Crystal Cmcm [40]	−0.24	−0.24	−0.10
α-AlMnSi	Approximant Pm3 [20]	−0.27	−0.26	−0.16
Al_6Mn	Liquid[(a)]		−0.02 [(b)]	−0.00 [(b)]

(a) From a calculation by molecular dynamics [7].

(b) In the structure of the liquid there is a pair of Mn first neighbors. Thus it is necessary to add a repulsive potential to $V^{\text{eff}}_{\text{Mn-Mn}}$. Following a classical approximation, we used an exponential potential, $b\exp(-\alpha d_{\text{Mn-Mn}})$, where the parameters α and b are chosen to obtain the first minimum of the potential at $d_{\text{Mn-Mn}} = 2.7\,\text{Å}$.

25.4.3.2 Comparison Liquid–Crystal–Quasicrystal. The analysis of the energies presented in Table 25.1, gives much useful information on the stability and the magnetism of crystals, approximants and liquids. First of all, as far as the energy of the Mn sublattice is concerned, there is no significant difference between stable crystals and approximants. But the behavior of the liquid is completely different.

For crystals and approximants, the free energy per TM atom, $\mathcal{E} = \mathcal{E}_{\text{Mn lattice}} + \mathcal{E}_1$, is minimized for $m = 0$. For instance in the case of Al_6Mn crystals, if $m = 0$, $\mathcal{E} = -0.24\,\text{eV}$ (because $\mathcal{E}_1(m = 0) = 0$); whereas if $m = 2\,\mu_B$, $\mathcal{E} = -0.15\,\text{eV}$ (assuming $\mathcal{E}_1(m = 2\,\mu_B) = -0.05\,\text{eV}$). Therefore Mn atoms are not magnetic in the crystal Al_6Mn and in the approximant α-AlMnSi. Similar calculations done for other approximants show that in approximants most of Mn are non-magnetic and are not closed from the magnetic/non-magnetic transition. We have studied in detail the case of the approximant μ-Al_4Mn [35], that contains a small proportion of localized magnetic moment. The free energy calculation of the sublattice of Mn leads us to identify the magnetic Mn sites and non-magnetic Mn sites. The behavior of quasicrystals is expected to be the same as that of large approximants.

In liquids, the variation of $|\mathcal{E}_{\text{Mn lattice}}|$ with the magnetic moment is smaller than the energy $|\mathcal{E}_1(m_i)|$. The situation is almost equivalent to the impurity case, for which the Mn impurity is expected to be close to the magnetic/non-magnetic transition. For instance in the case of liquid Al_6Mn, $\mathcal{E}(m = 0) = -0.02\,\text{eV}$ and $\mathcal{E}(m = 2\,\mu_B) = -0.05\,\text{eV}$. Therefore Mn atoms should be magnetic. Moreover, in the liquid, one should consider the fact that displacements of the atoms are important. The magnetic moment may change with the position of the atom and varies from zero to a finite value. The fluctuations of the atomic positions as well as the fluctuating spin orientations due to temperature should also favor the appearance of magnetic moments in the liquid.

25.5 Conclusion

In this chapter we presented a theoretical analysis of the condition for the occurrence of localized magnetic moments in crystalline, quasicrystalline and liquid AlTM phases. We focused on AlMn alloys that have the most interesting behavior. Our conclusions agree fairly well with the experimental investigations and with numerical calculations.

In crystals, approximants and quasicrystals most of the Mn atoms are non-magnetic. This is due to the effect of the band energy which is maximized if there is no magnetic moment. We showed that the main contribution to the energy is due to the medium-range Mn-Mn interaction that is strong up to ~ 12 Å. In these alloys, the magnetic Mn sites should correspond to defects or particular sites of the perfect structure.

In liquids and disordered AlMn phases, the medium-range atomic order is strongly damped out and the Mn atoms are close to the magnetic/non-magnetic transition, as in dilute **Al**Mn. Because of the thermal fluctuations the local magnetic moment on each Mn atom may fluctuate from zero to a finite amplitude.

Acknowledgement

We are grateful to F. Hippert, R. Bellissent, D. Nguyen-Manh, A. Pasturel, M. Audier, C. Berger, J.J. Préjean and V. Simonet for stimulating and fruitful discussions. G.T.L. thanks CEA for financial support and the Laboratoire Léon Brillouin (CEA/CNRS) for its hospitality.

References

1. Andersen O.K., Phys. Rev. B 12 (1975) 3060
2. Anderson P.W., Phys. Rev. 124 (1961) 41
3. Ashcroft N.W., Mermin N.D., *Solid State Physics* (Sauders College Publishing, 1976)
4. Bancael A.P., Heiney P.A., Phys. Rev. B 33 (1986) 7917
5. Belin E., Dankházi Z., Sadoc A., Dubois J.M., Europhys. Lett. 26 (1994) 677
6. Berger C., *Lecture on Quasicrystals*, Eds. Hippert F., Gratias D. (Les Editions de Physique, Les Ulis, France, 1994) p. 463
7. Bratkovsky A.M., Smirnov A.V., Nguyen Manh D., Pasturel A., Phys. Rev. B 52 (1995) 3056
8. Cooper J.R., Miljak M., J. Phys. F 6 (1976) 2151
9. Cyrot-Lackmann F., Solid State Commun. 103 (1997) 123
10. Deutz J., Dederichs P.H., Zeller R., J. Phys. F 11 (1981) 1787
11. Dunlop J.B., Grüner G., Caplin A.D., J. Phys. F 4 (1974) 2203
12. Friedel J., Can. J. Phys. 34 (1956) 1190
13. Friedel J., Denoyer F., C. R. Acad. Sci. Paris Ser. II 305 (1987) 171
14. Friedel J., Helv. Phys. Acta 61 (1988) 538
15. Fujiwara T., Phys. Rev. B 40 (1989) 942; Fujiwara T., Yamamoto S., Trambly de Laissardière G., Phys. Rev. Lett. 71 (1993) 4166
16. Fujiwara T., Yokokawa T., Phys. Rev. Lett. 66 (1991) 333
17. Hafner J., Krajčí M., Phys. Rev. Lett. 68 (1992) 2321
18. Hausser J.J. et al., Phys. Rev. B 34 (1986) 4674
19. Heeger A.J., *Solid State Physic*, Vol. 23, Eds. Seitz F., Turnbull D., Ehrenreich H. (Academic Press, London, 1969) p. 283
20. Henley C.L., Phys. Rev. Lett. 55 (1985) 2883

21. Hippert F. et al., *Proceedings of ICQ5 Conference*, Eds. Janot C., Mosseri R. (World Scientific 1995) p. 464
22. Hippert F. et al., Phys. Rev. Lett. 76 (1996) 54
23. Krajčí M., Hafner J., Mihalkovic M., Phys. Rev. B 55 (1997) 843
24. Liu F. et al., Phys. Rev. B 48 (1993) 1295
25. Massalski T.B., Mizutani U., Prog. Mater. Sci. 22 (1978) 151
26. McHenry M.E. et al., Phys. Rev. Lett. 37 (1988) 10887
27. Nicol A.D.I., Acta Crystallogr. 6 (1953) 285; Bown M.G., Brown P.J., Acta Crystallogr. 9 (1956) 911; Raynor G.V., Waldron M.B., Philos. Mag. 40 (1949) 198; Douglas A.M.B., Acta Crystallogr. 3 (1950) 19
28. Phillips R. et al., Phys. Rev. B 49 (1994) 9322; Widom M., Cockayne E., Physica A (1997) 713
29. Préjean J.J. et al., *Proceedings of ICQ5 Conference*, Eds. Janot C., Mosseri R. (World Scientific 1995) p. 510
30. Raynor G.V., Prog. Met. Phys. 1 (1949) 1
31. Roche S., Mayou D., *Proceedings of ICQ5 Conference*, Eds. Janot C., Mosseri R. (World Scientific 1995), p 493
32. Roche S., Trambly de Laissardière G., Mayou D., J. Math. Phys. 38 (1997) 1794
33. Roche S., Berger, C., and Mayou D. (2002), see Chapter 16 of this book
34. Simonet V. et al., Phys Rev B 58 (1998) 6273
35. Simonet V. et al., Phys Rev B 58 (1998) R8865
36. Smith A.P., Ashcroft N.W., Phys. Rev. Lett. 59 (1987) 1365
37. Tang X.P. et al., Phys. Rev. Lett. 79 (1997) 1070
38. Trambly de Laissardière G., Mayou D., Nguyen Manh D., Europhys. Lett. 21 (1993) 25; Trambly de Laissardière G., Nguyen Manh D., Mayou D., J. Non-Cryst. Solids 153 (1993) 430
39. Trambly de Laissardière G., Fujiwara T., Phys. Rev. B 50 (1994) 5999; 50 (1994) 9843
40. Trambly de Laissardière G. et al., Phys. Rev. B (1995) 7920
41. Trambly de Laissardière G., PhD Thesis, University J. Fourier (Grenoble, 1996)
42. Trambly de Laissardière G., Mayou D., Phys. Rev. B 55 (1997) 2890; Trambly de Laissardière G., Roche S., Mayou D., Mater. Sci. Eng. A 226 (1997) 986
43. Trambly de Laissardière G., Mayou D., *submitted to Phys. Rev. Lett.*
44. Zou J., Carlsson A.E., Phys. Rev. Lett. 70 (1993) 3748

26 Bulk and Surface Properties of Quasicrystalline Materials and Their Potential Applications

Jean-Marie Dubois

This chapter is dedicated to Hans-Ude Nissen on the occasion of his 65th birthday.

Summary. The physical, chemical and mechanical properties of quasicrystalline alloys that may lead to technological applications are briefly reviewed. Some applications, either potential or close to the market, are presented, namely in the fields of energy savings (tribology and reduced adhesion, thermal barriers, solar light absorption) and of the production of high-strength materials. New prospects are raised in the domains of hydrogen storage and catalysis. Altogether, these developments tend to prove that quasicrystalline materials are no longer laboratory curiosities, yet are still of the greatest fundamental interest.

26.1 Introduction

Recently, I came across a short article in a newspaper [59] which reported on a successful attempt to run a ground test of an aircraft engine that carried turbine blades coated with quasicrystals. The purpose of this coating was to protect the Ni superalloy substrate of the blades from overheating and therefore increase the life time of these parts. It was fortunate to find this rather confidential matter disclosed so publicly. I was pleased to see that this very costly and difficult experiment we designed with our colleagues of the Spanish Aeronautic Research Centre, INTA, in Madrid at the time I was in charge of the scientific coordination of this R&D program [18] had finally come to a happy end. For sure, quasicrystals were no longer a laboratory curiosity, about thirteen years after their discovery was published [119]. As a matter of fact, it had already been shown a few years ago that these strange crystals may have more than academic virtues [38] and indeed they were the subject of several patents as early as 1987 and later [83,34,35,93,2].

The purpose of this chapter is to emphasize which properties of quasicrystals contain, to my knowledge, the most promising potential for applications. To this end, I will argue that quasicrystals may be useful for energy savings, either because they reduce friction, or wear or adhesion, or because they are heat insulators or thanks to their strong light absorption. Produced as particles in bulk materials, they yield outstanding mechanical properties. At the present stage of development, demonstrators were made available to confirm the usefulness of quasicrystals in the areas mentioned above. New possibilities

J.-B. Suck et al. (eds.), *Quasicrystals*
© Springer-Verlag Berlin Heidelberg 2002

are clearly pointed out, as yet in the laboratory, by the capability to store large amounts of hydrogen in Ti-Ni-Zr quasicrystals as well as in Zr-Ni-Cu-Al nanoquasicrystals prepared by crystallization of an amorphous precursor. Finally, intriguingly performing trends are indicated in patents for the purpose of catalysis and magnetic recording.

Due to the shortage of space, this chapter will mostly list properties in correspondence with these domains of applications. The reader may find more material about these issues elsewhere [65,100]. Also, I will not insist on metallurgical studies, including phase diagrams and processing, which form the background for the production of quasicrystals. This matter is also supplied in textbooks [65,100]. Up to now, quasicrystals are useful predominantly as coatings [40,125] or thin films [79] because their brittleness is so high that it forbids them to be used as bulk (pure) materials at ambient temperature. Taken as reinforcing precipitates, the issue is different however when they are mixed intimately with a soft matrix. This will be the subject of Sect. 26.6.

Nevertheless, I will not omit the scientific basis, or more abruptly, the guideline we have been using over recent years to strengthen our knowledge of quasicrystals and seek new potential applications. This is dealt with in the next section. Crystallography, largely evoked elsewhere in this book, is far beyond the scope of this chapter except on one point. Due to the existence of forbidden symmetries, the quasicrystalline state is easily identifiable. This point extends to approximants with pseudo-forbidden rotational symmetries. In the meantime, it guarantees that the properties of these compounds will be closer to those of the quasicrystals than of any conventional alloy with short lattice parameters. Quasicrystals and their approximants therefore belong to a large family of intermetallics which may be related to specific crystallographic characteristics in a straightforward way. Any claim for the application of a property is accordingly easy to substantiate in a patent by reference to a unique structural signature, the existence of one or several (pseudo-) 5-fold axes, or 10-fold or 8-fold axes, in an associated diffraction pattern (Fig. 26.1). Patents like the ones which are quoted in the following text most often rely upon this definition of the quasicrystalline material.

26.2 Recurrent Localization of Electronic States

Owing to the absence of translational symmetry, the breakdown of Bloch's theorem in quasicrystals leads to so-called critical states, neither extended as in a metal nor localized [123]. In most of these alloys, the interaction between d and sp states must also be taken into account, due to the transition elements [94,95]. As a result, the pseudo-gap which opens at the Fermi energy E_F because of the Hume–Rothery mechanism [50], is even deeper and broader than expected. As a matter of fact, this pseudo-gap was detected experimentally for the first time 12 years ago in metastable Al-Mn quasicrystals [133]. It is more marked in the more resistive, and stable, icosahedral phases [6].

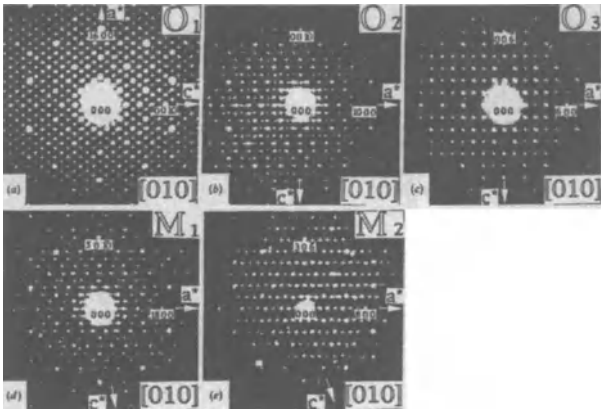

Fig. 26.1. Series of electron diffraction patterns with pseudo 10-fold symmetry which define the family of approximants of the decagonal phase in the Al-Cu-Fe-Cr system (O1: orthor., Bmm2, a = 3.25 nm, c = 2.37 nm; O2: orthor., P2mm, a = 2.36 nm, c = 2.01 nm; O3: orthor., Pnma, a = 1.46 nm, c = 1.24 nm; M1: monoc., a = 2.01 nm, c = 4.32 nm, $\beta = 98.3°$; M2: monoc., a = 1.24 nm, c = 2.01 nm, $\beta = 108°$; for all compounds, b = 1.22 nm) (taken from ref. [33, 87]). These alloys are preferred for the fabrication of low-adhesion, corrosion-resistant coatings

While the density of Al 3p states at the Fermi level, $n(E_F)$, decreases down to very small values in such alloys, it is also observed that the conduction states decay significantly in a range of a few eV beyond E_F. The two trends put together suggest that the stability of the quasicrystal does not arise only from scattering of the Fermi electrons by the few major Fourier components in reciprocal space which define a pseudo-Brillouin zone in contact with the Fermi sphere. Instead, every component, including very small ones which densely fill the reciprocal space, plays a role and opens a gap in the density of states (as long as the Fourier component and electronic life time satisfy Heisenberg's principle [30]). This is confirmed by IR absorption experiments [139] and *a contrario*, comparative, X-ray spectroscopy measurements on conventional Al-Cu Hume–Rothery alloys [7,49].

Another way to tackle this difficult problem was suggested by Janot and de Boissieu [62,64]. It is based upon the cluster description of the icosahedral structure that fits the available diffraction data obtained from various beam sources, mostly with i-AlPdMn single domain grains. This description is presented elsewhere in this book. Janot [64] assumes that the basic clusters , actually pseudo-Mackay icosahedra of 50 or 51 atoms, trap a magic number of electrons (i.e. 92) plus or minus a valence. Since the structure is hierarchically organized, the architecture of the basic cluster and its overlap with other groups of atoms is preserved at every stage of the growth. Thus, valencies are identical for atoms and for clusters. They keep constant the magic number of electrons over the whole range of hierarchic clusters. In

other words, the stability of the cluster imposes a one-to-one correspondence between hierarchical symmetry and valences of the constituents and clusters. Valence electrons, which would contribute to the Fermi sea in a conventional metallic alloy, are now localized in the clusters, starting with the basic one. Only part of them, those which yield the cluster valence, are promoted to the forthcoming cluster in the inflation series. The volume of the hierarchical clusters increases from step to step via an inflation factor of (nearly) τ^9 (τ is the golden section $(1+\sqrt{5})/2$) whereas the number of constituent clusters is constant (50 or 51). Accordingly, the density of nearly free electrons at zero temperature is expected to be vanishingly small, thus precluding an insulating behavior and diamagnetism as is indeed observed in samples of excellent lattice perfection [63,65].

Due to recurrent localization effects , the DOS is dominated by the contribution of the basic cluster to the valence band [62] (see Fig. 8.5 in the chapter by Janot and Dubois). The contributions coming from the next steps of the hierarchy are found closer and closer to the Fermi edge, decaying down in energy according to τ^{-6} and in intensity according to τ^{-3}. Above the Fermi level, conduction electrons form a parabolic-like band of small ($T \geq 0$ K) or vanishingly small ($T = 0$ K) intensity if the lattice of the icosahedral crystal is assumed perfect. Experimentally, the density of states was found to be constant, within experimental accuracy, with temperature below 300 K (E. Belin-Ferré, private communication), especially on the side of the conduction band. It may vary much more above 900 K when atomic movements are fast enough to become associated with a brittle–ductile transformation of the material [28,89]. This point requires further investigation.

Thus, the hierarchical nature of quasicrystals (icosahedral phases to be more precise) is dominated by a fairly specific electronic structure. This leads to special properties and temperature dependences as depicted by Janot in the references quoted above. It may also have an impact on growth and phase selection as examined in the next section.

26.3 Phase Selection and Preparation Conditions

In Janot's model, icosahedral quasicrystals are associated with strictly defined average electron densities (e.g. $< e/a > = 1.85\, e-/at$ in Al-TM-TM alloys) corresponding to a perfect icosahedral lattice. Perfection is unfortunately not easily achieved in real life and a scatter of values is expected when sampling for instance transport properties in a series of specimens. This addresses the question of the stability of quasicrystals on the one hand and raises constraints on the preparation methods and reproducibility of properties on the other.

Perfect icosahedral crystals can grow only if recurrent localization is satisfied at every stage of the hierarchy. On practical grounds, this may never happen either because the composition is not exactly stoichiometric (i.e. im-

purities cannot be avoided) or because of local fluctuations of the composition introduced by the preparation method. At elevated temperatures, these later defects may disappear rapidly enough thanks to the atomic diffusivity which becomes comparable to that in normal crystals [69]. Furthermore, hopping between isomorphically connected states [64] may smooth out the constraints from recurrent localization extending over every level of the hierarchy. This mechanism becomes efficient only at high temperature as its frequency increases according to the Boltzmann distribution law. It introduces an entropic stabilization term due to hopping electrons (not to phason jumps as in random tiling models [56] although coupling with atom equilibrium positions may exist). This favors the average icosahedral lattice in the high-temperature range.

Under infinitely slow cooling, this icosahedral state from high temperature could certainly not be preserved down to low temperatures with perfect icosahedral order, i.e. with a hierarchy extending to infinity. Indeed, preparation imperfections, as already mentioned, and more importantly the finite size of the sample necessarily break the recurrent localization scheme respectively in the bulk and at surfaces (hence keeping an inflation symmetry in two dimensions [113]). I will come back to this second point in the next section. Therefore, recurrent localization corresponds to an idealized concept, the icosahedral lattice, but not to an icosahedral crystal as a fundamental thermodynamic state at zero Kelvin. A detailed analysis of the diffuse scattering of i-AlPdMn single domain crystals of excellent lattice perfection at high temperature confirms this point [12,14]. This must be added to the many lattice instability studies published so far, see for instance [63].

The mechanism of recurrent localization strongly couples large numbers of atoms, first in the basic pseudo-Mackay cluster, then also beyond this size of about 1 nm in the next steps of the hierarchy. The quasicrystal behaves more as a molecular solid than any metallic alloy and therefore the kinetics of the transformations from an average icosahedral lattice to the low-temperature state must be very (or extremely) slow. This has some reminiscence of the glass transition mechanism in oxides but is relevant to the condensation of the nearly free electron states from the high-temperature regime into the successive cluster states of the hierarchy at lower temperature. The transition temperature is not necessarily identical to that of the brittle–ductile transition (about 870 K in i-AlCuFe [16]) which is supposed to accompany the decrease of cohesion between basic clusters upon heating [48]. One may even guess that a series of temperatures may be associated with the recurrent condensations of electrons in the cluster levels (in deflation order if temperature decreases).

It was already shown by real-time neutron diffraction experiments at a temperature just below that of the peritectic growth reaction that the velocity of the icosahedral crystal front is slowed down by several orders of magnitude as compared to that of a conventional intermetallic like Al_6Mn [32]. This

result goes along with the evidence provided by containerless experiments that the atomic clusters already form within the solid–liquid interfacial region [57]. It also means that reconstruction of the lattice, that would require to destroy first the stable clusters to rebuild them at another composition, will be a process far more time consuming than any usual peritectic reaction. This situation is encountered typically in Al-Cu-Fe icosahedral alloys which cannot be prepared without the nearby cubic CsCl-type phase except over very slow cooling or after high-temperature annealing. It is worth noting that the composition range of the metastable icosahedral phase is far away from that of the supposedly stable icosahedral phase. Reportedly, the stable state might always be a micro-twined approximant but this point is still a matter of debate [10,21].

A small composition change is associated with a shift of the average electron density $< e/a >$ that preserves the stability of the basic cluster, i.e. the magic number of electrons in the cluster level within a narrow range around 92. In terms of atomic content, the transition element like Mn or Fe in i-AlPdMn or i-AlCuFe, respectively, has the most drastic impact on this number whereas the cluster stability is less sensitive to variations of the Pd or Cu fractions. Hence, such fluctuations of 1 at% or less have a dramatic influence on the valency of the clusters and thus on their coordination, or equivalently on the extent of the hierarchical structure and clusters overlap. An estimate of this effect may be deduced from the stability region (Fig. 26.2) of the icosahedral phase and its approximants in the Al-Cu-Fe system [110]. A change of $< e/a >$ by $+0.06\ e-/at$ shifts the stability region at 970 K from the i-phase to the series of approximants (with $< e/a > \approx 1.92\ e-/at$). Although diffraction and HREM patterns show that the basic clusters are the same [86], it is the way the clusters are connected together which varies. Going further beyond this point, the structure of $Al_{55}Si_7Cu_{25.5}Fe_{5.5}Mn_7$ ($< e/a >= 1.86$ with 3, 4, 1, -2 and -3 valence electrons for the constituents, respectively) should be icosahedral since the average electron concentration is the same as that of the icosahedral phase. As a matter of fact, it is cubic (lattice parameter $a = 1.23$ nm), like the 1/1 approximant of composition $Al_{55}Si_7Cu_{25.5}Fe_{12.5}$ and $< e/a >=1.93\ e-/at$ [17,111]. This result is an indication that Si atoms do not substitute Al ones at random, nor Mn the Fe sites, and that valences of the individual clusters matter more than the average electron density, in strong support to Janot's model (Dubois J.M. and Zandona M., unpublished results).

To conclude on this section, it is clear that pure quasicrystals can be prepared only with the help of very well controlled processes, at least as far as the composition and temperature ramps are concerned. The purity and lattice perfection, which control the exaltation of the properties, are difficult to master without considering the very slow kinetics of the associated transitions, therefore their cost. For instance, the vapor deposition at nominal stoichiometry $Al_{62}Cu_{25.5}Fe_{12.5}$ (using magnetron PVD sputtering) of a coating on a

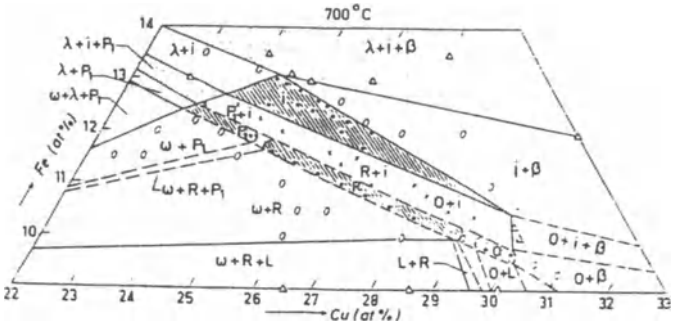

Fig. 26.2. Part of the Al-Cu-Fe phase diagram at 970 K showing the stability region of the icosahedral phase (labeled i) and of its pentagonal (P), rhombohedral (R) and orthorhombic (O) approximants. The neighboring crystalline phases are the β-cubic, λ-monoclinic and ω-tetragonal phases. The letter L denotes the liquid (taken from [110])

substrate held at room temperature produces an amorphous material. Upon annealing (Fig. 26.3) at 670 K, this material forms first the B2 cubic phase, which contains a large fraction of vacant sites and transforms later into a phasoned icosahedral phase [81,127]. The same trend is observed by starting from a mixture of powders alloyed by mechanical grinding [134] and also during annealing of Al/Cu/Fe multilayers [79,142]. Rapid cooling, fast diffusion or mechanical constraints do not allow the formation of the basic clusters in the initial stages of these processes and therefore the macroscopic quantum state which corresponds to idealized recurrent localization cannot take place. It requires thermal activation to install the icosahedral quasicrystal, albeit with slow kinetics. The observation [46] that the growth of isolated icosahedral particles of nanometer size does not proceed directly from a beam of individually evaporated atoms is consistent with this argument.

Due to process imperfections, it might be difficult to achieve a very precisely defined composition. Fortunately enough, for many of the properties we will see in the next section, it is sufficient to prepare either an approximant or a mixture of approximants and quasicrystal. Most often, the grain morphology appears then as a micro-twined intergrowth of the different compounds which shows enhanced ductility [71] but often at the expense of corrosion resistance. When doing so, the targeted stability region in the phase diagram is more open and falls in between that of the individual phases. The addition of chromium to Al-Fe-Cu alloys for instance makes the icosahedral phase disappear (due to the change of $\langle e/a \rangle$) but induces the growth of different orthorhombic approximants of the decagonal phase [33,87]. In this case, it has also a very favorable impact on the corrosion resistance in alkali or weakly acid solutions [90]. As a result, the optimal composition for the large-scale production of an Al-Cu-Fe-Cr alloy aimed at the manufacture of coatings on

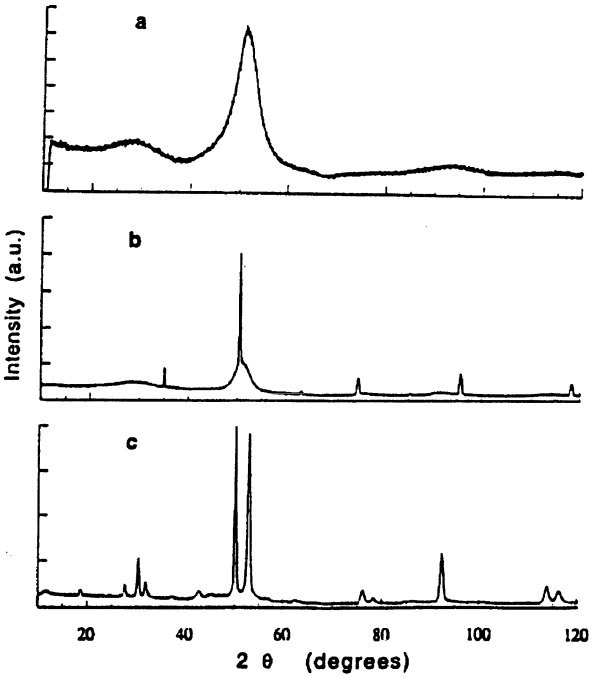

Fig. 26.3. Powder X-ray diffraction patterns for a 5 μm thick PVD deposit on a glass substrate: (**a**): after magnetron sputtering, (**b**): after temperature anneal at 673 K for 1 hour and (**c**): after 17 hours at 673 K. In (**a**), the coating is amorphous whereas about 50% of its volume has transformed to the β-cubic phase in (**b**). It is fully icosahedral in (**c**) (taken from [81, 127])

cooking utensils lies at the center of a broader concentration field [40]. This ensures a better control of the production whereas the properties involved in the application, here hardness, low adhesion and corrosion resistance, are preserved (if not enhanced).

26.4 Potential Applications of Transport Properties

The peculiar electron transport properties of quasicrystals have been described at length in many papers and textbooks [9,64,65,78,107,130,140] as well as in the present volume. The large negative temperature coefficient of the resistivity, in addition to the high resistivity values, suggests that quasicrystals might be used as temperature sensors with respectable sensitivity in a broad temperature range. Thin films of the i-AlCuFe phase processed by solid state interdiffusion of Al, Cu, and Fe multilayers obey Ohm's law perfectly over 7 orders of magnitude [80]. It was also suggested [60] that such alloys may be employed in the manufacturing of magnetic recording heads , albeit, the much more resistive i-$Al_{70.5}Pd_{21}Re_{8.5}$ icosahedral phase exhibits a

semiconductor-like behavior which is comparable to that of boron-rich compounds [131]. Consensus has not been fully achieved yet to determine whether this quasicrystal is an insulator or not at low temperature [88,104] but this material raises some prospects for its use in thermopower devices or thermocouples [29]. The strong dependence of the conductivity on composition and preparation [8,58] however throws some cold water on eventual industrial developments of thin films and coatings prepared with this alloy [55]. The i-AlCuRu phase, which also shows semiconductor-like electron transport [132], might be less demanding in this respect.

Applications based upon the optical conductivity of Al-Cu-Fe thin films sandwiched between dielectric films and plated on copper are closer to the market [47]. In a good metal, the optical conductivity $\sigma(\omega)$ is dominated by the Drude peak at $\omega = 0$ and decays to zero at very large frequencies. The opposite is observed with good quasicrystals. The conductivity $\sigma(\omega)$ is very weak at low frequencies and shows a broad peak at about 10^4 cm^{-1} [24]. Using spectrometers of sufficient resolution and samples of excellent lattice perfection allows (Fig. 26.4) the detection of the effect of the hierarchical nature of the Brillouin zone on the opening of a series of van Hove singularities in the DOS [30]. In decagonal quasicrystals, measurements of $\sigma(\omega)$ are sensitive to the anisotropy of the structure [5].

As already mentioned, the strong absorbance of quasicrystals in the visible and near infra-red range leads to potential applications for recovering solar light energy either as thick coatings [41] or as very thin films [44]. Now

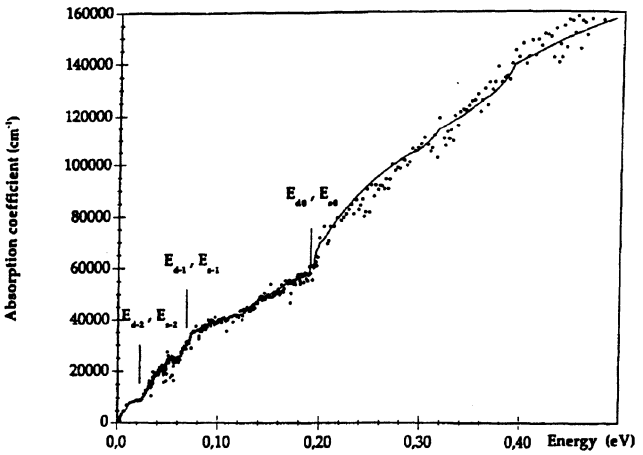

Fig. 26.4. IR light absorption coefficient deduced from a Kramer–Kronig analysis of the reflectance measured at room temperature for a i-$Al_{59}B_3Cu_{25.5}Fe_{12.5}$ sample of icosahedral phase (dots). The solid line is a fit of the data involving a series of direct transitions and van Hove singularities in the DOS which scale in energy according to an inflation rate of τ^2 (taken from [139])

that the metallurgy is better mastered in this latter case [46,47], demonstrators have been fabricated by the TiNOx company in München with rather promising performances [45]. For instance (Fig. 26.5), a 10 nm thick film of Al-Cu-Fe icosahedral phase plated onto a copper collector in between two Al_2O_3 films gives a strong absorbance in the visible and near IR ($\alpha \approx 0.8$) while the reflectivity at 493 K stays as low as a few percent. Industrialization of solar light collectors still requires the scaling up of the production of large areas of thin films but this invention seems very appealing.

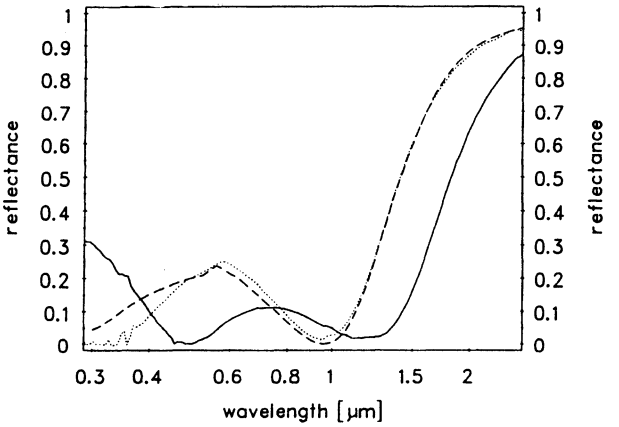

Fig. 26.5. Experimental reflectance measured as a function of wavelength with a sandwich of 10 nm i-AlCuFe phase between two layers of 50 and 70 nm of Al_2O_3 plated onto a copper collector (solid line). Also shown is the response (dashes) of a cermet containing 30% of i-AlCuFe nanoparticles dispersed in alumina. The dotted line is a fit of a theoretical model to the data (taken from [47])

Another use of a transport property of quasicrystals, namely heat insulation , is on its way to pre-industrial development [1,59]. In this case, the advantage of quasicrystals is two-fold. They are heat insulators as efficient as zirconia in a temperature range extending from room temperature to close to their melting point; furthermore, they become plastic above 870 K so that interfacial stresses arising at the contact with metallic substrates are canceled out [39]. This raises the prospect to use them as thermal barriers, hence in a lower-temperature domain as compared to that of zirconia (exit stage of air-craft engines, automotive engines, steam turbines, etc, ...) [36]. Another property of quasicrystals (Fig. 26.6) is the speed-up of cooling in contact with a liquid which is able to vaporize, like water. Due to the low effusivity of quasicrystals (i.e. the velocity with which heat propagates in the medium), the contact temperature of the liquid slightly exceeds that of the liquid–vapor transition. Especially with water, the vapor film which forms at the interface with the solid is not stable [98], thus enhancing the quenching rate of the

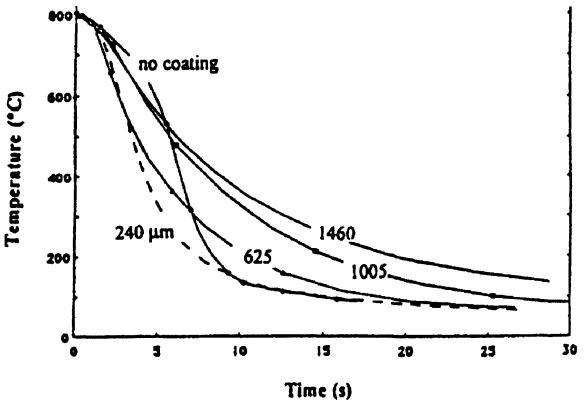

Fig. 26.6. Temperature versus time charts recorded at the center of nickel cylinders quenched in water from 1070 K. Note that the cylinder coated with a 240 μm thick quasicrystal coating cools faster than the one with no coating. With thicker coatings, the thermal barrier effect is observed (taken from [3])

solid since direct contact with the liquid takes place, yet at a temperature which exceeds that of the liquid–vapor transition. The case is very favorably represented by quasicrystal coatings on aluminium or nickel samples [3].

At low temperature, the propagation of heat in quasicrystals is vanishingly small. It increases first as a T^n power law ($3 \leq n \leq 2$), reaches a plateau in the 30 to 100 K region and then increases again [25,102]. This was interpreted by Janot [64–66] in terms of heat transport mostly due to acoustic phonons at low temperatures. It precludes a Dulong–Petit regime at a temperature where the phonon wavelength becomes comparable to the size of the basic clusters, i.e. at about 70 K. The point is consistent with neutron inelastic scattering data [11,109]. At room temperature and beyond, electron conductivity enters the game and contributes to heat transport in a way comparable to that of lattice vibrations [102]. This is far less than in usual metals and alloys. The details of the temperature dependence of heat conduction may be related to the interplay between phonons and defects (surfaces, phasons, etc, ...) [85,103]. However, owing to the absence of a well-defined Brillouin zone, or to its very limited size in approximants, the most efficient mechanism for the limitation of heat transport is the Umklapp process [70]. To my knowledge, application of quasicrystals for the purpose of heat insulation is the only case which considers pure and massive quasicrystals. The other applications, including light absorption, take advantage of the properties of thin films, as mentioned above, and of surfaces. This is the subject of the next section.

26.5 Surface Properties

In solid state physics, the studies of surfaces , preferably that of well-controlled single crystals, covers a very broad domain of active research, ranging from surface composition analysis and chemical reactivity to atomic structures, low-dimensional phase transitions and electronic structures (see e.g. [108]). The science of surfaces is usually restricted to the study of the ultimate atomic layers of the crystal but corrosion, which involves atomic transport from or to the bulk, and tribology, with the effect of very long range mechanical stresses, also belong to this vast class of materials investigations. In the domain of quasicrystals, this type of research is still in its infancy though its importance for potential applications had been recognized early [37,67]. In very recent years however, new and rather intriguing experimental results have been produced (for a review, see [68]).

The determination of atomic positions at the surface and just beneath is naturally the first issue to address in this respect. In spite of what we know already from high-dimensional crystallography on the 3D icosahedral network, it must be accepted at this stage that the evidence provided by various surface experiments is rather contradictory and that we are again left with the old question asked more than ten years ago [4]: where are the atoms? Scanning Tunneling Microscopy (STM) observations show two very different features, depending on the way the sample surface is prepared. On the one hand, a clean surface can be produced by cleaving an i-AlPdMn single crystal in the ultra-high vacuum (UHV) of the microscope. The images taken with such surfaces [43] show no atomic resolution whatsoever, though the STM is in principle able to achieve such a resolution with metals. Instead, a rough surface is revealed with protuberances slightly less than 1 nm in diameter. At lower magnification, aggregates of such clusters are visible. As a matter of fact, three distinct levels are distinguishable which nicely fit the hierarchical scheme presented in Sect. 26.2. As STM explores the contours of the electronic density at the surface, this experiment comes in strong support to the recurrent localization model . Right at the surface, nearly free electrons are detected [137]. Since the surface is created very far from equilibrium by cleavage, such electrons are expected in the framework of Janot's model because large clusters and probably also a few basic ones, which have been cut through during the propagation of the crack, are no longer acting as quantum wells. The electrons thus made free are confined in a narrow surface layer covering the other clusters kept intact by the crack passing around (like in computer simulations [97]). These clusters give rise to the image contrast and form a rough surface with hierarchical corrugation. Upon annealing, the cleaved surface is imaged with a better contrast, probably because reconstruction of the top layers enhances the perfection of the clusters and improves the electron localization. Hence, no atomic contrast is achieved with such samples closer to equilibrium.

A more conventional way to prepare the surface is to clean it first by ion etching (which leads to superficial amorphization) and then reconstruct it by careful annealing up to high temperature in UHV. Recording Low Energy Electron Diffraction (LEED) patterns in the course of the transformation has pointed out an intriguing phase transition [120], showing for instance that the appearance of an icosahedrally symmetric LEED pattern at 900 K is preceeded by a rhombic-like pattern of a fine grained surface in i-AlPdMn.

After such heat treatment, flat terraces are found at two-fold and five-fold surfaces of i-AlPdMn single crystals, most often surrounding facetted cavities [26]. Owing to appropriate image numerical treatment, it is even possible to distinguish atomic features but the most fascinating observation is obtained at moderate magnification [118]. Then, a series of terraces may be identified, with step heights taking values of either 0.42 or 0.67 nm [117]. These steps order according to a segment of the Fibonacci sequence when the crystal is viewed along a five-fold axis. Noticeably, these heights are about 2 (respectively 3) times larger than the distance separating two first neighbor close-packed planes in the structure model of the i-AlPdMn phase deduced from diffraction experiments [13]. It can therefore already be concluded that the surface terminating an icosahedral crystal (under thermodynamic equilibrium) is not similar to that of a usual close-packed metal which ends up on low Miller index planes (nor is it the same as the one obtained by cleavage). Furthermore, the distances of 0.42 and 0.67 nm correspond (Fig. 26.7) to separation distances between densely filled aluminium planes in the pseudo-Mackay cluster packing. This tendency to end up the crystal on an aluminium top layer is confirmed by oxidation experiments as described below.

A model [54] of the atomic structure of the surface was proposed on the basis of a comparison of experimental LEED patterns and calculated ones considering the bulk structure of i-AlPdMn [13] terminated on various planes chosen among the planar arrays of atoms present in the 3D structure (plus optimization of the interplanar spacings along the five-fold axis). The agreement with the LEED intensities is rather good and confirms the tendency to have an aluminium-rich outermost layer. However, despite the fact that comparison of model with experimental LEED intensities is satisfactory and similar to that of other surface structure determinations, I would suggest an alternative description.

First, it must be stressed that the two sets of observations – rough surfaces and flat terraces – can be mixed up, but represent two different kinds of terminating surfaces. Terraces arise from heating to equilibrium an initially disordered medium with a smooth, nearly flat surface. Its initial composition is far from the icosahedral phase stoichiometry due to preferential evaporation of Al during ion etching [67]. Upon annealing to the final state characterized by a five-fold symmetry (the two-fold symmetry was not studied in [54]), the metallic character of Mn atoms decays significantly [120] while the nominal composition is recovered. In this state, virtually no free electrons emerge

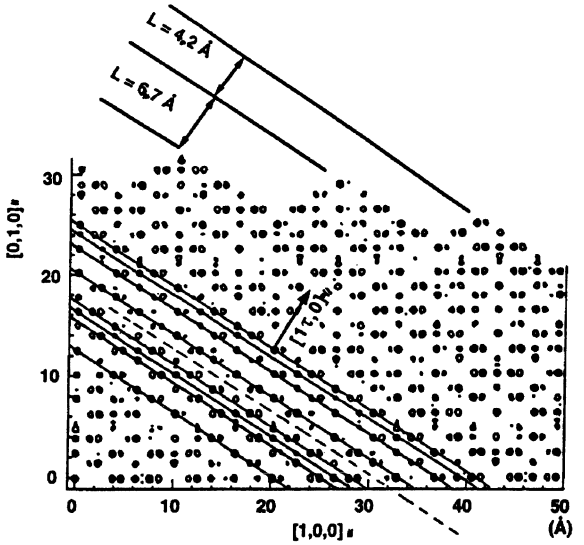

Fig. 26.7. Traces of the atoms in a two-fold plane of the i-AlPdMn structure containing a five-fold axis (labeled [1τ0]). A "surface" was cut, so as to pass in between complete pseudo-Mackay clusters. Terraces separated by distances of 0.42 and 0.67 nm are generated as shown. Note however that the average lateral extension of the terraces, in the plane of the figure and perpendicular to it, must be of the order of twice the diameter of the clusters so as to preserve complete clusters at the surface of a structure having full icosahedral symmetry. Therefore, this model is adapted to the images seen in [43] (after annealing). Flat terraces of much larger extent [117] require the introduction of periodicity by mapping the five-fold direction onto a periodic stacking axis in order to obtain statistically identical Al-rich, flat terminating planes with full clusters at the surface (taken from [65] and [13])

from the surface as STM experiments tell us (the optimum setting is as for semiconductors [26]) and X-ray photoelectron diffraction experiments are consistent with the presence of full pseudo-Mackay clusters in the ultimate layers of the single grain [99]. These two results are in line with Janot's model. Nevertheless, as observed [117], the lateral extension of the terraces is far too large to preserve complete clusters and planar Al-rich layers as the result of a straightforward two-dimensional cut through the icosahedral lattice. Rather, a corrugation should be observed as in [43], with wavelength similar or close to twice the cluster size (i.e. the characteristic length of this class of isomorphism, see Fig. 8.6 in the chapter by Janot and Dubois, this volume) if full clusters are to be preserved. This statement is exemplified in Fig. 26.7.

An alternative way to interpret the discrepancy between the two sets of data is the following. In the case of flat terraces, the top-most Al-rich layer yields an enhanced number of electrons ($V_{\mathrm{Al}} = 3$) and increases locally the

valence electron density $< e/a >$. In order to reach thermodynamic equilibrium, this may be accommodated, like in the bulk, by an approximant lattice. Appropriately, a shearing of the 6D lattice as described in [110] is able to produce a pentagonal structure with a five-fold axis perpendicular to the terrace. Such a structure, which keeps a generic inflation symmetry in the plane of the terraces [113], coincides with the icosahedral lattice along these two directions of space. It differs from it in the third direction by shifts of the interreticular spacings quite similar to the ones considered in [54]. Formally, this resembles the case of polytypism [72].

Comparatively, the oxidation resistance of i-AlCuFe [51,67,114] and i-AlPdMn [23] icosahedral phases appears to be rather similar. The thickness of the oxide layers after long-term exposure to ambient air falls in the range of a few nanometers but depends very much on the presence or not of humidity. On i-AlPdMn of stoichiometric composition, it seems nevertheless significantly lower than on aluminium metal [26]. Under oxygen flow in the Auger spectrometer, the i-AlCuFe phase oxidizes (Fig. 26.8) in three successive steps with increasing temperature [51,114]. A regime of little oxidation is observed between 290 and 670 K.

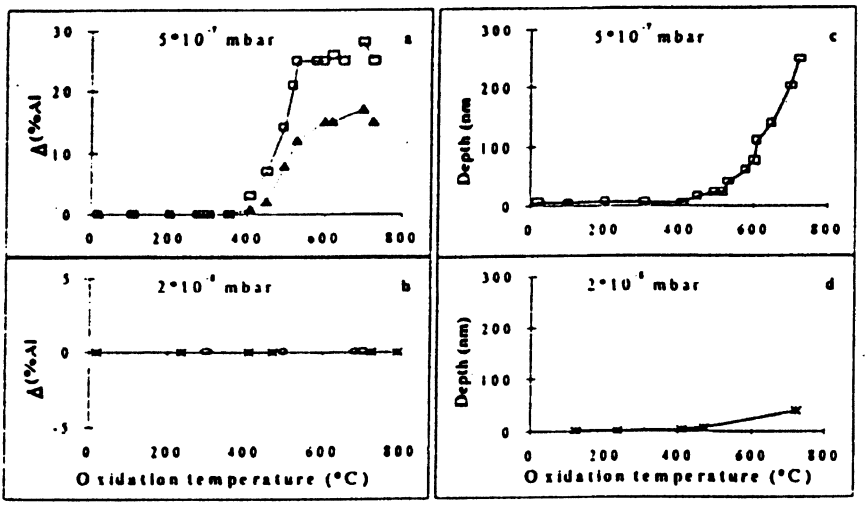

Fig. 26.8. Variation of the aluminium concentration in the surface layers of i-$Al_{62}Cu_{25.5}Fe_{12.5}$ relative to the nominal composition (**a, b**) and oxygen penetration depth (**c, d**) as functions of the sample temperature. Symbols are: □ for 7200 Langmuirs (L) of oxygen at 5.10^{-7} mbar pressure of the Auger vessel; △: 1700 L 5.10^{-7} mbar 0_2; ×: 1700 L, 2.10^{-8} mbar 0_2; o: 600 L, $2.10^{-}8$ mbar 0_2 (taken from [51, 114])

The thickness of the oxygen adsorption layer then remains below 2 nm and no change of the alloy surface composition is detected. From 670 K up to about 800 K, the thickness of the oxide rises steeply and the composition moves at the surface from 62 at% Al to more than 80%. Meanwhile, stoichiometric Al_2O_3 alumina is detected. Finally, beyond 820 K, the aluminium concentration is nearly stable at the surface but the penetration of oxygen in the material still goes on. This effect was also detected by a Secondary Ion Mass Spectroscopy (SIMS) analysis of icosahedral grains submitted to long-term annealing in air [74]. Together with substantial oxygen diffusion in the icosahedral lattice, it was associated with a shift of the phase stability towards that of the β-cubic phase in thin areas. In massive samples, the remarkable penetration of oxygen in the bulk only affected the lattice perfection [141]. During such experiments on i-$Al_{63}Cu_{25}Fe_{12}$, it was shown that the alumina layer grows first in the γ-cubic allotropic form and transforms after further oxidation into nodules of corundum-type α–Al_2O_3.

A study of the XPS signals from the three constituents of i-AlPdMn submitted to oxidation in vacuum or in dry air indicated that only aluminium binds to oxygen atoms [23]. This was no longer true when the experiment was done in immersion in water or in the presence of H_2O vapor [67,106]. It was then observed that water is a more efficient oxidant than oxygen, consistent with previous observations on aluminium alloys. This goes along with a drastic enhancement of the aluminium concentration at the surface whereas the contents of the two other elements decrease by a factor of 5 with respect to the nominal composition.

A similar trend was observed during corrosion tests of a $Al_{71}Cu_8Fe_{10.5}Cr_{10.5}$ coating immersed in dilute acetic acid (4% of CH3COOH in water) at 368 K [91]. This electrolyte is called vinegar in the kitchen. The test was designed in view of the manufacture of cooking utensils [40]. The equilibrium state of this alloy is an orthorhombic approximant of the decagonal phase as already mentioned in Sect. 26.3. The actual structure may depend on the cooling conditions encountered during the plasma processing of the alloy [40]. Most often, the coating as-prepared contains a mixture of β-cubic, primitive icosahedral and decagonal phases which may be turned into the equilibrium structure by high-temperature annealing. Conventional potential-current corrosion tests, as well as chemical analysis of the Al, Cu, Fe and Cr content of the electrolyte after testing for several hours, have shown that the corrosion rate of the fully annealed coating is negligible. Its response to this specific test is then intermediate between that of austenitic and of ferritic stainless steels[1] which however exhibit far less surface defects and porosity than that due to rolling (Fig. 26.9). Just after plasma spraying and polishing, the situation is not so favorable, because of the presence of interphase grain boundaries

[1] Austenitic steels contain large amounts of Ni and Cr and are fcc. Ferritic steels, with a bcc Bravais lattice and less Cr, exhibit less corrosion resistance but are cheaper.

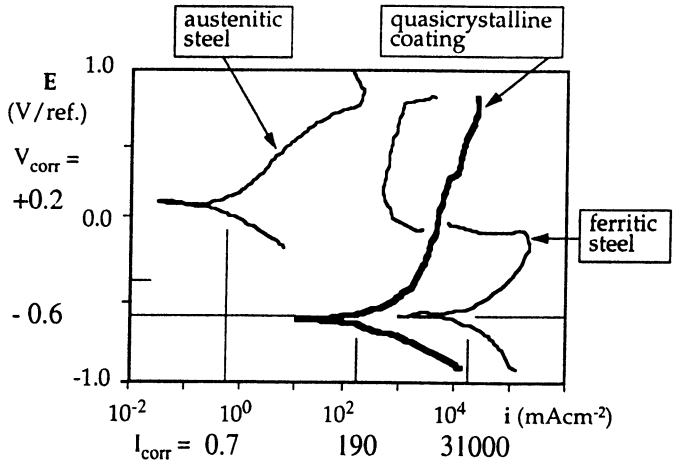

Fig. 26.9. Plots of the potential versus corrosion current measured in dilute acetic acid at 368 K for two rolled plates of stainless steel and a polished Al-Cu-Fe-Cr coating. The corrosion resistance of this latter sample is intermediate between that of the two stainless steel plates (taken from [91])

and mostly fluctuations of the Cu concentration between Cu-rich β-phase grains and the other phases. A preferential dissolution of aluminium is then observed (whereas Cu mainly does not go into solution in the electrolyte). Nonetheless, the corrosion rate observed in this case is still a factor 2 below that of aluminium alloys currently used for cooking utensils. In a number of atoms, it is comparable to the corrosion rate of low-carbon steel.

Thus, the first application of quasicrystals that went close enough to the market [27] was based on a compromise between good corrosion resistance , high hardness and respectably low surface energy for the sake of reducing the adhesion forces to food. This affair is no longer a question of laboratory development but nowadays a matter of industrial up-scaling and marketing. Up to now, the surface energy of quasicrystals has been studied only marginally. Indices, from fairly negligible resistance against crack propagation ($K_{IC} \leq 0.5$ MPa $m^{1/2}$) [16] or from very limited growth of precipitates [61,113], suggest that it must be low in contrast to metals and alloys. Indeed, metals have surface energies of the order of 1000 mJ/m^2, basically because the wavefunction of free electrons does not cancel to zero right at the surface but outside. Actually, such a surface energy (it corresponds to half the cleavage energy) is barely measurable, neither by cleavage experiments nor at the surface of a clean metal (gold, mercury). Oxidation, which goes along with the growth of a foreign surface layer, changes the nature of the surface and reduces the apparent surface energy of the metal.

This surface energy γ_S is often estimated with the help of wetting experiments, assuming that the equilibrium shape of the liquid droplet is the result

of a balance between energies of the solid–liquid, solid–vapor and liquid–vapor interfaces. These energies reflect the electrostatic interactions between dipolar moments carried by the liquid molecules and localized at the surface of the solid [22]. If γ_S is small enough, of the order or less than 50 mJ/m^2, it is safe to separate the contributions from interactions between instantaneous dipolar moments, which give rise to so-called London forces (or dispersive terms), and permanent moments (also called the polar contribution). The crystal field in an ionic solid brings up such a component as well. For this reason, water which is a very asymmetric molecule with the strongest polar contribution, wets easily most solids which show a non-zero permanent surface energy contribution γ_S^P whereas it hardly wets many polymers, especially Teflon (PTFE), which are characterized by $\gamma_S^P = 0$.

A simple experiment can thus be designed to estimate the apparent surface energy of quasicrystals and related alloys. To this end, it suffices to deposit a minute droplet of water on the surface of a sample and to measure the contact angle between liquid and solid. If this angle is above 90 degrees, the liquid does not wet (this is the case for water on Teflon) whereas angles below 90 degrees show a tendency to wetting, thus a larger solid surface energy γ_S. If γ_S is larger than the cohesive energy of the liquid, then total wetting occurs and the contact angle is no longer defined. Actually, it is possible to obtain quantitative estimates of the two components of γ_S by using a series of different liquids with varying dispersive and permanent contributions [22].

This was done for several quasicrystalline samples, approximant and amorphous alloys as well as for metallic alloys and reference solids such as PTFE and single crystalline alumina. For the sake of making the comparison more valid, the surfaces of these samples were all grinded to mirror polish (with final arithmetic roughness of 0.1 μm or less) so that the contributions to γ_S coming from local curvature and pining were similar [113]. It appeared (Fig. 26.10) from this study that pure icosahedral materials, either single grains or polycrystalline, exhibit a wetting behavior by water comparable to that of Teflon whereas more metallic specimens do not. This is due to the permanent component which is negligible for the best quasicrystalline samples. It also indicated that the very thin oxide layer , which forms at ambient temperature in air just after polishing, does not change the surface energy and is not detectable. On the contrary, after ageing above 673 K, this layer grows thick enough and moves the surface wetting behavior to that of Al_2O_3 [51,114]. After such a treatment, the polar component of γ_S is far more important than for specimens kept at room temperature. It would presumably increase as well after corrosion tests or immersion in water. Surprisingly enough, the polar component of γ_S correlates with the density of Al-3p states measured by X-ray spectroscopy [42]. This effect, which was predicted some time ago [113], is observable only if the surface oxide is very thin, so as to allow an interaction with the liquid by tunneling (assuming that artifacts due to surface contamination were eliminated). Application is straightforward to coatings of

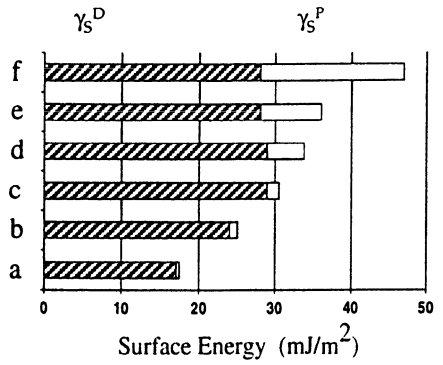

Fig. 26.10. Histograms of the surface energy components (black: dispersive term; white: polar contribution) measured with PTFE (*a*), a i-AlPdMn single grain (*b*), polycrystalline i-AlCuFe (*c*) and β-cubic AlCuFe (*d*), freshly polished fcc aluminium (*e*) and single crystalline alumina (*f*) (taken from [65] and [42])

polymer moulds, cooking utensils, chemistry reactors, etc, ... which require to keep the adherence of the reactants to the container surface as weak as possible for further demoulding, cleaning, etc, ...

When the surface oxide grows thick enough, wetting experiments show a trend typical of the pure alumina oxide. This has a dramatic influence not only on adhesion with liquids but also on solid–solid contact friction [124]. Multiple pass scratch tests [31], followed by a careful chemical determination of the composition of the oxide phases encountered in wear debris removed from the surface of a sintered i-AlCuFeB bulk specimen by a WC indentor, have shown that the cohesion of the quasicrystal–oxide interface plays a determining role in the weakness of the friction experienced with these materials [122]. Hence, the friction coefficient remains low in comparison to that of WC on to metallic alloys.

This is indeed an attractive feature which may be exploited for the purpose of reducing energy losses due to friction and wear between mechanical parts in contact with each other [2,34,83,93]. Characteristic friction coefficients fall in the range $\mu = 0.08$ to 0.15 for hard steel gliding on a $Al_{59}B_3Cu_{25.5}Fe_{12.5}$ icosahedral phase (Fig. 26.11) which presents an enhanced yield stress and slightly larger ductility as compared to the boron-free material [71]. With respect to diamond gliders, the friction figure is much lower and goes down to 0.04–0.05, i.e. close to the ploughing component one can calculate from the elastic characteristics of the contacting partners (no lubricant is involved) [128]. This is one order of magnitude below the friction of the same indentor on conventional Al-based alloys [73] and quite comparable to the friction of diamond onto itself [112].

The unavoidable presence of oxide at the surface of the samples as well as the brittle propagation of cracks make scratch tests very sensitive to preparation defects such as pores or inclusions. Coatings on mechanical parts are especially prone to such drawbacks as well and their technical exploitation in view of the reduction of friction and wear requires additional solutions to limit brittle damage. One such ingredient consists of mixing a small amount

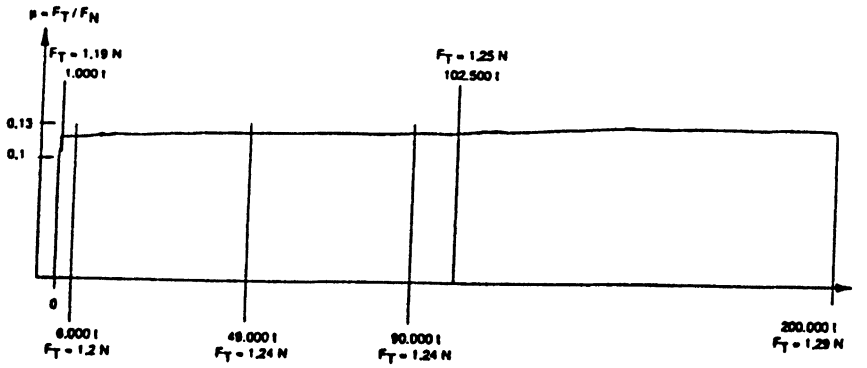

Fig. 26.11. Pin-on-disk chart curve recorded during a 6-hour run of a hard steel ball gliding on a i-$Al_{59}B_3Cu_{25.5}Fe_{12.5}$ finely polished coating (normal load: 10 N, diameter of the trace: 30 mm, relative velocity: 0.55 m/s, diameter of the indentor ball: 6 mm, 200 000 turns in total, no lubricant) (taken from [65])

of ductile Al-Fe intermetallic powder with the quasicrystal prior to projection [126]. Wear abrasion due to brittle spalling of particles is then very significantly reduced. To conclude this section, it is also worth mentioning that contact mechanical and adhesion properties of quasicrystals is not only a promising technological issue, actually considered by industrial companies [18,19], it also has deep relevance to the nature of so-called critical states at the surface of the quasicrystal. This was already alluded to in this section but the most outstanding result in this respect is provided by friction experiments of surface-clean, single grain i-AlPdMn specimens sliding on each other [53]. The measurement was done in the ultra-high vacuum of an Auger spectrometer after ion etching of the surfaces and thermal annealing. In these specific conditions, the friction coefficient is low, $\mu = 0.6$, whereas metals would simply stick. For instance, Ni(100) and Cu(111) single crystals give very high static friction $\mu \geq 4$ [52,96]. This is direct evidence that the electron wavefunctions (nearly) vanish at the surface of the quasicrystal if it is appropriately prepared.

It might also be inferred from these results that applications of quasicrystals which involve a surface property are very much dependent upon the preparation of that surface and its persistence upon ageing and/or reactivity with the environmental atmosphere. For instance, mechanical grinding is detrimental to the lattice perfection [15] but this operation is mandatory after plasma spraying in order to remove the roughness resulting from liquid droplets which have piled up, one after the other, on the substrate during the coating process. On the contrary, a very perturbed quasicrystalline surface may show an enhanced reactivity, a plausible explanation for the remarkable catalytic activity (Fig. 26.12) of ultra-fine quasicrystalline particles as compared to conventional Pd fine grains [101].

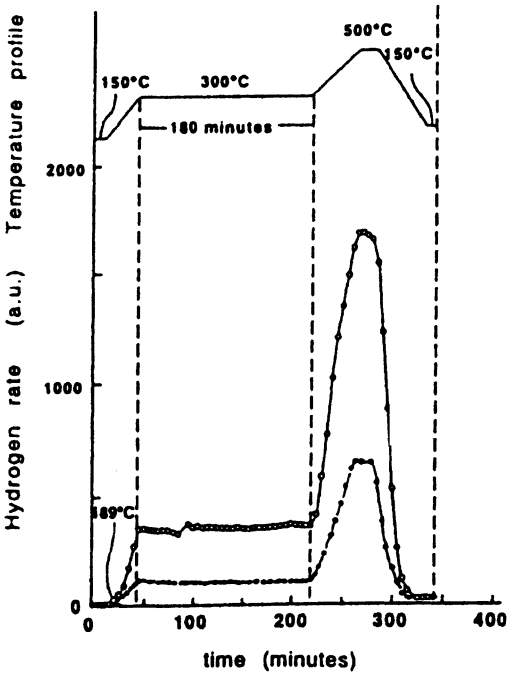

Fig. 26.12. Rate of hydrogen gas obtained through methanol cracking reaction (the temperature profile is indicated at the top of the figure) either with nanosized icosahedral Al-Pd powder (open symbols) or conventional Pd catalyst powder of comparable size (black symbols) (redrawn from [101])

26.6 Strengthening of Metallic Matrices

Several attempts have been made to incorporate quasicrystalline powders in soft metallic alloys in order to raise their yield strength and hardness. The most straightforward way is to homogenize and sinter powders of aluminium alloys and quasicrystal by ball-milling followed by hot pressing [135] or, taking the mixture as such, by sintering within the liquid–solid temperature range [143]. A substantial increase of the mechanical characteristics was observed with for instance hardness reaching 1200 MPa, i.e. twice as much as with SiC particles incorporated in the aluminium alloy at the same volume fraction, or friction being reduced (Fig. 26.13).

It is also possible to take advantage of the low surface tension of quasicrystals. Upon undercooling, for instance through atomization of the liquid alloy, quasicrystal grains nucleate and grow to a critical size that is proportional to the interface energy with the matrix. It was observed that the precipitate radius is typically less than 5 nm in Al-Li-Cu-Mg alloys [115]. It is even smaller in Al-Mn-Ce or Al-Mn-Co alloys prepared by atomization or melt-spinning techniques which impose severe cooling rates of the order of 10^6 Ks^{-1} or beyond [61]. Examination by HREM of such samples shows that finely dispersed nanoscale precipitates have grown up in an fcc-Al matrix, apparently free of grain boundaries. Crystaline precipitates of similar dimension are obtained when the matrix is amorphous. These two features,

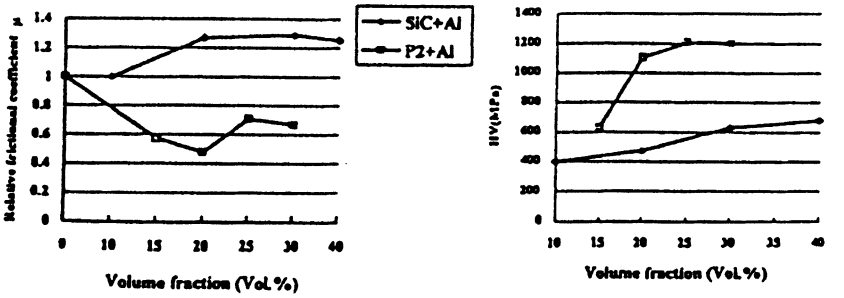

Fig. 26.13. Typical relative friction coefficient (left) and hardness (right) as functions of the volume fraction in an fcc aluminium matrix of a melt-spun $Al_{65}Cu_{20}Cr_{15}$ icosahedral alloy (P2) or of SiC powders. The samples were prepared by uniaxial hot pressing at Dalian Maritime University, China (Courtesy of Pr. Z.K. Hei and [143])

the extremely small size of the reinforcing particles and the cohesion of the matrix, make these alloys very valuable for the production of massive rods upon subsequent compaction of the powders by extrusion [77,92]. The tensile yield strength obtained so far with bulk samples is quite comparable to that of the best aeronautic alloys whereas the deformation at rupture is much larger (Fig. 26.14). Since the specific weight is the same, these alloys form

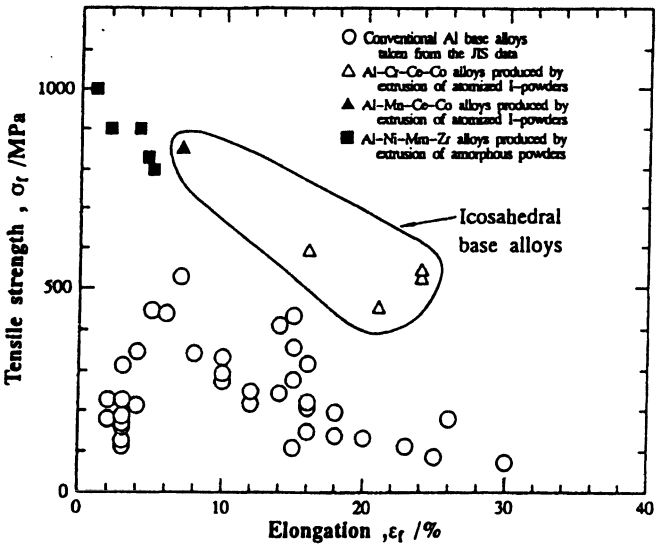
Conventional Al base alloys taken from the JIS data
Al-Cr-Ce-Co alloys produced by extrusion of atomized I-powders
Al-Mn-Ce-Co alloys produced by extrusion of atomized I-powders
Al-Ni-Mm-Zr alloys produced by extrusion of amorphous powders
Icosahedral base alloys
Tensile strength , σ_f /MPa
Elongation ,ε_f /%

Fig. 26.14. Room temperature tensile yield strength versus deformation at rupture obtained for industrial aluminium alloys (circles), extruded amorphous powders (squares) and quasicrystalline-containing materials (triangles). The best performing Al-based aeronautic alloy corresponds to the top-most circle (taken from [61])

a new, competitive family of light, high-strength materials that production industries should no longer ignore.

A precipitation and growth of icosahedral nuclei occurs as well during tempering of maraging steels [121]. Upon well-controlled annealing conditions, it was observed that the particles retain an icosahedral structure whereas they transform into Laves compounds at higher temperatures [105]. This material continuously hardens when it is annealed below 850 K for very long times, thus reaching a final hardness of more than 700 HV (Vickers units) and yield strength close to 3000 MPa. This maraging steel [129] is now available on the market as e.g. wires adapted to the fabrication of surgery tools, probably the first actually available application of quasicrystals.

Clearly enough, another way to benefit from the properties of bulk quasicrystals is to process them by sintering like technical ceramics [65]. Substantial progress has already been made in this direction in Nancy and Ames as demonstrated by the surface mechanical properties of sintered or isostatically pressed (HIP) specimens which were reported in the previous section. Applications are in the domain of small, net-shaped parts such as medical protheses [65].

26.7 Hydrogen Storage

Absorption and storage of hydrogen is of great importance for the availability of a non-polluent fuel which, when combined with oxygen, delivers energy in combustion engines, rejecting only water as a by-product. Also, it is the particle which transports electricity in batteries. It is therefore the focus of many R&D programs aimed at large-scale applications in the domain of domestic utilization, urban transport, robotics, etc, ... Different materials may be used for this purpose, ranging from liquid hydrogen, magnesium, intermetallic powders, etc, ... for storing hydrogen. In batteries, conducting polymers, rare earths, and intermetallic compounds are suitable like the old-fashioned, yet still very much in use, manganese or lead oxides. It has been demonstrated in recent years [75] that some icosahedral quasicrystals offer an alternative solution that may become very competitive if long-term cycling and reproducibly of the components are actually guaranteed [116].

The first example known so far of a quasicrystal suitable for hydrogen storage is the i-$Ti_{45}Ni_{17}Zr_{38}$ icosahedral phase and its C14 Laves approximant [116,138]. Right at the stoichiometric composition, the icosahedral phase seems to be stable [76]. Another example of hydrogen storage material was found more recently in Zr-Cu-Ni-Al glasses which transform upon annealing into nanosized quasicrystals [82]. This latter material is able to store hydrogen in large amounts, leading to a ratio of hydrogen to matrix atoms H/M larger than 1.6. In the Ti-Ni-Zr quasicrystal, the H/M ratio is the same or larger, depending on the loading method. For instance (Fig. 26.15), H/M = 1.7 was obtained thanks to loading in hydrogen gas at 500 K and pres-

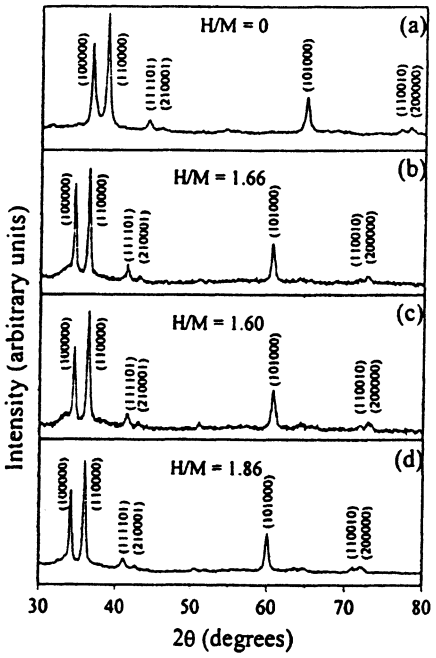

Fig. 26.15. Powder X-ray diffraction patterns of the as-quenched $Ti_{45}Ni_{17}Zr_{38}$ icosahedral phase (**a**), after hydrogen loading from gas phase at 500 K and 27 atm (**b**), after ball-miling in 5 atm H_2 at 300 K (**c**) and after electrolytic loading of hydrogen. (**d**) The saturation hydrogen to metal atom ratio is indicated (taken from [75])

sure of 27 atm. It reached nearly H/M = 1.9 with electrolytic loading in 5M KOH [75]. The hydrogen atom density was then 5.6 10^{22} H at/cm^3 of metal, a figure quite comparable to that of TiFe or $LaNi_5$ intermetallics after full H-absorption.

This density is larger than in liquid hydrogen. The crystalline approximant is not as good, with H/M $\approx$ 1 whereas the metallic glass gives H/M $\approx$ 0.15. The Y-Mg-Zn icosahedral phase also seems to be able to store hydrogen, yet seemingly with less performance [136]. The adsorption of such large amounts of hydrogen atoms induces important size expansion effects (Fig. 26.16) and disordering of the icosahedral lattice. It has been remarked that the storing is, at least partially, reversible and that the fraction of stable hydrides formed in the course of loading is small. The control of these properties is very

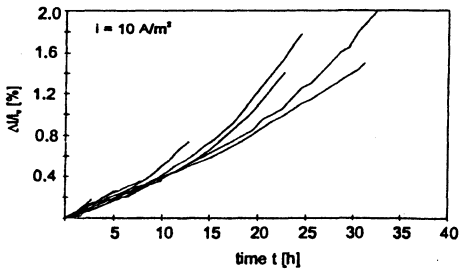

Fig. 26.16. Elongation of quasicrystalline $Zr_{69.5}Cu_{12}Ni_{11}Al_{7.5}$ samples measured *insitu* during loading in a 2:1 glycerine-phosphoric acid electrolyte at a current density of 10 A/m^2 (taken from [82])

much related to surface effects and requires additional solutions such as e.g. the plating of the surface with a thin Pd layer preventing oxidation [76]. If long-term recycling is indeed feasible, as these preliminary experiments hopefully indicate, then the preparation of energy storing demonstrators, and later the production of commercial batteries, will become a major issue for technological applications of quasicrystalline materials. The way to this end will however be long and difficult, starting with the hydrogen permeation problems encountered at the surface of the material. This is where the other storage media find their limit, especially with the requirements of long life time and perfect reproducibility of the devices.

26.8 At the Edge of a New Era in Quasicrystals Science

It took 12 years, from the initial publication of the existence of quasicrystals [119] to nowadays to establish the paradigm and reality of this new type of order in condensed matter [20]. This was the time of a revolution from which emerged a new crystallography and, owing to the fascinating properties that were discovered later, a completely renewed insight into condensed matter physics. Now, with these key issues settled, it appears necessary to explore the quasicrystal world in detail, within systematic investigations of phase diagrams, to establish the basics of this metallurgy and obtain a broad knowledge of all properties. Meanwhile, new quasicrystals with original properties will be discovered, not necessarily because the rules that govern their formation and stability will be better or fully understood but more probably thanks to accidents, good luck and mental preparation.

Science gets support nowadays only if some practical usefulness is manifest or at least potentially visible. With quasicrystals becoming useful in different respects, this quality is now rather well secured and we should aim more at a broad-ranging study of properties and applied physics than at the development of actual applications which are in other hands than ours. In this respect, the forthcoming decade will presumably be more characterized by tailoring the properties of known quasicrystalline alloys for technological purposes and by the emergence of process studies. On this way, the competition for raising not only research funds but simply interest will become harder as other subjects of more fashionable appearance also exhibit high-level scientific promise and potential applications. This represents a major change with respect to previous years. Presumably, are we thus right at the edge of a new era in quasicrystal science.

Acknowledgments

It is a pleasure to acknowledge many fruitful discussions over past and recent years with G. Beck, H. Begorre, E. Belin-Ferré, L. Bresson, J. Chevrier, F. Cyrot-Lackmann, C. Dong, T. Eisenhammer, T. Fujiwara, A.J. Gellman, A.I.

Goldman, D. Gratias, C. Janot, K.H. Kuo, R. Lück, B. Maudinas, U. Mizutani, F. Moreaux, H.U. Nissen, A. Sanchez-Pascual, D.J. Sordelet, Y. Sueur, C. Tadic, H.R. Trebin, P.A. Thiel, A.P. Tsai, K. Urban and the collaboration with the participants of the research project on aperiodic intermetallics in Nancy.

References

1. Agüero A., Algaba J.M., Alvarez J., Garcia de Blas F.J., Sanchez-Pascual A., Torre Albarsang M. de la and Vallés P., Proc. Int. Conf. on Metallurgical Coatings and Thin Films, San Diego (1997)
2. Anderson A.I., Ellis T., Goldman A.I., McCallum R.W., Shield J.E. and Sordelet D.J., US Patent no. 5433978 (1995)
3. Archambault P., in "New Horizons in Quasicrystals: Research and Applications", Goldman A.I., Sordelet D.J., Thiel P.A. and Dubois J.M. (Eds), World Scientific, Singapore (1997) p. 232
4. Bak P., Phys. Rev. Lett. 56 (1986) 861
5. Basov D.N., Timusk T., Barakat F., Greedan J. and Grushko B., Phys. Rev. Lett. 72-12 (1994) 1937.
6. Belin-Ferré E. and Dubois J.M., J. Phys. Cond. Matter 8 (1996), L717
7. Belin-Ferré E. (2002), see Chapter 17 of this book.
8. Berger C., Grenet T., Lindqvist P., Grieco J.C., Fourcaudot G. and Cyrot-Lackmann F., Sol. St. Comm. 87-11 (1993) 977
9. Berger C. in Lectures on Quasicrystals, Hippert F. and Gratias D. (Eds), Les Editions de Physique, Les Ulis (1994) p. 463
10. Bletry J., Colloque Français sur les Quasicristaux, Grenoble (1997), unpublished
11. Boissieu M. de, Boudard M., Bellissent R., Quilichini M., Hennion B., Currat R., Goldman A.I. and Janot C., J. Phys. Cond. Matter 5 (1993) 4945
12. Boissieu M. de, Boudard M., Hennion B., Bellissent R., Kycia S., Goldman A.I., Janot C. and Audier M., Phys. Rev. Lett. 75-1 (1995) 89
13. Boudard M., Boissieu M. de, Janot C., Heger G., Beeli C., Nissen H.U., Vincent H., Ibberson R., Audier M., Dubois J.M., J. Phys. Cond. Matter 4 (1992) 10149
14. Boudard M., Boissieu M. de, Letoublon A., Hennion B., Bellissent R. and Janot C., Europhysics Lett. 33(3) (1996) 199
15. Boudard M., Boissieu M. de, Simon J.P., Berar J.F. and Doisneau B., Phil. Mag. Lett. 74-6 (1996) 429
16. Bresson L. in Lectures on Quasicrystals, Hippert F. and Gratias D. (Eds), Les Editions de Physique, Les Ulis (1994) p. 549
17. Bresson L., Quivy A., Faudot F., Quiquandon M. and Calvayrac Y. in Proceedings of the 6th Int. Conf. on Quasicrystals, Takeuchi S. and Fujiwara T. (Eds), World Scientific, Singapore 1998, p. 211
18. Brite-Euram project no. 5188, contract no. BRE2-CT92-0171: "New metallic alloys for high performance thermal insulation and tribological applications"
19. Brite-Euram Project "Non Stick Coating of Mold Used for Composite ...", contract no. BR PR 960273

20. Cahn J.W. in Quasicrystals, Proceedings of the 5th Int. Conf. on Quasicrystals, Janot C., Mosseri R. (Eds), World Scientific, Singapore (1995), p. 807
21. Calvayrac Y., Quivy A., Bessière M., Lefebvre S., Cornier-Quiquandon M., Gratias D., J. Phys. France 51 (1990) 417
22. Carré A., in Phénomènes d'Interface, Agents de Surface, Briant J. (Ed.), Technip, Paris (1989) p. 93
23. Chang S.-L., Anderegg J.W. and Thiel P.A., J. Non Cryst. Sol. 195 (1996) 95
24. Chernikov M.A., Degiorgi L., Bernasconi A., Beeli C. and Ott H.R., Physica B 194 (1994) 405
25. Chernikov M.A., Bianchi A. and Ott H.R., Phys. Rev. B 51-1 (1995) 153; Chernikov M.A., Bianchi A., Müller H. and Ott H.R. in Quasicrystals, Proceedings of the 5th Int. Conf. on Quasicrystals, Janot C., Mosseri R. (Eds), World Scientific, Singapore (1995), p. 569; Chernikov M.A., Bianchi A., Felder E., Gubler U. and Ott H.R., Europhysics Lett. 35(6) (1996) 431
26. Chevrier J., Cappello G., Comin F. and Palmasi J.P., "New Horizons in Quasicrystals: Research and Applications", Goldman A.I., Sordelet D.J., Thiel P.A. and Dubois J.M. (Eds), World Scientific, Singapore (1997), p. 144; Chevrier J., Colloque Français sur les Quasicristaux, Grenoble (1997), unpublished
27. CNRS Info n^{c}*irc.* 196 (1990) 5; Le Monde 09-03-90 (1990); French Advances in Science and Technology 4-3 (1990) 3; Technology Review, January issue (1991) 19
28. Coddens G., Bellissent R., Calvayrac Y. and Ambroise J.P., Europhysics Lett. 16(3) (1991) 271; Coddens G., Ann. Chim. Fr. 18 (1993) 513
29. Cyrot-Lackmann F., Grenet T., Berger C., Fourcaudot G. and Gignoux C., French Patent no. 9503938 (1995)
30. Cyrot-Lackmann F. in "New Horizons in Quasicrystals: Research and Applications", Goldman A.I., Sordelet D.J., Thiel P.A. and Dubois J.M. (Eds), World Scientific, Singapore (1997) p. 216
31. Darbeida A., Stebut J. von, Assoul M. and Mignot J., Int. J. Mach. Tools Manufact. 35 (1995) 177
32. Dong C., Dubois J.M., Boissieu M. de, Boudard M. and Janot C., J. Mater. Res. 6 (1991) 2637
33. Dong C., Dubois J.M., Kang S.S. and Audier M., Phil. Mag. B 65-1 (1992) 107
34. Dubois J.M. and Weinland P., French Patent no. 8810559 (1988)
35. Dubois J.M. and Pianelli A., French Patent no. 9100549 (1991)
36. Dubois J.M., Archambault P. and Colleret B., French Patent no. 9115866 (1991); Dubois J.M. and Cathonnet P., French Patent no. 9215659 (1992)
37. Dubois J.M., Kang S.S. and Stebut J. von, J. Mat. Sc. Lett. 10 (1991) 537
38. Dubois J.M., Physica Scripta T49 (1993) 17; Dubois J.M., Kang S.S. and Perrot A., Mater. Sci. Eng. A179-180 (1994) 122
39. Dubois J.M., Kang S.S., Archambault P. and Colleret B., J. Mater. Res. 8 (1993) 38
40. Dubois J.M., Proner A., Bucaille B., Cathonnet P., Dong C., Richard V., Pianelli A., Massiani Y., Aït-Yaazza S., Belin-Ferré E., Ann. Chimie Fr. 19 (1994) 3
41. Dubois J.M. and Machizaud F., French Patent no. 9503939 (1995)
42. Dubois J.M., Plaindoux P., Belin-Ferré, E., Tamura N. and Sordelet D.J. in Proceedings of the 6th Int. Conf. on Quasicrystals, Takeuchi S. and Fujiwara T. (Eds), World Scientific, Singapore 1998, p. 733

43. Ebert P., Feuerbacher M., Tamura N., Wollgarten M. and Urban K., Phys. Rev. Lett. 77 (1996) 3827
44. Eisenhammer T. and Lazarov M., German Patent no. 4425140 (1994)
45. Eisenhammer T., Thin Solid Films, 270 (1995) 1
46. Eisenhammer T. and Trampert A., Phys. Rev. Lett. 78-2 (1997) 262
47. Eisenhammer T. in "New Horizons in Quasicrystals: Research and Applications", Goldman A.I., Sordelet D.J., Thiel P.A. and Dubois J.M. (Eds), World Scientific, Singapore (1997) p. 304
48. Feuerbacher M., Banfeld B., Rosenfeld R., Bartsch M., Hanke G., Beyos M., Wollgarten M., Messerschmidt U., Urban K., Phil. Mag. Lett. 71 (1995) 91
49. Fournée V., Belin-Ferré E. and Dubois J.M., J. Phys. Cond. Matter 10 (1998) 4231
50. Friedel J. and Denoyer F., C.R. Acad. Sci. Paris, 305-II (1987) 171
51. Gavatz M., Rouxel D., Pigeat P., Weber B. and Dubois J.M. in Proceedings of the 6th Int. Conf. on Quasicrystals, Takeuchi S.and Fujiwara T. (Eds), World Scientific, Singapore 1998, p. 765
52. Gellman A.J., J. Vac. Sci. Techn. A 10(1) (1992) 180
53. Gellman A.J., APS March 97 Meeting, Kansas City (1997); Ko J.S., Gellman A.J., Lograsso T.A.; Jenks C.J. and Thiel P.A., Surface Science 423 (1999) 243
54. Gierer M., Hove M.A. van, Goldman A.I., Shen Z., Chang S.-L., Jenks C.J., Zhang C.M. and Thiel P.A., Phys. Rev. Lett. 78(1997) 467
55. Gignoux C., PhD Thesis, Grenoble (1997)
56. Henley C.L., in "Quasicrystals: the State of the Art", Di Vicenzo D.P. and Steinhart P.J. (Eds), World Scientific, Singapore (1991), p. 429
57. Holland-Moritz D., Herlach D.M. and Urban K., Phys. Rev. Lett. 71 (1993) 1196
58. Honda Y., Edagawa K., Yoshioka A., Hashimoto T. and Takeuchi S., Japan J. Appl. Phys. 33 (1994) 4929
59. Industries et Techniques (1997), July issue: "Des quasicristaux dans un moteur d'avion" (Quasicrystals in an air-craft engine)
60. Inoue A., Masumoto T. and Nagahora J., Japanese Patent no. 20662692 (1992)
61. Inoue A., Kimura H. and Kita K. in "New Horizons in Quasicrystals: Research and Applications", Goldman A.I., Sordelet D.J., Thiel P.A. and Dubois J.M. (Eds), World Scientific, Singapore (1997) p. 256
62. Janot C. and Boissieu M. de, Phys. Rev. Lett. 72 (1994) 1674
63. Janot C., "Quasicrystals: a Primer", Oxford Science Pub., 2nd edition, Clarendon Press, Oxford (1994).
64. Janot C., Phys. Rev. B53 (1996) 181; J. Phys. Cond. Matter 9 (1997) 1493
65. Janot C. and Dubois J.M., "Les Quasicristaux: Matière à Paradoxes", Les Editions de Physique, Les Ulis (1997)
66. Janot C. in "New Horizons in Quasicrystals: Research and Applications", Goldman A.I., Sordelet D.J., Thiel P.A. and Dubois J.M. (Eds), World Scientific, Singapore (1997) p. 240
67. Jenks C.J., Pinhero P.J., Chang S.L., Anderegg J.W., Besser M.F., Sordelet D.J. and Thiel P.A. in "New Horizons in Quasicrystals: Research and Applications", Goldman A.I., Sordelet D.J., Thiel P.A. and Dubois J.M. (Eds), World Scientific, Singapore (1997) p. 157

68. Jenks C.J., Pinhero P.J., Shen Z., Lograsso T.A., Delaney D.W., Bloomer T.E., Chang S.-L., Zhang C.M., Anderegg J.W., Islam A.H., Goldman A.I. and Thiel P.A., in Proceedings of the 6th Int. Conf. on Quasicrystals, Takeuchi S. and Fujiwara T. (Eds), World Scientific, Singapore 1998, p. 741
69. Joulaud J.L., Bernardini J., Gas P., Bergman C., Dubois J.M., Calvayrac Y. and Gratias D., Phil. Mag. A 75-5 (1997) 1287
70. Kalugin P.A., Chernikov M.A., Bianchi A. and Ott H.R., Phys. Rev. 53 (1996) 14145
71. Kang S.S. and Dubois J.M., Phil. Mag. A 66-1 (1992) 151
72. Kang S.S. and Dubois J.M., J. Phys. Cond. Matter 4 (1992) 10169
73. Kang S.S., Dubois J.M. and Stebut J. von, J. Mater. Research 8 (1993) 2471
74. Kang S.S. and Dubois J.M., J. Mater. Research 10 (1995) 5
75. Kelton K.F., Viano A.M., Stroud R.M., Majzoub E.H., Gibbons P.C., Misture S.T., Goldman A.I., Kramer M.J. in "New Horizons in Quasicrystals: Research and Applications", Goldman A.I., Sordelet D.J., Thiel P.A. and Dubois J.M. (Eds), World Scientific, Singapore (1997) p. 272
76. Kelton K.F., Kim J.Y., Majzoub E.H., Gibbons P.C., Viano A.M. and Stround R.M., in Proceedings of the 6th Int. Conf. on Quasicrystals, Takeuchi S. and Fujiwara T. (Eds), World Scientific, Singapore 1998, p. 261
77. Kita K., Japanese Patent no. 24325392 (1992)
78. Klein T., Berger C., Mayou D. and Cyrot-Lackmann F., Phys. Rev. Lett. 66 (1991) 2907
79. Klein T. and Symko O.G., Appl. Phys. Lett., 64-4 (1994) 431
80. Klein T. and Symko O.G., Phys. Rev. Lett. 73-16 (1994) 2248
81. Kleiter S., Rapport EEIGM (1997), unpublished
82. Köster U., Zander D., Meinhardt J., Eliaz N. and Eliezer D. in Proceedings of the 6th Int. Conf. on Quasicrystals, Takeuchi S. and Fujiwara T. (Eds), World Scientific, Singapore 1998, p. 313
83. Kreider K.G., US Patent no. 6553087 (1987)
84. Ledieu J., Muntz A.W., Parker T.M. McGrath R., Diehl R.D., Delaney D.W. and Lograsso T.A., in Quasicrystals, Mat. Res. Soc., Symp. Proc., Vol. 553 (Materials Research Society, Warrendale, 1999)
85. Legault S., Ellman B., Ström-Olsen J., Taillefer L., Lograsso T. and Delaney D. in Proceedings of the 6th Int. Conf. on Quasicrystals, Takeuchi S. and Fujiwara T. (Eds), World Scientific, Singapore 1998, p. 475
86. Le Lann A. and Devaud J. in Quasicrystals, Proceedings of the 5th Int. Conf. on Quasicrystals, Janot C., Mosseri R. (Eds), World Scientific, Singapore (1995) p. 672
87. Li X.Z., Dong C. and Dubois J.M., J. Appl. Cryst. 28 (1995) 96
88. Lin C.R., Chou S.L. and Lin S.T., J. Phys. Cond. Matter 8 (1996) L725
89. Lyonnard S., Coddens G., Hennion B. and Calvayrac Y. in Proceedings of the 6th Int. Conf. on Quasicrystals, Takeuchi S.and Fujiwara T. (Eds), World Scientific, Singapore 1998, p. 463
90. Massiani Y., Aït-Yaazza S., Crouzier J.P. and Dubois J.M., J. Non Cryst. Sol. 159 (1993) 92
91. Massiani Y., Aït-Yaazza S., Crouzier J.P. and Dubois J.M., Matériaux et Techniques 3-4 (1996) 39; Massiani Y., Aït-Yaazza S. and Dubois J.M. in Quasicrystals, Proceedings of the 5th Int. Conf. on Quasicrystals, Janot C., Mosseri R. (Eds), World Scientific, Singapore (1995), p. 790

92. Masumoto T., Inoue A., Watanabe M., Nagahora J. and Shibata T., Japanese Patent no. 6256692 (1992)
93. Masumoto T., Inoue A., Kimura H., Shinohara Y., Horio Y. and Kita K., Japanese Patent no. 5914594 (1994)
94. Mayou D. in Lectures on Quasicrystals, Hippert F. and Gratias D. (Eds), Les Editions de Physique, Les Ulis (1994) p. 417
95. Mayou D., Roche S., Trambly de Laissardière G., Berger C., Gignoux C. in Proceedings of the 6th Int. Conf. on Quasicrystals, Takeuchi S. and Fujiwara T. (Eds), World Scientific, Singapore 1998, p. 555
96. McFadden C.F. and Gellman A.J., Langmuir 11 (1995) 273
97. Mikulla R., Krul F., Gumbsch P. and Trebin H.R. in "New Horizons in Quasicrystals: Research and Applications", Goldman A.I., Sordelet D.J., Thiel P.A. and Dubois J.M. (Eds), World Scientific, Singapore (1997) p. 200
98. Moreaux F., Chevrier J.C. and Beck G., Int. J. Multiphase Flow 2 (1975) 183
99. Naumovic D., Aebi P., Schlapbach L. and Beeli C. in "New Horizons in Quasicrystals": Research and Applications, Goldman A.I., Sordelet D.J., Thiel P.A. and Dubois J.M. (Eds), World Scientific, Singapore (1997) p. 86
100. "New Horizons in Quasicrystals: Research and Applications", Goldman A.I., Sordelet D.J., Thiel P.A. and Dubois J.M. (Eds), World Scientific, Singapore (1997)
101. Nosaki K., Masumoto T., Inoue A. and Yamaguchi T., Japanese Patent no. 26559193 (1993)
102. Perrot A., Dubois J.M., Cassart M. and Issi J.P. in Quasicrystals, Proceedings of the 5th Int. Conf. on Quasicrystals, Janot C., Mosseri R. (Eds), World Scientific, Singapore (1995), p. 588
103. Perrot A., PhD Thesis, Nancy (1997)
104. Pierce F.S., Guo Q. and Poon S.J., Phys. Rev. Lett. 73-16 (1994) 2220
105. Ping Liu, Stigenberg A.H. and Nilsson J.O., Acta Metall. Mater. 43-7 (1995) 2881
106. Pinhero P.J., Chang S.-L., Anderegg J.W. and Thiel P.A., Phil. Mag. B 75-2 (1997) 271
107. Poon S.J., Adv. Phys. 41 (1992) 303
108. Prutton M., Introduction to Surface Physics, Oxford Science Pub., Oxford (1994)
109. Quilichini M. and Janssen T., Rev. Modern Phys. 69-1 (1997) 277
110. Quiquandon M., Quivy A., Devaud J., Faudot F., Lefebvre S., Bessière M., Calvayrac Y., J., Phys. Cond. Matter 8 (1996) 2487
111. Quivy A., Quiquandon M., Calvayrac Y., Faudot F., Gratias D., Berger C., Brand R.A., Simonet V., Hippert F., J. Phys. Cond. Matter 8 (1996) 4223
112. Ravch A., Martinn L., Hawthorne H.M. and Wertheimer M.R., Surfc. Coatings Techn. 58 (1993) 45
113. Rivier N. in "New Horizons in Quasicrystals: Research and Applications", Goldman A.I., Sordelet D.J., Thiel P.A. and Dubois J.M. (Eds), World Scientific, Singapore (1997) p. 138; J. Non Cryst. Sol., 153-154 (1993) 458
114. Rouxel D., Gavatz M., Pigeat P., Weber B. and Plaindoux P., "New Horizons in Quasicrystals: Research and Applications", p. 173
115. Sainfort P. and Dubost B., 4th Int. Conf. on Al-Li, Paris (1987), see ref. 112
116. Sawa T., Inaba T. and Takahashi Y., Japanese Patent no. 32437393 (1993)
117. Schaub T.M., Bürgler D.E., Güntherodt H.J. and Suck J.B., Phys. Rev. Lett. 73 (1994) 1255

118. Schaub T.M., Colloque Français sur les Quasicristaux, Grenoble (1997), unpubl. and APS March 97 Meeting, Kansas City (1997)
119. Shechtman D., Blech I., Gratias D. and Cahn J.W., Phys. Rev. Lett. 53 (1984) 1951
120. Shen Z., Jenks C.J., Anderegg J.W., Delaney D.W., Lograsso T.A., Thiel P.A. and Goldman A.I., Phys. Rev. Lett. 78-6 (1997) 1050
121. Sidhom H. and Portier R., Phil. Mag. Lett. 59-3 (1989) 131
122. Singer I.L., Dubois J.M., Soro J.M., Rouxel D. and Stebut J. von, in Proceedings of the 6th Int. Conf. on Quasicrystals, Takeuchi S. and Fujiwara T. (Eds), World Scientific, Singapore 1998, p. 769
123. Sire C., in Lectures on Quasicrystals, Hippert F. and Gratias D. (Eds), Les Editions de Physique, Les Ulis (1994) p. 505
124. Sordelet D.J., Kramer M.J., Andersson I.E. and Besser M.F. in Quasicrystals, Proceedings of the 5th Int. Conf. on Quasicrystals, Janot C., Mosseri R. (Eds), World Scientific, Singapore (1995), p. 778
125. Sordelet D.J., Besser M.F. and Anderson I.E., J. Thermal Spray Techn., 5 (1996) 161
126. Sordelet D.J., Bloomer T.A., Kramer M.J. and Unal O., J. Mat. Sci. Lett. 15 (1996) 935
127. Soro, J.M., Comte C., Hunn Loi T., Billard A. and Stebut J. von, ICMCTF San Diego (2000) in press
128. Stebut J. von, Strobel C. and Dubois J.M. in Quasicrystals, Proceedings of the 5th Int. Conf. on Quasicrystals, Janot C., Mosseri R. (Eds), World Scientific, Singapore (1995), p. 704
129. Stigenberg A.H., Nilsson J.O. and Ping Liu, Swedish Patent no. 9303280 (1993)
130. Takeuchi T. and Mizutani U., Phys. Rev. B 52-13 (1995) 9300
131. Takeda M., Tamura R., Sakairi Y. and Kimura K. in Proceedings of the 6th Int. Conf. on Quasicrystals, Takeuchi S. and Fujiwara T. (Eds), World Scientific, Singapore 1998, p. 571
132. Tamura R., Waseda A., Kimura K. and Ino H., Phys. Rev. B 50-13 (1994) 9640
133. Traverse A., Dumoulin L., Belin E. and Senemaud C., in Quasicrystalline Materials, Janot C. and Dubois J.M. (Eds), World Scientific, Singapore (1988), p. 399
134. Tsai A.P., Tsurni T., Memezawa A., Aoki K., Inoue A. and Masumoto T., Phil. Mag. Lett. 67-6 (1993) 393
135. Tsai A.P., Aoki K., Inoue A. and Masumoto T., J. Mater. Research 8 (1993) 5
136. Tsai A.P., Niikura A., Inoue A. and Masumoto T. in Quasicrystals, Proceedings of the 5th Int. Conf. on Quasicrystals, Janot C., Mosseri R. (Eds), World Scientific, Singapore, (1995), p. 628; Tsai A.P., Niikura A., Aoki K. and Masumoto T., Int. Conf. on Metal Hydrides (1996), unpublished
137. Urban K., APS March 97 Meeting, Kansas City (1997) unpublished
138. Viano A.M., Stroud R.M., Gibbons P.C., McDowell A.F., Conradi M.S. and Kelton K.F., Phys. Rev. B 51-17 (1995) 12026
139. Vigneron B., Perrot A., Machizaud F., Dubois J.M., Jeandel G. and Wyncke B., Phil. Mag. Lett. B 77-3 (1998) 849
140. Wagner J.L., Wong K.M. and Poon S.J., Phys. Rev. B 39-12 (1989) 8091

141. Wehner B.I. and Köster U. in Proceedings of the 6th Int. Conf. on Quasicrystals, Takeuchi S. and Fujiwara T. (Eds), World Scientific, Singapore 1998, p. 773
142. Yoshioka A., Edagawa K., Kimura K. and Takeuchi S., Japan J. Appl. Phys. 34 (1995) 1606
143. Yuhong Q., Zhanping Z., Zukun H. and Dong C., unpublished report, Dalian University Techn. (1997)

A Further Reading: Literature on Quasicrystals

Michael Baake and Uwe Grimm

In what follows, we list further references on quasicrystals and related topics. In view of the vast body of literature, we restrict ourselves to books and proceedings, plus some of the reviews not already contained in the former. Some extra comments on the content of books are included if their titles do not speak for themselves. This is meant to facilitate potential search for those readers who want or need more, but, at the end of this book, (hopefully) know what type of literature they are after.

Further information – in particular, on research groups and their current work – can, to a large extent, be found on the world wide web (e.g. one can search for keywords such as "quasicrystals", "tilings", etc. with the familiar Internet search engines – but be aware that you may have to work your way through zillions of links before you really find what you are looking for).

References

Amann, A., Cederbaum, L., Gans, W. [Eds.] (1988): *Fractals, Quasicrystals, Chaos, Knots and Algebraic Quantum Mechanics.* (NATO ASI Series C: Mathematical and Physical Sciences, vol. 235) Kluwer, Dordrecht
Proceedings of a NATO Advanced Study Institute on New Theoretical Concepts in Physical Chemistry, Acquafredda di Maratea, Italy (1987).

Axel, F., Denoyer, F., and Gazeau, J.-P. [Eds.] (2000): *From Quasicrystals to More Complex Systems.* Springer, Berlin; EDP Sciences, Les Ulis
Proceedings of a summer school at Les Houches, France (1998).

Axel, F., Gratias, D. [Eds.] (1995): *Beyond Quasicrystals.* Springer, Berlin; Les Editions de Physique, Les Ulis
Proceedings of a summer school at Les Houches, France (1994), with review articles mainly on theoretical and mathematical issues.

Baake, M. [Ed.] (1993): *Selected Topics in the Theory of Quasicrystals.* Int. J. Mod. Phys. B **7**, nos. 6–7 (special issue). World Scientific, Singapore
Collection of theoretical research articles dedicated to Peter Kramer on the occasion of his 60th birthday.

Baake, M., Moody, R.V. [Eds.] (2000): *Directions in Mathematical Quasicrystals.* (CRM Monograph Series, vol. 13) American Mathematical Society, Providence, RI

J.-B. Suck et al. (eds.), *Quasicrystals*
© Springer-Verlag Berlin Heidelberg 2002

A collection of invited mathematical articles on the present state of the art, originating from a meeting in Oberwolfach, Germany (1998).

Belin-Ferré, E., Berger, C., Quiquandon, M., Sadoc, A. [Eds.] (2000): *Quasicrystals – Current Topics.* World Scientific, Singapore
Proceedings of the Spring School on Quasicrystals, held at Aussois, France (1999).

Bellissard, J., Bovier, A., Ghez, J.M. (1992): Gap labelling theorems for one-dimensional discrete Schrödinger operators. Rev. Math. Phys. **4** 1–37

Boissieu, M. de, Verger-Gaugry, J.-L., Currat, R. [Eds.] (1998): *Aperiodic '97.* World Scientific, Singapore
Proceedings of the International Conference on Aperiodic Crystals, Alpe d'Huez, France (1997).

Böttger, H., Kasner, G. (1991): Quasicrystals. Phys. Stat. Sol. (b) **164** 11–38

Chapuis, G., Paciorek, W. [Eds.] (1995): *Aperiodic '94.* World Scientific, Singapore
Proceedings of the International Conference on Aperiodic Crystals, Les Diablerets, Switzerland (1994).

Corbel, C. [Ed.] (1996): *Les intermétalliques: des superalliages aux quasicristaux.* J. de Physique IV **6** Coll. C2. Les Editions de Physique, Les Ulis
Proceedings of the 38ème Colloque de Métallurgie de l'INSTN at Saclay, France (1995).

DiVincenzo, D.P., Steinhardt, P.J. [Eds.] (1991): *Quasicrystals: The State of the Art.* (Directions in Condensed Matter Physics, vol. 11) World Scientific, Singapore
Collection of original review articles. The second edition (1999) contains some short updating notes by the authors as well as two new chapters.

Doebner, H.-D., Scherer, W., Schulte, C. [Eds.] (1997): *GROUP 21 – Physical Applications and Mathematical Aspects of Geometry, Groups, and Algebras*, vol. 2. World Scientific, Singapore
Proceedings of the XXI International Colloquium on Group Theoretical Methods in Physics, Goslar, Germany (1996). These contain a section on Crystallography and Aperiodical Order (pp. 937–1002).

Dubois, J.-M. (2001): *Useful Quasicrystals.* World Scientific, Singapore (to appear)

Farkas-Jahnke, M., Pai, E. [Eds.] (1993): *Modulated Structures, Polytypes and Quasicrystals.* Phase Transitions B **43&44** (special issue). Gordon and Breach, Yverdon
Proceedings of an International Conference (MOSPOQ '91) in Balatonszeplak, Hungary.

Fujiwara, T., Ogawa, T. [Eds.] (1990): *Quasicrystals.* (Springer Series in Solid-State Sciences, vol. 93) Springer, Berlin
Proceedings of the 12th Taniguchi Symposium, held at Shima, Mie Prefecture, Japan (1989).

Gähler F., Kramer P., Trebin H.-R., Urban K. (2000): *Proceedings of the 7th International Conference on Quasicrystals.* Mat. Sci. Eng. A **294–296** (special issue)
Proceedings of a conference held in Stuttgart, Germany (1999).

Godrèche, C. [Ed.] (1988): *Du cristal à l'amorphe.* Les Editions de Physique, Les Ulis
Proceedings of a workshop with articles in French and in English.

Goldman, A.I., Kelton, K.F. (1993): Quasicrystals and crystalline approximants. Rev. Mod. Phys. **65** 213–230

Goldman, A.I., Sordelet, D.J., Thiel, P.A., Dubois, J.-M. [Eds.] (1997): *New Horizons in Quasicrystals – Research and Applications.* World Scientific, Singapore
Proceedings of an application-oriented meeting in Ames, Iowa (1996).

Gratias, D., Michel, L. [Eds.] (1986): *International Workshop on Aperiodic Crystals.* J. de Physique **47**, Coll. C3, suppl. 7. Les Editions de Physique, Les Ulis
Proceedings of a workshop held at Les Houches, France (1986).

Grimm, U., Scheffer, M., *Incommensurate Crystals and Quasicrystals*, Encyclopedia of Physical Science and Technology, 3rd ed., edit. Robert A. Meyers, Academic Press, San Diego 7 (2001) 731–750.

Grünbaum, B., Shephard, G.C. (1987): *Tilings and Patterns.* W.H. Freeman, New York
The tiling bible.

Guyot, P., Kramer, P., de Boissieu, M. (1989): Quasicrystals. Rep. Prog. Phys. **54** 1373–1425

Hargittai, I. [Ed.] (1990): *Quasicrystals, Networks, and Molecules of Fivefold Symmetry.* VCH Publishers, New York
Collection of original review articles.

Hargittai, I. [Ed.] (1992): *Fivefold Symmetry.* World Scientific, Singapore
Ancient patterns, and a lot of cultural and natural background.

Hippert, F., Gratias, D. [Eds.] (1994): *Lectures on Quasicrystals.* Les Editions de Physique, Les Ulis
Proceedings of a winter school at Aussois, France (1994), with articles on experimental and theoretical aspects of quasicrystals.

Janot, C. (1994): *Quasicrystals: A Primer* (2nd edition). Clarendon Press, Oxford
The physical primer.

Janot, C., Dubois, J.M. [Eds.] (1988): *Quasicrystalline Materials.* World Scientific, Singapore
Proceedings of the ILL/CODEST Workshop, Grenoble, France (1988).

Janot, C., Dubois, J.M. (1998): *Les quasicristeaux – matière à paradoxes.* EDP Sciences, Les Ulis

Janot, C., Mosseri, R. [Eds.] (1995): *Quasicrystals.* World Scientific, Singapore
Proceedings of the 5th International Conference on Quasicrystals, Avignon, France (1995).

Janssen, T. (1988): Aperiodic Crystals: A Contradictio in Terminis? Phys. Rep. **168** 55–113

Jarić, M.V. [Ed.] (1988): *Introduction to Quasicrystals.* (Aperiodicity and Order, vol. 1) Academic Press, San Diego
First volume of a book series with invited review articles on quasicrystals.

Jarić, M.V. [Ed.] (1989): *Introduction to the Mathematics of Quasicrystals.* (Aperiodicity and Order, vol. 2) Academic Press, San Diego

Jarić, M.V., Gratias, D. [Eds.] (1989): *Extended Icosahedral Structures.* (Aperiodicity and Order, vol. 3) Academic Press, San Diego

Jarić, M.V., Lundqvist, S. [Eds.] (1990): *Quasicrystals.* World Scientific, Singapore
Proceedings of the Anniversary Adriatico Research Conference, Trieste, Italy (1989).

Kelton, K.F., Gibbons, P.C., Goldman, A.I. [Eds.] (1993): *Quasicrystals 4.* J. Non-Cryst. Solids **153&154** (special issue). North-Holland, Amsterdam
Proceedings of the Fourth International Conference on Quasicrystals, St. Louis, Missouri (1992).

Kuo, K.H. [Ed.] (1987): *Quasicrystals.* (Materials Science Forum, vols. 22–24) Trans Tech Publications, Aedermannsdorf
Proceedings of an International Workshop on Quasicrystals, Beijing, China (1987).

Kuo, K.H., Ninomiya, T. [Eds.] (1991): *Quasicrystals.* World Scientific, Singapore
Proceedings of China-Japan Seminars in Tokyo (1989) and Beijing (1990).

Kuo, K.H., Takeuchi, S. [Eds.] (1994): *Quasicrystals and Imperfectly Ordered Crystals.* (Materials Science Forum, vols. 150–151) Trans Tech Publications, Aedermannsdorf
Proceedings of an International Symposium in Chengde, China (1993).

Loreto, L., Ronchetti, M. [Eds.] (1990): *Topics on Contemporary Crystallography and Quasicrystals.* Per. Mineral. **LIX**, nos. 1–3 (special issue)
Contains an extensive bibliography on quasicrystals until 1991 (pp. 219–257).

Luck, J.-M., Moussa, P., Waldschmidt, M. [Eds.] (1990): *Number Theory and Physics.* (Springer Proceedings in Physics, vol. 47) Springer, Berlin
Part II (pp. 77–137) deals with quasicrystals and related geometrical structures.

Meyer, Y. (1972): *Algebraic Numbers and Harmonic Analysis.* North-Holland, Amsterdam
Many results on the structure of quasiperiodic point sets are already contained in this book because they are special cases of Meyer's harmonious sets. A classic.

Miękisz J. (1993): *Quasicrystals. Microscopic models on nonperiodic structures.* Leuven University Press, Leuven
Models with energy-minimizing aperiodic ground-state configurations are constructed and investigated.

Moody, R.V. [Ed.] (1997): *The Mathematics of Long-Range Aperiodic Order.* (NATO ASI Series C: Mathematical and Physical Sciences, vol. 489) Kluwer, Dordrecht
Proceedings of a NATO Advanced Study Institute at the Fields Institute, Waterloo, Canada (1995). Summary of the present mathematical knowledge of the field, first part.

Pandey, D., Vinod, K., Wadhawan, V.K. [Eds.] (1989): *Modulated Structures, Polytypes and Quasicrystals.* Phase Transitions **16&17** (special issue). Gordon and Breach, New York
Proceedings of an international conference (MOSPOQ '88) in Varanasi, India.

Patera, J. [Ed.] (1998): *Quasicrystals and Discrete Geometry.* (Fields Institute Monographs, vol. 10) American Mathematical Society, Providence, RI
Invited research articles from a long-term research program at the Fields Institute, Toronto, Canada (1995). Summary of the present mathematical knowledge of the field, second part.

Pérez-Mato, J.M., Zúñiga, F.J., Madariga, G. [Eds.] (1991): *Methods of Structural Analysis of Modulated Structures and Quasicrystals.* World Scientific, Singapore
Proceedings of an international workshop in Lekeitio-Bilbao, Spain (1991).

Pokrovsky, V., Uimin, G. (1993): *Modulated Structures: Commensurate, Incommensurate, Stochastic Structures and Quasicrystals.* (Series on Modern Condensed Matter Physics, vol. 3) World Scientific, Singapore

Poon S.J. (1992): Electronic properties of quasicrystals: An experimental review. Adv. in Phys. **41** 303–363

Quilichini, M., Janssen, T. (1997): Phonon excitations in quasicrystals. Rev. Mod. Phys. **69** 277–314

Radin C. (1999): *Miles of Tiles.* American Mathematical Society, Providence, RI
Short introductory textbook focussing particularly on 'pinwheel' or 'quaquaversal' tilings that are invariant under infinite rotation groups.

Ranganathan S., Chattopadhyay K., Singh A., Kelton K.F. (1997): Decagonal quasicrystals. Prog. Mater. Sci. **41** 195–240

Schulz-Baldes H., Bellissard J. (1998): Anomalous transport: A mathematical framework. Rev. Math. Phys. **10** 1–46

Scott, J.F., Clark, N.A. (1987): *Incommensurate Crystals, Liquid Crystals and Quasi-crystals.* (NATO ASI Series B, vol. 166) Plenum Press, New York
Proceedings of a NATO Advanced Research Workshop in Boulder, Colorado (1986).

Senechal, M. (1995): *Quasicrystals and Geometry.* Cambridge University Press, Cambridge; corrected reprint (1997)
The geometric primer.

Sordelet, D.J., Dubois, J.M. [Eds.] (1997): *Quasicrystals.* MRS Bulletin **22** no. 11
Collection of articles on metallurgy, physical properties and potential applications of quasicrystals.

Stadnik Z.M. [Ed.] (1999): *Physical Properties of Quasicrystals.* (Springer Series in Solid-State Sciences, vol. 126) Springer, Berlin
Collection of articles on physical properties of quasicrystals with an emphasis on experimental results.

Steinhardt, P.J., Ostlund, S. [Eds.] (1987): *The Physics of Quasicrystals.* World Scientific, Singapore
Reprint volume which contains many of the early articles until 1987.

Steurer W. (1990): The structure of quasicrystals. Z. Kristall. **190** 179–234

Steurer, W. (1996): The Structure of Quasicrystals. In: *Physical Metallurgy,* vol. I. Ed. by R.W. Cahn and P. Haasen. Elsevier, Amsterdam, pp. 371–411

Takeuchi, S., Fujiwara, T. [Eds.] (1998): *Proceedings of the 6th International Conference on Quasicrystals.* World Scientific, Singapore
Proceedings of a conference held in Tokyo, Japan (1997).

Tolédano, P., Dmitriev, V. (1996): *Reconstructive Phase Transitions in Crystals and Quasicrystals.* World Scientific, Singapore

Yacamán, M.J., Torres, M. [Eds.] (1993): *Crystal-Quasicrystal Transitions.* North-Holland, Amsterdam
Collection of invited research and review articles.

Yacamán, M.J., Romeu, D., Castaño, V., Gómez, A. [Eds.] (1990): *Quasicrystals and Incommensurate Structures in Condensed Matter.* World Scientific, Singapore
Proceedings of the Third International Meeting on Quasicrystals, Vista Hermosa, Mexico (1989).

Yamamoto, A. (1996): Crystallography of Quasiperiodic Crystals. *Acta Cryst.* A **52** 509–560.

Index

α-AlMnSi 145
α-AlCuFe 322
α-AlMnSi 322
α-AlSiCuFe 323
β-Al_3Mg_2 152
δ-Al_3Ni_2 120
ϵ-Al_3Pd 120
$\gamma_2Al_8Cr_5$ 120
γ-Al_2Cu_3 353
λ-$Al_{13}Fe_4$ 352
ω-Al_7Cu_2Fe 352
ω-Al_7Cu_2Fe 323
ϕ-$Al_{10}Cu_{10}Fe$ 353
σ-phase 150
θ-Al_2Cu 352
ζ-Al_3Cu_4 353
$(\boldsymbol{Q}, \omega)$ space 439
"parent" crystal 10
$\mathbb{Z}$-module 69
3D quasilattice 9
6D models 108
6D periodic Bravais lattices 94

A15 structure 150
Abbé Principle 121
absolutely continuous spectrum 393, 433
absorption spectroscopy 327
acceptance domain 26, 58, 59, 135, 140, 207
acoustic mode 407, 430
acoustic phonons 418, 441
activation 324
– area 308
– barrier 235
– distance 307
– enthalpy 308, 309, 311, 315
– entropy 308
– volume 308, 315, 316
additional contrast 104
aggregation 199, 206
AKK-rhombohedra 117, 118, 140, 147
AKK-tiling 140, 147
Al_3Ni_2 121
AlCoCu 117, 126, 154, 156, 159
AlCoCuSi 126
AlCoNi 115, 117, 119, 120, 126, 130–134, 137–139, 153, 155, 156, 221, 227, 341
AlCrCu 117
AlCu 353
AlCuCo 119, 254, 301, 396, 413–417
AlCuCoSi 280, 281, 293, 299, 301, 303
AlCuFe 115, 119, 141, 143–146, 251, 321, 340, 350, 368
AlCuFeSi 324
AlCuLi 115, 117, 119, 139–141, 145, 146, 396, 399, 405, 413, 418
AlCuRu 347
AlCuTM 117
AlFe 353
AlFeGeMn 117
AlFeNi 117
AlGaMgZn 323
AlLiCu 225
AlMg 152
AlMgPd 117
AlMn 115, 116, 120, 355, 357, 406–408, 416, 418
AlMnPd 115, 117, 119, 120, 126–129, 139, 141, 145, 146, 155, 156, 158, 221, 251
AlMnPdSi 146, 147
AlMnSi 119, 145, 151, 322
almost periodic functions 24
AlNiCo 418

AlNiRh 355
AlNiRu 117
AlPdMn 225, 293, 298, 302, 321, 342, 350, 352, 396, 399, 406, 411, 413, 416, 418
AlPdRe 117, 321, 323, 335, 358, 359, 415, 416, 418
AlPdTM 117
AlRu 324, 358, 359
AlTM 119
aluminium top layer 519
AlZnMg 172
Ammann tiling 280, 295, 296
Ammann–Beenker tiling 19, 59
Ammann–Kowalevski–Kramer rhombohedra 117
Ammann–Kramer tiling 29
amorphous 116, 229, 230, 291, 344, 352, 358–360, 366, 369, 376
– alloys 472
– system 199
amplitude phase diagram (APD) 269
amplitudons 426
anelastic properties 305
angular resolved photoemission spectroscopy 342
angular straggling 290, 291
anisotropy 333, 334, 417, 418, 459
anisotropy of the dispersion 443
annealing experiments 313
annealing out the defects 462
annealing out of phasons 480
anomalous
– diffusion 321, 326, 328, 334
– Hall effect 488
– quantum diffusion 326
– transport 322, 323, 326, 329
– transport properties 415
anti-Penrose tiling 62
antibonding states 495
antiphase domains 130
aperiodic 423
aperiodic tiling of the plane 5
applications 507
approximant 129, 130, 140, 145, 146, 154, 230, 321–324, 326, 328, 342, 348, 351–353, 394, 397, 408, 411, 416, 428, 431, 446, 481, 502, 508
– phase 210
– structures 209
atom cluster 130, 131
atom density 285
atomic
– domain 195
– hypersurfaces 58, 263, 274
– movement 338
– order 488
– plane 287, 294
– position 200, 209, 215
– row 286, 294
– scattering factor 80
– surface 59, 72, 89, 253, 423, 480
– transport 338, 360
autocorrelation 21, 330
average
– electron density 510, 512
– icosahedral lattice 511
– potential 288
– structure 118, 141, 142, 145
averaged dispersion curves 462
Avrami exponent 477
axial channeling 283, 285, 289, 290
axial stress 306

backscattering yield 285, 291, 292, 295
ball milling 230
band energy 503
basic building units 7
basic clusters 509
Beer–Lambert law 344
Bergmann cluster 7, 146, 147, 158
BiMn 148
binary tiling 146, 254, 258, 259
bipartite 382, 389
Bloch
– function 424
– spectral function 401, 403, 405, 411, 413
– states 326
– theorem 27, 397
– wave 436
– wave method 123
– wave representation 441
Bloch–Boltzmann approximation 332
Bloch–Boltzmann conductivity 328
block diagonalization 399
blocking 286, 298

body centered 94
Boltzmann factor 213
Boltzmann transport theory 416
bond directions 13
bond orientation correlation function 13
bond-orientational order 118
bond-oriented glass 211
Bose factor 451
Bose thermal factors 440
box function 138
Bragg
– peak 20, 92, 116, 209, 352, 406
– plane orientations 272
– reflection 115, 123, 124
Bravais lattice 118
Bravais module 427
Bremsstrahlung 293
bright field image 268
Brillouin zone 352, 394, 398, 436, 441
brittle–ductile transition 511
brittleness 508
broadening of the phonon peaks 445
bcc phases 9
building blocks 117, 145, 151
Burgers vector 257, 271, 306, 313
Burgers vector component 274

calorimeter 473
CALPHAD method 228
canonical cell tiling 212
Cantor spectrum 27
catalytic activity 526
catalytic potency factor 235
CBED 116, 122, 154, 155, 272
centrosymmetrical 86
chair tiling 51
channel center 287, 289, 290
channel wall 281, 286, 287, 302
channeled ion 282, 283, 290
channeling 155
– condition 282, 283, 288, 289
– minimum 283, 287
– profil 281, 299–303
characteristic irrational number 11
charge density 283
charge density waves 10
chemical
– decoration 146
– decorations 193
– disorder 135, 139, 201
– potential 212
– reactivity 191
– short-range ordering 476
– stability 328
chromatic aberration 124
classical theory of nucleation 234
classification scheme 41
closeness condition 480
cluster 184, 201, 204, 206, 208, 209, 211, 215, 235, 428, 479, 518
– density 186
– friction model 316
– virtual bound states 192
co-sputtering 366, 373
coating 507, 522
coherent scattering 457
coincidences 209
cold neutrons 458
column approximation 268
compensating gauge transformation 73
compositional incommensurate modulation 10
compression tests 306
conductance 379, 382
conduction electron 357
conductivity 190, 224, 322–324, 326–330, 332, 333, 340, 358, 373–375, 416, 417
configurational
– disorder 200
– entropy 139, 204, 211, 236
–– entropy of the interface 244
confined states 383
constraints 108
containerless undercooling methods 237
continued fraction 400
continued fraction expansion 425
continuous fraction development 325
continuous spectrum 334, 393
continuum potential 289
contrast
– simulation 129
– transfer function 124
– variation 87

convergent beam electron diffraction (CBED) 115, 116, 122, 154, 262
convolution 124, 125, 345
Conway's theorem 393, 395
correlation function 438
correlation length 119, 140
corrosion
– rate 523
– resistance 523
– tests 522
Coulomb gap 321, 335
coupling function 456
covering 185, 208
covering matching rules 185
$Cr_5Ni_3Si_2$ 151
crack propagation 259
critical
– angle 283–285, 297, 298
– eigenstates 393, 433
– states 526
CrNi 116, 148, 151
CrNiSi 116
cross-section 440
crystal growth 199
crystallization energy 234
crystallographic 19
crystallographic restriction 19
CTF 124, 125
cubic quasicrystal 115, 148, 152
cuboctahedral BOO 14
cuboctahedron 7
curved space 5
cut effects 103
cut method 87
cut-and-project sets 25
cut-and-projection method 50, 118
cut-and-projection scheme 209

d resonance 491
damped harmonic oscillator 440
Danzer model 382, 391
Danzer tiling 30
dart–rhombus random tiling 44
de Bruijn's grid method 61
dead surface 203, 212
Debye model 455
Debye–Waller factor 404
decagonal 3
– decagonal cluster 148, 159
– decagonal phase 213
– decagonal quasicrystal 115–117, 119, 126, 159, 225, 292, 297, 396, 406, 412, 416, 417
– decagonal structures 209
decagons 9
decahedral-recursive model 208
decapods 204
dechanneling 283, 291, 297, 298
deconvolution 302, 303
decoration 118, 140, 147, 280, 281, 298, 299
decoration rule 167
defect 42, 118, 119, 200, 204, 228, 285
defected quasilattice 264
defective icosahedral phase 14
deflation 5
deflation symmetry 255
deformation softening 310
degenerate d orbitals 489
Delone set 18
dendritic morphology 240
density 193
– functional 408
– of quasicrystalline grains 238
– of states 324–326, 330, 338, 340, 400, 401, 418, 429
destructive interference 99
detailed balance 213
diagonal order 330
diagonalization 398
diamagnetism 191, 488
dielectric constant 356
different chemical occupation 112
differential scanning calorimeter 224, 473
differential thermal analysis 224, 226
diffraction 20
– by Bragg planes 494, 497
– contrast analysis 272
– disk 272
– experiment 83, 210
– of conduction electron 498
– pattern 71, 82, 122, 123, 138, 139, 141, 154, 158, 200, 209
– peak 206, 211, 215
– rods 267
diffuse background 209

diffuse scattering 138, 140
diffusion 216
– constant 328
– equation 205
– limited aggregation 205
diffusivity 326, 327, 333
dihedral groups 78
dilatometry 227
Dirac comb 21
direct space 106
direction of the Burgers vector 271
disclination pairs 13
disclinations 13
discrete spectrum 152, 433
dislocation 251, 256, 268, 306, 327
– annihilation 315
– density 311
– energy 275–277
– in decagonal quasicrystals 271
– motion 257
– pairs 12
– slip-plane 314
disorder 199, 316, 488
disorder parameter 332
disordered condensed matter 11
dispersion 326, 342, 343
– of the bands 416
– of the phasons 11
– relation 406, 408, 413
dispersionless excitation 445
displacement 139, 288, 291
displacive incommensurate modulation 10
dissociation of dislocation 275, 277
distribution of the valence electrons 195
DLO model 207
dodecagonal 3
– quasicrystal 115, 148–152, 212, 419
– rings 149
dodecahedral local ordering model 207
dodecahedron 112, 145
dodecahedron sites 193
domain structure 10
domains 118, 128, 130, 134, 193
double differential scattering cross-section 457
double roller 229
DR model 208
drop tube 238
Drude 327, 357
DSC 224
DTA 224
dual lattice 22
dualization 59
dualization method 26, 51
ductility 525
dynamical
– contrast calculation 144
– electron scattering 118
– image 141
– matrix 397, 398, 402, 440
– scattering 132, 133, 158
– structure factor 404, 429, 440, 441
– theory 121, 123

EBSP 158
ECP 158
EELS 354–356
effective
– coupling strength 494
– medium 494
– pair potential 500
– pseudo-potential 499
– shear stress 307
eigenmodes 440
eigenstate 321, 325, 328, 329, 331, 334
eigenvalue 385
– problem 397
– spectrum 397–399, 403, 418
eigenvector 397, 440
elastic
– coefficients 442
– constant 43, 211, 459
– properties 305
– scattering 438
– scattering of electrons 370
electrical conductivity 416
electrodynamic response 357
electron 393, 408
– affinity 189
– backscattering diffraction 115
– channeling 156
– channeling pattern technique 158
– density 352

– diffraction 115, 122, 154, 155, 224, 343, 352, 355
– energy loss spectroscopy 354
– interference effects 155
– micrograph 118, 135, 136
– microscopy 126, 143, 224
– transport 322
– wavelength 124
electron-electron interaction 321, 324, 335, 375
electron-energy loss 338
electron-hole pairs 346
electron-matter interaction 121
electronic
– density of states 190, 338, 412, 414, 415
– energy distribution 338
– interband transition 357
– localization 501
– property 321, 338, 360
– specific heat 481
– specific heat data 479
– stability 328
– states 358
– structure 193, 325, 326, 338, 351, 356, 359, 408, 418
– structure of clusters 188
– transport properties 416, 514
electronically induced peak 370
elementary charge 283
elementary excitations 393, 396
embedding method 118
embedding space 118
enantiomorphism 154
endothermic effect 224
energetic conditions 186
energetically stable 200
energy
– distribution 338, 340, 342, 345
– resolution 439
– sensitive detector 283
– transfer 457
enthalpy 473
enthalpy of formation 481
entropic 215
entropic contribution 200
entropic stabilization 228, 480, 482
entropically stabilized structures 184
entropy 42, 139, 201, 212, 216, 228, 473
– of formation 475
– of mixing 477
equation of motion 424
equilibrium 213, 214
equilibrium random tilings 216
equipotential line 289, 290
Euclidean space 5
Euler function 74
eutectic reaction 223
eutectoid reaction 223
evaporation 365
Ewald sphere 153
exothermic effect 224
expansion 464
experimental activation volume 308
extended eigenstates 393, 416
extended modes 403
extended states 345, 349
extinction condition for dislocations 271
extinction rules 81, 94
extra 474

F-type quasicrystal 141, 144, 147
F2-phase 141, 143
face centered 94
fat rhombus 5
Fermi
– energy 324, 326, 328, 479
– level 323, 326, 328, 340, 351
– sphere 353
– surface 323, 352, 418, 479
Fibonacci 134, 160, 325, 330, 333
– chain 25, 50, 55, 253, 427
– number 55, 397
– quasilattice 415
– sequence 55, 203
fine structure 466
finite-size effects 400
five-fold symmetry 5
flash-evaporation 366
flip motion 253
flux peak 286
flux quantum 381
flux-density distribution 286, 302
force constants 402
form factor 84
formation of the qc phase 462

Fourier
– filtering method 159
– module 5, 69
– spectrum 394
– transform 22, 121, 122, 125, 138
fracture and failure 305
Frank's rule 276
Frank–Kasper phases 7, 12, 233, 479
Frank–Kasper type of i-structure 463
Fraunhofer diffraction function 121, 122
free
– atomic clusters 187
– carrier density 358
– electron states 418
– electrons 489
– energy 307
friction
– and wear 525
– coefficient 525
– experiments 526
– force 307
Friedel oscillations 500
Friedel wavelength 372
Friedel–Anderson model 489
fundamental reflections 98

GaCoCu 116
GaCuFeSi 116
GaMgZn 117
GaNiSiV 116
gap 325, 441
– in the spectrum 416
– labeling theorem 325
– opening 449
– openings 449
gas-solid reaction 151
Gaussian distribution 138, 288
generalized
– Cherns–Preston rule 273
– Penrose tilings 41
– symmetry 31
– vibrational density of states (GVDOS) 458
geometrical constraints 10
geometrical models 184
Gibbs
– energy 473
– energy of mixing 476
– equation 307
– free energy 234, 308
– phase rule 222
– triangle 222
glass model 118
golden mean 6, 50, 57, 134, 206, 325, 397
golden ratio 56
grain boundary 159
Green function 400, 401
grid method 51, 61
growth 199, 204
– algorithm 151, 199, 212, 215
– instability 213
– mechanism 210
– model 201, 205, 206, 208, 209, 212, 213
– of icosahedral quasicrystals 189
– of isolated icosahedral particles 513
– rule 204

H-phase 150
Hamiltonian 325, 331, 333, 398, 409, 494
Hamiltonian matrix 397, 401
hardness 523, 529
harmonic approximation 402, 423, 466
harmonic phonon process 440
Harper equation 387
heat capacity 474
heat insulation 516
Henley–Elser decoration 396
heterogeneous nucleation 235
hexatic phase 13
hierarchical clusters 510
hierarchical order 430
high-resolution transmission electron microscopy 115, 121, 224
high-temperature phase 9
high-temperature plastic deformation 275
homogeneous nucleation 235
homogenization 229
Hooke's law 308
hopping 324–327, 330, 333, 334
HRTEM image 123–131, 133, 137–140, 142–144, 149–151, 159
HRTEM micrograph 118
Hume–Rothery 352, 370, 411, 418, 493

- alloys 479, 498
- pseudo-gap 488
- stabilization 501
- stabilization mechanism 412
hybridization 328, 348–350, 352, 354, 411
hydrogen atom density 529
hypercubic
- Bravais lattice 94
- lattice 59, 135
- reciprocal lattices 94
hyperlattice 257, 263
hyperplane 135, 136
hyperspace 396, 481
hypersurface 135, 136, 301

IC composites 70
icosahedral 3
- Al-Pd-Re 373
- axes 295
- bond orientational order 12
- building units 12
- cluster 11, 140, 145–147, 227, 328, 476
- configuration 6
- glass 13, 210, 211
- glass model 118, 119
- groups 76
- lattice 395
- order 352
- phase in condensed matter 14
- point-group 115
- quasicrystal 207, 209, 395, 405
- short-range order 233
- SRO in undercooled melts 233
- structures 209
- subunits 11
- symmetry 29, 115, 139, 141, 157
icosahedratic phase 13
ideal
- crystals 200
- glass temperature 243
- quasicrystal 117, 118
- solution model 475
IDOS 325
image
- contrast 124, 125, 134, 135, 141, 149, 155, 159, 268
- formation 121, 122, 268
- simulation 123, 125, 134
incident electron energy 355
incommensurable modulation 10, 11
incommensurate 70
- lattice spacings 269
- phases 9
independent electron scheme 321
indexing of the diffraction pattern 94
inelastic nuclear scattering 456
inflation 5, 57, 61, 193, 194
inflation rule 9, 50, 52, 60
inflation–deflation symmetry 39, 254
infra-red
- catastrophe 346
- conductivity 359
- property 357
integrated density of states 325, 429
intensity-normalization scheme 354
interaction
- of dislocations 275
- potential 83
- range 83
interatomic
- pair potentials 403
- potential 207, 402
- short distances 108
interdiffusion 149, 230
interfacial energy 234, 242
interference pattern 122
intermetallic compounds 472
internal
- coordinate 73
- space 74
- stresses 307
interplanar distance 285, 295, 297
intraband transition 357
intrinsic
- defect 291
- disorder 119, 193
- linewidth 444
inverse Matthiessen rule 369, 374, 376
ion channeling 280, 281, 286, 288, 294, 303
ion incidence 283, 286–288, 291–294, 301
ion trajectory 282
isomorphic substitution 87
isopleth 222, 225–227, 229

isotropy of the longitudinal and transverse acoustic branch 448
itinerant electron 328, 329

jellium model 187
Johnson–Mehl–Avrami 477
Jones zone diameter 370

Kikuchi band 153
Kikuchi line 115, 152, 153, 158, 159
kinematic approximation 264
kinematic factor 293
kinematical diffraction 268
kinematical theory 121
kinetically stabilized 478
kinetics 511
Klotz construction 59
Knudsen cell 476
Kondo temperature 492
Kossel cone 153
Kramers–Kronig 356, 358
Kubo–Greenwood 326, 328–331

Landau
– band 385
– diamagnetism 488
– gauge 381
Landauer formula 380
large-angle collision 283, 293
latent heats 474
lattice 19
– gas 210
– part of the specific heat 460
– vibration 284, 473
Laue zone 153, 154
Laves phases 479
Lennard–Jones potential 205
level order 188
levitation techniques 237
LI class 31, 32, 51, 58, 63
light microscopy 224
limit translation module 36
Lindhard theory 281, 290
line glide resistance 307
linear
– muffin-tin orbitals 408
– phason field 265
– phason strain 126, 136
– phason strain field 263, 268
– response 380
– response theory 328
lineshapes 439
liquid 502
– state 226, 227
– state reaction 229
liquidus
– groove 223, 226
– projection 221, 225, 226, 229
– surface 223, 227, 229, 230
LMTO calculations 492, 499
LMTO method 408
local
– atomic environment 488
– derivability 35
– disorder 118
– environment 489
– equivalence 35
– growth algorithm 201
– indistinguishability 31
– indistinguishability class 51
– isomorphism 31
– isomorphism class 51
– magnetic moment 487, 491
– order 322, 348
– structure 5, 501
– symmetry 493
– topological order 341
localization 321, 324–326, 328, 333–335, 354, 357, 358, 371, 403
localization of optic modes 446
localized
– eigenstates 393
– magnetic moments 488
– modes 403, 441
– moment 493
– states 190, 416
London forces 524
long-range
– bond orientational order 5
– diffusion 126
– icosahedral BOO 14
– order 13, 139, 323, 456, 500
longitudinal modes 407
low
– energy electron diffraction 158
– energy modes (LEM) 460
– surface tension 527

– temperature state 130
lower yield point 309

Mackay
– cluster 145
– icosahedra 108, 463
– icosahedron 7, 186
– type clusters 316
magic
– clusters 188
– number 187, 190
– number of electrons 509
magnetic
– field 375
– impurity 497, 498
– Mn sites 502
– moments 418, 493
– recording heads 514
– scattering 438
– susceptibility 224
magnetic/non-magnetic transition 502
magnetoconductance 380, 391
magnitude of the strain fields 272
mapping 327
matching rule 5, 9, 40, 51, 63, 184, 200, 201, 204, 212
matching rule violations 11, 270, 316
Mathematica 49, 51
Matthiessen rule 322, 327
maximizing the density 185
maximum flow stress 310
maximum undercoolability 237
mean
– expansion 467
– free time 327
– velocity 326
mechanical brittleness 191
mechanical grinding 513, 526
medium-range atomic order 503
melt quenching 229
melt spinning 119, 229
mesoscopic homogeneity 325
metal cluster formation 11
metal insulator transition 321, 324, 326, 328, 330, 373
metallic amorphous systems 11
metallic glass 461
metallurgy 116
metastable 460
metric tensor 77
MgAl 116
MgREZn 117
MgSEZn 117
Miller indices 9
minimal embedding 28
minimum yield 284, 285, 291, 298, 299
MIT 327
mixing enthalpy 476
MLD class 35, 38
mobility of dislocations 275
modulated crystal phases 424
modulated crystals 70
modulated spring model 425
modulation 141, 142, 333
modulus of the partial structure factors 94
Moilière's screening function 284
Moilière-potential 288
molar heat 473
molecular dynamics simulations 258
momentum transfer 457
monograin sample 103
Monte Carlo 205, 210, 213
Monte Carlo simulation 286, 290, 297, 302
most localized basis 409
muffin-tin orbitals 408
multi-slice technique 123, 132
multifractal states 327
multiphonons 458

nano-quasicrystalline 460
nanosized quasicrystals 529
narrow pseudo-gap 488
nearest-neighbor configurations 185
nearly free
– electron 411, 510, 518
– electron like 493
– electron states 511
negative enthalpy of formation 474
negentropic model 236, 244
neutron
– diffraction 139, 145
– inelastic scattering 438, 457
– scattering 83, 406
–– cross-section 438

-- length 84
$Ni_{16}V_6Si_7$ 152
NiTiZr 117
NiV 148, 151
NiVSi 148
non-ballistic propagation 326
non-channeled ion 285
non-crystallographic symmetries 19
non-equilibrium process 213
non-locality 201, 204
non-magnetic impurity 497, 498
non-magnetic Mn sites 502
non-periodic functions 4
non-periodic tiling 5
nuclear charge 283
nuclear scattering 438
nucleation 199, 208, 235
- of a solid 234
- site 235
nucleus 235
number density 285, 295, 298
number of confined electrons 195
numerical techniques 396

object transmission function 121
obstacles to the dislocation motion 316
obtuse rhombohedron 9
occupation density 291, 297
octagonal 3
- quasicrystal 115, 151
- tiling 59, 253, 256
octogonal tiling 325
one-dimensional quasilattice 263
one-electron approximation 343, 345
one-phonon coherent inelastic scattering law 440
one-phonon cross-section 441
optic modes 449
optic-like phonons 441
optical
- conductivity 357–359, 515
- modes 407
- spectroscopy 356
orientation diagram 292, 297–299
orientation-sensitive interaction 14
orientational order 115, 201
orientational symmetry 215
Orowan relation 306
orthogonal space 252
orthogonal subspaces 88
orthorhombic approximant 129
oscillatory motion 281
OSDS growth algorithm 204
OSDS rule 201
overlap between orbitals 492
overlapping clusters 193
overlapping rules 185
oxidation resistance 521
oxide layer 524
oxygen diffusion 522

P-type quasicrystal 141, 143
packing of clusters 479
packing of hard or soft spheres 6
pair
- correlation function 86
- interactions 501
- potential 168
parallel orientation 132, 134, 155
parallel space 88, 135
partial
- d DOS 493
- Debye–Waller coefficients 440
- density of states 458
- structure factor 100
participation ratio 403, 416
patents 508
Patterson
- analysis 97
- function 21, 86
- map 145
Pauli paramagnetism 488
Peierls mechanism 315
penetration depth 282, 286
Penrose rhombs 63
Penrose tiling 24, 51, 62, 63, 117, 130, 135–137, 139, 201, 207, 208, 212, 325, 342, 427
pentagonal
- cluster 134
- dodecahedron 7
- lines 206
- tiling 206
pentagrid 62
perfect
- and partial dislocations 274
- icosahedral crystals 510

– icosahedral phase 14
– matching rule 40, 51, 201, 208
– quasicrystal 200
periodic 19
– approximant 231, 321, 325, 328, 335, 397
– image in a higher-dimensional space 88
– lattices 5
periodicity 118
peritectic reaction 223, 226, 229
perpendicular space 58, 74, 88, 97, 135–138, 140
PES 338–340, 342
phase 86
– diagram 116, 119, 120, 472, 481
– difference 94
– information 10
– reconstruction 98
– transformation 223, 231, 268
– transition 12, 78, 519
phason 11, 59, 211, 228, 251, 291, 298, 303, 313, 327, 426, 459, 480
– defect 119, 139, 142, 144, 184, 193, 274, 275, 474
– disorder 138, 139, 208, 317
– energy 276
– flip 138, 139, 254, 255, 257, 297, 298
– flipping 480
– fluctuation 205, 206, 210, 213, 216
– instability 213
– jump 58
– movement 147
– shift 252, 253
– strain 205, 210, 214, 270, 314, 460
– strain field 271
– strain matrices 267
– unlocking transition 481
– wall 256, 257
phonon 393, 402
– components 313
– creation or annihilation 440
– density of states (PDOS) 440, 455
– in decagonal quasicrystal 406
– in icosahedral quasicrystal 405
– strain 270
– strain field 271
photoelectron 115, 157, 158, 338, 339, 342
– intensity 157
– spectroscopy 157, 339, 414
photoemission 338–340, 342
photoemission spectrum 415, 417
physical
– properties 183, 394
– reciprocal space 265
– space 58, 72, 74, 88, 263
PIXE 291, 293, 294, 297, 300–303
planar channeling 283–285, 287, 290
plastic
– deformation 258
– ductility 257
– flow 306
– properties 305
point
– group 71, 399
–– symbol 74
–– symmetry 116
– spectrum 393
– symmetry 3, 31, 115, 116, 154, 156
Poisson summation formula 22
polarization 407
polyhedral cluster 148
polytetrahedral SRO 233
porosity 522
positional order 118
potential contour 290
potential parameters 410
powder diffraction 116
power spectrum 134
precipitates 527
primary crystallization 226
primary formation 229
primitive 94
projected density of states 400, 401
projection 92, 206
– direction 129, 130, 134, 139–142
– method 25, 50
– scheme 59, 63
propagating modes 443
propagation of heat 517
pseudo-Brillouin zone 430, 441, 479, 493
– boundaries 449
– concept 446

pseudo-forbidden rotational symmetries 508
pseudo-gap 326, 333, 342, 343, 348, 351, 353–355, 358, 359, 372, 373, 375, 376, 411, 413–415, 418, 431, 493, 495, 498, 508
pseudo-localized character 430
pseudo-Mackay cluster 112, 145–147, 156–158
Pseudo-Mackay Icosahedra (PMI) 191
pseudo-potential 499
pseudobinary intersection 221, 222
pseudodecagonal
– approximant 120
– axis 134
– direction 130
puzzle 63, 200

QIE 324
quantum
– diffusion 330
– dynamic 330
– interference effect 324, 488
– well 351
quasi-Brillouin zone 394, 395, 411, 418
quasi-Brillouin zone boundaries 406
quasibinary intersection 222
quasicontainerless methods 238
quasicrystal 70
– formation 208
– growth 199, 215
– surfaces 195
quasicrystalline approximant 399
quasicrystalline order 359
quasilattice 118
quasiparticle 438
quasiperiodic 69, 423
– function 4, 71
– order 199, 321, 322, 334
– tiling 50, 117, 200, 201, 205, 211
quasiperiodicity 25
quaternary system 222

R-phase 140
radial distribution function 11
radiation damage 280
random
– growth model 201
– packing 201, 209
– tiling 42, 49, 118, 119, 135, 138, 150, 151, 201, 205, 211, 215, 481
– tiling hypotheses 44
randomness 136, 330, 331, 333
range of the icosahedral BOO 13
rank of the Fourier module 5
rank of the module 69
rapid
– quench 462
– quenching 126, 127, 151, 152, 221, 237
– solidification 152
rational approximant 397, 463
RBS 282, 289, 291–293, 297, 299, 300
reaction scheme 223
reciprocal
– hyperlattice points 265
– lattice 69, 72, 85, 264, 265, 395
– quasilattice 394
– space 106, 394
reconstruction 512, 518
rectangle–triangle random tiling 213
rectangle–triangle tiling 419
recurrence property 330
recurrence relation 399
recurrent localization 511
–– effects 510
–– model 518
recurrently localized states 195
recursion method 329, 330, 399, 410
reduction of heterogeneous nucleation 237
refinement method 129, 140
regular grid 61
regular patterns 33
reinforcing particles 528
relaxation time 326, 416
residual factor 107
resistivity 224, 323, 324, 327, 338, 351, 352, 360
resolution function 439, 459
resonant-like scattering 371
rhombic triacontahedra 9
rhombic triacontrahedron 7
rhombicosidodecahedral building blocks 12
rigid band approximation 498
rigid band model 491

RKKY interaction 488
Robinson tiling 36
rocking movement 158
root lattices 28
rotation-symmetric function 138
rotational invariant order parameters 14
rule of reversibility 286
Rutherford backscattering 282, 302

S-MLD class 38
SAED 115, 123, 126, 128, 130–132, 134, 138, 139, 141, 142, 148, 149, 151–154, 158, 224
sample size 439
satellite reflection 123
satellites 10
scaling 141, 321, 325–329, 334, 335
scanning electron microscope 158
scanning tunneling microscopy 115, 159, 224
scattering law 439
scattering strength 297
Scheil reaction scheme 223
Scherzer condition 125, 141, 142
Schmid factor 306
screening 409
screening length 288
secondary electron imaging 115, 155
segregation 229
SEI 155–157
selected area electron diffraction 115
selection rule 441
self-consistent Hartree–Fock equation 498
self-correlation function 440
self-similar 5, 190
– character 425
– packing of building blocks 191
– tiling 51
self-similarity 194, 393
semi-classical approximation 328
shape of the AO 99
shear stress 306
shift of the GVDOS 468
short-range order 227, 456
simpleton flip 253–255
single quasicrystals 103
single-scattering cluster calculation 158
singular continuous spectrum 393, 415, 433
singular patterns 33
sintering 529
skinny rhombus 5
sliding mode 427
slip system 306, 313
slip velocity 306
slow kinetics 512
small oscillations 423
small-angle collision 281
smooth GVDOS 462
Socolar–Steinhardt tiling 30
soft mode 426
soft X-ray spectroscopy 414
solar light energy 515
solid–liquid interfacial energy 235
solid-state reaction 149
solidification in free fall 238
solidus area 229
soliton-like domain walls 10
sound velocities 442, 451
sp-d
– coupling 494
– hybridization 493, 499
– interaction 489
space group 73, 399
space group symmetry 71
sparse matrix 399
specific heat 473
spectral function 401
spectral property 325
spherical aberration 123–125
spherical model 105, 107
spike 342
spiky structure 414, 418
spin glass 488
spin order 488
splatcooling 239
spot shifts 267
square–triangle random tiling 212
square–triangle tiling 28, 150, 213
SSC 158
SSDS 209
stability 188, 370, 411, 472
– of atomic clusters 187

– of quasicrystals 200, 478, 510
stabilization 42, 227, 478
stable in the thermodynamic sense 478
stacking disorder 137
stacking randomness 137
standard functions 473
star short-distance scheme 209
stationary modes 406
stationary states 416, 418
steady-state nucleation rate 235
steering force 281, 297
stereo analysis 313
stereographic projection 158
STM image 156, 159, 160
storage of hydrogen 529
strain 306
– accommodation parameter (SAP) 274, 277, 313
– energy ratio 276
– rate 306
streaks 10
stress 306
stress-relaxation 308
stress-transient dip tests 311
strip projection 57
strong extinction condition (SEC) 270
structural
– effects on nucleation 243
– energy 501
– models 396
– phase transition 10
structure
– and stability of quasicrystals 183
– constants 410
– determination 169
– factor 80, 84, 499
– of amorphous metal 14
– refinement 172
sub-ballistic regime 326
subdirect product 74
substitution
– matrix 56
– rule 55
– sequence 50, 56
supercluster 190
supercooled liquid metals 13
supercooling 229, 230
superspace 5
superspace group 74
superstructural ordering 105
superstructure 96, 130–132, 134, 137, 138, 141, 142, 227, 231
superstructure reflections 96, 98
surface 202, 204, 207, 208, 213, 216, 518
– annealing 213
– defects 522
– energy 523
– layer 115, 155, 157, 285, 291, 341
– oxide 341, 342
– peak 283
– phonons 442
– reconstruction 195
surface-barrier detector 291
surface-induced phonons 434
symmetry
– analysis 34
– axes 141, 158
– element 115, 116, 152, 154, 157
symmetry-breaking phase transition 78
synchrotron radiation 456
synchrotron radiation diffraction 134

T-phase 28, 116, 294, 295, 299–301, 407
Tübingen triangle tiling 37, 254, 258
TaTe 117, 148–151, 419
$TaTe_2$ 149
TB-LMTO method 410
TDOS 326, 332, 333
tears 206, 210, 213
TEM 115
temperature dependence 466
temperature sensors 514
temperature–time transformation diagram 238
tensile yield strength 528
tension 306
terminator 400
ternary
– alloy system 221
– peritectic reaction 223, 225, 231
– phase diagram 126, 221, 229
– quasi-peritectic 223

– quasicrystal 221
– reaction 223
terrace 159, 160, 519
tetragonal structure 12
tetrahedra 9
tetrahedral SRO 236
tetrahedron 222
texture 126, 158, 159
theory 477
thermal
– activation 513
– expansion 224, 492
– neutrons 457
thermally activated dislocation motion 315
thermodynamic functions 473
thermopower 372, 373, 375, 377
thin films 369, 370, 376
Thomas–Fermi screening 284
Thomson scattering 84
three-axis spectrometer 437, 439
Thue–Morse sequence 56
tie line 222, 229
tight-binding 380
– Hamiltonian 409
– model 325, 330
tile 118, 119, 127, 128, 137, 138, 150
tiling 5, 396
– decoration 167
– of canonical cells 173
– towers 41
time-of-flight 458
timely averaged confinement 195
topologically inequivalent sites 411
torus parametrization 32
total dislocation energy 277
total wetting 524
transfer matrix 500
transformation enthalpy 477
transition element 512
translational parts 75
transmission
– cross-coefficient 125
– electron microscope 121, 123, 124, 139, 158
– electron microscopy 115, 116, 122, 224
– photoabsorption 354
transport properties 416, 418
transverse modes 407
triacontahedron 108
tridiagonalization 399
truncated icosahedron 7
truncation effects 103
twined crystal 209
twined crystalline structures 206
two kinds of long-range order 13
two-beam condition (TBC) 268
two-dimensional clusters 196

ultrasonic attenuation 442
undercoolability 241
undercoolability of melts 234
undercooled liquid 12
unit cell 85
universality class 322
unlocalized states 190
upper yield point 309
UPS 339, 342

vacancy 200
van Hove singularities 414
van Hove singularity 455
vapor deposition 512
velocity-velocity correlation 327
vertex 135, 137
vertex distribution 136
vibrational
– density of states (VDOS) 405, 407, 454
– eigenmodes 403
– Green function 404
– spectral function 405
– spectrum 403
virtual bound state 328, 493, 497
virtual bound state model 489, 491
virtual image 123
viscosity 243
VNiSi 116
Vogel–Fulcher–Tammann ansatz 236
volume of the AO 99

wave-packet dynamic 329
wavenumber space 395
weak
– disorder 329
– extinction condition (WEC) 270

– localization 359, 360
– phase object approximation 124
wetting 523, 524
width of the spectrum 429
width of the transverse mode 448
Wigner–Seitz area 285
window 26, 58
worm 203
WPOA 124
Wyckoff positions 80

X-ray 115, 116
– diffraction 139, 140, 145, 156, 224
– emission 282, 291, 327, 338, 343
– excitation 287
– fluorescence radiation 457
– investigation 119
– photoabsorption 338
– photoabsorption spectroscopy 344
– photoelectron diffraction 157
– photoelectron scattering 157
– photoelectron spectroscopy 157, 339
XAS 345, 346, 350, 351, 353, 355, 356
XES 343–348, 350, 351, 353, 358
XPD 157
XPS 339, 342, 345–347, 353, 355–357

yield strength 529
yield strength and hardness 527
yield stress 525

zone axis 141
Zr_4Al_3 150
$ZrAl_3$ 150

Springer Series in

MATERIALS SCIENCE

Editors: R. Hull R. M. Osgood, Jr. J. Parisi A. Zunger

1 **Chemical Processing with Lasers***
By D. Bäuerle

2 **Laser-Beam Interactions with Materials**
Physical Principles and Applications
By M. von Allmen and A. Blatter
2nd Edition

3 **Laser Processing of Thin Films and Microstructures**
Oxidation, Deposition and Etching of Insulators
By. I. W. Boyd

4 **Microclusters**
Editors: S. Sugano, Y. Nishina, and S. Ohnishi

5 **Graphite Fibers and Filaments**
By M. S. Dresselhaus, G. Dresselhaus, K. Sugihara, I. L. Spain, and H. A. Goldberg

6 **Elemental and Molecular Clusters**
Editors: G. Benedek, T. P. Martin, and G. Pacchioni

7 **Molecular Beam Epitaxy**
Fundamentals and Current Status
By M. A. Herman and H. Sitter 2nd Edition

8 **Physical Chemistry of, in and on Silicon**
By G. F. Cerofolini and L. Meda

9 **Tritium and Helium-3 in Metals**
By R. Lässer

10 **Computer Simulation of Ion-Solid Interactions**
By W. Eckstein

11 **Mechanisms of High Temperature Superconductivity**
Editors: H. Kamimura and A. Oshiyama

12 **Dislocation Dynamics and Plasticity**
By T. Suzuki, S. Takeuchi, and H. Yoshinaga

13 **Semiconductor Silicon**
Materials Science and Technology
Editors: G. Harbeke and M. J. Schulz

14 **Graphite Intercalation Compounds I**
Structure and Dynamics
Editors: H. Zabel and S. A. Solin

15 **Crystal Chemistry of High-T_c Superconducting Copper Oxides**
By B. Raveau, C. Michel, M. Hervieu, and D. Groult

16 **Hydrogen in Semiconductors**
By S. J. Pearton, M. Stavola, and J. W. Corbett

17 **Ordering at Surfaces and Interfaces**
Editors: A. Yoshimori, T. Shinjo, and H. Watanabe

18 **Graphite Intercalation Compounds II**
Editors: S. A. Solin and H. Zabel

19 **Laser-Assisted Microtechnology**
By S. M. Metev and V. P. Veiko
2nd Edition

20 **Microcluster Physics**
By S. Sugano and H. Koizumi
2nd Edition

21 **The Metal-Hydrogen System**
By Y. Fukai

22 **Ion Implantation in Diamond, Graphite and Related Materials**
By M. S. Dresselhaus and R. Kalish

23 **The Real Structure of High-T_c Superconductors**
Editor: V. Sh. Shekhtman

24 **Metal Impurities in Silicon-Device Fabrication**
By K. Graff 2nd Edition

25 **Optical Properties of Metal Clusters**
By U. Kreibig and M. Vollmer

26 **Gas Source Molecular Beam Epitaxy**
Growth and Properties of Phosphorus Containing III–V Heterostructures
By M. B. Panish and H. Temkin

27 **Physics of New Materials**
Editor: F. E. Fujita 2nd Edition

28 **Laser Ablation**
Principles and Applications
Editor: J. C. Miller

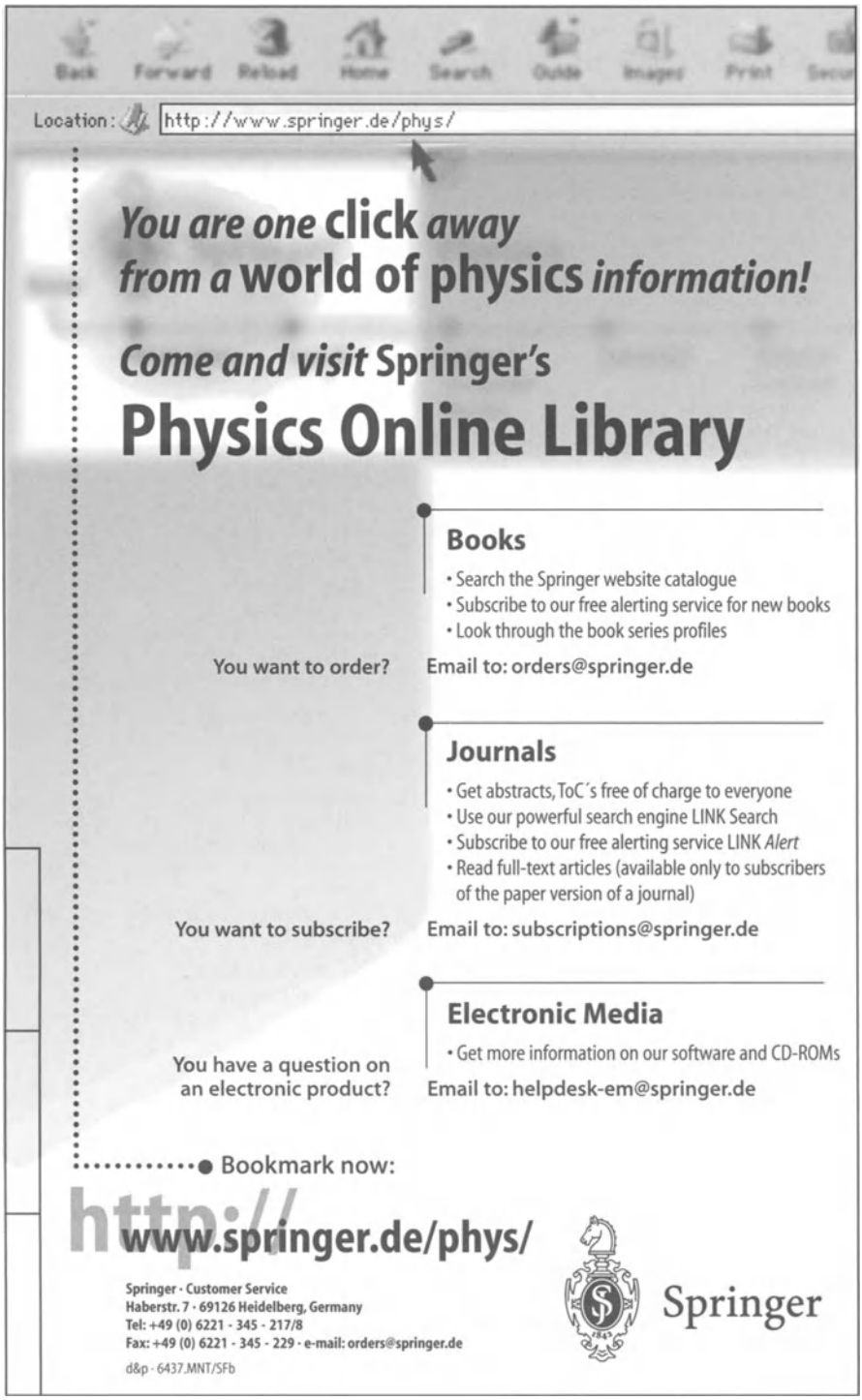
Back
Forward
Reload
Home
Search
Guide
Images
Print
Location:
http://www.springer.de/phys/
You are one click away
from a world of physics information!
Come and visit Springer's
Physics Online Library
Books
• Search the Springer website catalogue
• Subscribe to our free alerting service for new books
• Look through the book series profiles
You want to order?
Email to: orders@springer.de
Journals
• Get abstracts, ToC´s free of charge to everyone
• Use our powerful search engine LINK Search
• Subscribe to our free alerting service LINK Alert
• Read full-text articles (available only to subscribers of the paper version of a journal)
You want to subscribe?
Email to: subscriptions@springer.de
Electronic Media
• Get more information on our software and CD-ROMs
You have a question on an electronic product?
Email to: helpdesk-em@springer.de
Bookmark now:
http://www.springer.de/phys/
Springer · Customer Service
Haberstr. 7 · 69126 Heidelberg, Germany
Tel: +49 (0) 6221 - 345 - 217/8
Fax: +49 (0) 6221 - 345 - 229 · e-mail: orders@springer.de
d&p · 6437.MNT/SFb
Springer

Springer Series in

MATERIALS SCIENCE

Editors: R. Hull R. M. Osgood, Jr. J. Parisi A. Zunger

29 **Elements of Rapid Solidification**
Fundamentals and Applications
Editor: M. A. Otooni

30 **Process Technology for Semiconductor Lasers**
Crystal Growth and Microprocesses
By K. Iga and S. Kinoshita

31 **Nanostructures and Quantum Effects**
By H. Sakaki and H. Noge

32 **Nitride Semiconductors and Devices**
By H. Morkoç

33 **Supercarbon**
Synthesis, Properties and Applications
Editors: S. Yoshimura and R. P. H. Chang

34 **Computational Materials Design**
Editor: T. Saito

35 **Macromolecular Science and Engineering**
New Aspects
Editor: Y. Tanabe

36 **Ceramics**
Mechanical Properties, Failure Behaviour, Materials Selection
By D. Munz and T. Fett

37 **Technology and Applications of Amorphous Silicon**
Editor: R. A. Street

38 **Fullerene Polymers and Fullerene Polymer Composites**
Editors: P. C. Eklund and A. M. Rao

39 **Semiconducting Silicides**
Editor: V. E. Borisenko

40 **Reference Materials in Analytical Chemistry**
A Guide for Selection and Use
Editor: A. Zschunke

41 **Organic Electronic Materials**
Conjugated Polymers and Low Molecular Weight Organic Solids
Editors: R. Farchioni and G. Grosso

42 **Raman Scattering in Materials Science**
Editors: W. H. Weber and R. Merlin

43 **The Atomistic Nature of Crystal Growth**
By B. Mutaftschiev

44 **Thermodynamic Basis of Crystal Growth**
P–T–X Phase Equilibrium and Non-Stoichiometry
By J. Greenberg

45 **Thermoelectrics**
Basic Principles and New Materials Developments
By G. S. Nolas, J. Sharp, and H. J. Goldsmid

46 **Fundamental Aspects of Silicon Oxidation**
Editor: Y. J. Chabal

47 **Disorder and Order in Strongly Nonstoichiometric Compounds**
Transition Metal Carbides, Nitrides and Oxides
By A. I. Gusev, A. A. Rempel, and A. J. Magerl

48 **The Glass Transition**
Relaxation Dynamics in Liquids and Disordered Materials
By E. Donth

49 **Alkali Halides**
A Handbook of Physical Properties
By D. B. Sirdeshmukh, L. Sirdeshmukh, and K. G. Subhadra

50 **High-Resolution Imaging and Spectrometry of Materials**
Editors: F. Ernst and M. Rühle